Transactions of the ASME

The Journal of Engineering for Power (ISSN 0022-
25) is published quarterly for $72 per year by The
erican Society of Mechanical Engineers, 345 East
47th Street, New York, NY 10017. Second class
postage paid at New York, NY and additional
mailing offices. POSTMASTER: Send address
nge to The Journal of Engineering for Power, c/o
The AMERICAN SOCIETY OF MECHANICAL
NGINEERS, P.O. Box 3199, Grand Central Station,
New York, NY 10163.
ANGES OF ADDRESS must be received at Society
headquarters seven weeks before they are to be
effective. Please send old label and new address.
PRICES: To members, $36.00, annually; to
nonmembers, $90.00. Single copies, $24.00 each.
Add $6.00 for postage to countries outside the
United States and Canada.

INDEXED by the Engineering Index, Inc.

Journal of Engineering for Power

Published Quarterly by The American Society of Mechanical Engineers

VOLUME 105 • NUMBER 4 • OCTOBER 1983

TECHNICAL PAPERS

(Contents Continued on pg. 741)

(Contents Continued)

Status of Design Code Work in Germany Concerning Materials and Structural Aspects for the Heat Exchanger Components of Advanced HTR's

F. Schubert
Nuclear Research Center Juelich,
Institute for Reactor Materials,
D-5170 Juelich, West Germany

H. J. Seehafer
GHT/INTERATOM GmbH,
D-5060 Bensberg, West Germany

E. Bodmann
Hochtemperatur-Reaktorbau GmbH,
D-6800 Mannheim, West Germany

A brief status report on the work concerning design codes for HTR components with service temperatures above 800°C is given. The evaluation of experimental test work and preliminary time-dependent design data are reviewed and some design analyses for an IHX concerning fatigue, creep buckling, and creep ratcheting are described as a basis for critical discussion of some features of ASME Code Case N 47.

1 Introduction

The helium-gas-cooled, high-temperature reactor (HTR) is under intensive research and development in the Federal Republic of Germany [1]. Beside the generation of electricity, the potential of this reactor system is for the supply of nuclear process heat. In utilization of nuclear heat for a steam reforming process, or via an intermediate heat exchanger (IHX) for coal gasification, primary helium temperatures up to about 950°C are necessary.

For these high temperatures, from the nuclear engineering point of view, no design code is available but experience in stress analysis of nuclear power plant components for elevated service temperatures are documented in the ASME Code Case N 47 [2]. In this code case, the problems of time-dependent material properties are taken into consideration. Would it not then be logical to take this design code and to expand it by a supplement of data for the required materials? This type of extrapolation, however, can only be partially successful. This is not only because the candidate materials have not yet been adopted in nuclear specifications, but also because the materials response to the expected operating conditions proves to be somewhat different at these high temperatures. Beside the lack of materials data at temperatures above 800°C, the creep behavior must be considered even in short term loading and the possibility of environmental effects has to be considered.

In addition to these materials aspects, typical features of advanced HTR systems, characterized by the low pressure differences during normal operation, the small transients and the gas-dependent heat transfer, must be taken into account.

This situation requires the establishment of a basis for a nuclear design code. The object of the research project is to compile the basis for a "design by rule" and "design by analysis." Open questions—both scientific and technological—are to be defined and possible solutions derived in the course of this work. The task can only be achieved through the sponsorship of the Federal Ministry of Internal Affairs, the Federal Ministry of Research and Technology, and the State of North-Rhine-Westfalia, as well as the close cooperation between scientific institutions, licensing authorities, and in particular, the industrial partners involved in the HTR development. It must also be emphasized that not only designers, strength analysis experts, and material scientists are involved in this work, but also representatives of the licensing institutions.

The German project work on advanced HTR systems for the evaluation of materials data for commercial alloys at temperatures above 800°C has reached a status which allows preliminary design values and methods to be considered. This deals with the problems resulting from design and stress analysis of an intermediate heat exchanger. Before going into detail, the status of the work can be summarized as follows:

Physical properties: Sufficiently known for the design.

Mechanical properties: Creep data for the constructional materials, such as Hastelloy X and Inconel 617, (in this paper the trade names of the alloys are used) are available and extrapolation for times in excess of 50,000 hrs is allowable. Preliminary design curves for low cycle fatigue can be derived. Calculation of service time accumulation is possible. Short-term properties after simulated service exposure have been determined.

Safety margins and constitutive equations: Work in this area has been intensified during the last two years.

Inelastic stress analysis and simplified methods: Progress in this field depends on progress in the development of constitutive equations.

Contributed by the Nuclear Engineering Division and presented at the 1982 Joint Power Generation Conference, Denver, Colorado, October 17–21, 1982. Manuscript received at ASME Headquarters July 14, 1982. Paper No. 82-JPGC/NE-1.

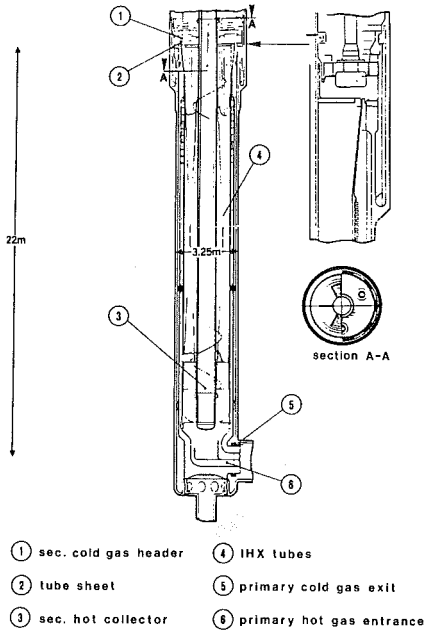

Fig. 1 Intermediate heat exchanger (helix type)

Table 1 Basic nominal values and representative dimensions

Nominal primary coolant inlet temperature	°C	950
Nominal secondary coolant outlet temperature	°C	900
Nominal pressure difference at normal operating condition	bar	2
Pressure difference at pressure loss accident of emergency condition	bar	40
Desired service life time	h	140 000
Temperature transients at normal operating condition	K/min	±2
Maximum temperature transients	K/min	−10
Heat exchanging tubes:		
Diameter	(mm)	20
Wall thickness	(mm)	2
Hot He-Header:		
Diameter	(mm)	1.080
Wall thickness	(mm)	100

2 Operational Conditions and Constructional Features

2.1 Loading Conditions. Two types of intermediate heat exchanger (IHX) are under construction for the PNP plant. These are the helical (Fig. 1) and the U-tube type. Considering the characteristic features of the structural components (pressure retaining function, barrier of primary circuit, and operation at a high temperature level), examples of critical parts are the secondary hot helium header and the heat exchanging tubes. A brief survey of nominal loading values envisaged for normal, upset, and emergency conditions is given in Table 1.

In addition, temperature and pressure rise due to hot streams, fluctuation effects, and control uncertainties have also been considered by the design calculations.

2.2 Structual Failure Modes. Calculations of highly loaded parts have been performed in order to protect against following failure modes:

- Fracture from short term loadings
- Failure due to creep rupture
- Failure due to creep fatigue

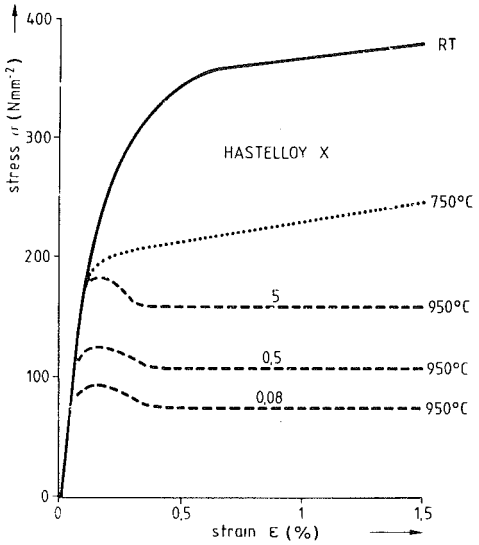

Fig. 2 Load elongation curves for Hastelloy X, (schematic)

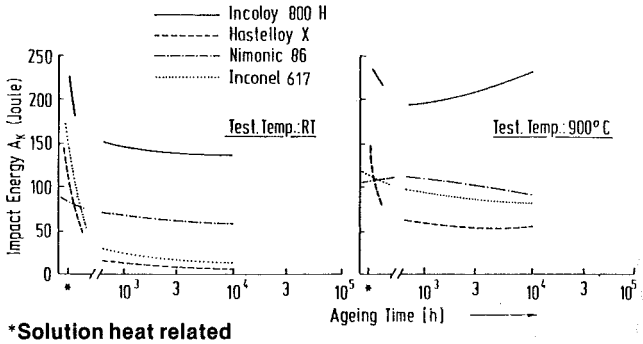

*Solution heat related

Fig. 3 Impact strength of PNP reference alloys after exposure at 900°C

- Distortion due to ratcheting
- Buckling due to short and long term loadings.

Further design aspects concerning (*i*) environmental and irradiation effects, (*ii*) welding problems in connection with limited ductility potential, (*iii*) prevention of brittle fracture, and (*iv*) multiaxiality are being theoretically and experimentally investigated.

3 Evaluation of Design Values

3.1 Short Term Properties. The scatterband evaluation of hot tensile properties [4] of the material in the as-received and aged conditions shows that above 800°C the data gained by a strain-rate controlled tensile test are strongly influenced by creep. In Fig. 2, the σ-ϵ curves for specimens of Hastelloy X show strain hardening effects at 750°C and creep effects at 950°C.

Tensile and impact tests on aged material at room temperature, Fig. 3, indicated a tendency for decreasing ductility. Therefore, the measures against failure due to short term loading—ductile fracture or brittle fracture—cannot be derived from the existing rules for LWR materials or from the evaluation of elastic limits given in the 3 S_m-criterion. It is therefore proposed that at working temperatures above 800°C the components should be safeguarded against the "yield point." The tolerable stress limit may be determined by a formula consisting of descriptions for the elastic behavior and the creep behavior. These equations have to be established for the beginning and end of life status of the material. Below

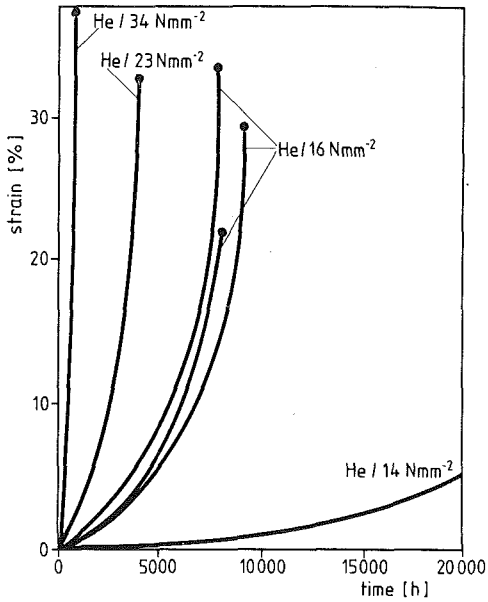

Fig. 4 Creep curves of Inconel 617 at 950°C

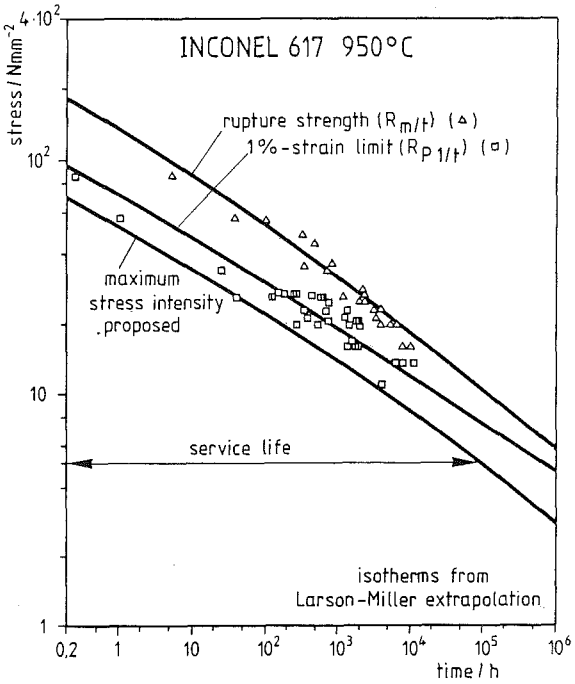

Fig. 5 Creep data of Inconel at 950°C

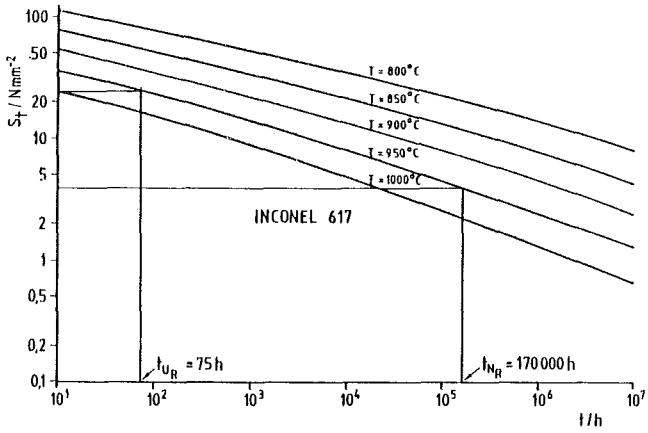

Fig. 6 Preliminary maximum design stresses S_t calculated from ASME Code, Case N 47, rules

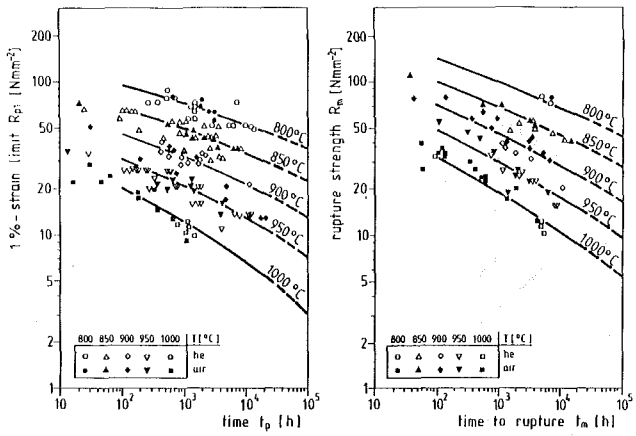

Fig. 7 Creep properties of Inconel 617

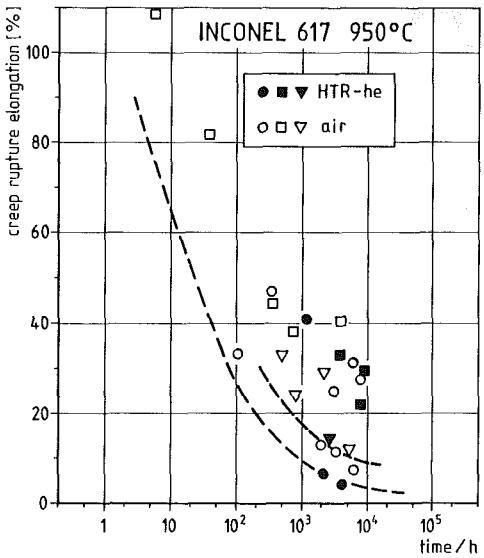

Fig. 8 Creep rupture ductility of Inconel 617

800°C, as plastic deformation and strain hardening are observed, the methods of ASME Code, Case N 47 may be tolerable.

From the metallurgical point of view, high creep strength and high room temperature ductility after overaging are contradictory, and consequently a limit for room temperature ductility or impact strength as given for austenitic steels for LWR application does not appear to be acceptable.

3.2 Long Term Creep Behavior. The dimensions of the high-temperature components are based on the S_t value given by ASME Code Case N 47.

Typical creep curves for Inconel 617 are shown in Fig. 4. Based on literature data and the results of the materials test program, this alloy is the strongest candidate material [5]. However, even for this alloy, the creep behavior at 950°C is different from the typical creep behavior of austenitic steels at temperatures about 550°C. A well-defined region of secondary creep is missing, and the determination of the onset of tertiary creep cannot be reliably carried out. Therefore, for the high temperatures, the beginning of tertiary creep has not been included in the evaluation.

As shown in Fig. 5, the minimum stress for the 1 percent creep strain is design-limiting at higher stress levels and rupture strength at low stress levels. In Fig. 6, a set of

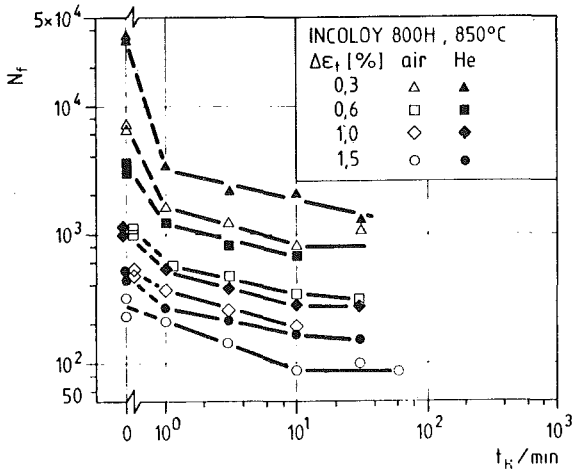

Fig. 9 Influence of hold time on LCF – behavior of Incoloy 800H

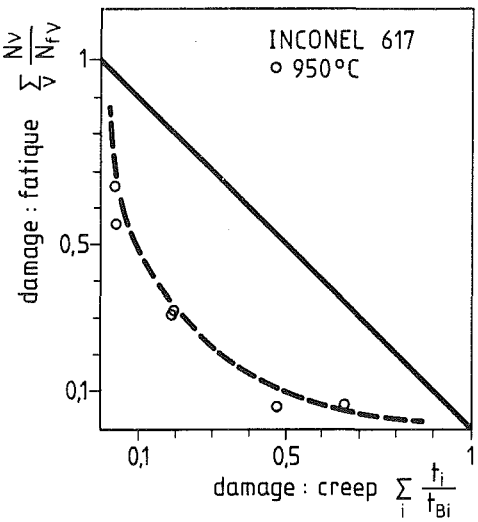

Fig. 11 Linear damage accumulation for creep fatigue interaction

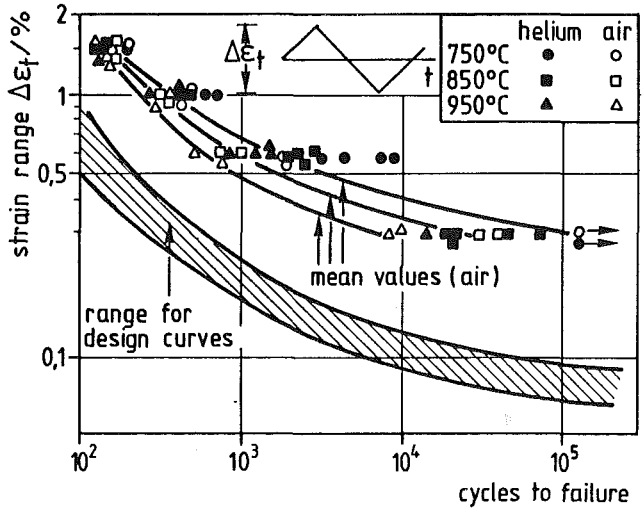

Fig. 10 LCF results for Inconel 617

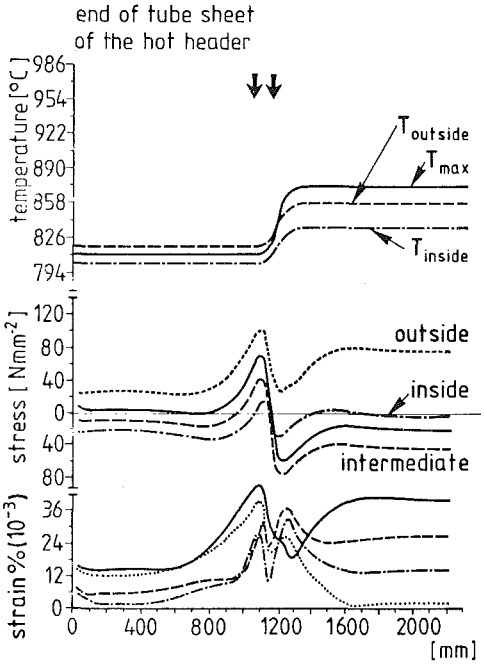

Fig. 12 Distribution of stress and strain along the hot gas header

calculated S_t-curves for different temperatures is given. These are extrapolated values based on experimental results with test times of up to 20,000 hrs. The scatterbands of results for three heats tested in air and simulated HTR-helium for the 1 percent strain limit and the creep rupture strength are overlapping (Fig. 7).

As there seemed to be a small effect of impure helium on creep rupture ductility (Fig. 8), the criteria for strain limitation as proposed by ASME Code Case N 47 may be adopted as follows:

- Maximum allowable strain through the thickness: 1 percent
- Maximum allowable strain at the surface due to an equivalent linear distribution of strain through the thickness: 2 percent
- Maximum local strain: 5 percent

The foregoing limits apply to computed strains accumulated over the operating life-time.

With experiments on tubing, the transferability of creep data obtained in monotonic uniaxial creep tests to multiaxial loading conditions is being examined. Tests of welded specimens both in uniaxial and multiaxial condition should lead to a better description of the creep behavior of welds, as well as to better evaluation of safety margins.

3.3 Creep Fatigue. A number of analytical methods for correlation of creep and fatigue are given in the literature [6, 7]. Cyclic loading in pure creep and in pure fatigue results in a consumption of service lifetime. The damage of material is defined in ASME Code, Case N 47 as the time ratio and the cyclic ratio. Other theories regarded the accumulated strains as measures for the damage [8]. In newer models, damage is the nucleation and the growth of microstructural voids and cracks [9]. For the designer, the linear damage accumulation rule is the most common, being a combination of the theories of Robinson and Palmgreen-Miner [6, 7].

The experimental basis for the design are low cycle fatigue tests with hold times in the stress region. In Fig. 9, for example, the number of cycles to failure for a set of strain ranges is correlated with the hold time for specimens of Incoloy 800 H, tested in air and simulated PNP-helium given [10]. There are some indications that increasing hold times above 1 hr at temperatures above 800°C produces no further decrease in number of cycles to failure.

The region for design curves at temperatures above 800°C

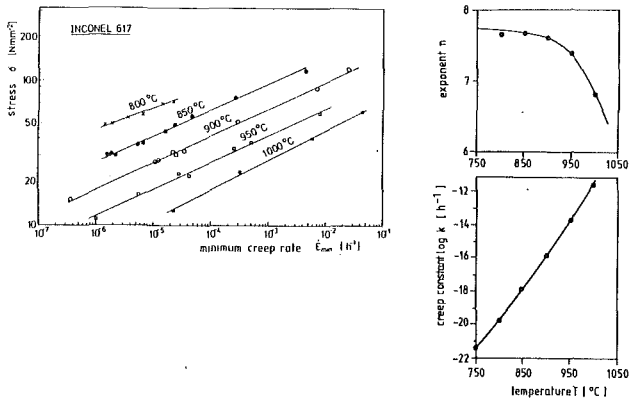

Fig. 13 Norton's creep law parameters for Inconel 617

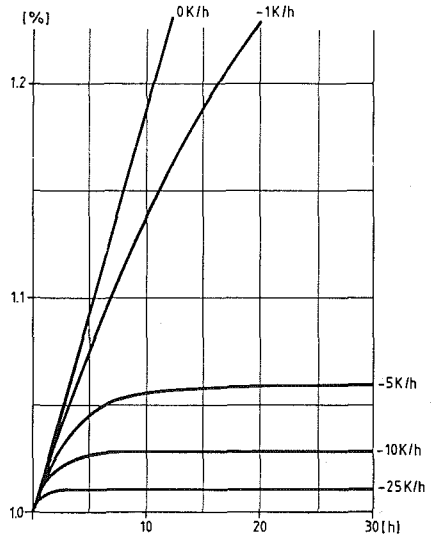

Fig. 14 Influence of temperature gradients on creep buckling

is given in Fig. 10. For the as-received material, the number of cycles to failure is greater in simulated HTR-helium than in air; disregarding environmental effects, this seems to be sufficiently conservative.

Taking the results of the minimum values for creep rupture strength and the minimum number of cycles to failure, and using the linear accumulation rule as described in ASME Code, Case N 47, the analysis of LCF tests with hold times are shown in Fig. 11. The points are below the expected curves. The linear damage rule is therefore not suitable for the very high temperatures.

The current understanding of lifetime prediction methods do not allow the formulation of a proposal for a fixed rule. Further experimental work is needed to establish damage accumulation rules.

3.4 Influence of Environment. In the case of a PNP-prototype plant the low scattered neutron influence reaching heat exchanging components can be neglected for materials properties.

The influence of impurities in HTR-helium, as far as material properties are concerned, may be also neglected to temperatures up to about 900°C. Above these temperatures, a wall thickness margin must be considered for heat exchanger tubes.

4 Examples of Applied Methods

Comprehensive analyses have been performed in order to protect highly loaded structures against the failure modes listed in 2.2.

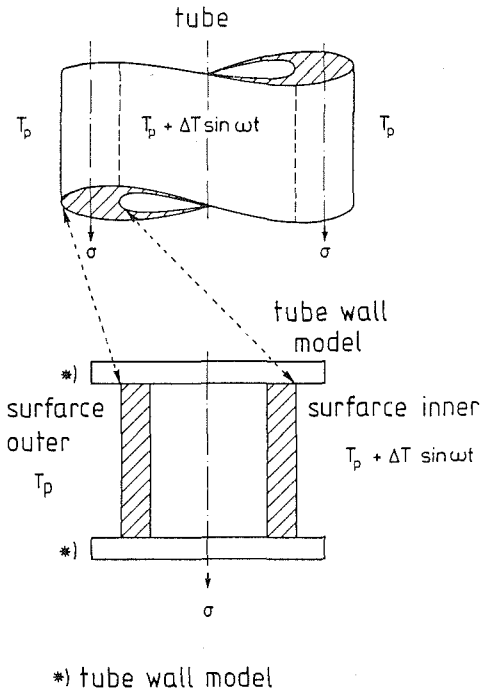

Fig. 15 Model for creep ratcheting evaluation

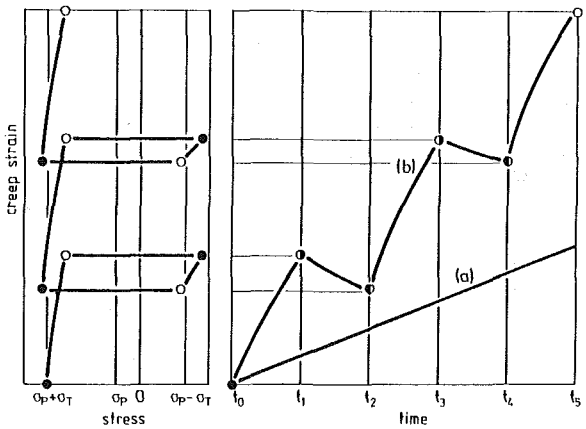

Fig. 16 Stress and creep strain as function time during creep ratcheting

The following three examples have been selected: fatigue analyses, creep buckling studies, and ratcheting evaluations.

4.1 Fatigue Analysis. The hot gas header has a relatively large wall thickness and structural discontinuities, with two-dimensional (axial and radial) temperature distributions at the transition to the secondary coolant inlet, which lead to cyclic strains during operation. The design procedure performed can be characterized by the following steps:

- Finite element, stress strain analyses taking into account two-dimensional temperature fields and geometrical discontinuities
- Evaluation of maximum equivalent strain range per cycle
- Comparison with fatigue design curve considering maximum hold time effects (Fig. 9) and maximum temperature level per cycle
- Evaluation of total use fraction sum by applying linear damage rule.

The results have indicated that the applied procedure seems to be rather conservative. In reality, the maximum strain range imposed will be sustained for only a few minutes during

start up periods at considerably lower temperatures than assumed. Figure 12 shows characteristic stress and strain curves along the axial axis of the hot gas header. The results lead to design optimizations and have indicated that emphasis must be placed on discussion and investigation of improved damage rules as well as of defined allowable use fractions considering coolant effects, strain rate and hold time effects.

4.2 Creep Buckling Analyses. The pressure difference between primary and secondary circuit is kept at a very low level during normal operation as shown in Table 1. The pressure loss of the secondary circuit is a postulated accident leading to a pressure difference of about 40 bar for a limited time period.

As creep effects are significant, the hot gas header must be protected against the failure mode "instability due to creep buckling." Many studies have been performed in order to investigate the influence of the design parameters. These concern:

- Ovality due to fabrication tolerance and circumferential temperature distribution
- Temperature level as well as temperature variations with time
- Creep behavior of the material

For the application of creep buckling theories, a set of creep equations must be evaluated. In the Fig. 13, the values of the Norton creep law are given.

The results have been presented and discussed in [11]. Figure 14 shows the increase of ovality with time for several conditions of temperature decrease rate.

As the axial length of the hot gas header is limited by end caps having an axial temperature gradient, the calculations have been completed by taking these effects into account. It was shown, that the assumptions in [11] of infinite length and constant axial temperature are very conservative.

The buckling calculations have been performed following the procedure recommended in [2]. This procedure is characterized by considering a load related safety factor of 1.5 leading to pressure difference consideration of 60 bar.

Applying Hoff's theory [12] and Norton's creep law, the creep exponent, n, has an important influence on ovality. As n is dependent on stress level, the safety potential related to an assumed time related safety factor will also be dependent on stress level.

Summarizing the present results:

(*i*) Temperature level as well as temperature variation with time and creep resistance of the material have an important influence on creep buckling.

(*ii*) Limitations should not be neglected in order not to be over conservative.

(*iii*) In order to reduce calculation times, application of load related safety factors are recommended, considering however dependence of stress level on creep exponent, n.

Full-scale experiments are being planned in KVK (Komponenten-Versuchskreislauf) at INTERATOM in order to verify these results. The theoretical evaluation will be done on model tube specimens at KFA.

4.3 Phenomena of Plastic and Creep Ratcheting. Ratcheting is defined as progressive cyclic inelastic deformation in a component. It is a superposition of mechanical secondary stress, thermal secondary stress, or both, on a sustained primary stress.

First analysis of creep ratcheting has been made with a simplified model [13] (Fig. 15). The total creep strain is successively increased in comparison with the creep under primary stress level (Fig. 16).

A critical application of ASME Code, Case N 47 criteria illustrated very well that at the high temperature only one criterion, test number 2, can be applied. However, this criterion is very conservative due to the limitation by the 10^4 S_t-value. New relevant models must be developed.

5 Final Remarks

The status of work from the material science and stress analysis points of view is as follows:

Information on materials is available to such an extent that the basis for a design can be determined and the design carried out. An allowable service time for a heat exchanger of about 50,000 hrs seemed to be realistic.

There are some uncertainties in the definition of safety margins and the development of simplified methods. The problems regarding structural mechanics are:

- Further evaluation of experimental work up to longer test times for
  (*a*) confirmation of existing models
  (*b*) incorporation of models in technically applicable rules
- Nuclear approval of HTR materials

Experimental investigations are required for:

- Transferability of uniaxial test results to multiaxial loading
- Creep ratcheting evaluation
- Structural integrity tests
- Damage accumulation
- Fracture mechanics

In addition to these problems, a better understanding of the requirements of in-service inspection and of repair and maintenance rules must be further discussed.

Design rules for HTR heat exchanging components will be formulated in a concluding report after the current research and development has been completed.

Acknowledgment

This work has been performed within the framework of the German HTR- R and D Company (Entwicklungsgesellschaft HTR). The project is sponsored by the Minister for Research and Technology and the Minister of Internal Affairs of the Federal Republic of Germany and by the State of North-Rhine-Westfalia.

References

1 Nickel, H., Ennis, P. J., Schubert, F., and Schuster, H., "Qualification of Metallic Materials for Application in Advanced High-Temperature, Gas-Cooled Reactors," *Nuclear Technology*, Vol. 58, 1982, p. 90.

2 ASME Code Case N 47 - 15, "Class 1 Components in Elevated Temperature Service, Division 1," ASME, New York, 1979.

3 Design by Gebr. Sulzer GmbH, CH-Winterthur, INTERATOM GmbH, D-Bensberg and Steinmüller, D-Gummersbach.

4 Schuhmacher, R., Diehl, H., Ennis, P. E., Schubot, J., te Heesen, H., and Ullrich, G., 'Kurzzeiteigenschaften ohne und mit Vorbeanspruchung," *Energie - Politik*, Bd14 (1982) p. 119.

5 Schubert, F., Bruch, U., Cook, R., Diehl, H., Jakobeit, W., teHeesen, H., Ullrich, G., and Weber, H., "Zeitstandverhalten," *Energie - Politik*, Bd14 (1982) p. 134.

6 Robinson, E. L., ASME *Transactions*, Vol. 60, 1938, p. 253.

7 Miner, A. A., *Journal of Applied Mechanics*, Vol. 12, 1945, p. 159.

8 Monsau, S. S., Halford, G. R., and Hirschberg, M. H., "Creep-Fatigue Analysis by Strain Range Partitioning," NASA TMX - 67838, 1971.

9 Kachanow, L. M., "Theorie des Kriechens" (in Russian), *Gos. Izdat. Fis. Mat. Lit.*, Moscow, 1960.

10 Meurer, H. P., Breitling, H., and Grosser, E. D., "Low Cycle Fatigue Behavior of High-Temperature Alloys in HTR-Helium," IAEA-Specialists' Meeting, Vienna, Austria, May 1981, OFZS-Ber. 4086.

11 Schulze, R., and Seehafer, H. J., "Creep Buckling Analysis of Cylindrical HTR-components," 6th SMIRT Conference 1981, L 13/2.

12 Hoff, N. J., Jahsman, W. E., and Nachbar, W., "A Study of Creep Collapse of a Long Circular Cylindrical Shell Under Uniform External Pressure," *J. Aero/Space Sc.*, Vol. 26, No. 10, 1959.

13 Over, H. H., KFA-internal report, IRW-TN 102/81.

13 Schubert, F., Oves, H. H., Zottmaier, R., "Darstellung des Krichratcheting," *Proceedings of RWTüV-Seminar*, 1983.

LMFBR Steam Generator Materials Development at Westinghouse

M. A. Hebbar
Manager, Materials and Processes.

C. E. Sessions
Principal Engineer.

Breeder Reactor Components Project,
Westinghouse Nuclear Components Division,
Tampa, Fla.

The impact of Materials and Processes (M and P) development activities at the Nuclear Components Division - Breeder Reactor Components Project of Westinghouse are described. Nine specific M and P programs have been performed over the past five years and the conclusions drawn from each are summarized herein. These engineering activities could be classified as component design, fabrication, and testing results. However, the discussion presented is from a materials engineer's viewpoint as to how the previously proposed development tasks have answered existing questions about either design, manufacturing, or plant operation. The nine areas which are discussed include (i) double-wall tubing, (ii) tube-to-tubesheet welding, (iii) few tube model fabrication and testing, (iv) tube support plates, (v) shell welding, (vi) convoluted shell expansion joint, (vii) water chemistry and corrosion behavior, (viii) chemical cleaning, and (ix) surface contamination protection.

Introduction

The M and P activities, still required for development of reliable steam generators for LMFBR (Liquid Metal Fast Breeder Reactor) service are quite numerous. The issues have been highlighted repeatedly at both materials and nuclear power conferences over the last decade [1-5]. Major emphasis in the United States has been placed on ASME Boiler and Pressure Vessel Code mechanical property data generation and fabrication technology for the ferritic steel, 2-1/4 Cr-1Mo. In the remainder of the world, the emphasis has been upon a wider range of materials for potential application in the LMFBR steam generator environment. Emphasis on sodium decarburization, compatibility with water/steam, and influence of heat treatment and corrosive species on mechanical properties have been particularly active areas of materials R and D abroad.

A decision to concentrate on 2-1/4, Cr-1Mo steel rather than Alloy 800 or a higher chromium ferritic steel was made about 1973 and since that time most design, analysis, and materials development has been in support of that decision. The steam generator vendors in this country have been designing, analyzing, and building hardware of this material for Fast Breeder Reactor (FBR) development testing while the national laboratories have been generating the large bulk of corrosion and mechanical property data to support the on-going steam generator vendor design and manufacturing activities.

The issue of using either a single or double-wall tube in a sodium-to-water heat exchanger (steam generator) has been with the liquid sodium reactor industry since its inception in the early 1950's because of the concern for the potential of sodium/water reactions. Early model tests utilized single, double, and even triple-walled tubes in various heat transfer models. The history of the development of liquid metal heat exchanger technology has been recently published by Stone et al. [6]. Statistical reliability studies performed by Westinghouse as early as 1973 confirmed several orders of magnitude improvement in the steam generator availability of a double-wall concept as compared to a single-wall design [7]. However, the absolute reliability of even the more common single-wall reference steam generator designs was not firmly established because of the lack of a mature data base concerning actual single-wall tube steam generator operational experience in the LMFBR environment.

Westinghouse has been involved in LMFBR steam generator development for approximately 20 years. In 1977, a major Department of Energy contract for a large plant steam generator design was initiated on a straight, once-through concept utilizing radially prestressed double-wall tubes. Major developments in the metallurgical area were required to bring the initial conceptual design to the current state of readiness for potential commercial application. This paper describes these developments with particular emphasis on the materials and processing tasks.

Design Features

The Westinghouse steam generator design [6, 8, 9, 10] provides a double barrier between sodium and water, and leak detection capability between the two barriers. The design consists of double-wall tubes with integral third-fluid leak detection, the key elements of which are illustrated in Figs. 1-3. Penetration of the water side results in steam leaking into the helium, which is detected in the upper helium plenum by moisture (hygrometers) or pressure detectors (transducer). Penetration of the sodium side results in helium leaking into the sodium, which is detected at the sodium outlet by a gas sparger and a gas chromatograph.

Contributed by the Nuclear Engineering Division and presented at the 1982 Joint Power Generation Conference, Denver, Colorado, October 17-21, 1982. Manuscript received at ASME Headquarters July 23, 1982. Paper No. 82-JPGC/NE-2.

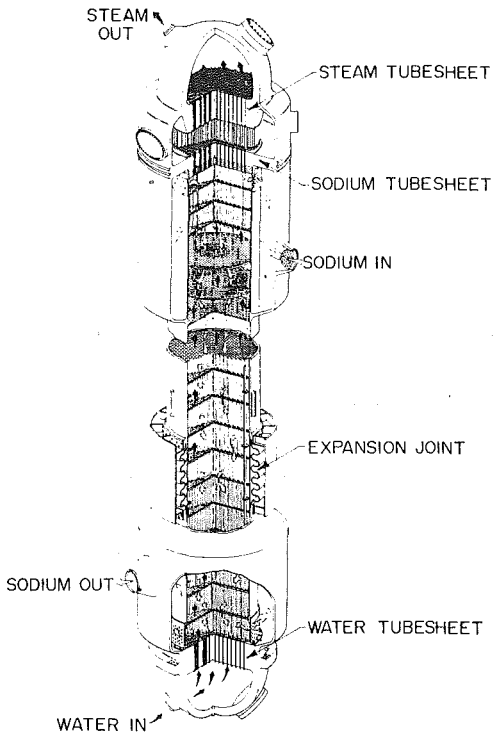

Fig. 1 Westinghouse sodium heated steam generator

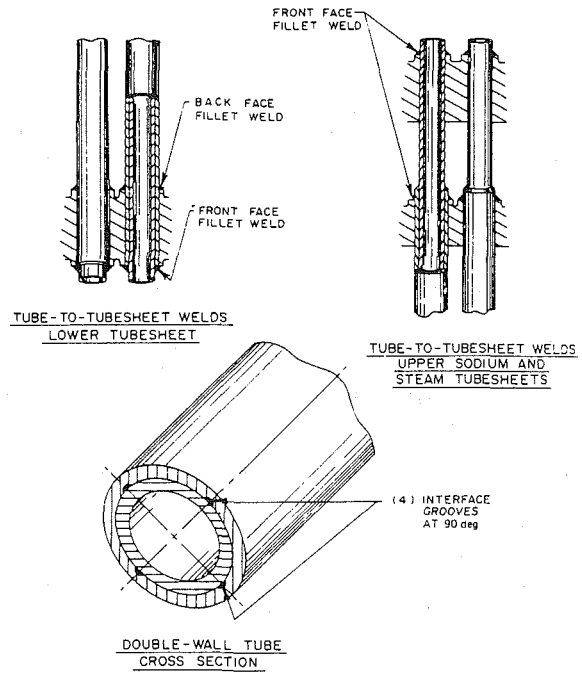

Fig. 2 Double-wall tube and tube-to-tubesheet weld locations

Figure 1 illustrates the reference Benson-cycle (once-through) steam generator, which evaporates and superheats the water in a single shell. It is a vertically oriented, shell-and-tube counterflow heat exchanger, with water/steam on the tube side, sodium on the shell side, and a static helium third-fluid between the tube walls. A helium plenum is formed between the two tubesheets at the top of the unit for leak detection. A convoluted shell expansion joint (CSEJ) in the shell provides differential thermal expansion between the shell and tube bundle.

The double-wall tubes are radially prestressed and contain linear grooves at 90 deg intervals on the inner surface of the outer tube as illustrated in Fig. 2. The inner and outer tubes are individually welded to the double tubesheet at the top of the steam generator, and to both sides of the single tubesheet at the bottom of the unit, maintaining the double barrier between sodium and water.

Table 1 Steam generator materials selected by various countries

	EVAPORATOR	SUPERHEATER
United Kingdom (PFR)	2 1/4 Cr-1Mo-Nb	316SS
United Kingdom (CDFR)	9 Cr-1Mo	9 Cr-1Mo
French (Phenix)	2 1/4 Cr-1Mo	321SS
French (Superphenix)	Inconel 800	(once-through)
Germany (SNR)	2 1/4 Cr-1Mo-Nb	2 1/4 Cr-1Mo-Nb
Russia	2 1/4 Cr-1Mo	2 1/4 Cr-1Mo
Japan (Monju)	2 1/4 Cr-1Mo	321SS
United States (CRBR)	2 1/4 Cr-1Mo	2 1/4 Cr-1Mo

A number of design features are included to satisfy the structural requirements. The CSEJ is used in the lower part of the shell to accommodate differential thermal expansion between the tube bundle and the shell. Individual tube differential thermal expansion is controlled by the thermal hydraulic design. Differential thermal expansion between the tube bundle and shell in the upper double tubesheet region is provided by connecting flanged and dished heads. Differential thermal expansion between the tube and tubesheet at the bottom is eliminated by a full-depth expansion of the tubes into the lower tubesheet. Alloy 718 thermal shielding plates are used on the sodium side of the upper sodium tubesheet to limit creep-fatigue operating and transient effects between the solid outer ring and perforated area. Thirty-nine support plates are used to support the tubes in the sodium chamber and are connected together by a compliant stayrod design.

Interface wear caused by relative motion between the double walls due to gross thermal transients and departure from nucleate boiling (DNB) has been extensively studied. This study has resulted in tube sizing margin to accommodate the saturating wear if, for any reason, the prestress between tube walls was lost.

Materials Selection

The selection of the reference material for the LMFBR steam generator has been the subject of numerous discussions both in the United States and in other countries where LM FBR research and development is underway. Understandably, there is little consensus in the selection of the reference material (Table 1). Many general requirements may be imposed on the alloy for use as the steam generator material of construction. In the United States, the base technology program sponsored by the DOE almost 10 years ago selected unstabilized 2-1/4, Cr-1Mo low alloy steel as the reference material for the steam generator. Mechanical behavior, corrosion resistance, and cost are some of the more convincing points in favor of the steel. The industrial and fabrication experience with the 2-1/4 Cr-1Mo steel is vast and sufficient to outweigh most uncertainties present. These uncertainties include the lack of a complete understanding of creep-fatigue interaction at elevated temperatures and the concern about its decarburization by sodium and water corrosion over the 30 or 40 year design life of the steam generator. The evidence in favor of 2-1/4 Cr-1Mo steel far outweighed the unknowns, and it was selected as the reference material for the Westinghouse steam generator. Alloy 718 was selected for some of the tube support plates by virtue of its wear properties against 2-1/4 Cr-1Mo under sodium and for its strength to accommodate high side loads during seismic events. Alloy 600 and Alloy 800H are used for miscellaneous parts such as instrumentation jackets, spool pieces for safe ends etc.

Material specifications were written for pressure boundary, nonpressure boundary, and weld materials to include contractual, ASME Code and Westinghouse design requirements. As a rule, pressure boundary materials specification were written to meet the ASME Code Section III, Class 1 requirements, whereas Section II material specifications (SA or SB) were factored into nonpressure boundary materials, as a minimum. Code Case N-47, paragraph 2000 requirements were also made applicable to the pressure boundary components.

During the development of material specifications, the advantages of advanced steel-making practices were realized, and this had a significant impact on both the design and the fabrication of the steam generator. Cladding of the 2-1/4, Cr-1Mo steel tubesheet with a 2-1/4 Cr-1Mo filler metal of controlled chemistry was conceived in the beginning of the program as a means of creating a clean, low inclusion and low residual elements surface to which the tubes would be welded. Since tube-to-tubesheet (T/TS) welds are critical for successful operation of the steam generator, this extra step was considered necessary due to the lack of confidence in the cleanliness of a conventionally produced forging. However, when the ability of remelt qualify forgings—electroslag remelt (ESR) or vacuum arc remelt (VAR)—to achieve the same end were known and the availability of ESR/VAR forgings in large sizes suitable for plant unit steam generators was confirmed, the cladding development program was dropped. This is estimated to have saved a significant amount of development and fabrication cost. The second application of ESR/VAR forgings was made in the CSEJ design. The details follow later on, but it is sufficient to mention here that the excellent quality obtained in the ESR/VAR forgings made it possible to manufacture the CSEJ by machining and, therefore, made the design of the straight shell/straight tube steam generator possible and fully reliable. The advantages of remelt, 2-1/4, Cr-1Mo steel include microcleanliness and property uniformity (isotropy).

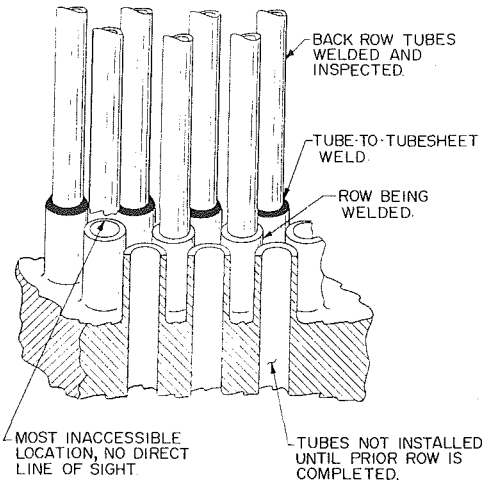

Fig. 3 Tube-to-tubesheet welding sequence

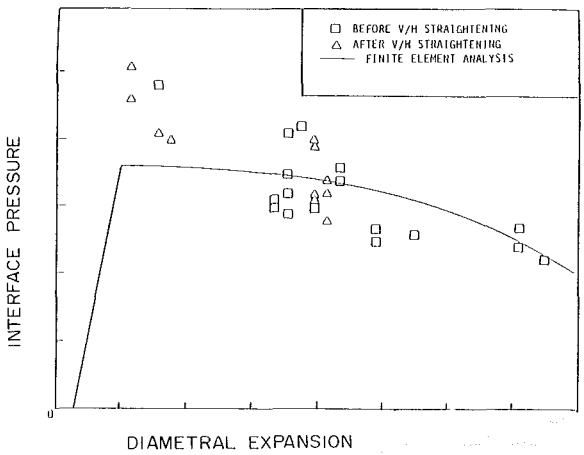

Fig. 4 Agreement between theoretical prediction of interface prestress and actual measurements on tube samples

Impact of Materials and Processes Development on the Design

Major M and P development tasks addressed the following activities: (*i*) double-wall tubing, (*ii*) tube-to-tubesheet welding, (*iii*) tube support plate manufacture, (*iv*) few tube model and (*v*) convoluted shell expansion joint qualification. Lesser, but still significant, M and P efforts were required in other developmental areas as follows: (*vi*) shell welding, (*vii*) water chemistry, (*viii*) chemical cleaning, and (*ix*) surface contamination protection. This section will present a summary of the major conclusions [12, 13, 14, 15, 16] that have evolved from these developments in the metallurgical area.

Double-Wall Tubing. The accomplishments of the double-wall tubing development activity have been presented previously [11, 12]. The tube specification that has evolved since 1973 is now extensive and covers the permissible processes and the range of physical attributes which must be maintained to produce an acceptable product from both a metallurgical and a residual stress viewpoint. The specified yield strength range, before the prestressing, is established such that a vendor must use a fast cool from the austenization temperature followed by tempering. The use of isothermal annealing, although desirable, would produce yield strength values on the average below that specified by Westinghouse to produce the desired amount of tubing prestress.

The decarburization behavior of normalized and tempered 2-1/4, Cr-1Mo steel in sodium, the creep behavior, and the fatigue properties are known [4, 5] to be different from those of isothermally annealed 2-1/4, Cr-1Mo steel for which so much of the materials characterization work has been done. However, these differences are considered to be acceptable in the design.

Several problems were experienced during the tubing manufacturing development but were successfully overcome. They include the achievement of the proper groove depth and shape, proper heat treatment to obtain mechanical properties without metallurgical bonding, control of tube dimensions prior to and following the prestressing operation, interface cleanliness, achievement of the desired prestress, and maintenance of acceptable prestress after final straightening.

Figure 4 illustrates the good agreement between theoretical finite element predictions of tubing prestress and the experimental values from tubing produced to our specifications. Acceptability of light vertical/horizontal straightening of the prestressed tubing is also illustrated in Fig. 4.

The major conclusion drawn from the tubing development is that the product can be practically manufactured at a reasonable cost even though the technical requirements are quite extensive and an appreciable vendor learning curve was required to successfully and reproducibly manufacture this prestressed double-wall tube product.

Tube-To-Tubesheet Welding. Tube-to-tubesheet (T/TS) welding has included three distinct areas of development [10, 13]: (*i*) tube-in-tubesheet expansion, (*ii*) weld gun and parameter development, and (*iii*) post-weld heat treatment process development. In the steam generator design, each tube is welded to the three tubesheets in four locations—on both

sides of the water tubesheet and on the top faces of the sodium and steam tubesheets. With this arrangement, two T/TS welds on the same tube must fail before a sodium water reaction can occur. To accomplish the "inaccessible"[1] welds, a welding gun was developed to operate within the tight confines of 5/8-in. (16-mm) spacing. This inaccessibility also requires a row-by-row insertion of tubes and the completion of all production operations on a given row before proceeding with the adjacent row. A schematic of the T/TS welding sequence is shown in Fig. 3.

Tube expansion is performed hydraulically and full-depth in all three tubesheets to maximize both the weldability and the heat transfer performance. High pressures, ~60,000 psi (414 MPa), precise sizing of the hydraulic expansion mandrels and seals, and precise positioning within the tubesheets are required.

Various joint geometries and filler pass sequences were tried for the T/TS welds before a satisfactory combination of fusion pass and filler passes was arrived at for each of the four weld joints. All filler passes were with cold wire feed (CWF). The Gas Tungsten Arc Welding (GTAW-CWF) process was specified to provide the cleanest process with the best accessibility and to enable one to control the chemistry of the deposit. The pulsed current technique was employed which aided in choosing the optimum puddle control/penetration combination for varied conditions such as the root pass and the third filler pass.

Welding devices for accessible, inaccessible, and repair welding were designed, built, tested, and modified as needed. The automatic weld guns were purchased from an outside vendor, whereas the repair welding gun was built by Westinghouse. The repair welding gun was actually used to make all welds successfully in the fabrication of a seven-tube model (identified as Few Tube Model, FTM). The reason was that the FTM was fabricated prior to procurement of the two automatic welding devices.

High-frequency induction heating was selected for use in post weld heat treatment (PWHT) of the T/TS welds. The technical requirements were defined by Westinghouse and the equipment was designed and built by an outside vendor. In order to reduce the mismatch in strength between the base metal (tube and tubesheet) and weld metal and at the same time reduce the weld hardness after PWHT, a low-carbon, 2-1/4, Cr-1Mo filler metal was selected for T/TS welds. An extensive experimental investigation conducted on prototypic T/TS weld samples, heat treated at different temperatures and times, indicated that the reference temperature of 1375°F (746°C) for 10 min provided optimum softening of the weld and the heat affected zone (HAZ). The combination of rapid induction heating and short heat treatment times also prevented significant thermal growth and reduced residual stresses in the tubesheets.

The heat treating of individual T/TS welds is performed using an induction coil and an infra red sensing device that automatically controls the temperature within a few degrees. The equipment is programmed for fast heating, a hold period of 10 min, and a fast cool down from the soaking temperature.

Problems with porosity within the welds, as determined by the microfocus rod anode throughout this weld development work, have occurred. The schedule for fabrication requires resolution of these difficulties by December 1982. A detailed investigation of the cause of the porosity, which has also plagued other FBR steam generator vendors, is underway at a high level of priority.

Tube Support Plate (TSP). The subject of design and development of tube-support-plates for LMFBR application is complicated because of the influence which sodium has on the inherent wear behavior of these materials couples. The design and metallurgical development of the support plates manufacturing approach was previously addressed [13, 14] and an update is presented at this same conference [15].

The status below is presented to briefly summarize the design/development conclusions to date. Both 2-1/4 Cr-1Mo and Alloy 718 were expected to be utilized in the diffusion coated conditon to improve the tribological properties in sodium. The location of a specific type of TSP was dictated by the calculated loads that the support plates would see during operation or by strength requirements during seismic events. Attempts to qualify two vendors to perform diffusion treatment of model size, 44-in. (1118-mm) dia tube support plates of both materials have recently been hampered because of dimensional changes of the parts that occur during the coating cycle. Due to either the relaxation of residual machining stresses or to thermal distortion during the diffusion cycle, it was determined that the tight control on the tube hole position (±.005 in. or .13 mm) cannot be maintained. The approach which is currently favored is to utilize uncoated Alloy 718 for all the tube support plates within the design. In previous tests done in support of liquid sodium systems, Alloy 718 was demonstrated to possess very good tribological properties when rubbed against itself or against 2-1/4 Cr-1Mo steel. The bypass diversion rings located between support plates do not experience appreciable side loading in service and will continue to be made from 2-1/4 Cr-1Mo steel.

Few Tube Model. The few tube model with seven full length tubes was designed, built, and tested during the period, 1979 through 1981. It is currently being destructively examined after a successful test period for confirmation of the design adequacy of an LMFBR plant unit. A subsequent 70 MWt model with 804 tubes will also be tested, and is currently being manufactured by Westinghouse in Pensacola. The purpose of the FTM development program was to prove the heat transfer performance and structural adequacy of the steam generator design through both steady-state and transient testing. The major input to the FTM from the M and P discipline was in design, fabrication, and post-test-examination of the model. Design input involved welding, defining ordering specifications, drawing review, and vendor interaction. The input to fabrication included cleanliness requirements, process specifications, and resolution of supplier and shop manufacturing deviations.

The post test examination of the FTM is intended to supply information on dimensional changes, if any, visual appearance of the internals, levels of interface prestress, wear behavior, T/TS weld integrity, and water/steam corrosion performance of the tubing following the approximately 5000 hrs of testing. The dissection of the FTM is now complete and detailed metallographic and prestress measurements should be available soon.

Convoluted Shell Expansion Joint (CSEJ). The CSEJ program [16] produced a unique approach to fabrication/design of an expansion-type device to be used in the shell of a straight-tube steam generator. The idea, proven by manufacturing development of an outside vendor, was that a thick wall convoluted shell could be made from a ring forging by three-dimensional machining of approximately 85 percent of the initial volume of the ring forging. Although three metallurgical concerns (below) were raised initially about this approach, they were subsequently proven to be unwarranted concerns by the procurement of electroslag remelt (ESR) quality forgings.

(*a*) Flow lines/CSEJ surface interaction. The machining

[1] Inaccessible means that there is no direct line of sight around the tube as the welding is performed.

Fig. 5 Convoluted shell expansion joint machined from a ring forging

technique is contrary to the traditional practice of allowing the flow lines to follow the contour of the component.

(*b*) Grain size anisotropy. In a thick wall forging, grain size anisotropy could be expected from midwall to the surface. This would give rise to strength inhomogeneity in various parts of the CSEJ. Further, the ultrasonic testing of the ring forging would be extremely difficult if grain size inhomogeneity were present.

(*c*) Anisotropic mechanical properties. Because of the different working in the three directions and different cooling rates in a thick wall forging, the three-dimensional tensile properties might show large variations.

An investigation into the advantages of ESR/VAR steel forgings concluded that the foregoing concerns could be eliminated by the use of one of these remelt techniques because of their inherent cleanliness and homogeneity. Two ESR ring forgings were procured from Japan and successfully machined in the United States by Allis Chalmers. One CSEJ was tested structurally and the second will be used for the 70-MWt model. The properties of the ring forgings far exceeded the most optimistic expectations in terms of uniformity in tensile properties, toughness, conformity to the specified chemistry, inclusion content, and uniformity in the grain size. The three-dimensional properties at the midwall and the surface were remarkably uniform [16]. In addition, the microstructure at these locations indicated a homogeneous forging responding uniformly to the heat treatment with no signs of directionality of the flow lines.

The CSEJ (Fig. 5) was machined to within 1/4 in. (6.35 mm) of the final OD and ID dimensions on a vertical boring mill. Contouring was performed by a tracer technique. At this stage, the CSEJ was stress relieved and ultrasonically tested. The CSEJ was then machined to the final dimension of 0.75-in. (19-mm) wall thickness. The dimensional control on the final machined contour was excellent and what appeared to be an extremely difficult, and intricate machining operation was completed successfully without significant problems and at low cost. The details of the manufacturing and machining of the CSEJ have been presented previously [13, 16].

Several smaller M and P development activities have produced a variety of interesting conclusions concerning materials engineering for this steam generator design. Discussed in the following section, these are: shell welding [6], water chemistry [7], chemical cleaning [8], and surface contamination protection [9].

Shell Welding. Shell welding development activities produced an ASME Code qualification of two welding procedures—submerged arc welding (SAW), and shielded metal arc welding (SMAW)—over a one year time frame. These procedure qualifications covered plate thickness ranges between 5/8 in. (15.87 mm) and 8 in. (203 mm), a range that covers both the present 70 MWt model steam generator and plant size design requirements.

Water Chemistry and Corrosion Behavior. One of the basic issues concerning the commitment of 2-1/4, Cr-1Mo steel to both the evaporator and superheater of an LMFBR steam generator was its water/steam corrosion performance. Although prior successful application of this material in superheater service has occurred historically in fossil boilers, the specific corrosion rates in the evaporator and on the steam side of the superheater were not well characterized because the fire-side corrosion resistance of this material normally posed the major concern in fossil systems. Thus, few quantitative data under germane heat flux conditions were available initially concerning its performance in water/steam.

Three major programs provided meaningful corrosion rate data in water/steam under representative heat flux and off-normal water chemistry conditions, such that design corrosion allowances could be substantiated. The three programs included a superheat steam corrosion study at Oak Ridge National Laboratories [17], a single-tube model evaporator post test examination at General Electric Company [20], and a similar single-tube model program at Westinghouse [18, 19]. In addition, water chemistry specifications have been established by General Electric, Westinghouse, and Rockwell for future plant designs based in part on this characterization of the corrosion behavior of 2-1/4, Cr-1Mo steel.

The 1974 Nuclear Systems Materials Handbook (NSMH) recommended approach to calculation of corrosion allowances for 2-1/4, Cr-1Mo steel was based upon an Ahrenius correlation of isothermal corrosion rate data for steady-state oxidation tests. No water phase corrosion results were included, and in fact, even carbon steel data were included in the oxidation rate analysis. A factor of 1.5 was recommended to be used to account for the effect of heat transfer. To account for the rapid build up of the oxide after a chemical cleaning operation, the NSMH included data on the temperature dependence of the parabolic portion of the oxidation curve.

The recent model tests corrosion data generated by Westinghouse and General Electric in support of the Clinch River Breeder Reactor steam generators development therefore provided some of the first data specifically addressing the effect of steady-state operation and off-normal water chemistry behavior on 2-1/4 Cr-1Mo in the water and steam phases and at DNB. Maximum rates of corrosion based upon linear extrapolation of the model post test examination results gave values of 0.8 and 0.9 mils/yr (0.020 and 0.023 mm/yr), respectively, for the General Electric and Westinghouse tests. No accelerated corrosion was found at DNB, although prior concern existed about the possibility of accelerated corrosion at that point. Test results and model operating conditions are presented in Table 2. These upper limits established on the corrosion rate of 2-1/4, Cr-1Mo steel were appreciably higher than expected for the water phase.

The water chemistry requirements which were specified for the Westinghouse steam generator, based in part upon a review of the corrosion behavior of 2-1/4 Cr-1Mo, are similar to those reported by Simpson et al. [21] for CRBRP.

Chemical Cleaning. A literature review of the ef-

Table 2 Operation and corrosion results for General Electric and Westinghouse 2-1/4, Cr-1Mo steel model tests

	Westinghouse	General Electric
Na Content in Feedwater (ppb)	30	9 ± 3
Max. Heat Flux (Mw/m^2)	0.76	1.26
Exposure Time (Hr.)	8494-10455	2820-4180
Max. Temperature (°C)		
Nucleate Boiling (ID)	327	326
Film Boiling (ID)	402	407
Cation Conductivity at 25°C (micro ohm/cm)	2 (max)	2 (max)
Oxygen (ppb)	7 (max)	7
Copper (ppb)	11 (max)	12 (max)
Iron (ppb)	55 (max)	60 (max)
Chloride (ppb)	20 (max)	30 (avg)
ID Decrease at DNB (mm)	NA*	.013
Oxide Thickness (mm)	.005-.022	NA*
Max. Deposition at DNB (mm)	0.013	0.005
Max. Inferred Corrosion (mm)	.010-.022	0.010
Max. Rate (Corrosion observed//Time of Exposure) (mm/yr)	0.0086-.023	0.020

*Not available

fectiveness of various solvents used in fossil boilers and now being studied for application in PWR's and LMFBR's was recently made. The reliability of both steam generators and turbine generators can be enhanced by the routine application of an appropriate chemical cleaning procedure that removes oxides, scales, and mass transfer deposits from heat transfer surfaces. However, whether to apply a chemical cleaning procedure and what frequency to use even if applied is not at all straightforward.

The accumulation of deposits on heat transfer surfaces is a time-dependent phenomenon that can be accelerated by off-normal water chemistry or thermal transients that change the flow rates and/or the solute concentration levels of the coolant. A theoretical model of the boiling process within porous deposits has been formulated [22] and experimental observations tend to confirm the fact that in the deposit a higher solute concentration of the liquid phase is generated because the boiling process selectively enriches the liquid with respect to the steam which leaves through the pores. The corrosiveness of this enriched liquid remaining in contact with the wall of the heat transfer surface can be significant depending upon factors such as (*i*) the bulk solute concentration of the incoming feedwater, (*ii*) the heat flux across the porous deposit, and (*iii*) the effectiveness of the deposit to permit selective boiling without mixing of the residual and the bulk liquid.

Potential advantages of periodic chemical cleaning include (*i*) removal of the sites for possible concentration of impurities, (*ii*) removal of oxides that could potentially spall and damage the turbine, and (*iii*) restoration of the original heat transfer and pressure drop performance degraded by the presence of the deposits. One major disadvantage of chemical cleaning relates to the large risk associated with the possible damage due to corrosion attack by the cleaning solvent of either a general, localized, or galvanic nature.

A number of groups have studied various EDTA (Ethylene diamine tetra-acetate) and citric acid mixtures (solvents) for different cleaning applications, and these studies tend to reinforce the position taken by FBR vendors that EDTA and citric acid is a good FBR steam generator chemical cleaning candidate. However, a rather tight control is required to use this solvent at its optimum penetration rate, which might well make application of these solvents difficult, unless shell heaters are installed on large components that can maintain solvent temperatures at the desired levels.

A draft chemical cleaning procedure has been defined by Westinghouse for use on the Westinghouse double-wall steam generator. It involves the application of ammoniated EDTA and citric acid at 176°F (80°C) using shell heaters to control the temperature of the solvent during cleaning. Criteria for when chemical cleaning should be performed remain to be established.

Surface Contamination Protection. Limited Westinghouse experience in fabrication of steam generators from the low-alloy steel 2-1/4 Cr-1Mo initiated a task to expose and examine coupons within the shop environment. A variety of procedures were tried to characterize the tendency for rust to form on freshly machined surfaces and the effectiveness of elevated temperatures and different protective covers to prohibit rust formation. Scanning electron microscopy and Auger analysis were used to characterize the nature of contaminants at the interface of tube samples after the shop exposure. Three methods were generally concluded to provide adequate rust protection.

(*i*) Keeping the steel at least 30°F (16.5°C) above ambient to prohibit condensation on the parts

(*ii*) Using Vapor Phase Inhibitor (VPI) powder or paper in plastic sleeves or bags around a part

(*iii*) Using oil based products such as "Weld Kleen" on a periodic basis by spraying

Techniques (*i*) and (*ii*) generally were followed for different parts during the fabrication of the FTM in the shop in Tampa, Florida with acceptable results. Technique (*iii*) was not generally applied during the FTM fabrication because of concern for its effect on weld quality. Each of the seven tubes in the FTM passed a gas flow test through the grooves over the 77-ft (23.4-mm) length to confirm that tubing interface contamination had not occurred during FTM fabrication.

Important application of these conclusions will occur during fabrication of the 70-MWt model in Westinghouse at Pensacola, Florida during the next two years prior to shipment of the model to ETEC for a year of testing beginning in 1985.

Project Status and Future Plans

The results of these M and P and other engineering development activities not presented here, have been factored into a preliminary design of a plant unit and a 70-MWt model of the double-wall tube steam generator for commercial application. In 1981, a fabrication release design review resulted in resolution of all key outstanding technical items and release for fabrication of the model was granted to Westinghouse by the U.S. Department of Energy.

Several ongoing procurements continue at this time, such as double-wall tubing, welding heads, post-weld heat treatment equipment, and rod anode X-ray equipment for production use during the fabrication of the 70-MWt model. At the present time, production welding of nozzles and shell barrels is progressing well and structuring of the tube bundle is expected to begin in October 1982. Tube-to-tubesheet welding,

Table 3 Comparison of plant and model steam generators

	PLANT STEAM GENERATOR	MODEL STEAM GENERATOR
RATING MWt	293	70
UNIT LENGTH, FEET (M)	85.6 (26.1)	81.6 (24.9)
TUBE LENGTH, FEET (M)	76.9 (23.4)	76.9 (23.4)
TUBE O.D., INCH (MM)	0.812 (20.6)	0.812 (20.6)
NUMBER OF TUBES	3366	804
SHELL O.D., INCH (MM)	92 (2337)	47 (1194)
SODIUM INLET TEMPERATURE °F (°C)	900 (482)	900 (482)
STEAM OUTLET TEMPERATURE °F (°C)	855 (457)	855 (457)
STEAM OUTLET PRESSURE PSIA (MPa)	2290 (15.8)	2290 (15.8)

PWHT, and radiography of the welds are scheduled for second quarter of 1983. Barring any major unforeseen difficulties with the procurements and the Westinghouse fabrication requirements of the existing design, shipment of the highly instrumented model is scheduled from the Westinghouse Pensacola, Florida facility in July 1984 for testing at the DOE Energy Technology Test facility near Los Angeles in 1985. A brief comparison of the model being fabricated currently and the plant unit design for future commercialization is presented in Table 3. As can be seen, the model is 25 percent the capacity of the plant-size unit, but is fully prototypic in terms of length (except for steam heads), operating conditions, and manufacturing processes.

Acknowledgments

We would like to achnowledge the many capable materials suppliers, fabricators, and vendors that contributed to the developments reported herein. Several individuals in the Breeder Reactor Components Project, too many to name individually, contributed significantly to the success of the development programs. We also gratefully acknowledge Argonne National Laboratory/Department of Energy management and funding, the reviewers of this paper C. R. Adkins and W. G. Harris, and the typist Ms. Dawn Clark.

References

1 First International Conference on Materials for Nuclear Steam Generators - Gatlinburg, Tenn., *Proceedings*, *Nuclear Technology*, Vol. 28, No. 3, 1976.

2 *Proceedings International Conference on Liquid Metals Technology in Energy Production*, Champion, Pa., May 3-6, 1976, CONF 760503-P1 and P2, 1977.

3 International Conference on Ferritic Steel for Fast Breeder Reactor Steam Generators, May 30-June 2, 1977, BNES London, England.

4 *Proceedings Second International Conference on Liquid Metals Technology for Energy Systems*, Richland, Wash., Apr. 20-24, 1980, CONF 800401, 1980.

5 Materials Performance in Nuclear Steam Generators, Conference held St. Petersburg Beach, Fla., Oct. 6-9, 1980; *Nuclear Technology*, Oct. and Nov. 1981.

6 Stone, C., et al., "Experience with LMFBR Steam Generators - U.S. Design," *Nuclear Technology*, Vol. 55, No. 1, Oct. 1981, pp. 66-87.

7 Lohmeier, A., Westinghouse paper in U.S./USSR LMFBR Steam Generator Seminar, Los Angeles, Calif., 1974.

8 Adkins, C. R., Bongaards, D. J., and Smith, P. G., "Double-Wall Tube Steam Generator for Breeder Nuclear Plants," ASME Paper No. 81-JPGC-NE-2, 1981.

9 Adkins, C. R., and Bongaards, D. J., "Straight Double-Wall Tube Steam Generator with Third Fluid Leak Detection Capability for LMFBR Application," ASME Paper No. 80-C2/NE-27, 1980.

10 Kiefer, J. H., and Hebbar, M. A., "Tube to Tubesheet Welding Development for the Westinghouse LMFBR Steam Generator," Topical Meeting on LMFBR Steam Generators, Genoa, Italy, Nov. 30-Dec. 2, 1981, to be published as proceedings.

11 Uber, C. F., and Langford, P. J., "Analysis of Prestressed Double-Wall Tubing for LMFBR Steam Generators," ASME Paper No. 81-PVP-25, 1981.

12 Sessions, C. E., and Uber, C. F., "Steam Generator Tubing Development for Commercial Fast Breeder Reactors," *Nuclear Technology*, Vol. 55, No. 2, Nov. 1981, pp. 280-288.

13 Sessions, C. E., Reynolds, S. D. Jr., Hebbar, M. A., Lewis, J. F., and Kiefer, J. H., "Materials Development for a Fast Breeder Reactor Steam Generator Concept," *Nuclear Technology*, Vol. 55, No. 2, Nov. 1981, pp. 270-279.

14 Duke, J. M., Hebbar, M. A., Reynolds, S. D., and Lewis, J. F., "Material Considerations for Large Sodium Heat Steam Generators," ANS Abstract announcement of Winter AWS meeting Nov. 27-Dec. 2, 1977.

15 Bieberbach, G., and Hebbar, M. A., "Design of Tube Supports for the Westinghouse Straight Double-Wall Tube Liquid Metal Steam Generator," paper submitted for presentation at ASME meeting Oct. 1982 in Denver.

16 Hebbar, M. A., "A Metallurgical and Manufacturing Solution to Large Diameter Thick Walled Expansion Joints," Paper No. 82-PVP-5, ASME Pressure Vessel and Piping Conference and Exhibition, June 27-July 2, 1982, Orlando, Fla.

17 Griess, J. C., DeVan, J. H., and Maxwell, W. A., "The Effect of a High Heat Flux on the Oxidation of 2-1/4, Cr-1Mo Steel Tubing in Superheated Steam," *Material Performance*, Vol. 19, 1980, pp. 46-52.

18 Cohen, P., Padden, T., Schmidt, D., and Efferding, L. E., "Accelerated Corrosion Testing of a Sodium Heated 2-1/4 Cr-1Mo Steel Steam Generator Tube," Paper No. 65, International Conference on Ferritic Steel for Fast Reactor Steam Generators May 30-June 2, 1977, BNES, London, England.

19 Efferding, L. E., and Hwang, J. Y., "Interim Evaluation of Exposure Conditions for the Water-Side Corrosion Test of a Sodium Heated Steam Generator Evaporator Model Employing a Duplex Tube," ASME Paper No. 76-JPGC-NE-5, June 16, 1976.

20 Rush, D. J., Hampton, L. V., Spalaris, C. N., Schmidt, D. K., and Padden, T. R., "Corrosion and Deposition Effects under DNB Conditions," Paper No. 4, First Joint US/Japan Seminar on LMFBR Steam Generators, Japan, CONF 780203, Vol. 1, Feb. 1978.

21 Simpson, J. L., Robles, M. N., Spalaris, C. N., and Moss, S. A., "Water Chemistry of Breeder Reactor Steam Generators," *Nuclear Technology*, Vol. 55, No. 2, Nov. 1981, pp. 339-348.

22 Cohen, P., "Chemical Thermohydraulics of Steam Generating Systems," *Nuclear Technology*, Vol. 55, No. 1, Oct. 1981, pp. 105-116.

Materials Development for HTGR Heat Exchangers

W. R. Johnson

D. I. Roberts

GA Technologies, Inc.
San Diego, Calif. 92138

High-temperature, gas-cooled reactors (HTGR's) are uranium/thorium-fueled, graphite-moderated, helium-cooled systems capable of producing high-temperature primary coolant. Several variants of this system are under active development in the United States and worldwide. In one version, the primary coolant heat is transferred to steam generators producing 538°C/16.5 MPa steam for use in electricity generation or process heat applications. The materials and design technology for steam generators in this system are well developed, relying heavily upon prior experience with fossil-fired steam generators and the steam generators of the commercial HTGR's. The major work that remains to be done is to complete qualification of the materials and to respond to evolving rules pertinent to elevated-temperature nuclear design and construction. Other versions of the HTGR generate much higher primary coolant gas temperatures (850° to 950°C) and exchange this heat, through intermediate heat exchangers (IHX's), to a secondary loop for higher temperature process heat applications. Although IHX's for these systems are typically pressure-balanced (low-stress) units, their design involves several challenges, including the potential interactions between structural materials and impurities present in the HTGR primary coolant. Considerable work is required to qualify materials for IHX applications, including detailed mechanical property characterization, determination of environmental influences on performance, provision of welding materials and procedures for producing joints of adequate strength and integrity, and provisions for wear protection. Some of the work currently under way addressing these issues is described.

Introduction

High-temperature gas-cooled reactor systems have been under development for 20 years or more, and during that time several have been constructed (see Table 1). The three early reactors were small prototype units. The FSV and THTR reactors are demonstration plants designed for commercial power generation.

Operating experience with the reactor systems has generally been very good. Although the FSV reactor experienced several problems during its early startup phase that caused some delay in the reactor schedule, performance has been satisfactory since the plant began operation in 1976. The relatively low fission product levels in the primary coolant systems in these reactors have allowed plant operation and maintenance with minimum exposure of operating personnel to radiation. During the later stages of operation of the Dragon reactor and during recent operation of the AVR, the potential of these reactor systems for generating very high primary coolant outlet temperatures (up to 950°C) has also been demonstrated.

As a result of this prior experience, interest exists in several countries of the world in further developing this reactor system for a variety of potential applications. In the United States interest has focused upon four potential variants (Table 2). The HTGR-SC is aimed at electricity generation and is similar in concept to the FSV, Peach Bottom, and THTR reactors. The HTGR-SC/C is aimed at exploiting the HTGR in a situation where maximum economic benefit can be derived from the potential of the system for electricity generation and for the generation of steam for chemical process applications. The HTGR-GT and HTGR-PH variants are more advanced systems characterized by significantly higher primary coolant outlet temperatures. Both these systems have received considerable study in recent years and the process heat system, in particular, continues to receive considerable effort in the United States, Germany, and Japan.

Each HTGR variant features heat exchangers that must perform efficiently and reliably for the advantages of the reactor system to be realized. In the HTGR-SC and SC/C versions, the heat exchangers are steam generators that transfer heat from the high-temperature (~700°C) helium gas primary coolant to produce 538°C/16.5 MPa steam in the secondary coolant. In the HTGR-GT direct cycle, there are large recuperators that exchange heat between the hot and cold loops of the helium coolant and precoolers that extract heat from the helium gas immediately prior to compression and recirculation. In the indirect cycle version of the HTGR-

Contributed by the Nuclear Engineering Division and presented at the Joint Power Generation Conference, Denver, Colorado, October 17-21, 1982. Manuscript received at ASME Headquarters August 6, 1982. Paper No. 82-JPGC/NE-14.

Table 1 HTGR's constructed to date

Name	Size [MW(t)]	Sponsor/Owner	Location	Type	Status
Dragon	20	Organization for Economic Cooperation and Development/Nuclear Energy Agency	Winfrith, U.K.	Experimental unit	Operated 1966 to 1976, now decommissioned
Arbeitsgemeinschaft Versuch Reaktor (AVR)	46	Kernforschungsanlage	Julich, Federal Republic of Germany (FRG)	Experimental unit	In operation since 1967
Peach Bottom	115	U.S. Atomic Energy Commission (AEC) [U.S. Department of Energy (DOE)]/Philadelphia Electric Company	Pennsylvania	Small prototype	Operated 1967 to 1974, now decommissioned
Fort St. Vrain (FSV)	842	AEC (DOE)/Public Service Company of Colorado	Colorado	Demonstration reactor	In operation since December 1976
Thorium Hoch Temperatur Reaktor (THTR)	762	Vereinigte Elecktriziatswerke Westfalen	Schmeehausen, FRG	Demonstration reactor	Scheduled for startup 1985

Table 2 HTGR systems

Reactor Type	Maximum Primary Coolant Temperature (°C)	Remarks
Steam cycle, electricity generation (HTGR-SC)	700 to 750	FSV and Peach Bottom of this type
Steam cycle/cogeneration (HTGR-SC/C)	700	
Gas turbine (HTGR-GT)	850	May be direct or indirect cycle
Process heat (HTGR-PH)	850 to 950	Indirect cycle

Table 3 Principal features of HTGR steam generators

Plant	Maximum Primary Coolant Temperature (°C)	Steam/Water Conditions		Steam Generator Configuration and Type
		Temperature (°C)	Pressure (MPa)	
Dragon	830	203	1.6	Not used for power generation
AVR	950	505	7.5	Involute tube
Peach Bottom	700	536	10.2	U-tube forced recirculation
FSV	775	Main steam 538 Reheat steam 538	16.5 4.9	Once-through helical bundles with reheat
THTR	750	Main steam 530 Reheat steam 530	18.0 5.6	Once-through helical bundles with reheat
HTGR-SC	690	540	16.5	Once-through helical bundles

Table 4 Behavior considerations important in selection of materials for HTGR steam generators

1. Tensile, creep-rupture, low-cycle fatigue and creep-fatigue interaction behavior
2. Interaction of materials with environments (impure helium, steam/water, temperature) and effects on mechanical properties
3. Thermal aging and embrittlement
4. Fabricability (weldability, formability, availability of required product forms, etc.); matching or appropriate properties in welds
5. Resistance to friction wear and adhesion in HTGR helium
6. Cost

GT and the HTGR-PH systems, IHX's transfer heat from the primary to the secondary helium loops at temperatures up to 950°C.

The heat exchangers are critical components from performance, economic, and safety viewpoints and achievement of the necessary integrity requires the availability of substantial materials and fabrication technology, particularly for the most challenging of the heat exchangers - steam generators and the IHX. This paper reviews the status of the development of pertinent heat exchanger materials technology for HTGR steam generators and IHX's.

Steam Generator Materials Technology

Four of the reactor systems shown in Table 1 (Peach Bottom, FSV, THTR, and HTGR-SC) have featured steam generators that produce modern, high-pressure, high-temperature steam (Table 3). The Peach Bottom reactor was operated for 7 years and has been shut down and decommissioned, and the steam generators have been examined. The FSV reactor has entered commercial operation, and substantial operating experience has been accumulated. The THTR is under construction in the FRG and substantial fabrication-related experience has been developed.

As a result of this prior experience, considerable knowledge and technology exist in all aspects of HTGR steam generators, and this is reflected in current reactor design activities.

Several versions of the HTGR feature a multicavity prestressed concrete reactor pressure vessel (PCRV), which houses the components of the primary coolant system. Figure 1 shows a typical layout of a steam-generating version of the plant, and Fig. 2 presents a schematic flow diagram.

Since the cost of an HTGR plant is influenced by the size of the PCRV, it is desirable that the steam generator occupy a relatively small volume. As a result, compact high-performance steam generator designs are employed. In current U.S. HTGR designs, the steam generators are once-through, uphill boiling units in which a large fraction of the heat transfer section consists of densely packed, helically wound tubes with the water/steam on the inside of the tube and the primary coolant helium on the outside. A typical wound, once-through steam generator module used in the FSV reactor is shown in Fig. 3.

The key considerations governing the selection of materials for steam generators are summarized in Table 4. In addition, selection is strongly influenced by earlier HTGR experience supplemented by relevant operating experience with fossil-fired steam generators. (It should be noted that HTGR steam generators generate steam at temperatures and pressures similar to those found in most modern fossil-fired power plants.) Alloy 800H, which was used as the superheater/reheater of the Peach Bottom, FSV, and THTR plants, will be employed for the higher-temperature superheaters of the HTGR-SC/C system. The lower-temperature superheater, together with the evaporator and economizer sections, will be fabricated from 2-1/4 Cr - 1Mo in the annealed condition, based on prior HTGR and fossil plant experience.

In HTGR's, the steam generator tubing constitutes the primary coolant boundary, and as such, design, analysis, and fabrication are governed by Section III and Code Cases N-47

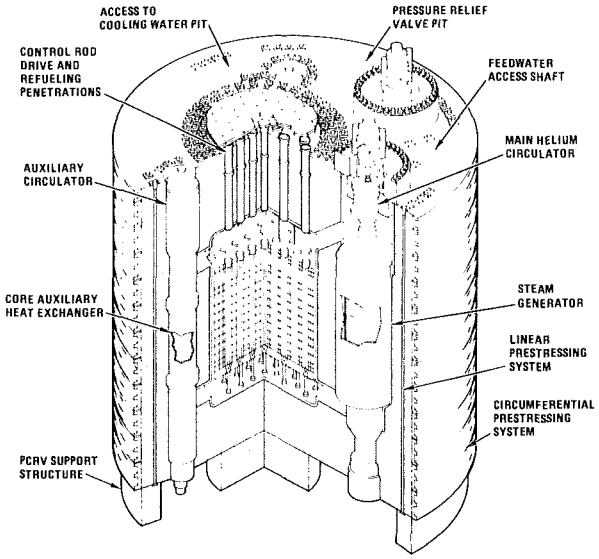

Fig. 1 HTGR-SC/C nuclear steam supply system

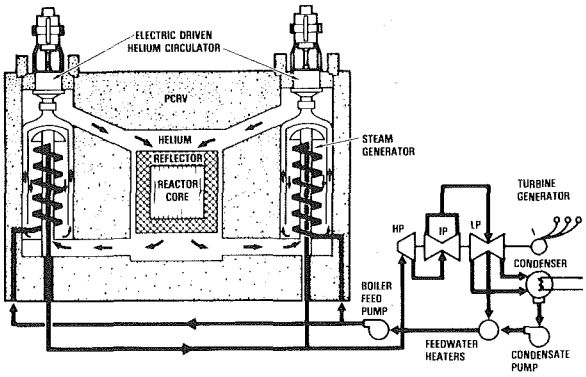

Fig. 2 Schematic flow diagram of HTGR-SC/C

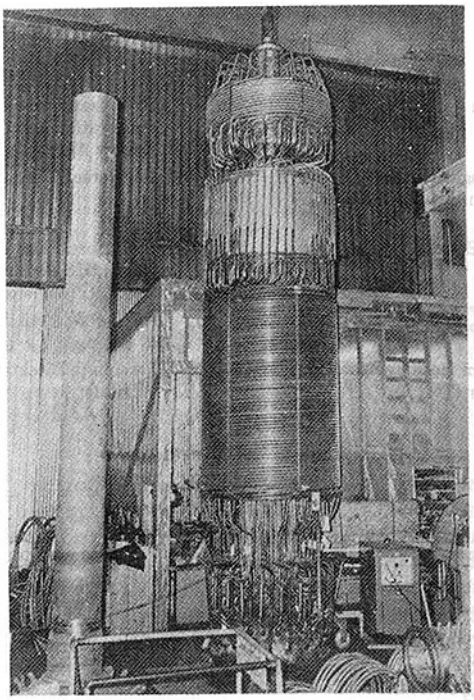

Fig. 3 FSV steam generator module

Table 5 Variables under study in fatigue and creep-fatigue program on Alloy 800H

Temperature range	538° to 760°C
Test conditions	Continuous cycling
	Hold time (creep-fatigue) tests with holds in tension, compression, or both
Environmental effects	Tests in air and HTGR helium

Table 6 Expected range of impurities in primary coolant of HTGR-SC/C

Impurity	Expected Range (Pa)
H_2	9-18
H_2O	0.1-5
CO	5-10
CO_2	1-2
CH_4	0.5-1

and N-48 of the ASME Boiler and Pressure Vessel Code. Analysis in accordance with these rules requires the availability of complete data adequate to form a basis for assessment of time-dependent and time-independent properties, such as tensile, creep, rupture, fatigue, creep-fatigue, and deformation behavior throughout design life. In addition, Case N-47 requires that the designer explicitly account for any environmental degradation of materials that may occur in service. Since HTGR steam generators are designed for a 40-year life, a substantial body of data is required to permit all the required analyses to be performed. Accordingly, even though there is substantial extant data on Alloy 800H and 2-1/4 Cr - 1Mo, additional information is required to allow a complete assessment in accordance with these rules. Generation of this information is the purpose of an important part of the U.S. DOE HTGR materials programs.

With respect to the properties noted in Table 4, the basic mechanical property data for both Alloy 800H and 2-1/4 Cr - 1Mo are contained in ASME Code Case N-47. However, because of the strong influence of creep-fatigue in component design, considerable work is under way to better characterize this behavior aspect of Alloy 800H. The variables under current study are shown in Table 5.

The tests employ parallel-section (as opposed to hourglass) specimens with axial extensometers. This permits accurate testing at the small strain ranges that are relevant to the design of reactor components. As this testing progresses, it has become apparent that the observed sum of creep and fatigue damage fractions at failure for Alloy 800H test specimens can often be substantially less than unity, particularly in tests that are performed at near design conditions, such as at lower temperatures and lower strain ranges and with larger hold times. The significance of this is under current study.

A unique feature of the HTGR is the presence of the helium primary coolant gas. Helium is, of course, chemically inert. However, there are practical limits to the purity levels that can be obtained in a circulating primary coolant gas, and interactions can occur between the impurities and the structural materials. Table 6 illustrates some of the typical impurities expected to be present in the primary coolant of an HTGR-SC/C plant during normal operation. Examination of these impurity species from a thermodynamic standpoint indicates, as shown in Fig. 4, that a wide range of material responses can be expected. For example, within the expected impurity range for the SC/C system it is possible to find environments that are decarburizing to both high- and low-chromium alloys and environments in which high-alloy materials may carburize while low-chromium ferritic steels will be decarburized. Analysis of the data generated in laboratory experiments using a range of possible simulated HTGR primary coolant gases shows that these phenomena are, in fact, observed. Figure 5 shows data obtained on the exposure of 2-1/4 Cr - 1Mo to a simulated HTGR helium

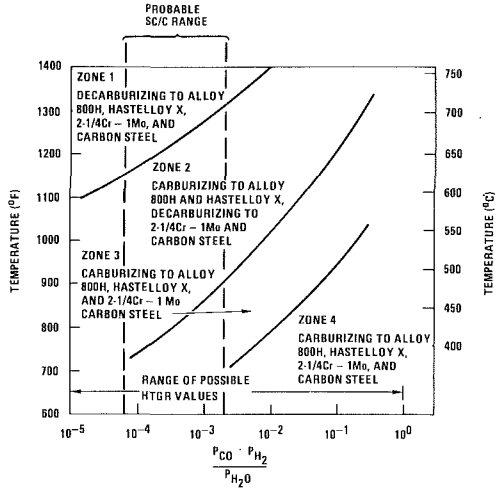

Fig. 4 Carburizing/decarburizing potential of HTGR primary coolant based on the CO + H ⇌ C + H_2O reaction (ignoring the influence of CH_4)

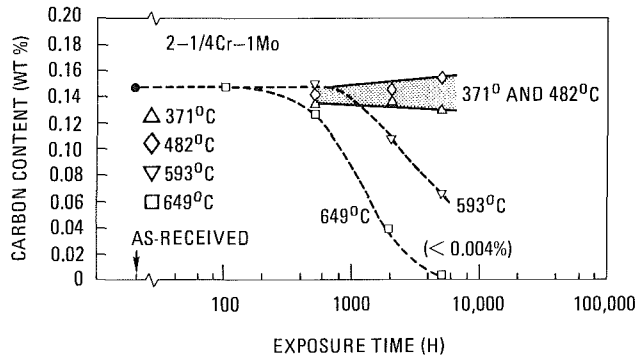

Fig. 5 Bulk carbon content of 2-1/4 Cr · 1Mo after exposure in an HTGR helium environment containing 20 Pa H_2, 10 Pa CO, 2 Pa CH_4, 5 Pa H_2O, and 0.5 Pa CO_2 for various times in comparison with that of as-received material. (Carbon content detection limit is 0.004 wt percent)

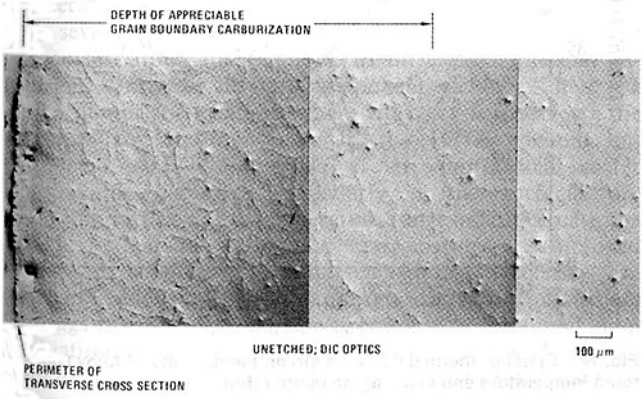

Fig. 6 Carburization in Alloy 800H creep specimen (0.53 percent ϵ_c) observed after 19 000 hrs exposure in dry, controlled-impurity helium at 800°C

environment at a variety of temperatures. As indicated, at high temperatures significant decarburization occurred. Figure 6 shows the microstructure of Alloy 800H exposed to simulated HTGR coolant gas for 19,000 hrs and illustrates carburization that occurred as a result of that exposure.

Environmental interactions such as carburization and decarburization can exert a significant influence on the properties of structural materials, and substantial testing has been performed to assess these effects. The influence of the helium environment on fatigue properties is generally benign (Fig. 7). With respect to creep-rupture properties, data now available suggest that, while there is some influence, effects

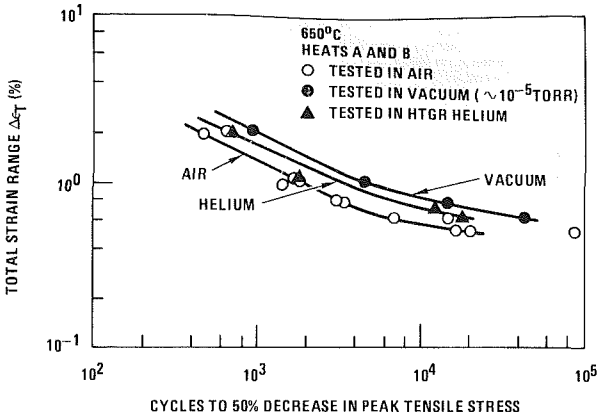

Fig. 7 Number of cycles to 50 percent decrease from maximum value of peak tensile stress as a function of total axial strain range for Alloy 800H specimens tested under strain control in air, vacuum, and HTGR helium at 650°C (strain rate = 4 × 10^{-3} s^{-1})

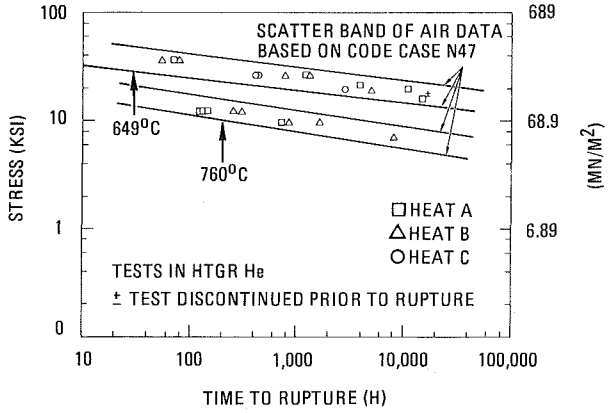

Fig. 8 Stress-rupture data of Alloy 800H (9.5-mm-dia specimens) tested in HTGR helium containing 150 Pa H_2, 45 Pa CO, 5 Pa CH_4, 5 Pa H_2O, and 0.5 Pa Co_2

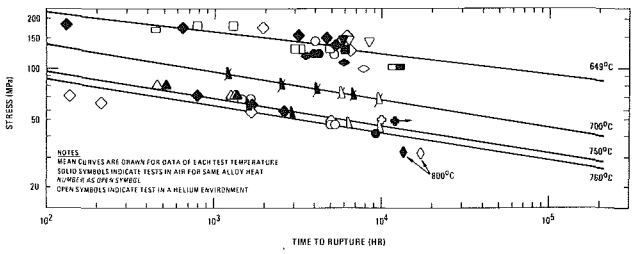

Fig. 9 Stress-rupture values for Alloy 800 and Alloy 800H in air and in *controlled-impurity helium test environments. (Test materials were* Alloy 800H or Alloy 800 having wt percent C ≥ 0.025 and grain size coarser than ASTM No. 5.)

seem generally to be fairly small. This is illustrated, in the case of Alloy 800H, by Figs. 8 and 9. Figure 8 shows that data generated in a variety of helium environments generally fall within the expected scatterband of air data for this alloy. Similarly, Fig. 9 shows that data from air and helium tests on the same heats of material generally fall within the same scatterband. However, more detailed examination (Fig. 10) shows that the HTGR helium environment does have some minor degrading effect. Figures 11 and 12 illustrate similar effects for 2-1/4 Cr - 1Mo steel.

At the temperatures that prevail in HTGR steam generators, many of the high-temperature alloys of interest undergo microstructural changes that may cause embrittlement, which occasionally can be serious. Because it is necessary to show that reactor structures can absorb high-strain-rate events (such as seismic loads) after extended high-

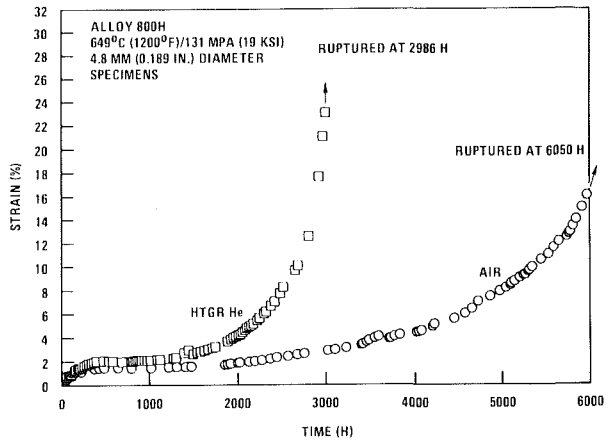

Fig. 10 Comparison of creep curves for one heat of Alloy 800H tested in helium and air environments (helium impurities 150 Pa H_2, 45 Pa CO, 5 Pa CH_4, 5 Pa H_2O, and 0.5 Pa CO_2)

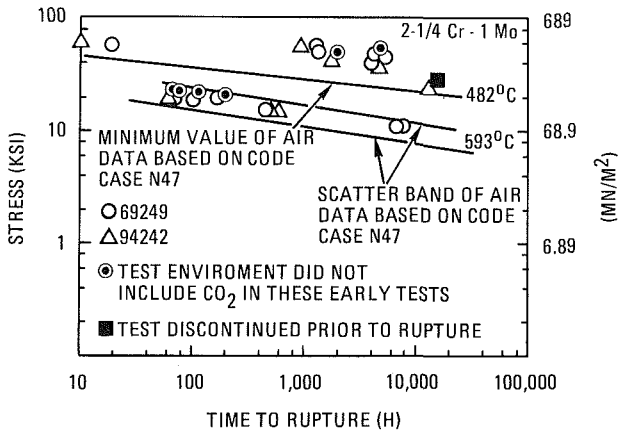

Fig. 11 Comparison of stress-rupture behavior of several heats of annealed 2-1/4 Cr - 1Mo steel in HTGR helium and the scatter band of air data for the alloy

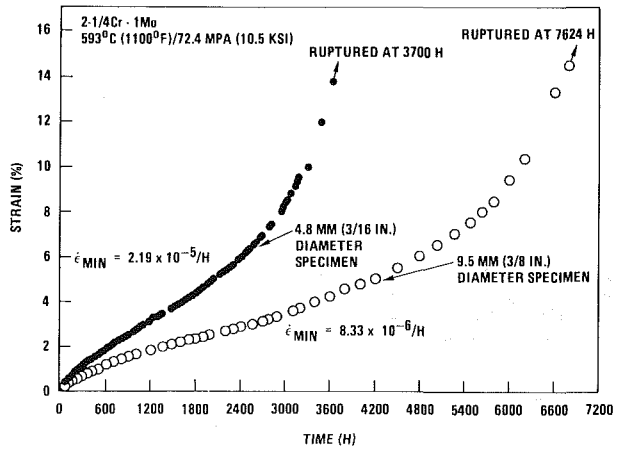

Fig. 12 Comparison of creep curves for one heat of 2-1/4 Cr - 1Mo (4.8 and 9.5-mm dia specimens) tested at 593°C and 72.4 MPa in HTGR helium (helium impurities same as Fig. 8)

temperature operation, it is important to understand the extent to which aging causes changes in properties. Figures 13 and 14 indicate changes produced in the tensile characteristics of Alloy 800H as a result of 20,000 hrs aging at various temperatures. Figure 15 illustrates a general trend of toughness of this alloy with extended aging at different temperatures. The Charpy V-notch data shown in Fig. 15 are a convenient way of illustrating the changes that occur. However, for design purposes, more quantifiable fracture

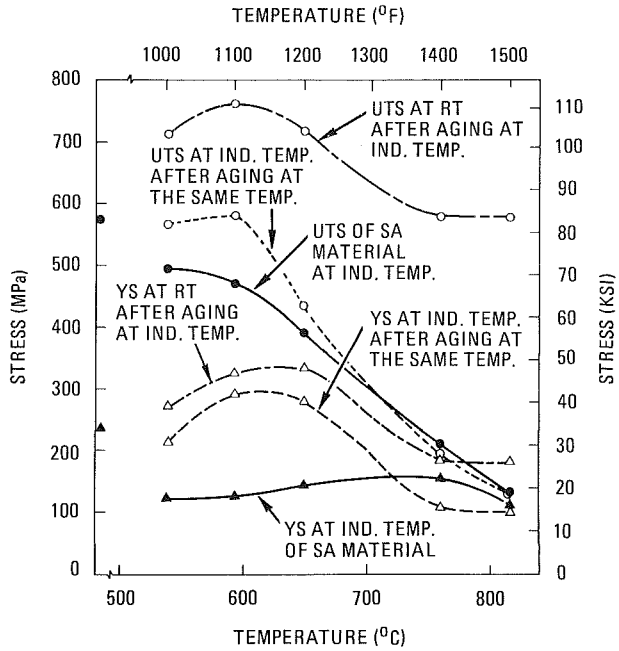

Fig. 13 Effects of 20,000-hrs thermal aging (in air) on the strength of Alloy 800H at room temperature and at the aging temperature (grain size No. 3, 0.05 wt percent C, 0.39 wt percent Al, 0.44 wt percent T)

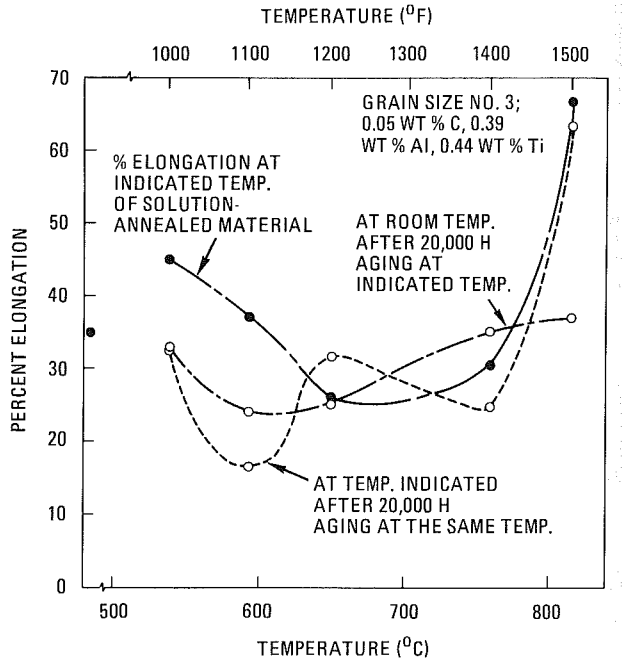

Fig. 14 Effect of thermal aging (in air) on the ductility of Alloy 800H at room temperature and at the aging temperature

toughness information (such as that generated by compact tension testing) is required, and such data are currently being generated. However, in general, it appears that this alloy retains adequate toughness after long-time aging.

The HTGR steam generator components are, of course, fabricated by welding, and it is important to establish that the properties of the resulting weld joints are compatible with those of the base metal. This is being assessed in a program of elevated-temperature testing of all-weld-metal and cross-weld specimens on Alloy 800H and 2-1/4 Cr - 1Mo. Data available to date suggest that, on the average, the rupture strengths of the weld metals used to join Alloy 800H to itself and to join 2-1/4 Cr - 1Mo may be slightly lower than those of the base metal at the longest times/highest temperatures. Accordingly, consideration is being given to the introduction of weld metal

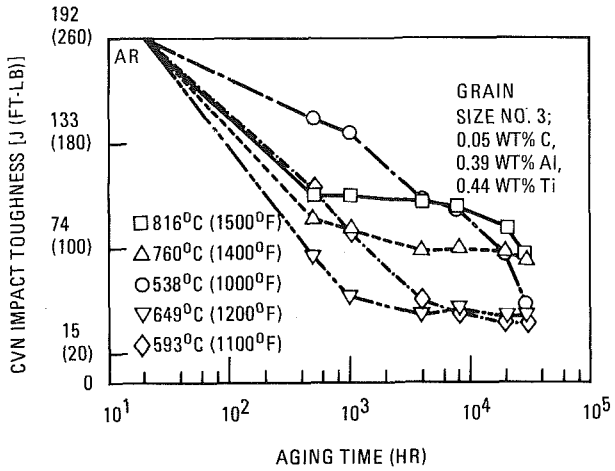

Fig. 15 Room-temperature CVN impact strength of one heat of Alloy 800H aged in air at various temperatures for up to 30,000 hrs

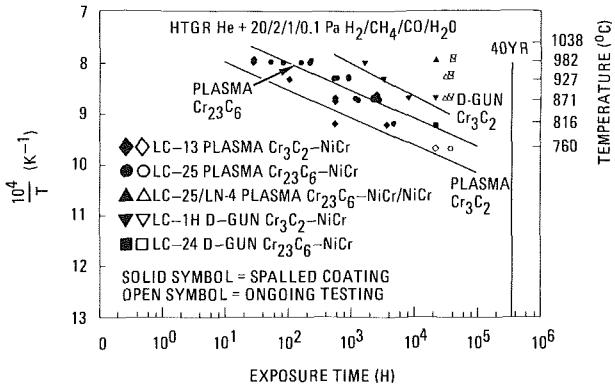

Fig. 16 Spallation chart of chromium carbide - nichrome coatings on Alloy 800H

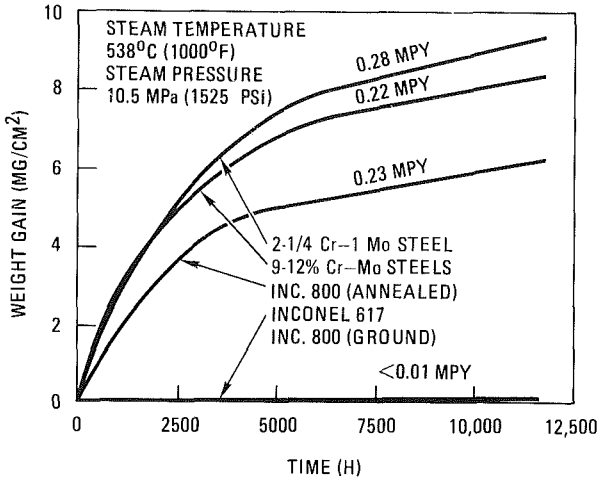

Fig. 17 Corrosion rate of candidate HTGR steam generator materials in superheated steam at 538°C

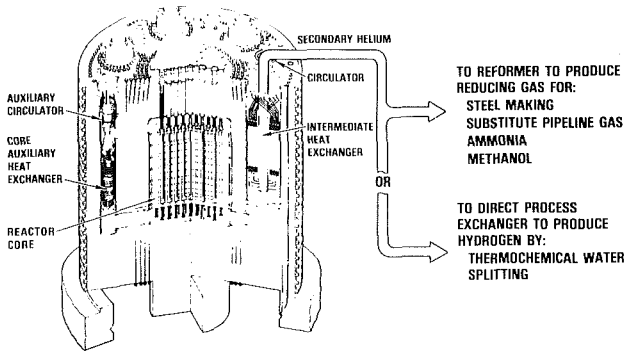

Fig. 18 Nuclear heart of an HTGR-PH system

factors into the allowable stresses used for long-time, high-temperature design with these materials.

In several regions of the HTGR steam generators, relative movements (due, for example, to differential thermal expansion) can occur between component surfaces. There are also a number of locations where vibratory forces create the potential for fretting wear. In the HTGR helium environment, such surfaces can, if left unprotected, suffer considerable damage, particularly if the surfaces are operating in the higher-temperature ranges. To decrease the potential effects of friction and wear, coatings are employed at critical locations. Chromium-carbide-based coatings are currently under study for this application. Evaluation of these coatings consists of sliding and fretting wear tests, including evaluation of the effects of sliding velocity, contact load, etc. In addition, it has been noted that after extended elevated-temperature exposure to HTGR helium, some of these coatings will undergo spallation (Fig. 16), and care must be taken to select a coating suitable for the intended service conditions.

The materials in the HTGR-SC/C heat exchangers are also exposed to water and steam environments, and it is important to establish the compatibility of the materials employed with these environments. The feed-water employed in the steam generator is, of course, of ultra-high purity, with pH and oxygen control. In general, the compatibility of the materials used in the steam generator with environments of this kind is well established. However, it was considered prudent to determine experimentally the long-time corrosion behavior of the materials used in the highest-temperature region of the steam generator in a representative steam environment. To this end, pertinent tests were performed by the Oak Ridge National Laboratory. These tests, which extended for 28,000 hrs, showed that corrosion rates of Alloy 800 were low, predictable, and satisfactory (Fig. 17) [1]. Another important consideration in the steam generators is the influence of steam flow velocity relative to causing erosion-corrosion of the low alloy steel components. Extensive tests were performed to show that erosion-corrosion behavior was satisfactory provided that pH was maintained in a specified regime, flow velocities were maintained at moderate values, and where appropriate, low alloy steels were employed.

Intermediate Heat Exchanger Materials Technology

The layout of the nuclear heart of a typical GA-designed HTGR-PH system is shown in Fig. 18. The function of the IHX in this system is to transfer heat from the primary to the secondary helium coolant. For process applications, it is economically desirable for the secondary loop to be able to deliver heat to the user process at relatively high temperatures (significantly above 800°C). As a result, the goal for the HTGR-PH system is to operate with core outlet temperatures of at least 850°C and, ultimately, 950°C. The key component limiting the ability to achieve these temperatures is the IHX.

To function at such elevated temperatures, several important features are designed into the IHX. For example, for all normal operation, the pressure in the primary and secondary coolant loops is balanced so that the pressure differential carried across the heat transfer tubing is essentially zero. As a result, relatively thin-walled tubing can be employed. In fact, in an actual IHX design, the wall thickness of the tubing is sized by the ability to carry the short-time loads that occur due to the pressure differential resulting from the accidental depressurization of one loop. The use of thin-walled tubing allows temperature differentials across tube

Table 7 Impurity levels expected in the primary coolant of the HTGR-PH system

Impurity	Concentration (Pa)
H_2O	0.05
H_2	50
CO	5
CH_4	5
CO_2	<0.1
N_2	1.5
O_2	<<<0.1

Table 8 Carburization-resistant coatings under study

Aluminized coatings	Preformed oxide coatings
Al	In air
Al + Cr	In controlled environments
Al + Pt	
Al + Rh	
M-Cr-Al-Y coatings	Claddings
M = Fe or Ni	Fe-Cr-Al-Mo-Hf
	Fe-Cr-Al-Y
	Udimet 720
	Inco clad 671/800H

walls to be minimized, thus minimizing creep-fatigue effects.

Another recognized feature of the IHX is that because of the very high operating temperatures, it may be appropriate to design the heat exchanger for a shorter life than the reactor as a whole.

Despite these design features, the design of a 950°C IHX remains very challenging, particularly with respect to materials selection. The types of material considerations that are important in an IHX are generally similar to those shown in Table 4 as pertinent to the steam generator. However, because of the much higher operating temperature of the IHX, many of the property changes and environmental effects considered are accelerated. In addition, new phenomena, such as evaporation of alloying elements, can become important considerations in very high-temperature IHX design.

One aspect of materials behavior over which temperature exercises a strong influence is the interaction of materials with primary coolant impurities. One reason for this is that, in an HTGR-PH system with 950°C core outlet temperature, it is expected that the combination of impurities present in the primary coolant gas will tend to be more reducing (less oxidizing) and more carburizing than in an HTGR-SC system. Typical expected HTGR-PH impurity values are shown in Table 7.

Extensive experimental evaluations of materials behavior in this environment have been carried out over the past ~10 years. The results of these programs clearly show that predicted carburization rates in an HTGR-PH environment such as that shown in Table 7 become very high for commercially available wrought alloys such as Alloy 800H, Inconel 617, and Hastelloy X at temperatures above ~700°C, as shown in Fig. 19.

Other alloys, such as the cast nickel-base superalloys and MoTZM show much lower carburization rates. However, these alloys are not suitable for the construction of large welded heat exchangers of thin-walled tubing.

The occurrence of carburization is undesirable from several standpoints. Severe carburization causes embrittlement of many wrought alloys. Figure 20 shows the effects of carburization on the room-temperature tensile ductility of Hastelloy X. Similar effects are observed for carburized Alloy 800H and Inconel 617.

Carburization has also been observed to produce dimensional changes (swelling) in some alloys [2] and has the potential to affect other key properties such as creep, rupture, fatigue, and creep-fatigue.

The potentially deleterious effects of carburization on wrought alloy candidate materials for the higher-temperature

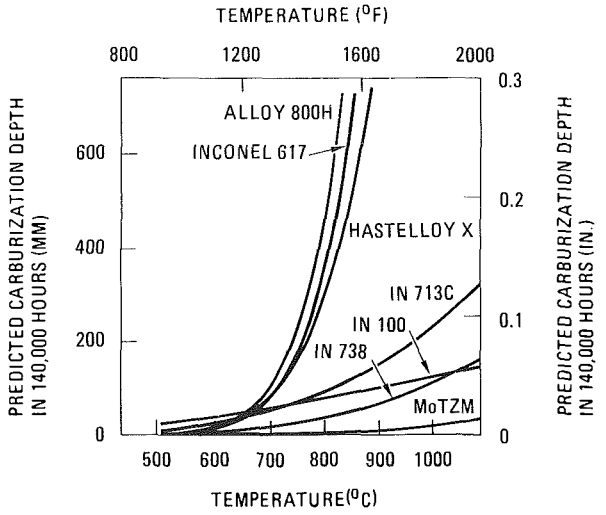

Fig. 19 Comparative carburization behavior of metals in HTGR-PH helium

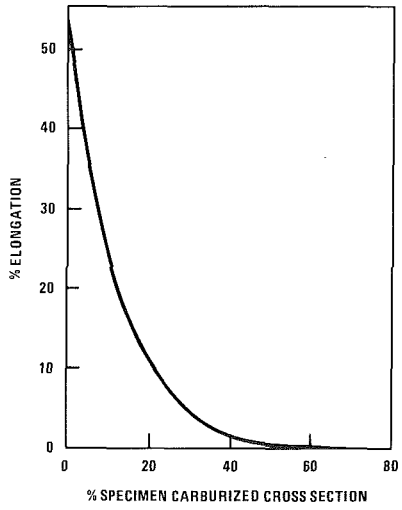

Fig. 20 Effect of precarburization at 1100°C on the room-temperature elongation of Hastelloy X

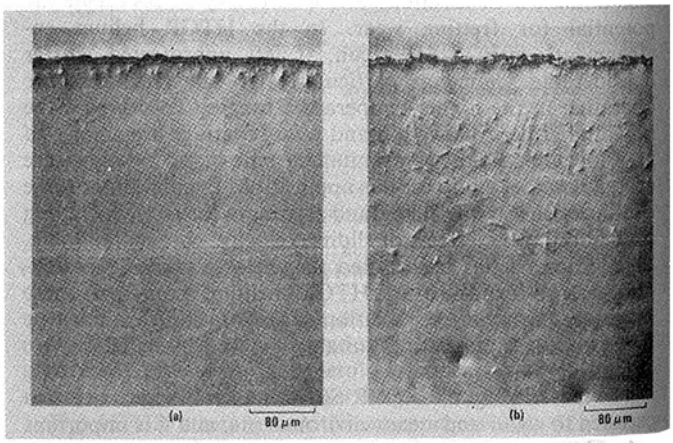

Fig. 21 Differential interference contrast photomicrographs showing Hastelloy X specimens exposed for 3000 hrs at 900°C in controlled-impurity helium containing 50 Pa H_2, 5 Pa CO, 5 Pa CH_4, and <0.05 Pa H_2O. Prior to exposure, specimen surface condition was (a) preoxidized for 10 hrs at 900°C and (b) standard machined surface.

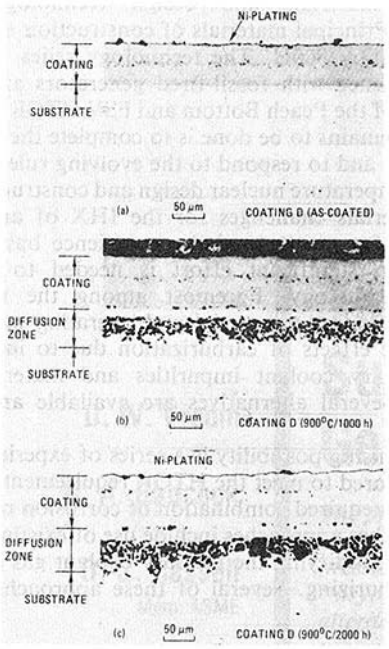

Fig. 22 Optical photomicrographs of aluminide-coated Hastelloy X showing (*a*) no pores in the as-coated condition and (*b*, *c*) extensive pores in the diffusion zone after exposure to controlled-impurity helium (50 Pa H_2, 5 Pa CO, 5 Pa CH_4, <0.1 Pa H_2O) at 900°C for 1000 and 2000 hrs, respectively (unetched)

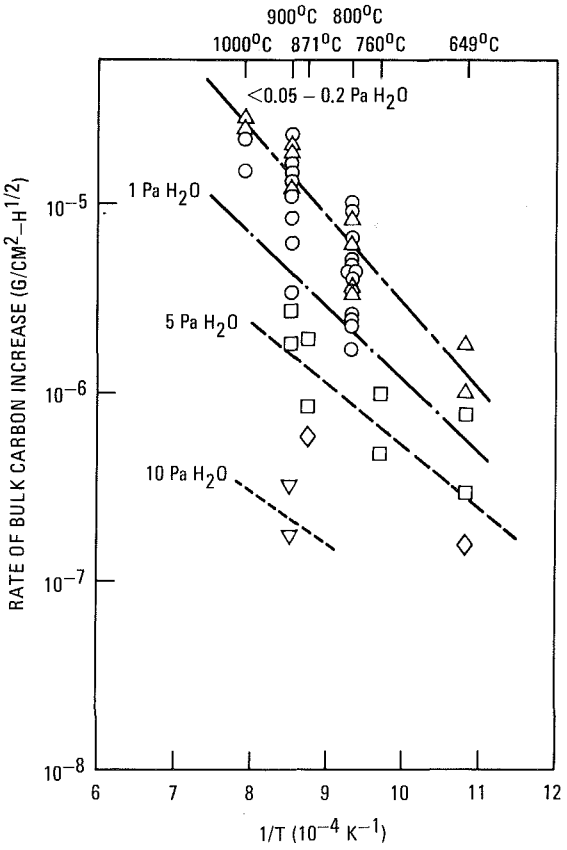

Fig. 23 Effect of moisture content on carburization behavior of Hastelloy X in helium containing 50 Pa H_2, 5 Pa CH_4, and 5 Pa CO

reactor systems have prompted a search for protective coatings. Table 8 lists the coatings and claddings being studied at GA.

Preformed oxides offer the potential for a simple means of protection against carburization, and preliminary results are very encouraging. For example, it has been shown that

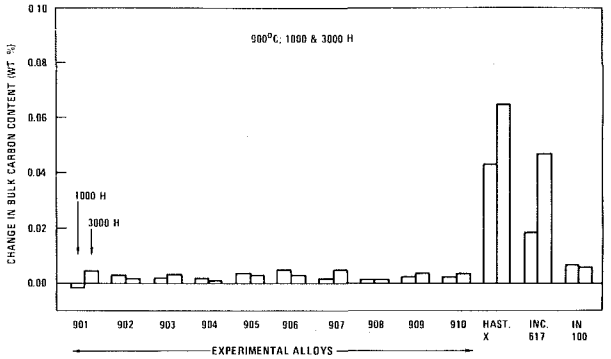

Fig. 24 Change in bulk carbon content of experimental alloys Hastelloy X, Inconel 617, and IN100 after 1000 and 3000 hrs exposure in simulated HTGR-PH helium at 900°C

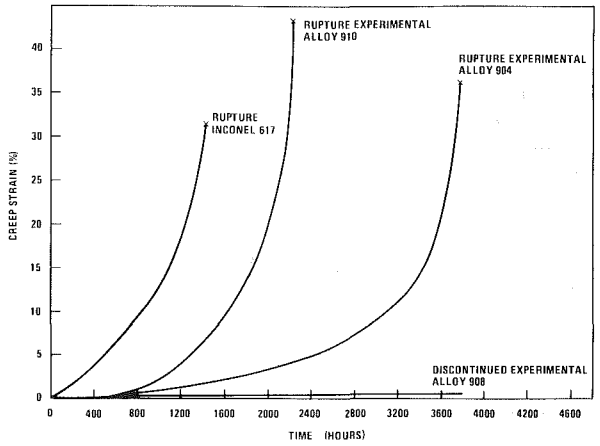

Fig. 25 Creep-rupture behavior in HTGR-PH helium of several alloys at 51.7 MPa and 900°C. (Alloy 908 discontinued after 3800 hrs)

preoxidation of Hastelloy X in air at 900°C for 10 hrs produces an oxide coating that is effective in protecting against carburization in HTGR helium. This is illustrated in Fig. 21, which shows the cross-sectional appearance of Hastelloy X exposed at 900°C for 3000 hrs with and without preoxidized coating.

Diffused coating methods, such as aluminizing, offer another potentially attractive solution, and exposures in HTGR helium show that such coatings can provide effective protection. However, a difficulty that has been observed with these coatings is the tendency during long-time exposure for formation of pores at the coating-substrate interface (Fig. 22). These pores are believed to be Kirkendall voids, and their formation and development can ultimately lead to coating separation. It is believed that this process will limit use of diffused coatings for this application unless coating compositions can be developed that minimize the interdiffusion of elements causing this effect.

Another possible approach to the control of carburization in wrought alloys is based on the observation that carburization rates in HTGR helium are very sensitive to the water content of the gas. As shown in Fig. 23, carburization rates for Hastelloy X can be reduced by almost two orders of magnitude with sufficient water present. Unfortunately, there are limits to the permissible water content in HTGR helium imposed by control of graphite oxidation. At present time, more work is needed to determine if a "window" exists within which satisfactory corrosion rates can be obtained in both metal and graphite components. It is also important to consider, in this regard, possible behavior in crevice regions or regions of semistagnant gas wherein the water content of the gas may be depleted, allowing rapid local carburization to occur.

A further approach to control of the environmental interaction issue is to develop 'tailored' alloys intrinsically suitable for this application. Work in this direction is underway and preliminary results look encouraging. A series of experimental alloys have been developed in which the surface protection against carburization results from the formation of surface films of aluminum and titanium oxides. (These oxides are stable under all credible HTGR operating conditions.) To permit the preferential formation of these oxides, the alloys have a low chromium content. Strengthening in the alloys is achieved through the use of molybdenum and tungsten together with the effects of aluminum, titanium, carbon, and zirconium. Initial results for these alloys are most encouraging. Tests in HTGR-PH helium have shown that carbon pickup in the experimental alloys is very low, compared to Hastelloy X, Inconel 617, and Alloy 800H (Fig. 24). Mechanical property tests have shown several of the experimental alloys to possess excellent creep and rupture strength (Fig. 25) with good retention of toughness and ductility. Tests on additional heats of these alloys are currently underway to more fully establish their capability and potential.

Clearly, for an IHX, there are many materials issues that will require development and qualification. These will include protective coatings to decrease the effects of friction and wear and vibration, development of welds with adequate high-temperature properties, and an improved understanding of creep-fatigue behavior at these very elevated temperatures and related effects. However, establishment of these data must await completion of the basic studies to identify viable candidate materials of construction.

Conclusions

Heat exchangers play a key role in HTGR's, and considerable materials technology is required to support their design. For the HTGR-SC steam generators, there is considerable prior experience and established knowledge. Accordingly, materials and design technology are well developed. Principal materials of construction are 2-1/4 Cr - 1Mo and Alloy 800H. The technology relies heavily upon prior experience with fossil-fired generators and the steam generators of the Peach Bottom and FSV HTGR's. The major work that remains to be done is to complete the qualification of materials and to respond to the evolving rules pertinent to elevated-temperature nuclear design and construction.

The materials challenges for the IHX of an HTGR-PH system are far greater and the experience base is far less. Accordingly, significant effort is needed to develop the required technology. Foremost among the issues to be resolved is finding a material and operating mode that will mitigate the effects of carburization due to interaction between primary coolant impurities and materials of construction. Several alternatives are available and are being explored.

One promising possibility is a series of experimental alloys that are tailored to meet the HTGR requirements and appear to offer the required combination of corrosion resistance and strength. Other approaches include use of existing alloys with coatings or modifying the primary coolant gas impurities to be less carburizing. Several of these approaches are under current study.

Acknowledgment

This work was performed in part under Department of Energy Contract DE-AT03-76ET35301.

References

1 Greiss, J. C., and Maxwell, W. A., "The Corrosion of Several Alloys in Superheated Steam at 482° and 538°C," Oak Ridge National Laboratory Report ORNL/TM-6465, Nov. 1978.

2 Inouye, H., and Rittenhouse, P. L., "Relationship Between Carburization and Zero-Applied-Stress Dilation in Alloy 800H and Hastelloy X," in *Proceedings of the IAEA Specialists Meeting on High-Temperature Metallic Materials for Application in Gas-Cooled Reactors, Vienna, Austria, May 4-6, 1981*," Austrian Research Center, Seibersdorf, Austria, p. L-1.

Thermal/Hydraulic Tests of Tube Supports in a Multitube Steam Generator Model

D. W. Vroom

D. A. Babcock

D. S. Cassell
Mem. ASME

CE Power Systems,
Combustion Engineering, Inc.
Windsor, Conn.

The presence of tube supports in PWR steam generator tube bundles creates regions of restricted flow which may result in altered heat transfer effects and increased pressure drop. One heat transfer effect which can occur is localized vaporization or "dryout." At higher heat flux levels this may result in a stable vapor blanket or an alternate wetting and drying occurring with an accompanying increase in the local tubewall surface temperature. A test program was conducted to determine the thermal/hydraulic conditions at the inception of the tubewall temperature excursion for selected tube support designs and to measure the pressure drop across the supports using a multitube steam generator model. Tests were performed on each of four tube supports over a broad range of shellside quality/subcooling conditions and pressures, temperatures, and mass flow rates that are prototypical of PWR steam generator operating conditions. Photographs and high-speed movies were taken of the flow both above and below the test piece.

Introduction

Tube supports used in the tube bundles of PWR steam generators have consisted of mechanical devices located at intervals along the tube bundle. Support configurations have consisted of plates with flow passages provided or a lattice work of interlocking metal strips or bars. Drilled plates with annular flow passages between the plate and tubes are examples of the plate type. Another example of the plate type is the trefoil which is a plate with three flow lobes integral with the hole for the tube. The "eggcrate," which consists of interlocking strips of slotted bars, is an example of the second type of support.

The presence of tube supports creates regions of restricted flow with altered flow patterns and increased pressure drop. An additional and very important effect is also the possibility of local complete vaporization, or "dryout," occurring in the tube/support flow passages and crevices. The thermal/hydraulic conditions at which dryout occurs are of particular interest because of the possibility of the deposition of dissolved solids with the occurrence of dryout. As long term build-up of solid depositions could have a deleterious effect, knowledge of the conditions at which dryout occurs would possibly provide a means to avoid this build-up.

A test program, sponsored by the Steam Generator Project Office of the Electric Power Research Institute, was conducted to determine the thermal/hydraulic conditions at which dryout occurred for selected tube supports. The liquid deficient heat transfer associated with dryout will cause a local tubewall temperature rise, i.e., a tubewall temperature excursion. The onset of this tubewall temperature excursion was measured and assumed to indicate the initiation of dryout. Pressure drops across the supports were also measured and photographic documentation of the flow both above and below the supports was made. Test conditions covered the range of typical PWR steam generator operating conditions.

Test Model, Instrumentation, and Loop Description

A schematic of the test model is shown in Fig. 1. The model consisted of a seven-tube bundle of 3/4-in. (19.1-mm) Inconel tubes on a 1-in. (25.4-mm) triangular pitch. Bayonet type tube assemblies were made up of 7/16-in. (11.1-mm) inner tubes for flow upward through the inner tube, reversed at the top, and downward through the annulus between the inner and outer tubes. A flange at the top of the model provided a means to remove and replace the individual tube supports. Separate inlets were provided at the bottom of the model for the steam and water of the secondary flow. Mixing occurred along the 18-in. heated length between the inlet plenums and the support location. A sleeve concentric with the tubes prevented water from flowing into the steam plenum. Water entered the bundle region through the annulus between the sleeve and tube. Steam entered the bundle region from the annulus through the sleeve and the top plate of the steam plenum. Two viewports in the model, located above and below the test support, consisted of windows of 2-in. (50.8-mm) dia quartz flat on the outside and contoured to a 1.5-in. (38.1-mm) radius on the inside.

Model instrumentation included thermocouples embedded in the walls of three tubes, six pressure taps along the model shell, and resistance temperature devices for measuring the

Contributed by the Nuclear Engineering Division and presented at the Joint Power Generation Conference, Denver, Colorado, October 17-21, 1982. Manuscript received by the Nuclear Engineering Division July 27, 1982. Paper No. 82-JPGC-NE-5.

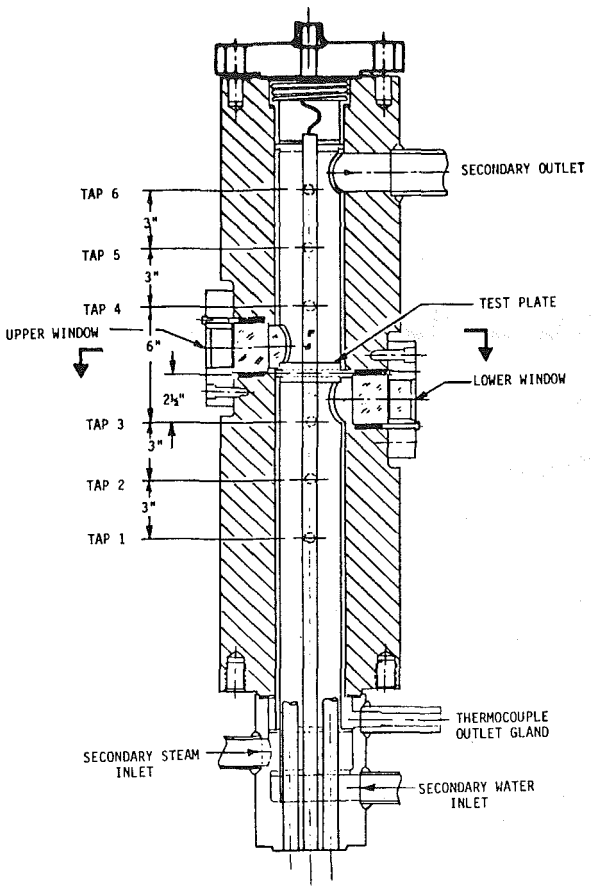

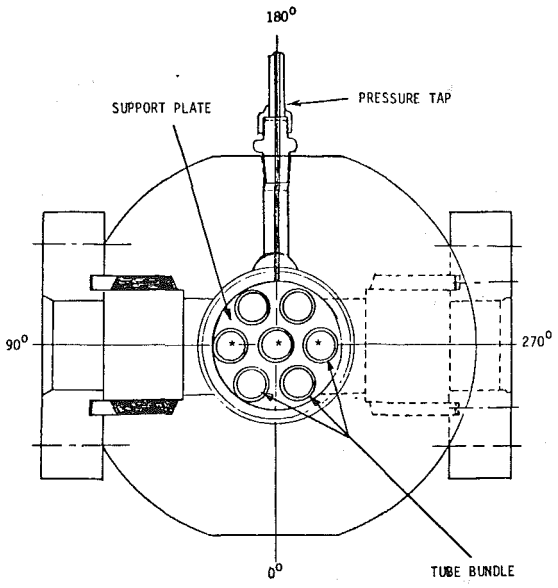

*INSTRUMENTED TUBES

Fig. 1 Test model schematic. Conversion factor: 1 in. = 25.4 mm.

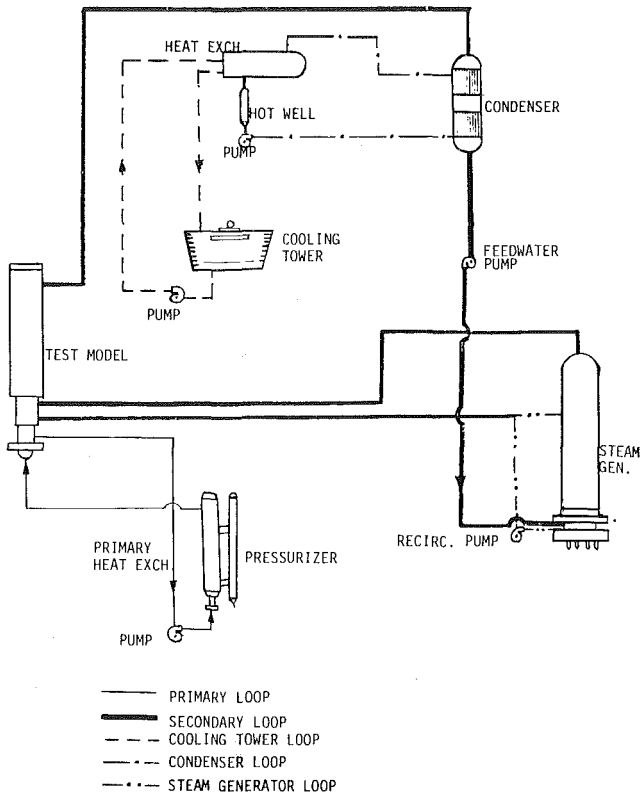

Fig. 2 Test loop schematic

primary fluid inlet and outlet temperature. The three instrumented tubes each had ten 0.020-in. (0.51-mm) dia thermocouples brazed into 0.022-in. (0.56-mm) deep slots in the 0.048-in. (1.22-mm) thick tubewalls which measured the circumferential tubewall temperature distribution at the support location and an upstream tubewall temperature. An instrumented tube was located in the center of the bundle and adjacent to each viewport.

The loop schematic is shown in Fig. 2. The 2.2 MW steam generator provided sufficient steam to test at high secondary qualities. The 0.18 MW primary heat exchanger provided model heat fluxes over a range of zero to >120,000 Btu/hr-ft^2 (379 kW/m^2). High-pressure/temperature, canned-rotor pumps gave loop capacities of 21,000 lbs/hr (9530 kg/hr) primary flow and secondary flow rates of 22,000 lbs/hr (9980 kg/hr). Design pressures were 1200 psia (8.27 MPa absolute) and 2500 psia (17.2 MPa absolute) for the secondary and primary, respectively.

Testing

Four supports were tested over ranges of secondary heat flux, mass flux, and quality, and at secondary side saturation pressures representative of their in-service environment. The supports tested were a trefoil, an eggcrate, and two drilled plates with 0.031-in. (0.787-mm) and 0.078-in. (1.98-mm) diametrical clearances, respectively. The range of conditions

Nomenclature

g_c = conversion factor
K = pressure loss coefficient
V_s = average velocity through the support
x_s = secondary quality at the support
Δp_s = pressure drop across the support
ρ_l = density of the secondary saturated liquid
ρ_s = density of the secondary fluid at the support
ρ_v = density of the secondary saturated vapor

Table 1 Test matrix

Support	Range of conditions
Trefoil	
pressure (psia)	800 & 1100
mass velocity (lb/hr-ft^2)	42,000 - 168,000
heat flux (Btu/hr-ft^2)	0 - 120,000
quality (%)	2 - 100
Eggcrate	
pressure (psia)	800 & 1100
mass velocity	87,000 - 347,000
heat flux (Btu/hr-ft^2)	0 - 120,000
subcooling - quality	31°F - 100%
Small hole drilled plate (0.031-in. diametrical clearance)	
pressure (psia)	800 & 1100
mass velocity (lb/hr-ft^2)	55,000 - 220,000
heat flux (Btu/hr-ft^2)	0 - 120,000
subcooling - quality	77°F - 29%
Large hole drilled plate (0.078-in. diametrical clearance)	
pressure (psia)	800 & 1100
mass velocity (lb/hr-ft^2)	74,000 - 295,000
heat flux (Btu/hr-ft^2)	0 - 120,000
subcooling - quality	96°F - 20%

1 psia = 6.985 kPa
1 lb/hr-ft^2 = 4.882 kg/hr-m^2
1 Btu/hr-ft^2 = 3.155 W/m^2
1°F = 0.5556°C
1 in. = 25.4 mm

tested is given for each support in Table 1. Contact was established between the instrumented tubes and the supports by mechanical means to promote dryout. Figures 3 through 5 show the contact locations and thermocouple positions relative to the tube and tube support.

The test procedure for each run consisted of first establishing fixed primary and secondary flow rates, secondary flow inlet conditions, and the secondary pressure. At the set conditions the primary temperature was slowly increased at a 2°F/min (1.11°C/min) ramp rate, to average heat fluxes in excess of 120,000 Btu/hr-ft^2 (379 kW/m^2). During the ramp, data were sampled and stored on magnetic disk every 25 s. The 2°F/min (1.11°C/min) ramp rate was established as a reasonable compromise between achieving steady-state conditions and minimizing test time. A slower ramp rate would more closely approach steady-state conditions but would significantly increase both test time and cost. Strip chart recordings were made of four tubewall temperatures during all runs.

Photographs of the flow above and below the support were taken at the beginning and end of all runs. High-speed movies (2000 frames/s) were taken of selected runs.

Analysis

The amount of heat transferred from the primary to the

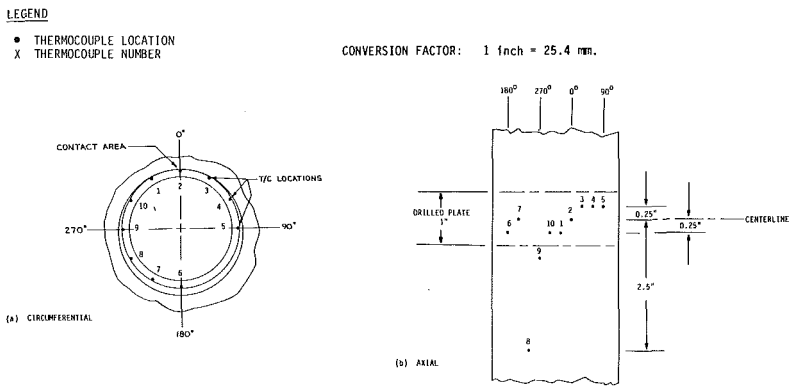

Fig. 3 Drilled plate tube/tube support thermocouple orientation

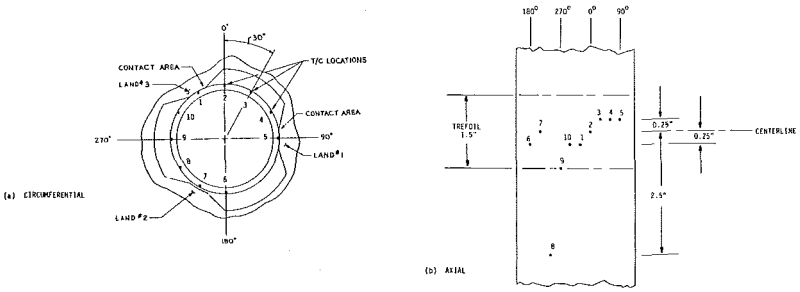

Fig.4 Trefoil tube/tube support thermocouple orientation

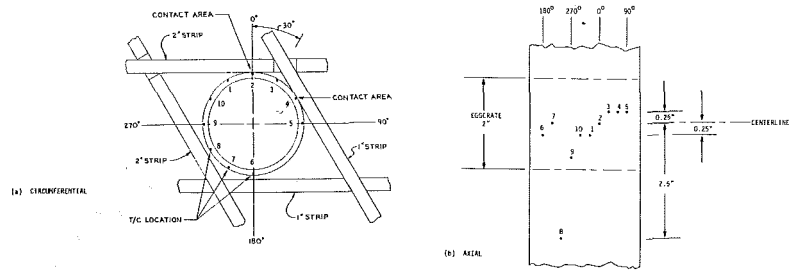

Fig. 5 Eggcrate tube/tube support thermocouple orientation

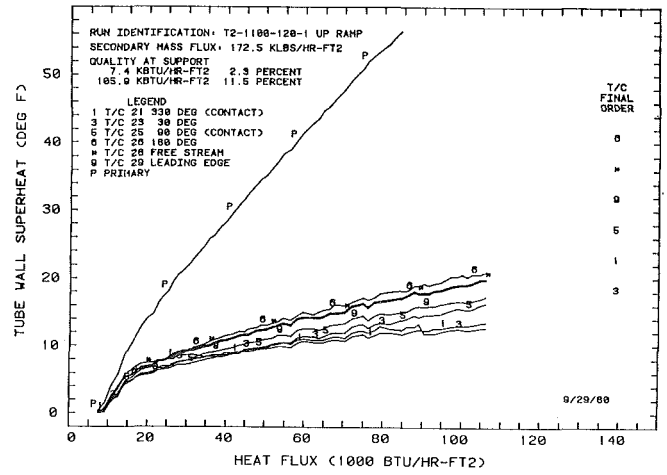

(a) TREFOIL AT LOW QUALITY (~10%)

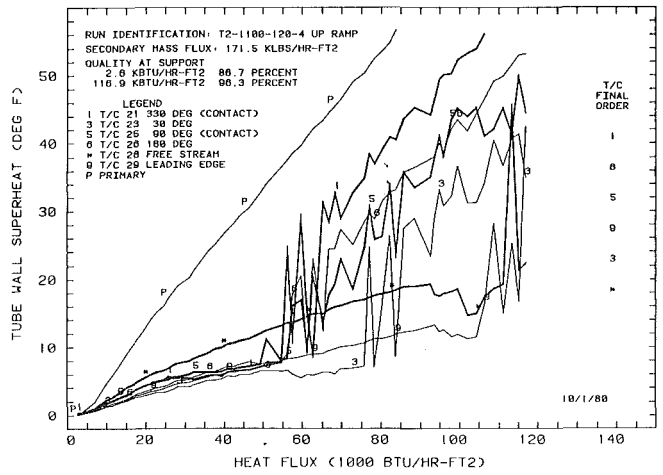

(b) TREFOIL AT HIGH QUALITY (~90%)

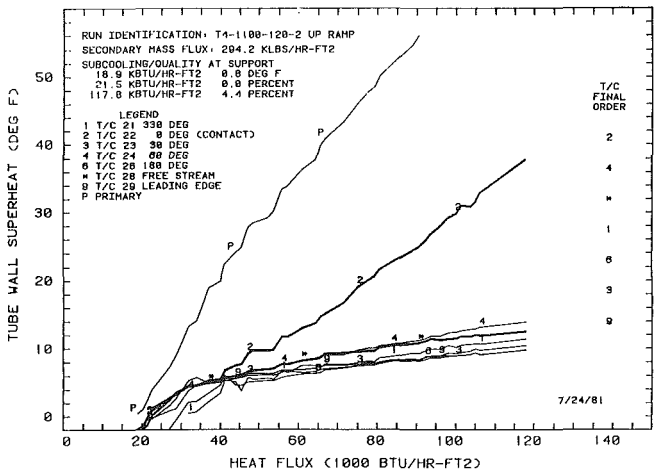

(c) DRILLED PLATE

Fig. 6 Tubewall superheat in support crevice as a function of heat flux. Conversion factors: 1 Btu/hr-ft^2 = 3.155 W/m^2; 1 lb/hr-ft^2 = 4.882 kg/hr-m^2; 1°F (ΔT) = 0.5556°C (ΔT).

secondary was determined based on the sensible heat loss of the primary. The heat flux used in the evaluation of the results to simulate the local heat flux was the average heat flux in the model neglecting both the heat flux variation along the length of the bundle and the local perturbation in the region of the support. Analyses of a bare tube (i.e., no support plate present) showed that there was less than 10 percent variation between the average heat flux and the local value at the position where the support would be.

Similarly the secondary side conditions at the support (quality or subcooling) were determined from a heat balance using the bundle average heat flux and measured values of the individual inlet steam and water flow rates and conditions.

The pressure loss coefficients (K) were determined based on the defining equation

$$\Delta p_s = \frac{K V_s^2 \rho_s}{2 g_c} \tag{1}$$

with the density at the support (ρ_s) given by

$$\rho_s = \left[\frac{x_s}{\rho_v} + \frac{1 - x_s}{\rho_l} \right]^{-1} \tag{2}$$

The pressure drop due to the support only, Δp_s, was found by assuming that the pressure gradient in the vicinity of the support with no support present would be the same as the pressure gradient below the support if the support were in place. The pressure taps below support location were used to establish the nominal bundle pressure gradient. Taps above and below the support location were used to determine the combined bundle and support pressure drop. Data from the tap in the flow recovery region just past the plate and at the exit of the model were not used. A calculation considering heat addition showed the pressure gradient remained essentially constant below and in the vicinity of the support region. In this manner, the effects of acceleration, density and friction were readily accounted for and their individual contributions did not need to be considered.

Results

Heat Transfer. Typical results are illustrated in Figs. 6(a–c) which show the measured tubewall superheat (measured tubewall temperature, i.e., thermocouple indicated value minus secondary saturation temperature) versus average tube bundle heat flux for a constant mass flux. The run identification number and the secondary mass flux are given in the top left corner. The secondary subcooling and/or quality condition is given for the corresponding heat flux at the beginning and end of the primary ramp. For the case of initial subcooling with a transition to two-phase, the flux at which the secondary becomes saturated liquid at the support location is given. The thick lines distinguish the free-stream and contact thermocouple temperatures from the other tubewall temperatures. The thermocouple final order corresponds to the magnitude of temperatures at the top of the ramp. Dryout is assumed to be indicated by a significant change in the slope of the tubewall temperature versus heat flux curve, i.e., a tubewall excursion, since the reduced heat transfer associated with a vapor film will cause a rise in the local tubewall temperature which may approach the primary temperature.

Figure 6(a), which is for the trefoil, illustrates the case in which there is no evidence of dryout. Figure 6(b), also for the trefoil, shows the type of dryout which was found only at very high (~90 percent) qualities. Similar results were obtained for the eggcrate. However, qualities at dryout were approximately twice those which occur in the service application of a recirculating PWR steam generator.

A different type of dryout was obtained for the drilled plates and is illustrated in Fig. 6(c). As shown, only the contact thermocouple exhibited a tubewall temperature excursion indicating dryout. This result was typical for both drilled plates and was obtained over the entire range of quality/subcooling tested.

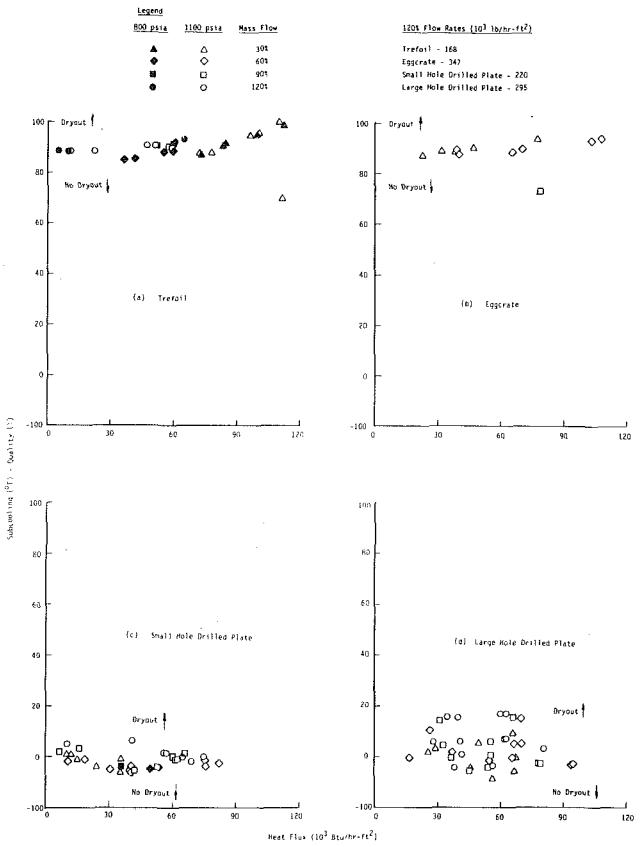

Fig. 7 Tubewall superheat excursion onset conditions. Conversion factors: 1 Btu/hr-ft^2 = 3.155 W/m^2; 1 lb/hr-ft^2 = 4.882 kg/hr-m^2; 1°F (ΔT) = 0.5556°C (ΔT)

From the superheat plots obtained, the conditions of heat flux and local quality/subcooling at which temperature excursions occurred were determined. Figure 7 presents a graphical summary of the tubewall superheat excursion onset conditions obtained for the four supports.

Strip chart recordings were made to observe transient thermocouple response during the course of testing. Figure 8 shows strip chart results for the trefoil support at high heat flux. The cyclic temperature response which was obtained by some thermocouples is shown. At lower heat fluxes (below an excursion point) the temperature response was flat. Similar results were obtained with all supports.

Hydraulic. Pressure gradients obtained were typical of those illustrated in Fig. 9, which shows pressure drop versus length along the tube bundle for several heat fluxes at a constant mass flux. The run identification and secondary mass flux is in the top left corner. The plate location symbol is in the proper orientation with its width to scale. The plotted lines correspond to different heat fluxes and, consequently, quality/subcooling conditions at the support location.

Results of the pressure drop plots were used to determine the pressure loss coefficient (K-factor) for the supports. Table 2 shows a summary of the measured and predicted loss coefficients.

For each run the pressure loss coefficient was calculated for three regimes of operation: low heat flux, about 15,000 Btu/hr-ft^2 (47 kW/m^2); medium heat flux about 50,000 Btu/hr-ft^2 (158 kW/m^2); and high heat flux, about 110,000 Btu/hr-ft^2 (347 kW/m^2). Figure 10 shows a plot of the experimental loss coefficients versus Reynolds number, which was obtained for the small hole drilled plate.

Visuals. Still photographs and high-speed movies were

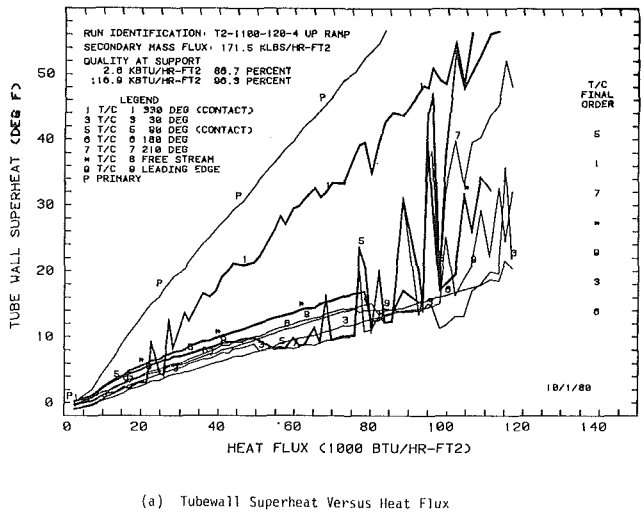

(a) Tubewall Superheat Versus Heat Flux

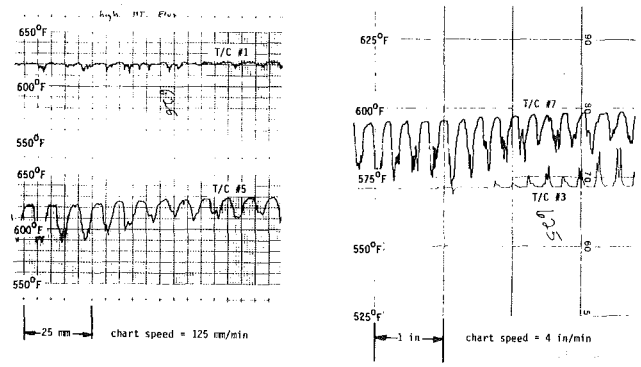

Fig. 8 Trefoil strip chart example, 105,000 Btu/hr-ft^2 (331 kW/m^2) heat flux, 69°F (21°C) superheat. Conversion factors: 1 Btu/hr-ft^2 = 3.155 W/m^2; 1 lb/hr-ft^2 = 4.882 kg/hr-ft^2; °C = 5/9 [(°F) − 32]; 1°F (ΔT) = 0.5556°C (ΔT), 1 in. = 25.4 mm.

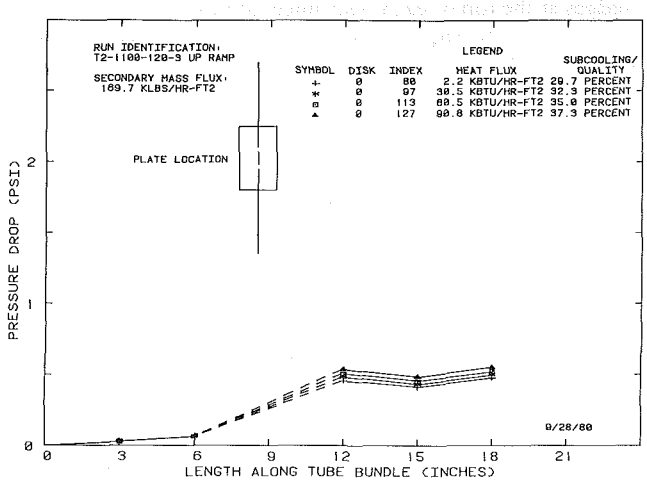

Fig. 9 Trefoil secondary flow pressure drop versus length along tube bundle. Conversion factors: 1 Btu/hr-ft^2 = 3.155 W/m^2; 1 lb/hr-ft^2 = 4.882 kg/hr-m^2; 1 psi = 6.895 kPa; 1 in. = 25.4 mm.

obtained for flow below and above the supports and in general showed uniform, well-mixed flow below the supports, and jetting, swirling, and recirculating flow above the supports.

Discussion of Results

Heat Transfer. A characteristic of both the trefoil and

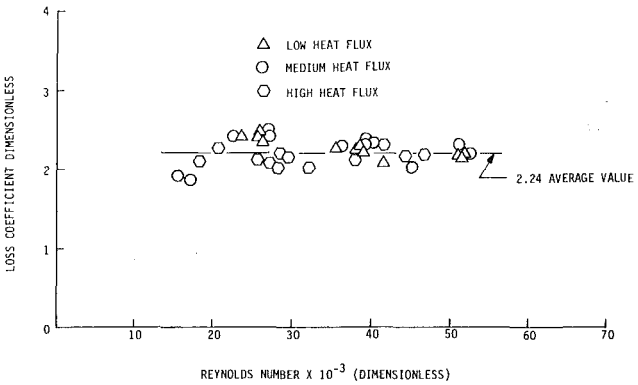

Fig. 10 Loss coefficient versus Reynolds number small hole drilled plate

egg-crate supports was that the tube wall temperature excursions only occurred at high qualities, ~90 percent. The observed tubewall temperature fluctuations possibly indicate alternate wetting and drying within the crevice. Such fluctuating wall temperatures may be the result of a departure from nucleate boiling (DNB). In contrast to the trefoil and eggcrate, temperature excursions occurred on every run for the two drilled plates. Dryout occurred at the plate with subcooled water as well as with low quality flow. No significant variation was found with mass flow or pressure level for any of the supports tested.

A strong influence of geometry was particularly evident in the drilled plate results. Of the two active instrumented tubes for the small clearance drilled plate, only one tube indicated dryout (and did so for each test run). The other instrumented tube never indicated dryout. From this result, it was concluded the tube exhibiting dryout had sufficient contact (line contact) with the plate to cause dryout to occur, whereas the tube which did not exhibit dryout was assumed not to be in line contact. Contact between the supports and the plate had been achieved for the first three supports tested by adjustable wedges at the top of each instrumented tube which could bend the tube in the required direction. Contact was confirmed both visually and by touch prior to the test of each support. This procedure established and confirmed contact on assembly but did not necessarily establish or confirm line contact.

Consequently, it was decided for the large clearance drilled plate (the fourth plate to be tested) to make special provisions to insure line contact for the two active instrumented tubes. The original test piece was replaced with one fabricated to particularly tight tolerances and with adjusting screws, which allowed the support to be tilted. With these provisions and the wedge system, line contact, which was confirmed visually and by touch, was apparently obtained on assembly. As expected, dryout was indicated by both active instrumented tubes at the contact line thermocouple for all test runs. In addition to these results, other investigators have found that gap thicknesses of more than approximately 0.001 in. (0.0254 mm) may prevent dryout from occurring [1].

One phenomenon evident from the supports tested was that tubewall thermocouples away from the vicinity of the contact line recorded temperatures below the free stream wall temperature, indicating enhanced heat transfer in the support region. This is apparently due to the restriction in flow area and consequent increase in flow velocity. However, in the extreme localized area of the crevice where strong viscous forces predominate, i.e., near the contact line, the velocity approaches zero, allowing the fluid in this part of the crevice to vaporize. The contact point or line between concentric cylinders, such as the drilled plate supports and tubes, is much more likely to produce dryout due to the long narrow crevice formed. The eggcrate contact line is similar to the tangent of a plane to a cylinder, and the trefoil contact line is similar to the intersection of a short concave surface and a cylinder. Both have wider crevices than the drilled plate supports. The test results were consistent with the above with dryout always occurring in the drilled plates and apparently never occurring in the trefoil and eggcrate supports except at very high qualities.

It has been suggested that a preliminary phenomenon to complete steam blanketing of the crevice is alternate wetting and drying [2]. Strip chart results did show a cyclic temperature response which could be associated with an alternate wetting and drying of the crevice. It appeared that the crevice may have alternated from a predominately wet to intermittently dry condition at the lower heat fluxes and a predominately dry to an intermittently wet condition at the higher heat fluxes.

Hydraulic. Pressure loss coefficients versus the approach Reynolds number were determined for the four supports. Loss coefficients were found to be constant with respect to Reynolds number and heat flux. Loss coefficients generated at a secondary system pressure of 800 psia (5.52 MPa absolute) agree with those determined for a secondary system pressure of 1100 psia (7.58 MPa absolute). Comparisons of the experimentally determined loss coefficients with theoretical models [3] agreed within 10 percent.

A constant pressure gradient was observed upstream of the supports. Downstream of the support, the varying gradient observed was attributed to recovery and turning effects.

Visuals. Results of both the still photographs and high-speed movies indicated the flow was well mixed and essentially homogeneous below all supports at all test conditions. The method of steam and water introduction apparently produced satisfactory mixing and a representative flow condition at the support. Flow upstream (below) of the support appeared unperturbed by the presence of the support except for a slight necking of the flow observed for the drilled plates. Flow downstream (above) of the support was characterized by jetting, swirling, and recirculation patterns, the intensity of which was dependent upon the flow velocity through the support, apparently due to the two-phase flow transition from a high velocity to a low velocity. Excellent visibility was obtained with the viewports during the entire test series.

Conclusions

The main conclusion obtained from the heat transfer portion of the program was that geometry was the single most important parameter affecting the occurrence of dryout. This finding is consistent with the findings of other investigators for single tube tests [1, 2]. The agreement was qualitative since the multitube geometries (tolerances, etc.) tested were not identical to the single tube geometries. The three types of supports tested were fabricated in accordance with actual shop practice. Tubes were in contact with the supports, the most conducive position for dryout to occur, thus representing a typical worst case for operating units. A fourth support specially fabricated to insure line contact gave results with more quantitative agreement with the single tube test results.

The primary conclusion of the hydraulic tests was that pressure loss coefficients of tube supports in two-phase flow over nominal PWR steam generator operating conditions are a function of the flow area ratio (support flow area to bundle flow area) and are essentially independent of quality, heat

flux and mass flux. The agreement between the measured loss coefficients and those predicted by one method in the literature [3] was within 10 percent.

No particular conclusions were reached from the visual studies of the flow. Flow upstream of the support appeared unperturbed by the presence of the support. Flow downstream of the support was characterized by jetting, swirling, and recirculation flow patterns possibly due to the two-phase flow transition from a high-velocity flow to a low-velocity flow.

The design concept and design details of the model were satisfactory. Features that were of particular concern were tested in separate mock-ups prior to model fabrication. These consisted of the viewports, the mixing chamber, the tubewall thermocouple installation, and the thermocouple routing through the secondary flow field. Excellent visibility was obtained with the viewports. Apparently good mixing of the steam and water was obtained below the supports. Thermocouple performance appeared satisfactory and no vibration/fatigue failure of the leads in the secondary flow occurred.

Acknowledgments

This work was done by Combustion Engineering, Inc., sponsored by the Steam Generator Project Office of the Electric Power Research Institute, as Contract S121-1. Dr. C. L. Williams was project manager.

References

1 Johnson, B. S., Sharon, A., Kozawa, Y., and Bankoff, S. G., "Boiling Heat Transfer In A Narrow Eccentric Annulus," ASME paper presented at the 1982 Joint Power Generation Conference, October 17–21, 1982, Denver, Colo.

2 Baum, A. J., and Curlee, N. J., 'An Experimental and Analytical Investigation of Dryout and Chemical Concentration in Confined Geometries," ASME Paper No. 80-C2-NE-6, 1980.

3 Idel'chik, I. E., "Handbook of Hydraulic Resistances," 1960, AEC-TR-6630, translated 1966, reproduced by the United States Atomic Energy Commission, Oak Ridge, Tenn.

B. S. Johnston[1]

A. Sharon[2]

Y. Kozawa[3]

S. G. Bankoff[4]

Department of Chemical Engineering,
Northwestern University,
Evanston, Ill. 60201
Mem. ASME

Boiling Heat Transfer in a Narrow Eccentric Annulus, Part I: Dryout

An experimental apparatus was used to simulate the annular crevice formed by a heated tube and drilled tube support plate (TSP) in a pressurized water reactor recirculating steam generator. The aim of the experiment was to explore the conditions required for the formation and maintenance of a dry region. Water at 0.69 MPa or atmospheric pressure was circulated through the crevice. Visual observations and tube wall temperature measurements were obtained and compared to synthesize a description of the crevice boiling processes. It was determiend that a stable dry patch exists about a line of contact between tube and TSP above a wall superheat of 2–3°C. However, separating the tube and TSP by about 0.025 mm allows the dry patch to be rewet.

Introduction

The PWR recirculating steam generator is basically a vertical shellside boiler. The single-phase primary water flows in a U-tube bundle; these tubes are supported by a tubesheet at the bottom, straps at the top, and several tube support plates. The secondary water flows vertically upwards as a boiling, two-phase mixture. The quality at the top of the tube bundle is nominally 33 percent; corresponding to an internal recirculation ratio of three to one. The steam passes through droplet separators and dryers before exiting the steam generator, while the separated liquid is collected in a downcomer and returned to bottom. Williams [1] and Baum [2] discuss steam generators in greater detail.

In the thermohydraulic design of nuclear power plants, much more attention was given to the reactor than to the steam generator [3]. However, operating experience has shown that steam generators have a variety of endemic problems [3–4].

A particularly severe problem is "denting," or deformation of the tubes in the region of the tube support plate (TSP). The tubes pass through holes in the TSP, resulting in a small annular clearance. Corrosion of the carbon steel TSP results in the formation of an oxide occupying nearly twice the volume of the original iron. This corrosion product has been observed to fill the crevice and squeeze the tube. As denting proceeds, the support plate may deform. In severe cases both tube and support plate may crack.

Corrosion is judged to arise from the concentration of an aggressive chemical species in a localized area. Green and Steininger [4] state that dented tube and support plate sections removed from steam generators showed high chloride concentrations. Laboratory tests were cited which showed that local chloride concentration was related to corrosion, and ultimately to denting. Baum [2] postulates that chemical concentration can result from a dryout condition in the annular crevice between tube and TSP.

Baum and Curlee [5] report a study directly applicable to steam generator tube support crevices. This experiment featured a flowing water stream at typical steam generator conditions. Furthermore, the experimental crevices were completely eccentric, the inner tube touching the confining wall. Two types of tests were run. In the first, tube wall temperatures were measured within a support plate crevice geometry. High readings, as compared to measurements obtained at locations presumed to be in nucleate boiling, were taken to represent a dryout condition. In the second test, a dissolved chemical was allowed to precipitate in the crevices. The authors were able to demonstrate a definite correlation between the existence of dryout and the concentration of chemicals in tube support crevices.

An earlier study of some relevance to tube support crevices was made by Ishibashi and Nishikawa [6]. These researchers experimented with saturated pool boiling in a vertical concentric annulus, utilizing an electrically heated inner surface. Two fundamentally different boiling regimes were identified. The first, the isolated bubble regime, differed little in appearance from normal pool boiling, exhibiting the nucleation of small bubbles at numerous sites. In the second, the coalesced bubble regime, this nucleation was replaced by the formation of large bubbles that filled the crevice, left a liquid film on the heater surface. and departed at a slow regular frequency.

Jensen, Cooper, and Bergles [7] studied saturated pool boiling of water at atmospheric pressure in horizontal annuli utilizing an electrically heated inner surface. The experimental apparatus was intended to simulate the baffle plate tube clearance in a shell-and-tube heat exchanger. The majority of the configurations were concentric, but two misalignments of eccentricity, 0.38 and 0.49, were examined as well. The critical heat flux (CHF) was observed to occur with the ap-

[1] Present address: E.I. duPont de Nemours, Savannah River Laboratory, Aiken, S.C. 29808

[2] Present address: Fauske and Associates, Inc., Burr Ridge, Ill. 60521

[3] Visiting Scholar: present address: Research Laboratory for Nuclear Reactors, Tokyo Institute of Technology, Tokyo, Japan

[4] Author to whom communications whould be addressed

Contributed by the Nuclear Engineering Division and presented at the Joint Power Generation Conference, Denver, Colorado, October 17-21, 1982. Manuscript received by the Nuclear Engineering Division July 27, 1982. Paper No. 82-JPGC/NE-7.

pearance of a small overheated area within the crevice on the top of the tube. Melting of the tube followed quickly unless the power was shut off. The measured CHF was found to decrease with decreasing radial clearance. The smallest clearance tested exhibited a CHF one-tenth of that of the bare tube. Critical heat fluxes for the eccentric alignments did not differ markedly.

It seems that the term "critical heat flux" has different impliciations in each study. In [7], a small dry patch was observed which quickly spread and led to tube melting. By contrast, Baum and Curlee [5] were able to maintain a stable localized dryout condition at a lower heat flux, also using electric power. The difference is probably due to the condition of contact between tube and plate in the latter study, rather than to flow or vertical orientation. Since Jensen et al. found that eccentricities of 0.38 and 0.49 did not affect their CHF results, the indication is that contact in the annulus ($\epsilon = 1.0$) is fundamentally different from noncontact alignments.

The postulation that corrosion in tube support plate crevices is caused by local chemical concentration is considered to be well-founded. In addition, it is felt that the postulated occurrence of dryout in these crevices provides a plausible mechanism for such chemical concentration. While the presence of dissolved impurities may be minimized by advances in water chemistry, and the severity of corrosion may be minimized by improved materials of construction, the formation and maintenance of dry regions, as an initiator of TSP damage, is a problem of heat transfer and fluid mechanics. The present study considers the process of boiling and dryout in a narrow annular tube support plate crevice, without the complication of dissolved or suspended solids. It is desirable to explore conditions of contact and near-contact between tube and TSP, providing more detail about contact boiling than has been available, and relating this to the concentric studies of [6] and [7].

Experimental

The test system was chosen to be a single 18.9-mm, o.d. inconel tube passing through a drilled hole in a simulated tube support plate. The circular hole was surrounded by four "flow holes," as shown in Fig. 1. Several support plates were made with different hole diameters such that the diametral gap between tube and plate could be varied. The tube, plates, and surrounding vessel were constructed so as to provide for line contact between the tube and hole.

The tube was heated by a downward flowing water stream designated the primary loop. This water was pressurized with compressed nitrogen to 1.7 MPa. Flowing outside the tube, vertically upward within the surrounding vessel, was the secondary water. This flow loop was pressurized to 0.69 MPa with its own vapor. It could also be run at atmospheric pressure.

The flow loops were entirely separate, interacting only to exchange heat in the test section. Each was heated (or cooled), pumped, and metered independently. Both were filled with water treated in a fabric filter, charcoal filter, and two ion-exchange columns. Treatment of pH and oxygen content, necessary at higher temperatures, was not done in this experiment. In order to preserve water cleanliness, 304 and 316

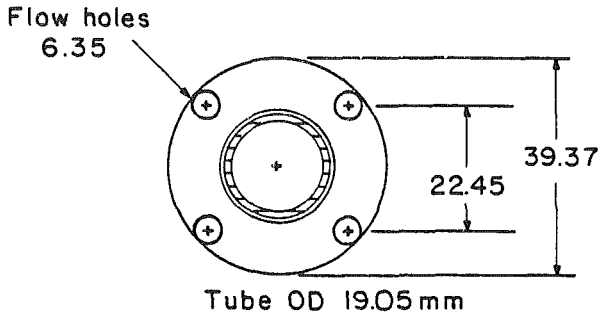

Fig. 1 Tube support plate geometry (note the narrow crevice about the tube)

stainless steels were used in construction, excepting the copper lines to the differential pressure transmitters.

The tube support plates were constructed of polished quartz. As a result, it was possible to observe the boiling and flow phenomena in the narrow annular crevice between the tube and the drilled hole. In the wall of the tube were embedded 24 0.51-mm o.d. steel-sheathed thermocouples. The junctions of these were located within the region of the annular crevice, except for one placed approximately 25 mm below the TSP. Thus, both visual observations and temperature and pressure drop measurements were available.

The instrumented tube was calibrated to allow the surface temperature to be obtained by one-dimensional extrapolation from the wall thermocouple readings and primary bulk temperature. This was done by placing the tube in well-defined flow fields, calculating the appropriate film coefficients, and thus establishing the ideal radial temperature profile in the tube wall. The "virtual" radial position of each thermocouple was then calculated by comparing its reading with this profile.

By varying both the temperature and gradient in the tube wall during the calibration runs, it was determined that the virtual position of a thermocouple was a unique, monotonically-increasing function of its reading during calibration. In taking data, the reading of a thermocouple could be used to determine its virtual radial location. This location, the primary temperature, and the appropriate inside wall film coefficient were then used to extrapolate to the outer surface temperature. The result of using the calculated virtual position of the thermocouple junction was to obtain the surface temperature which would exist were the thermocouple not present.

For a particular support plate, an experimental run involved setting the secondary flow rate and inlet enthalpy, and maintaining these while varying the heat flux. The experiment began with the primary temperature close to that of the secondary. The primary temperature was then increased, usually about 1°C/min. At regular intervals, depending on the duration of the experiment, the thermocouples were sampled and recorded. The resulting periodic scans of temperature were not obtained after the equipment had attained a steady state, but were rather taken in passing. However, the tube wall adjustment to changes in primary temperature was quite rapid. Results for experiments run

Nomenclature

l = thermal diffusion in liquid
M = molecular weight
P = pressure
r^* = radius of vapor nucleus
R = ideal gas constant
T_s = saturation temperature
T_w = temperature of tube outer surface
ΔT_s^* = superheat required for equilibrium of a vapor nucleus
α_l = liquid thermal diffusivity
ϵ = eccentricity of tube and drilled hole
λ = heat of vaporization
σ = surface tension

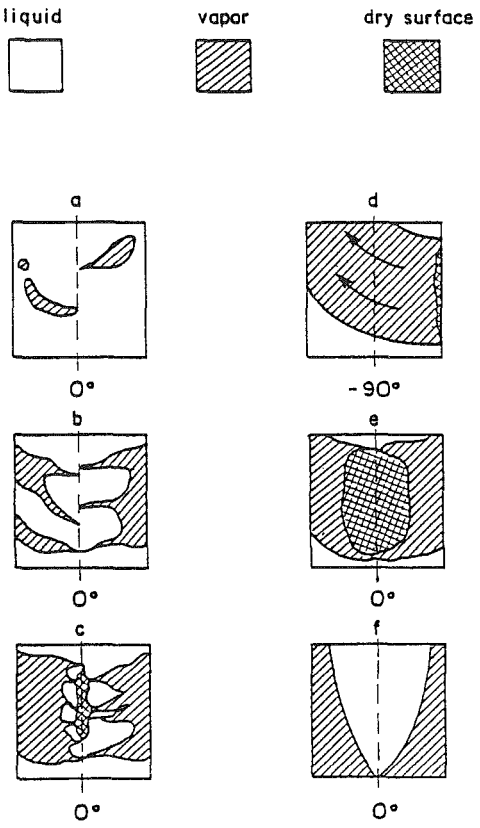

Fig. 2 Visual appearance of crevice boiling phenomena

three times as fast showed no systematic deviation from those obtained at the pace stated above. Additional detail on experimental design, construction, calibration, and operation is available elsewhere [8].

It is appropriate first to describe the visual appearance of the crevice boiling and flow phenomena. Visual observations will be found to show a strong correlation to temperature measurements. Several descriptive terms will be introduced for later use in presentation of heat transfer results. The observations given are general; not every detail will occur in every experiment. However, the observations are equally applicable to experiments run at 0.69 MPa and at atmospheric pressure.

For a given secondary flow rate, slightly subcooled, the primary temperature is imagined initially to be equal to that of the secondary. The flow through the TSP is thus entirely single-phase liquid. The primary temperature is gradually increased. Boiling is initiated in the vicinity of the contact line. High-speed films reveal that the bubbles leave the nucleation site traveling circumferentially about 5 deg in 0.001 s, or 0.76 m/s. The bubbles are pancake-shaped, squeezed in between tube and plate, about 0.25 to 0.76 mm in diameter. They depart with increasing frequency, appearing to the eye to merge into continuous *vapor streams*. As shown in Fig. 2(*a*), these streams flow tangentially outward from the contact line before turning to flow upward, out of the support plate crevice. Increasing the primary temperature increases the number of these active sites. Their streams tend to merge into a tangential *vapor sweep* which fills the gap as shown in Fig. 2(*b*).

The *dry patch* usually occurs suddenly. It is visible as an oblong region at the contact line with a definite boundary inside which no liquid motion occurs. High-speed films reveal that the boundary at this stage is stationary. The vapor produced along this boundary pierces the surrounding liquid as small *tendrils* which merge into the vapor sweep, as shown in Fig. 2(*c*). The sweep dominates the motion in the crevice, the tangential vapor turning up to exit the test section between 75 and 135 deg from the contact line (see Fig. 2(*d*)).

The dry patch spreads circumferentially as the primary temperature is increased. The sides of the patch tend to be vertical; there is negligible indication of progressive widening with increasing axial position. The patch tends to occupy the middle of the TSP, the contact line at the top and often the bottom remaining wetted (see Fig. 2(*e*)). In addition, the boundary region of the patch becomes more agitated, exhibiting a gradual transition from the vapor tendrils in a continuous liquid to liquid droplets in a continuous vapor. At substantial heat fluxes, the vapor from each side of the patch meets in the wide portion of the crevice, 180 deg from the contact line. In a greatly subcooled flow, the vapor produced in the contact region may condense in the wider portion of the gap before exiting the crevice.

The initiation and development of the patch proceed in exactly the same manner under conditions of high-void flow. Under the initial condition of equal primary and secondary temperatures, the two-phase flow is confined to the wider portion of the gap, leaving the tube surface adjacent to the contact line completly wet. The locus of nearest vapor approach appears as in Fig. 2(*f*). Thus, at the contact line, a two-phase flow is indistinguishable from that of a saturated liquid. Not only is the patch growth identical; as the primary temperature is decreased, the patch retraces its development, being extinguished to vapor streams, and finally leaving the contact region completely wet.

High-speed movies of a fully-developed dry patch indicate that there is a tangential fluctuation in the boundary of the patch over approximately 3 to 10 deg of tube surface. The motion is roughly periodic with a frequency on the order of 100 Hz. Liquid appears to flow toward the contact line, reaching a position of "minimum patch width." Vaporization and expulsion then occur in about 0.0005 s, blowing the liquid away and resulting in a departing bubble which, when viewed by eye, comprises the vapor sweep. Following this bubble, a thin liquid layer evaporates from the tube surface, with the edge of the layer moving away from the contact line. By the time this has moved between 3 and 10 deg on the surface (roughly 0.004 s), the liquid again presses toward the minimum patch width.

The overall impression is that of a stable dry patch whose boundary fluctuates at a small amplitude. There is no indication of a complete alternate dryout and rewetting process. The vapor produced at the boundary flows tangentially away from the patch as a vapor sweep. Thus, the dominant flow field in the narrow crevice is not in the direction of the bulk flow.

Contact Line Boiling

The influence of heat flux on narrow gap boiling has been described implicitly in the discussion of visual observations Its effect is, simply, to initiate and develop a dry patch in the tube surface. Under conditions of line contact between tube and plate,boiling at or near the contact line occurs at a wall superheat between 0 and 1°C. This is in striking contrast to more conventional unconfined boiling, in which wall superheats of 10–15°C may be required to initiate boiling [9]. In addition, this behavior is observed at both atmospheric pressure and 0.69 MPa.

The explanation is found in terms of the criteria for bubble growth in a heated liquid. An equation for the mechanical equilibrium of a spherical vapor nucleus is given by Collier [9].

$$\Delta T_s^* = \frac{RT_s^2}{\lambda M}\frac{2\sigma}{\mathrm{Pr}^*} \tag{1}$$

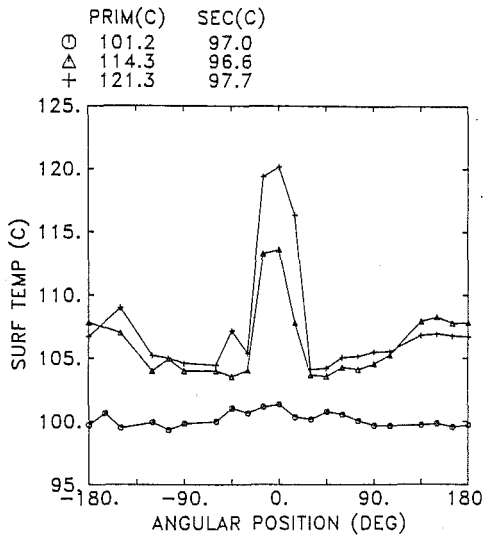

Fig. 3 Angular distribution of tube surface temperature as the primary temperature is increased; pressure = 0.12 MPa; diametral gap = 0.48 mm; flow rate = 730 kg/m^2 s

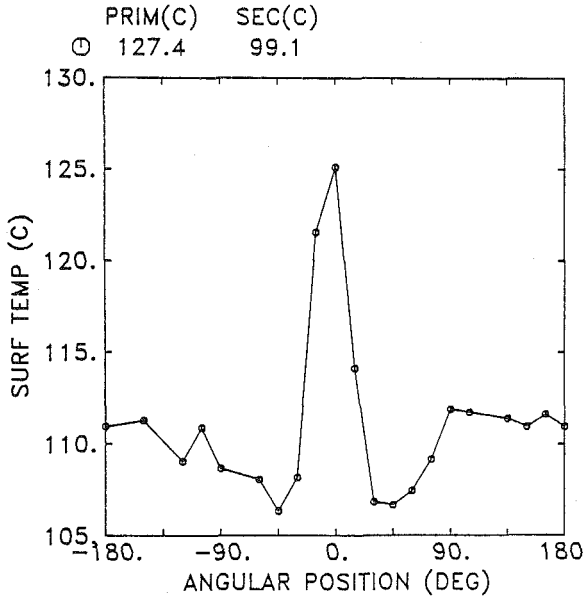

Fig. 4 Angular distribution of tube surface temperature demonstrating "W-shape": pressure = 0.12 MPa; diametral gap = 0.48 mm; flow rate = 2750 kg/m^2 s

This equation relates the nucleus radius r^* to the liquid superheat required for equilibrium in terms of physical properties and the imposed pressure, P. For the bubble to grow, the liquid superheat must exceed this value.

In heterogeneous nucleation, one is concerned with the growth of bubbles from cavities on a solid surface immersed in a liquid. By geometrical arguments [9] it may be shown that the radius, r^*, may be equated to the radius of the mouth of the cavity in which the bubble is growing. Under a temperature gradient from the solid surface, the superheat determined from equation (1) is actually that required at some distance from the surface; therefore, the surface itself must be hotter.

In the present situation, the liquid in the vicinity of the contact line is flowing with a low velocity between a heated wall, the tube, and a wall of low thermal conductivity, the quartz TSP. It is not unreasonable to expect the liquid to be heated to the wall temperature rather quickly. As an approximation, consider the unsteady heat flow in a solid slab of thickness, l, and thermal diffusivity, α_l. One wall is maintained at temperature, T_w, the other insulated. The initial temperature is constant at T_s. The solution to this problem is well known [10]. In one time constant l^2/α_l, the temperature at the insulated wall is $T_s + 0.9(T_w - T_s)$. Taking l to be the distance between tube and plate 5 deg from the contact line, the time constant is about 10^{-4} s. Thus the liquid in the vicinity of the contact line rapidly reaches the tube wall temperature. This value may be calculated directly from equation (1). For a common active cavity size [9] of 0.01 mm the superheat required for nucleation is about 0.3°C. This is well within the range measured here.

Temperature Measurements

The measured tube wall temperatures were extrapolated to the surface values under the assumptions discussed above. These are most conveniently displayed as a function of the angular location of each thermocouple. Such an angular distribution plot is shown in Fig. 3. These are experimental results; the surface temperature distribution is given for indicated values of the primary temperature.

At a primary temperature of 101°C, the secondary fluid is completely liquid. The surface temperature is distributed from a maximum at the contact line (0 deg) to a minimum at 180 deg. This is reasonable, since velocity, and thus convective heat transfer, increase circumferentially from the contact line. The remaining data were taken under dryout conditions. The domain of the dry patch is easily identified by the high temperatures around the contact line. This demarcation is made much more striking by the low temperatures at ± 30 deg. Instead of the possible intuitive expectation of a high temperature at the contact line decreasing to a minimum at 180 deg, the distribution has a pronounced W-shape. The maximum at the contact line falls rapidly to a minimum adjacent to the patch and then rises to a relative maximum in the wide portion of the gap. An increase in the primary temperature is seen to affect the patch temperature more than that of the remainder of the gap. The contact temperature is little less than the primary temperature, while surface temperatures between ± 30 deg and ± 120 deg are little more than the saturation value.

The thermocouple junctions were placed at various axial locations within the crevice. The temperature distributions in this plot and in others obtained show no consistent trend attributable to axial location. The variations that do exist are small and equally attributable to uncertainty in the radial depth calibration. For this reason, no further attention will be given in this paper to possible axial dependence of the measured quantities. The variation of the tube surface temperature and crevice flow phenomena will be discussed only as a function of circumferential location with respect to the contact line.

The angular distribution of surface temperature shows excellent correspondence to visual observations of flow phenomena. In the experiment resulting in Fig. 4, thermocouples at 0 and ± 15 deg were in the dry patch. That is to say no liquid was observed to wet the tube surface over these thermocouple locations. The patch actually extended as far as −30 deg from the contact line, but this thermocouple, located high in the crevice, was within the wetted boundary region. As evidenced by the low measured surface temperature, the heat transfer was quite effective. Thermocouples from 30 to 75 deg and −45 to −90 deg show similarly low readings. These regions of the tube surface are swept by vapor from the contact region. In this region of the vapor sweep, the bubbles leave a thin sheared liquid film on the tube surface as they pass. No nucleation is observed.

The remainder of the wide gap region shows a higher surface temperature than that under the vapor sweep. The

flow here was relatively undisturbed, flowing axially through the crevice. It seems that this axial flow provides a less effective means of heat transfer, since the surface temperature is higher here than under the vapor sweep.

In summary, the temperature measurements taken with visual observations have revealed that different heat transfer mechanisms are in effect at different circumferential locations in the crevice. About the contact line there exists a region of high temperatures corresponding to the dry tube surface. This dry patch is bounded by a region of minimum surface temperature corresponding to evaporation of a sheared film of liquid. The surface temperature rises to some extent into the wider portion of the crevice. This region also exhibits thin film evaporation, under the vapor sweep. The widest portion of the crevice may feature axial flow, with or without nucleate boiling, or a possible mixing of the vapor sweeps from both sides of the patch.

Near Contact Behavior

Above a wall superheat of 2°C, under a condition of line contact, a stable dry patch was found to exist in all crevices studied. It is now desired to examine the process of dryout as the tube and plate are brought into contact at a moderate prevailing heat flux. Figure 5 is a plot of tube surface temperature at the 0 deg (contact line) position versus the distance between tube and plate at that position. The diametral gap was 0.48 mm. Also plotted are the prevailing primary and saturation temperatures. The relative position of the tube surface temperature between these is an indication of the heat transfer conditions at the outer surface.

At line contact, the surface temperature was 3°C lower than the primary temperature. This condition remained as the tube was moved 0.025 mm away from the TSP. Between 0.025 mm and 0.076 mm, the surface temperature decreased rapidly. At a given position within this range, the temperature measurements showed a good deal of scatter, indicating a transition boiling condition. At a separation exceeding 0.076 mm, the temperature appeared to be relatively constant, about 3°C above saturation.

Notes of visual observations and high-speed movies were made during this experiment. These will now be discussed for detailed comparison with the temperature measurements in Fig. 5.

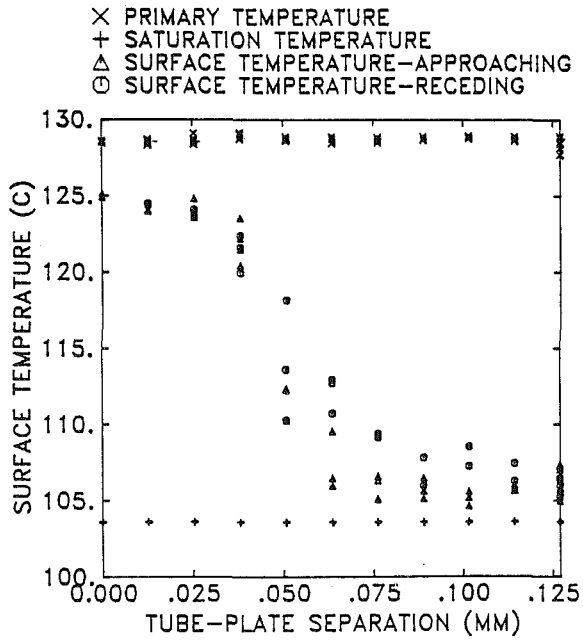

Fig. 5 Variation of tube surface temperature at the contact line as tube and TSP are separated. Diametral gap = 0.48 mm.

0.127 mm: very fast nucleation and churning of the fluid appear in the contact region. High-speed movies reveal that an individual bubble forms and quickly grows to fill over 90 deg of the crevice in about 0.010 s. It is then expelled by the inflowing liquid. The nucleation frquency is roughly 20–50 Hz. No dry surface is observed. These large deformed bubbles are in great contrast to the tiny bubbles present at the initiation of boiling near the line of contact. The behavior here is similar to the "coalesced bubble region" boiling described by Ishibashi and Nishikawa [6], but at a much greater frequency of bubble departure.

0.076 mm: Spherical fluid bodies appear in rapid motion in the crevice. There is a tendency for some tangential flow away from the more constricted portion of the crevice. High-speed films indicate that new bubbles are nucleating before the previous bubble has completely departed. Bubbles form only in the liquid-filled portion of the crevice; no rupturing is observed of the thin liquid film remaining on the tube surface under a departing bubble. The violent interaction of colliding bubbles produces liquid bodies within the bubble which remains stationary as the bubble departs.

0.051 mm: The apparent spherical bodies are more evident over the whole contact region. There is a more pronounced vapor sweep to the wide portion of the gap. No stationary liquid-vapor interface is apparent. The films show that multiple nucleation is taking place, with the colliding bubbles filling the contact region with small liquid droplets. The nucleation frequency is high enough and the departure slow enough that the upper portion of the crevice is usually vapor filled. In this region some transient dryout occurs.

0.025 mm: The liquid droplets appear to move more slowly around a stable liquid-vapor interface. The tube surface is dry between −5 and 20 deg. The patch is broken by rivulets running toward the center. High-speed films indicate that the tube surface is dry in the upper part of the crevice. The mechanism of nucleation followed by bubble displacement is still in effect, the bubble never being completely displaced before new bubbles form in the axially flowing displacing liquid. The rapid nucleation and bubble collision create liquid droplets which are strewn across the glass over the dry tube. These appear as rivulets when viewed by eye.

Contact: a stable dry patch exists from −20 to 30 deg, with a fluctuating boundary. No liquid motion is visible in the dry patch. The films reveal that the condition of contact has greatly diminished the tendency of the liquid to displace the stable bubble. In addition, vaporization now takes place at the bubble interface, not as nucleation within the encroaching liquid. This mechanism has been described previously. The droplets formed as the rapid vaporization shatters the liquid phase now remain outside the patch boundary, in the region of the vapor sweep.

Figure 6 is a plot of surface temperature at a position −15 deg from the contact line. This temperature is plotted against the same abscissa as in Fig. 5, and is shown between prevailing primary and saturation temperatures for reference. For this plot, the behavior is much the same as at the contact line. The dryout temperature is lower than that in Fig. 5, but the temperature for a separation greater than 0.076 mm is about the same. The temperature at 180 deg, Fig. 7, shows a very slight decrease as tube and plate are separated. Of course, this corresponds to a reduction of the space available for this location.

Figure 8 is an angular distribution plot for this experiment. Data are plotted for different tube-plate separation distances. As the previous plots have indicated, the wide gap region shows little change as the tube is moved; the dramatic changes occur over the extent of the dry patch. As the tube and TSP

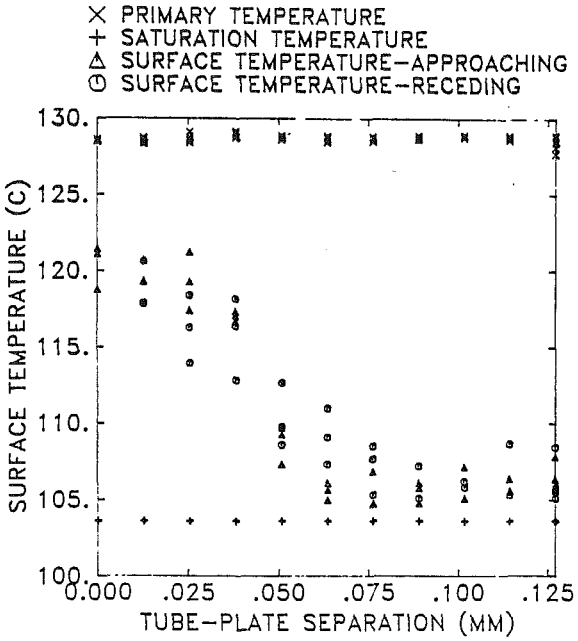

Fig. 6 Variation of tube surface temperature −15 deg from the contact line as tube and TSP are separated. Diametral gap = 0.48 mm.

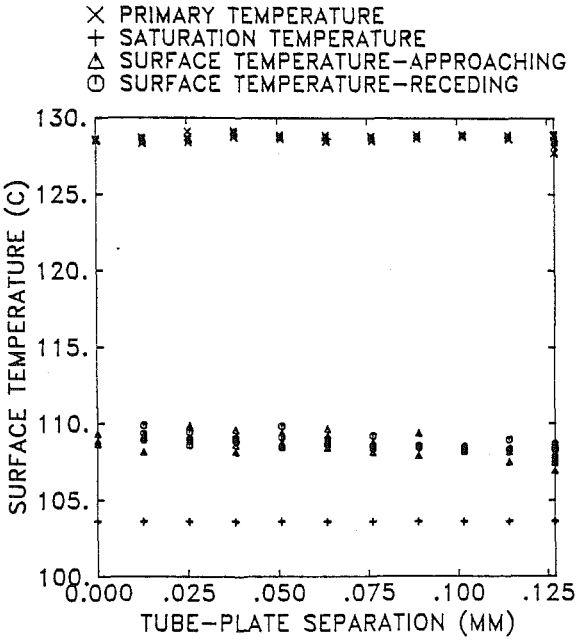

Fig. 7 Variation of tube surface temperature 180 deg from the contact line as tube and TSP are separated. Diametral gap = 0.48 mm.

are separated, the region of maximum temperature becomes the minimum temperature region.

As was anticipated earlier, the varying eccentricity experiment described previously shows that the differences between concentric and non contact eccentric alignment are small compared to the extreme condition of line contact. This is a fundamentally different mode of narrow-crevice heat transfer. Instead of the scattered nucleation and spread of bubbles, followed by their displacement from the crevice, line contact heat transfer involves a stable dry patch and dominant flow field. The unsteady boundary behavior happens over short time and distance scales, such that the apparent result is

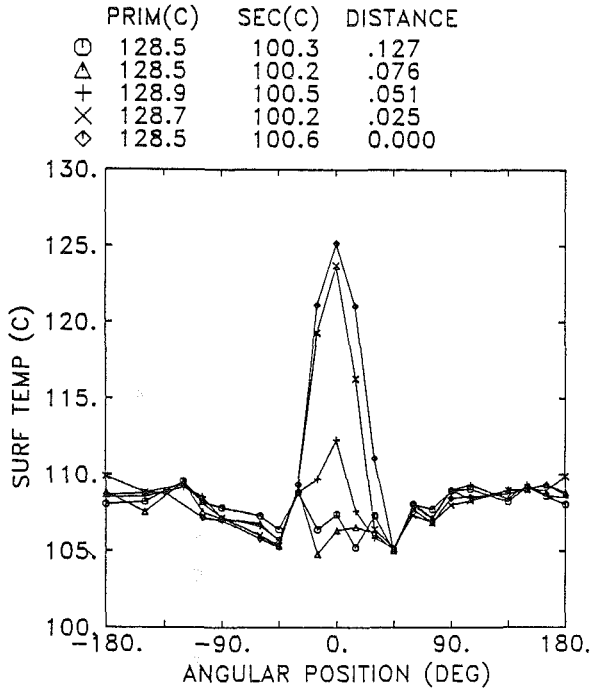

Fig. 8 Angular distribution of tube surface temperature as tube and plate are separated: pressure = 0.12 MPa; diametral gap = 0.48 mm; flow rate = 1630 kg/m^2 s

a steady temperature profile with extreme tangential gradients. The contact line thus becomes a stabilizing focus for the entire crevice.

Acknowledgment

The authors wish to acknowledge the support of the Electric Power Research Institute under Contract S133-1. In addtion, we wish to thank Dr. C. L. Williams, Steam Generators Owners Group and the Electric Power Research Institute, for many helpful comments, and the Japanese Government for the support of one of us (YZ) while a Visiting Scholar at Northwestern University (1978).

References

1 Williams, H. K., "System 80™ NSSS Steam Generator Design," American Power Conference, Chicago, 1976.

2 Baum, A. J., "The Mechanics of Concentration Processes in Recirculating Nuclear Steam Generators," Conference on Water Chemistry and Corrosion in the Steam-Water Loops of Nuclear Power Stations, Seillac, France, 1980.

3 Williams, C. L., and Green, S. J., "Thermal and Hydraulic Aspects of PWR Steam Generators," ANS/ASME International Topical Meeting on Nuclear Reactor Thermal-Hydraulics, Saratoga Springs, N.Y., 1980.

4 Green, S. J., and Steininger, D. A., "Pressurized Water Steam Generators-Problems and Progress," ASME Century 2 Nuclear Engineering Conference, San Francisco, Calif., 1980.

5 Baum, A. J., and Curlee, N. J., "An Experimental and Analytical Investigation of Dryout and Chemical Concentration in Confined Geometries," ASME Century 2 Nuclear Engineering Conference, San Francisco, Calif., 1980.

6 Ishibashi, E., and Nishikawa, K., "Saturated Boiling Heat Transfer in Narrow Spaces," *International Journal of Heat and Mass Transfer*, Vol. 12, 1969, pp. 863–893.

7 Jensen, M. K., Cooper, P. E., and Bergles, A. E., "Boiling Heat Transfer and Dryout in Restricted Annular Geometries," AIChE Symposium Series, Vol. 73, 1977, pp. 205–214.

8 Johnston, B. S., Ph.D. thesis, Northwestern University, 1981.

9 Collier, J. C., *Convective Boiling and Condensation*, McGraw-Hill, New York, 1972, pp. 111–123.

10 Carslaw, H. S., and Jaeger, J. C., *Conduction of Heat in Solids*, 2d ed., Oxford University Press, 1959, p. 98.

B. S. Johnston[1]

A. Sharon[2]

S. G. Bankoff
Mem. ASME

Department of Chemical Engineering,
Northwestern University,
Evanston, Ill. 60201

Boiling Heat Transfer in a Narrow Eccentric Annulus, Part II: Heat Transfer

An experimental apparatus was used to simulate the annular crevice formed by a heated tube and drilled tube support plate (TSP) in a pressurized water reactor recirculating steam generator. A previous paper [1] has described the stable dryout phenomena which occur. This paper discusses the heat transfer mechanisms in the contact and wide gap regions of the crevice. Changes in flow rate and inlet enthalpy are found to have little effect on the patch extent and contact line temperature, while an increase in diametral gap size decreases both. Increasing the thermal conductivity of the TSP also reduces the contact line temperature, but does not affect the wide gap region.

Introduction

Problems of tube denting in PWR steam generators are postulated to result, in part, from a localized dryout condition in tube support plate (TSP) crevices. These narrow annular crevices are formed by the passage of a heated tube through drilled holes in the TSP. A previous paper [1] has shown stable dryout to be a condition which easily occurs if the tube is in line contact with the plate. The dry patch is centered about the line of contact. Vaporization occurs at the patch boundary, and the resulting vapor flows circumferentially away from the patch, leaving a thin sheared film of liquid on the tube surface.

The thin film evaporation mechanism of heat transfer in narrow crevices was identified earlier by Ishibashi and Nishikawa [2]. These researchers experimented with saturated pool boiling in a vertical concentric annulus, utilizing an electrically heated inner surface. Two fundamentally different boiling regimes were identified. The first, the isolated bubble regime, differed little in appearance from normal pool boiling, exhibiting the nucleation of small bubbles at numerous sites. In the second, the coalesced bubble regime, this nucleation was replaced by the formation of large bubbles which filled the crevice, left a liquid film on the heater surface, and departed at a slow regular frequency. These regimes were separated by a critical gap size, which varied with fluid properties. The isolated bubble regime was present in larger crevices. Below the critical crevice dimension, the coalesced bubble regime was observed.

Jensen, Cooper, and Bergles [3] studied saturated pool boiling of water at atmospheric pressure in horizontal annuli utilizing an electrically heated inner surface. They observed that boiling was initiated in the crevice prior to the remainder of the heated tube surface. The bubbles exiting the crevice were generally large. This would be consistent with coalesced bubble regime boiling; it is noted that all radial clearances in this experiment were smaller than the 3.0 mm critical size determined by Ishibashi and Nishikawa for water at atmospheric pressure. However, the authors did not report detailed visual observations in the crevice itself. The surface temperature was found to be lower within the gap than on the unconfined tube surface. Crevice heat transfer coefficients were as much as 230 percent greater than those measured for normal pool boiling; they tended to increase with decreasing gap size. These results are also consistent with those of Ishibashi and Nishikawa. Jensen et al. postulated that this behavior is due to a thin film evaporation mechanism; a decreasing gap size results in higher vapor escape velocities and thus higher heat transfer rates.

In this paper we will examine the heat transfer characteristics of different regions within the crevice. Local boiling curves will be used to illustrate the effects of varying the flow rate and enthalpy of the water entering the crevice. In addition, the diametral gap size and the tube support plate thermal conductivity will be shown to influence the crevice phenomena.

Experimental

The single tube and TSP test section, with supporting primary and secondary flow loops, was described in [1]. Quartz tube support plates were used with diametral gaps of 0.48 and 2.13 mm. A stainless steel TSP, providing a diametral gap of 2.13 mm, was also used. For a particular support plate, an experimental run involved setting the flow rate and inlet enthalpy, maintaining these while varying the heat flux.

Regions Within the Crevice

We sought to examine the heat transfer processes at a given

[1] Present address: E. I. duPont De Nemours, Savannah River Laboratory, Aiken S.C. 29808

[2] Present address: Fauske and Associates, Inc., Burr Ridge, Ill. 60521

Contributed by the Nuclear Engineering Division for publication in the Journal of Engineering for Power. Manuscript received at ASME Headquarters March 21, 1983.

location in the crevice. For this purpose it is useful to obtain the boiling curve for the tube surface relating the local heat flux to the wall superheat. As described in [1], the experimental heat fluxes and surface temperatures are calculated by one-dimensional extrapolation from measured temperature data. The experimental boiling curves should then be designated "one-dimensional" boiling curves to distinguish them from "actual" boiling curves. The actual boiling curve presents the true outer surface heat flux

$$q = -k_i \frac{\partial T}{\partial r}\bigg|_{r=r_o} \tag{1}$$

as opposed to the extrapolation

$$q_1 = U(T_p - T_w) \tag{2}$$

where U is suitably defined.

If the tangential temperature gradient in the tube wall is small, q_1 is equal to q (within experimental uncertainty). As the tangential gradient becomes large at a given location, the two heat fluxes diverge. For example, the tube wall below a dry patch is cooled by radial conduction into the patch, as well as tangential conduction in either direction. The one-dimensional surface heat flux, equation (2), attributes this entirely to radial conduction, and thus exceeds the actual heat flux, equation (1).

In spite of this limitation, the one-dimensional boiling curves prove quite useful in distinguishing among various mechanisms of heat transfer at a given surface position. A basic division can be made between local boiling curves for the contact region and for the wide gap region. The contact region is roughly designated as that portion of the tube surface swept by vapor at the initiation of boiling in the narrow crevice. The wide gap region is the remainder of the tube surface.

The contact region as defined includes portions of the tube surface which do not dry out. For finer detail, it is possible to divide the contact region into a dry patch and a boundary region. The reason for considering these subregions together is that their boiling curves show similar characteristics. On the other hand, the boiling curves for the wide gap region show different characteristics of appearance. These will be described below. Reference will also be made to the visual appearance of the crevice phenomena.

A typical contact region local boiling curve is given in Fig. 1, describing the progress of an experiment in which the primary temperature is raised to a maximum and then lowered. Such an experiment would be run at a fixed secondary flow rate and inlet enthalpy.

Curve A-B describes convective heat transfer. The secondary fluid is entirely liquid; no boiling occurs. The local heat flux is on the order of 3000 W/m^2. This low value is indicative of the low velocities near the contact line in the crevice. Point B is designated the departure point. It has been found to occur at a superheat of 0 – 1 °C. Visually, point B corresponds to the initiation of boiling in the contact region. This first boiling usually consists of vapor streams moving horizontally away from contact. During cooling of the primary temperature, point B is reached as the last vapor streams extinguish. The sharp departure is made striking because the convective heat flux is so low here.

Curve B-D is characterized by a rapid rise in heat flux with little increase in wall superheat. The rise regime tends to be convex leftward. Heat is transferred through a thin sheared film of liquid. Curve D-E is a plateau in which the tube wall temperature increases with little change in heat flux. This heat flux varies with gap size and angular position. The slope of the plateau varies as well, and may be positive or negative. During this stage no liquid wets the tube surface. Heat is transferred into the vapor blanket. Curve D-F is observed in that part of the contact region which does not dry out.

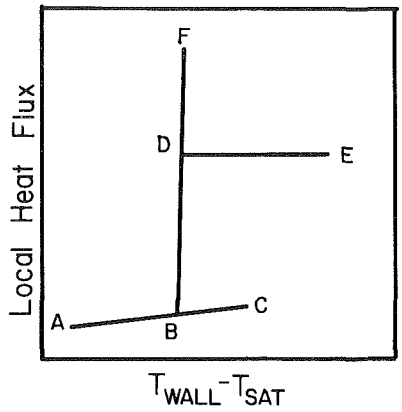

Fig. 1 Typical contact region boiling curve

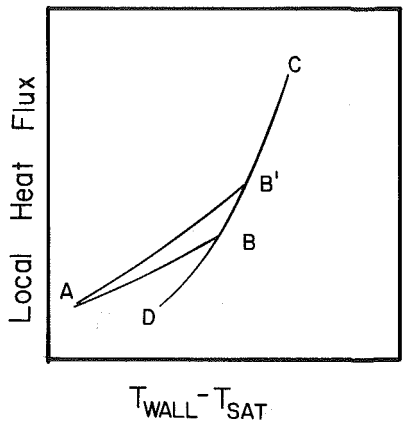

Fig. 2 Typical wide gap region boiling curve

Curve B-C is an extension of the convective region to high wall superheat. This overshoot is an unstable condition which occurs as the primary temperature is rising. It does not occur in all experiments and has not been observed as the primary temperature is decreased. It is most likely to occur when the secondary fluid is subcooled. The wall superheat at point C varies from run to run; it has been observed to be as high as 10 °C. The transition from point C is rapid; in about 1 s, the wall temperature falls, and the heat flux rises to a condition in the mid-rise region. A large superheat at point C results in a large heat flux after transition. Visually, patch development is instantaneous. There is usually no boiling prior to point C.

The wide gap boiling curve has the appearance of a conventional forced convective boiling curve [4]. Referring to Fig. 2, curve A-B describes single phase convective heat transfer. The effect of increased velocity is shown by curve A-B′. Heat transfer in the convective regime is improved, but the curve merges smoothly into the rise regime. Curve D-B is characteristic of a saturated or positive-quality fluid.

Nomenclature

k_i = thermal conductivity, tube
q = local heat flux
q_1 = local heat flux calculated by one-dimensional extrapolation
r = radial coordinate
r_o = tube outside radius
T = temperature
T_p = temperature of primary fluid
T_w = temperature of tube outer surface
U = overall heat transfer coefficient, primary to outer wall

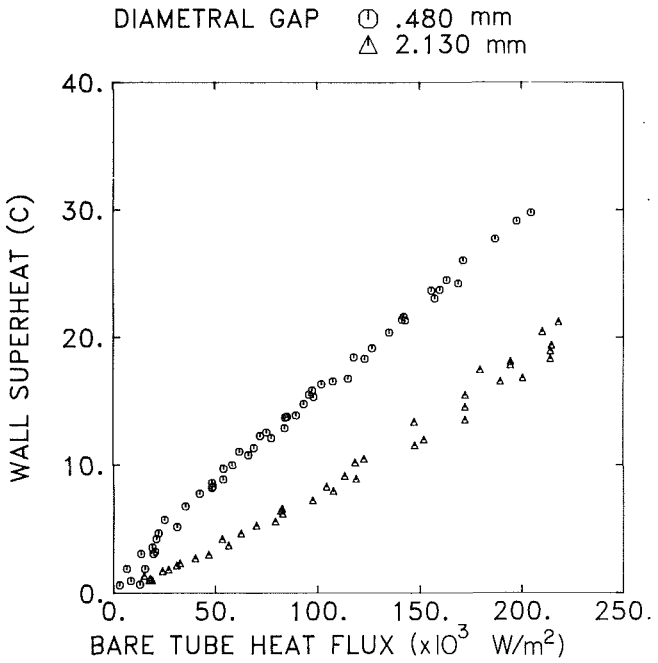

Fig. 3 Maximum wall superheat in crevice versus bare tube heat flux: pressure = 0.69 MPa; diametral gap = 0.48 mm and 2.13 mm

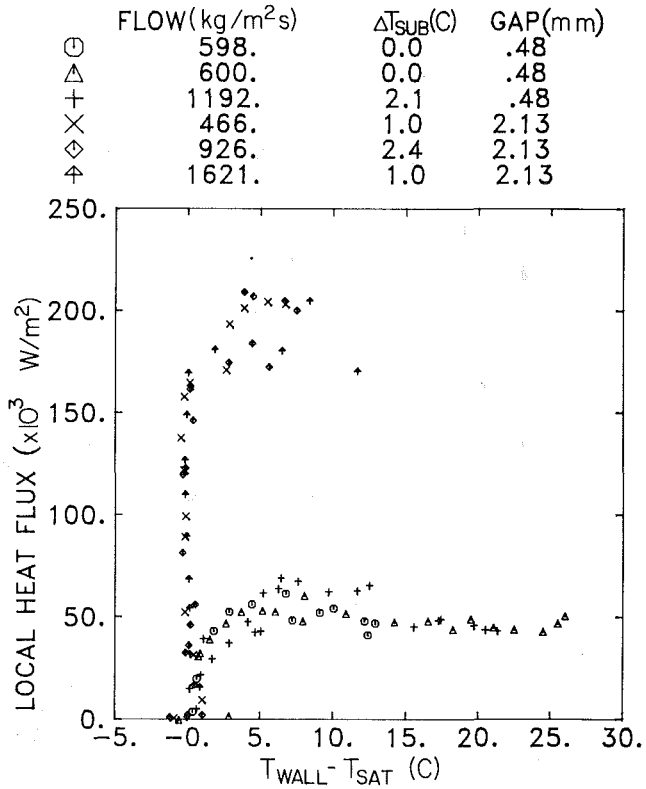

Fig. 4 Effect of gap size on boiling curve at − 15 deg from the contact line: pressure = 0.69 MPa; gap size, 0.48 mm and 2.13 mm; flow rate = 466-1621 kg/m²s; inlet enthalpy, 2.4°C subcooling to 0.002 quality

In the rise regime the heat flux increases rapidly with increasing wall temperature. Curve B-C tends to be concave leftward. The heat transfer mechanism is most often thin film evaporation under the vapor sweep, but can be nucleate boiling. The behavior of this regime is somewhat more complicated than has been indicated here. This will be further discussed below. The departure point B is not as pronounced as in the contact region, because (by definition) the vapor

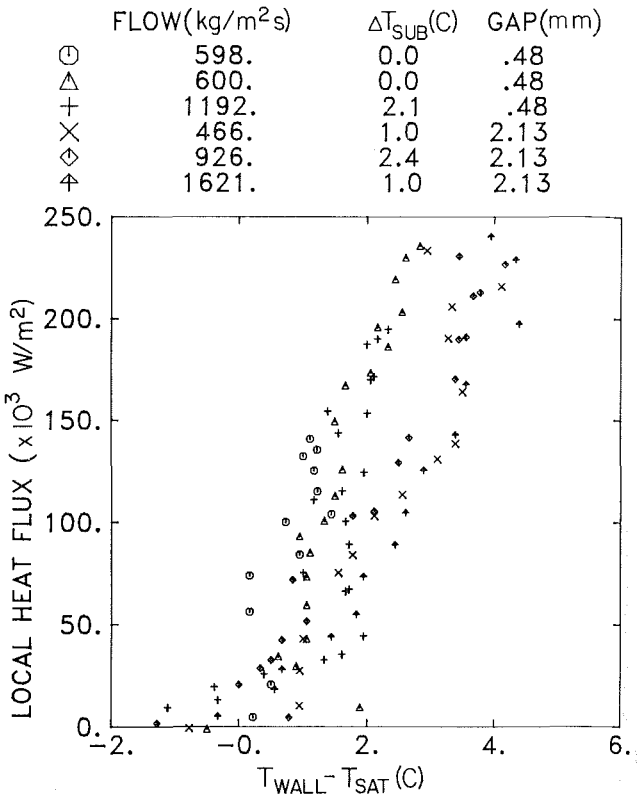

Fig. 5 Effect of gap size on boiling curve at 60 deg from the contact line (conditions same as Fig. 4)

produced at the initiation of boiling does not reach the wide gap region.

Effect of Gap Size

In the concentric annulus boiling study of [2], a "critical gap size" was found to determine which boiling regime prevailed. Under conditions of line contact, however, a dry patch is always observed. Visual observations indicate that increasing heat flux increases the patch width for any gap size, but the gap size determines the general magnitude of the patch. The hot tube wall under the dry patch is cooled by radial conduction into the vapor blanket as well as tangential conduction in the tube wall. As a corollary to the patch width observations mentioned above, it would be expected that the temperature at the contact line would increase with decreasing gap size for a given heat flux. Figure 3 shows that this is so. The contact line superheat for various experiments is plotted against the bare tube heat flux. The experiments reflect the full range of flow and enthalpy conditions. The data are clearly divided by gap size.

Figures 4 and 5 illustrate the effects of gap size at specific locations within the crevice. At − 15 deg from the line of contact, Fig. 4 shows that the local heat flux is considerably reduced in the smaller gap. The greater surface temperature, as shown earlier, is illustrated here as well. Both gap sizes show the typical contact region departure and rise; however, the spreading dry patch limits the local heat flux in the 0.48-mm crevice to a value approximately one-fourth of the plateau heat flux in the 2.13-mm gap. In the wide gap region the trend is reversed. Figure 5 shows the heat transfer coefficient in the smaller crevice to exceed that in the larger. Since the heat transfer mechanism throughout much of the wide gap region is thin film evaporation under the vapor sweep, it is expected (as in [3]) that a smaller crevice dimension will lead to higher sweep velocities and thus improved heat transfer coefficients. This expectation is borne out by the data.

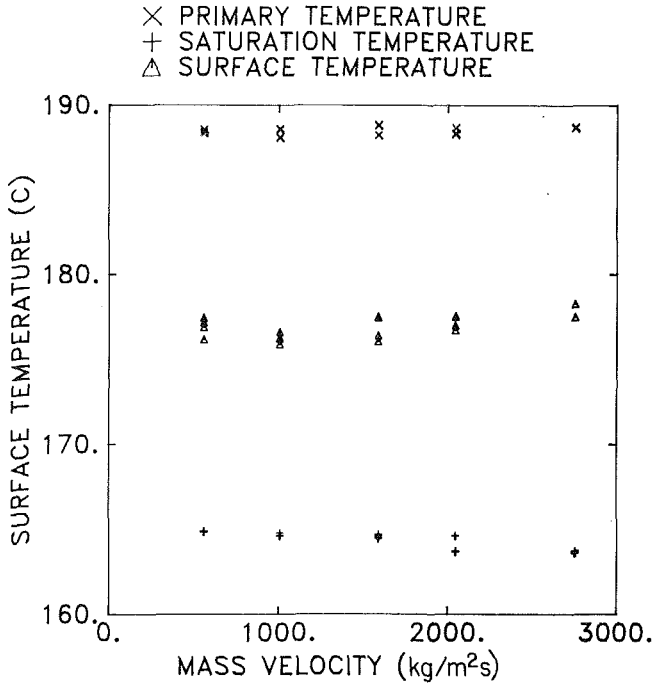

Fig. 6 Surface temperature variation with flow rate at the contact line: pressure = 0.69 MPa; diametral gap = 0.48 mm; flow rate = 488-2780 kg/m^{2}s

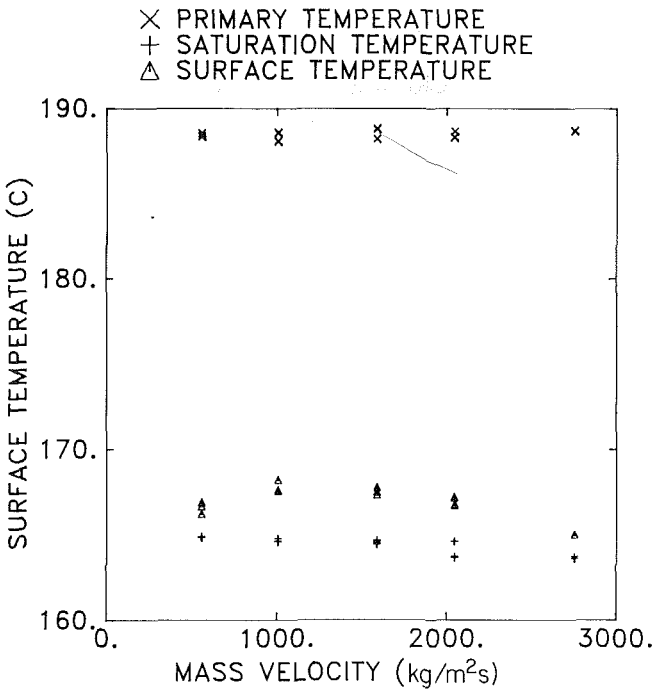

Fig. 7 Same as Fig. 6, except at 105 deg from the contact line

Effect of Flow Rate

The influence of the secondary flow rate was studied by running experiments at various flow rates. Illustrative boiling curves from these experiments will be presented. Prior to this, however, it will be instructive to consider the results of a special experiment in which the flow rate was varied directly. The secondary temperature was held at saturation, and the primary temperature was set to give a fully developed dry patch. These temperatures were maintained while the secondary flow rate was varied between 488 and 2780 kg/m^{2}s. The plate pressure drop varied between 0.0004 and 0.0044

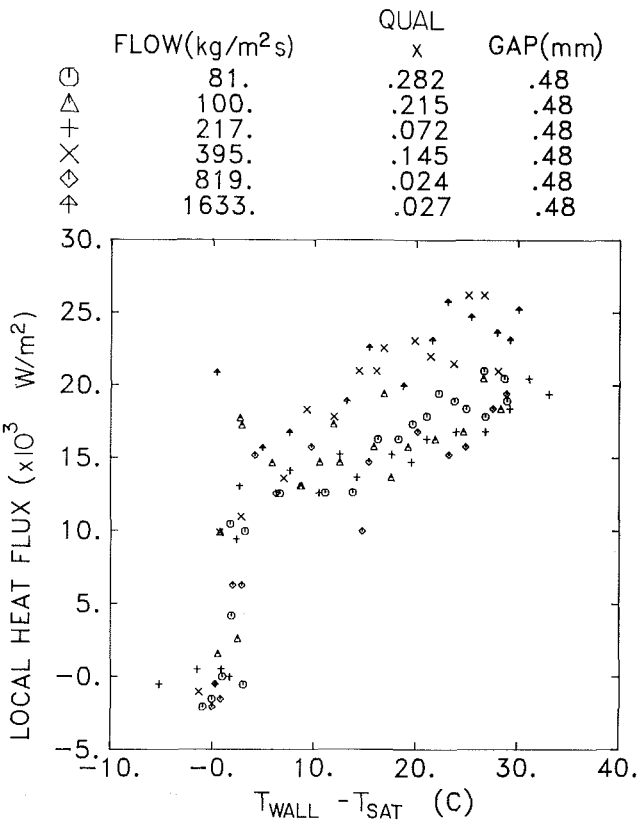

Fig. 8 Local boiling curve at the contact line: pressure = 0.68 MPa; diametral gap = 0.48 mm; flow rate = 81-1633 kg/m^{2}s; inlet quality = 0.024-0.282

MPa. At the highest flow rate, the patch was observed to be narrower by about 10 deg of tube surface than at the lowest flow; however, it retained its integrity. Figure 6 shows that the contact line temperature varied very little with flow rate changes.

The increase in flow rate was observed to decrease the extent of the vapor sweep. At the lowest flow rate, the vapor from each side of the patch met in the widest portion of the crevice. The highest flow rate drove the vapor sweep from the crevice about 75 deg from the contact line. This behavior is reflected in the surface temperature measurements of Fig. (7). The temperature shows a general decline with increasing flow, except for the very lowest flow rate measured. This is thought to be evidence of competing heat transfer mechanisms. At the lowest flow rate, the vapor sweep dominates the crevice. The resulting thin film evaporation provides excellent heat transfer. Higher flow rates displace the vapor sweep, but this convective heat transfer mechanism is not as effective until the highest flow rates. While the wide gap behavior is interesting in itself, the temperature changes involved, about 3 °C, are minor compared to the temperature across the patch boundary [1].

Superimposed boiling curves show the effects of flow rate over the full range of heat flux. For the dry patch, the previous discussion suggests that little change will be observed. This is the case, as shown in Fig. 8. The previous discussion on competing heat transfer mechanisms in the wide gap region suggests that these boiling curves may not be so coincidental. Figure 9 is a plot for various flow rates in which the increasing flow increases convective regime heat transfer in the customary manner. Above the saturation temperature, however, the curves shift to the right, a decrease in heat transfer rate with increasing flow. The vapor sweep increases in velocity and volume with increasing heat flux. It is evident from the data that its displacement by axial flow is more

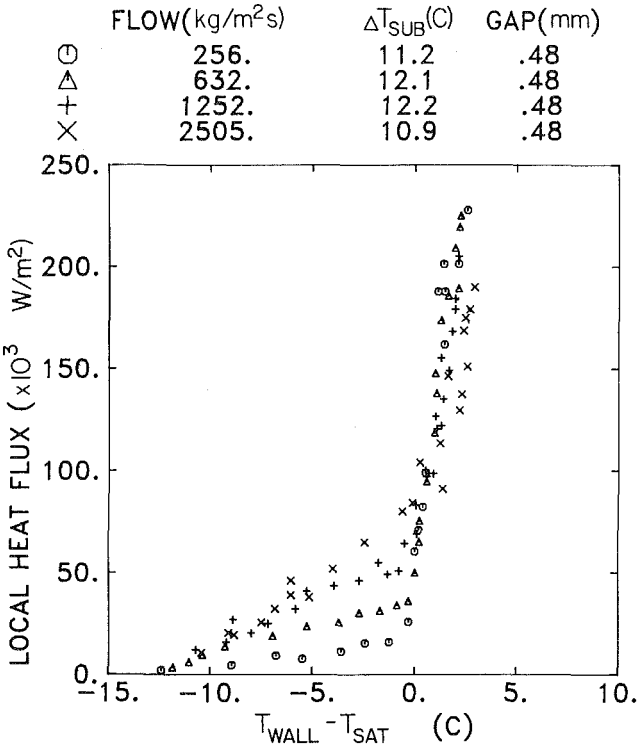

Fig. 9 Local boiling curve 75 deg from the contact line: pressure = 0.69 MPa; diametral gap = 0.48 mm; flow rate = 256-2505 kg/m²s; inlet subcooling = 10.9-12.2°C

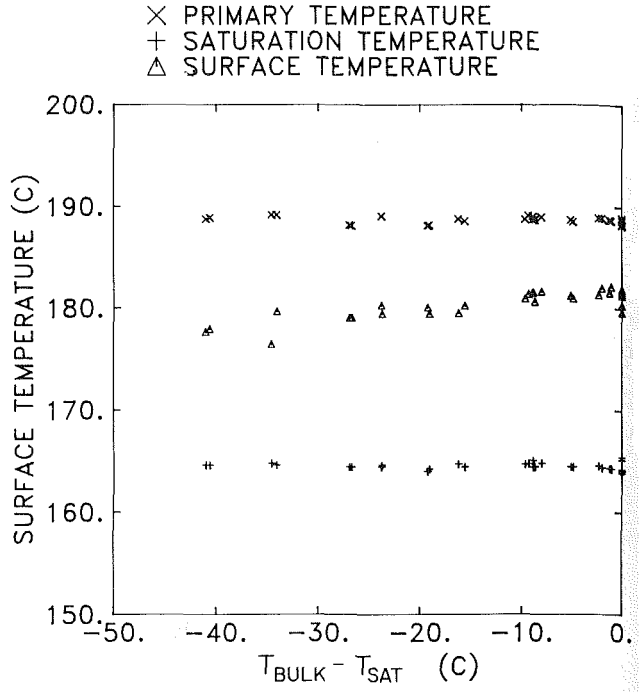

Fig. 10 Surface temperature variation with subcooling at the contact line: pressure = 0.69 MPa; diametral gap = 0.48 mm; flow rate = 1590 kg/m²s

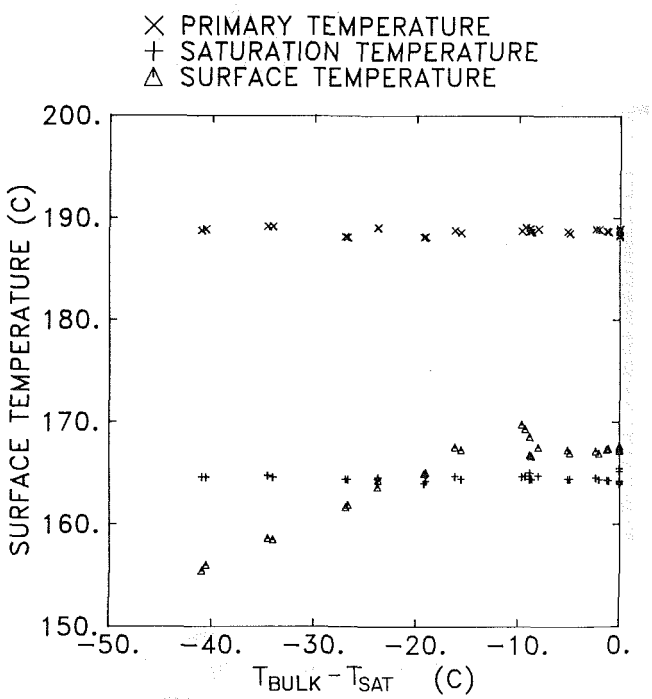

Fig. 11 Same as Fig. 10, except 180 deg from the contact line

detrimental to heat transfer at high fluxes. In assessing the importance of this result it must be noted that the temperature spread is less than 2 °C. This is only slightly larger than the margin of uncertainty in surface temperature measurements. Thus, however real the mechanism of vapor sweep displacement may be, its effects are small.

Effect of Inlet Enthalpy

An experiment was run to determine the stability of the dry patch under a secondary bulk subcooling much greater than that found in normal steam generator operation. The flow rate was maintained at about 1590 kg/m²s and the primary temperature and secondary pressure kept constant as well. The dry patch results are shown in Fig. 10. The surface temperature decreases smoothly to a small extent over a 42 °C subcooling. The relatively high surface temperature indicates that the dry region remained in existence. This is precisely what was observed visually. The decrease in temperature is probably due to tangential conduction in the tube wall.

In the wide gap, the vapor sweep began to condense in the crevice as the secondary fluid was subcooled. Figure 11 shows that at about 25 °C subcooling of the bulk fluid, the wall temperature dropped to the saturation temperature. Further subcooling decreased the wall temperature even more; hence, the increased tangential conduction from the dry patch. By contrast, heat transfer from the bare tube was much poorer. Figure 12 shows that the wall temperature remained above the saturation temperature for the greatest subcooling attained. This experiment showed the patch to be stable under bulk subcooling, even though the remainder of the crevice was below the saturation temperature.

A boiling plot for experiments run at various inlet enthalpy conditions indicates good coincidence of the contact line data, Fig. 13. The wide gap might be expected to show some effects due to the competing mechanisms of heat transfer which have been discussed previously. Figure 14 shows that the data are rather neatly divided into a subcooled group and a saturated group. The saturated data fall smoothly on a step rise; this rise is due to thin film evaporation under the vapor sweep. As a result, the convective regime persists to a greater wall superheat before the vapor sweep mechanism begins to dominate. This occurs at higher heat fluxes, and as the data show, the curves then merge.

Metal Tube Support Plate

The information gained from experiments with the transparent tube support plates has provided a good picture of the processes which occur in narrow crevice boiling. In order to

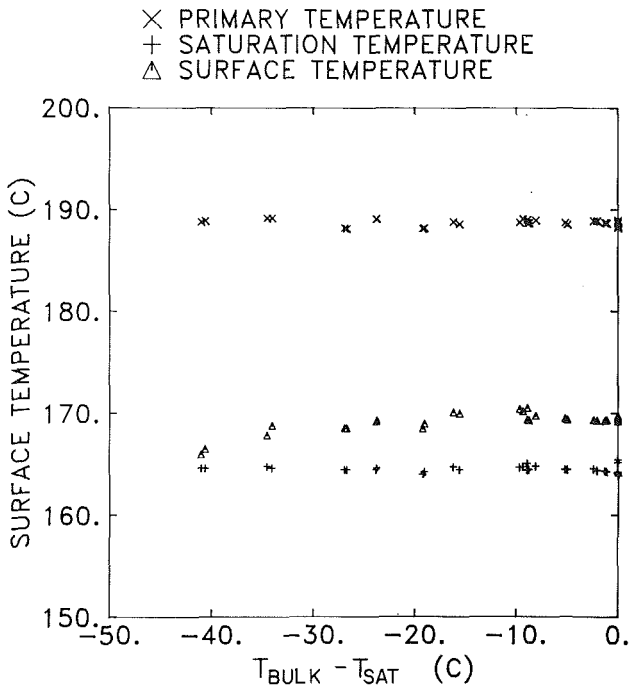

Fig. 12 Same as Fig. 10, except bare tube, outside of crevice

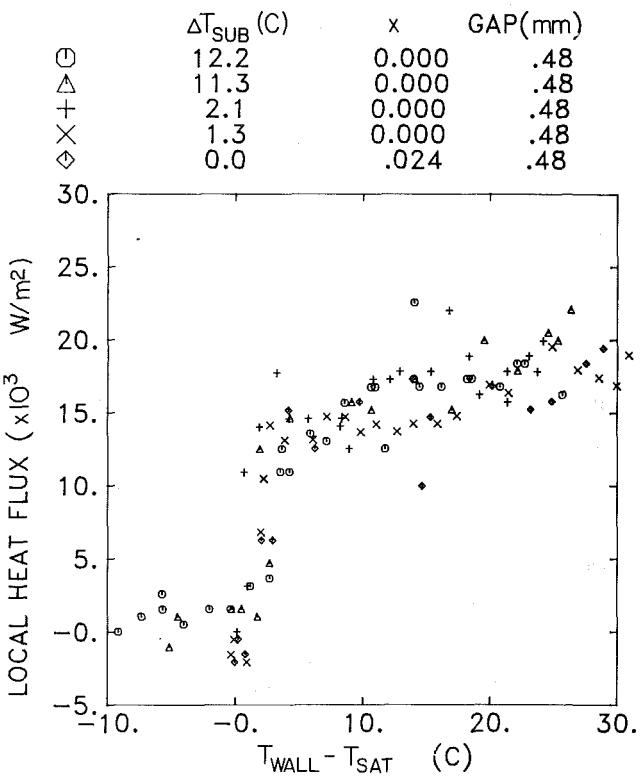

Fig. 13 Local boiling curve at the contact line: pressure = 0.69 MPa; diametral gap = 0.48 mm;

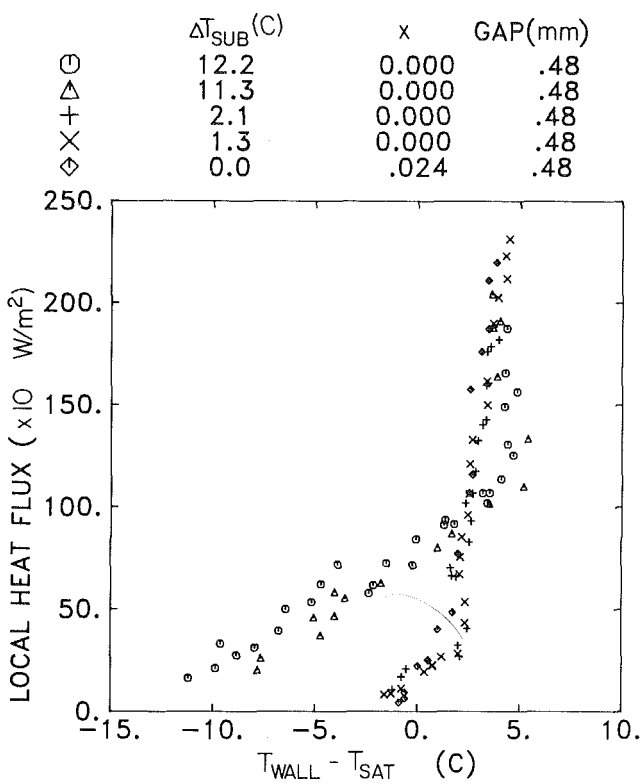

Fig. 14 Same as Fig. 13, except 135 deg from the contact line

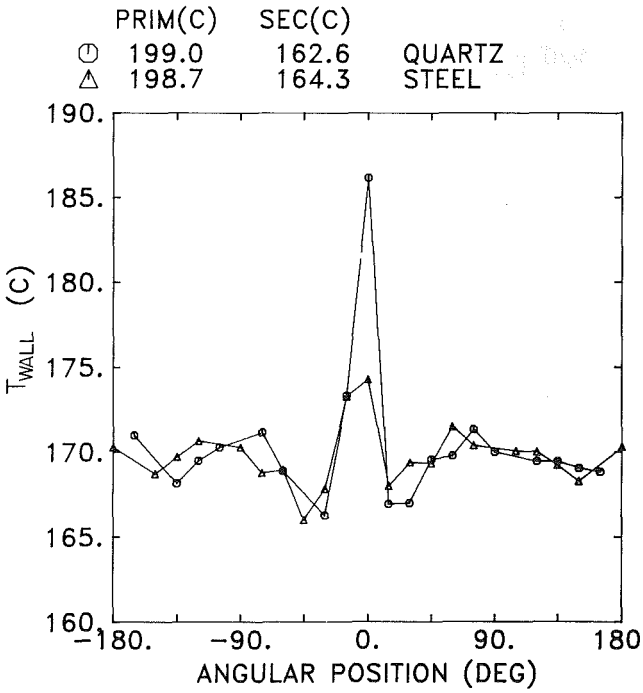

Fig. 15 Comparison of surface temperature for glass and metal TSP: pressure = 0.69 MPa; diametral gap = 2.13 mm; flow rate = 463 kg/m²s

assess the effect of support plate thermal conductivity, several experiments were run with a stainless steel TSP. Consistent with the results presented above, the varying flow rate and inlet enthalpy conditions had little effect. Therefore, it will be sufficient to examine only one of these runs in detail.

Figure 15 is an angular distribution plot for similar experiments using quartz and steel support plates. For each experiment are presented surface temperature data taken at a similar primary temperature. The quartz plate results are typical of what has previously been presented [1]. The W-shaped temperature distribution features a maximum at the contact line and a minimum on either side of the dry patch. For the steel TSP, the profile is seen to feature a W-shape as well.

In comparing the two experiments, it is noted that the wide gap region temperature profiles are much the same. Similarly,

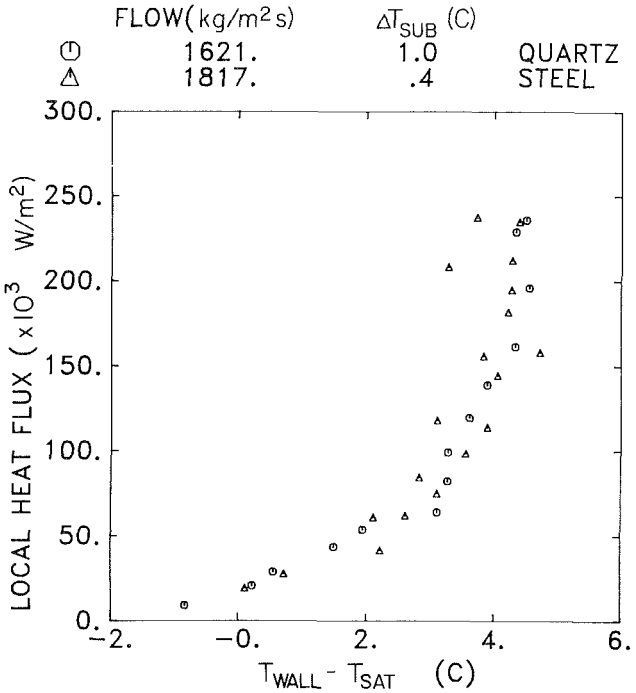

Fig. 16 Local boiling curves at 135 deg from the contact line for glass and metal TSP: pressure = 0.69 MPa; diametral gap = 2.13 mm; flow rate = 1621 and 1817 kg/m^{2}s

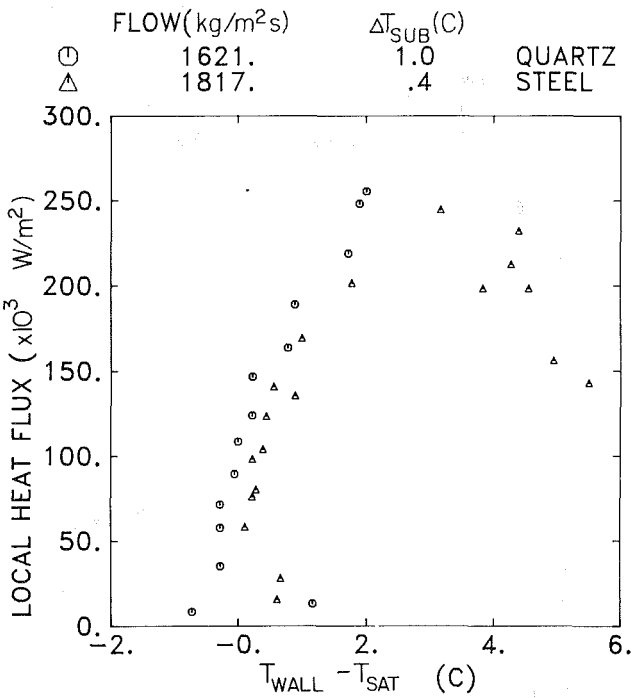

Fig. 17 Same as Fig. 16, except 15 deg from the contact line

the minimum temperature in the distributions are nearly equal. The major difference is that the maximum temperature for the steel plate is some 11 °C lower than the contact line temperature for the quartz TSP. In addition, it exceeds the average wide gap temperature by a mere 4 °C. From this alone it is not clear if dryout has occurred.

In examining the comparative boiling curves, Fig. 16 shows that the wide gap behavior is the same for both support plates. Figure 17 presents data taken 15 deg from the contact line. Here it can be seen again that the behavior is similar for both support plates. The metal TSP boiling curve reaches a definite

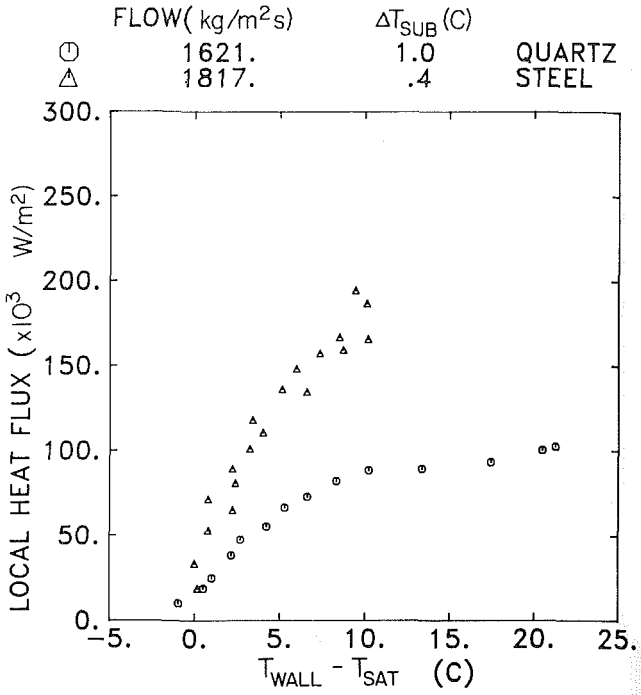

Fig. 18 Same as Fig. 16, except at the contact line

plateau. Although the wall superheat attained is not great, it is obvious that a major change in heat transfer mechanism has taken place. By analogy with what has been observed using transparent plates, the most reasonable explanation is that contact line dryout has in fact occurred. In order to examine this dryout condition, consider the 0 deg boiling curve, Fig. 18. As was indicated in the angular distribution plot, the wall superheat is lower for the steel support plate and the heat flux generally twice as great.

In conclusion, for a stainless steel support plate, under the conditions studied, contact region boiling begins at a wall superheat between 0 and 1 °C as indicated by contact region boiling curves. A dry patch forms, as indicated by these plots and by the maximum temperature at the contact line. The W-shaped temperature distribution provides evidence that the vapor sweep mechanism is in effect. Coincidence of wide gap boiling curves for metal and glass support plates shows that TSP thermal conductivity is not important there. Thermal conductivity is important only in the vicinity of the dry patch, where the metal TSP provides a lower tube wall temperature.

Acknowledgments

The authors wish to acknowledge the support of the Electric Power Research Institute under Contract S133-1. In addition, we wish to thank Drs. C. L. Williams and G. Hetsroni, who monitored the contract for the Electric Power Research Institute, for many helpful comments; and Dr. Y. Kozawa, Tokyo Institute of Technology, for the original design of this apparatus while a Visiting Scholar at Northwestern University (1978) under a grant from the Japanese Government.

References

1 Johnston, B. S., Sharon, A., Kozawa, Y., and Bankoff, S. G., "Boiling Heat Transfer in a Narrow Eccentric Annulus—Part I: Dryout," ASME JOURNAL OF ENGINEERING FOR POWER.

2 Ishibashi, E., and Nishikawa, K., "Saturated Boiling Heat Transfer in Narrow Spaces," *International Journal of Heat and Mass Transfer*, Vol. 12, 1969, pp. 863-893.

3 Jensen, M. K., Cooper, P. E., and Bergles, A. E., "Boiling Heat Transfer and Dryout and Restricted Annular Geometries," AIChe Symposium Series, 164, Vol. 73, 1977, pp. 205-214.

4 Rohsenow, W. M., and Hartnett, J. P., eds., *Handbook of Heat Transfer*, McGraw-Hill, New York, 1973, pp. 13.2-13.75.

F. Nordmann
FRAMATOME,
Groupe Chimie et Corrosion,
Paris La Défense, France

G. Pinard-Legry
CEA,
Section de'Etude de la
Corrosion Aqueuse,
Centre de Fontenay-aux-Roses, France

J. Daret
CEA,
Section d'Etude de la
Corrosion Aqueuse,
Centre de La Hague, France

J. P. Brunet
CEA,
Service d'Etude et de
Dévelopment de la Technologie
des Reácteurs à Eau,
Centre de Cadarache, France

Experimental Investigation on Denting in PWR Steam Generators: Causes and Corrective Actions

Denting studies have been undertaken in order to assess the influence of the most important parameters which could initiate corrosion of the carbon steel occurring in the tube-tube support plate crevices of some PWR steam generators. Tests have been carried out in model boilers where feedwater was polluted with sea or river water. Specific effects of chloride or sulfate and influence of oxygen content, magnetite addition and pH value were investigated. In magnetite prepacked crevices, denting is obtained within 1000 hrs for seawater pollution of 0.3 ppm chloride at the blowdown. In neutral chloride or in river water, denting is observed only with oxygen addition. Denting prevention is effective in the case of an on-line addition of phosphate, boric acid, or calcium hydroxide. For denting stopping, boric acid or calcium hydroxide is efficient even with a high seawater pollution. Soaks cannot stop denting if they are not followed by an on-line treatment (boric acid, calcium hydroxide). With quadrifoil holes, denting doesn't occur. In very severe test conditions, 13 percent Cr steel can be corroded, but the corrosion rate is low and oxide morphology is different from that growing on carbon steel.

Introduction

About seven years ago, inspections in PWR steam generators detected some diametral reductions of Inconel-600 tubes in the region of intersections between tubes and tube-support plates (TSP).

After examinations, this phenomenon, called denting, was associated with an abnormal corrosion of the C-steel TSP developed in the crevices of the intersections [1]. Magnetite formed in these regions, having a higher volume than the parent base metal, (about twice) exerts high radial compressive stresses on the tubes, which are then diametrically constricted.

A first consequence of this deformation is to hinder the passing of eddy current probes inside the tubes; secondary consequences are Inconel-600 stress corrosion cracking problems associated with the formation of high stresses on the tubes in the dented regions or in the U-bends due to the distortion of the legs. At last, a deformation of the TSP occurs in the less stiff regions (flow slot hourglassing) and in some cases ligament ruptures are observed.

Many works have been carried out to study the causes and remedies of this phenomenon [2-8]. It is now well established that this fast growth of magnetite is due to the build up in the tube/TSP crevice of an acidic chloride medium. These impurities come from condenser in-leakage and cooling water ingress into the steam generator. The role of the pH on the corrosion of the carbon steel, the oxidation rate of which increases sharply for values below 3 [8], is well known. Some uncertainties still remain concerning the role of the other chemical species and possible synergistic effects [9—13].

CEA (Commissariat à l'Energie Atomique) and FRAMATOME have been undertaking an extensive study on the mechanism of denting with laboratory tests (high-temperature electrochemical measurements, autoclave tests) and by implementation of large-scale experiments in specially designed experimental loops.

This paper reviews the results obtained with these last facilities; the first part of the program was conducted in order to have a better understanding of the effect of various chemical species—Cl^-, $SO_4^=$, O_2—on the denting occurrence and to assess the consequences of sea water or river water ingress in the steam generator.

The second part of the work is related to the study of denting stopping or prevention by using various methods such as soaks or additions of hydrazine, calcium hydroxide, lithium phosphate, or boric acid in presence of a continuous contamination. Denting prevention by modifications of the TSP design is also investigated and tests results on broached or drilled 13 percent chromium steel are reported.

Contributed by the Nuclear Engineering Division and presented at the Joint Power Generation Conference, Denver, Colorado, October 17-21, 1982. Manuscript received by the Nuclear Engineering Division July 27, 1982. Paper No. 82-JPGC/NE-4.

Experimental Facilities

Description of the Loops. All the experiments have been

Table 1 Technical characteristics of the loops

	AJAX	CLARINETTE
Primary Circuit		
Material	AISI 316	Carbon steel
Operating temperature	320°C	330°C
Operating pressure	140 bars	170 bars
Electric heater power	192 kW	500 kW
Chemistry	H_3BO_3, LiOH and H_2	LiOH
Secondary circuits		
Number of Model Boilers	16 { 8 (AJAX II); 2 × 4 (AJAX I and III)	12 { 3 (2.5-m tube); 9 (0.5-m tube)
Wrapper and/or tube sheet	Carbon steel	Carbon steel
Operating temperature (t sat)	*275°C*	*270°C*
Heat flux on tubes	400 kW•m^{-2}	400 kW•m^{-2}
Mass of water for one MB	5 kg	14 kg or 35 kg
Continuous feed and blowdown flow rates (Operating values)	1.5 l.h^{-1}	4 l.h^{-1} or 15 l.h^{-1}

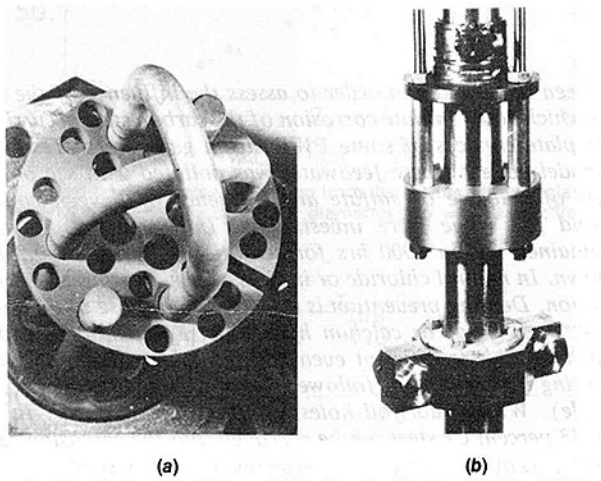

(a) (b)

Fig. 1 Crevice devices used in model boilers for denting studies (7/8-in., In-600 tubes): (a) carbon steel tube support plate (TSP) with two U-bend tubes (In-600, first row radius) in an AJAX model boiler; (b) carbon steel ring used for open crevices (upper part) or prepacked devices (lower part) with sintered caps and magnetite packed in the crevice

performed in pressurized loops reproducing the operating conditions of a PWR Steam Generator.

These loops named AJAX and CLARINETTE are designed with primary circuit heat exchanging with several steam generators or model boilers (MB). In AJAX tests, one or two U-bend tube R1) are set in each of the 16 MB; in the CLARINETTE loop the 12 test sections are straight tubes. The main technical characteristics of the loops are reported in Table 1.

Primary water circulates inside the MB tubes. Stability of the secondary water temperature is obtained by adjusting the flow rate of the condenser cooling water. Usually, all the condensate is recirculated without steam bleed.

Every MB secondary circuit is independent and has continuous injection and blowdown. Makeup water is prepared for each boiler with the planned composition (NH_3, N_2H_4, contaminants, inhibitors . . .) and then injected with flow rates as mentioned in Table 1. Various oxygen levels are obtained by adjusting the N_2/O_2 ratio in the cover gas of the make-up tanks or by using aerated water.

In some tests, the MB are continuously fed with magnetite.

A common feature of these loops is the heat flux through the Inconel tubes (30-40 W•cm^{-2}) similar to the flux on hot legs in a PWR Steam generator and the high "available superheat," which represents the Δt between primary water temperature and saturation temperature of the secondary water (45°C in AJAX and 40–60°C in CLARINETTE).

Feedwaters and blowdowns are periodically analyzed by ion chromatography (DIONEX) and colorimetry; pH and conductivities are continuously monitored on each MB blowdown.

Crevice Devices. In order to simulate the geometry of the tube/TSP intersections, carbon steel (A 285) rings (in one or two pieces) are set around the IN-600 tubes. In addition, drilled carbon steel plates are also used in AJAX loops (Fig. 1).

The average gap between devices and Inconel tube is 0.2 mm. Normally, crevices are empty at the beginning of the tests (open crevices) and injection of magnetite in the boiler simulates the sludge formation occuring in a real secondary circuit. Nevertheless, in some tests, crevices are initially filled with powder (prepacked crevices) to reproduce the situation of predenting, i.e., after the first step which is the filling of the gap by corrosion products. In this case, the triggering of denting occurs in a shorter time period, due to the local thermohydraulic conditions giving easily high concentration of impurities in the crevice.

Experimental Procedure. Usual tests durations range from 1000 to 5000 hrs. Denting evaluation is done at each shutdown every 1000 hrs) by measuring the internal diameter of the test tubes. The measurement is achieved with a two-leg mechanical probe shifted all along four generating lines of the tube. An example of the recorded diameter variations is given on Fig. 2.

Denting values are expressed as being the difference between the tube diameter values in the nonaffected zone and in the more dented area. The four azimuthal values thus obtained give an idea on the shape in the dented zone and specially on its ovalization. On graphs presented below, two kinds of denting amplitude values are usually reported: the maximum value observed in the dented zone (D_{max}) or the average of the four directions maximum denting values. In some cases a decreasing value of the denting is observed: it corresponds to a relaxation of the tube in the dented zone.

At the end of the runs, destructive examinations are performed on the tube/TSP assemblies. Investigations include optical and scanning electron microscope with microprobe analysis, specially in the crevice region, and chemical determinations of the species filling the gap between In-600 and carbon-steel.

Influence of Chemistry

Many MB tests on AJAX and CLARINETTE loops have been run to define the nature, the threshold, and the synergy of chemical contaminants able to produce denting.

Sea Water Concentration Threshold. The first part of the experimental study concerns sea water (SW) contaminations

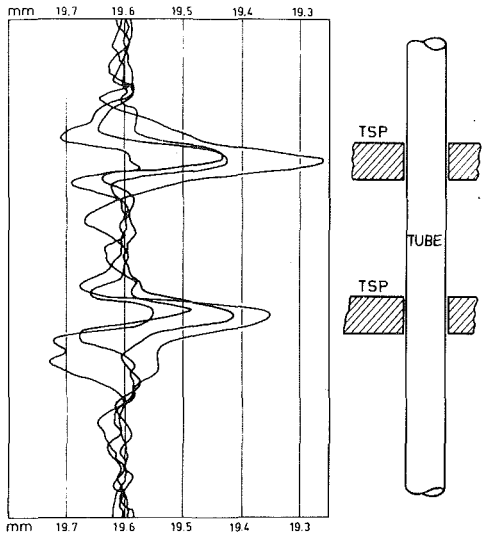

Fig. 2 Example of internal diameter recording in four directions indicating tube denting of both TSP intersections

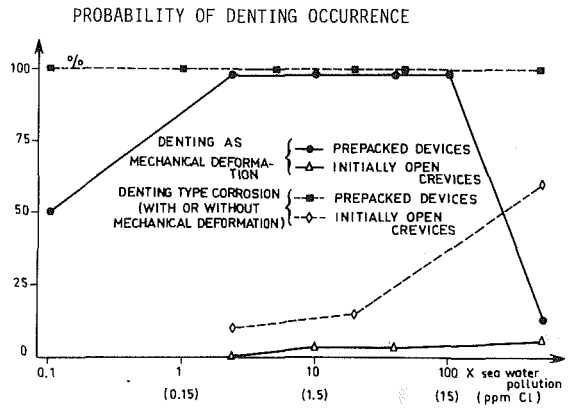

Fig. 3 Probability of denting or denting type corrosion occurrence with only seawater contamination

which are of major concern for denting occurrence in PWR plants.

With a total of about 100 prepacked devices and 100 initially open crevices, MB have been operated with natural sea water contaminations ranging from about 0.1 X to 500 X. One X corresponds to the limited value of cation conductivity allowed for normal power operation in steam generator blowdown of Framatome plants: 2 $\mu S \cdot cm^{-1}$ or 0.15 ppm chloride.

Figure 3 shows the probability of denting occurrence versus SW contamination level. In this figure, data are related to denting process, either at its early stage, which is the laminated oxide type of carbon-steel corrosion, or at its final stage, which is the mechanical deformation of the tube.

With prepacked devices, the denting type corrosion occurs, whatever the SW contamination level is. A crevice filled with porous oxide is able to concentrate any residual chloride and to produce the accelerated corrosion of carbon-steel.

However, at the lowest SW concentration (0.1 X), it is more difficult to maintain a sufficient chloride level in the crevice through the concentrating process and to get mechanical deformation, once the deposit in the crevice has been blocked.

On the other hand, if the test is performed with a very high SW content, sea water salts can deposit early in the porous magnetite, so limiting the denting process evolution. It should be considered that the sequences of the denting process are somewhat different in that case than with initially open crevices as they are in real plants. Thus, it is more realistic to

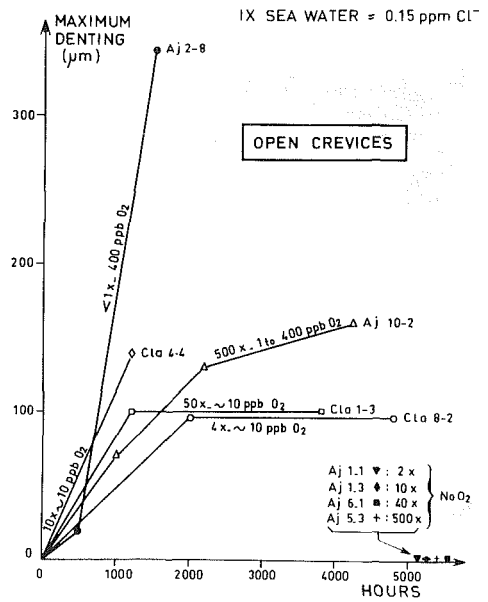

Fig. 4 Comparative tests of denting kinetics with or without oxygen contamination or magnetite addition, for various seawater contamination levels

consider, from Fig. 3 with open crevices, that denting occurrence probability increases when the SW concentration increases.

Oxygen Threshold. Some discrepancy in the results of the tests with SW contamination seems to indicate that denting occurrrence probability is much higher if a small oxygen content (either as air ingress or as a larger amount of magnetite brought into the system) is present. For example, with prepacked devices, the higher possibility of getting denting, as compared to open crevices, can be attributed to the porous concentrating medium but perhaps also to the presence of an oxygen content higher than the stoichiometry in the magnetite which has been placed initially in ambient atmosphere.

With open crevices, denting type corrosion may occur either with high SW content (500 X) and long test durations (5000 hrs), or at any SW content provided that a small amount of oxygen has been introduced in the MB during the test.

Figure 4 gives some examples of comparative tests performed with a small amount of oxygen in the feedwater (about 10 ppb) producing denting or with a careful elimination of oxygen which did not produce denting on open crevices.

The AJAX 2.8 test without SW contamination (chloride content in steam generator blowdown lower than 0.1 ppm) gave significant denting in the presence of high oxygen (as air) contamination. An example of micrographic examination showing the laminated denting type corrosion obtained in this test is presented on Fig. 5.

pH Influence. When $FeCl_2$ (0.1 to 1 ppm Fe) or $CuCl_2$ (0.2 ppm Cu) is added to a MB with a 40 X SW contamination, denting occurrence probability on open crevices is about 70 percent (after 1000 hrs). Should be magnetite also be continuously injected into the MB, the mechanical denting probability reaches 94 percent (within 1000 hrs).

Thus, the addition of hydrolysable salts, producing a more acidic condition than SW contaminations, increases denting occurrence probability and denting kinetics on open crevices.

On the other hand, a test with neutral chloride (NaCl) did not dent the open crevices in 2500 hrs, while the two prepacked devices dented. This confirms that the prepacked devices constitute a pessimistic experimental condition.

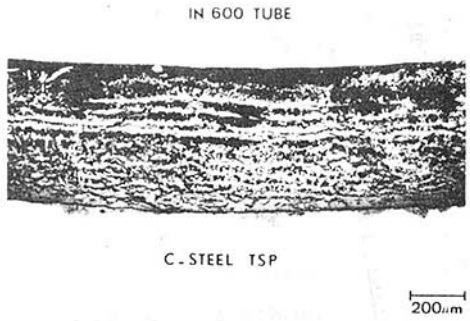

Fig. 5 Transverse section of an initially open crevice showing that denting can be obtained within 2700 hrs in the case of high oxygen content (400 ppb 0_2) and magnetite injection, without other pollution

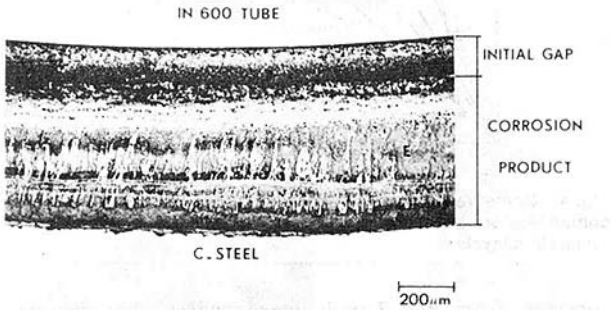

Fig. 6 Transverse section of a precracked device where denting was obtained using Loire river water pollution (conductivity = 10 $\mu s \cdot cm^{-1}$) and a high oxygen ingress (400 ppb 0_2 in the feed water) during 2000 hrs

Th oxygen-pH synergy has been also deduced from river water tests.

The river waters used are coming from French nuclear sites (Loire and Rhone rivers) and are alkaline forming under heating and concentration process.

In these tests, none of the open crevices dented, even in the presence of oxygen, and the prepacked devices need a high oxygen contamination to dent (denting type corrosion is shown on Fig. 6). With river water contaminations of 10 $\mu S \cdot cm^{-1}$ total conductivity at the MB blowdown, the laminated type corrosion also occurred in an open crevice, with a high oxygen level (0.1 ppm in the feedwater).

In addition to the pH influence, lowering the denting occurrence in river water contamination tests, several neutral or alkaline nonaggressive compounds (calcium hydroxide for example) are able to plug the crevice by precipitation, according to their low solubilities.

Sulfate Influence. It appears interesting to compare the chloride and sulfate influence on denting occurrence in order to define the specific effect of the anion on denting and to know if sulfate contaminations have a beneficial or detrimental effect. Such contaminations may come from chemicals used for resin regeneration in demineralization plants or from releases of resin fines which decomposes. Sulfate salts are also present, beside chlorides, in the raw water for condenser cooling.

Comparative tests about respective effect of chloride and sulfate have been run. A test with sea water (40 X) plus $FeCl_2$ (1 ppm Fe) plus magnetite addition gives 100 μm of denting after 1000 hrs on open crevices. Another test, with the same cation contamination, but where chloride have been replaced by sulfate, did not produce denting after 3000 hrs.

Moreover, an oxygen addition in a test with neutral plus acidic sulfates did not produce denting after 3000 hrs on open crevices.

Discussion. All these results on chemistry influence show the following points:

- A sea water contamination (containing about 10 percent of its chloride in potentially acidic form $-MgCl_2$—and 90 percent in neutral form—NaCl) is able to produce denting, particularly if a small amount of oxygen is present (either as air ingress, or as magnetite which has been exposed to air).
- A high oxygen contamination would be sufficient to produce denting, even if the system is not particularly contamined by chlorides (less than 0.1 ppm at the MB blowdown).
- If more acidic chlorides (from $FeCl_2$) are added with sea water, denting can be easily obtained.
- If an alkaline contamination (river water condenser ingress) occurs, the denting phenomenon will probably require the simultaneous presence of oxygen contamination, because the presence of alkaline compounds decreases the ability to build up an acidic chloride medium in the crevice.
- Sulfate ions, even in acidic conditions, does not have the same capability as chlorides to produce denting, perhaps due to the complexing role of Cl^- [11].

Water Soak—Switch to a Pure AVT Chemistry Hydrazine Treatment

The use of additives which could concentrate in the steam generator or deposit on various parts of the secondary system always potentially presents side effects. As a consequence, another procedure without this inconvenience has been tested.

It consists, after a seawater (SW) polluted test sequence, in a "water soak" followed by an operation with a pure all volatile (AVT) chemistry. The water soak is a low power operation of a limited duration, with a very low heat flux on the steam generator tubing. Such a procedure is intended to simulate an attempt to return from hide-out the chloride and the other compounds which have been concentrated and/or deposited in the crevice during a contaminated phase.

Applied on already dented devices in MB, it shows clearly that it is not able to stop an active denting which nearly remains as much active during the last sequence of the test (normal power operation in pure AVT conditions) as if the SW contamination had been maintained.

As an example, a test with eight prepacked devices, operating for 1400 hrs with a 40 × SW contamination, has been "water soaked" and then operated with only ammonia (0.25 ppm NH_3) and hydrazine (0.2 ppm N_2H_4) for 4600 hrs. The denting remained active on all the devices and the average denting (for the 8 devices), which was of about 130 μm at the water-soak time, reached 400 μm at the end of the test.

Considering that such water soaks were ineffective for denting stopping, the procedure has been applied periodically (every 500 hrs) on open crevices in order to try to prevent denting.

The results showed that the water soak was able to return from hide-out about 90 percent of the chloride contained in the devices; however, during the following operation sequence with SW contamination, the chloride concentration process resumed very quickly so as the water soak was worthless.

The only case where the water soak might be of some benefit, is when a SW contamination occurs. The plant could be immediately water-soaked to try to return from hide out as much chloride as possible, and then operated without contamination. However, confirming this beneficial effect on MB tests would be difficult, since it would take very long test durations on many MB in order to take into account the discrepancy of such results on open crevices.

Thus, the water soak procedure without subsequent AVT operation is not considered efficient to prevent or to stop denting; on the other hand, it has been shown that the oxygen has an important synergistic effect when SW is present, and that oxygen should be present to produce denting with river water contamination. This is the reason why another kind of

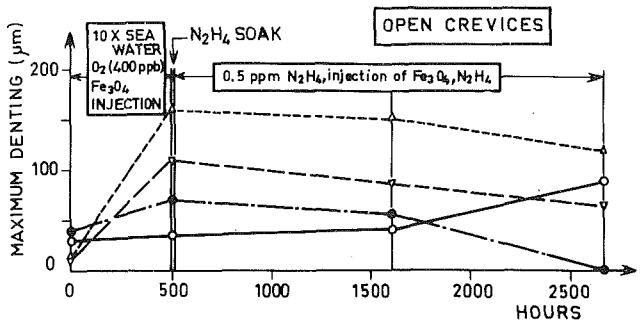

Fig. 7 Denting stopping by hydrazine soak, plus on-line treatment

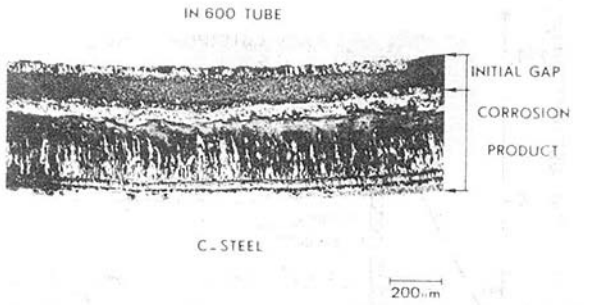

Fig. 8 Transverse section of a prepacked device showing that phosphates are not always efficient to prevent accelerated denting type corrosion (1200 hrs, 10 X, i.e., 1.5 ppm Cl^- as seawater, and lithium phosphate addition: 4 ppm PO_4)

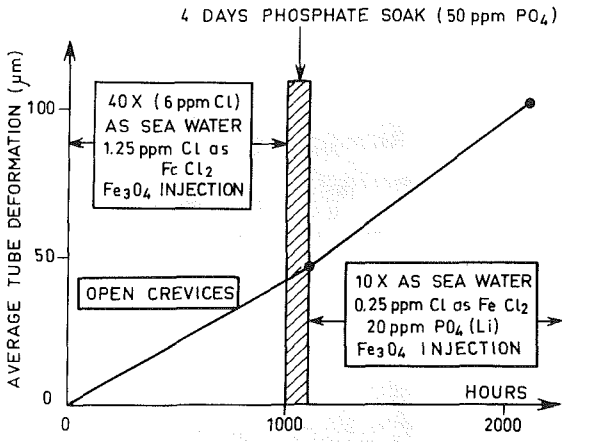

Fig. 9 Attempt to stop denting by soak, plus on-line phosphate treatment

treatment has been tested: the hydrazine soak followed by an on-line treatment.

The soak is performed with a high hydrazine content in the MB (150 ppm); the on-line treatment is a normal operation but with higher hydrazine concentrations (0.5 to 5 ppm) than usual.

A few tests started with a hydrazine soak in order to reduce the oxygen excess present in the MB after its opening during the shutdown, the tests operated with an on-line hydrazine treatment and 10 X or 40 X SW contaminations.

This was not able to prevent denting occurrence on prepacked devices (about 150 μm of maximum denting after 1000 hrs) or on open crevices where $FeCl_2$ and Fe_3O_4 were continuously added into the MB (same denting kinetics as above).

One test which had been started with 10 X SW, oxygen and magnetite contamination, gave denting on open crevices as expected (Fig. 7). Then, the hydrazine soak followed by the on-line treatment without contamination (besides the magnetite) was able to stop denting, whereas a water soak followed by a pure AVT operation (without particular hydrazine addition) would probably not have been able to stop it.

Destructive micrographic examinations clearly indicated that a transition to a nondenting type corrosion occurred and that hydrazine treatment, in addition to chloride removal, helped to remove the corrosion products from the crevice.

A river water contamination test was conducted where denting had been obtained in presence of oxygen elimination and the hydrazine soak followed by the on-line treatment stopped the denting, even while maintaining the river water pollution.

Such results show that the hydrazine soak plus on-line treatment may help to stop denting with a rather good efficiency, provided that the sea water ingress be discontinued.

Use of Chemical Additives to Inhibit Crevice Denting Corrosion

If one assumes that the rapid corrosion of carbon steel, which is the cause of denting, is due to the concentration of aggressive, generally acid and chlorinated species in some areas of steam generators, then the use of chemical additives able either to neutralize these media, to prevent their formation, or to protect the carbon steel might be an effective way to inhibit the phenomenon.

Therefore, tests were performed with seawater contaminations that used different neutralizers or boric acid, which acted as a reaction product transport inhibitor or a pore plugger [4].

Use of Neutralizers.

Phosphates. The first neutralizing additives which have been tested as potential denting inhibitors were the sodium or lithium phosphates (4 to 20 ppm PO_4, Na/PO_4 or Li/PO_4 molar ratio equals 2.5). The advantage of using lithium phosphate would be to avoid the problems formerly encountered with caustic stress corrosion cracking of Inconel 600.

Phosphate additions from the start-up, simultaneously with pollutions which otherwise give denting, are efficient to prevent the tube deformation, but not always to prevent accelerated corrosion of TSP carbon steel (see Fig. 8). Difficulties to maintain the correct molar ratio have been confirmed. In other tests, phosphate was added after denting was established. This on-line addition had no noticeable effect. Then tests were performed with phosphate applied as low heat flux soak (50 ppm PO_4) followed by on-line addition (20 ppm PO_4) on open crevices previously dented in sea water and ferrous chloride medium.

This procedure was generally ineffective to stop the denting progression (Fig. 9).

So, lithium or sodium phosphates are not held to be satisfactory denting stopping inhibitors.

Calcium Hydroxide. The second neutralizing additive that has been tested is calcium hydroxide. Laboratory tests with continuous injection of $Ca(OH)_2$ (10^{-4} mole$\cdot$kg^{-1}) from the start-up show that this treatment is effective to prevent tube denting.

In another test $Ca(OH)_2$ was applied, afer denting was established, as a soak (10^{-4} mole$\cdot$kg^{-1}) followed by a 1000 hrs on-line addition (10^{-4} mole$\cdot$kg^{-1}). This treatment has a very good efficiency, and a memory effect was noted in the last 2000 hrs where calcium hydroxide was no longer added (Fig. 10).

The cause of this effectiveness and of this memory effect is that a lot of calcium compounds are precipitated in the crevices, causing alkaline conditions in these restricted areas, but also plugging the TSP crevices and thus probably

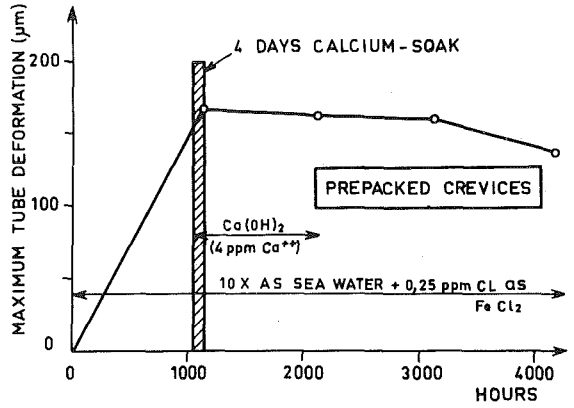

Fig. 10 Denting stopping with soak, plus on-line calcium hydroxide treatment. Memory effect during the last 2000 hrs.

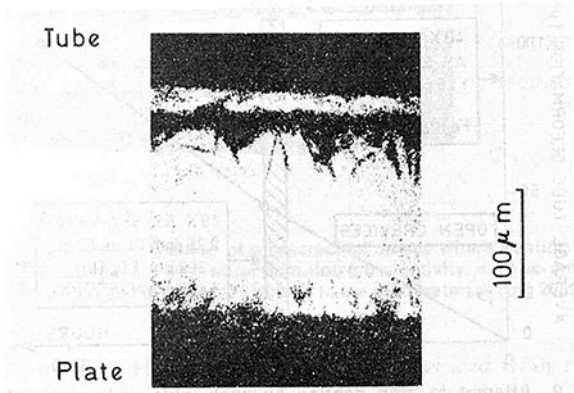

Fig. 11 Electron microprobe microanalysis of a transverse section. Image of calcium deposited in an open crevice, preventing denting to appear in presence of 10 X (i.e., 1.5 ppm Cl as seawater) during all the test (5700 hrs) and of calcium hydroxyde (10^{-4} mole·kg^{-1}-during 2400 hrs

preventing further penetration of impurities (Fig. 11). It must be noted that for test durations up to 6000 hrs, only a slight deposit has been observed on the straight parts of the tubes outside the crevices. That is in a good agreement with the predictions of a computer program developed by FRAMATOME, which indicates that with such level of pollution and Ca $(OH)_2$ addition, calcium hydroxide is precipitated in crevices and not on outside parts of the tubes. The last point which remains to be verified is that calcium hydroxide keeps its effectiveness in presence of dissolved oxygen.

Use of Boric Acid. Let us recall that the idea of using boric acid as an inhibitor came from the TURKEY POINT experience, where an ingress of boric acid due to a primary to secondary leak resulted in a decrease in the level of corrosion induced hydrogen.

Laboratory tests confirm that boric acid addition (2 to 10 ppm B) from the start-up is efficient to prevent denting in the case of sea water pollutions and absence of dissolved oxygen. The reason for this effectiveness might be the formation of iron boron compounds within the corrosion product layers, but the subsequent role of these insoluble species is not yet clear.

Moreover some doubts appeared about boric acid effectiveness to prevent denting in the case of dissolved oxygen presence together with sea water pollution. To clear the matter up, a test has been conducted first without oxygen and then with a high level of dissolved oxygen (up to 400 ppb in the feedwater). Figure 12 shows the deleterious effect of the oxygen presence. Secondary ion mass spectrometry (SIMS) is

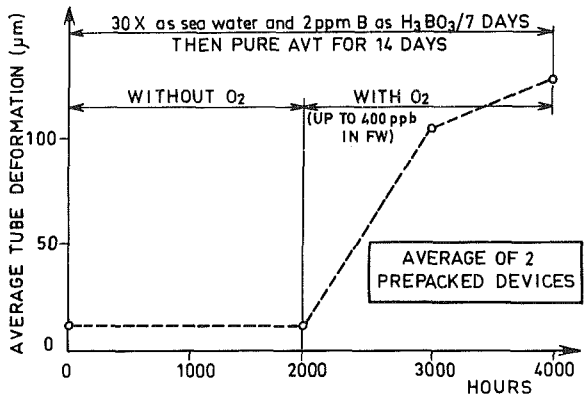

Fig. 12 Consequence of dissolved oxygen on boric acid effectiveness to prevent denting

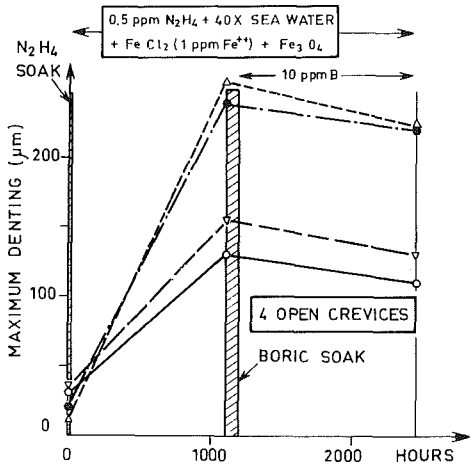

Fig. 13 Denting stopping by soak, plus on-line boric acid treatment

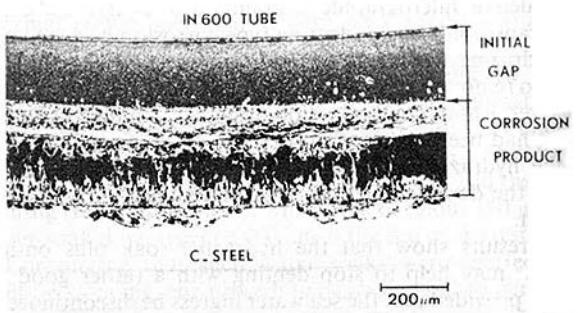

Fig. 14 Transverse section of a prepacked device where tube deformation has been stopped by a boric-soak (4 days, 25 ppm B) followed by a 4000 hrs on-line boric acid addition (2 to 10 ppm B). Sea water and ferrous chloride (1.75 ppm total Cl^{-1}) were present all the time. The penetrations beneath the regular front of denting-type corrosion are always associated with the arrest of tube deformation.

in progress to see if there is a difference in the corrosion product layers.

Boric acid efficiency to stop an established denting has also been verified in laboratory tests without dissolved oxygen. Several procedures were tested, combining low heat flux soaks (25 to 50 ppm B as H_3BO_3) with on-line additions (10 ppm B). A typical result is presented in Figs. 13 and 14, showing a very good effect of boric acid.

Discussion. Among the chemical additives susceptible to inhibit crevice denting corrosion, calcium hyroxide and boric acid seem very efficient, on condition that oxygen is absent in the feedwater. If such is the case, on-line addition of any of these products prevents the onset of denting, and a combined

soak and on-line treatment, with either calcium hydroxide or boric acid, is effective in arresting tube deformation. Some problems may occur if dissolved oxygen is present in the feedwater, showing once again that this element is very harmful to steam generator integrity.

Modified Tube Support Plates

Beside the chemical treatment, the denting problem can be overcome by modifying the design of the TSP to limit the crevice effect and by changing the carbon steel to a more noble alloy. For this reason, studies have been performed to assess the respective advantages of the two modifications:

- Broached instead of drilled TSP
- Thirteen percent chromium ferritic alloy to replace the A 285 carbon steel

It should be noted that in the new French steam generators, TSP are made of broached chromium ferritic steel.

Description of the Tests. For the effect of the material, comparison is done between 13 percent Cr steel (Z 10 C 13) and carbon steel (A 285). Devices, set in the same model boilers, are prepared in the following conditions:

- Drilled and magnetite prepacked devices
- Drilled open crevices

For evaluation of the effect of the geometry, broached (quadrifoiled) TSP made of both alloys were used.

Duration of experiments ranged from 2000 hrs to 9000 hrs with various levels of sea water pollutions, the most corrosive conditions being AVT + 50 X (sea water) + 1 ppm ($FeCl_2$) and magnetite injection.

Results

Material Effect. In the open drilled crevices, denting was only observed with carbon-steel TSP and never with 13 percent Cr-steel even in the most aggressive conditions after a 9000 hrs duration test.

With 13 percent prepacked devices which cannot be considered as fully representative, only one case of minor deformation has been observed with the most severe contamination. However, in this case, the denting rate was from 10 to 30 μm per 1000 hrs, whereas in the same test, the denting rate was 150–200 μm/1000 hrs in the carbon-steel. Moreover, micrographic examinations seem incompatible with a deformation possibility. Indeed the volume of the oxide does not seem higher than that of the parent metal (Fig. 15).

Geometry Effect. Denting was not detected in any tubes fitted with broached C-steel or Cr-steel TSP in the experimental conditions mentioned above.

Micrographic Examinations. In Z 10 C 13, open-drilled plates, an irregular corrosion of the steel is observed (Fig. 16).

After 9000 hrs with 40 X + $FeCl_2$, the thickness of the oxide layer is less than 0.2 mm. The aspect of the oxide seems less compact than the thick magnetite formed on C-steel.

The corrosion is more irregular and localized when the chemical conditions are less aggressive (Fig. 17).

In the case of broached TSP, corrosion of the carbon steel is observed on the zone touching the tube. The thickness of the remaining oxide layer is irregular (Fig. 18) and does not have the same compact aspect as in dented crevices. However, even if there is no denting, the consequence of such a corrosion in a very severe chemical condition, is to increase the gap and to allow a higher amplitude for the displacement of the tube.

Conclusions

From the results of the tests presented in this paper, it is possible to outline some conclusions concerning the onset of denting and the procedures which seem to be effective to prevent or stop this phenomenon in PWR Steam Generators.

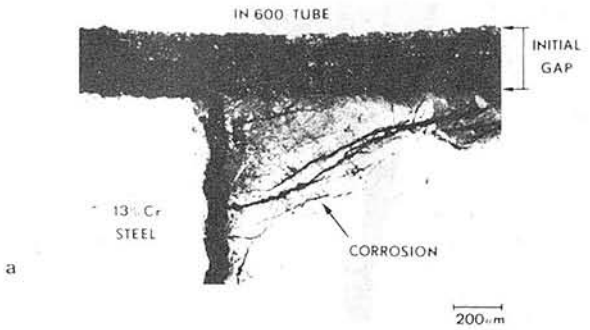

(a) View of the maximum corrosion observed on the 13 percent Cr-steel, at the junction of the two pieces of the device. The corrosion products do not have the laminated morphology observed on carbon steel and generally associated with tube denting. On the left part, the initial gap does not seen to have increased.

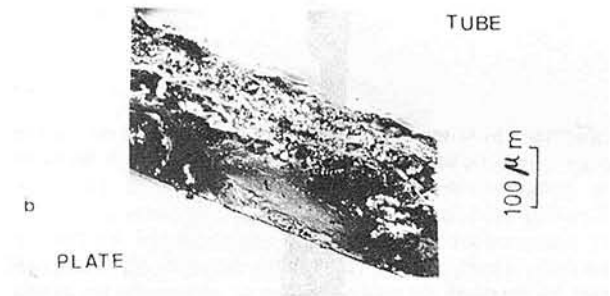

(b) Irregular generalize corrosion showing locally less compact oxides.

Fig. 15 Transverse section of the prepacked 13 percent Cr-steel device where tube deformation occurred (7400 hrs, 7.5 ppm Cl^- as seawater, 1.25 ppm Cl^{-1} as $FeCl_2$, magnetite injection).

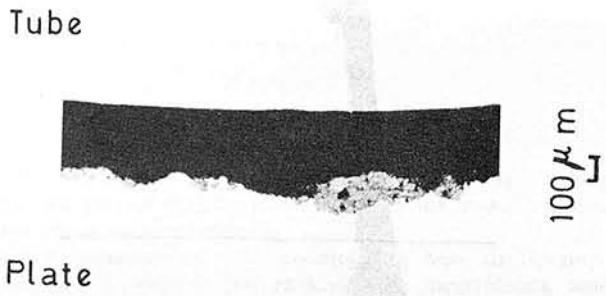

Fig. 16 Transverse section of a 13 percent Cr-steel TSP with an initially open crevice. The oxide layer is narrow as compared to that obtained in same chemical conditions (7.5 ppm Cl as seawater, 1.25 ppm Cl as $FeCl_2$, magnetite injection, 7400 hrs) on carbon steel. The oxide morphology is not laminated as when denting occurs on carbon steel TSP.

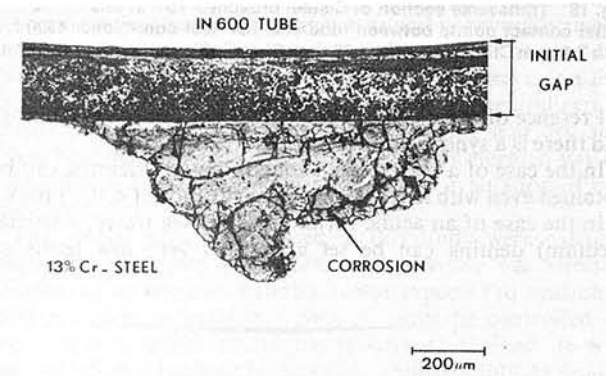

Fig. 17 Transverse section of a prepacked device showing the type of corrosion generally observed on 13 percent Cr-steel: deep but localized, and different from that obtained on carbon steel (2000 hrs with Loire river water pollution—70 $\mu s \cdot cm^{-1}$—and high oxygen ingress: 400 ppb O_2)

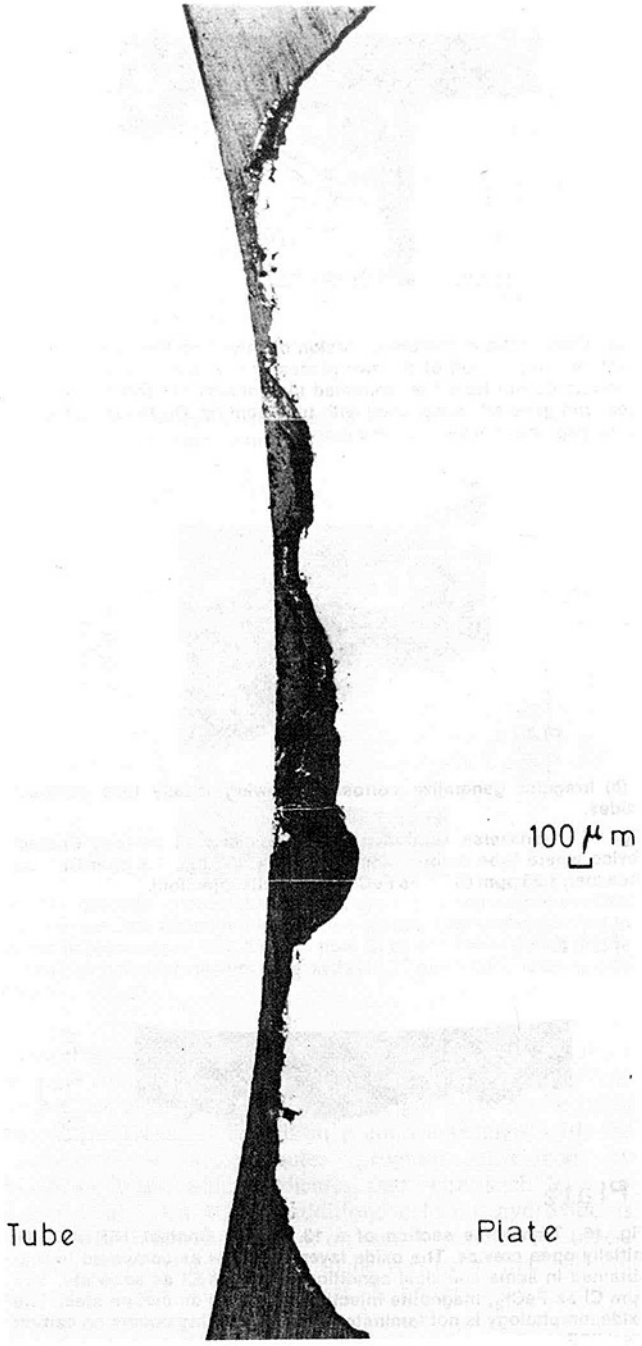

Fig. 18 Transverse section of C-steel broached TSP at one of the two initial contact points between tube and TSP test conditions: 4300 hrs with 7.5 ppm Cl as sea water, 1.25 ppm Cl as $FeCl_2$ magnetite injection

Presence of chloride appears to be necessary to get denting, and there is a synergistic effect with oxygen.

In the case of a high oxygen contamination, denting can be obtained even with low chloride concentrations (< 0.1 ppm).

In the case of an acidic forming water (sea water, artificial medium) denting can be set even with very low levels of chloride. In the case of alkaline forming river water, oxygen is a triggering element for denting evolution. For this reason, in the case of river water cooling, the best way to prevent denting is to avoid oxygen ingress into the steam generator, by, for instance, hydrazine injection in the appropriate part of the system. This procedure would be also convenient for stopping denting in the same case.

Boric acid and calcium hydroxide are efficient inhibitors to prevent or to stop denting. The best procedure is to perform a soak followed by an on-line addition.

However, the inhibitors effectiveness might be limited in case of simultaneous significant sea water contamination (1.5 ppm Cl) and oxygen ingress (400 ppb in feedwater).

In the absence of chloride, sulfate even in very acidic conditions does not lead to denting.

Acknowledgment

This CEA and FRAMATOME work has been performed in a research program part of an agreement between CEA, EDF, FRAMATOME and WESTINGHOUSE. We thank the other parties for permitting publications.

Special thanks to MM. Lefevre, Y., Colin, G., and Vincent, J., for the metallographic examinations and to the team of AJAX and CLARINETTE loops for their experimental assistance.

References

1 Van Rooyen, D., and Weeks, J. R., "Denting of Inconel Steam Generator Tubes in Pressurized Water Reactors," BNL - NUREG 50778, 1978.

2 Wootten, M. J., Economy, G., Pebler, A. R., and Lindsay Jr., W. T., "Laboratory Investigations of the Denting Phenomenon in Nuclear Steam Generators," *Materials Performance*, Vol. 17, No. 2, 1978, p. 30.

3 Vaia, A. R., Economy, G., Wootten, M. J., and Aspden, R. G., "Denting of Steam Generator Tubes in PWR Plants," *Materials Performance*, Vol. 19, No. 2, 1980, pp. 9-24.

4 Wolfe, C. R., Esposito, J. N., Whyte, D. D., Gilkinson, J. M., Balavage, J. R., Wootten, M. J., and Wozniak, S. M., "Model Boiler Inhibition Studies of the Nuclear Steam Generator Denting Phenomenon," *Nuclear Technology*, Vol. 55, No. 2, 1981, pp. 405-421.

5 Brown, J., Gonzalez, F., Iley, D., and Mc Kay, A., "Studies of Denting of Steam Generators With Simulated Fresh Water In-Leakage," *Nuclear Technology*, Vol. 55, No. 2, 1981, pp. 513-524.

6 White, E. L., and Berry, W. E., "Effects of Cu and Ni Compounds on the Corrosion of Pressurized Water Reactor Steam Generator Materials," *Nuclear Technology*, Vol. 55, No. 1, 1981, pp. 135-150.

7 Pathania, R. S., and Mc Vey, E. G., "Evaluation of Sodium Phosphate as a Denting Inhibitor," *Nuclear Technology*, Vol. 55, No. 1, 1981, pp. 178-190.

8 Campan, J. L., Pinard Legry, G., and Vignes, A., "Denting Mechanism and Kinetics With Sea Water Pollution," paper presented at the ANS 2nd International Conference, Oct. 6-10, 1980, St. Petersburgh, Fla.

9 Ashford, J. H., Garnsey, R., and Mann, G. M. W., "Corrosion of Mild Steel Under Heat Transfer in High-Temperature Aerated Sodium Chloride Solutions," *Corrosion Science*, Vol. 14, 1974, pp. 515-525.

10 Bianchi, G., Formaro, L., Mazza, F., and Torchio, S., "An Electrochemical Model for the Interpretation of the Morphology of the Laminated Magnetite in the Corrosion on Load of Boiler Tubes," *Proceedings of 7th International Congress on Metallic Corrosion*, 1978, Rio de Janeiro, pp. 1489-1501.

11 Scheiman, M. A., "Kinetics of the Chloride-Induced Oxidation of Iron at 300°C," *Corrosion Science*, Vol. 12, 1972, pp. 477-494.

12 Castle, R., and Mann, G. W., "Denting Corrosion of PWR Steam Generators, Heated Crevice Experiments With Feedwater Containing Dissolved Oxygen," EPRI Workshop on Causes of Denting, May 11-13, 1981, New York.

13 Garnsey, R., "PWR Steam Generator Denting: a Problem Solved but not yet Quantified," EPRI Workshop on Causes of Denting, May 11-13, 1981, New York.

T. A. Beineke

J. F. Hall

K. E. Marugg

D. B. Scott

R. M. Orsulak

E. E. Grondahl

E. J. Silva

G. C. Fink

Combustion Engineering, Inc,
Materials and Chemistry Department,
Windsor, Conn. 06095

Chemical Neutralization to Control Denting in Nuclear Steam Generators

Laboratory testing at Combustion Engineering has indicated promise in controlling simulated steam generator tube denting through chemical neutralization. Testing was limited to on-line treatment, and two neutralizers have been evaluated: (i) calcium hydroxide, and (ii) boric acid. On-line treatment with calcium hydroxide successfully halted active denting whenever the bulk calcium concentration (in ppm) equaled or exceeded the bulk chloride concentration (in ppm). Calcium hydroxide also was effective as an alternative to ammonia as a pH controlling agent in two tests conducted without ingress of chloride. On-line treatment with boric acid consisted of a four-day soak at simulated low (approximately 30 percent) power with 50 ppm B followed by one month full-power operation with 10 ppm B. This treatment also halted denting. Nondestructive and destructive examination of test boilers gave no indication of adverse side effects associated with either neutralizer.

Introduction

In some nuclear steam generators, accelerated corrosion of carbon steel tube support plates has occurred at their intersections with heat transfer tubing. The resulting oxide, a hard, adherent, nonprotective magnetite, fills the space between the tube and the support and can exert compressive forces on the tubing sufficient to produce local deformation. This phenomenon is known as denting, and can lead to support plate cracking and may induce stress corrosion cracking of the tubing. Denting has generally been associated with contaminant ingress from condenser leakage and the subsequent concentration of these impurities, particularly chlorides, in crevice areas, followed by the breakdown of the normally protective magnetite film.

Most investigators agree that an acidic chloride environment can promote the breakdown of the protective magnetite film. In laboratory-produced dents, concentrations of chloride have been found under nonprotective magnetite, near the corroding interface between oxide and carbon steel in regions isolated from direct contact with the bulk environment. As a consequence of this accumulation of chloride, denting, once initiated, may continue without the presence of high levels of chlorides in the bulk environment. Dented steam generators have continued to experience denting even after impurity ingress to the steam generators was substantially reduced, although laboratory testing indicates that the rate of denting is substantially lower when chloride concentrations are reduced.

The objective of this investigation was to develop a chemical procedure for removing or neutralizing acidic chlorides in crevices and thereby arrest dent progression.

Low-temperature, isothermal soaks to halt denting were first considered as near-term actions that could be rapidly developed for field application. The risk of deleterious side effects from isothermal soaks was considered low, due to the short exposure time and the lack of a crevice concentrating mechanism. Isothermal soaking was found to be ineffective in arresting denting leading to the evaluation of on-line additions of neutralizers. Unlike isothermal soaks, on-line power operations were expected to concentrate neutralizers in crevices because of heat flux, surface boiling and dry-out. These benefits, however, are accompanied by elevated risk of deleterious side effects, requiring a careful evaluation of on-line neutralization.

The on-line neutralizers used in this study were calcium hydroxide and boric acid. Calcium hydroxide was selected because, as an alkaline material, it was expected to neutralize crevice acidity. Alkalinity, however, must be controlled to avoid caustic attack of tubing at stressed regions. It was anticipated that calcium hydroxide's limited solubility would minimize or preclude caustic attack. Boric acid was chosen for on-line testing based on past success in halting denting in testing conducted by another NSSS vendor [1-3].

The principle objective of this study was to develop a

Contributed by the Nuclear Engineering Division and presented at the Joint Power Generation Conference, Denver, Colorado, October 17-21, 1982. Manuscript received by the Nuclear Engineering Division July 27, 1982. Paper No. 82-JPGC/NE-11

Table 1 Test boiler thermal hydraulics

Test Vehicle	Inlet Primary Temp.	Secondary Pressure	Maximum Primary to Secondary ΔT^a
Pot 1M	600°F (590K)	1000 psig (6.9 MPa)	54°F (30K)
Pot 7F (100% power)	600°F (590K)	1000 psig (6.9 MPa)	54°F (30K)
Pot 7F (30% power)	560°F (570K)	950 psig (6.6 MPa)	20°F (11K)
Pot 9A	600°F (590K)	1030 psig (7.1 MPa)	50°F (28K)
Pot 10	600°F (590K)	1000 psig (6.9 MPa)	54°F (30K)
Pot 11A	600°F (590K)	960 psig (6.6 MPa)	58°F (32K)
Model 4	620°F (600K)	1055 psig (7.3 MPa)	67°F (37K)
Model 8 (100% power)	620°F (600K)	1055 psig (7.3 MPa)	67°F (37K)
Model 8 (30% power)	580°F (580K)	1055 psig (7.3 MPa)	27°F (15K)

[a] Maximum primary to secondary ΔT in T_{in} (primary) - T_{sat} (secondary)

Table 2 Comparison of test units with steam generators

Type of unit	Heat flux	Bulk water volume-to-crevice volume ratio
Pot boiler	10,000–20,000 Btu/hr/ft^2 (30,000–60,000 W/m^2)	11,000
Model steam generator	40,000 Btu/hr/ft^2 (120,000 W/m^2)	44,000
Field unit (i.e., actual steam generator)	100,000 Btu/hr/ft^2 (300,000 W/m^2)	8,000

neutralization procedure applicable to operating plants which would limit dent growth.

Experimental

Test Facilities. On-line neutralization procedures were evaluted in two test vehicles—pot boilers and model steam generators. Pot boilers are small refluxing autoclaves heated internally by the circulation of pressurized water [600°F (590K) at approximately 2000 psig (1.34 MPa)] through four inverted U-tubes. Steam produced on the secondary side is condensed at system pressure and returned to the pot by gravity. The pot boiler environment includes boiling heat transfer on the tube and dryout in concentrating crevices. Tube denting at simulated tube supports is induced by seawater and simulated copper alloy feedtrain corrosion product ingress. Model steam generators are similar to pot boilers, but have 16 inverted U-tubes, increased heat fluxes, and a tube bundle shroud to achieve natural circulation between downcomer region and tube bundle. Thermal hydraulic information for each test vehicle is summarized in Table 1.

Although these units differ markedly in size and detail, major features are comparable as illustrated in Fig. 1. Suitable instrumentation was installed to control secondary temperature, pressure, and water level. Sample and blowdown lines were afixed at various elevations to provide flexibility of testing and control. Various support structures and steam blanketed regions were simulated as described below. Since the objective of this testing was to evaluate crevice corrosion, selected crevices in both units were instrumented with high-temperature strain gauges. The measurement of strain was the primary experimental measurement which was related to denting. Trends and changes in denting rates were indicated qualitatively but clearly by strain gauges, although there is no quantitative means to equate strain with denting. The principal differences between these test units and actual steam generators were the reduced heat fluxes in these units and the substantially increased bulk water volume-to-crevice volume ratio as shown in Table 2.

The four alloy 600 tubes in the pot boiler were widely

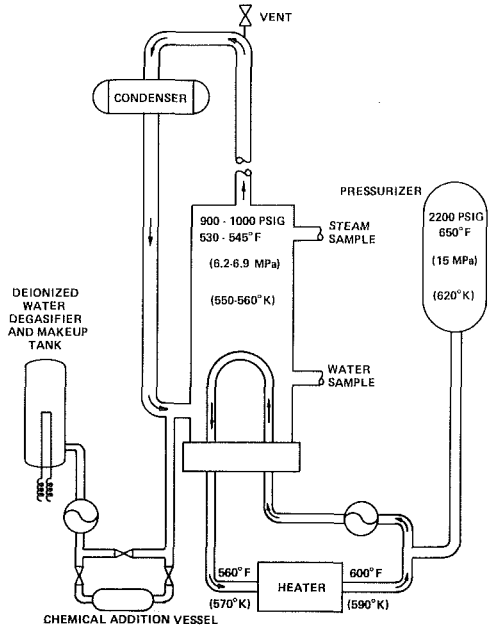

Fig. 1 Test facility schematic

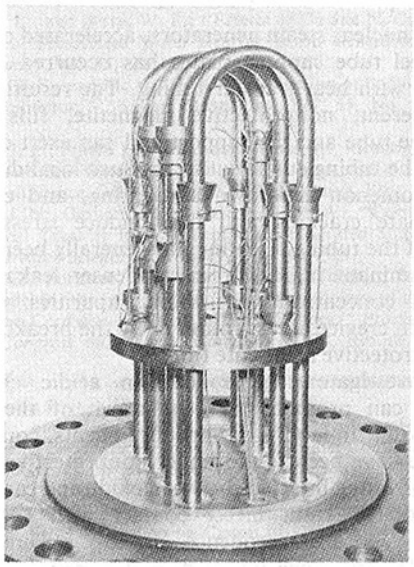

Fig. 2 Typical pot boiler before steaming

spaced to permit use of a variety of concentrating devices as shown in Fig. 2. Support structures were simulated by a full diameter carbon steel support plate and rings of various materials. In two tests, carbon steel sandwich plates were bolted across one of the U-bends in order to provide a region of steam blanketing and associated dryout at a location where

the tubing material is highly stressed. The lack of a tube bundle shroud and the wide spacing of tubes, resulted in low steam quality and fluid velocities in the bundle region.

The 16-tube model steam generators used in this project consisted of closely packed triangular pitch tube bundles of Alloy 600, Alloy 690, and Alloy 800 tube materials, as shown in Fig. 3. The support structures used in these units were similar to field units, and included eggcrate supports and drilled support plates with flow holes. Although not shown in this figure, each unit had a tube-bundle shroud which directed the flow of recirculating water. Details of pot boiler and model steam generator construction have been presented previously in [4]. Of greatest interest in this study was denting corrosion of carbon steel support structures at the intersections with Alloy 600 tubing.

Neutralization Test Procedure. Three pot boilers and two model steam generators were used in evaluating on-line chemical additions of calcium hydroxide and boric acid as a remedy for tube denting. In addition, two pot boilers were used to determine the side effects of a calcium hydroxide alternative bulk chemistry on steam generator internals.

A preliminary progress report on this work has appeared previously [5, 6].

There were four phases of operation for neutralization tests. In phase 1, denting was induced by steaming under all volatile treatment (AVT) faulted with a mixture of seawater and cupric chloride along with additions of synthetic feed train corrosion products. The onset of denting was indicated by strain gauge response. An interim inspection followed the denting phase.

At the beginning of phase 2, prior to neutralization, the units were operated from one to two weeks under faulted volatile chemistry control with chloride concentrations closer to those likely to be found in field units. The objective of the reduction in chloride concentration was to establish a constant denting rate (as indicated by strain gauges) under these conditions to be used as a base line for evaluating the effect of neutralization.

After a base line was established, neutralization was performed. Additions of calcium hydroxide were made with no interruption in operation, while boric acid additions were preceded by a four-day low power soak. Strain gauge response was monitored to follow the course of denting during neutralization. The residual effects of neutralization were evaluated in phase 3. The units were operated for about 30 days without neutralizer addition, while maintaining the same impurity chemistry control as during phase 2. During phase 4, the units were operated for one to two weeks under high fault conditions in order to reinitiate denting to verify the operability of the strain gauges.

After testing was completed, the test vehicle internals were destructively examined. The tube bundle was disassembled to provide specimens for more detailed examination by light or scanning electron microscopy. Specimens were taken at ring and support plate locations where tube denting had occurred. These were further sectioned to give longitudinal samples for metallographic examination.

Alternative Chemistry Testing. In the alternative chemistry tests, calcium hydroxide was used with AVT for alternative chemistry control. The purpose of these tests was to determine if deleterious side effects could be associated with the continuous use of calcium hydroxide in the bulk water. In these tests, calcium concentrations were successively increased during full power steaming. Interim examinations were performed on the tubes, supports, and corrosion coupons for indications of caustic attack. At the conclusion of testing, a destructive examination of the tubes and support structures was performed.

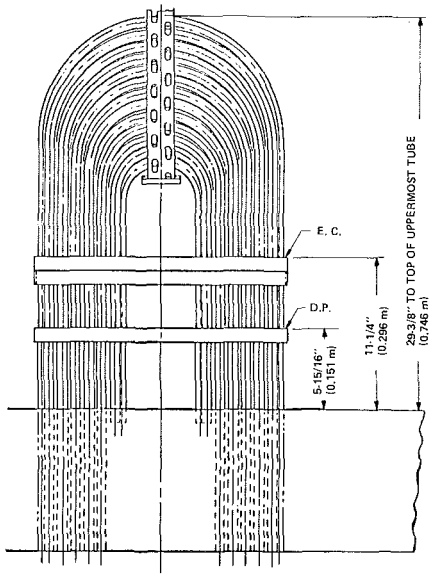

SUPPORT MATERIALS

COLD LEG DRILLED PLATE	405 STAINLESS
HOT LEG DRILLED PLATE	CARBON STEEL
COLD LEG EGG CRATE	CARBON STEEL
HOT LEG EGG CRATE	409 STAINLESS
VENTILATED SUPPORT	STAINLESS

Fig. 3 Model no. 4 tube support system

Examinations. Nondestructive techniques including eddy current testing and profilometry were used at interim examinations to confirm strain gauge data. The eddy current technique measures average tube deformation whereas profilometry measures deformation at eight azimuthal locations. Profilometry is useful in observing asymmetric dents, but for the purposes of this study, the arithmetic average of the eight profilometry observations at each defect, are presented and compared with eddy current values.

Selected crevice areas from pot boilers and model steam generators were destructively examined. Samples were sectioned longitudinally and examined by optical microscopy. Areas of interest were subjected to further examination by scanning electron microscopy (SEM), energy dispersive spectrometry (EDS), electron microprobe (EMP), and wavelength dispersive spectrometry (WDS), which provided a sensitive x-ray mapping of the elemental distribution. In addition, deposits were collected from pot boilers and model steam generators for characterization by x-ray fluorescence (XRF) and x-ray diffraction (XRD). These examinations yielded valuable information on corrosion product distribution and the morphology of denting corrosion, along with possible side effects of neutralization.

On-Line Application of Calcium Hydroxide

Neutralization Results. Calcium hydroxide on-line neutralization testing was conducted in two pot boilers (pots 10 and 11A) and one model steam generator (model 4). Chemistry conditions for all tests are indicated on the strain gauge plots, Figs. 4 and 5. Eddy current and profilometry data are presented in Tables 3 to 5.

In all tests, strain rates showed a pronounced decline upon addition of calcium hydroxide. Recall that calcium hydroxide was added under full steaming conditions after a stable strain rate had been established with representative impurity concentrations. No other changes were made in chemical or thermal hydraulic conditions. Consequently, any change in strain rates could be attributed directly to the addition of calcium hydroxide.

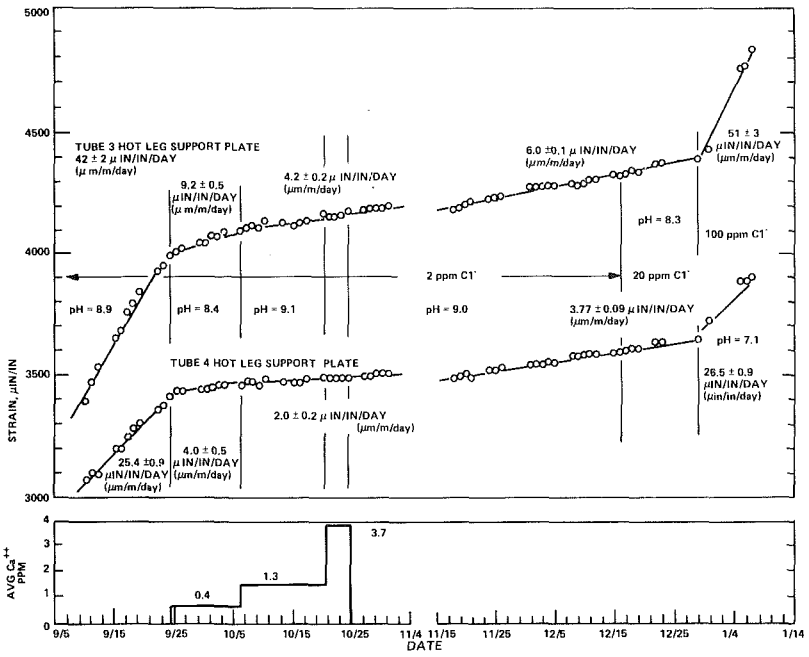

Fig. 4 Calcium hydroxide neutralization pot 11A strain gauge data

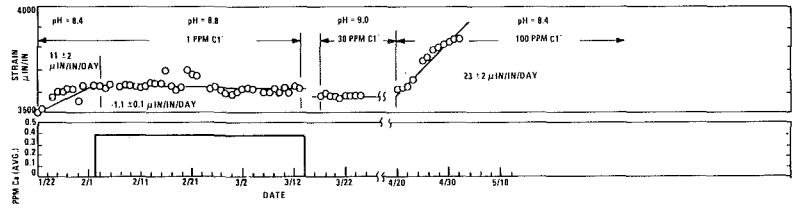

Fig. 5(a) Calcium hydroxide neutralization model 4 strain gauge data tube 10 hot leg support plate

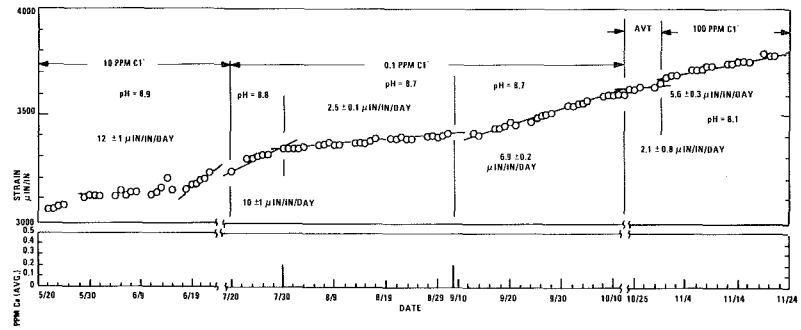

Fig. 5(b) Calcium hydroxide neutralization pot 10 strain gauge data tube 4 hot leg ring

The most definite observation of neutralization was made in pot 11A. Two of the five strain gauges installed in this pot boiler remained operational for the duration of testing compared to one gauge each in model 4 and pot 10. The following is an expanded description of the testing in pot 11A.

Base line strain rates of 42 and 25 μin./in./day (μm/m/day) were established for the two active strain gauges, by operation under low chloride fault conditions prior to neutralization with calcium hydroxide.

Neutralization was attempted by injection of calcium hydroxide for 13 days, during steaming operation, to obtain a bulk water concentration of 0.4 ppm Ca. During this time, strain rates decreased to approximately 9 and 4 μin/in./day (μm/m/day) for the active strain gauges. These strain rates, higher than instrument drift ranges of 2–4 μin/in./day (μm/m/day) indicated continued denting at reduced rates. Subsequently, the calcium hydroxide concentration was increased to a bulk water Ca concentration of 1.3 ppm, which resulted in additional reductions in strain rates to approximately 4 and 2 μin/in./day (μm/m/day), indicating the cessation of denting.

After two weeks of operation at 1.3 ppm Ca, the calcium hydroxide concentration was increased to 3.7 ppm Ca to determine if the strain rates could be further reduced. This increase in Ca concentration did not affect the strain rates indicating complete cessation of denting at 1.3 ppm Ca. After

Table 3 Pot 11A eddy current and profilometry results in mils (μm) off radius

Dent Location	End of phase 1 exam		End of phase 4 exam	
	EC	prof. avg.	EC	prof. avg.
Tube 3 hot leg support plate	13.0 (330)	11.8 (300)	16.2 (410)	16.2 (410)
Tube 4 hot leg support plate	12.5 (320)	11.2 (280)	15.9 (400)	17.0 (430)
Tube 3 hot leg CS ring	11.5 (290)	----	13.0 (330)	13.0 (330)

Table 4 Model 4 eddy current and profilometry results (all dents at CS support plate in mils (μm) off radius)

Dent location tube no.	End of phase 1 exam		End of phase 4 exam	
	EC	prof. avg.	EC	prof. avg.
4	16 (410)	15.6 (440)	16 (410)	16.2 (410)
5	6 (150)	5.4 (140)	6 (150)	6.6 (170)
5A	7 (180)	6.5 (170)	7 (180)	7.6 (190)
6	8 (200)	7.6 (190)	9 (230)	8.8 (220)
7A	6 (150)	6.4 (160)	6 (150)	7.4 (190)
9	7 (180)	6.6 (160)	7 (180)	9.7 (250)
9A	4 (100)	5.6 (240)	4 (100)	5.8 (150)
10	6 (150)	7.8 (200)	5 (130)	6.3 (160)
11	9 (230)	8.6 (220)	10 (250)	10.3 (260)
11A	6 (150)	6.4 (160)	6 (150)	6.4 (160)
12	5 (130)	5.3 (130)	4 (100)	4.9 (120)
13	5 (130)	4.5 (110)	4 (100)	5.0 (130)
13A	7 (180)	6.0 (150)	6 (150)	6.4 (160)

Table 5 Pot 10 eddy current and profilometry results in mils (μm) radius

Dent Location	End of phase 1		End of phase 2		End of phase 3		End of phase 4	
	EC	prof. avg.	EC	prof. avg.	EC	prof. avg.	EC	prof. avg.
hot.leg ring	4.5 (110)	4.5 (110)	4.4 (110)	4.4 (110)	4.4 (110)	5.2 (130)	5.2 (130)	4.8 (120)
Tube 3 hot leg ring	1.0 (25)	----	1.0 (25)	----	1.0 (25)	----	1.2 (30)	----
Tube 4 hot leg support plate	11.6 (290)	10.7 (270)	11.6 (290)	12.4 (310)	11.6 (290)	12.6 (320)	13.5 (340)	13.4 (340)
Tube 4 hot leg tubesheet	3.0 (75)	2.1 (50)	3.0 (75)	2.6 (65)	3.0 (75)	2.5 (65)	3.0 (75)	3.2 (80)

four days at 3.7 ppm, the calcium concentration was reduced by blowdown to 0.4 ppm to prepare for phase 3 (residual effects) operation.

Strain rates during post-neutralization, low-fault steaming, approximately 6 and 3.8 μin/in./day (μm/m/day), were an order of magnitude lower than the pre-neutralization strain rates, but statistically greater than the strain rates during neutralization. These lower strain rates may indicate a limited residual effect associated with the calcium hydroxide treatment. After one month of residual effects testing, the chloride concentration was increased in discrete steps to reinitiate denting and check the operability of the strain gauges. There were no measurable increases in strain rates after 7 days at 20 ppm Cl; strain rates increased when the chloride concentration was raised to 100 ppm indicating that the strain gauges remained operable throughout the test.

Eddy current and profilometry examinations were conducted after the pre-neutralization phase and at the end of the test (see Table 4). Increases in dent sizes (3.2, 3.4, and 1.5 mils radially as measured by eddy current) are attributed to continued denting between the eddy current inspections when the pot boiler was steamed under chloride fault conditions before and after calcium hydroxide neutralization.

The results from model 4 and pot 10 were similar to those obtained in pot 11A. The addition of calcium hydroxide produced an immediate reduction in the strain rate. In pot 10, the strain rate was reduced from a pre-neutralization rate of 10 μin/in./day to 2.5 μin/in./day (μm/m/day) by on-line calcium hydroxide additions. The strain rate in model 4 was reduced from 10.8 μin/in./day (μm/m/day) to −1.1 μin/in./day (μm/m/day).

A negative strain rate is indicative of strain relief, not just a cessation of denting. It would be unreasonable to expect the addition of calcium hydroxide to cause relief of strain. At the conclusion of testing, the support plate in model 4 was found to be extensively cracked. There is no indication from test data as to when plate cracking and expansion began, but in view of model 4's extensive steaming exposure to high concentrations of chloride prior to this test, it is reasonable to assume that plate cracking initiated before neutralization. If this occurred, there would be an underlying relief of crevice stress against which all strain gauge measurements were made

during this test. In other words, the negative 1.1 ± 0.1 μin/in./day (μm/m/day) strain rate during neutralization is quite probably the strain gauge drift rate as the support plate continues to expand following cracking. These observations do not alter the fact that denting was halted by additions of calcium hydroxide.

In both tests, the strain rate during post-neutralization, low-fault steaming was intermediate to the pre-neutralization and neutralization rates, an indication of a possible residual effect of the treatment. However, past experience with pot boilers (exclusive of neutralizer additions) has shown that after the denting rate has been reduced, it is difficult to increase the denting rate during subsequent operation. This is an alternative explanation to the residual effects hypothesis concerning the reduced strain rate during post-neutralization operation [5]. Additional details on this testing are in [4] and [5].

Representative crevice specimens from each test vehicle were destructively examined to look for evidence of calcium hydroxide in crevice magnetite and to determine if there were adverse side effects attributable to the calcium hydroxide concentration. Observations were made via optical microscopy, scanning electron microscopy (SEM), energy dispersive spectrometry (EDS), and wavelength dispersive spectrometry (WDS).

All oxide morphologies were typical of nonprotective magnetite grown in an acid chloride environment. There was no evidence of calcium hydroxide induced corrosion, contrary to a previous observation [5, 6]. Complete details are presented in [4]. Calcium was found in localized areas within crevice magnetite, usually associated with sulfur. This distribution had been observed previously in pots and models steamed with seawater fault. There was no indication of a general penetration by calcium hydroxide of the crevice magnetite, at least not in excess of the lower limit of detection which was 1–3 percent.

Alternative Chemistry Tests. Two pot boilers (pots 9A and 1M) were operated with calcium hydroxide as an alternative bulk chemistry. In these tests, secondary water chemistry was controlled with standard AVT plus on-line additions of calcium hydroxide. The purpose of the tests was to determine if deleterious side effects could be attributed to the use of calcium hydroxide. Pot 9A was operated with sequentially increasing concentrations of calcium hydroxide (0.2 to 0.6 ppm Ca), while pot 1M was operated at a constant calcium hydroxide concentration of 10 ppm Ca.

There was no calcium hydroxide-induced cracking or corrosion on heat transfer tube or support surfaces in either test. A white deposit was observed under umbrella cups in both tests. X-ray diffraction identified the deposit as calcium hydroxide. Scaling was evident on tubing in steam blanketed areas, but this is commonly observed in pots steamed on AVT chemistry. No scaling attributable to calcium hydroxide was observed.

These tests revealed no deleterious side effects caused by the use of calcium hydroxide in the bulk chemistry under the conditions tested. Heat fluxes more than twice those achieved in these test boilers, are present in actual steam generators. The possibility exists that calcium hydroxide added to steam generators may have side effects which result from the more aggressive environment therein. This matter is under continuing investigation at C-E.

On-Line Boric Acid Neutralization

On-line neutralization testing with boric acid was conducted in one pot boiler (pot 7F) and one model steam generator (model 8) following procedures developed by another NSSS vendor.[1,2] This procedure combined a low-power soak with on-line boric acid additions at full-power steaming conditions.

Denting was initiated by steaming under AVT faulted with chloride, 1/3 of which came from $CuCl_2$ and 2/3 from seawater. After an interim examination, the chloride concentrations were reduced to provide a baseline denting rate against which neutralizer effectiveness would be evaluated. The neutralization phase was initiated by simulating approximately 30 percent power and adding boric acid to maintain approximately 50 ppm B in the bulk coolant. After four days at low power, boric acid concentration was reduced via blowdown to 10 ppm B and full power operation was resumed. The full-power, on-line neutralization continued for approximately 30 days.

Thermal hydraulic conditions for the pot boiler and model steam generator during simulations of full power and low power (approximately 30 percent) were given previously in Table 1.

Chemistry conditions for the two tests are indicated on the strain rate plots, Fig. 6. Eddy current and profilometry data are presented in Table 6. In both tests, strain rates during the full-power, on-line operation with boric acid were significantly reduced from pre-neutralization rates and were close to the expected instrument drift rate. At the conclusion of the neutralization phase, boron levels were reduced via blowdown to about 1 ppm.

Prior to post-neutralization steaming, tube 1 was cut from pot 7F to preserve boron deposits. The tube 1 location was plugged, and the pot was steamed for one month on the low-fault, baseline chemistry. The strain rate during post-neutralization low fault steaming in pot 7F was half of the pre-neutralization rate, but higher than the rate during neutralization, possibly indicating limited residual effects associated with the treatment. The normal sluggishness of denting rates ot return to the normal rates after being reduced [5] is the more likely explanation. Strain gauge operability was confirmed by reactivation of denting after an increase in chloride fault to 100 ppm after one month of post-neutralization steaming.

Similar results were obtained for model 8 with a low-level fault concentration of 2 ppm chloride. The neutralization procedure was identical to that used for pot 7F. Again, strain rates were reduced by the treatment to essentially instrument drift rate. Testing was terminated at the conclusion of the neutralization phase for model 8.

Results of eddy current and profilometry tests generally confirmed denting trends indicated by strain gauge data. Denting was halted by the boric acid neutralization.

The pot boiler and the model steam generator were destructively examined at the conclusion of testing. This included examination by optical microscopy, scanning electron microscopy (SEM), energy dispersive spectroscopy (EDS), secondary ion mass spectroscopy (SIMS), and wavelength dispersive spectrometry (WDS).

All oxide morphologies were typical of nonprotective magnetite grown on carbon steel in an acid chloride environment. There were no indications that boric acid had an effect on oxide morphology, carbon steel support structures, ferritic stainless steel support strucures, or Alloy 600 tubing.

Boron, estimated at 50–150 ppm, was found by SIMS to be distributed throughout crevice magnetite in four specimens examined. For pot 7F, the specimen which had been removed from the pot immediately after the neutralization treatment contained 150 ppm B and 130 ppm Cl^- whereas the specimen which had been exposed to one month of post-neutralization residual effects steaming plus the final high fault phase contained 60 ppm B and 1000 ppm Cl^-. Although the boron concentrations are similar, there is some indication that boron was replaced by chlorides in the specimen subjected to post-

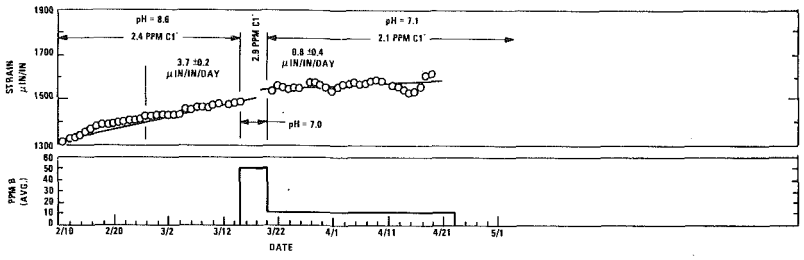

Fig. 6(*a*) Boric acid neutralization model 8 strain gauge data tube 6 hot leg support plate

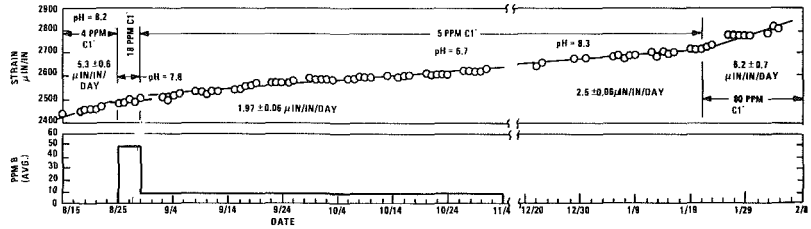

Fig. 6(*b*) Boric acid neutralization pot 7F strain gauge data tube 3 hot leg ring

Table 6 Eddy current and profilometry data from boric acid neutralization tests (all values are in mils (μm) off radius)

Location	Dent size at end of phase 1		Dent size at end of phase 2	
	EC	prof. ave.	EC	prof. ave.
Pot 7F				
Tube 4 cold leg ring	1.5 (38)	1.4 (36)	1.4 (36)	1.3 (33)
Tube 2 hot leg ring	2.4 (61)	2.3 (58)	2.0 (51)	2.4 (61)
Tube 3 hot leg ring	2.0 (51)	2.3 (58)	2.4 (61)	3.1 (79)
Tube 4 hot leg ring	2.3 (58)	----	2.4 (61)	2.5 (64)
Model 8				
4 HSP	5.0 (130)	----	3.0 (76)	2.3 (58)
5 HSP	6.0 (150)	----	3.5 (89)	3.2 (81)
5A HSP	----	----	----	1.4 (36)
6 HSP	6.0 (150)	----	7.0 (180)	5.0 (130)
7 HSP	----	----	----	0.3 (8)

Note: Profilometry indicates asymmetry of denting by measuring the tubewall deformation at eight azimuthal locations. The profilometer average which is tabulated is the arithmetic mean of the eight wall deformations.

neutralization low fault steaming plus the high fault phase. Similar amounts of boron were found in both specimens from model 8. The major observation is that boron was found uniformly throughout crevice magnetite with larger amounts observed in the more porous magnetite near the heat transfer tubing. These results reveal that boric acid penetrated the crevice magnetite.

Conclusions

On-line addition of calcium hydroxide in concentrations (measured as ppm Ca^{++}) equal to or greater than the ppm of chloride impurity is effective in stopping tube denting, as demonstrated in two pot boiler and one model steam generator tests.

Treatment with boric acid via a combination of low power soak at 50 ppm B and on-line treatment with 10 ppm B is effective in halting tube denting, as demonstrated in a pot boiler test and a model steam generator test.

Destructive evaluation of the test boilers did not reveal deleterious corrosion effects associated with addition of either neutralizer. This is under continuing investigation at C-E.

As illustrated in Table 2, there are significant thermal hydraulic differences between full-size steam generators and the test units used in this study. For this reason, concentrations of either calcium hydroxide or boric acid required to halt denting in field units may differ from those used in this study. In addition, as stated previously, the more aggressive environment of full size steam generators could cause side effects not observed in the test boilers.

Acknowledgment

This work was supported in part by the Electric Power Research Institute, E.P.R.I. Funding was provided under project RP-623-2.

References

1 Seager, J. S., "Background Data Report: A Summary of the Westinghouse Experience in Treating Steam Generators with Boric Acid," Steam Generator Owners Group Program S116-1, Westinghouse Electric Corporation, WCAP-9682, Dec. 1979.

2 Wolfe, C. R., Esposito, J. N., Economy, G., Charles, R. G., and Wooton, M. J., "Laboratory Studies of the Effectiveness of Boric Acid in Dent Inhibition," Steam Generator Owners Group Program S112-1, Westinghouse Electric Corporation, WCAP-9676, Feb. 1980.

3 Wozniak, S. M., Whyte, D. D., and Wolfe, C. R., "Laboratory Studies Related to Steam Generator Tube Denting," Steam Generator Owners Group Program S112-1, Sixth and Seventh Quarterly Report, Westinghouse Electric Corporation, Sept. 1980.

4 Grondahl, E. E., Beineke, T. A., Hall, J. F., Scott, D. B., Fink, G. C., Silva, E. J., and Marugg, K. E., "Tests of On-Line Additions of Calcium Hydroxide for Limiting Denting in Nuclear Steam Generators, Steam Generator Owners Group Program RP 623-2," Combustion Engineering, Inc., to be published.

5 Beineke, T. A., Hall, J. F., Morgan, D. J., Marugg, K. E., and Scott, D. B., "Evaluation of Calcium Hydroxide Chemistry to Control Denting in Nuclear Recirculating Steam Generators," TIS-6872, Oct. 1982, Combustion Engineering, Inc., Windsor, Conn.

6 Beineke, T. A., Hall, J. F., Morgan, D. J., Marugg, K. E., and Scott, D. B., "Evaluation of Calcium Hydroxide Chemistry to Control Denting in Nuclear Recirculating Steam Generators," *Proceedings • 42nd International Water Conference*, 1981, pp. 393–398.

7 Beineke, T. A., Morgan, D. J., Hall, J. F., Marugg, K. E., and Wiatrowski, M., "Tests of Isothermal Soaking Procedures for Limiting Tube Denting in Nuclear Steam Generators," EPRI NP-1761, Apr. 1981.

Modeling Considerations for the Analysis of LMFBR Steam Generator Tube Clamps

D. M. Lay

R. M. Piper

Stress Engineers,
Babcock & Wilcox,
Nuclear Equipment Division,
Barberton, Ohio 44203

In the design of the Babcock & Wilcox Helical Coil Liquid Metal Fast Breeder Reactor (LMFBR) Steam Generator, the tube bundle is connected to the feedwater and steam plenums via "inlet/outlet tubes." Of prime importance in the design of these tubes is the tube-to-tube and tube-to-shell clamps which are provided to prevent detrimental vibration. This paper presents a method of modeling the tube-to-tube clamps to accurately predict tube-to-clamp interaction in the finite element analysis. It is also the objective of this paper to demonstrate the validity of specific modeling assumptions in determining stresses in the clamp assembly. As this paper deals only with the analytical approach taken, no detailed results are presented.

Introduction

In the Liquid Metal Fast Breeder Reactor (LMFBR) program, one of the designs for the steam generator features a once-through, helically coiled tube bundle concept [1]. A configuration of tubes called "inlet tubes" is used to transport feedwater from the feedwater tubesheet to the bottom of the helical bundle. Likewise, "outlet tubes" transport superheated steam from the top of the tube bundle to the steam outlet tubesheet (see Fig. 1). The tubes have varying routing paths to provide adequate tube flexibility for maintaining structural integrity of the tubes during operating conditions (2).

Because the tube flexibility creates a concern for vibrations, the inlet and outlet tubes are supported by four types of tube-to-tube and tube-to-shell clamps known as A, B, B-1 and B-2 clamps. The main purpose of these clamps is to eliminate damaging tube vibration while allowing sufficient tube flexibility for structural integrity.

The thermal/mechanical stress analysis of these clamps is performed using the finite element method. The primary purposes of the analysis are:

1 To determine load in the clamp bolts during operating conditions
2 To assess slippage of the tube in the clamp
3 To determine stresses in the bolt, clamp, and tube

This paper presents special modeling considerations which are being used in the analysis of the B-clamp (see Fig. 2). These modeling considerations have been chosen to accurately reflect the behavior of this clamp while serving to minimize computing time.

Specific aspects of the modeling techniques discussed in this paper include:

- Model refinement in the tube and clamp using 20-node solid elements
- Simulation of bolts which develop clamping force between tube and clamp
- Monitoring of tube-to-clamp interface boundary for contact area and relative motion (slippage)
- Application of thermal/hydraulic boundary conditions
- Application of mechanical loads and constraints

Description of Clamp

The four types of clamps are required because of different tube spacings and restraint needs at different locations in the inlet/outlet tube routings. The B-2 clamps provide a relatively fixed support for all of the tubes. The two A-clamps constrain groups of tubes to displace as a unit. The B-1 clamp connects individual tubes to the vessel shell. The B-clamps connect one tube to another and permit differential thermal growth between tubes. The B-clamp geometry is the clamp-type specifically covered in this paper.

A typical B-clamp assembly is shown in Fig. 2. The clamps are basically comprised of two rectangular blocks with partial circular cutouts that are attached around the tube by preloading two symmetrically spaced bolts. The clamps are in turn interconnected by straight bar linkages (link-arms), which can rotate about the clamp bolt at each end. Cylindrical bushings are used to maintain the compatibility of thermal expansion between the two bolts by providing equal stressed lengths and to transfer loads from the bolts to the grips without restricting the rotational capability of the link-arms. Note that the link-arms are designed to provide horizontal vibration support while allowing for differential vertical motion between tubes due to temperature differences. The most severe differential vertical motion occurs when a clamp

Contributed by the Nuclear Engineering Division and presented at the Joint Power Generation Conference, Denver, Colorado, October 17-21, 1982. Manuscript received by the Nuclear Engineering Department July 27, 1982. Paper No. 82-JPGC/NE-9.

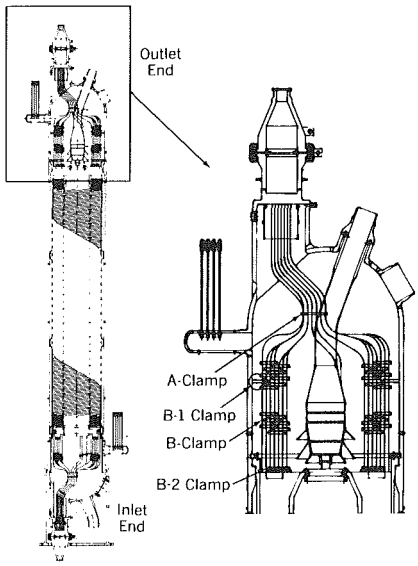

Fig. 1 70 MWt prototype steam generator and clamp locations

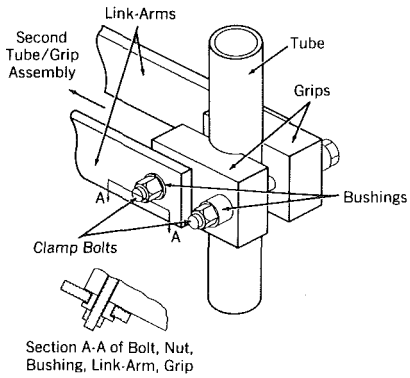

Fig. 2 Typical B-clamp assembly

connects an active tube and a plugged tube that contains no water and thus experiences quite different thermal expansion.

The tube, grips, and link arms are constructed of 2-1/4 Cr-1 Mo low-alloy steel. The bolts, nuts, and bushings are high nickel Alloy 718 material because of its resistance to creep and relaxation, which is important in terms of maintaining preload. Since the coefficient of thermal expansion of the bolts is greater than for the grips of the clamp, preload in the bolt decreases as the overall clamp temperature is raised from ambient to operating conditions. Since the primary source of stress in the clamp is the load in the bolts (which is accomplished with a very small amount of prestrain), it is imperative to obtain results from the finite element analysis that reflect actual clamp conditions.

Clamp Environment

As shown in Fig. 1, B-clamps are located at both the inlet and outlet ends of the vessel. At the inlet end, the clamps are surrounded by sodium, which flows from the bundle to the outlet nozzle. The tube contains water flowing from the feedwater nozzle to the helical bundle. At the outlet end, the clamps are also surrounded by sodium exiting from the sodium distributor. The tube contains superheated steam flowing from the helical bundle to the steam outlet nozzle.

The load in the bolts, and hence the stress in the clamp, is determined by bolt prestrain, the pressure in the tube, the overall clamp temperature, the link arm loads, and the temperature difference between the bolts, grips, and tube. The bolt is initially loaded with prestrain. Internal pressure in the tube tends to dilate the tube, and thus increase the bolt load.

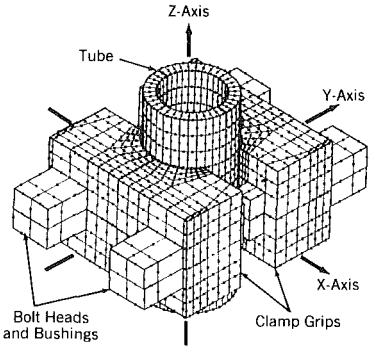

Fig. 3 B-clamp finite element model – full model

If the clamp experiences a uniform increase or decrease in temperature, the bolt load decreases or increases, respectively. The sodium-to-water temperature differential, which in turn induces a temperature differential between the bolts and the tube, is the primary factor in determining bolt load. The hotter the bolt as compared to the tube, the lower the bolt load.

Finite Element Modeling

General purpose Babcock & Wilcox finite element programs which are used for this analysis include FETAP (Finite Element Thermal Analysis Program) and FESAP (Finite Element Stress Analysis Program) [3].

The finite element B-clamp model generated for the thermal and mechanical analysis is shown in Fig. 3. It consists of three-dimensional, 20-node, curved isoparametric elements in combination with beam elements and two-dimensional plate elements. The beams and plates are used to induce special behavior in the model.

Convergence studies were performed on various submodels to determine the necessary grid refinement and to assure that the stress results reflect those obtained from classical formulae. For example, the length of tube included in the model is sufficient to attenuate the stresses produced by the clamp.

Due to numerous interaction effects between the tube and the clamp and between the various parts of the clamp itself, certain modeling assumptions are required.

Clamp Bolt Modeling. The clamp grip bolts are modeled as beam elements to permit a concentration of nodes and elements around more critical regions of the clamp, such as the thin ligament in the grip. These beams are given geometric properties representive of the actual bolts. Additional plate and beam elements, with modified properties, are connected to the bolt beam elements to assure that the beams reflect the behavior (both structurally and thermally) of the actual bolt and to properly connect the beams to the three-dimensional solid elements comprising the rest of the clamp. The configuration of these various elements is depicted in Fig. 4.

In order to simulate the preload in the bolt, a prestrain is induced in the bolt model by the use of a very short beam element termed a "preload element." The thermal expansion coefficient of this element is modified such that it contracts an initial fixed amount to produce the tensile preload, while permitting normal thermal expansion and contraction in the remainder of the bolt. The coefficient of expansion is temperature-dependent and is set so that the effect of the initial prestrain is maintained throughout the temperature range experienced by the bolt. This allows the overall bolt load to vary during transient events, which is more accurate than an applied force that would simply maintain a constant bolt load.

Special two-dimensional plate elements are connected to the bolt elements to provide surface area for heat transfer

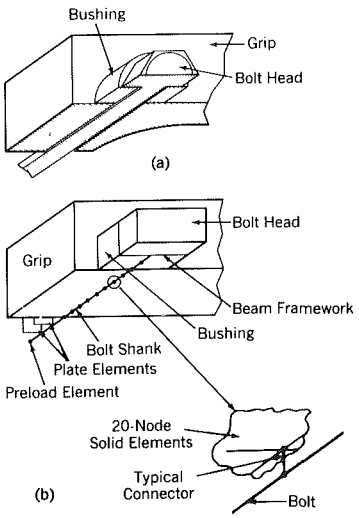

Fig. 4 B-clamp-bolt finite element model: (*a*) bolt-clamp cut-away; (*b*) finite element representation

through the exposed surface of the bolt between the clamp grip segments. These plate elements are given modified properties (arbitrarily high conductivity and low specific heat) so that they provide surface area only and offer essentially no thermal resistance to the heat flowing within the beam elements.

Heat flows from the grip material that surrounds the bolt hole to the bolt through very short connector beams which join the nodes in the bolt to the corresponding nodes in the grip. In order to model the capability of the bolt to slide within the bolt hole, these connectors are equipped with special joints at their two ends (nodes), which permit axial bolt motion while constraining lateral motion. This constraint allows the beams to move freely in the longitudinal direction (slide in the bolt hole) while forcing the beams to bend as the clamp deforms. This is required due to a close clearance between the bolt and bolt hole in the actual clamp.

The major connection between the bolt (beams) and the grip is a framework of rigid beam elements connected to the nodes in the bolt head. These are used to transfer bolt load from the beam elements representing the shank of the bolt to the three-dimensional elements which represent the bolt head and bushings. The framework spreads out the bolt load over an area representative of the bushing and serves to minimize the concentration of stress at the beam element three-dimensional element interface (a result of the mathematics of the finite element method).

Tube-Grip Contact Surface. The outside radius of the tube is smaller than the radius of the partial circular cutout in the grips. Therefore, the amount of bearing surface between the tube and the grip varies, depending upon the clamping force and tube loads that are applied. In order to determine the extent of the contact surface, a method is devised using beam elements to bridge the "gap" between the elements in the tube and the elements in the grip.

These "gap elements" have a modified thermal expansion coefficient such that their lengths shrink to zero at operating temperature, forcing the tube and grip model surfaces to conform. If tension is developed in a gap element under load, it is deleted and a second iteration of the same loading is performed (the tension force means that the surfaces at that point are actually not in contact). Eventually, only the gap elements in compression remain in the model and represent the anticipated contact surface between the tube and the grip.

If some portion of the tube exceeds yield stress under the clamping load, the actual tube/grip contact surface is somewhat larger than that determined by the preceding calculations. This is due to the redistribution of load in the tube as the material plastically distorts and conforms more closely to the shape of the curved cutouts in the grip.

In this case, a measure of the tube/grip surface is also obtained by an iterative process. The contact surface is initially set slightly greater than the value calculated elastically, with the gap elements used only for load transfer between tube and grip (instead of forcing the contact surfaces together as before). If tube stresses are still above yield under clamp load, a second iteration is performed with the contact surface increased even more from that used in the first iteration. This process continues until tube stresses are below yield. At this point, the tube/grip contact surface is defined.

Additional Modeling Considerations. In order to minimize the number of nodes and elements in noncritical areas of the model, the cylindrical bolt hole, the bushing, and the hexagonal bolt head are modeled as three-dimensional rectangular elements. In all three cases, there is more material represented in the finite element model than actually exists in the clamp, so the material properties of these elements are modified by a ratio of the actual volume to the modeled volume to yield the same stiffness and heat transfer characteristics.

Using the modified material properties, the effects of the bolt hole, bolt head, and bushing are simulated. The modulus of elasticity is reduced in mechanical analyses, while density is reduced and thermal conductivity is increased for the thermal analyses.

Certain areas of the model, such as the tube elements and the elements adjacent to the bolt, are not sufficiently refined to pick up peak stresses. The region surrounding the bolt does not require refinement since stresses in this area can be calculated by hand using classical formulae. A more refined tube in the full clamp model would easily exceed most computers' storage capacities, so a separate refined model of the tube is generated (see Fig. 5). Displacements from the analysis of the clamps using the coarse tube are imposed on the refined tube submodel to determine peak stresses. Since the region representing the contact surface of the refined tube model has many more nodes than the corresponding region of the grip, a framework of beam elements is used to distribute the loads from the grip model over the contact surface of the refined tube model (see Fig. 5).

Load Application

The model itself is symmetric about three orthogonal planes. Certain loads are aligned with the various planes of symmetry in the model, so the entire model need not be used to analyze all loads (see Fig. 6). Pressure, preload, and thermal loads are symmetric about all three planes, so only 1/8 of the full clamp model need be used for the majority of the analyses. Other loads, such as tube bending and tube shear can be resolved into components which are symmetric about one plane, so that only 1/2 of the full clamp model is used for these loads. As a result, only loads involving tube torsion and link arm loads require the full model for analysis.

The link-arms connecting a B-clamp on one tube to a B-clamp on another tube are not included in the model. Instead, the loads calculated from a separate finite element analysis of the inlet/outlet tubes [2] are applied directly to the bushing elements as a contact pressure.

The actual analysis is performed using unit loads for pressure, link-arm loads, and tube loads. Typical loading conditions are shown in Fig. 7. Any load may be represented by a combination of these basic loading conditions. By

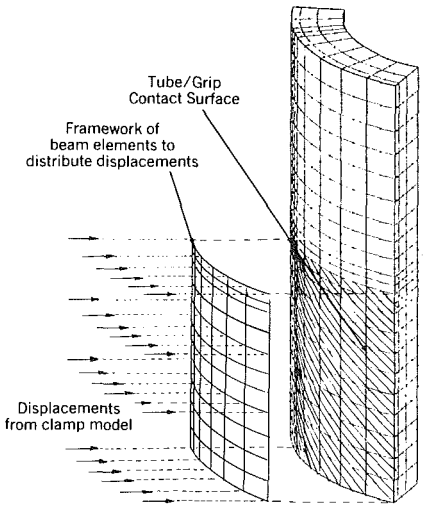

Fig. 5 Refined tube model

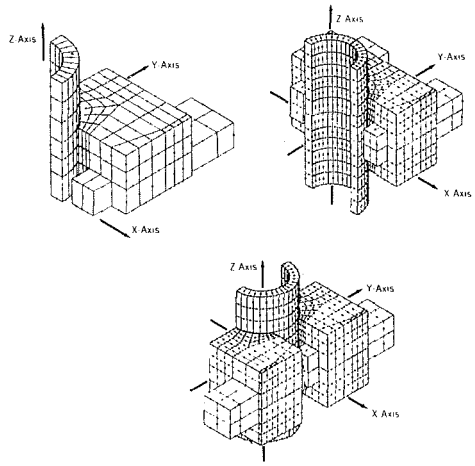

Fig. 6 1/8 clamp and 1/2 clamp models

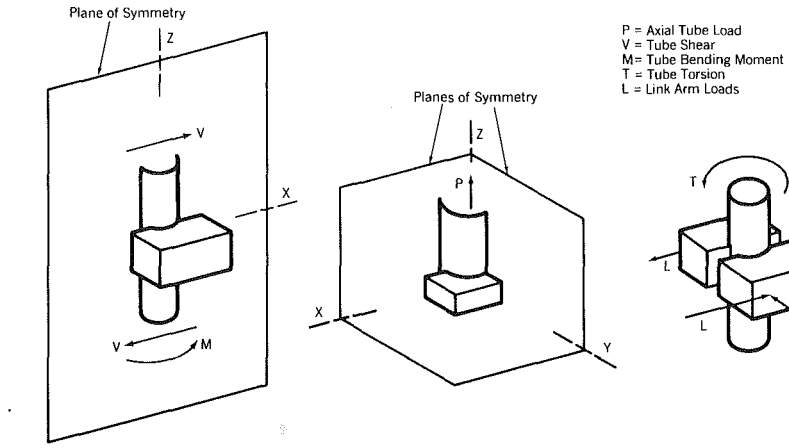

Fig. 7 Typical B-clamp loading conditions

superposition of stress results from the basic loads, stress results for any actual clamp loading may be calculated.

Summary

This paper presents special modeling considerations for use in the finite element analysis of the tube-to-tube clamps in an LMFBR steam generator. The primary topics of interest are the bolts that provide clamping force and the contact surface between the clamp and the tube it restrains.

The bolts are modeled as beam elements to permit a concentration of nodes and elements around more critical regions of the clamp. A "preload" element is devised that contracts a prescribed amount at operating temperature to induce a tension prestrain in the bolt. In order to provide for heat transfer through exposed surfaces of the bolt, two-dimensional plate elements are connected to the bolt to provide surface area for the heat flowing to and from the bolt. The material properties of the solid elements that represent the bolt hole are also modified to approximate the behavior of the actual geometry.

In order to determine the extent of the contact surface between the clamp and tube, beam elements with modified material properties are used in an iterative process to connect the tube model to the clamp model. When the stresses in the tube are below yield, this iterative process results in an accurate determination of the contact surface. When stresses exceed yield, an iterative process based on changing areas provides an approximate measure of the contact surface.

Also, it is shown that the entire model need not be used to analyze all loads since certain loads are aligned with various planes of symmetry in the model. This leads to a savings in time and computer costs.

Acknowledgments

This paper was sponsored by the Department of Energy, Division of Reactor Development and Demonstration, Contract No. DE-AC02-77ET37209. The authors wish to thank Mr. R. G. Carlson and Mr. J. R. Woolsey for the guidance in the preparation of this paper.

References

1 Grant, G., "Design and Development of a Once-Through Helical Coil Steam Generator for Large LMFBR Plants," ASME Paper No. 80-C2/NE-29.

2 Pedani, A. J., and Figliomeni, F. J., "Modeling of Internal Tubing and Supports in an LMFBR Steam Generator," ASME Joint Power Generation Conference, Denver, Colorado, Oct. 17-21, 1982.

3 Van Fossen, D. B., "FESAP—Design Program for Static and Dynamic Structural Analysis," *Computers and Structures*, Vol. 9, Oct. 1978, pp. 371-376.

The Effect of Flat Bar Supports on the Crossflow Induced Response of Heat Exchanger U-Tubes

D. S. Weaver
Department of Mechanical Engineering,
McMaster University,
Hamilton, Ontario, Canada L8S 4L7

W. Schneider
Babcock and Wilcox,
Canada, Limited,
Cambridge, Ontario, Canada

A wind tunnel study was conducted to determine the effect of flat bar supports on the crossflow induced response of heat exchanger U-tubes. The 13-mm-dia tubes formed a triangular array with a pitch ratio of 1.57 and a mean U-bend diameter of about 1.5 m. A 0.3-m-long section of the array was exposed to a flow parallel to the plane of the U-bends. Experiments were conducted with no supports, with one set of flat bars at the apex, and with two sets of flat bar supports at the apex and 45 deg points. In each case, the tube response was monitored to a flow velocity beyond that required for fluid elastic instability. Limited experiments were also conducted to examine the effect of tube support clearance on tube response. Conclusions are drawn regarding the effectiveness of flat bars as U-bend antivibration supports.

Introduction

Flow-induced vibrations in heat exchangers is recognized as a serious problem, which can lead to tube failure through fretting wear or fatigue [1-3]. Such failures have resulted in numerous plant shutdowns, which were often very costly, especially in the case of nuclear power stations. While fluid-elastic instability will almost certainly lead to tube failure in a relatively short period of time, this can be avoided by limiting the flow velocity across the tubes. However, some tube response due to turbulent buffeting or vortex shedding cannot be avoided, and this may lead to long term fretting failure due to tube impacting at the supports. For a given flow velocity through a tube bundle, the only practical way of reducing tube response in most cases is to alter the tube support design. While support effective spacing is very important, support geometry and tube-to-support clearances are also significant parameters.

In spite of its importance, there is virtually no reference in the open literature to the effect of tube support design on the crossflow response of heat exchanger tubes. Some work has been reported on the effect of tube support impacting under conditions of no flow [4-8]. Computer programs based on the finite element method have been developed to predict tube dynamics and impact forces at the supports. It has been shown that small support clearances do not have a significant effect on tube natural frequencies. Reasonable agreement has been found with experiments for tube response and impact forces for some relatively simple tube and support configurations. Some excellent work has also been done on the effect of clearance and materials on fretting wear rates [9, 10]. It is clear that the larger the impact force and/or support clearance, the greater is the wear rate. It is also clear that the dynamics of tube response under conditions of support impacting are nonlinear. Goyder [11] has recently developed a method for measuring the natural frequencies and damping of loosely supported tubes. His experiments show that the effect of support clearance on natural frequency and damping is dependent on mode shape and lateral load at the supports.

All of the aforementioned work has been done for straight tubes under no flow conditions and most of it has considered relatively simple support geometry such as a plate with a drilled hole. A variety of other support arrangements have been used in heat exchangers and, amongst these, flat bars offer significant advantages for use in U-bend regions. While such supports have been used in steam generators with apparent success, their flow induced vibration characteristics have not been documented. Since these supports do not appear to restrict in-plane tube motions, research into their efficacy is warranted. This paper reports the results of an experimental program to investigate the effectiveness of flat bars as antivibration supports for U-tubes. The experiments were conducted using a bundle of steam generator U-tubes in a wind tunnel. A brief discussion is given of some of the criteria that must be considered when designing tube supports, and some alternative support geometries are examined. Then experiments are described and results reported for tube response with zero, one, and two sets of flat bar supports. The effect of support clearance is also investigated, and a comparison is made to tube response with scalloped bar supports.

U-Bend Support Criteria and Alternatives. The design of U-bend supports is difficult because of the numerous conflicting design criteria, some of which are as follows:

(*a*) Provision of a support sufficiently stiff to minimize flow-induced vibration (FIV) response, even where high flow rates are used to maximize thermal efficiency and minimize deposition of impurities on the tubes

(*b*) Maintenance of a good flow distribution throughout the U-bend region

Contributed by the Nuclear Engineering Division and presented at the Joint Power Generation Conference, Denver, Colorado, October 17-21, 1982. Manuscript received by the Nuclear Engineering Division July 27, 1983. Paper No. 82-JPGC/NE-12.

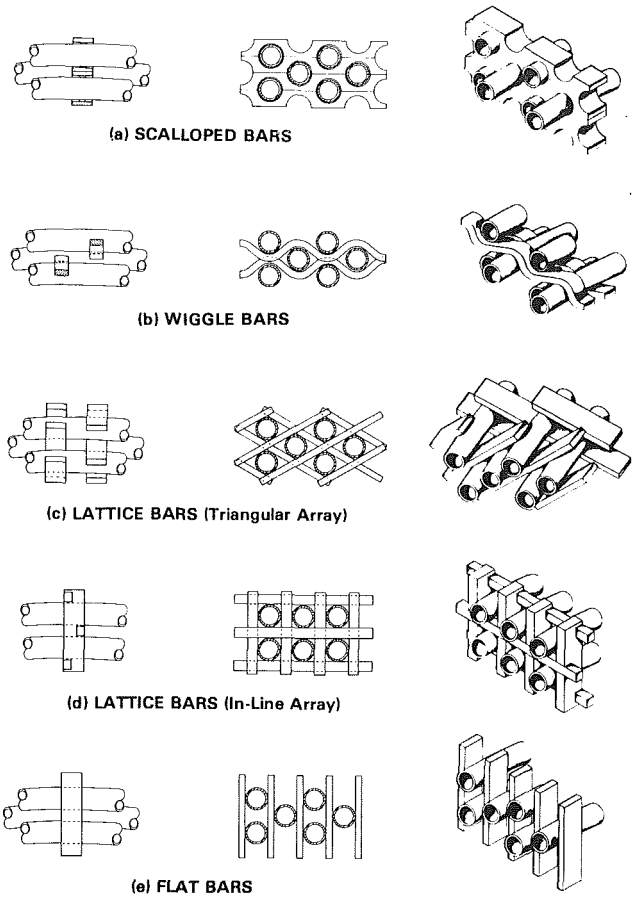

Fig. 1 Various U-tube support configurations

(*c*) A minimum support contact area to minimize deposition of corrosion causing impurities

(*d*) Avoidance of trapped spaces which could cause dryout or build-up of deposits

(*e*) A contact area sufficiently large to minimize contact stresses, and hence, fretting wear

(*f*) A support stiff enough to sustain lateral seismic and handling forces without tube damage

(*g*) A support with sufficient clearance or flexibility to accommodate tube motions related to differential thermal expansion effects and manufacturing tolerances.

In view of all these criteria, it is not surprising that a variety of U-bend support configurations have evolved. Some of these are presented below and their relative advantages and disadvantages are discussed briefly. The list is not intended to be all-inclusive but rather to illustrate the principal types of supports used.

Scalloped Bars. A drilled hole type of support can be created in the U-bend by drilling a stack of bars at the parting lines so as to generate the tube hole pattern in the assembled stack, Fig. 1(*a*). These "scalloped bars" may then be installed, a bar at a time, after each row of common radius tubes is installed. The built-up assembly in effect forms a plate with the tubes passing through it. It is structurally very strong and provides excellent tube support. At the same time, it causes severe blockage of flow and the annular support area around each tube is not well vented for release of steam and impurities. It is also very rigid relative to differential tube motions.

Wiggle Bars. A variation of the above may be created by offsetting alternate scalloped bars to create a structure which is more open to the flow. The same type of support may be created by forming "wiggle bars" from strip (see Fig. 1(*b*)). This greatly improves openness to flow, although the tube is still covered over 180 deg at the land area. The radial flexibility of the tube bundle is somewhat enhanced in this arrangement.

Lattice Network (Triangular Arrays). A lattice type of support may be built up of flat bars to provide a diamond-shaped support space for each tube (see Fig. 1(*c*)). With this configuration the bars may only be installed after tubing, a practice which is not desirable for large bundles or close support clearances. Radial flexibility is quite limited since the entire tube bundle is tied together. However, if the bars are not interlocked, they may flex somewhat to accommodate relative tube motion. The arrangement does provide a very open structure to the flow with line contact support so as to reduce the potential for the build-up of deposits.

Lattice Bars (In-Line Arrays). A variation of the lattice bar arrangement is shown in Fig. 1(*d*). Here, large bars are placed on the plane of the U-bends with additional bars perpendicular to the U-bend plane. This arrangement ties the entire U-bend assembly rigidly together. Thus, relative tube motion at the support is prevented and differential axial tube motion must be absorbed by tube flexing. While line support contact is provided, there may be poorly vented spaces if the bars are wide.

Flat Bars. U-bend support may also be provided by placing flat bars in the plane of the U-bends, radially or otherwise (see Fig. 1(*e*)). In some designs, the bars drop into and back out of the U-bend assembly in a boomerang shape where both ends of the bars are outside the bundle. Flat bars may be staggered or lined up with one another as shown in the figure. This type of support is very open to the flow and has only line contact with the tubes. Trapped cavities or stagnant spaces can be avoided so as to minimize problems with dryout or deposition. Flat bars also provide great flexibility to accommodate differential tube motions in operation. These may be caused by temperature differentials and by thermal expansion coefficient differentials.

The preceding discussion suggests that flat bars may best meet the various criteria for effective U-bend supports. However, they apparently provide little, if any, support against in-plane tube motions. In large steam generators, the outside tube length above the straight leg supports may exceed 4 m, and hence have very low, in-plane frequencies. Such low, in-plane modes should become unstable at very low flow velocities, at least theoretically, and, if this were the case, flat bars would fail to be effective antivibration supports. Nevertheless, the apparent success of these supports in heat exchangers in service and their significant advantages suggest that a study of their FIV characteristics would be very worthwhile. This paper presents the results of such a study.

Experimental Rig and Instrumentation

Detailed reports of flow induced vibration of full U-bend tubes in the literature are essentially nonexistent for good reason. The size of practical U-bend tube bundles and the simulation of the actual radial flow distribution make model testing extremely difficult and expensive. Nevertheless, for the purposes of the work reported here, it was considered important to make the experiments as realistic as possible. Therefore, it was decided that a reasonable compromise would be to use a bundle of steam generator U-tubes and radial flow across only a portion of the bundle (partial admission).

The experimental rig developed is shown in Fig. 2. The 13-mm-dia Inconel 600 tubes are arrayed in a parallel triangular pattern with a pitch of 20 mm. The bundle is six rows deep

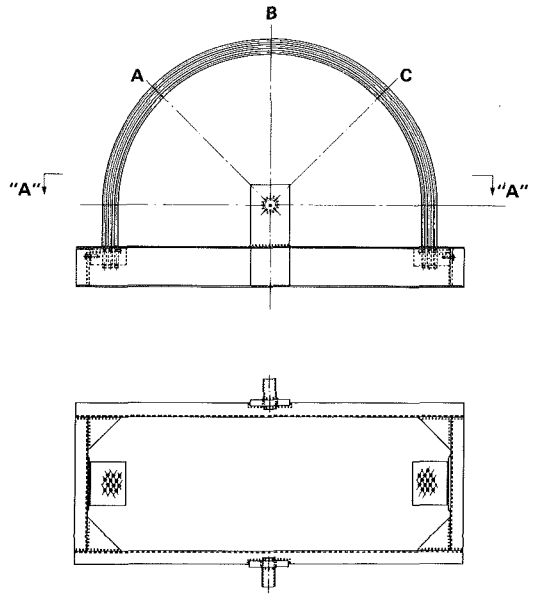

Fig. 2 Experimental U-tube bundle and support frame

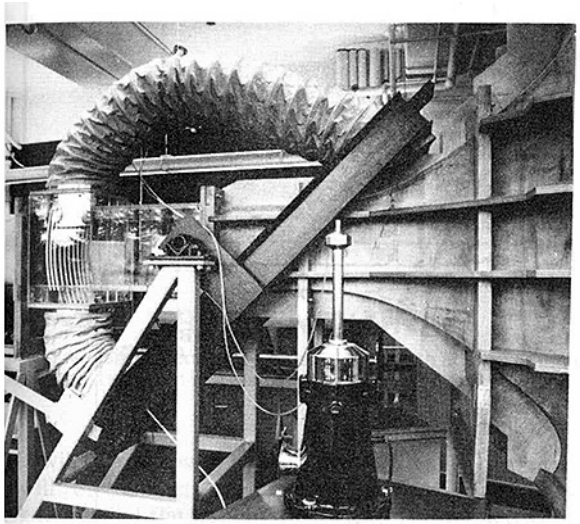

Fig. 3 Photograph of U-bend rig in wind tunnel

which has been shown to be sufficient for studying FIV in tube banks [12]. The tubes in the bundle have U-bend radii from 0.68 m to 0.73 m, plus a 0.162 m straight leg section at each end and are roll-expanded into steel blocks of 0.076-m thickness. These blocks are fixed to a heavy rectangular frame which has trunnions such that the flow could be directed radially over any 0.305-m section of the bundle away from the ends. In the experiments reported here, the wind tunnel test section was centered over the 45 deg line marked A in Fig. 2. The apex, marked B, and the other 45 deg line, marked C, were the locations used for the 410 stainless steel flat bar supports. Figure 3 shows a photograph of the U-bend rig in the wind tunnel. The bellows cover over the U-tubes seen in the figure was used to prevent leakage of flow into the wind tunnel where the bundle penetrated the test section. Details of the wind tunnel facility may be found in [13]. The upstream velocity profile is flat within 1 percent outside the boundary layers, and the turbulence intensity is less than 0.2 percent.

In order to fill out the 0.305-m width of the test section and minimize edge effects, lengths of the same curved "dummy" tubes similar to those of the flexible bundle were arranged as shown in Fig. 4. Also seen in this photograph are the solid

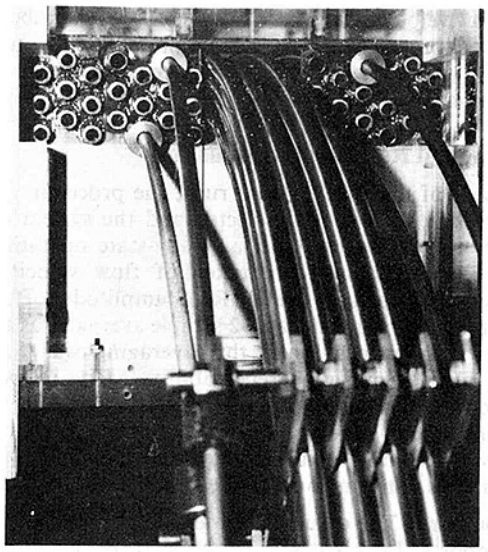

Fig. 4 Close-up of top of test section showing dummy tubes, tube bundle and 1 set of flat bar supports

Table 1

	Out-of-plane		In-plane	
Mode	Frequency (Hz)	Damping (%)	Freqency (Hz)	Damping (%)
1	9	2.18	19.4	0.10
2	25.7	0.17	44.5	0.01
3	54.7	0.12	83.9	0.10
4	95.3	0.07	131.2	0.32

curved rods that were passed through dummy tubes and attached to the end support blocks. These rods provided a base to which the support bars were fixed. A set of flat bar supports are seen in place in the bottom of the photograph.

The streamwise and transverse tube response was monitored using two MTI noncontacting capacitance displacement probes (ASP 10) and a MTI Accumeasure 1000 Bridge. The probes were fixed near the base plate at one end of a tube in the fifth row from the front of the bundle. Accessability problems made it impossible to monitor tubes in the center of the bundle, and it is desirable to have the monitored tube surrounded by flexible tubes. Also, the tubes with larger U-bend radii towards the outside of the bundle have lower natural frequencies and, hence, should become unstable first. Thus, a fifth row tube appears to be the best choice for monitoring. Other tubes could be observed visually through the acrylic test section. The first four out-of-plane and in-plane natural frequencies of the monitored tube measured in still air are given in Table 1. Of course, the tubes in different rows had somewhat different natural frequencies because of their different radii. For example, the first out-of-plane natural frequencies varied from 7.8 Hz to 9.4 Hz for the first row and sixth row tubes, respectively. The damping was highest in these lowest modes as expected, being 2.2 percent for the first out-of-plane mode of the monitored tube. With no supports, the damping in the higher modes was less than 1 percent.

The tube frequency spectra were obtained using Spectral Dynamics 335 real time frequency analyzer and plotted using a Hewlett-Packard 7004B X-Y plotter. The overall RMS tube response was obtained by taking the square root of the sum of squares of the transverse and streamwise responses from the SD 335 analyzer. Tube mode shape was observed on a Tektronix 564 B dual trace oscilloscope.

The flow velocity was obtained upstream of the tube bundle using a calibrated DISA 90 deg miniature hot wire probe together with a DISA 55A01 constant temperature anemometer.

Experimental Results and Discussion

For each of the experimental runs, the procedure was the same. A flow velocity was selected and the system allowed some 15 minutes to establish a steady-state operating condition. Then, readings were taken of flow velocity, tube frequency response and overall RMS amplitudes. The latter were obtained through at least 32 sample averages, as the tube response was unsteady, and this averaging was found to produce results with good repeatability. Mode shapes were observed, visual observations made and then the flow velocity was incremented and the entire process repeated until the bundle was well into the unstable range. The various support arrangements tested are outlined separately below.

No Supports. The datum case was a test conducted with no tube supports. In this case, the mode corresponding to the lowest natural frequency, the first out-of-plane mode at 9 Hz, is expected to become unstable. The overall RMS amplitude response as a function of flow velocity is plotted in Fig. 5. The pitch velocity, V_p, is used in all graphs and is defined as $V_p = (p/p-d)\ V_u = 2.76\ V_u$ were p is the tube pitch, d is the tube diameter, and V_u is the measured upstream velocity. It is seen that the monitored tube becomes unstable in the first out-of-plane mode at about 4.2 m/s. In order to compare the critical flow velocity for tubes with different natural frequencies, it is customary to nondimensionalize flow velocity with the natural frequency at instability and tube diameter. This so-called "reduced velocity," V_p/fd, is about 35.9 in the present case. The experiment was terminated when tube-to-tube clashing was clearly audible.

One Set of Flat Bars. One set of flat bars were inserted at the apex as shown in Fig. 4. For this experiment, the thickness of the flat bars was such that the diametral clearance was 0.08 mm. This was sufficient to allow free motion of a pure in-plane mode but completely suppress the first out-of-plane mode. The lowest natural frequencies are then 19 Hz (first-in-plane mode) and 25.7 Hz (second out-of-plane mode).

The amplitude-velocity curve is shown in Fig. 5. It is seen that the monitored tube becomes unstable in the second out-of-plane mode at about 12 m/s. This corresponds to a reduced velocity of 36.9, slightly higher than that found for the case of no supports. Interestingly, there was no evidence whatever of significant motion in an in-plane mode which theoretically should have become unstable first at about 9 m/s. Note particularly that the flow over the bundle is in the plane of the flat bars, and thus, the fluid drag force is not forcing the tubes against the supports.

Two Sets of Flat Bars. In this experiment, in addition to the apex supports a second set of flat bar supports were inserted at the 45 deg point (supports at points B and C in Fig. 2). These supports had the same small clearance as those at the apex. Again, the in-plane modes were apparently unsupported but now the second out-of-plane mode is suppressed.

The amplitude-velocity plot is also shown in Fig. 5. In this case, the monitored tube becomes unstable in an unsymmetric out-of-plane mode at about 16.2 m/s. Using the 35.6 Hz frequency, the reduced velocity at instability is computed to be 35.0, very close to the values found previously for the cases of no supports and one set of flat bar supports.

Again, in spite of the fact that the flow velocity was taken to above twice that theoretically required to produce instability in the first in-plane mode, no significant in-plane motions were observed.

In all of the above cases, the stability thresholds were

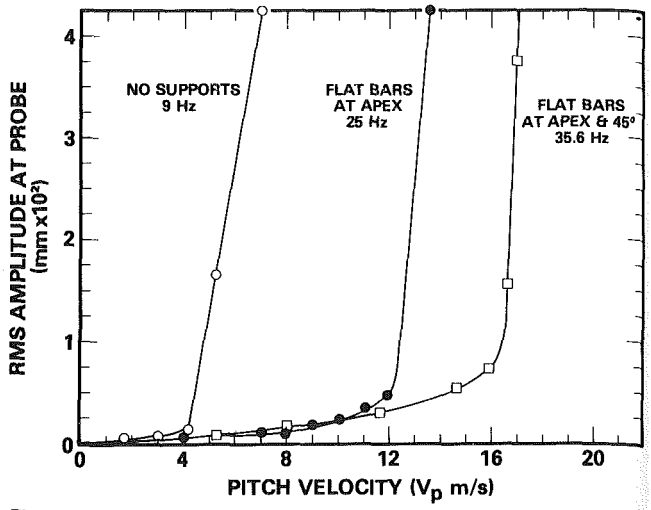

Fig. 5 Amplitude-velocity response curves for three support cases—flat bars with 0.08-mm diametral clearance

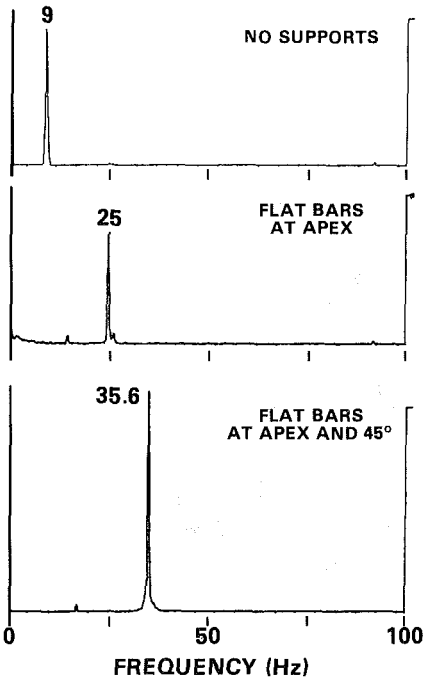

Fig. 6 Frequency spectra in the unstable range. Flat bar supports with 0.08-mm diametral clearance

relatively well defined and the unstable modes were "pure" out-of-plane modes at a well defined frequency as shown in Fig. 6. These frequency spectra all correspond to flow velocities above the respective stability thresholds and are typical of the unstable response of tubes when the support clearances are small.

Effect of Tube Support Clearance. Numerous experiments were conducted with various thicknesses of flat bars to assess the effect of support clearance on flow-induced tube response. During these experiments, a variety of difficulties were encountered, and considerable variability between results was observed. However, after many trials and repetitions, some understanding was gained and trends developed. In what follows, these insights will be summarized briefly.

First, it is instructive to discuss some of the difficulties in conducting these experiments. The bending of tubes for U-bends causes ovalling of the cross section which depends on U-bend radius. Thus, the precise distance between adjacent

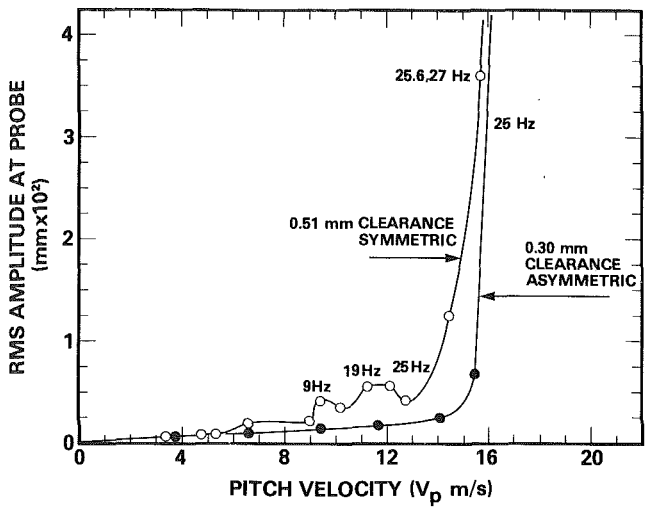

Fig. 7 Amplitude-velocity response curves—one set of flat bar supports, variable clearance

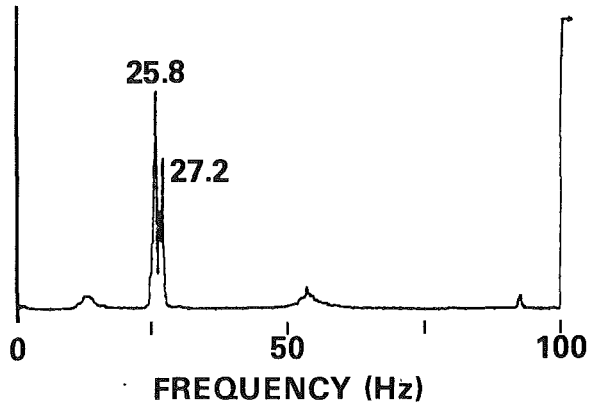

Fig. 8 Frequency spectrum—unstable range with one set of flat bars, tube centered with 0.51-mm diametral clearance

tubes will increase with U-bend radius (smaller ovalling) and so will the diametral clearance provided by a constant thickness radial flat bar. In addition, it is extremely difficult to build a rig, such as shown in Fig. 2, with all of the U-tubes exactly parallel. Thus, when some tubes are located centrally between flat bar supports, others will be off-center or even slightly loaded against a support on one side. Thus, the exact nature of the tube-support interaction will vary from tube to tube and even from one support to another for a given tube with multiple supports. The fact that the tubes have different in-plane and out-of-plane frequencies and these frequencies are dependent on tube radius which varies through the bundle, adds further variability to the expected results [14], [15]. Of course, all of these effects are typical of practical heat exchangers and it follows that similar variability is expected for such equipment in service.

Two typical results for one set of flat bar supports at the apex are shown in Fig. 7. In both cases, the unstable mode is the second out-of-plane mode as expected. In the lower curve, the tube had a diametral clearance of 0.30 mm, but the supports were located such that the monitored tube was at one side of the space. The stability threshold is delayed somewhat, the reduced velocity being about 46. The response curve is quite regular, and the delay in stability threshold is likely due to friction damping at the support.

When the support clearance was increased to 0.51 mm and the supports placed such that the monitored tube was centrally located, the critical reduced velocity was about 39. Not

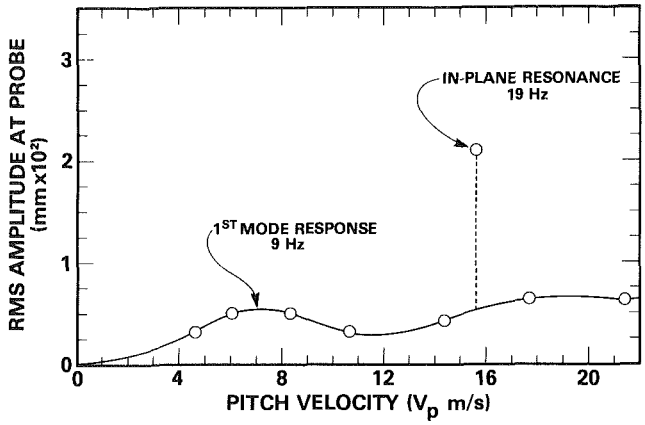

Fig. 9 Amplitude-velocity response curve—two sets of scalloped bars with 0.51 mm diametral clearance

surprisingly, the tube displacement at subcritical flow velocities is larger in this case. Particularly significant are the lumps in the amplitude-velocity curve. These correspond to motions of modes suppressed by those supports with smaller clearances, that is, the first out-of-plane and in-plane modes at 9 Hz and 19 Hz, respectively. They also occur at flow velocities above those expected to produce instability in these modes and were accompanied by audible rattling of the tubes between the supports. These observations offer a logical explanation of the recorded behavior. When the support clearance is sufficiently large and the tube is centrally located, the lower modes are effectively unsupported. At a high enough flow velocity, these modes attempt to become unstable but are suppressed when tube support impacting occurs. As the flow velocity is increased, each mode appears in order of increasing natural frequency until instability occurs in the lowest completely unsupported mode.

An indication of the nonlinear nature of the support given by large clearance is shown in the frequency spectrum of Fig. 8. This corresponds to the case of 0.51 symmetric clearance and for flow velocities in the unstable range. The second out-of-plane mode shows a split frequency at 25.8 and 27.2 Hz. This behavior undoubtedly accounts for the slight delay in stability threshold over the case for small tube clearance. In none of the various support arrangements tested was the stability threshold lower than that found for the case of carefully centered tubes between supports of small clearance.

Effect of Two Sets of Scalloped Bars. Some tests were conducted to compare the performance of the flat bars as antivibration bars with scalloped bars. The scalloped bars used were typical of those currently in use and had a nominal diametral clearance of 0.51 mm. The introduction of scalloped bar supports introduced another difficulty in testing in that any variability in U-tube radius produced contact with the supports. In extreme cases, this would move the tube in-plane and produce in-plane loads on the tube at the supports.

The flow tests showed that the performance of the scalloped bars was essentially the same as flat bars with the same 0.51 mm diametral clearance. Of particular interest are the results of two sets of scalloped bars (apex and 45 deg), as shown in Fig. 9. As is seen, there was no instability of the monitored tube. However, it is clear that the turbulence-induced vibration amplitudes are much larger than permitted by flat bars with small clearance. The peak at around 7 m/s corresponds to a response primarily in the first out-of-plane mode at 9 Hz, a mode which is theoretically suppressed by the supports. Also seen is an apparent resonance at 19 Hz in the first in-plane mode at 15.6 m/s. This response peak was very narrow, but persistent. It appeared at a given flow velocity in repeated tests and disappeared when the flow velocity was

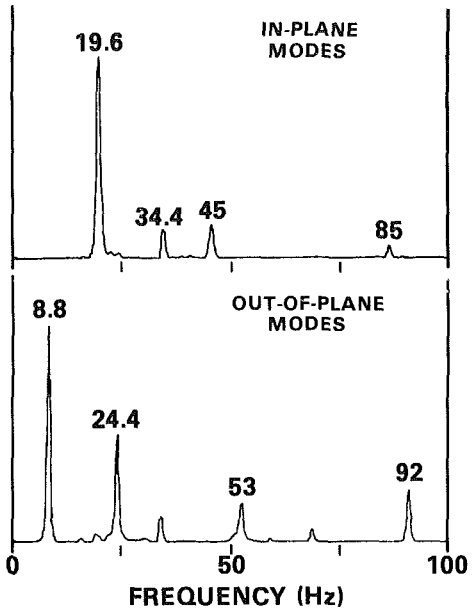

Fig. 10 Frequency spectra at low flow velocity—two sets of scalloped bar supports with 0.51-mm clearance

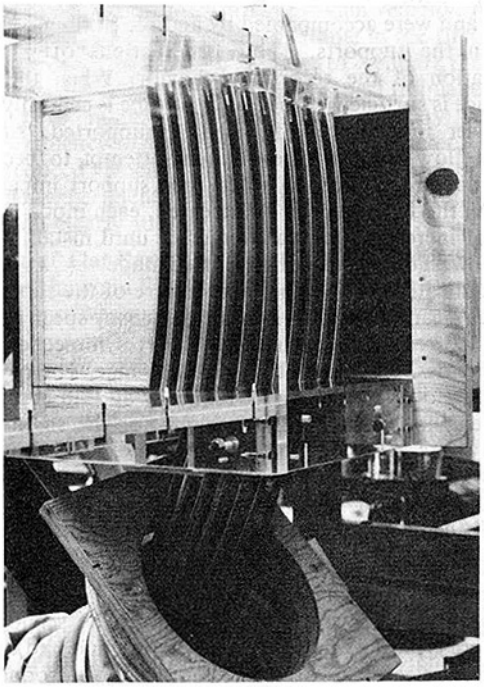

Fig. 11 Photographs of the tube bundle with out-of-plane flow

incremented slightly. This behavior is not understood but was always accompanied by audible rattlings of the tubes in the supports and perhaps was induced by some tubes in the middle of the bundle being unstable. It is interesting to note that, while these tests were conducted to determine the ability of flat bars to restrain in-plane modes, the largest in-plane response was observed for scalloped bars which are assumed in vibration analysis to provide nodal points for both in-plane and out-of-plane modes.

While large support clearances and/or lateral loads induced by tube contact at supports may be instrumental in delaying the stability threshold of some tubes, they may also be responsible for inducing premature failure through fretting wear. Tube in-plane and out-of-plane frequency spectra taken at a low flow velocity are shown in Fig. 10. The monitored tube was centrally located at both scalloped bar supports and all in-plane and out-of-plane natural frequencies are clearly visible. Most obvious are the large responses in the lowest modes which are theoretically restrained. As the flow velocity was increased, the amplitudes in the lower modes would increase until suppressed by impacting at the supports. These modes would then give way to significant amplitudes in the next higher modes. Thus, when support clearances are large, significant tube motions may occur at relatively low flow velocities, presumably because the lowest modes attempt to become unstable until quenched by support impacting. This impacting may lead to fretting failure after some period of time and it follows that, from a vibration point of view, support clearances should be kept as small as practicable.

Effect of Out-of-Plane Flow. The out-of-plane motions discussed above were all for in-plane flows, that is, the tube instabilities were invariably transverse to the flow direction. While the water tunnel tests reported in [15] showed that instability occurs in the lowest mode whether in the transverse or streamwise direction, it was considered desirable to run a test with the tube bundle turned sideways in the wind tunnel. In this way, the flow is transverse to the plane of the U-bends and the out-of-plane modes would be streamwise to the flow. This arrangement is shown in Fig. 11. As can be seen, the flow channel through the bundle is curved and the portion of the wind tunnel test section inside and outside of the tube bundle had to be blocked. The array pattern is a normal triangle, and as the depth of the bundle is now 17 rows, the pressure drop across the tubes is much greater. This configuration severely taxed the capacity of the wind tunnel. Nevertheless, the tests showed that the lowest out-of-plane, now streamwise, mode was the critical one and no in-plane instabilities were observed.

Conclusions

Tube supports are generally required in the U-bend regions of heat exchangers to prevent fluid-elastic instability. The support design influences such factors as flow distribution, tube denting, wastage due to corrosion, deposition problems, and fretting wear. Flat bars appear to have excellent capability as U-bend supports and a series of tests have been conducted to test their efficiency as antivibration bars. The conclusions drawn are as follows:

1 The effect of flat bar supports with small clearance is to act as apparent nodal points for flow-induced tube response. They not only prevented the out-of-plane modes as expected, but also the in-plane modes. No in-plane instabilities were observed, even when the flow velocity was increased to three times that expected to cause instability in the apparently unsupported first in-plane mode.

2 Experiments with the tube bundle rotated such that the flow was normal to the plane of the U-bends showed that the out-of-plane modes were still critical. Hence, the lack of observed in-plane instabilities must be due to the flat bar supports and not the inability of the flow to excite streamwise tube motion.

3 The most consistent experimental results, as well as the lowest and best defined stability thresholds, were found for flat bars with small but nonzero, clearance.

4 When the support clearance is large, the tubes rattle around in whatever space is available. The supports cannot act as nodal points until they are impacted and significant response in theoretically restrained modes occurs at relatively low flow velocities. It follows that, from a fretting point of view, the support clearance should be kept as small as practically possible.

5 The effect of zero clearance, contact force at tube supports or large clearance was to produce less consistent

results and some delay of the stability threshold. These effects are undoubtedly due in part to friction and impact damping. With large clearances, the damping and stiffness are both decidedly nonlinear. This, together with the different natural frequencies between in-plane and out-of-plane modes as well as between tubes with different radii are bound to aggravate the problem of obtaining consistent results with well defined stability thresholds.

Acknowledgment

The authors gratefully acknowledge the assistance of J. H. Lever, D. Harburn, and M. El Kashlan for running the many experiments which formed an essential part of this research program.

References

1 Paidoussis, M. P., "Flow-Induced Vibrations in Nuclear Reactors and Heat Exchangers," *Proceedings of the IUTAM-IAHR Symposium on Practical Experiences with Flow Induced Vibrations*, Karlsruhe, 1979, edited by E. Naudascher, and D. Rockwell, Springer Verlag, Berlin, 1980, pp. 1-80.

2 Halle, H., Chenoweth, J. M., and Wambsganss, M. W., "DOE/ANL/HTRI Heat Exchanger Tube Vibration Data Bank," Argonne National Laboratory Technical Memorandum, ANL-CT-80-3. 1980.

3 Pettigrew, M. J., "Flow-Induced Vibration Phenomena in Nuclear Power Station Components," *Power Industry Research*, Vol. 1, 1981, pp. 97-133.

4 Blevins, R. D., "Vibration of a Loosely Held Tube," ASME *Journal of Engineering for Industry*, Vol. 97, 1975, pp. 1301-1304.

5 Rogers, R. J., and Pick, R. J., "On the Dynamic Spatial Response of a Heat Exchanger Tube with Intermittent Baffle Contacts," *Nuclear Engineering and Design*, Jan. 1976, pp. 81-90.

6 Shin, Y. S., Jendrzejczyk, J. A., and Wambsganss, M. W., "The Effect of Tube-Support Interaction on the Dynamic Response of Heat Exchanger Tubes," Paper F6/5, *Transactions of the 4th International Conference on Structural Mechanics in Reactor Technology*, San Francisco, Calif., 1977.

7 Shin, Y. S., Sass, D. E., and Jendrzejczyk, J. A., "Vibro-Impact Response of a Tube With Tube-Baffle Interaction," Argonne National Laboratory Technical Memorandum ANL-CT-78-11, 1978.

8 Ko, P. L., and Rogers, R. J., Analytical and Experimental Studies of Tube/Support Interaction in Multi-Span Heat Exchanger Tubes," Paper F9/4, *Transactions 5th International Conference on Structural Mechanics in Reactor Technology*, Berlin, 1979.

9 Ko, P. L., "Experimental Studies of Tube Fretting in Steam Generators and Heat Exchangers," ASME *Journal of Pressure Vessel Technology*, Vol. 101, 1979, pp. 125-133.

10 Pettigrew, M. J., and Ko, P. L., "A Comprehensive Approach to Avoid Vibration and Fretting in Shell-and-Tube Heat Exchangers," *Flow Induced Vibration of Power Plant Components*, edited by M. K. Au-Yang, PVP-41, 1980, ASME, New York, pp. 1-18.

11 Goyder, H. G. C., "Measurement of the Natural Frequencies and Damping of Loosely Supported Tubes in Heat Exchangers," *Proceedings of the BNES Conference on Vibration in Nuclear Plant*, Keswick, May 1982.

12 Weaver, D. S., and El Kashlan, M., "On the Number of Tube Rows Required to Study Cross-Flow Induced Vibrations in Tube Banks," *Journal of Sound and Vibration*, Vol. 75, No. 2, 1981, pp. 265-273.

13 Grover, L. K., and Weaver, D. S., "Cross Flow Induced Vibrations in a Tube Bank—Vortex Shedding," *Journal of Sound and Vibration*, Vol. 59, 1978, pp. 263-276.

14 Weaver, D. S., and Lever, J., "Tube Frequency Effects on Cross Flow Induced Vibrations in Tube Arrays," *Proceedings of the Fifth Biennial Symposium on Turbulence*, University of Missouri-Rolla, Mo., Science Press, Princeton, N.J., 1977, pp. 323-331.

15 Weaver, D. S., and Koroyannakis, D., "Flow Induced Vibrations of Heat Exchanger U-Tubes, A Simulation to Study the Effects of Asymmetric Stiffness," ASME *Journal of Vibration, Acoustics, Stress, and Reliability in Design*, Vol. 105, Jan. 1983, pp. 67-75.

Shock Wave/Boundary Layer Interaction in Dry and Wet Transonic Steam

N. A. Evans[1]
Advisory Engineer,
Westinghouse Electric Corporation,
Steam Turbine-Generation Division,
Lester, Pa.

As part of the continuing technological advance towards the design of transonic steam turbine blades by analysis, rather than by experience based on time-consuming field testing, a series of experiments in a one-dimensional Laval nozzle was conducted to determine the nature of self-excited fluctuations due to shock wave/boundary layer interaction. Results in superheated steam flow showed peak-to-peak pressure fluctuations reaching 80 percent of the ideal across a normal shock wave, with a frequency spectrum having a fairly flat response to 150 Hz. Results in wet flow showed a distinctly different spectrum with decreased activity up to 200 Hz, but a shock wave interacting with incipient condensation near the nozzle throat produced additional broad spectral strength at 500 and 700 Hz. In addition, shock wave fluctuation in supercooled flow could trigger condensation in advance of the natural Wilson point.

Introduction

Past blade design practice has used a strength index (commonly referred to as a magnification factor) based on the steady steam bending stress in the blade and the strength of the material under vibratory loading. The magnitude of this index was calibrated using field experience.

More recently, the blading strength index has been upgraded to include the response of the blade in the various untuned modes and the strength of the blade in the actual operating environment. Upper bounds on expected response have been determined by statistically examining model test results. In this procedure, the difference in expected excitation levels between subsonic and supersonic flow has been explicitly identified, but again based on observed results.

At this point, blade design technology appears ready for a more rapid advance in the use of predictive inputs concerning excitation levels, especially in the case of tuned rotating blades in the last stages of large, low-pressure turbines. In this section of the turbine, the flow is typically transonic, and any oscillation in a blade passage of the accompanying shock wave system, with its discontinuous changes in pressure, represents a significant source of blade excitation. Such an oscillation can arise when a shock wave interacts unfavorably with a blade surface boundary layer, causing unsteady flow separation and reattachment.

In addition to interaction effects, the intrinsic nature of transonic flow causes blade loading to be sensitively dependent on small perturbations in pressure (such as those produced by upstream nozzle wakes), and in geometry (such as deviations and nonuniformities produced during manufacture). As an example of this sensitivity aspect, it is seen in Fig. 1 that there is a significant change in shock wave pattern, and hence in the blade loading, when the pressure ratio across the blade passage is changed by only 4 percent, which is directly comparable to the magnitude of upstream nozzle wake pressure perturbations.

Since previous work in a two-dimensional blade cascade has shown that unsteady interaction effects are extremely complex and difficult to interpret, an experimental and theoretical program has been started in a one-dimensional transonic steam nozzle in order to improve basic understanding of the fluid physics involved.

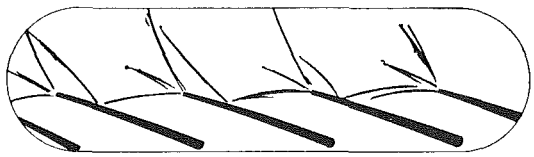

EXIT MACH NUMBER $M_{ex} = 1.18$

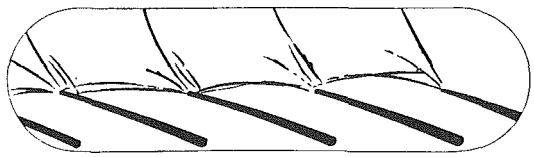

$M_{ex} = 1.22$

THE UPPER SHOCK WAVE PATTERN WILL DEVELOP INTO THE LOWER ONE FOR A DECREASE IN PRESSURE RATIO $\Delta \left(\frac{p_b}{p_t} \right) = 4\%$

Fig. 1 Sensitivity of shock wave geometry to overall pressure ratio

[1] Currently at Sandia National Laboratory, Albuquerque, New Mexico.

Contributed by the Gas Turbine Division for publication in the JOURNAL OF ENGINEERING FOR POWER. Manuscript received by the Gas Turbine Division June 18, 1982.

Related Work

The subject of shock wave/boundary layer interaction has received attention mostly in connection with high-speed wing buffeting, but the closely related topics of oscillatory nozzle flow, and unsteady flow in the inlets to supersonic aircraft propulsion systems (especially when operating at off-design conditions) have been recently investigated in quite considerable depth.

In a basic experimental study of unsteady transonic Laval nozzle flow using air, Meier [1] gave a detailed explanation of how the initial shock-wave-induced flow separation point (just downstream of the shock wave) moves upstream to meet the shock wave, thus causing the shock wave position to be inconsistent with its pressure environment. The excess downstream pressure occurring induces the shock wave to move upstream towards the nozzle throat (and into the subsonic converging section as a "bang wave"), taking the separation point with it, and ultimately producing an all-subsonic, separated flow in the diverging section. The maintained pressure difference across the nozzle then causes reestablishment of supersonic flow and repeat of the self-excited cycle in a nearly periodic fashion. In concentrating on determining the nature of the fluctuating flow mechanism, Meier did not present oscillation frequencies directly, but from oscillograms included in his paper for one set of operating conditions, it can be deduced that such frequencies were of the order of 200 to 300 Hz, with static pressure amplitudes Δp of the order of 40 percent of the stagnation pressure p_t, corresponding to one-dimensional motion of a normal shock wave at Mach numbers in the region of 1.5.

Chen, Sajben, and Kroutil [2] studied shock wave oscillations in a diffuser flow related to air inlets for supersonic aircraft propulsion. In previous work, they had identified five qualitatively different flow modes involving the nature of the separation mechanism (pressure gradient- or shock-wave-induced), the length of the separation zone, and the shock wave geometry (initially normal, and then becoming lambda-shaped (λ) as the pressure ratio across the nozzle was increased). Using wall-mounted, fast-response pressure transducers and Schlieren film taken at 44,000 frames/s, they presented quantitative results and detailed interpretations for the behavior of the unsteady flow, and concluded that the specific character of the fluctuations depended on the immediate cause of the flow separation, and were associated with fast, weak, upstream-moving perturbations in the core flow, and slow, strong, downstream-moving waves in the separated boundary layer region.

Boundary layer separation and shock wave oscillation was investigated by Troyanovskii et al. [3] in blade cascades. They performed detailed analyses on shock wave geometries and incorporated experimental results to produce specific recommendations for the peripheral zone profile of blade backs and trailing edge thickness to minimize fluctuations and profile losses in converging passages, depending on the exit Mach number, M_{ex}, up to $M_{ex} = 2.2$. For $M_{ex} > 1.5$, they recommended a diverging passage, provided a shroud was fitted, and operation was at high end-loadings.

Sensitivity of Wall Load and Shock Wave Position to Pressure Perturbations and Variations in Specific Heat Ratio

As mentioned in the Introduction, transonic flow causes blade loading to be sensitively dependent on small perturbations in certain parameters. This will now be illustrated by a simple theoretical example in one-dimensional flow for perturbations in pressure ratio, and a second example will show how shock wave location depends sensitively on the value of the specific heat ratio. A further example from the experimental results to be discussed later is concerned with sensitivity to small perturbations in geometry.

Although one-dimensional geometry was adopted for simplification purposes, it, nevertheless, simulated as closely as possible a typical blade passage. By this is meant, for example, the nozzle developed expansion rates and an exit Mach number that were similar to a typical L-1 rotor blade passage, which has, from time to time, exhibited deficiencies in reliability and performance.

Consider the diverging portion of a plane wall Laval nozzle with an exit to throat area ratio $A_{ex}/A^* = 1.1$. With a ratio of specific heats $\gamma = 1.1$ for wet steam (as might be encountered in the final stages of a low pressure turbine) and an entry stagnation pressure p_t with inviscid flow, a certain back pressure p_b will produce a Mach number $M_A = 1.34$ at station A immediately ahead of a normal shock wave in the exit plane. This occurs for $p_b/p_t = 0.72$, as shown in Fig. 2, which gives the pressure distribution along the nozzle from the choked throat, and includes a sketch of the corresponding nozzle geometry using arbitrary length units.

The hatched area under the pressure distribution curve

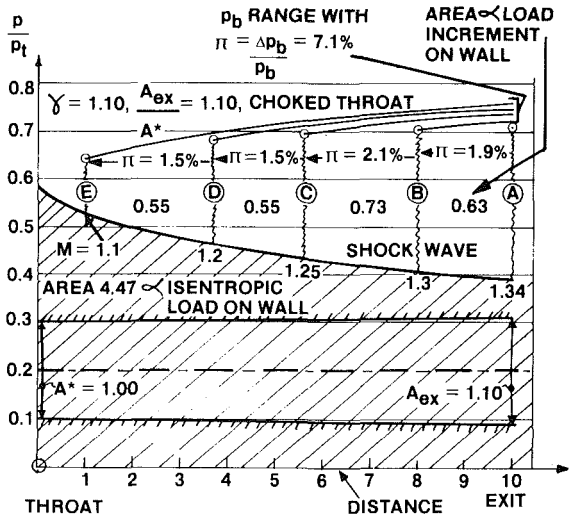

Fig. 2 Dependence of shock wave position on back pressure in a one-dimensional nozzle

Nomenclature

A = area
L = load
M = Mach number
p = pressure
T = temperature
x = axial distance
γ = specific heat ratio
Δ = change in
λ = sensitivity factor, $(\Delta L/L)/(\Delta p_b/p_b)$
λ' = sensitivity factor, $(\Delta L/L)/(\Delta\gamma/\gamma)$
π = $\Delta p_b/p_b$

Subscripts and Superscripts

A,B,C,D,E = shock wave position
b = back
ex = exit
t = total
$*$ = value at sonic condition
$\hat{\ }\ \hat{\ }$ = peak-to-peak value

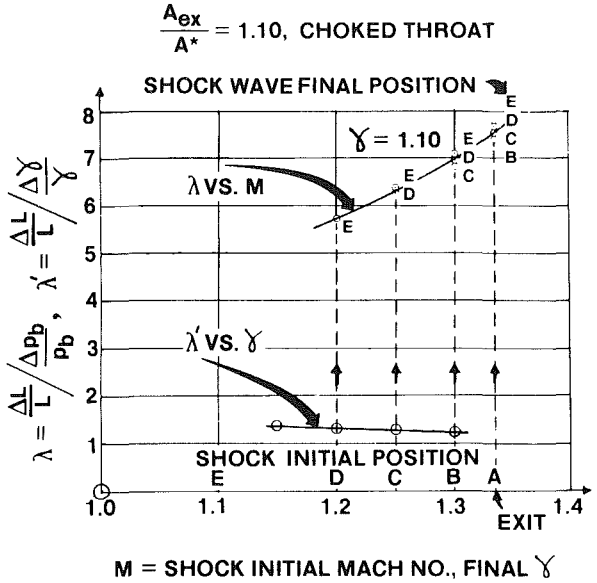

Fig. 3 Variation of load sensitivity factors with shock Mach number and final specific heat ratio

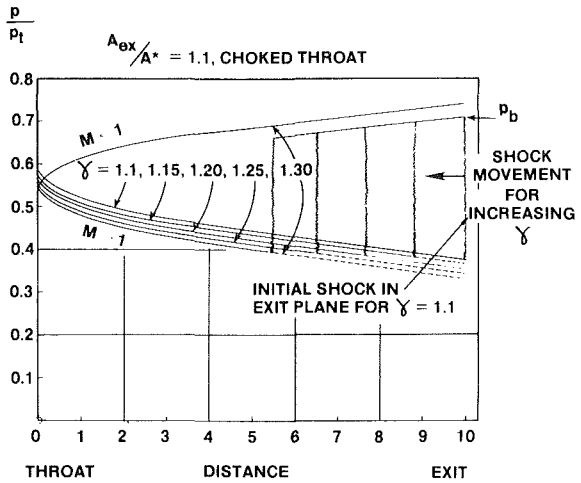

Fig. 4 Effect of variation of specific heat ratio on shock position for fixed back pressure

(4.47 units) is proportional to the isentropic load, L_A, on the nozzle wall. If the back pressure ratio is increased by an amount Δp_b, so that $\pi = (=\Delta p_b/p_b A) = 1.9$ percent, the shock wave moves upstream to position B where $M_B = 1.3$, and increases the nozzle wall load by an amount, ΔL_{AB}, proportional to 0.63 units, giving $\Delta L_{AB}/L_A = 14.1$ percent. Defining a load sensitivity factor $\lambda = (\Delta L/L_A)/(\Delta p_b/p_b)$ gives $\lambda_{AB} = 14.1/1.9 = 7.4$ for shock wave movement from A to B, as shown in Fig. 3. Additional values of λ for Fig. 3 can be generated by considering a shock wave initially at any point A, B, C, or D and moving to any upstream location B, C, D, or E, such as B to E.

The results indicate that a relatively modest change in back pressure $\Delta p_b/p_b$ can exert significant leverage (typical values of $\lambda = 7$ or 8) on the wall load increment ratio $\Delta L/L$ when moving a shock wave. It is also seen from Fig. 3 that λ increases with M at the initial shock wave location and is relatively insensitive to the final shock wave position. Another way to emphasize the nature of the sensitivity is to note that, once the shock wave has been established in the exit plane at $M_A = 1.34$, a back pressure ratio change of just $\pi = 7.1$ percent will drive the shock wave almost to the throat. Since the shock wave position is specifically dictated by p_b/p_t, changes in position of a similar order will also occur with variation Δp_t in p_t, and it is readily appreciated that such changes from upstream, as might be produced in an actual turbine by periodic stator wake pressure deficits, could lead to oscillating wall loads at a level significantly higher than when applying the effects of Δp_t to the walls directly.

If γ is increased from 1.1 to 1.3, a typical superheated value, the preceding values of λ decrease by less than 3 percent for a shock wave initially at $M = 1.34$ and induced to move upstream to $M = 1.25$ by changing p_b. While this situation shows no sensitive dependence of λ on variation in γ, a fairly dramatic sensitivity for shock wave relocation arises as follows. Consider a moist flow ($\gamma = 1.1$) with $p_b/p_t = 0.712$ so that a shock wave is in the nozzle exit plane at $x = 10$ units. If p_b and p_t are held constant, but γ is increased to 1.3 corresponding to superheted flow, the shock wave moves to $x = 5.5$ units, almost halfway up the nozzle, as shown on Fig. 4. Similarly, a shock wave in wet flow at $x = 6$ units will vanish upstream in the throat with maintained p_b/p_t if the flow becomes superheated.

A load sensitivity $\lambda' = (\Delta L/L)/(\Delta\gamma/\gamma)$ can be determined in a manner similar to that for λ due to changes in p_b, and the results for an initial value of $\gamma = 1.1$ and varying final value of γ, are shown on Fig. 3. The maximum calculated value of λ' at 1.35 is much smaller than λ (typically 7.5) due to cancellation of wall loading effects upstream and downstream of the final shock wave location after changing γ (see Fig. 4), but the combined, multiplied value, $\lambda \cdot \lambda'$, is a full order of magnitude. However, with respect to λ' alone, the large change in shock wave position could, in an actual turbine, result in boundary layer separation on the back of a blade, with consequent oscillatory flow, loss of performance, and vibratory excitation.

Experimental Objective, Apparatus, and Procedure

The experimental objective was to determine, both qualitatively and quantitatively, the nature of shock wave/boundary layer interaction in one-dimensional transonic steam nozzle flow. This would represent the first step for improving the design procedure to enhance transonic turbine blade performance and reliability. For an observed instability in superheated flow, it was therefore necessary to determine the dependence of its amplitude, frequency, position and movement range on the nozzle operation parameters of total pressure, back pressure, and total temperature.

The work was conducted at the Westinghouse R&D Center in Pittsburgh using a side leg of the Steam Test Facility which is capable of operating at full scale Mach and Reynolds numbers when testing cascades of the largest low pressure turbine blades. The principal facility components are a boiler, throttle, desuperheater, separator, test nozzle section, and condenser. The boiler can produce steam mass flow rates up to 9000 lb/hr and the condensor can achieve pressures down to 1.5 in HgA, depending on the steam load and the ambient characteristics acting on the cooling tower. The steam inlet conditions range typically from 100°F superheat to approximately saturated, depending on the mass flow and limitations of the desuperheater and separator.

The test nozzle section contained components, such as a flow straightener, diffusers (maximum wall divergence angle 5 deg), and a contraction section to the test nozzle (area ratio 24:1) to ensure a high-quality, steady flow. The final diffuser (between the nozzle exit and the condenser) terminated with an eight-petal grid valve capable of fine adjustment to given precise control over the nozzle back pressure for positioning of the shock wave.

The original test nozzle (Fig. 5) had a nominal sonic throat

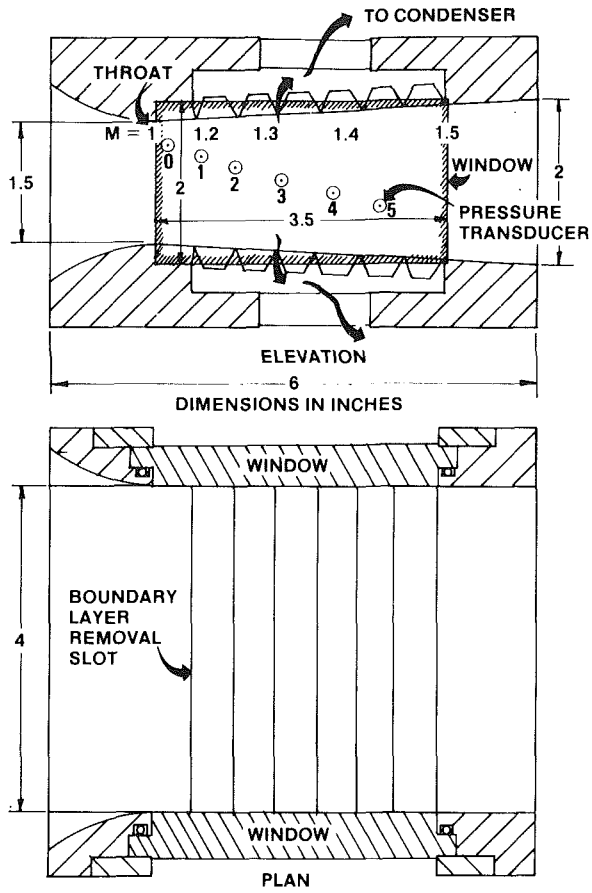

Fig. 5 Test nozzle geometry

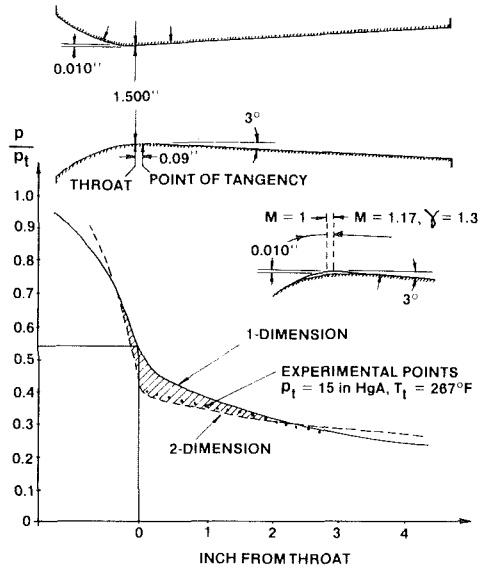

Fig. 6 Initial pressure distribution in original nozzle and geometric modifications

height of 1.500 in. and a width of 4 in., followed by plane parallel side walls, and top and bottom plane walls, each 4.75 in. before connecting with the diffuser. For work with full boundary layers, the top and bottom walls were solid, but each could be replaced by six flush-mounted strips, 3.875-in. long × 0.5-in. wide with adjustable intervening slit spacing for upstream from the nozzle throat; the subsonic appraoch on all four walls was a surface segment of radius 1.75 in., which then became tangent to plane walls at 45 deg in the settling chamber.

Downstream of the throat, the nozzle sidewalls were composed of high optical quality fused silica windows for shadowgraph flow visualization, using a double-pass light beam system. Shadowgraph records were obtained on a still camera having a focal plane shutter with calibrated slit speed, and on a motion picture camera at 400 frames/s with an individual frame exposure of 1/4000 s. The windows could be replaced with sidewalls containing, on one side, 16 static pressure taps connected to a Scanivalve and Statham transducer for steady or averaged measurements. Over a period of approximately 0.25 s, each prepurged tap was scanned for five readings, which were then averaged by a PDP8 computer before result printing. The 17th port on the Scanivalve was used for measuring the pressure, p_t, in the settling chamber. The other sidewall contained six fast-response (50 kHz), hermetically sealed Kulite transducers principally for unsteady measurements, with the conditioned signals recorded on a Honeywell type 101 FM tape recorder for subsequent digital processing. Each transducer output could be switched to oscilloscopes and an rms voltmeter to give immediate observations for positioning of the shock wave at a particular location by adjustment of the downstream petal valve.

Tests were performed at 9 points in superheated steam covering the total pressure range from 3.5 to 20 in. Hg absolute. For each value of p_t, static pressure measurements were recorded for shock-free flow, and for the shock wave positioned for maximum activity at each transducer location in turn. Several tests were also performed in wet steam in order to make comparisons with the above results involving superheat.

Results and Discussion

Superheated Flow. For shock-free, superheated flow, the pressure distribution in the original nozzle was below the theoretical one-dimensional prediction, with the disagreement increasing towards the throat, as shown in Fig. 6. Even though the slender nozzle geometry, having a total divergence angle of 6 deg between one pair of walls with the other pair parallel, might be readily accepted as satisfying normal one-dimensional flow assumptions, it appears that, near $M = 1$ in the throat, the discrepancy was caused by a significant two-dimensional flow condition, as follows. For $\gamma = 1.3$, turning a sonic flow past the throat through an expansion angle of 3 deg to follow one wall will theoretically induce a Mach number $M = 1.17$, with pressure lower than the local one-dimensional value at the tangency point (Fig. 6), which is less than 0.1 in. downstream of the throat. In addition, similar, steep expansion waves from the throat region of the opposite wall will further increase the Mach number in excess of the one-dimensional value. To support this assertion, the results of a two-dimensional prediction technique are seen in Fig. 6 to agree quite closely with the experimental points. The shaded area between one- and two-dimensional pressure distributions represents a wall loading difference which may be regraded as due to a sensitive dependence on geometry in a flow near sonic conditions.

In order to improve the experimental pressure distribution and restore part of the test range in Mach number for $M <$ 1.2, the nozzle throat region was very slightly modified as shown in Fig. 6, by removing 0.010 in. from each wall and then producing a smoothly blended contour at points approximately 0.5 in. on each side of the throat. In this way, the measurement points nearest the throat, which originally anticipated the theoretical one-dimensional pressure distribution by an upstream distance of approximately 0.75

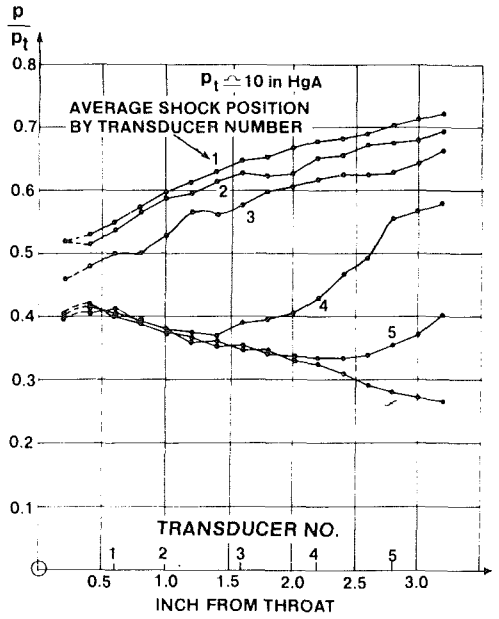

Fig. 7 Averaged pressure distribution along channel with different oscillating shock wave locations

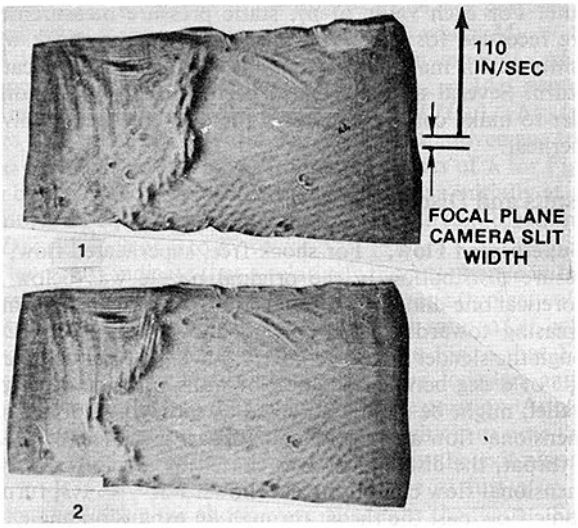

Fig. 8 Shadowgraphs of oscillating shock wave in superheated flow using a focal plane camera

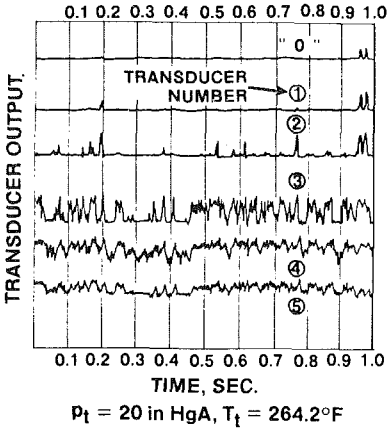

Fig. 9 Simultaneous overlay of pressure transducer signals for shock wave oscillation mostly at transducer 3 in superheated flow

in. (Fig. 6), showed better agreement with the upstream anticipation distance. However, with the modified nozzle, measurements from the first tap (dashed curve segments on Figs. 7, 12, and 13) were often low, presumably due to sensitive overexpansion at a slight wall junction imperfection just downstream of the throat between the nozzle and the removable window section (also used for mounting the pressure taps, Fig. 5).

The sensitive manner in which a small change in throat geometry decreased wall loading is potentially significant for the performance of forged turbine blades which have generous dimensional tolerances to accommodate the manufacturing process, resulting, for example, in the requirement for custom-fitted shrouds. While such geometric deviations could affect steady loading, variations from geometric deviations during vibration (especially for long blades) could produce coupled blade excitation. These aspects will be incorporated in a formal program to determine an acceptable balance between reasonably achievable manufacturing tolerances and consequent performance and reliability, especially in the case of blades for converging-diverging passages.

Time-averaged pressure measurements in the modified nozzle are shown in Fig. 7 for $p_t \simeq 10$ in. Hg absolute. The lowest curve is for isentropic flow (shock wave at ∞) and the improvement at the upstram end over the corresponding curve for the original nozzle (see Fig. 6) should be noted. The slight general waviness to the curve is attributed to the effect of noncancelled pressure waves in supersonic flow from the top and bottom plane, diverging walls. The other curves of Fig. 7 correspond to cases in which a shock wave was positioned for maximum activity (as observed on rms voltmeter) over the transducer number with locations as indicated on the distance axis. The irregular nature of the pressure distributions 1 through 5 is due to motion of the shock wave after interaction with the wall boundary layers, which resulted in flow separation in a manner similar to that described by Meier [1]. Although curves 1 through 3 are indicative of entirely subsonic flow, the corresponding transducer output traces clearly showed the bounded switch-on and -off characteristic of the passage, to and fro, of a shock wave. Furthermore, motion pictures at 400 frames/s, with each exposed at 1/4000 s, confirmed the presence of a normal shock wave in supersonic flow. Figure 8 shows shadowgraphs of the shock wave oscillation taken with a focal plane camera having a calibrated speed of the slit width. The shock wave was actually plane and normal, but during its motion, only a short segment was arrested at each instant as the slit rapidly traversed the film plane, with the result that the shock wave appeared to be twisting. From these shadowgraphs the oscillation frequencies were calculated to be of the order of 100 to 200 Hz, and it is seen that the motion was quite erratic. The fact that the measured pressure distributions at the wall were far different in form from the theoretical distributions given in Fig. 2 is an indication of the disruptive complexity caused by interaction with the boundary layer. However, it should be noted that these nozzle wall readings are of particular importance, since they simulate what might be felt by the surface of a turbine blade in an analogous flow situation. Additional measurements taken along the nozzle centerline would be desirable for further improvement in understanding of the fluid physics involved.

Figure 9 shows the simultaneous a-c output component of transducers 0 through 6 over a period of one second for a shock wave with an average position mostly over transducer

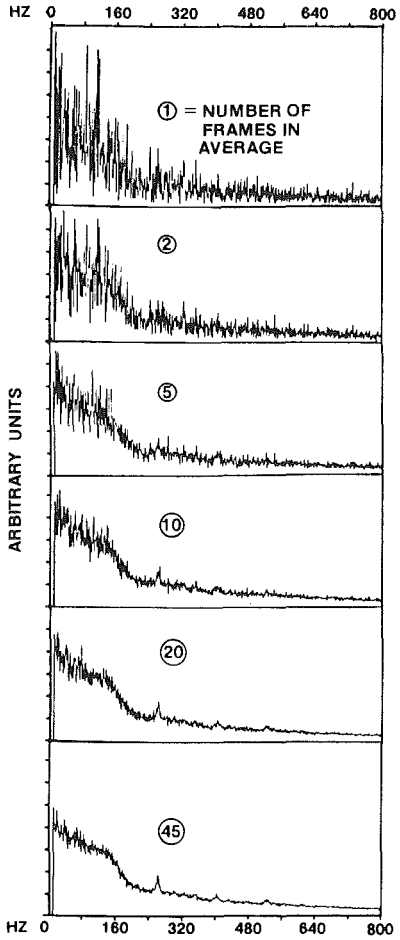

Fig. 10 Effect of multiframe averaging of frequency spectrum

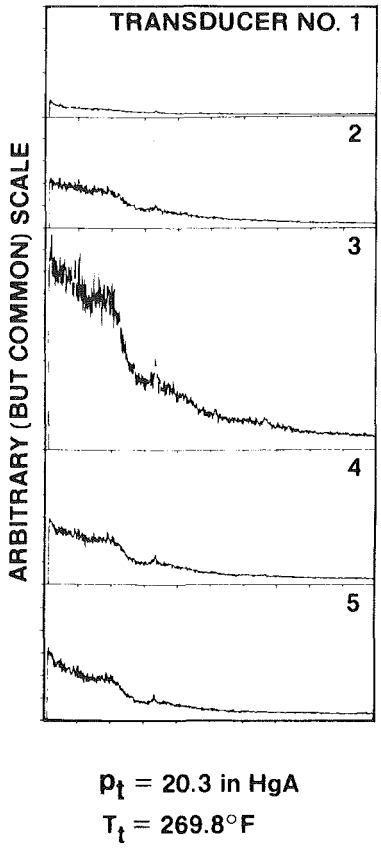

Fig. 11 Spectra for shock wave oscillation in superheated flow, with average shock wave position over transducer No. 3

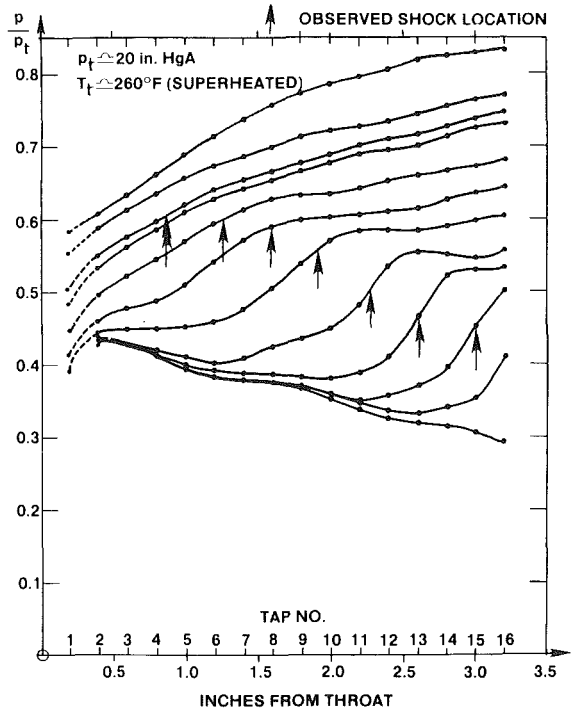

Fig. 12 Pressure distribution for arrested shock wave with reduced boundary layers

3. The bounded nature of trace 3 is evident, together with the wide variability in oscillation frequency and movement range along the channel. Relatable pressure peaks are seen to have occurred across all six transducers at 0.2, 0.96, and 0.975 s. With the failure of one transducer, the remaining results are reported for transducers in locations 1 through 5.

Initial processing of transducer output for spectral content used a tape record length of 1 s, and a typical fast Fourier analysis result is shown in the frame labeled (1) in Fig. 10. To improve interpretability, additional 1-s data lengths were averaged, the total number involved for a particular result being indicated by the circled number in the remaining frames of Fig. 10. It is seen that the 45-frame average spectrum is considerably cleaner than for the single-frame case and has a slowly decreasing frequency response up to approximately 150 Hz, followed by a break with faster response decay to a 200 Hz, and then roughly linear decay to 800 Hz, and presumably beyond. The peaks at 260, 400, and 530 Hz correspond to the organ pipe (standing wave) harmonics produced by the subsonic flow length in the nozzle combined with the diffuser at a steam sonic speed of approximately 1500 ft/s. The organ pipe quarter wavelength fundamental frequency is approximately 125 Hz, and this can be readily detected on other spectra, such as in Fig. 15, to be discussed later. The finite bandwidth of these peaks is probably due to the slight change in subsonic resonance length as the shock wave oscillated in the nozzle.

It turned out that this spectrum shape with a shoulder-type break at 150 Hz was particularly characteristic of a shock wave oscillating in superheated flow, and will subsequently be referred to as a "shoulder spectrum." The relatively flat shoulder is especially significant: since it occurred as the result of multi-frame averaging, it may be interpreted as all frequencies up to 150 Hz having roughly equal probability of being exicted. This, in turn, implies a high susceptibility to tuning to a particular frequency up to 150 Hz by an excitation

source external to the channel, analogously to upstream nozzle wakes in an actual turbine. Further examples of shoulder spectra along the channel length at p_t = 20 in. Hg absolute, with a shock 3, are shown in Fig. 11. In these and succeeding sets of spectra, the vertical axis has the same scale throughout for direct comparision of amplitudes, with the spectra in a column corresponding downwards to transducers 1 through 5.

From the unbounded transducer output trace (of the type shown in Fig. 9) at station 3 corresponding to p_t = 20.3 in. Hg absolute, an estimate of the maximum peak to peak oscillating static pressure gives $\hat{p}/\hat{p}_t$ = 28.7 percent. This is 81 percent of the theoretical value produced by the static pressure discontinuity across an ideal normal shock wave at the same location and Mach number. While the measured values still represent very substantial fluctuating pressure levels, the deficiency of the measured value with respect to the ideal was due to the local complication of the shock wave geometry when interacting with the boundary layer. It is well documented that the foot of the shock wave at the thickening, or separating, boundary layer edge is lambda-shaped, so that the pressure rise is spread over a distance of many boundary layer thicknesses upstream and downstream, causing a decrease in the degree of the pressure rise at a specific location. In pipe flow cases, a length equivalent to several diameters is required to achieve the full pressure increase, which then closely approaches the theoretical value for a normal shock wave in inviscid flow.

With the boundary layer removal strips installed in the top and bottom of the nozzle (see Fig. 5) with slit widths of 0.005 in. increasing to 0.009 in. downstream, shock wave oscillation could be reduced to a slight flutter over a total distance of about 0.2 in., but the measured pressure gradients (Fig. 12), (although steeper at the observed shock wave locations at the downstream end of the nozzle than when previously measured without boundary layer removal) were still far less than the ideal, discontinuous profile. This was probably due, in spite of substantial steadying of the shock wave, to persisting boundary layer interaction effects, especially on the plain sidewall windows, and provides further emphasis for the desirability to make center line pressure measurements in the core flow.

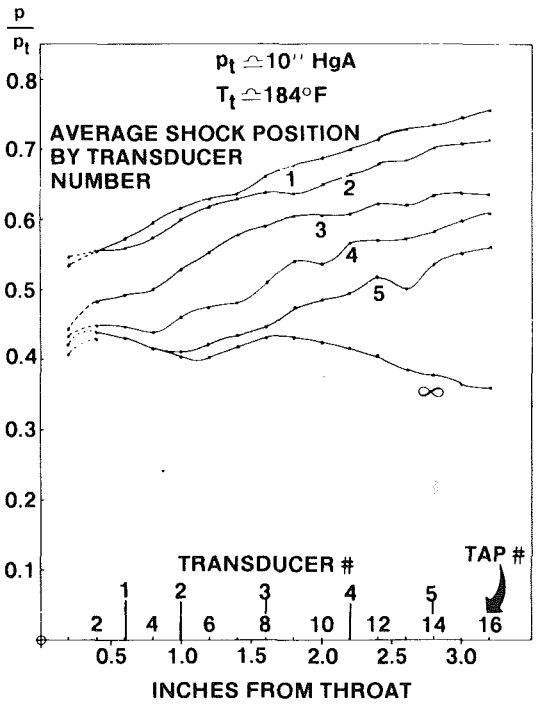

Fig. 13 Averaged pressure distribution with condensation in mid-channel, varying shock wave location and full boundary layers

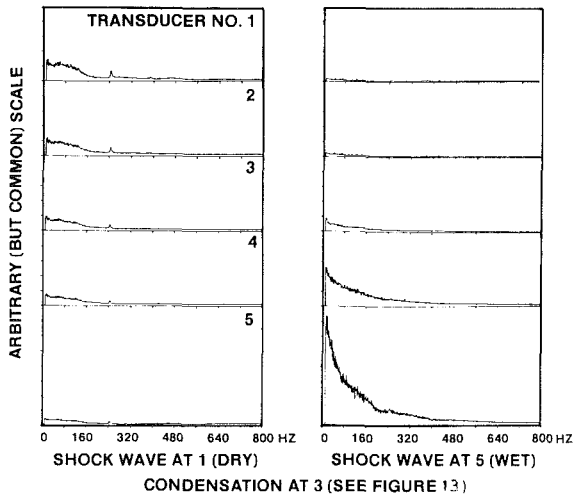

Fig. 14 Spectra for shock wave oscillation upstream and downstream of condensation with full boundary layers

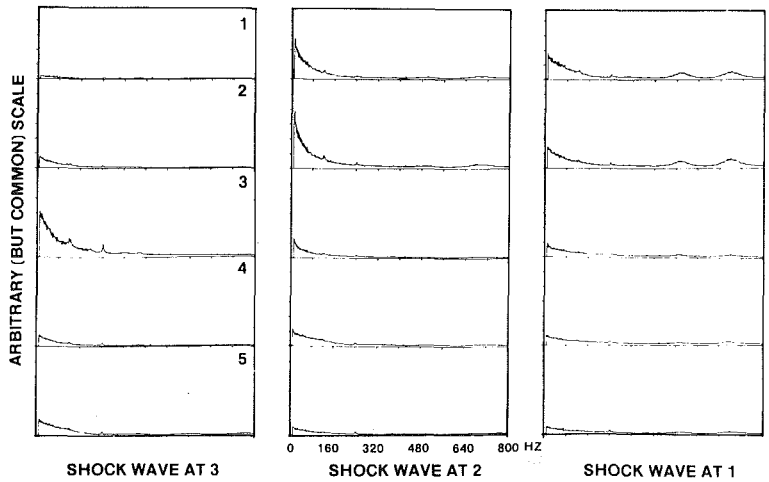

Fig. 15 Spectra for shock wave oscillation with condensation occurring near nozzle throat at T_t = 165 F with full boundary layers

Wet Flow. With operation of the desuperheater, steady pressure measurements with spontaneous condensation in shock free flow are shown in Fig. 13 for the curve labelled ∞. At p_t = 10 in. Hg absolute, and T_t = 184°F with high flow speed, the steam became supercooled in the nozzle and then went through a rapid approach to equilibrium at the Wilson point, where the sudden latent heat release caused an associated static pressure increase, but this was not sufficient to cause boundary layer separation. Under these operating conditions, the condensation was clearly visible on the shadowgraph as a steady, plane front, almost halfway along the nozzle.

The introduction of a shock wave, as with superheated flow, caused fluctuations, but the characteristic spectrum shape in wet flow was similar to hyperbolic, as opposed to the shoulder type in superheated flow. In Fig. 14, which corresponds to the conditions for Fig. 13, this hyperbolic shape is seen for a shock wave positioned at station 5 in the wet flow, whereas the shoulder type is evident along the entire nozzle for a shock wave positioned at station 1 in the superheated flow (the response here is of necessity lower than for the wet flow case because the shock wave is weaker at the smaller Mach number near the throat). The persistence of the shoulder spectrum along the nozzle indicates that the upstream shock wave (at 1 < M < 1.25 approximately) inhibited the condensation process.

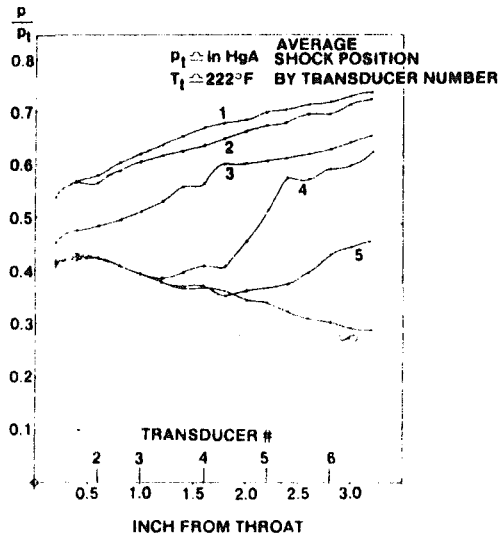

Fig. 16 Averaged pressure distribution with modest superheat, varying shock wave location and full boundary layers

It also appears that, once the moisture had sufficiently condensed, the shock wave did not cause rapid reevaporation, as seen in Fig. 15, where the low value of T_t = 165 F induced shock-free spontaneous condensation quite close to the throat. However, shock waves located at stations 3, 2, and 1 all produced the hyperbolic profile, indicating the persisting presence of moisture.

With condensation near the throat, the particular case of the shock wave at station 1 (but also discernible when at station 2) produced broad response peaks at 500 and 700 Hz along the nozzle (Fig. 15). Here the shock wave was reinforcing the condensation pressure rise near the throat and probably caused the thermal choking limits to be exceeded at the relatively low supersonic Mach number. As a result, the flow would seek readjustment, possibly in a manner similar to that observed by other investigators, such as Barschdorff [4], who measured frequencies of the order of 500 to 1000 Hz. Such frequencies occurred when spontaneous condensation alone, sufficiently close to a very slender throat, had exceeded the thermal choking limit.

For a modest degree of superheat (T_t = 220°F at p_t = 10 in. Hg absolute), Fig. 16, curve ∞, shows that condensation did not occur in shock-free flow within the measurement length of the nozzle. However, introducing a shock wave produced unsteadiness, and a particularly large time-averaged pressure rise when located at M ≃ 1.35 at station 4 (Fig. 16, curve 4). Examination of the corresponding spectra (Fig. 17) shows a hyperbolic profile with the shock wave at station 4, indicating that the shock wave had triggered condensation well ahead of the Wilson point. With the shock wave located at station 5, a transitional spectrum with higher frequency content occurred and was possibly due to the shock wave interacting with incipient unsteady condensation (perhaps partially triggered ahead of where it would naturally have occurred) and reevaporation, similar in some respects to the high frequency situation when a shock wave interacted with condensation close to the throat (Fig. 15, shock wave at

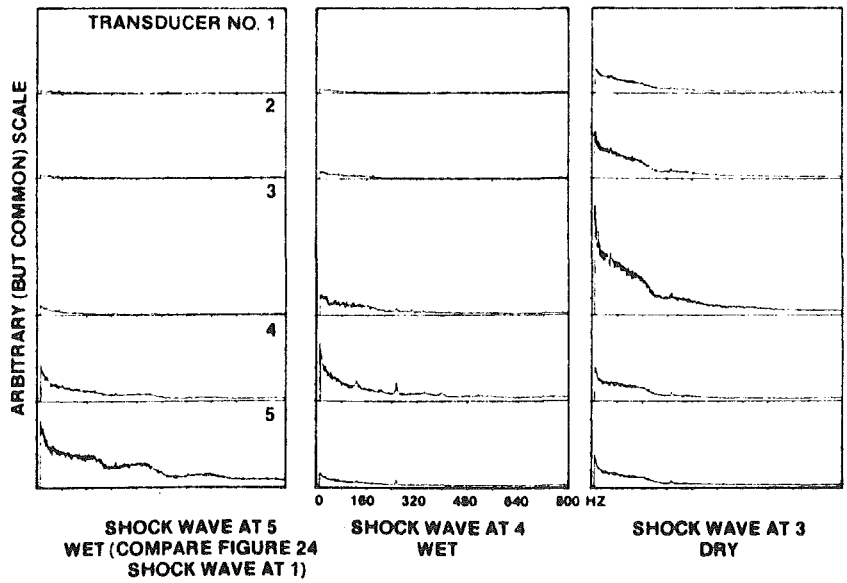

Fig. 17 Spectra showing condensation triggered by shock wave oscillation

station 1). The shock wave located at 3 was too far upstream to trigger condensation, and the spectra are all of the shoulder type for dry flow throughout. For better clarity of comparison and contrast, the features described above for the interaction between a fluctuating shock wave and condensation under various conditions are summarized together in the next section.

Conclusions and Implications for Turbine Blade Design

From an experimental investigation of shock wave/boundary layer interaction in one-dimensional, transonic steam nozzle flow, the following conclusions were drawn, together with implications (as appropriate at this stage in the program) that could affect turbine blade design with respect to reliability and performance.

In Superheated Flow. 1 Self-excited shock wave oscillation produced a charactertistic "shoulder-type" frequency spectrum with a relatively flat, broad peak to 150 Hz for all operating conditions, suggesting high susceptibility to tuning by an external excitation source. In an actual turbine, such tuning could be readily associated with upstream nozzle wakes.

2 Peak-to-peak oscillating static pressures reached 80 percent of the theoretical value for an ideal normal shock wave, with the deficiency attributed to the shock wave structure where it interacted with the boundarylayer. Such pressures suggest highly significant blade excitation inputs in an actual turbine, with a minimum stimulus that is great than the presently acknowledged design value of 3.75 percent in the transonic flow regime.

3 The shock wave could be significantly arrested by boundary layer removal, but the axial pressure gradients measured at the wall were still far short of the characteristic for a normal shock wave, suggesting local complexity in shock wave structure.

4 The wall loading was particularly sensitive to geometric perturbations in the sonic region, and this has bearing on manufacturing tolerances, especially for blades for converging-diverging passages and would require acceptable trade-offs amongst cost, performance, and reliability.

In Wet Flow. 1 The characteristic frequency spectrum for self-excited shock wave oscillation was approximately hyperbolic in shape for all wet operating conditions, with frequencies of significance restricted to less than 200 Hz, and was easily distinguishable from the shoulder spectrum for superheated flow. This point, together with item 2 below, suggests that wetness would give some relief from reliability problems, but it is well established that a deterioration in performance would occur.

2 A shock wave fluctuating in a mature wet flow did not appear to cause significant reevaporation, but the rms pressure activity was clearly less than for the corresponding superheated case.

3 A shock wave fluctuating near the throat ($1 < M < 1.25$) under the influence of a separated boundary layer and interacting locally with incipient condensation showed broad spectral strength at 500 and 700 Hz, suggesting the possibility of a type of critical operating condition to be avoided in an actual turbine.

4 A shock wave fluctuating near the throat ($1 < M < 1.25$) under the influence of a separated boundary layer could inhibit condensation that would normally occur further downstream beyond a shock-free Mach number of approximately 1.3.

5 A shock wave fluctuating in midchannel ($M \simeq 1.35$) within a certain distance upstream of the normal Wilson point could trigger condensation, indicating that certain types of flow nonuniformity, as may be encountered in an actual turbine, could inhibit supercooling and its consequent undesirable effects.

Note that items 2 to 5 represent a fairly complicated but progressive interplay amongst shock strength and position, and the tendency to induce, inhibit, or reevaporate moisture, and could justify further investigation of these phenomena.

In anticipation of actual conditions occurring in a turbine, it was also shown theoretically that the wall loading is sensitively dependent on shock wave movement that might be induced by perturbations in total pressure or back pressure. In addition, changes in steam state, as indicted by the value of γ, could significantly affect the shock wave position in the nozzle, but in this case the wall loading increase was very modest.

Acknowledgment

This investigation was supported by the Electric Power Research Institute under contract RP 1407-1.

The provision of two-dimensional nozzle flow calculations by D. K. Whirlow (R&D Center, Pittsburgh), the assistance of G. Miklos (R&D Center, Pittsburgh) in the operation of the experiments, and the contributions of D. I. Minnig and B. W. Patullo (Steam Turbine-Generator Division, Lester) towards the data reduction are gratefully acknowledged.

Thanks are also due to Beverly Anne Powell for typing this paper with support provided by R & D Associates of Albuquerque, New Mexico.

References

1 Meier, G. E. A., "Shock-Induced Flow Oscillations in a Laval Nozzle," *IUTAM Symposium*, 1975, Göttingen.

2 Chen, C. P., Sajben, M., and Kroutil, J. C., "Shock Wave Oscillations in a Transonic Diffuser Flow," *AIAA J.*, Vol. 17, No. 10, Oct. 1979, pp. 1076–1083.

3 Troyanovskii, B. N., Maiorskii, E. V., Lukin, V. V., and Yaragulya, B. A., "Supersonic Cascades in the Last Stages of High Capacity Steam Turbines," *Teploenergetika*, Vol. 24, No. 10, 1977, pp. 7–12.

4 Barschdorff, D., "Droplet Formation, Influence of Shock Waves and Instationary Flow Patterns by Condensation Phenomena at Supersonic Speeds," *Third Int. Conf. Rain Erosion and Allied Phenomena*, 1970, Farnborough.

Droplet Size Effects on NO_x Formation in a One-Dimensional Monodisperse Spray Combustion System

H. Sarv

A. A. Nizami

N. P. Cernansky

Department of Mechanical Engineering,
Drexel University,
Philadelphia, Pa. 19104

A one-dimensional monodisperse aerosol spray combustion facility is described and experimental results of post-flame NO/NO_x emissions are presented. Four different hydrocarbon fuels were studied: isopropanol, methanol, n-heptane, and n-octane. The results indicate an optimum droplet size in the range of 43–58 microns for minimizing NO/NO_x production for all of the test fuels. This NO_x behavior is associated with droplet interactions and the transition from diffusive type of spray burning to that of a prevaporized and premixed case. Decreasing the droplet size results in a trend of increasing droplet interactions, which suppresses temperatures and reduces NO_x. This trend continues until prevaporization effects begin to dominate and the system tends towards the premixed limit. The occurrence of the minimum NO_x point at different droplet diameters for the different fuels appears to be governed by the extent of prevaporization of the fuel in the spray and is consistent with theoretical calculations based on each fuel's physical properties.

Introduction

The combustion of liquid fuel sprays is currently responsible for a large portion of the total energy consumption of the world. For example, most practical combustion systems, such as oil-fired, base load power plants and home heating units, gas turbines, diesel engines, direct-injected stratified charge engines, etc., operate using liquid fuel spray firing of the combustor. In these systems, a detailed understanding of the spray combustion phenomena is required in order to improve combustion efficiency and to predict and control pollutant formation and emissions. However, spray combustion depends upon and is governed by complex physical and chemical phenomena including simultaneous heat, mass, and momentum transfer, and the associated energy liberating chemical reactions. These factors are influenced by fuel type, droplet size distribution and number density, spray aerodynamics, ambient gas composition, and the local temperature and pressure. Because of these complexities and because of difficulties in direct measurement under actual operating conditions, the basic combustion processes, the rate of burning of fuel droplets, and the pollutant formation processes in spray combustion systems are not well understood at this time.

In view of its importance, the problem of spray burning has received considerable experimental and theoretical attention and has been the subject of several extensive reviews (e.g., Faeth [6]; Chigier [5]; Nizami [10, 11]; and others). Of particular interest and importance is the behavior of spray systems in the "transition region." In this region, which encompasses droplet sizes in the region of 15–80 μm dia, the mixing and evaporation processes are both incomplete at the flame front and the burning occurs in a combined diffusive and premixed fashion. Under these conditions, the relative importance of heterogeneous and homogeneous effects in dominating the combustion process is switched and gives rise to a number of interesting and important effects. For example, maxima in burning velocities (Polymeropoulos and Das [14]; Hayashi *et al.* [7]), extension of flammability limits (Burgoyne and Cohen [3], minima in ignition energies (Rao and Lefebvre [15]; Ballal and Lefebvre [1]; Chan and Polymeropoulos [4]), and minima in pollutant emissions (Nizami and Cernansky [11, 12]; Nizami *et al.* [13]) have all been observed and reported. These transition region effects have been reviewed and discussed by Nizami *et al.* [13]. A brief overview of the behavior of oxides of nitrogen (NO_x) emissions in the transition region is given below.

In their studies of NO_x production in aerodynamically stabilized, 40–80 μm diameter, monodisperse isopropanol/air spray flames, Nizami and Cernansky [11, 12] observed significant droplet size effects in the transition region and an optimum droplet diameter with regard to lowest NO_x levels. In general, as the droplet diameter in the spray decreases, NO_x also decreases reaching a minimum value around 50 microns droplet diameter. Further reduction in droplet diameter increases the NO_x, ultimately reaching the constant premixed value. At an equivalence ratio of 1.39, a 61 percent reduction in NO_x and a 87.5 percent reduction in NO were observed from the maximum values recorded in the two

Contributed by the Gas Turbine Division and presented at the Joint Power Generation Conference, Denver, Colorado, October 17–21, 1982. Manuscript received by the Gas Turbine Division July 17, 1982. Paper No. 82-JPGC/GT-10.

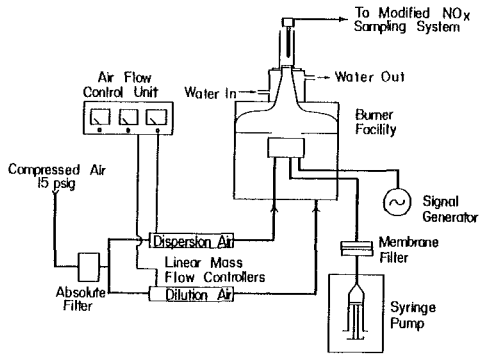

Fig. 1 Schematic of experimental facility

respective modes. These studies were extended later to include five additional hydrocarbon fuels with similar results (Nizami [11]; Nizami *et al.* [13]). Typically, NO_x reductions at the optimum droplet diameter were in the range of 40–70 percent and the optimum droplet diameter occurred from 48–55 microns. The occurrence of the minimum NO_x point at different droplet diameters for the different fuels appeared to be governed by the extent of prevaporization of the fuel in the spray and was consistent with each fuel's physical properties. The minimum in NO_x production as droplet size was varied was associated with droplet interaction effects and the transition from diffusive to premixed burning. Droplet interactions can result in a local temperature suppression with a subsequent reduction in NO_x production; the transition point, and hence the significance of the droplet interaction effects, is governed by the extent of prevaporization.

While the experimental data and analysis were consistent for the foregoing work, the general experimental configuration with an aerodynamically stabilized flame had undefined aerodynamic and mixing effects. Such effects could possibly be important and significant in biasing or affecting the data and conclusions. Thus, the basic experimental facility was modified to stabilize the flame on a screen flame holder and one dimensionalize the flow system, thereby eliminating these factors. This paper describes this modified experimental facility and reports new experimental data and results collected in the absence of mixing and aerodynamic effects on NO_x formation in monodisperse spray combustion systems.

Experimental Apparatus and Procedure

The basic experimental facility is shown schematically in Fig. 1. The facility included a Berglund-Liu Vibrating Orifice Monodisperse Aerosol Generator (Model 3050). This instrument, when operating in its monodisperse range, produces a uniform droplet stream with a standard deviation of less than 1 percent of the mean droplet size which, in turn, can be calculated to an accuracy of 2 percent or better from the generator operating conditions. To form a monodisperse aerosol, this stream of uniform droplets must be dispersed and diluted before significant coagulation occurs. This is accomplished by using dispersion and dilution air flows. The monodispersion ranges of the generator were established for a variety of orifices using the manufacturer's recommended "jet deflection" method and further confirmed by an impaction slide and microphotograph techniques. The monodispersion ranges for the 20, 25, and 35 μm orifice plates used in the present study are shown in Fig. 2. Further details and characterization of the basic experimental facility are presented elsewhere (Nizami [10]; Nizami and Cernansky [11]).

After generation and dispersion, the spray of monodisperse droplets is supplied to the desired combustion system. In the original configuration used by Nizami and Cernansky [12], the monodisperse fuel aerosols were supplied to and burned in

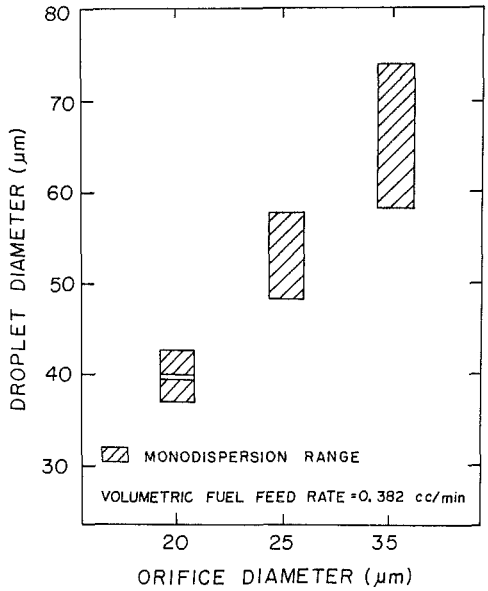

Fig. 2 Monodispersion ranges of single orifice aerosol generation system

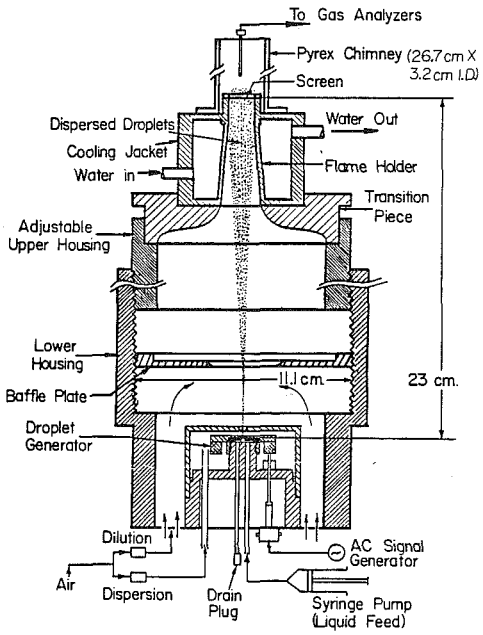

Fig. 3 One-dimensional vibrating orifice burner detail

an aerodynamically stabilized self-supporting flame inside a pyrex combustion tube. Primarily because of the uncontrolled mixing and aerodynamic effects in this configuration, as described earlier, the facility was modified to provide flame stabilization and one dimensional flow in the burner section. The combustion tubes were replaced with reducing and flow control sections directing the air/fuel aerosol to a 40 × 40 mesh stainless steel screen flame holder. The new system includes: a water cooled flame holder to prevent uncontrolled fuel evaporation; a transition piece with geometrically streamlined curvatures; adjustable upper and lower housings to provide flexibility in burner height adjustment; and a baffle plate to improve and control the mixing of the dilution air with the dispersed aerosol. The current system configuration is shown in more detail in Fig. 3.

The spray of monodisperse droplets was burned in a screen stabilized one dimensional flame inside a pyrex chimney (i.d. = 32 mm, length = 267 mm). Fuel feed rate through the system was held constant at 0.382 cc/min. Measurements

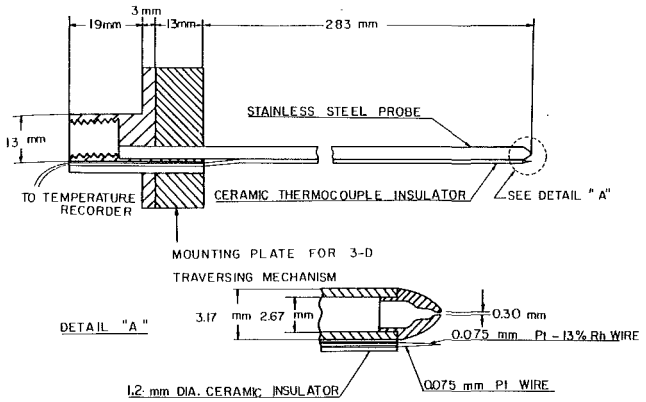

Fig. 4 Combination temperature and gas sampling probe

were made over the monodispersion operating range of the system encompassing droplet diameters from 36–70 μm and equivalence ratios from 0.8–1.2. To change the equivalence ratio, the dilution air flow rate was varied keeping the dispersion air flow rate constant at 1300 cc/min. The ambient air temperature was 24°C for all the experiments. Flame holders were primarily selected to provide a stable flame and also to give approximately the same approach velocity at the screen flame holder. Thus, the combustor residence times were approximately the same at all conditions, and consequently, any residence time effects on NO_x formation for the different operating conditions are expected to be insignificant.

Prevaporized and premixed conditions were examined as well to give the small droplet size limit. These prevaporized mixtures were made by mixing the fuel and dispersion air in a tee and then passing it through a vertical three-loop-helix wrapped with heating tape. The liquid fuel was vaporized and the mixture was heated to about 65°C before being introduced into the burner through the normal dispersion air path. This heating was sufficient to keep the mixture above the dew point of the fuel and to avoid condensation of fuel vapor on the combustor walls. Normal cooling of the mixture after leaving the vaporizer resulted in mixture temperatures near the flame holder of about 26°C.

Four liquid hydrocarbon fuels (isopropanol, methanol, n-octane, and n-heptane) were used for the experimental measurements. Post flame NO/NO_x data were collected using an uncooled aerodynamically quenched stainless steel probe (0.30 mm orifice) at a fixed axial location of 5 cm above the screen flame holder. Nitric oxide and total oxides of nitrogen were analyzed using a Thermoelectron chemiluminescent NO/NO_x analyzer, modified for low pressure sampling. The accuracy of these measurements was ± 0.5 ppm with a ± 1 ppm day to day reproducibility. Temperature measurements were made with a Pt/Pt-13 percent Rh fine wire thermocouple (0.003 in/0.075-mm dia) attached to the gas sampling probe. This combination temperature and gas sampling probe is shown schematically in Fig. 4.

Experimental Results

One dimensionality and symmetry of the flame for three different droplet sizes were examined by traversing the combination gas sampling/thermocouple probe across the combustion tube 4 mm above the flame holder screen. The flame thickness for the 26.7 and 55.8 μm droplet sprays was about 3 mm and looked fairly flat. However, the flame shape for 69.1 μm droplets was extended to about 6 mm at the center. With the exception of 69.1 μm droplets, radial profiles of both NO_x and temperature are indeed flat across the screen flame holder, as shown in Figs. 5 and 6, thus confirming the one dimensionality of the burner system.

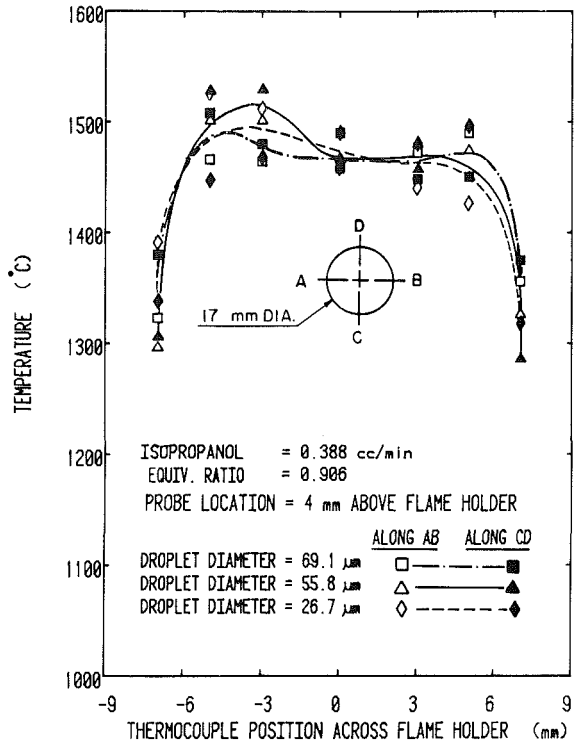

Fig. 5 Temperature traverse across the burner

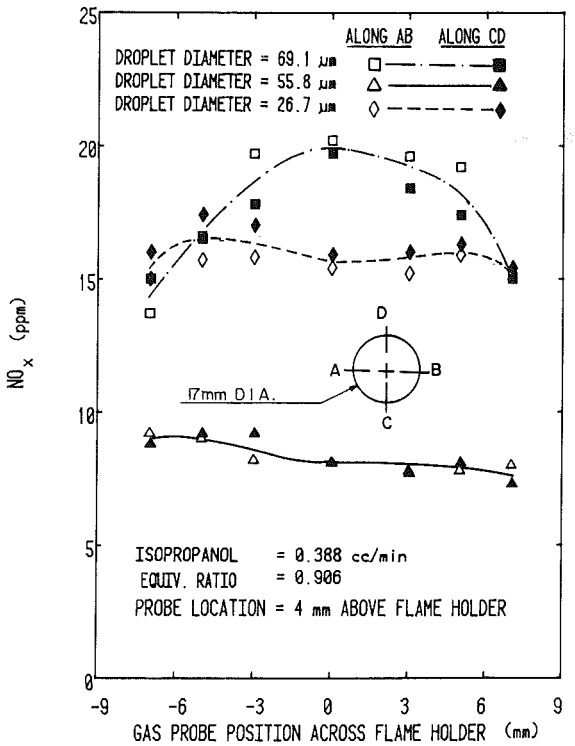

Fig. 6 NO_x traverse across the burner

Axial traverses along the centerline of the burner were made as well. Representative temperature and NO_x data for three droplet sizes and the associated premixed limit are shown in Fig. 7. The data show the peaking of NO_x and temperature in the flame zone with some reduction in the post flame region to nearly steady or slowly diminishing levels. The relative thickness of the flame zone is indicated in these types of plots. Based upon this information for the range of fuels being

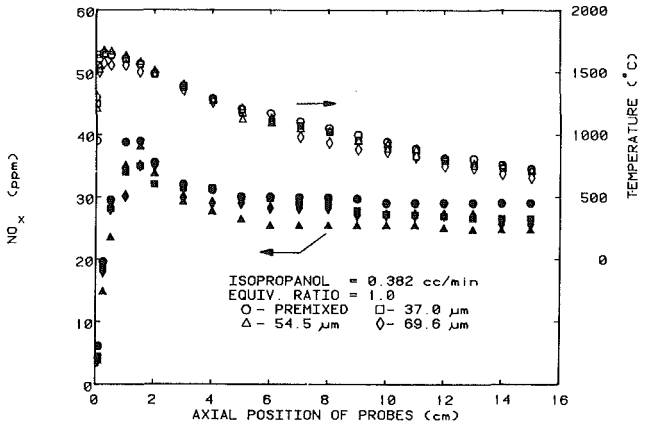

Fig. 7 Axial temperature and NO_x profiles along the burner centerline

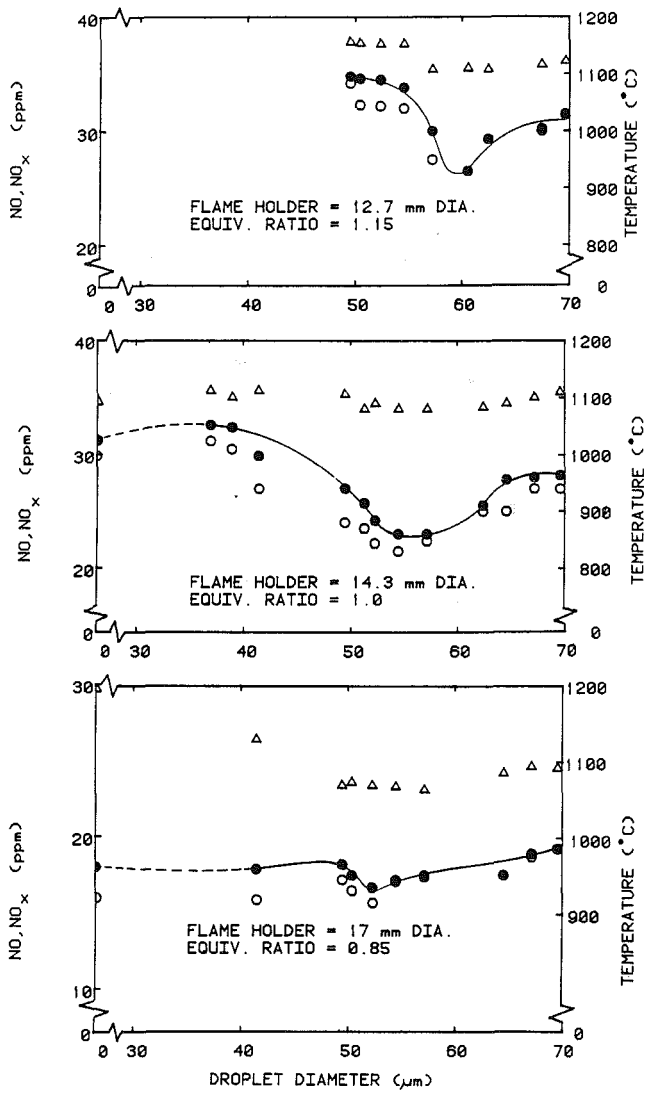

Fig. 8 Droplet size effect on post-flame temperature, NO and NO_x formation in monodisperse aerosol combustion for various equivalence ratios at a fuel feed rate of 0.382 cc/min. using isopropanol as fuel: ○ - NO; ● - NO_x; Δ - temperature

tested, a fixed sampling location on the burner centerline 5 cm above the screen flame holder was selected for fuel and droplet size comparison studies. This sampling location avoids regions of high temperature and concentration gradients.

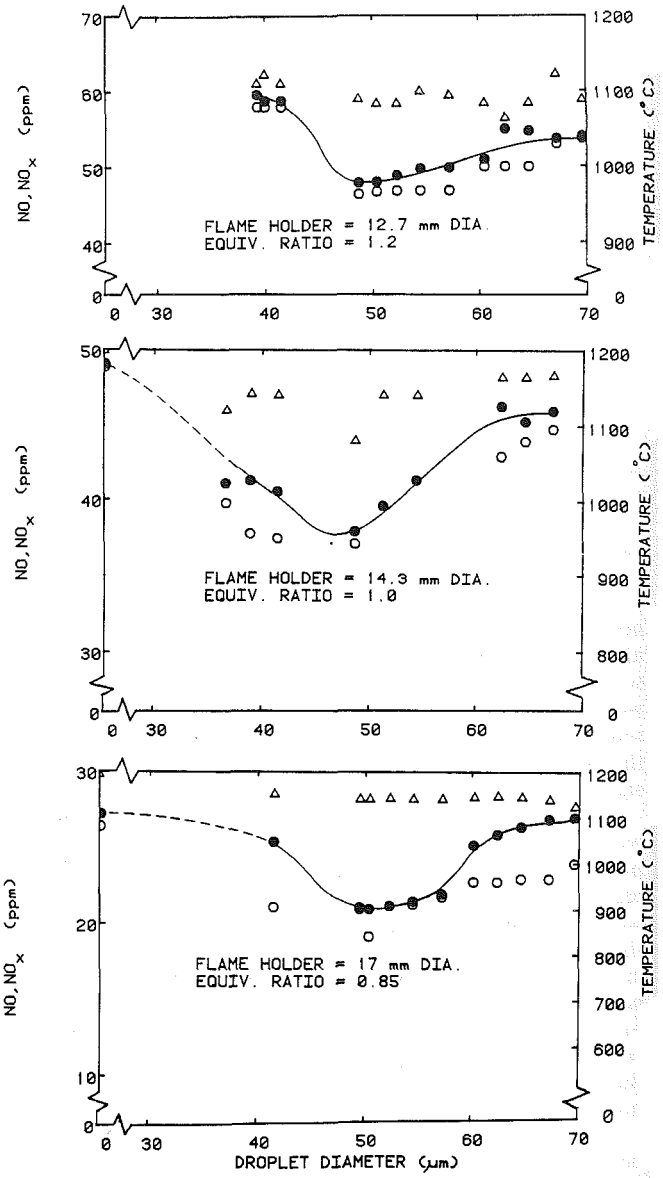

Fig. 9 Droplet size effect on post-flame temperature, NO and NO_x formation in monodisperse aerosol combustion for various equivalence ratios at a fuel feed rate of 0.382 cc/min. using N-heptane as fuel: ○ - NO; ● - NO_x; Δ - temperature

Representative temperature and NO_x results showing the effect of droplet diameter over a range of equivalence ratios are shown in Figs. 8–11. Where available, premixed limit data are shown as data points at zero droplet diameter. For smaller droplet sizes, the flame was pale blue and nonluminous. Imbedded within the pale blue zone were smaller darker blue centers. The luminosity increased for heavier fuels. The thickness of the flame increased for larger droplet sizes, presumably because larger drops take longer to burn and thus travel for a greater distance before burnout at the same flow velocity. A general trend in these plots is that NO_x decreases as the droplet diameter is decreased, reaching a minimum around 43–58 μm, and then increases to a fairly constant value with any further decrease in droplet diameter. Although the temperature and concentration gradients are steep near the flame, this trend is also illustrated in the radial traverses, Fig. 6, where lower NO_x levels are indicated with 55.8 μm than with 26.7 or 69.1 μm droplets. The small droplet size limit is generally close to and approaches the prevaporized premixed experiment results. The above mentioned general trend in NO_x variation with droplet size was observed for all the fuels

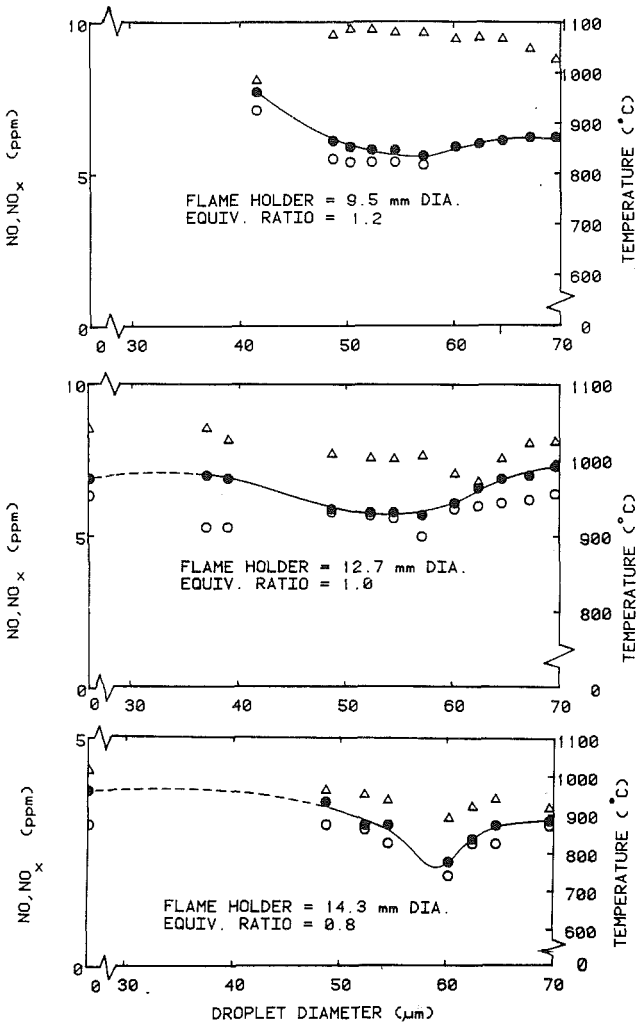

Fig. 10 Droplet size effect on post-flame temperature, NO and NO_x formation in monodisperse aerosol combustion for various equivalence ratios at a fuel feed rate of 0.382 cc/min. using methanol as fuel: ○ - NO; ● - NO_x; Δ - temperature

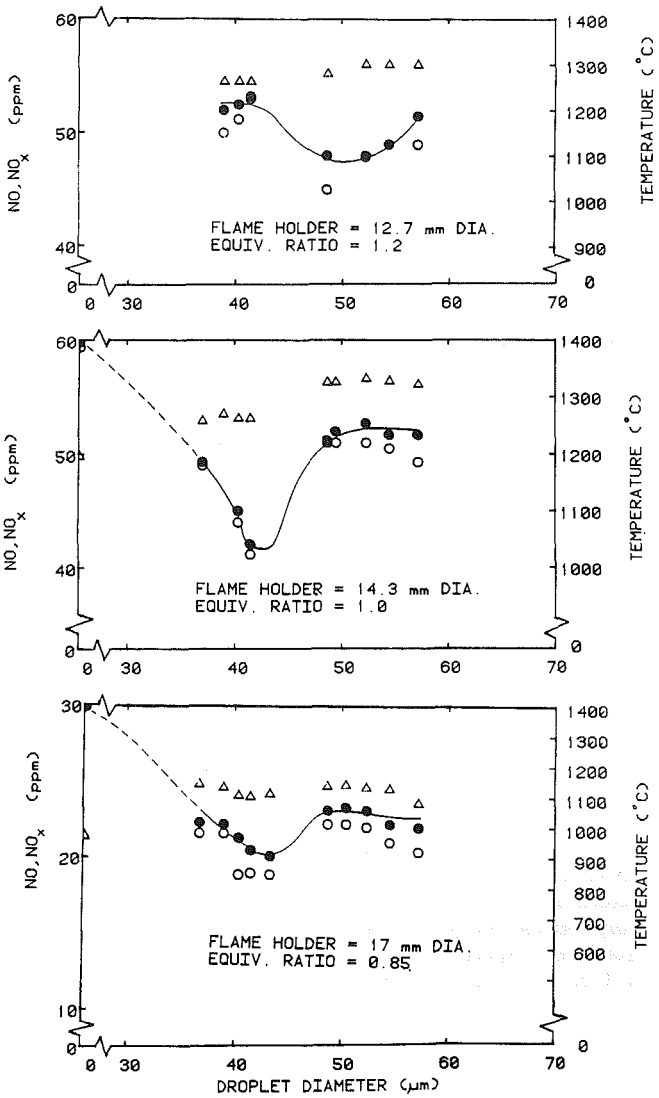

Fig. 11 Droplet size effect on post-flame temperature, NO and NO_x formation in monodisperse aerosol combustion for various equivalence ratios at a fuel feed rate of 0.382 cc/min. using N-octane as fuel: ○ - NO; ● - NO_x; Δ - temperature

tested in rich, lean, and stoichiometric burning situations. Also, it appears that, while the NO_x minimum points are not sharply defined in the current data, the methanol minima are shifted to slightly larger droplet diameters and the n-heptane and n-octane data are shifted to slightly smaller droplet diameters relative to isopropanol. These general trends are in agreement with the theoretical calculations and the experimental data reported by Nizami et al. [13] in their aerodynamically stabilized flame measurements. Thus, since aerodynamic and mixing effects have been minimized in the current system, these results and behavior indicate a true droplet size effect on NO_x formation.

Discussion

The results just presented indicate that relative to larger droplet diameters (>60 microns), where diffusive type of burning dominates, NO and NO_x decrease with decreasing droplet diameter. These results are in agreement with the theoretical and experimental studies of Bracco [2], Kesten [9], Labowski [8], and others. For individual droplet burning, decreasing the droplet size increases the flame to droplet diameter ratio, reduces the flame temperature, and therefore, results in reduced NO_x production. In contrast to individual droplet combustion, spray burning results in droplet interactions which decrease the local oxygen concentration around burning droplets, resulting in a subsequent reduction of flame temperature and NO_x.

At smaller droplet diameters (<30 microns), where premixed type of burning dominates, NO and NO_x remain relatively constant with decreasing droplet diameter. In this regime, sufficient fuel is prevaporized and premixed prior to the flame front so that the situation approaches the premixed case.

In the transition region (30–70 microns), where the NO_x minimum is observed, the combustion undergoes a transition from diffusive to premixed burning domination of the system. As the droplet size is reduced, additional fuel is prevaporized until the situation resembles vaporized fuel seeded with small liquid droplets, which eventually approaches the premixed case. As this transition takes place, relatively less oxygen depletion occurs, and therefore, the temperature and NO_x go through minimum and gradually increase to their prevaporized and premixed levels.

The apparent shifts in the droplet diameters associated with the NO_x minimum points for the various fuels were found to be consistent with the thermophysical properties of the fuels; some of these thermophysical properties and evaporation parameters, as reported by Nizami et al. [13], are given in Table 1. The evaporation constants and extent of prevaporization for the different fuels were calculated and

Table 1 Thermophysical properties of fuels and computed evaporation parameters[a]

Fuel	Chemical formula	Molecular weight	Latent heat cal/gm	Vapor pressure[b] 20°C, torr	Mass transfer no. B_{ev}	Evap. constant $K_{ev} X 10^{-3}$ $cm^2/sec.$	Mass ratio $W_{fuel}/W_{isopropanol}$
Isopropanol	C_3H_80	60.10	160.0	65.95	0.197	0.455	1.000
Normal Octane	C_8H_{18}	114.2	86.5	3.37	0.017	0.048	0.079
Normal Heptane	C_7H_{16}	100.1	87.1	19.26	0.089	0.243	0.787
Methanol	CH_4O	32.0	263.0	231.04	0.482	0.963	3.608

[a]Nizami et al. [13]
[b]Other vapor pressure correlations yielding slightly different values do not significantly affect the evaporation parameter computations.

compared following the approach used by Nizami et al. [13]. The procedure yields reasonable relative results for extent of prevaporization prior to the fuel spray reaching the flame zone. Using isopropanol as the base case, the mass ratios of fuel evaporated relative to isopropanol for fixed initial droplet diameters were calculated. The mass ratio for methanol was larger than one and the mass ratios for n-heptane and n-octane were less than one. Thus, methanol with its higher evaporation ratio, requires larger droplets to produce the same levels of prevaporization as the isopropanol base case. N-octane and n-heptane, on the other hand, required smaller droplets to achieve the same levels of prevaporization. Thus, these calculations are consistent with the experimental data and indicate the importance of the extent of prevaporization in determining the NO_x minimum point.

Nizami et al. [13] have also suggested that single component heavy fuels are expected to shift the minimum NO_x point to lower droplet diameters than 50 microns. Further, in the case of multicomponent heavy fuels, the behavior is expected to be governed by the lighter components because they will determine the prevaporization characteristics of the fuel. In a polydisperse spray of a heavy multicomponent fuel, similar trends are expected. However, additional experimental work will be required in order to eludicate the NO_x behavior in practical combustion systems, which have different pressure and temperature environments, and widely varying droplet sizes.

Conclusions

A one-dimensional aerosol spray combustion facility has been developed and characterized. Experimental results of post flame NO/NO_x emissions utilizing liquid hydrocarbon fuels in this combustion system have been presented. A significant droplet size effect on NO/NO_x emissions was observed for the four fuels tested. Both NO and NO_x decrease with decreasing droplet diameter, reach minima (around 43–58 μm droplet diameter), and then increase again with further decreases in droplet size, eventually approaching the premixed combustion limit. Further, the minimum NO/NO_x point shifts towards a smaller droplet size for lower vapor pressure single component fuels.

Overall the observed effects are attributed to droplet interactions and the transition from diffusive to prevaporized and premixed burning. Droplet interactions apparently result in local temperature suppression with a subsequent reduction in NO_x production. The observed occurrence of the minimum NO_x point at different droplet diameters for individual fuels is explained through theoretical calculations of the extent of prevaporization of the fuel in the spray. The theoretical analysis and experimental evidence indicate that the extent of prevaporization is an important factor in determining the minimum NO_x point.

This study confirms the existence of a droplet size dependence on NO_x emissions in the transition region in the absence of mixing and aerodynamic effects. Consequently, reduced NO_x production should be obtainable through appropriate droplet size control. This fact (and the associated experimental data) may be useful in designing and optimizing hydrocarbon fuel spray combustion systems.

Acknowledgments

This paper is based on research supported by the Lewis Research Center of the National Aeronautics and Space Administration through grant number NASA NAG 3-1. The authors would like to thank Dr. Surendra Singh for his efforts in developing the experimental facility.

References

1 Ballal, D. R., and Lefebvre, A. H., "Ignition of Liquid Fuel Sprays at Subatmospheric Pressures," *Combustion and Flame*, Vol. 31, 1978, p. 115.

2 Bracco, F. V., "Nitric Oxide Formation in Droplet Diffusion Flames," *Fourteenth Symposium (Int'l.) on Combustion*, The Combustion Institute, 1973, p. 831.

3 Burgoyne, J. H., and Cohen, L., "The Effect of Drop Size on Flame Propagation in Liquid Aerosols," *Proc. of The Royal Society: Series A: Mathematical and Physical Sciences*, Vol. 225, No. 1162, 1954, p. 375.

4 Chan, K. K., and Polymeropoulos, C. E., "An Experimental Investigation of the Minimum Ignition Energy of Monodisperse Sprays," Paper No. ESSCI 81-21, Eastern States Section, The Combustion Institute Meeting, Nov. 1981.

5 Chigier, N. A., "The Atomization and Burning of Liquid Fuel Sprays," *Progress in Energy and Combustion Science*, Vol. 2, 1975, pp. 97–114.

6 Faeth, G. M., "Spray Combustion Models—A Review," AIAA Paper 79-0293, 17th Aerospace Sciences Meeting, Jan. 1979.

7 Hayashi, S., Kumagai, S., and Sakai, T., "Propagation Velocity and Structure of Flames in Droplet-Vapor-Air Mixtures," *Combustion Science and Technology*, Vol. 15, 1976, p. 169.

8 Labowski, M., "Calculation of the Burning Rates of Interacting Fuel Droplets," *Combustion Science and Technology*, Vol. 22, 1980, p. 217.

9 Kesten, A. S., "Analysis of NO Formation in Single Droplet Combustion," *Combustion Science and Technology*, Vol. 6, 1972, p. 115.

10 Nizami, A. A., "An Experimental Study of NO_x Formation in Monodisperse Fuel Spray Combustion," Ph.D. thesis, Drexel University, Philadelphia, Pa., 1978.

11 Nizami, A. A., and Cernansky, N. P., "A Monodisperse Spray Combustion System and the Measurement of Oxides of Nitrogen," Paper No. 78-37, Western States Section, The Combustion Institute, 1978.

12 Nizami, A. A., and Cernansky, N. P., "NO_x Formation in Monodisperse Fuel Spray Combustion," *Seventeenth Symposium (International) on Combustion*, The Combustion Institute, 1979, p. 475.

13 Nizami, A. A., Singh, S., and Cernansky, N. P., "Formation of Oxides in Nitrogen in Monodisperse Spray Combustion of Hydrocarbon Fuels," *Combustion Science and Technology*, Vol. 28, 1982, p. 97.

14 Polymeropoulos, C. E., and Das, S., "The Effect of Droplet Size on the Burning Velocity of Kerosine - Air Sprays," *Combustion and Flame*, Vol. 25, 1975, p. 247.

15 Rao, H. N. S., and Lefebvre, A. H., "Ignition of Kerosine Fuel Sprays in a Flowing Air Stream," *Combustion Science and Technology*, Vol. 8, 1973, p. 95.

G. L. Touchton
Engineer.

L. C. Szema
Engineer.

M. B. Cutrone
Manager.

General Electric Company,
Schenectady, N.Y. 12345

R. Cellamare
Engineer,
Acurex Corporation,
Mountain View, Calif.

W. Vonkleinsmid
Research Director,
Southern California Edison Company,
Rosemead, Calif.

Design of a Catalytic Combustor for Heavy-Duty Gas Turbines

Laboratory tests of catalytic combustors with distillate fuel have achieved ultralow NO_x formation at catalytic reactor exit temperatures and combustion efficiencies consistent with state-of-the-art gas turbine requirements. Concomitant with these features, however, are design limitations such as narrow turn-down range and unique reactor mounting requirements. This paper presents fully analyzed conceptual design solutions to these problems within the constraints of fixed geometry, full catalytic combustion over 80 percent of the turbine load range, and retrofit to an existing gas turbine. The combustor design incorporates (a) a gutter stabilized pilot burner downstream of the reactor for operation from ignition to full-speed no-load, (b) a segmented fuel-air preparation system for fuel staging of the reactor, (c) a reactor mounting system which accommodates thermal growth and start-up and shutdown transients, and (d) a graded cell reactor. These features were achieved while maintaining low reactor face velocities and system pressure drops.

Introduction

Catalysts are widely used in the chemical and petroleum refining industries to accelerate reactions or to promote desired reactions. However, catalysts have not been used in practical gas turbine combustion systems. In part, this neglect is due to technical difficulties in the practical application of catalytic reactors to heavy-duty gas turbine equipment, but the overriding considerations are the ease of generation and ease of maintenance of turbulent diffusion flames. The flames are maintained in sophisticated, jet-mixed, vortex-stabilized reactors. These combustion systems are smokeless, are stable, have a wide apparent turn-down ratio, and operate at very high efficiencies and volumetric heat release rates. However, the underlying flame structure which gives rise to these features also leads to very high emissions of nitrogen oxides.

The dominance of the vortex-stabilized diffusion flame combustor has been challenged in the last decade because of pressure for the reduction of nitrogen oxides emissions. The environmental and health effects of these compounds have been known for some time, but their role in the photochemical smog cycle has led to greatly increased regulatory activity.

Figure 1 summarizes regulatory levels and actual abatement achieved as a function of time. Inert injection (e.g., steam and water) has been pushed to its practical limit at roughly 30 ppmv. Dry low NO_x technology is immature and may reach levels as low as 30 ppmv in the future, but is probably limited by stability even with the use of variable geometry combustion systems. Only catalytic combustion has the potential to meet Selective Catalytic Reduction (SCR) levels by direct combustion system modification.

This paper presents the results of a preliminary design study undertaken by General Electric under the sponsorship of Southern California Edison Company. The design, which is complete to the detailed layout stage, satisfies the operating requirements of a state-of-the-art, heavy-duty gas turbine within the constraints of presently available catalysts and substrates. The program objective was the design of a practical, durable catalytic combustion system which would achieve NO_x emissions less than 20 ppmv for baseload operation with low nitrogen content petroleum distillate fuel (less than 500 ppmv nitrogen). The design machine cycle produces approximately 80 MWe power with a nominal 12:1 pressure ratio. The combustion system for this machine includes ten individual combustor cans of the reverse flow type.

An isometric view of the resulting combustion system (Fig. 2(*a*)) shows its essential features as follows:

(*i*) A radially segmented graded cell catalytic reactor loaded compressively in an air cooled metallic support structure

(*ii*) A multiple injection point fuel and air preparation system

(*iii*) Venturi tube air blase atomizers

(*iv*) A V-gutter stabilized auxiliary burner incorporating an air atomized fuel injection system

The air flow path and position of the combustion system within the combustor casing are shown in Fig. 2(*b*).

In the following sections the unique features and constraints of the catalytic reactor and the operating

Contributed by the Gas Turbine Division and presented at the 1982 Joint Power Generation Conference, Denver, Colorado, October 17-21, 1982. Manuscript received at ASME Headquarters August 5, 1982. Paper No. 82-JPGC-24.

requirements of the gas turbine are detailed. Then, the design of the components is discussed. Finally, the operating modes and expected performance of the combustion system over the gas turbine load range are outlined.

Catalyst and Substrate Operating Limits

A fixed-geometry catalytic combustion system operating at bulk mean catalytic reactor exit temperature of 1700 K (2600°F) at peak-load would have a reactor exit temperature of approximately 980 K (1300°F) at full-speed no-load (FSNL). This temperature range is required to meet turbine cycle requirements. Two major factors prevent a simple catalytic reactor from operating efficiently over this range. These are as follows:

(*i*) The temperature range cannot be handled by one type of catalyst, i.e., a single catalyst which provides sufficiently high catalytic activity at low temperatures while also avoiding degradation of activity at the highest exit temperatures required (2600–2800°F).

(*ii*) The oxidation rate of carbon monoxide and unburned hydrocarbons is so slow at the lower temperature that a prohibitively large reactor is required for satisfactory emissions performance and efficiency at low reactor exit temperatures.

The low temperature operating limit of the catalytic reactor is therefore set by considerations of minimum acceptable combustion efficiency. The high temperature operating limit of a catalytic reactor depends on both catalyst type and the substrate material. Also, for the present application an overriding maximum operating temperature is that of approximately 1920 K (3000°F) where NO_x formation becomes unacceptable. The design approach selected to maximize the range of effective catalytic operation combines the use of a hybrid reactor design with fuel staging of individual reactor segments. The design includes a noble metal catalyst for

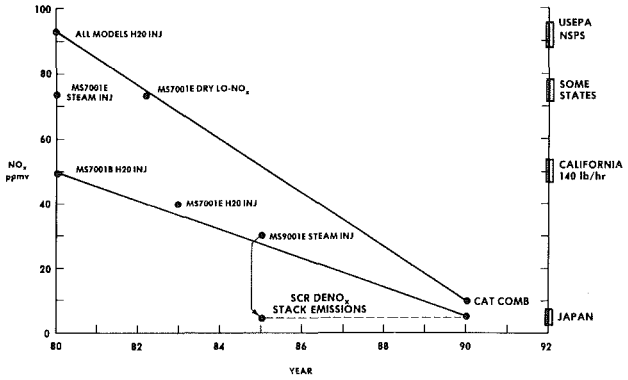

Fig. 1 NO_x emission technology development

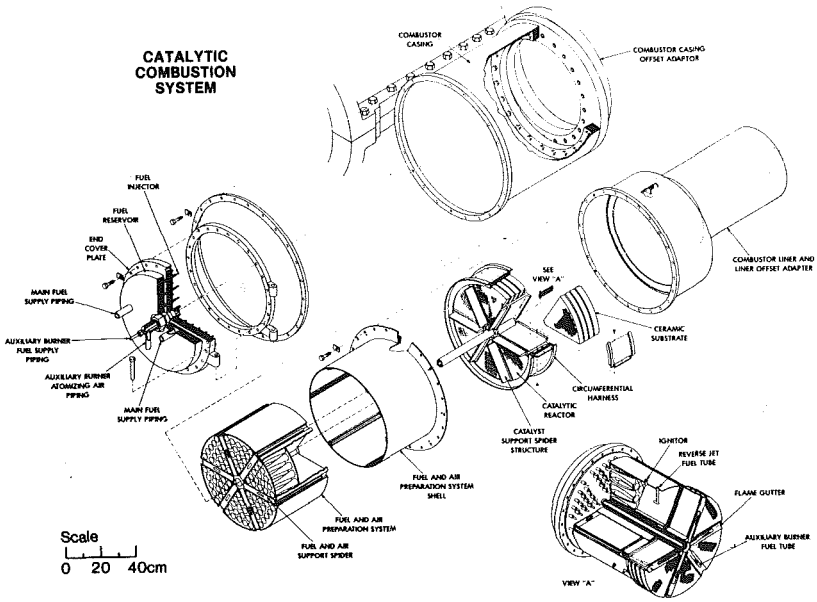

Fig. 2(*a*) Catalytic combustion system

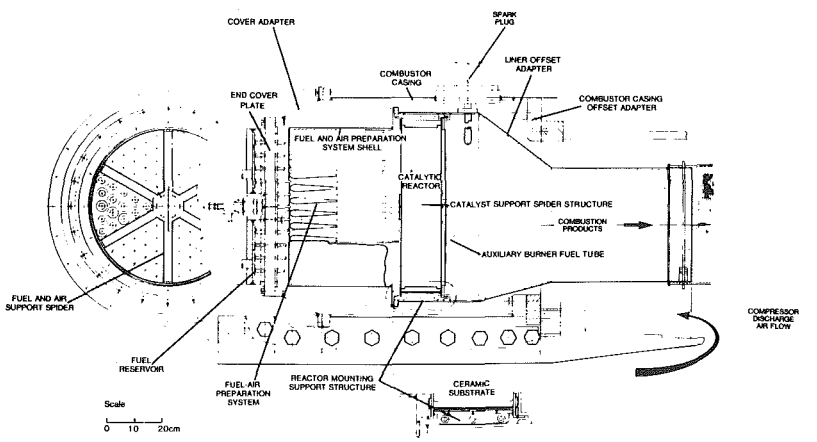

Fig. 2(*b*) Layout of catalytic combustion system

Table 1 Steady-state operating characteristics of various catalyst systems

SYSTEM NO.	INVESTIGATOR	CATALYST BED DIMEN.[f] & TYPE	CATALYST	FUEL	INLET TEMP. °K (°F)	FACE VELOCITY m/sec (ft/sec)	COMBUSTOR PRESSURE MPa (atma)	CATALYST BED TEMP. K (°F)	HEAT RELEASE RATE MJ/hr-Pa-m³ (MBtu/hr-atm-ft²)	EMISSIONS NO_x ppm	CO ppm	UHC ppm
1	ACUREX	12.7 x 10.2 (5 x 4)	Cr_2O_3 & UOP NOBLE METAL	DIESEL[a]	633 (680)	15.2 (48.8)	0.31 (3.1)	1686 (2575)*	10.7 (28)	38	27	33
				DIESEL[b]	636 (685)	8.9 (29.3)	0.53 (5.2)	1228 (1750)*	1.3 (3.5)	9	2235	306
2	ACUREX	5.1 x 7.6 (2 x 3)	Tb-Ce-Th & UOP NOBLE METAL	PROPANE	744 (880)	13.4 (44.1)	0.10 (1.0)	1700 (2600)*	3.9 (11)	5	20	0
3	ENGELHARD	2.5 x 15.2 (1 x 6)	DXB-222 (PROPRIETARY)	DIESEL	628 (670)	12.9 (42.3)	0.10 (1.0)	1595 (2411)	1.5 (4.2)	4	60	1
4	ENGELHARD	2.5 x 15.2 (1 x 6)	DXE-442 (PROPRIETARY)	DIESEL	633 (680)	14.2 (46.6)	0.50 (5)	1539 (2310)	4.0 (11)	5	2420	146
5	ENGELHARD	15.2 x 17.8 (6 x 7)	DXA-111	DIESEL	633 (680)	42.7 (140)	0.30 (3.0)	**	**	2	25	1

[a]MAXIMUM THROUGHPUT TEST

[b]LOW BED TEMPERATURE TEST

[f]DIAMETER x LENGTH

*MAXIMUM RECORDED BED TEMPERATURE

**NOT REPORTED

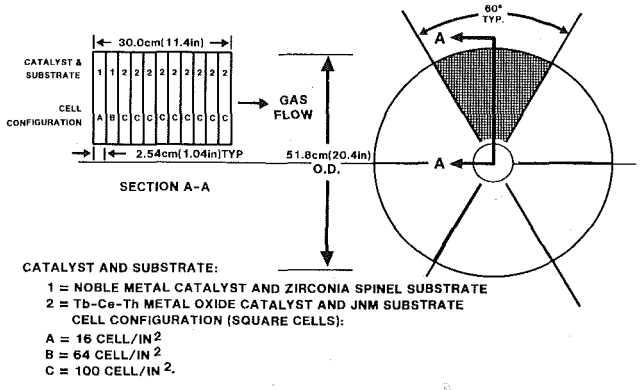

Fig. 3 Catalytic reactor segments

Table 2 Predicted catalytic reactor emissions performance

Inlet Conditions:	
Face Velocity	18 m/sec (59 ft/sec)
Inlet Temperature	583-616°K (590-650°F)
Inlet Pressure	1.0-1.2 MPa (145-175 psia)
Fuel Vaporization	>90%
Fuel Mixture Variation	±10% of Mean
Exit Conditions:	
Reactor Exit Temperature	1370-1700°K (2000-2600°F)
NO_x	1-5 ppmv
CO	3-15 ppmv
UHC as C_3H_8	0-2 ppmv
Efficiency	99+%
Reactor Exit Temperature	1256°K (1800°F)
NO_x	<1 ppmv
CO	100 ppmv
UHC as C_3H_8	2000 ppmv
Efficiency	85%

upstream sections of the catalytic reactor and a metal oxide for downstream sections.

There are two major types of combustion catalysts: noble metals and base metal oxides. The noble metal catalysts may be employed up to 1590 K (2400°F). At higher temperatures they degrade rapidly due to evaporation and sintering. The metal oxide catalysts operate effectively at temperatures up to 1810 K (2800°F) but exhibit unacceptable fuel oxidation rates below 1590 K (2400°F). Even for the noble metal catalysts, the oxidation rates for unburned hydrocarbons and fuel are unacceptable below 1370 K (2000°F).

The upper operating temperature limit of the catalyst can only be achieved if a compatible substrate with adequate durability and life can be found. Various substrate/catalyst material combinations were tested at Acurex [1]. Based upon these tests, a zirconia spinel was chosen as the substrate material for the noble metal sections of the reactor, while a proprietary substrate (designated JNM) was chosen for those sections of the reactor using a base metal oxide catalyst. The maximum acceptable operating temperatures are estimated from Table 1, which outlines actual test performance [2].

In addition to adequate combustion efficiency at low reactor temperatures and durability at high exit temperatures, another essential requirement of the catalytic reactor is an acceptably low temperature at which sustained combustion can be initiated, i.e., the lightoff temperature. Use of a noble metal catalyst at the upstream end of the reactor is expected to result in lightoff temperatures of 630 K (675°F), [3, 4].

Catalytic Reactor Design Features

Based on the above catalyst/substrate considerations, two key concepts have been employed in the combustor design which extend the operating range of the catalytic reactor beyond the limits indicated by the above discussion. These are:

(*i*) The use of a hybrid reactor, i.e., a reactor containing both noble metal and metal oxide catalyst sections

(*ii*) The use of a graded cell reactor in which the cell size is varied in the flow direction

A hybrid reactor design was selected to achieve maximum reactor operating temperature range. The upstream noble metal catalyst provides the high activity required at the low end of the operating temperature range. The downstream metal oxide catalyst segments provide the capability of operating at an upper temperature of 1700 K (2600°F). At that operating point, the upstream catalyst will radiate sufficient energy to maintain its temperature below the 1590 K (2400°F) maximum allowable for noble metal catalysts. The large cells at the upstream end of the graded cell reactor enhance reactor ignition and provide greater heat release rate than does a nongraded cell configuration. Also, the graded

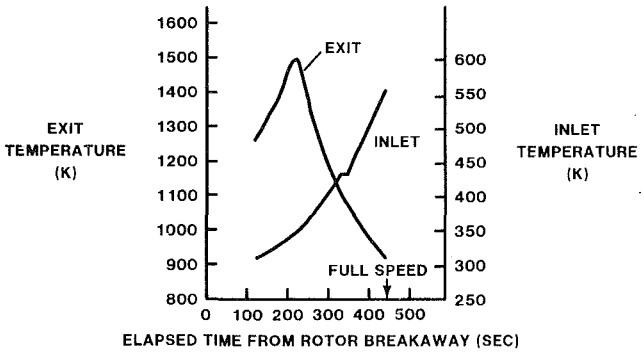

Fig. 4 Pilot or catalytic reactor exit and inlet temperature

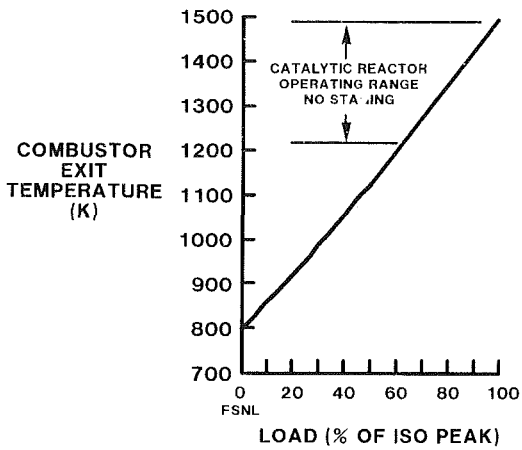

Fig. 5 Load range combustor requirements

cell reactor has a more uniform axial temperature distribution which reduces thermal stresses.

The downstream segments provide high mass transfer rates due to a high cell density. The overall length of this section is sufficient to initiate gas phase combustion down to an exit temperature of 1367 K (2000°F) with an inlet temperature of 616 K (650°F). This results in essentially complete combustion from this section alone. In combination with the upstream segments, the reactor has considerable operating margin.

As schematically illustrated in Fig. 3, the reactor has a 51.8-cm (20.4-in.) o.d., is 30-cm (11.4-in.) long, and is composed of 11 equal length axial segments with each axial segment split into six pie-shaped segments. A zirconia spinel monolith substrate coated with a Universal Oil Products (UOP) proprietary noble metal catalyst was selected for the first two axial segments of the reactor, with 2.5 cells/cm^2 in the first axial segment and 10 cells/cm^2 in the second segment. The third and subsequent axial segments use a JNM monolith substrate coated with Tb-Ce-Th metal oxide catalyst with a cell configuration of 16 cells/cm^2. Square cell shapes were selected based on experience and availability. A broad range of honeycomb materials with square cells have been successfully tested at Acurex.

Because of the favorable effects of low reactor face velocities on pressure losses, minimum operating fuel to air ratio, and minimum catalyst lightoff temperature, the combustor casing was expanded to the maximum diameter consistent with retrofit to the current turbine. This resulted in a 51.8-cm (20.4-in.) dia reactor with a nominal 18.3 m/s (60 ft/s) face velocity. The permanent pressure losses of the reactor for ISO day conditions are predicted to be 3.2 percent at peak load conditions.

The expected steady-state emissions performance of the catalytic reactor over its operating range is shown in Table 2. Even with the long reactor, 1256 K (1800°F) is not an acceptable steady-state operating point. The increased reactor length simply adds some margin to the lightoff temperature limit and to the tolerance of the reactor for variation in fuel mixture and fuel vaporization. However, operation of the combustor at exit temperatures below 1800°F is accomplished in this design by fuel staging of the reactor segments. A later section of this paper discusses the fuel staging approach employed to accomplish catalytic reactor operation over the range of combustor exit temperatures from 922 to 1489 K (1200 to 2220°F).

Design Cycle Conditions and Combustion System Requirements

The design cycle conditions for a single-shaft, heavy-duty gas turbine fall logically into two parts: (*i*) The startup transient from shaft on turning gear to shaft full-speed, no-generator load, and (*ii*) the load range from generator synchronization to peak load during which shaft speed is constant. Each of these operating regions and the associated combustion system requirements are discussed below.

The combustor inlet and exit temperatures during the start-up sequence are shown in Fig. 4. Start-up via catalytic combustion is immediately ruled out by the low inlet temperatures. Therefore, the necessary energy to the turbine must be supplied by an auxiliary burner in parallel or series with the main burner. If a parallel system were employed, variable geometry or air staging would be necessary to achieve fully catalytic combustion at peak load. Both of these alternatives were unacceptable in terms of retrofit capability; therefore, a series design was selected.

For a fixed geometry combustion system employing an auxiliary burner upstream of the catalytic reactor, Fig. 4 also represents the temperature variation to which a catalytic reactor would be subjected. In addition, there would be ignition temperature spikes from the auxiliary burner which are not shown. These spikes are a function of the exact speed, fuel-to-air ratio, efficiency at ignition, and the time lag between fuel flow and ignition. These parameters vary widely for satisfactorily operating gas turbines because of differing maintenance histories, and can easily lead to temperatures which would result in catalytic reactor failure in only a few start cycles.

In light of the above arguments, the design alternative selected for the present program was a series auxiliary burner located downstream of the catalytic reactor. Thus, the temperature excursion for the catalyst during the start-up cycle is reduced to the gradual increase compressor discharge temperature from ambient to 560 K (550°F), shown as combustor inlet on Fig. 4.

The combustor exit temperatures required for operation from FSNL to peak load are plotted in Fig. 5. Also shown on this plot is the operating range of the catalytic reactor without fuel staging. Therefore, in order to operate the catalytic reactor over any appreciable portion of the load range, fuel staging is necessary. This maintains the fueled catalyst segments within the acceptable limits, i.e., from 1370 K (2000°F) set by combustor efficiency, to the 1700 K (2600°F) limit which assures substrate and catalyst durability.

Catalytic Combustion System Description

The preliminary combustion system design satisfies the turbine requirements within the cycle and catalytic reactor constraints. The overall design is modular (Fig. 2). Fuel is vaporized and mixed with compressor discharge air in the upstream fuel-air preparation section and then enters the catalytic reactor section. The reactor, in this design, is a graded cell array. An auxiliary burner section, downstream of

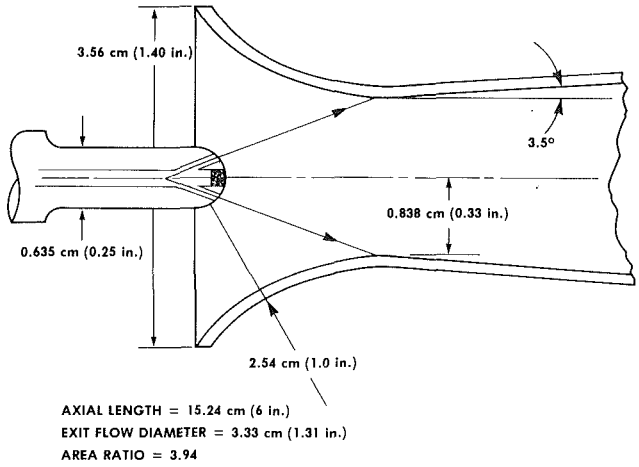

Fig. 6 GE multiple Venturi tube injector fuel injection tube – Venturi detail

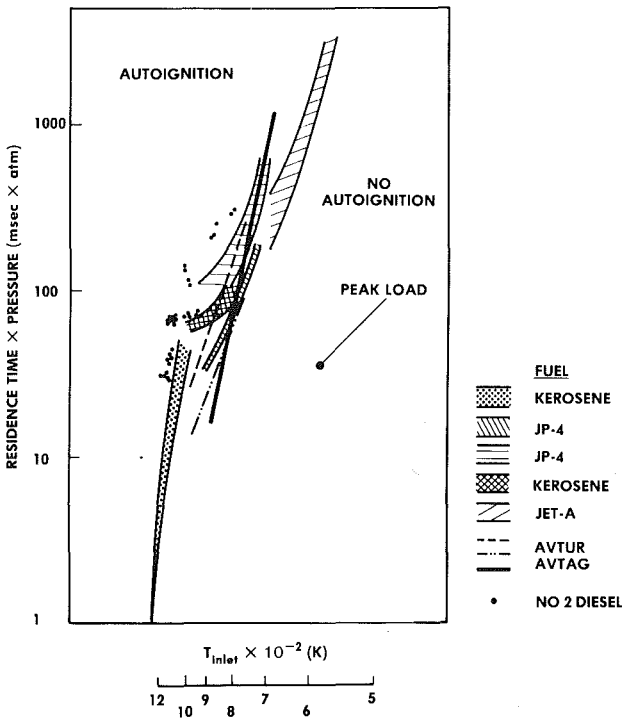

Fig. 7 Autoignition of liquid hydrocarbon fuel sprays in air

the reactor section, is used for combustor ignition, acceleration to FSNL, and operation to approximately 20 percent power. At that load point, fuel transfer occurs to ignite selected reactor segments. Further load increases to turbine full-load power are accommodated by fuel transfers to and ignition of additional reactor segments. Each module is functionally distinct and is explained below.

Fuel-Air Preparation Section. The fuel vaporizing and premixing system is based upon the NASA multiple conical and multiple Venturi tube injection systems [5–8]. These designs have been extensively tested in a number of programs and have demonstrated performance that satisfies this project's design goals. The concept is a multipoint injection system that utilizes high-velocity air in the Venturi throat to atomize the fuel. The air and fuel mixture is then decelerated in a diffuser to recover pressure. Finally, the diffuser exits are dumped into a flow section to mix the individual streams. The multiplicity of injection points and fine atomization should result in greater than 90 percent vaporization and extremely flat fuel air mixture profiles at the design mixing length of 33.6 cm. The diffusing section recovers pressure and minimizes overall losses.

The Venturi tubes were designed with an inlet with a large radius of curvature to minimize inlet losses and to present a flat velocity profile at the throat, as seen in Fig. 6. The throat section has a 4.5 to 1 reduction in area from the entrance. This reduces the influence of inlet flow conditions on the throat velocity profile and therefore minimizes their effect on diffuser losses. The diffuser itself is a maximum pressure recovery design. The data of MacDonald and Fox was used in the design [9].

The Venturi tubes are formed into an array and positioned in the fuel and air support spider by sheet metal partitions fore and aft. A series of bleed jets is incorporated in the current design. These jets prevent local recirculation but are small enough that dilution effects are mixed out before the face of the catalyst is reached. The overall mixing length of 20 throat diameters from the throat to the catalyst face for this design is slightly greater than the 18 throat diameters reported for the NASA multiple conical fuel injector [5].

Fuel is injected into the Venturi throats from a series of tubes which penetrate the combustor casing end cover (Fig. 2). These tubes are located in a region of increasing air velocity but block only 7 percent of the inlet area. Minor misalignments will therefore have little effect on Venturi throat velocity profiles. The tubes are fed by an external reservoir, which is separated from the cover plate by an air gap to allow convective cooling and thereby prevent coking or other thermal degradation of the fuel. The reservoir is internally baffled. One set of baffles provides for the segmentation of the fuel injector tubes to match that of the catalytic reactor and fuel-air preparation system. The other set of baffles or channels provide equal length fuel passages for each of the injection points so that the catalyst segment receives fuel evenly when flow is initiated. This is essential to assure fuel uniformity across the face of the reactor and thus achieve optimal emissions performance and avoid excessive temperature gradients.

Each segment of the fuel-air preparation system is provided with a reverse-jet ignitor. Figure 2 – View "A" – shows the ignitor placement. The reverse jet ignitor has for some time been used in catalytic combustor laboratory testing by Acurex Corporation [10]. It is a tube oriented so that a jet of gaseous fuel issuing from the tube opposes the main stream flow. A stagnation or "bow" surface is formed which effectively holds flame. This flame is initiated by means of a spark ignitor. When the catalyst ignition sequence is complete, fuel flow is terminated. Since the reverse jet tube alone does not provide a sufficiently stable wake for flame holding, all burning upstream of the catalytic reactor is extinguished.

Auto-ignition poses little problem for the residence times and inlet operating conditions of the present design. Figure 7 shows the ISO Peak Load operating point plotted with the results from [11]. This point is clearly in the zone of no auto-ignition. So long as the physical delay times are near those calculated on a one-dimensional basis, there is no concern with auto-ignition. Essentially, the only way the physical times can deviate from the calculated is through the existence of bluff body wakes and recirculation at the exit plane of the Venturi tubes. This concern has been addressed through the bleed jets discussed above.

Heating of the fuel droplets by radiation from the upstream reactor face has the beneficial effect of increasing vaporization. If this heating caused auto-ignition before mixing was complete, an upstream section of inactive substrate would be needed as a radiation shield. However, radiant heating poses no problem since only a small fraction of the energy radiated from a grey body (such as the reactor)

Table 3 Auxiliary burner performance

OPERATING CONDITION	PRESSURE MPa(psia)	TEMPERATURE °K(°R)	VELOCITY m/sec (ft/sec)	AUX BURNER AIR FLOW kg/sec (lbm/sec)	AUX BURNER FUEL TO AIR mass fuel / mass air	LOCAL FUEL TO AIR RATIO LIMITS* RICH	LEAN	ESTIMATED EFFICIENCY** %
IGNITION	0.11(16)	306(550)	6.4(21)	1.2(2.7)	0.035	0.145	0.036	85-99
MAX ACCEL FUEL TO AIR RATIO	0.16(24)	350(630)	7.9(26)	2.0(4.4)	0.0318	0.150	0.036	78-92
FULL SPEED NO LOAD	0.91(132)	571(1028)	22.5(74)	18.9(41.7)	0.00999	0.16	0.036	62-89
20% OF PEAK LOAD	0.97(141)	581(1046)	21.3(70)	18.8(41.5)	0.0110	0.16	0.036	67-92

*Calculated using [17]
**Low and high calculated for 45 cm (18 in.) and 61 cm (24 in.) effective flame propagation length respectively

* Registered trademark of the Brunswick Corporation

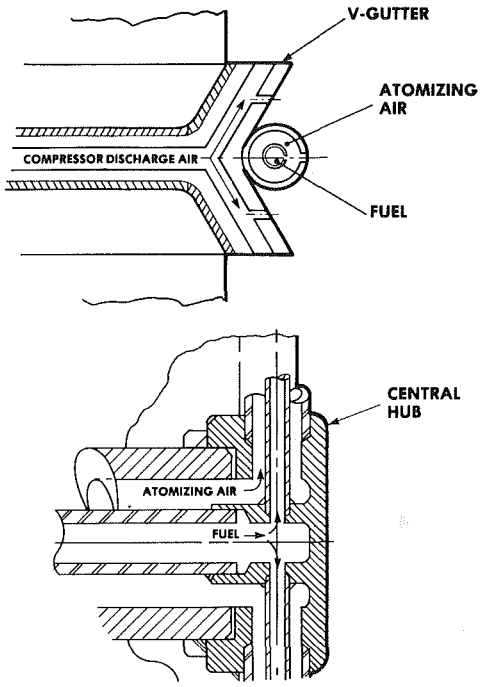

Fig. 8 Auxiliary burner fuel and atomizing air supply

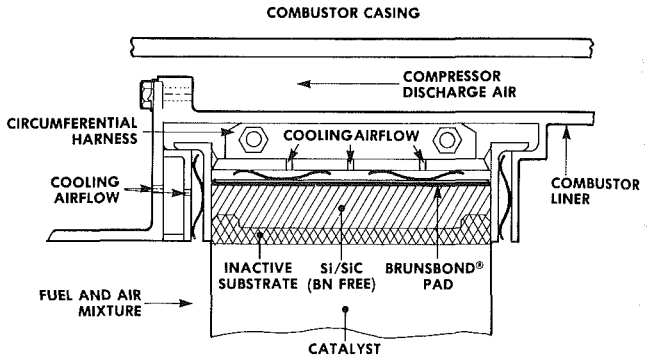

Fig. 9 Catalyst reactor mounting and support system

lies within the band from 3 to 4 micron wavelength where the fuel absorbs strongly. [12]

Flashback (upstream propagation of flame) in the boundary layer or mainstream flow should pose no problem for No. 2 distillate since its flame speed is 0.5 m/s (1.6 ft/s). Also, leakage flows interrupt the boundary layer on the walls of the fuel and air preparation system at its interface with the catalytic reactor. For the case of gaseous fuels with high flame velocities, tests have shown that a section of inert substrate must be used to arrest flashback. If the present system were used for an intermediate Btu coal gas, additional pressure loss should be anticipated due to these arrestors.

The Auxiliary Burner. The auxiliary burner is a baffle-stabilized system similar to an aircraft augmentor (afterburner). The baffles are a series of V-gutters which are structurally part of the catalyst support "spider" (see Fig. 2 – View A). These V-gutters are cooled convectively by compressor discharge air which passes through internal passages. Fuel and atomizing air are conveyed to the auxiliary burner via coaxial tubes. These tubes are located at the vertex of the V-gutters and supply an air atomized fuel spray to the recirculation zone formed behind them. The ignition source for the auxiliary burner is a retractable spark plug of conventional design.

The key operational advantages of the auxiliary burner design are (*i*) the use of the air passing through the catalytic reactor when it is not being fueled, and (*ii*) the "clean up" or afterburner action of the auxiliary burner when fuel flow is initiated to the catalytic reactor.

Performance. A baffle stabilized flame consists of two distinct regions. The first is a well-stirred region in the wake behind the V-gutters. The burnt products in this region ignite fresh fuel and air mixture in the wake boundary and stabilize the flame there. Downstream from this region, the flame spreads and coalesces with the flames from neighboring baffles. The operating parameters of most concern are the fuel rich and lean stability limits and the combustion efficiency.

Several investigators have presented semiempirical stability correlations for baffle stabilized reactors [13–16]. The stability limits for our case were calculated from the correlation of DeZubay, modified to account for inlet tempeature variations [17]. Table 3 shows that the local rich and lean limits for the combustor inlet conditions are nearly invariant over the operating range of the auxiliary burner.

The efficiency of the auxiliary burner (Table 3) was calculated by straightforward application of the method of Petrein, Longwell, and Weis [16], using the flame velocities of Zabetakis [18]. The efficiency, which is of the order of 70–90 percent, is considerably lower than that of the vortex stabilized burner. The trends shown are expected to be reasonably correct, but the absolute values have a low level of confidence due to the lack of an empirical calibration point.

Auxiliary Burner Fuel Injectors. Good performance from the auxiliary burner fuel injector requires a line source of atomized fuel droplets. The uniformity of this line source with respect to mixture strength, flow rate, and droplet size must

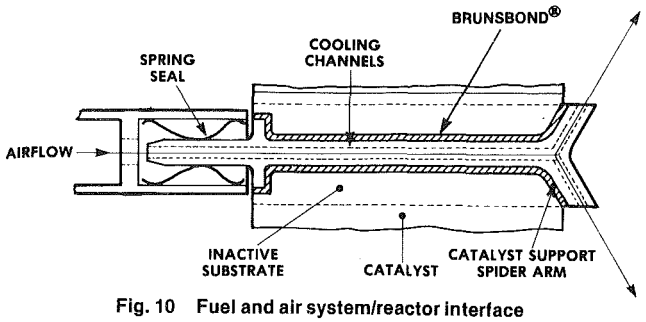

Fig. 10 Fuel and air system/reactor interface

be maintained. This is particularly important in light of the narrow operating limits of the gutter system noted above. Streaking or streaming filaments of inadequately atomized fuel will easily penetrate critical regions of the flow behind the baffle and discharge raw fuel from the combustor.

The atomization and delivery concept adopted for presentation in this report is a coaxial tube fuel and atomizing air system (Fig. 8). This system is simple and presents a minimum of problems at the interface with the central hub. Further, the fuel is surrounded by 200 to 250°F atomizing air. This eliminates all problems of fuel coking and fouling due to thermal decomposition.

Catalytic Reactor Mounting System. The major design challenges for the reactor mounting system are:

(*i*) The thermal mismatch between the reactor operating temperature and the allowable temperature limit of the metal support structure, which is of the order of 867 K (1100°F).

(*ii*) The radial differential thermal growth between the metal support structure and the ceramic reactor substrate. Typically, the expansion coefficient of the metal is four times that of the ceramic.

(*iii*) The stress due to axial thermal growth and pressure loading, when the catalyst is being ignited or shut down.

The thermal mismatch is accommodated by gradually lowering the temperature from the ceramic to the metal support through a series of insulating layers (Fig. 9). The first of these layers is a section of inactive channels of substrate that are blocked to prevent gas flow. The second layer, a compliant layer of Si/Si-C, borders the outer radial surface of the reactor segment. This layer is used for its stress relief properties. A layer of Brunsbond®* sintered metal fiber material is brazed to the circumferential metal harness [19]. The Brunsbond® layer[1] is a good insulator because of its porosity. Although this insulating quality will vary with density, it is approximately equivalent to a high-density ceramic. The bulk of the temperature drop will be absorbed by these insulating layers. Passages, as shown, have been provided for convective cooling of the circumferential harness and springs.

The stresses introduced by thermal growth differences between the ceramic and the circumferential support are absorbed by the Si/Si-C compliant layer and the Brunsbond® pad, while the leaf springs between the inner and outer support harnesses insure that an overall compressive force is applied to the ceramic segments at all times. In the axial direction, the ceramic segments are trapped by the flanges of the circumferential harness. This entire assembly is positioned in the combustion liner by a series of leaf springs, which absorb axial pressure loading forces and allow differential growth.

Figure 10 shows the inactive channels and use of the Brunsbond® pad at the support structure/substrate interface. Also shown are the internal cooling passages for the spider support arm. Heat transfer calculations show that the insulation results in minimal cooling flow being needed to achieve metal temperatures less than 700 K (800°F).

[1] Registered trademark of the Brunswick Corporation

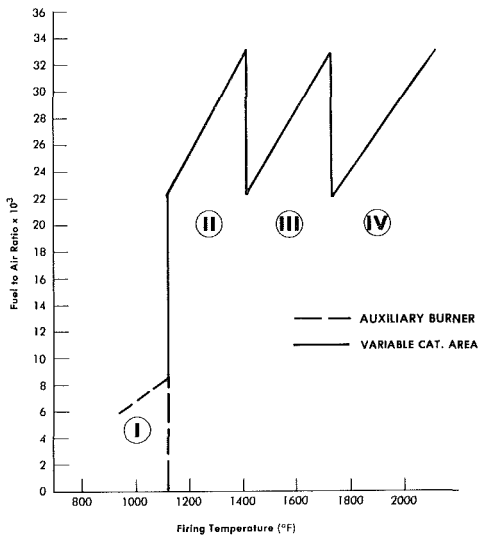

Fig. 11 Combustor fuel staging (full-speed no-load to peak)

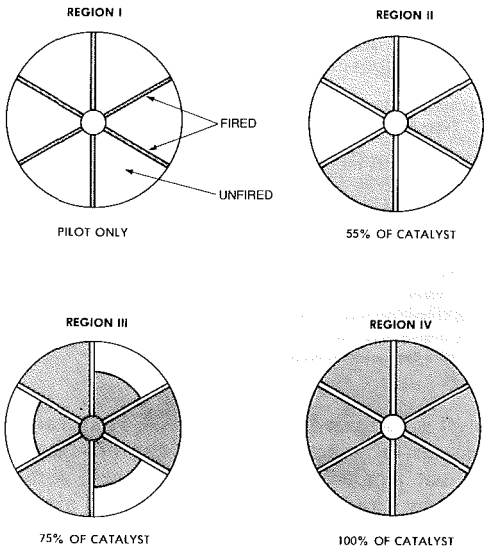

Fig. 12 Schematic of combustor staging modes

Combustion System Operating Modes

In order to span the range of combustor exit temperatures necessary to the operation of the gas turbine, fuel staging of the reactor segments is employed as shown in Fig. 11. The segments of the catalytic reactor involved in the staging process are shown schematically in Fig. 12.

Up to a firing temperature of 878 K (1120°F), the auxiliary burner supplies the operating energy for the turbine. At this point 55 percent of the catalyst is ignited and brought to the minimum operating fuel-to-air ratio of 0.0223. The sectors are of slightly different areas to match the staging requirements. In order to avoid load swings, the pilot burner is shut off as the catalytic reactor ignites such that a constant firing temperature is maintained. Once the transfer to catalytic combustion in three reactor segments is complete, the fuel to the operating portion of the catalyst is increased until the fuel to air ratio (0.0332), corresponding to the maximum catalyst operating temperature 1700 K (2600°F), is reached. At that point another constant load transfer is made, as follows. The exit temperature of the operating portion of

Table 4 Catalytic combustion system performance

PREDICTED CATALYTIC COMBUSTION SYSTEM EMISSIONS

CATALYTIC REACTOR OPERATIONAL (20% TO 100% OF PEAK LOAD)
AUXILIARY BURNER OFF
AVERAGE EXIT TEMPERATURE—2000 °F TO 2600 °F
EFFICIENCY – 99.0% +

SPECIES	CONCENTRATION (ppmv)	
	@ REACTOR EXIT	@ MACHINE EXHAUST
NO_x ($NO + NO_2$)	< 5	< 4
CO	< 15	< 11
UHC (as C_3H_8)	< 2	< 1.6
SMOKE	—	NO VISIBLE PLUME

PREDICTED PERMANENT PRESSURE LOSSES AT PEAK LOAD

PRESSURE LOSS	% OF PCD*
LOSSES, COMPRESSOR DIFFUSER TO COMBUSTOR INLET	0.5
LOSSES DUE TO FUEL-AIR PREPARATION SYSTEM	1.56
LOSSES ACROSS THE CATALYTIC REACTOR	3.24
TOTAL	5.3

NOTE:
(1) Catalyst face velocity = 59 ft/sec
(2) Catalyst exit temp. = 1700 °K (2600 °F)
(3) Original design goal = 5% pressure loss
* PCD = Compressor Discharge Pressure

Table 5 Catalytic combustion system emissions

STAGING POINT (WORST CASE)

CATALYTIC REACTOR - IGNITION
EXIT TEMPERATURE = 1800 °F
EFFICIENCY = 85%

SPECIES	CONCENTRATION (ppmv) AT REACTOR EXIT
NO_x	< 6
CO	100
UHC (AS C_3H_8)	2000

AUXILIARY BURNER
EXIT TEMPERATURE (1) = 1080 °F
EFFICIENCY = 98%

SPECIES	CONCENTRATION (ppmv) AT BURNER EXIT
NO_x	< 36 (3)
CO	< 120 (3)
UHC (AS C_3H_8)	< 20 (3)

MACHINE EXHAUST (2)

SPECIES	CONCENTRATION (ppmv)
NO_x	< 33
CO	< 150
UHC (AS C_3H_8)	< 1025
SMOKE	NO VISIBLE PLUME (3)

(1) Before catalyst ignition.
(2) No credit taken for cleanup of catalyst emissions by auxiliary burner.
(3) Design goal - Set at current levels.

the catalyst is decreased to 1370 K (2000°F) and an additional 20 percent of the reactor is ignited and brought to 1370 K (2000°F) exit temperature. Ignition of these sections is accomplished by a radial baffle in the fuel and air preparation channels. A total of 75 percent of the catalyst is now operating. This process is repeated again at a firing temperature of 1217 K (1730°F), and the entire reactor is operating. The fuel to the reactor can now be increased to attain full peak load operation.

The last staging point occurs at approximately 70 percent of peak load. Therefore, a base loaded machine would be operating with one fuel system in use. This is a major simplification over the parallel staged designs in which the pilot and catalytic reactor are both in operation. The end result is an increase in reliability.

The operating modes described above allow use of the catalytic reactor over 80 percent of the gas turbine load range (from 20 percent load to peak load) and allow full catalytic operation (no auxiliary burner) at all loads above 20 percent of peak load.

Overall Combustion System Performance

Expected emissions at the design conditions are shown in Table 4. The performance on NO_x, CO, UHC, and smoke are all predicted to be excellent. Table 5 illustrates the worst-case condition for emissions. This is the point at which the auxiliary burner is operating while initial catalyst ignition is accomplished. The emissions from the catalytic reactor and the auxiliary burner were combined proportionally with no credit taken for the clean-up of the reactor emissions by the auxiliary burner. (Note that the auxiliary burner emissions have been set at current levels.) Test and redesign will be necessary to achieve these levels.

Pressure losses for this system are somewhat higher than those for conventional systems due mainly to the long catalyst bed. Recall that this length was chosen to provide a margin for ignition and low-temperature operation. The total pressure loss of 5.3 percent is very close to the design goal of 5 percent (Fig. 4). This pressure drop was achieved by employing a large frontal area catalytic reactor and this, in turn, is made possible by expanding the combustion casing to the maximum practical diameter as described earlier.

Exhaust gas temperature profiles achieved by current production combustor designs should be easily achieved at all operating points where the entire reactor is fueled. The catalyst spider support structure cooling air will mix completely with the hot gases exiting the catalyst reactor in the recirculation zones behind the V-gutters. Also, when 55 or 75 percent of the catalyst is operating, the interleaved hot and cold flows form a symmetrical pattern. Again, the mixing should be rapid and complete.

The combustor as designed does not incorporate crossfiring. Each combustor for the turbine contains catalytic reactor ignition means and an auxiliary burner ignitor. Because of the segmented reactor design and the danger of holding flame upstream of the catalyst, crossfiring ignition of the catalytic reactor is impractical.

Conclusions and Recommendations

The preliminary design effort described in this paper has produced a ready-to-test design of a full-scale catalytic combustor for application to a heavy-duty gas turbine within the present level of understanding of catalytic combustion. In accomplishing this, it is apparent that the aerothermal portion

of the design has presented no barrier problems. The fuel-to-air premixing system work done by NASA provides good design data for a range of operating conditions that span those of heavy-duty gas turbines. The utilization of a downstream burner is conceptually sound, but detailed data are less available and generally are for conditions more applicable to augmentor ("afterburner") designs. Therefore, some development is necessary, but should be relatively straightforward. The cooling for the reactor mounting system is straightforward. The staging made necessary by the limited reactor operating range introduces complexities into the control system. These do not present a barrier problem and may be overcome using state of the art techniques with minimal effect on reliability.

Selected substrate and catalyst materials recently developed have demonstrated lifetimes and durabilities adequate for a laboratory test program. However, the barrier problems which must be overcome before a commercial catalytic combustor can be achieved lie primarily in this area. Materials development must be continued to extend maximum service temperatures, lifetimes, and durability of the substrates and catalysts. It is, therefore, strongly recommended that a materials development program be conducted in parallel with combustor development tests, both essential parts of a total catalytic combustor development program.

References

1 Cellamare, R., and Tong, H., "Stationary Gas Turbine Catalytic Combustion Development Program," prepared for General Electric Company, Acurex Technical Report 81-A3/EE, 90 pp., 1981.

2 Cellamare, R., Ibid., pg. 84.

3 Kesselring, J. P., Krill, W. V., Anderson, S. J., Chu, E. K., Friedman, M. A., Merrick, E. G., and Snow, G. C., "Catalytic Combustion Component Development and System Prototype Development," Acurex Project 7474, Second Annual Report Draft, EPA Contract No. 68-02-3122, Acurex Corporation, Energy & Environmental Division, Mountain View, Calif., Nov. 1980.

4 Snow, G. C., private correspondence for data not yet published, work performed under NASA Lewis Contract No. DEN3-83 and EPA Contract No. 68-02-3122, Acurex Corporation, Energy & Environmental Division, Mountain View, Calif., Nov. 1980.

5 Tacina, R. R., "Experimental Evaluation of Fuel Preparation Systems for an Automotive Gas Turbine Catalytic Converter," NASA TM-78856, 1977.

6 Tacina, R. R., "Degree of Vaporization Using an Airblast Type Injector for a Premixed-Prevaporization Combustor," NASA TM-78836, 1978.

7 Anderson, D. N., "Effects of Fuel-Injector Design on Ultra-Lean Combustion Performance," NASA TM-82624, 1981.

8 Tacina, R. R., "Performance of a Multiple Venturi Fuel-Air Preparation System," *Premixed Prevaporized Combustor Technology Forum*, NASA Conference Publication 2078, 1979, p. 85.

9 MacDonald, A. T., and Fox, R. W., "An Experimental Investigation of Incompressible Flow in Conical Diffusers," *Int. J. Mech. Sci.*, Vol. 8, 1966, pp. 125–139.

10 Anderson, S. K., Krill, W. V., and Kesselring, J. P., "Fuel Injector, Ignition, and Temperature Measurement Techniques for Catalytic Combustion," *Proceedings, 4th Workshop on Catalytic Combustion*, EPA 600/9-80-035, Aug. 1980.

11 TeVelde, J. A., and Spadaccini, "Autoignition Characteristics of No. 2 Diesel Fuel," NASA CR165315, 1981.

12 Berlad, A. L., and Hibbard, R. R., "Effect of Radiant Energy on Vaporization and Combustion of Liquid Fuels," NACA RME52109, 1952.

13 DeZubay, E. A., "Characteristics of Disk Controlled Flame," *Aero Digest*, July 1950, pp. 54–56 and 102–104.

14 Ballal, D. R., and Lefebvre, A. H., "Weak extinction Limits of Turbulent Flowing Mixtures," ASME Paper No. 78-GT-144, presented at the Gas Turbine Conference, London, England, Apr. 9–13, 1978.

15 Ballal, D. R., and Lefebvre, A. H., "Weak Extinction Limits of Turbulent Heterogeneous Fuel/Air Mixtures," ASME Paper No. 79-GT-157, presented at the Gas Turbine and Solar Energy Conference, San Diego, California, Mar. 12–15, 1979.

16 Petrein, R. J., Longwell, J. P., and Weiss, M. A., "Flame Spreading from Baffles," *Jet Propulsion*, Vol. 26, No. 2, Feb. 1956, pp. 81–86, 97.

17 Anon., "Design Practice — Combustor Aero Thermo-Thermal Design," Aircraft Engine Group, Evendale, Ohio, internal distribution only.

18 Zabetakis, M. G., "Flammability Characteristics of Combustible Gases and Vapors," U.S. Department of the Interior, Bureau of Mines Bulletin 62F, 1965.

19 Tolokan, R. P., Nablo, J. C., and Brady, J. B., "Ceramic to Metal Attachment Using Low Modulus Brunsbond Pad," ASME Paper No. 81-GT-160, presented at the International Gas Turbine Conference, Houston, Texas, Mar. 8–12, 1981.

Twenty-Five Years of Operating Experience With the Coal-Fired, Closed-Cycle Gas Turbine Cogeneration Plant at Coburg

K. Bammert
Professor Dr. —Ing.
University of Hannover,
Hannover, West Germany

The only commercially running closed-cycle gas turbine in the world delivering electricity as well as heat to a public utility and a heating network, is the heat and power station in Coburg, West Germany. The plant is fired exclusively with pulverized coal and uses air as the working medium. It has a maximum continuous electric power output of 6.6 MW into the grid and up to 16 MW of direct heating capacity into the town's heating network. The plant has accumulated 150,000 operating hours to date (approximately 7000 hrs per year); it is scheduled to remain in service during the following years due to its excellent performance. Since relatively little has been published about the plant in the technical literature, a report about its design and operating experience is presented here.

Introduction

The constraint of exploiting the limited indigenous fuels in a rational manner led to the construction of a number of heat and power stations in Germany several decades ago. This development gained additional impetus due to the general shortage and the consequent price rise of fossil fuels. In the course of time, different concepts of heat and power stations came into being. In principle, every thermal power conversion machine can be used for the cogeneration of heat and power but the question is, "How much of the fuel burned can be converted into mechanical power, and how simple and efficient is it to extract heat?"

Reflections of this nature were contemplated 25 years ago by the municipal public works of Coburg (Städtische Werke Coburg). The city had to expand its heating and power grid at this time. It was decided to erect a closed-cycle gas turbine plant fired with pulverized coal which offered special advantages in the medium output range in the cogeneration of heat and power. Waste heat occurs at higher-temperatures and due to the clean and dry working medium, air, the turbomachinery is not subjected to corrosion and erosion. Fouling of the heat exchangers is not expected. The output is controlled through the working medium pressure so the efficiency does not change much even when operating at part-load. The operation and control of the plant is very simple [1, 2]. Because the first successful operating results with a pulverized coal heater [3, 4] were already available and because the fabrication of turbomachinery and heat exchangers were considered to be without problems, it was generally believed that there was nothing to prevent the construction of a heat and power plant of the kind described in the following[1].

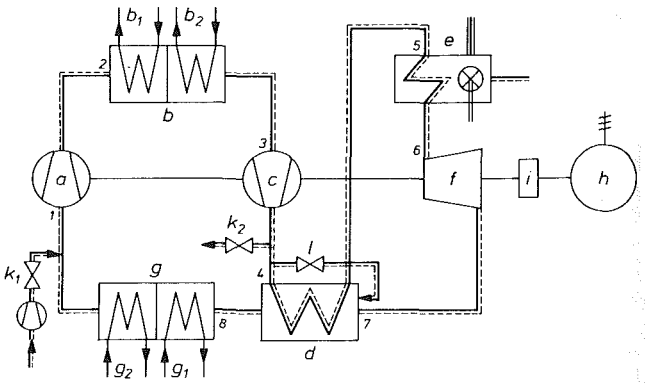

Fig. 1 Cycle diagram of the Coburg plant:

a	= LP compressor	g	= precooler
b	= intercooler	g_1	= heating part
b_1	= heating part	g_2	= cooling part
b_2	= cooling part	h	= alternator
c	= HP compressor	i	= gear box
d	= recuperator	k_1,k_2	= valves for inventory control
e	= coal-fired air heater	l	= bypass control valve
f	= turbine		

Contributed by the Gas Turbine Division of THE AMERICAN SOCIETY OF MECHANICAL ENGINEERS for presentation at the 28th International Gas Turbine Conference and Exhibit, Phoenix, Arizona, March 27-31, 1983. Manuscript received at ASME Headquarters December 7, 1982. Paper No. 83-GT-26.
Copies will be available until January 1984.

[1] The plant was built in the years 1957 to 1959 by Gutehoffnungshuette Sterkrade and rebuilt in 1962. Since then, the plant has been running 7000 hours per year; it will soon attain an operating time of 150,000 hours.

Table 1 Working medium conditions in the cycle

Maximum continuous rating 6.6 MW_e		design data	
Inlet spot	Component	temperature °C	pressure bar
1	LP-Compressor	20	7.88
2	Intercooler	76	13.08
3	HP-Compressor	20	12.91
4	Recuperator HP	125	31.72
5	Air heater	425	31.28
6	Turbine	680	29.66
7	Recuperator LP	445	8.47
8	Precooler	146	8.09

Table 2 Design data of the Coburg plant[a]

CYCLE			
Enthalpy drop of the turbine	Δh_t	= 260.34	kJ/kg
Enthalpy rise of the LP-compressor	$\Delta h'_v$	= 56.44	"
Enthalpy rise of the HP-compressor	$\Delta h''_v$	= 105.38	"
Effective enthalpy drop	Δh_e	= 98.52	"
Enthalpy increase in the heater	Δh_{he}	= 281.81	"
Heat input (fuel)	Δh_f	= 318.43	"
Cycle efficiency	η_{cy}	= 35	%
Thermal efficiency	η_{th}	= 31	%
Mass flow rate	$\dot{m}$	= 74.07	kg/s
POWER			
Electric Power	P_{max}	= 6.60	MW
Fuel power input	$\dot{Q}_f$	= 23.58	"
Heating power (precooler)		7.22	"
Heating power (intercooler)		1.98	"
Heating power total	$\dot{Q}$	= 9.20	"
Cooling power (precooler)		2.26	"
Cooling power (intercooler)		2.28	"
Cooling power total		4.54	"
EFFICIENCY			
Net electric efficiency	$\eta_{net} = P_{max}/\dot{Q}_f$	= 28	%
Net heating utilization	$\dot{Q}/\dot{Q}_f$	= 39	%
Net total utilization		67	%

[a] Point d in Fig. 4

Description of the Coburg Plant

The cycle diagram of the Coburg plant is shown in Fig. 1. Working air is compressed in the LP compressor, a, cooled in the intercooler, b, and raised to maximum process pressure in the HP compressor, c. Then it is preheated in the heat exchanger, d, followed by final heating to the maximum process temperature in the pulverized-coal fired air heater, e. In the turbine, f, the working fluid is expanded and in the heat exchanger, d, and precooler, g, returned to its starting conditions. The precooler, g, and the intercooler, b, are divided into two parts: the heating parts, b_1 and g_1, which transfer heat from the working medium to the hot water of the heating network and the cooling parts, b_2 and g_2, which transfer heat to the atmosphere. The turbo set (a, c, f) is coupled to one shaft. The alternator, h, runs by grid frequency. Both turbine and generator shafts are coupled via the gearbox, *i*. Valves, k_1 and k_2, serve to feed air from storage bottles into the piping upstream the LP compressor, or blow-off air from the piping downstream the HP compressor, respectively. The inlet valve, k_1, is used for power increase, and the outlet valve, k_2, for decreasing the load. In this manner the pressure level of the circulating working medium is controlled (so-called inventory control). The bypass valve, l, serves for short-term power decreases and for maintaining the heating power at low electric power requirements. The reference points 1–8 in Fig. 1 denote the entry of the working fluid into the respective cycle component. Table 1 lists the pressures and temperatures for these points. They correspond to a maximum continous electric power output of 6.6 MW.

At the design point the pressure upstream of the turbine is 29.66 bar and the temperature is 680°C, the temperature upstream of the compressors is 20°C, and the pressure upstream of the LP compressor is 7.88 bar. The turbine expansion ratio is 3.5. With a temperature difference on the hot side of the recuperator of 20°C, an inlet temperature of 425°C is thus obtained at the heater. For a maximum continuous electric output of 6.6 MW the mass flow rate, $\dot{m}$, is then 74.07 kg/s.

At the design point working air enters the precooler at a temperature of 146°C and the intercooler at 76°C. Due to these temperatures, it is possible to utilize almost 70 percent of the waste heat arising in the coolers as heating energy without affecting the electric power output. The inlet temperature of the heating water into the heating parts, b_1 and g_1, is 40°C (return water of the heating network). The water heated up in the heating parts is stored in hot water tanks before it is pumped into the piping system (heating network) at 100°C. Cooling water (mountain water) enters the cooling parts, b_2 and g_2, at 15°C and is heated by 25°C. According to Table 2, a total heating power of $\dot{Q}=9.20$ MW and a remaining cooling power of 4.54 MW are obtained.

The main data of the Coburg plant are shown in Table 2, based on a maximum continuous electric output $P_{max}=6.6$ MW. At an effective enthalpy drop of $\Delta h_e=\Delta h_t-(\Delta h'_v+\Delta h''_v)=98.52$ kJ/kg, where Δh_t is the enthalpy drop of the turbine and $\Delta h'_v$ and $\Delta h''_v$, respectively, denote the enthalpy rise of the compressors; and the increase in enthalpy of the working medium in the heater is $\Delta h_{he}=281.81$ kJ/kg; hence, the cycle efficiency, $\eta_{cy}=\Delta h_e/\Delta h_{he}$, is 35 percent. Since the efficiency of the pulverized coal-fired air heater is $\eta_{he}=88.5$ percent, the fuel heat supplied to the plant externally is $\Delta h_f=\Delta h_{he}/\eta_{he}=318.43$ kJ/kg. This results in a plant thermal efficiency of $\eta_{th}=\Delta h_e/\Delta h_f=31$ percent. If now the mechanical efficiency, η_m, of 98 percent, the gear box efficiency, η_g, of 96.5 percent, and the alternator efficiency, η_a, of 97.5 percent are taken into account as well as the internal efficiency factor η_i of 98 percent (ratio of the input power of the auxiliary units to P_{max}), then a net efficiency $\eta_{net}=\eta_{th}\times\eta_m\times\eta_g\times\eta_a\times\eta_i$ of 28 percent is obtained according to Table 2. It is identical to the ratio of the maximum continuous power, P_{max}, to the fuel power input in the heater $\dot{Q}_f=\dot{m}\times\Delta h_{he}/\eta_{he}$. Combined with the heating power of $\dot{Q}=9.20$ MW, the total utilization of the fuel is 67 percent.

Should greater heating power outputs be required over extended periods (extreme winter conditions), this can be achieved by increasing the inlet temperatures of the working medium upstream of the compressors [5, 6]. The effect of increased compressor inlet temperatures is shown in Table 3. Thus, for example, with a maximum continuous electric output of 6.6 MW_e and an inlet temperature at the compressor of $t_1=t_3=50$°C, a heating power output of about 16 MW can be obtained. Although the net efficiency for electric power generation is reduced from 28.0 to 24.3 percent, the fuel utilization increases to 83 percent. Table 3 lists the variation of compressor inlet temperature, $t_1=t_3$, from 20 to 50°C, with the turbine inlet temperature being constant at $t_6=680$°C. Of course, it is also possible to vary the turbine inlet temperature for controlling the heating power output,

Table 3 Peak heating power demand dependent on compressor inlet temperature at constant maximum electric power[a]

Compressor inlet temperature	$t_1 = t_3$	°C	20	30	40	50
Electric power	P_{max}	MW	6.60	6.60	6.60	6.60
Fuel power input	$\dot{Q}_f$	MW	23.58	24.68	25.78	27.12
Heating power total	$\dot{Q}$	MW	9.20	11.53	13.87	15.91
Net electric efficiency	$P_{max}/\dot{Q}_f$	%	28.0	26.7	25.6	24.3
Net heating utilization	$\dot{Q}/\dot{Q}_f$	%	39.0	46.7	53.8	58.7
Net total utilization	Σ	%	67.0	73.4	79.4	83.0

[a] Design point, d, in Fig. 4

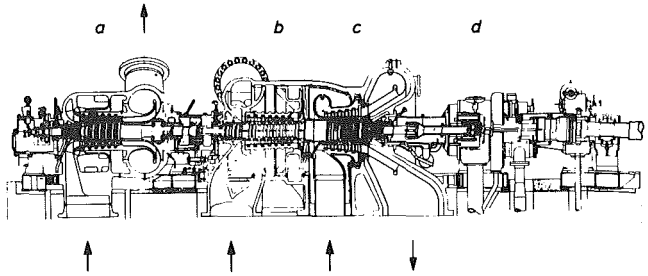

Fig. 2 Longitudinal section of the turbo set:

a = LP compressor
b = HP compressor
c = turbine
d = gear unit

but this temperature variation – especially towards still higher ranges – is limited.

The plant is generally operated at half load at night for power generation with the results that the heating power output is also reduced by one-half. However, to achieve higher heating power outputs even at part load, a bypass control valve (l in Fig. 1) is employed. This reduces the mass flow rate of the turbine and the net power output of the turbo set while keeping the mass flow rate of the compressors and the coolers practically unchanged. In contrast to pressure level control, the pressure ratio of the turbine decreases, which in turn results in an increase of turbine outlet temperature. Since the temperature conditions inside the coolers do not change much, heating power output not only remains constant but rises slightly. In order not to overload the coolers, the electric power output is reduced by decreasing the pressure level. This measure is taken for about 75 percent load (corresponding to 5 MW_e). At this point, the plant delivers a maximum heating power output of 11 MW. The subsequent bypass control, however, increases the heating power output at no load to a maximum of 14 MW. This method of control is of great advantage in terms of the heating output, but it is at the expense of a considerable loss of net electric efficiency.

The design of the turbomachinery and the heat exchangers takes into account the limiting data as listed in Table 3, whereby the inlet turbine temperature of $t_6 = 680°C$ is kept constant, and the maximum continuous electric output of $P_{max} = 6.6$ MW can always be achieved, as in all other operating conditions. The user had demanded at the time that in extreme cases a maximum heating output of $\dot{Q}_{max} = 16$ MW should be available without affecting the electric output. This requirement resulted in the pulverized-coal fired air heater being overdimensioned by $(27.12 - 23.58)/23.58 = 15$ percent, based on the input fuel. In other words, such an air heater is suited in regular operation to an electric power output of $(27.12 \times 0.28 =)$ 7.6 MW at compressor inlet temperatures of $t_1 = t_3 = 20°C$. An example in layout design [6] shows how the characteristics of the individual cycle components change in the plant when it is operated at the levels listed in Table 3 (pressure ratio, temperature difference in the heat exchanger, etc).

Table 4 shows pressure losses arising in the cycle based on design conditions (Tables 1 and 2). The relative total pressure loss Σ $(\Delta p/p)$ is 12.8 percent, and it comprises the relative individual pressure losses $\Delta p/p$ of the heat exchanging components, including the relevant piping. The relative pressure loss is calculated by dividing the pressure loss, Δp, by the respective inlet pressure, p, at each component.

Start of Operation

The construction of the plant began 25 years ago. Two years thereafter it was put into service. At that time it became apparent that the plant delivered only 2/3 of its design electric power output for the given layout data for mass flow rate and pressure level. Reasons for this were primarily the low efficiencies of LP and HP compressors, the low enthalpy rise of recuperator, and the excessive pressure loss in the heat transfer components, especially the recuperator itself.

The turbo-group was designed and built on the basis of the Ravensburg turbo set [1]. An axial turbine and a three-stage centrifugal compressor were mounted in a joint casing. The single-stage LP compressor was fitted with a double-entry impeller owing to a mass flow rate three times that of Ravensburg machine. The HP compressor had two centrifugal stages. Whereas both the compressors were designed for an efficiency of 83 percent, the LP compressor actually achieved 79 percent and the HP compressor 74.5 percent. Also, the turbo set had to be driven at a lower speed than originally intended due to the fact that static and dynamic stresses of an intensity hitherto unknown in conventional centrifugal compressors occurred in the wheel disks, shrouds, and blading of the centrifugal stages of the HP compressor. The highly charged cycle caused high load-dependent air forces which severely affected the stability and excitation of the machine. The lower speed of the turbo set caused a smaller pressure ratio. The plant had to be driven with higher mass flow rates so as to obtain the desired electric power output. This, however, resulted in high pressure losses over the entire cycle.

The heat exchanger (of the smooth-tube, counterflow design) constituted a further handicap. The HP air flowed inside the tubes and the LP air (in counterflow) flowed along the tube outer walls. Owing to shocks and jerks sustained during rail transport the tubes were shaken against each other and bent in such a way that about 30 percent of the free passages between the tubes were blocked on the low pressure side. The temperature difference of the heat exchanger was about 45°C instead of less than half of this value. The total pressure loss (on both HP and LP sides) was slightly more than double the design value.

Furthermore, it appeared that a safe operation of the air heater was impossible with the pulverized coal burners installed. Part loads below 80 percent of electric power could not be achieved without sustained gas firing.

Because all measures to improve the situation by individual corrections has been failing, the manufacturer decided to replace the centrifugal compressor (excluding the centrifugal discharge stage) by an axial compressor and the smooth-tube, counterflow heat exchanger by a corrugated strip fin tube heat exchanger. This led to a double-casing turbo set and a shorter heat exchanger, which at the same time enabled the inlet and outlet ducts of the coolers (which also showed high pressure losses) to be replaced by aerodynamic shaped connecting flanges. The burners of the air heater were also redesigned and installed during the same period (1961/62).

The reconstructed plant was commissioned on September 10, 1962. On September 17, 1962 it achieved for the first time the maximum continuous electric power output of 6.6 MW. The entire heating program was thoroughly tested in the

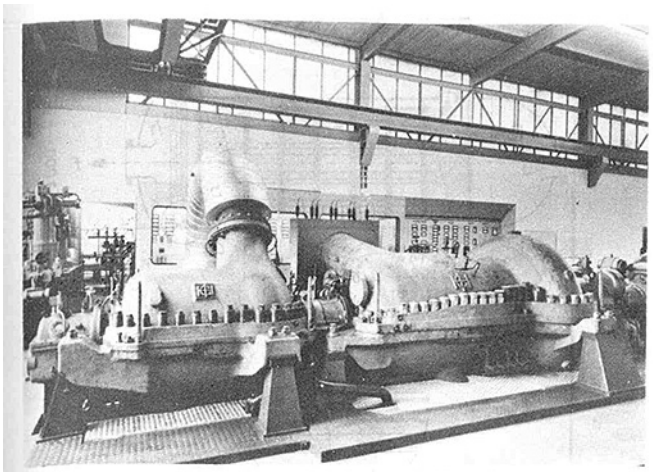

Fig. 3 View of the Coburg turbo set

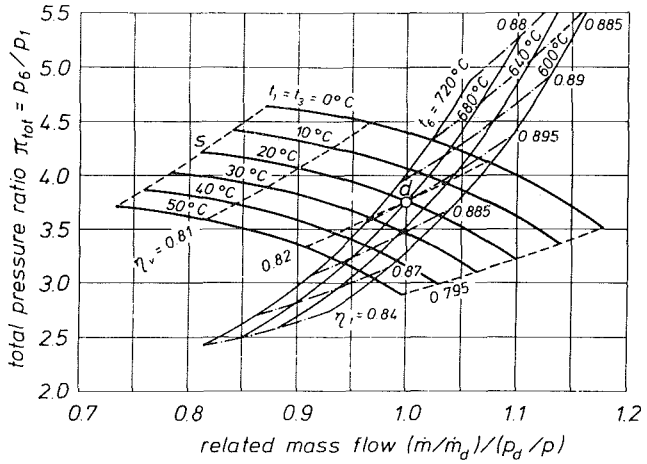

Fig. 4 Performance characteristics of the Coburg plant:

d = design point
s = surge line
n = 8217 rpm

ensuing winter. The electric power output, the heating power output and the efficiencies were all found to be commensurate with the original design with a guaranteed tolerance of 5 percent. The values listed in Tables 1-4 were achieved. Since recommissioning, the plant has been operating for more than 7000 hours a year, corresponding to an availability of over 80 percent. Annual inspection and overhaul are always performed in the months of July and August.

Components of the Coburg Plant

The figures and tables of this report all refer to the reconstructed plant only.

Turbo Set. The longitudinal section of the machine group is shown in Fig. 2. It comprises an LP compressor, a, in one casing and an HP compressor, b, and a turbine, c, in a second casing. Figure 3 shows a view of both casings of the turbo set. The LP rotor is coupled rigidly to the HP rotor by means of a bolt coupling. The axial thrust of the compressor acts in a direction opposite to that of the turbine. The remaining thrust is absorbed by a small compensating piston and a double-acting axial bearing located on the suction side of the LP compressor. The stator blade rings are fixed in special stator blade carriers mounted in the external casing. Due to large heat expansion the stator blade carrier is guided by an annular flange on the outlet side and centered by four radial sliding pads on the inlet side. The LP compressor has six axial stages and the HP compressor seven axial stages and one radial discharge stage. The first stator blade row for both compressors is adjustable so that it was possible to optimally coordinate the performance curves of the turbomachines during the test run. The turbine has five axial stages.

The LP compressor casing is made of spheroidal cast iron and the HP group casing of cast steel. This choice of materials was possible in spite of the high working air temperatures in the turbine because a gas-cooled double-jacket design was used for the turbine. The austenitic stator blade carrier and the austenitic inlet and outlet casings are isolated from each other by an insulating material. The rotor of the HP compressor and the turbine is in one piece and, owing to high temperatures in the turbine, it is made of austenitic material. The rotor of the LP compressor is of conventional ferritic material.

The pressure difference between the HP compressor and the turbine is minimal due to their close coupling. For this reason a short axial labyrinth seal is sufficient. Simultaneously, leakage air serves to cool the shaft between the compressor and the turbine. The shafts of both casings are sealed against the atmosphere by special seal-oil stuffing boxes. Both the casings are split horizontally in the usual manner. The effective power output of the turbo group is transmitted to the alternator through a planetary gear. The speed of the turbo set is 8217 rpm and that of the alternator 3000 rpm. The main oil pumps are flanged to the gearbox. The shaft bearing gear is mounted between the gearbox and the alternator.

Table 4 Pressure loss in the cycle

Air heater		4.8 %
Recuperator	high pressure side	1.1 %
	low pressure side	2.5 %
Precooler		2.6 %
Intercooler		1.8 %
Total		12.8 %

The performance characteristics in Fig. 4 depict the manner in which the efficiencies of the compressor and turbine change with varying inlet temperatures. The total pressure ratio, $\pi_{tot} = p_6/p_1$, is plotted aginst the related mass flow rate $(\dot{m}/\dot{m}_d)/(p_d/p)$ which is identical to $(\dot{V}/\dot{V}_d)/(T_d/T)$. Here, $\dot{m}$ denotes the mass flow rate, p the pressure, $\dot{V}$ the working air volume flow per unit of time, and T the absolute temperature. The point, d, in Fig. 4 refers to the design condition. Because of constant speed and pressure ratios at different points are proportional, and compressor and turbine discharges and expands, respectively, the same mass flow rate, the ordinate, and abscissa of both machines change in the same manner [6]. The characteristic lines can, therefore, be plotted in a single diagram. At the design point, d (the intersection of the compressor characteristic curve $t_1 = t_3 = 20°C$ and the turbine characteristic curve $t_6 = 680°C$), the total pressure ratio $\pi_{tot,d} = p_{6,d}/p_{1,d} = 29.66/7.88 = 3.76$ (Table 1). At this point, too, the efficiency curve of the turbine ($\eta_t = 89.5$ percent) intersects the efficiency curves of the two compressors ($\eta_v = 82$ percent). The individual efficiencies η_t and η_v decrease as the inlet temperatures of the compressors and the turbine move away from the design point, d.

Heat Exchanger. The amount of heat transferred internally in the heat exchanger by the LP air to the HP air roughly corresponds to the heat externally supplied to the cycle via the air heater by means of the fuel (coal). On the HP

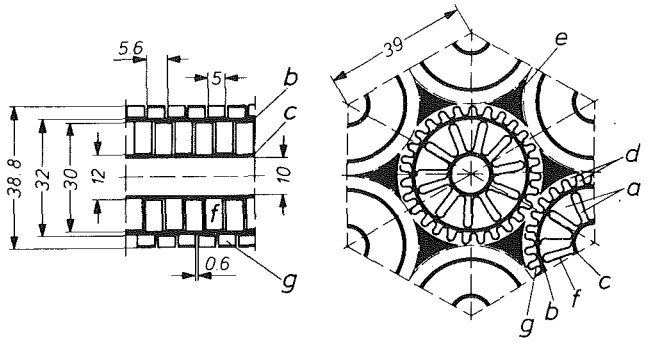

Fig. 5 Longitudinal and cross section of corrugated strip fin tube:

a = inner annulus
b = outer tube
c = inner tube
d = outer annulus
e = profiled bar
f = inner corrugated strip
g = outer corrugated strip
Dimensions in mm

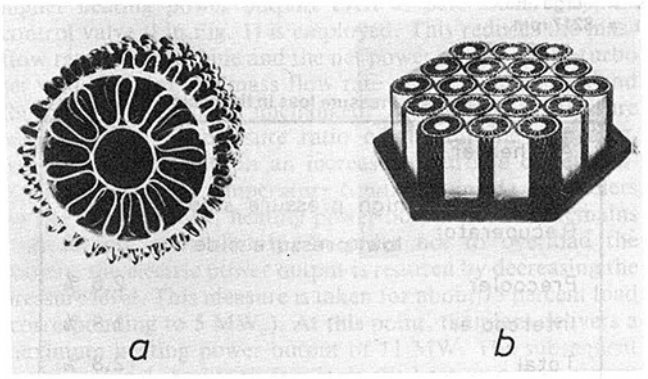

Fig. 6 Corrugated strip fin tubes

(*a*) single piece
(*b*) bundle piece

side, the temperature rise of the working medium in the heat exchanger is 300°C and in the air heater 255°C. According to Table 1, the working medium is heated on the HP side from 125 to 425°C and cooled on the LP side from 445 to 146°C. This corresponds to a temperature difference of 20°C between the HP and LP air or to a coefficient of heat utilization of 93.75 percent, if this value is calculated from the temperatures of the heat exchanger. For an overall assessment, it is also necessary to take into account the pressure losses on the HP and LP sides of the heat exchanger. These amount to a total of 3.6 percent (Table 4).

To achieve a simple, compact design, the heat exchanger has been fitted with corrugated strip fin tubes [7]. Figure 5 shows longitudinal and cross sections through a corrugated strip fin tube, and Fig. 6 is a photograph of a finned tube section. The LP air flows inside the annular space, a, (Fig. 5) between the inner wall of tube b and the outer wall of tube c. The HP air flows in counter current through the annular space, d, limited by the outer wall of tube b and the inner wall of the profiled triangle bars, e, placed in the gaps. The tube b is spirally wound with corrugated steel strips, f and g, inside and outside, and the strips are hard soldered to the inner and outer walls of tube b. Brazing is done inductively under a protective gas atmosphere. The tube c is closed and not exposed to air flow so that it does not participate in the heat exchange. The fins are manufactured from 5-mm wide steel strips. On the HP side they have a uniform thickness of 0.35 mm and on the LP side their thickness is chamfered along the direction of flow from 0.24 to 0.5 mm. By the staggered arrangement of the fins (Fig. 6(*a*)) the favourable heat transfer coefficients, characteristic for a not fully developed flow, are obtained.

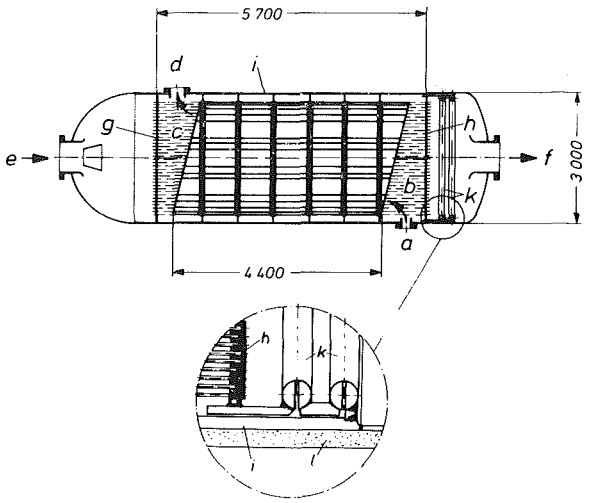

Fig. 7 Heat exchanger with corrugated strip fin tubes:

a = HP inlet
b,c = region of bundles
d = HP outlet
e = LP inlet
f = LP outlet
g,h = tube plate
i = outer plate
k = torus expansion joint
l = heat insulation
Dimensions in mm

The tubes are arranged in an equilateral triangle. To avoid bypass flow, it is necessary to fill up the space between the externally finned tubes b with profiled triangle aluminium bars. Nineteen corrugated strip fin tubes each make a bundle (Fig. 6(*b*)), having an unfinned tube connection at either end. A longitudinal section through a heat exchanger fitted with 4368 corrugated strip fin tubes is shown in Fig. 7. HP air enters the heat exchanger at a; it is deflected in the tube bundle end area b, it flows through the active finned external space (d in Fig. 5) 4400-mm long, it is again deflected in the area of tube bundle, c, and it leaves the heat exchanger at d. LP air enters the heat exchanger at e, it flows through the internally finned annular spaces (a in Fig. 5), and it leaves at f. The tube bundles are rolled in the left tube plate, g, and clamped by screwed joints in the right tube plate, h. The tube plate, g, is welded to the external shell, i. The tube plate, h, on the opposite end is mounted movably with 2 torus expansion joints, k. The outer liner, i, is enveloped by a heat insulation, l. This compact-sized corrugated-strip-fin-tube heat exchanger has relatively short tube lengths and connections. It has fulfilled all expectations without trouble.

Coolers. Both the precooler and the intercooler are divided into a heating part and a cooling part (Fig. 1). The heat exchanging surfaces consist of standard tubes which are internally smooth and externally finned. Heating water and fresh water, respectively, flow through the tubes in a cross-counter current to the working air which flows along the finned side of the tubes in the cooler longitudinal axis direction. Externally finned tubes were chosen because the coefficients of heat transfer are remarkably different on the water and air sides. The heat exchanging surfaces are divided into several equal-sized bundles. The precooler has nine bundles in the heating part and three bundles in the cooling part. The intercooler has four bundles in the heating part and three in the cooling part. Each bundle consists of 608 (38 × 16) tubes, having an inner diameter of 16 mm and an outer diameter of 18 mm. The finned outer diameter is 32 mm and the finned length is 1750 mm. Both the tubes and fins are of copper, the fins are soft soldered onto the tubes. The heat exchanging surface of one bundle including the fins is 3725 m^2. The bundles are connected to each other by short tubes on

Table 5 Main data of the radiation part

WORKING AIR (design point)	
Inlet temperature	517 °C
Outlet temperature	680 °C
Inlet pressure	31 bar
Pressure loss	3.8 %
Mass flow rate	74.07 kg/s
Thermal power	13.5 MW
Thermal power (max.)	15.8 MW
TUBE CAGE	
Number of tube panels	8
Number of tubes per panel	40
Total tube number	320
Tube material	X 8 CrNiMoNb 16 16
Irradiated tube length	10.15 m
Tube outer diameter	32 mm
Tube wall thickness	3.25 mm
Spacing ratio	1.62
Distance from wall	100 mm

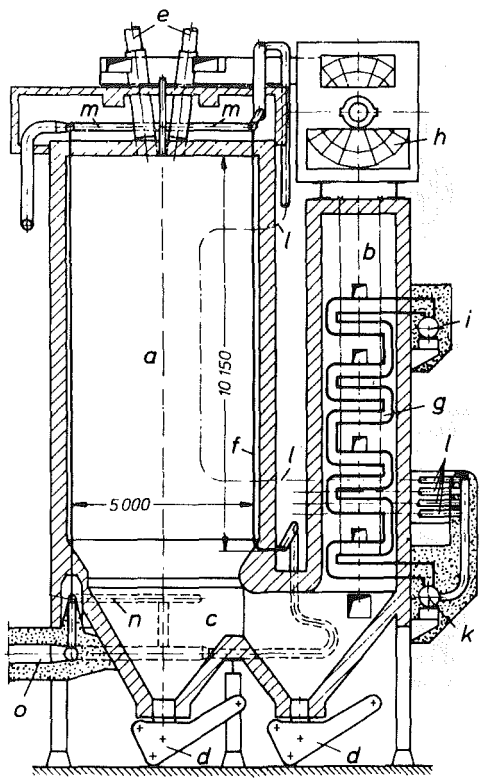

Fig. 8 Section through the coal fired air heater:

a = combustion chamber
b = convection part
c = gas reversal pass
d = wet ash extractor
e = burners
f = tubes of the radiation part
g = tubes of the convection part
h = air preheater
i = inlet header, convection part
k = outlet header, convection part
l = connecting pipes
m = inlet header, radiation part
n = outlet header, radiation part
o = double shell hot air pipe
Dimensions in mm

the water side. At the top and bottom of the tube sheets water chambers have been fastened. The upper tube sheets, from which bundles are suspended, are bolted into the frame of the cylindrical casing (outside shell) flattened on the top. After loosening of these bolts, the individual bundles can be vertically lifted by crane for cleaning. The tubes and deflection channels have been amply sized so that the heating water and fresh water need not be of great purity. The bundles can be easily cleaned. This cleaning is performed every year at the time of the annual inspection and overhaul of the heating and power plants (July/August).

The return water from the heating network is heated in the precooler from 40 to 140°C and in the intercooler from 40 to 76°C. This heating water is stored in two hot water tanks of 200 m^3 capacity each from where it is pumped into the heating network at a temperature level of 100°C. Fresh water enters the cooling part of the cooler at 15°C and is heated by 25°C. It is released to the river at 40°C.

Air Heater. The air heater plays a role similar to the boiler of a steam turbine plant. The transmission of heat from fuel to working medium is indirect, i.e., through heat transfer surfaces by radiation and convection; the combustion gases do not come into contact with the turbine and heat exchanger. Although the external structure of the air heater as well as the firing equipment and other auxiliary installations are similar to those of a boiler, it differs essentially from the latter and can best be compared to a direct fired superheater. It is generally of an U-pass, vertically arranged design [3, 4].

Figure 8 shows a section through the pulverized coal fired air heater at Coburg. The heater has for the design point a fuel power input of $\dot{Q}_f = 23.58$ MW and transfers a total power to the working medium of $\dot{Q}_{he} = 20.87$ MW. If a heating power output of $\dot{Q} = 16$ MW and an electric power of $P_{max} = 6.6$ MW are demanded, then $\dot{Q}_{f,max} = 27.12$ MW, and $\dot{Q}_{he,max} = 24.0$ MW (see Table 3).

The heater consists of the down-fired combustion chamber, a, and the upward pass, b. The two passes are connected at the bottom by a gas reversal duct, *c*. The ash is removed by the wet-ash extractors, d. Four burners, e, are arranged in the roof of the octogonal combustion chamber. The furnace is completely lined with tubes which constitute the radiant part, f. The convection part, g, is located in the upward pass. The coal/air mixture is ignited and burned in the combustion chamber. After delivering heat to the radiant part, the burned gases supply further heat to the convection part and the combustion air preheater, h. Then the flue gases are cleaned and led into the stack [4].

The working air – after being preheated in the heat exchanger (d in Fig. 1) – flows into the inlet header, i, and from there to the coiled tubes of the convection part in cross counter-current to the burned gases. Part of the circulating air is tapped off from the header, i, for cooling the support tubes of the convection part and protecting the lowest, most highly stressed tube coils. The tubes of the convection part including the support tubes and the protective loop lead to the common outlet header, k. From there the working air passes through the relatively thin and flexibily installed external, unheated pipes, l, to the inlet header, m, located above the combustion chamber roof. This header consists of eight individual segments. Each segment is attached to counterweights (not shown), and can move relatively freely due to flexible connecting pipes. The working medium flows from the header, m, downward in the tubes, f, parallel to the flue gases being raised to the final temperature of 680°C by radiant heat from

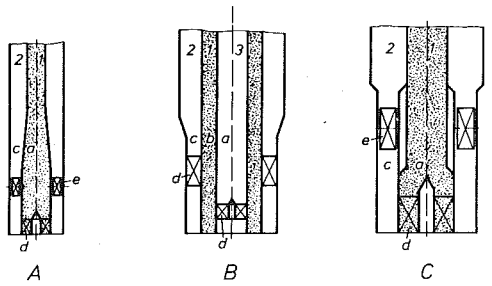

Fig. 9 Pulverized coal burner:

a = inner tube
b = innler annular tube
c = outer annular tube
d = fixed impeller
e = adjustable impeller
1 = primary air with pulverized coal
2 = secondary air
3 = tertiary air
A = RAVENSBURG burner
B = COBURG burner (first version)
C = COBURG burner (second and final version)

the burned gases. The circulating air is collected in eight outlet headers, n, from where it flows inside a double concentric hot air pipe, o, to the turbine. The outlet headers are the fixed points of the combustion tube lining. Thermal expansion of the tubes is taken up by the movable inlet header m mentioned above.

The design of the combustion chamber is rather difficult since many different, interrelated factors must be taken into consideration. These depend on the composition of the coal and the general layout of the cycle. For the combustion chamber austenitic materials are required. The higher the inlet temperature of the turbine, the better the material must be. The pressure drop of the working medium has also a decisive influence on the amount of tubing required and consequently on the cost of the air heater. The greater the internal heat transfer coefficient, the more the surface thermal loading can be increased, or the heating surface can be reduced without exceeding the permissible wall temperature of the tubes.

The most important data of the radiation part are set out in Table 5. When the working air enters the tubes of the combustion chamber, it has a temperature of about 517°C and a pressure of about 31 bar. Parallel to the flame, it is heated to 680°C mainly by radiation from the hot flue gases. With an air mass flow rate of 74.07 kg/s, the heat transfer to the working medium in the radiation part is 13.5 MW (maximum 15.8 MW). The relative pressure drop of the working air is 3.8 percent.

The tube cage of the combustion chamber consists of eight individual panels. The inside width of the tube cages is 5000 mm (Fig. 8). Each panel has 40 parallel tubes so that the tube cage consists of 320 tubes. The tubes have an outer diameter of 32 mm and a wall thickness of 3.25 mm. The radiated length is 10,150 mm, and the ratio of tube axis distance to outer diameter, the so-called spacing ratio, was fixed at 1.62. The distance between tube axis and combustion chamber inner wall is 100 mm. The tubes are made of high-alloy austenitic material X 8 CrNiMoNb 16 16.

Pulverized coal and combustion air are fed nearly axially into the combustion chamber. The four roof burners produce flame columns almost parallel to the axis of the combustion chamber. It has the advantage that roof firing produces a central flame core which ensures substantially uniform radiation on the wall. This effect is enhanced by a combustion chamber, usually of octogonal cross section, in which the distance from the flame surface to the tube walls is almost constant.

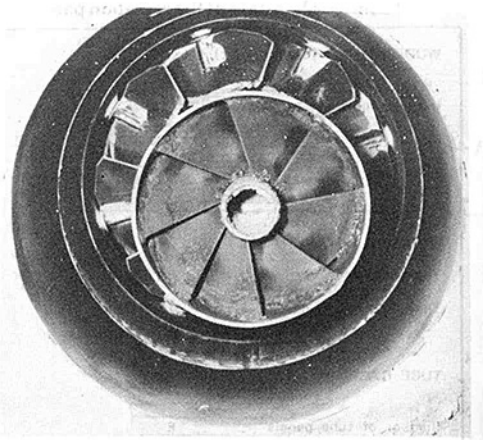

Fig. 10 View of the pulverized coal burner

Correct design of the combustion chamber requires knowledge of the combustion process. The combustion time is usually between 1.3 and 1.8 s. It depends, in general, on the fineness of grinding (percentage retained on the sieve) of the raw coal and on the turbulence of the gas-air mixture. The finer the grinding, the more rapid the combustion. Increased turbulence reduces the combustion time to the same extent as it is prolonged in the reverse case. The burner design is also of great importance: it must ensure intimate mixing of pulverized coal and air.

The plant at Coburg does not have a combustion chamber of the type used at Ravensburg, which has a relatively large ignition muffle [1, 3, 4]. For this reason the burner design had to be modified. The burner of the Ravenburg plant (type A, Fig. 9) consists of an inner tube, a, and an annular tube, c. The primary air containing pulverized coal flows through the inner tube. An impeller, d, (fixed installation at the tube end) gives a left-rotating swirl to the primary mixture at the entrance of the combustion chamber. Secondary air flows in the annular tube and receives a clockwise swirl from eight adjustable impeller blades, e. This results in an intimate mixing of the combustion air and the pulverized coal which in turn produces a stable flame. To achieve similar results at part loads the swirl imparted to the secondary air has to be increased.

At the Coburg plant, which had dropped the ignition muffle, it became necessary to obtain a more rapid ignition and a shorter burn-up time of the pulverized coal. Here the burner (type B, Fig. 9) consists of three tubes, a, b, and c, fitting one into the other. Tertiary air flowing through the inner tube, a, receives a left-rotating swirl by a fixed impeller, d. The primary mixture (pulverized coal and carrier air) enters the combustion chamber through the annular tube, b, without rotation. Secondary air flowing through the outer annular tube, c, gets a clockwise swirl from the fixed impeller, d. This type of burner (B) did not fulfill its expectation for two reasons. First, the flame became unstable at part loads below 80 percent. It was only possible with the help of an additional gas-fired ignition burner, installed centrally in the combustion chamber roof, to achieve part loads. Secondly, it became apparent that the flue gas temperatures at the end of the combustion chamber in the reversal duct exceeded the permissible values significantly. During the rebuilding of the plant in 1961/62, the B-type burners were also replaced by C-type burners (Fig. 9), which are similar to those of the A-type. The C-type burner consists of an inner tube, a, through which the primary mixture flows, and an annular tube, c, for the secondary air. Here, too, there is a fixed impeller, d, at the lower end of the inner tube which produces a clockwise swirl with its eight blades. There is an adjustable impeller, e, with

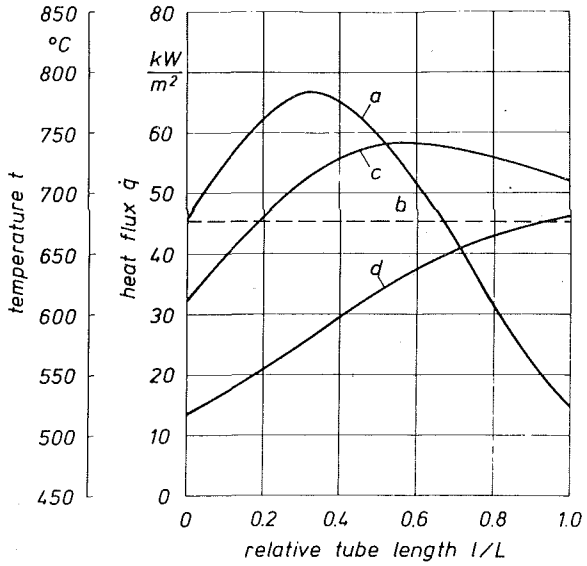

Fig. 11 Distribution of heat flux and temperatures of wall and working air versus specific tube length irradiated:

a = heat flux
b = mean heat transferred by unit surface area
c = max. tube wall temperature
d = temperature of working medium

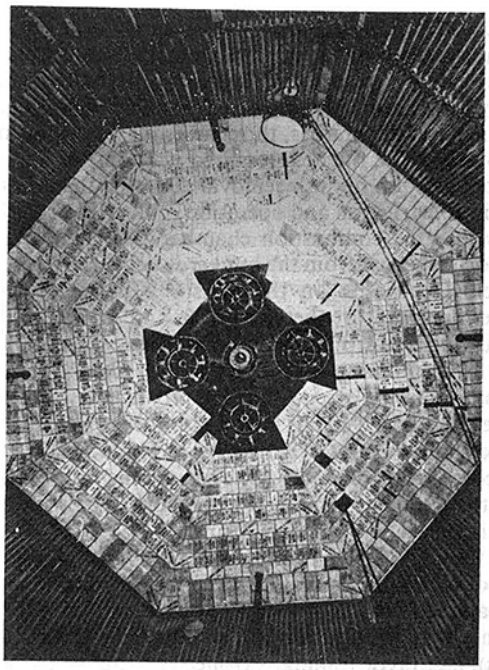

Fig. 12 View of the roof of the combustion chamber

ten blades in the annular tube to impart a left-rotating swirl to the secondary air. Figure 10 shows an installed burner of Type C, with which it is possible to obtain an optimum combustion for all load ranges with blade positions between 15 and 50 deg measured against the horizontal. The flue gas temperatures at the end of the combustion chamber reach their permissible values (1000–1050°C) without causing any slagging. Part load can be implemented down to about 30 percent without sustained firing.

The tube lining of the combustion chamber has to accept the heat radiated from the flame and to deliver it to the working air. Further, the combustion chamber wall consisting of ceramic materials must be protected from flame radiation so that temperature conditions behind the tubes are tolerable and no damage to the brickwork occurs. To achieve this, the tubes in front of the combustion chamber wall are placed with a spacing ratio of 1.62. This greater part of radiation passing through the gaps between the tubes is reflected from the wall onto the rear side of the tubes. This distributes the radiation around the periphery of the tubes and greatly reduces thermal stress due to nonuniform heat absorption [8, 9].

The gas temperatures attained in combustion correspond to definite amounts of heat radiated to the tube-lined wall of the combustion chamber. This quantity of heat related to unit area gives the heat flux density, $\dot{q}$, which varies over the combustion path. A quantity which has a great influence on the final temperature of the gases at the combustion chamber outlet is the "shape-factor" of the furnace. This is the ratio of surface to volume of the combustion chamber and depends on its size and shape [10]. The shape factor for the Coburg combustion chamber is 0.98.

In the chamber the working medium flows in the same direction as the flue gas because this leads to the lowest tube wall temperatures. The temperature of working air reaches a maximum at the end of the combustion chamber, Fig. 11. Here the heat flux, $\dot{q}$, absorbed by the working medium and referred to the tube surface area (curve a) is plotted against the relative tube length l/L, with l being the tube length coordinate and L the total irradiated tube length. Curve b (dotted line) gives the mean heat flux, and curve c shows the maximum tube wall temperature due to the irradiation pattern at the tube vertex facing the combustion chamber axis. In curve d the temperature of the working medium is shown as a function of the irradiated tube length. As mentioned before, the working medium enters the radiation part at $l/L=0$ with a temperature of about 517°C. Here it absorbs a heat flux of approx. 45 kW/m^2, whereby the maximum tube wall temperature is raised to a value of about 612°C. With increasing tube length there is first a rise in working medium temperature, in the maximum tube wall temperature, and in the heat flux absorbed by the working medium. The latter reaches its maximum value of 67 kW/m^2 at $l/L=0.32$. At this point, the maximum temperature difference between tube wall and working medium occurs. The maximum tube wall temperature reaches its peak at $l/L=0.6$, where it amounts to a value of about 742°C. Hence the peak values of heat flux and tube wall temperature are not coincident. At the outlet of the radiation part the working medium reaches a temperature of 680°C. The maximum tube wall temperature at this point is still 710°C and the heat flux 15 kW/m^2. Generally, it can be stated that accelerated combustion with which temperature and heat flux maxima occur more towards the burner, gives lower tube wall temperature than a retarded combustion process.

A further quantity which affects proportioning of the tube heating surfaces is the permissible "pressure drop" in radiation and convection parts of air heaters. To obtain the highest possible heat transfer in the tubes of the radiation part its pressure loss must be much greater than that of the convection part. For economic reasons the radiant part of the air heater has pressure loss of 3.8 percent and the convective part 1 percent. The total pressure loss amounts to 4.8 percent related to the inlet pressure of the working air. With an air pressure at the air heater inlet of 31.3 bar, the drop is 1.5 bar. A greater pressure drop, which would further reduce the temperature of the wall materials, is prohibitive when considering the overall efficiency of the plant. If, for example, pressure loss in the air heater is increased by 1 percent, efficiency of the plant is reduced by about 0.5 percent (percentage points). This reduction in efficiency could be compensated by raising the turbine inlet temperature of the working fluid by about 7°C.

The Coburg plant obtains 50 percent coal from the Ruhr

district (Germany) and imports 50 percent from Czechoslovakia. The latter is cheaper, but it has a higher ash content. The mixed raw coal is ground in a pulverizing plant to a powder of grain size suitable for combustion. The higher the proportion of volatiles, the coarser may be the grinding of the raw coal. The fineness required is about the same as for steam boilers with dry ash removal. To keep the milling plant simple in construction and operation, pulverized coal is blown directly into the combustion chamber. With this method of operation, raw coal from the bunker is delivered to the mill by a feeder. Depending on the moisture in the coal, with a classifier temperature between 100 and 170°C, a specific initial temperature of mill drying air is required. This temperature is automatically controlled by drawing in an appropriate quantity of cold air for mixing with hot air. The prepared pulverized coal is blown into the furnace through the classifiers and burners. The picture in Fig. 12 shows the roof of the combustion chamber. One can see the four coal burners and in the middle the igniter which is operated with town gas and, if required, for sustained firing.

The fouling of the heating surfaces depends on the air heater design and is mainly caused by chemical composition of the applied coal and its ahs. Low fusion temperatures of the ash, high proportions of sodium and potassium salts (alkalis), etc. favor fouling. Erroneous firing methods, where the air heater is operated with too little excess air, also leads to slagging of the combustion chamber tubes. Fouling of the heating surfaces in the combustion chamber reduces the heat absorption and increases the burned gas temperature at the entrance of the convection part. There is then a risk of exceeding the permissible temperature for the tube material. To restrict fouling, the air heater plant is provided with soot blowers. Retractable rotating blowers are used for the combustion chamber, and fixed-position multinozzle blowers are used for the convection part.

Operating experience has shown that tubes in the radiation part have never reached the 100,000 hrs life limit, for which they were calculated according to the ASME boiler code or the German pressure vessel specification. Service life of about 50,000 hrs could be achieved when pulverized coal flames were concentrated in such a way that the bright flame did not touch the tubes and noncombusted glowing or liquid carbon particles were not thrown onto the tubes. Requirements of this nature can be fulfilled largely by an appropriate design of the burners. They are set up optimally when primary air with carbon particles and preheated secondary air with carefully adjusted swirl and counterswirl intensities can be injected into the combustion chamber. In this way complete combustion at the end of the combustion chamber and flue gas temperatures below the ash melting point can be achieved. In addition, the flame must neither touch the irradiated tubes nor recirculate in such a way that the combustion chamber is endangered by liquid slag.

Even if flame positioning and combustion chamber design are such that corrosion, erosion, and deposits can be largely avoided, there is still the question whether the intense unilateral flame radiation (particle plus gas radiation) does not by itself produce – even in unchanged tube dimensions – stresses that have been overlooked so far and which limit the service life of the tubes. Tube wall thickness was calculated according to the ASME boiler code or German pressure vessel specification, i.e., dimensioned only in regard to interior pressure of the working medium. Creep strength in time is assumed as a value taking into account maximum material temperature at the exterior layer of the tube directly exposed to the front of the flame and the desired life expectancy. The safety factor is only dependent on the material.

The tubes in the combustion chamber were calculated according to this method. In the meantime, a procedure has been developed [8, 9] taking into account mechanical stresses in addition to stresses due to heat transfer phenomena. These heat stresses are produced by temperature gradients necessary for heat transfer in tube walls causing different dilations within the tube section. The largest amount of heat transfer by radiation takes place on the tube side facing the combustion chamber, while heat stress on the tube side facing the brick wall is relatively small. In addition to radial temperature gradients, such gradients in circumference and along the tube axis are also occurring.

Stresses caused by working medium pressure and heat stresses can be calculated separately from one another and superimposed. According to the deformation energy hypothesis, three-dimensional stress states can be reduced to a one-dimensional one. The result is a total stress in the sense of a reference stress $\sigma_{ref,t}$, dependent on the tube radius, segment angle, and tube length. In order not to overstress the tube material the reference stress must not exceed at any point of the tube cross section the allowable stress σ_{al}. Allowable stress is creep strength which depends on the temperature, expected service life, and a safety factor. As a comparative value for local stress the stress coefficient $\beta = \sigma_{ref,t}/\sigma_{al}$ is introduced. In every tube cross section there will be a maximum stress coefficient β_{max}. Its value is a function of working medium pressure and heat flux distribution. The optimum heat flux distribution (Bammert-criterion) will be reached for $\beta_{max} = 1.0$ for the entire radiated tube length [4, 8, 9].

When comparing the reference stress and the allowable stress, the life time of the tubes is less than 50,000 operating hrs. In reality, they reached a life time of a little more than 50,000 hrs. This contradiction can only be explained that calculated stresses – assuming linearly elastic behavior – are too large (as expected) and decreased by plastic deformation. It is understandable that this decrease is accomplished by shifting of stresses.

There are also other reasons why real occurring stresses can not be found out completely and why one is depending on experience especially in this case. The tubes in the combustion chamber suffer emaciation from corrosion and erosion, swelling by thermal overload, and strengthenning by carburization. These stresses work partly diametrically opposed to each other. They can be limited to a large extent if a stable and centrally located flame is produced inside the combustion chamber. Special attention has to be given to adjusting the burners when changing to different kinds of coal.

Conclusion

The cogeneration plant at Coburg has operated successfully ever since its refurbishing in 1962. Working in continuous operation, it achieves over 7000 operating hrs annually. This high availability is, to a great extent, due to meticulous supervision of the plant and its thorough inspection and overhaul once a year (July and August).

Special attention is being given to the tubes of the radiation part of the air heater. Thus, for example any changes in the diameter and wall thickness of the tubes are measured ultrasonically along the entire tube length; the extent of the emaciation occurring in the upper third of the combustion chamber and swelling occurring in the lower third are being recorded. The emaciations of the wall thickness occur on the side of the tube facing the flame due to corrosion (reducing atmosphere) and erosion (turbulent solid and liquid carbon particles). The swelling results from excessive flue gas temperatures at the end of the combustion chamber [4] which usually occur at continued overloads ($P_{max}, \dot{Q}_{f,max}$, Table 3). The tubes in the tube plates of the heat exchanger are rerolled at the time of the annual inspection. Small bypass flows cannot be avoided owing to increasing material embrittlement. The coolers only need cleaning once a year. For the turbo set it is necessary to check the bearing clearance,

tooth surface wear of the gearbox, etc.. Instability during operation and rotor vibrations can be avoided if limiting parameters gained through experience are adhered to. The blading, labyrinths, etc., have not suffered any damage to date.

A map of characteristic curves – once established for a closed-cycle gas turbine – enables the operator to follow changing demands in electricity and heating at an optimum (Fig. 4). In the first few years of operation, the turbine inlet temperature was raised above the design point in order to obtain a higher power generation efficiency (increased ratio of power-to-heat, $P/\dot{Q}$). Later, the growing demand in heating due to the oil crisis has led to increasing the compressor inlet temperature without decreasing the turbine inlet temperature, although both measures – either singly or jointly – increase the ratio of heat-to-power, $\dot{Q}/P$. In case of a higher heating power and low electric power demand, the bypass valve is operated.

The plant is in good working condition and can successfully operate for a few more years. The reduction of individual efficiencies due to aging (rough surfaces of flow channels, uncontrollable minor by-pass flows etc.) is insignificant and manifests itself in a correspondingly higher heating power output. Also, the economical operation of the plant is assured in the future, because the price of a kilowatt-hour for heating is about 60 to 70 percent of the price of an electric kilowatt-hour, and depreciation and interest payment have no book value any more.

The heating power is delivered to the consumers with a supply water temperature of 100°C. This power is evaluated according to the quantity of the return water based upon a temperature of 40°C. Large consumers, utilizing the heat in addition to the operation of air-conditioning and refrigeration units, succeed in obtaining even lower return water temperatures. This is an additional gain for them (department stores, banks, etc.) which, in turn, acts as an incentive for small consumers to strive to achieve low return water temperatures also.

References

1 Bammert, K., C. Keller, and H. Kress, "HeiBlufturbinenanlage mit Kohlenstaubfeuerung and Heizwärmelieferung," *BWK*, Vol. 8, No. 10, 1956, pp. 471–478.

2 Bammert, K., and C. Keller, "MeBergebnisse der ersten kohlenstaubgefeuerten HeiBlufturbinenanlage für Stromerzeugung and Heizwärmelieferung," *BWK*, Vol. 12, No. 2, 1960, pp. 62–64.

3 Bammert, K., and G. Groschup, "Status Report on Closed-Cycle Power Plants in the Federal Republic of Germany," ASME *Transactions*, Vol. 99, No. 1, 1977, pp. 37–46.

4 Bammert, K., "Long-term Experience With Coal-Fired Heaters in German Closed-Cycle Air Turbine Plants," *Atomkernenergie/Kerntechnik*, Vol. 38, No. 4, 1981, pp. 241–256.

5 Bammert, K., J. Rurik, and H. Griepentrog, "Highlights and Future Development of Closed-Cycle Gas Turbines," ASME *Transactions*, Vol. 96, No. 4, 1974, pp. 342–348.

6 Bammert, K., "Das Verhalten einer geschlossenen HeiBluftturbinenanlage als Heizkraftwerk bei veränderten Betriebsbedingungen," *Konstruktion*, Vol. 8, No. 11, 1956, pp. 443–452.

7 Haas, W., "Air Heater, Heat Exchanger, and Cooler for CCGT Plants," Special Edition of the *Escher Wyss News* for the Annual Meeting of the ASME, Zurich/Switzerland, 1966, pp. 22–31.

8 Bammert, K., and P. Seifert, "Tube Stresses in the Radiation Part of Solar Receivers and of Conventionally Fired Heaters," ASME Paper No. 81-GT-200, 26th Annual International Gas Turbine Conference. Houston, Texas, Mar. 1981.

9 Bammert, K., "The Thermal Load of Tubes in Radiation Heaters," *Forschung im Ingenieurwesen*, Vol. 48, No. 5, 1982, pp. 160–165.

10 Bammert, K., Th. Geissler, and E. Nickel, "Pulverized Coal Firing in Closed-Cycle Gas Turbines," Sixth World Power Conference, Melbourne, 1962, Paper No. 9. Australian National Committee 7, 1963, pp. 1–31.

J. W. Baughn
Professor.
Mem. ASME

A. A. McKillop
Professor.
Mem. ASME

K. Treleven[1]
Graduate Student.

Department of Mechanical Engineering,
University of California, Davis
Davis, Calif. 95616

An Analysis of the Performance of a Gas Turbine Cogeneration Plant

A computer program has been developed to analyze the thermodynamic performance of a cogeneration plant. Results of parametric studies using this program include partial load operation, inlet air cooling, and supercharging. Fuel chargeable to power, a previously used figure-of-merit, is used to evaluate the performance for partial-load operation. Fuel chargeable to incremental power and differential steam efficiency are two new figures-of-merit for evaluating other design alternatives: the former for incremental increases in electric power output, the latter for incremental increases in steam output at the expense of electrical power output.

Introduction

In this paper, cogeneration is considered to be the simultaneous production of electrical energy and steam from the same facility, although we are aware of cogeneration's broader definitions, which recognizes its potential for energy conservation in a variety of industrial processes [1, 2, 3]. While either type of energy can be considered to be the primary reason for the production of energy, Williams [4] suggests that practical problems limiting the transportation of steam confine cogeneration to locations where steam is needed and that electrical energy is the by-product. In this paper we describe and analyze a cogeneration plant that was built at the University of California at Davis (UCD) in 1977 [5]. A computer program has been written to simulate the thermodynamic performance of this plant. With this program we have analyzed the effect of two components on the power output and plant efficiency: a supercharger at the gas turbine inlet, and an inlet air cooling system. We have also examined the performance of the plant when it is operated at partial output, that is, when its output is deliberately decreased by reducing the turbine inlet temperature.

A key contribution of this paper is the development of two new figures-of-merit that describe quantitatively the unit change in performance of the plant for design alternatives and off-design operation. The fuel chargeable to power (FCP) is a common figure-of-merit [2] and is used here to examine the effect on partial output operation. For design alternatives such as supercharging and inlet cooling, we define and use, respectively, two corollaries of this expression: fuel chargeable to incremental power and differential steam efficiency; these new figures-of-merit are useful for the examination of design alternatives or operating modes which change the steam and/or electrical output.

The paper includes a brief description of the plant, a flow chart of the computer program with the pertinent equations, and results and discussion of the parametric studies of the plant.

Description of the Plant

The cogeneration plant at UCD was built in 1977 to deliver 3 MW of electrical power and 9070 kg/hr (20,000 lbs/hr) of 1.14 MPa (150 psig) steam to the campus. Since the minimum electrical and steam requirements of the campus are 8 MW and 10,000 kg/hr, respectively, this system alone cannot provide for the base load of the campus and thus is operated in conjunction with an existing central steam plant in an adjoining building.

A diagram of the UCD cogeneration system is shown in Fig. 1(*a*). It consists of a gas turbine directly coupled to a generator and an unfired waste heat recovery boiler that produces steam. As discussed below, unique features of this plant include: a turbine inlet air supercharger; a special heat-recovery system which extracts energy from some components in order to heat make-up water for the main boiler plant; and an inlet air cooler that uses chilled water from an existing plant. By following the diagram in Fig. 1, we can trace the three fluid flows of the system.

Air and Exhaust Gases. Air enters through silencers and filters, passes over the main cooling coils, and divides into two streams. One stream is used to cool the generator. Part of its energy is then transferred by heat exchanger to the make-up water recovery system; it then may be further cooled by a chilled water heat exchanger before being exhausted into the plant building at 22°C.

The second, larger flow of air, passes through a supercharger, enters the Allison 501 gas turbine where it is further compressed, is combusted with diesel fuel, and is expanded in the turbine whose shaftwork is transferred by way of a gearbox to the generator.

The combusted air - exhaust gas - from the turbine enters the waste heat recovery boiler, comprised of an evaporator and an economizer section, and a recirculation tank, as shown

[1] Now at Pacific Gas and Electric Company, San Francisco, California

Contributed by the Power Division for publication in the JOURNAL OF ENGINEERING FOR POWER. Manuscript received at ASME Headquarters March 24, 1983.

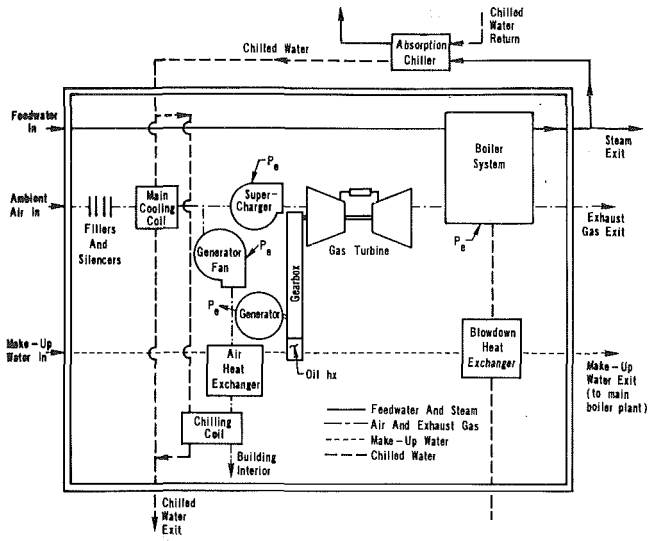

Fig. 1(*a*) Flow diagram of cogeneration plant

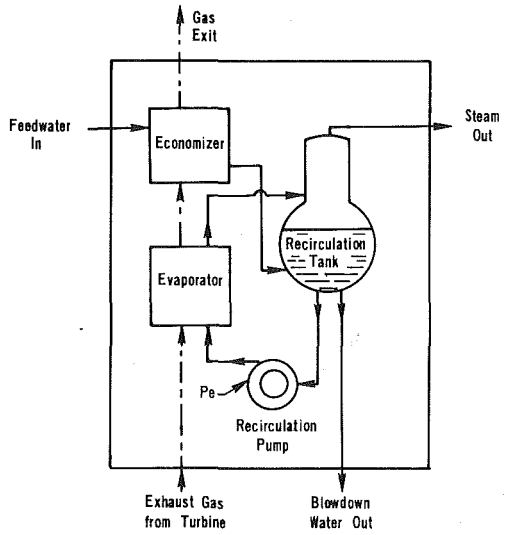

Fig. 1(*b*) Flow diagram of evaporator, economizer, and recirculation system

in Fig. 1(*b*). The exhaust gas finally passes through a silencer and is emitted from the stack at about 154°C.

Feedwater and Steam. Feedwater enters the cogeneration plant from the main boiler plant at 116°C. It flows through the economizer in which its temperature is raised to 181°C and then enters a recirculation tank. Water from this tank is continuously pumped through the evaporator, where about 10 percent of it is turned to steam at 1.14 MPa (150 psig) on each pass. The saturated steam is separated from the water in the tank and is passed back to the main boiler plant for distribution to the campus. Sedimentation in the tank is continuously removed by blowdown. Part of the energy in the blowdown water is transferred by a heat exchanger to the make-up water loop.

Make-Up Water. Make-up water for use in the central steam plant boilers (in the adjoining building) is preheated in the cogeneration plant by a heat recovery system. Water enters at ambient temperature and passes through three heat exchangers, picking up heat from hot air coming off the generator, the hot oil recirculating in the gearbox, and the hot blowdown water drawn off the boiler. The total temperature rise in make-up water passing through the system is typically 39–45°C for a fixed mass flow rate of about 1.4 kg/s (3 lbs/s).

Computer Program

The computational procedure used in the computer program used to simulate the thermodynamic operation of the plant is given in Appendix A, together with the pertinent equations solved in each step. The initial conditions read into the program include ambient conditions, component efficiencies and effectivenesses, and operation parameters such as turbine shaft speed, turbine inlet temperature, the amount of supercharging, the lower heating value, h_c, of the fuel, and pressure drop through the filters and silencers. Calculations are based on the following:

(*a*) Air was assumed to be a perfect gas for the purpose of calculating density and changes in enthalpy.
(*b*) Base enthalpy for air and gaseous products was set at 298 K (537 R).
(*c*) Performance characteristics of the Allison 501 gas turbine were digitized from the manufacturer's performance curves [6].
(*d*) The volumetric flow rate of air used to cool the generator ($\dot{V}$) was specified by the designer [5] and was used in all calculations.

Nomenclature

AF = air-to-fuel ratio
c = specific heat
$\dot{E}$ = useful energy rate
h = enthalpy
h_f = enthalpy of saturated liquid
h_v = enthalpy of saturated vapor
$h(t_{ml})$ = enthalpy of air based on feed water inlet temperature
$\dot{H}$ = total enthalpy rate
$\dot{m}$ = mass flow rate
p = pressure
P = electrical power
$\dot{q}$ = fuel energy rate
T = temperature
v = specific volume
$\dot{V}$ = volumetric flow rate of air in cooling of generator
ϵ = heat exchanger effectiveness or incremental efficiency
η = efficiency
η_i = isentropic efficiency

Subscripts

a = air
b = gear box
c = combustible fuel
d = blow down
e = electric
e = evaporator water
f = fan
g = generator
h = waste heat boiler
j = parasitic electric loads
k = chilling coils
l = main cooling coils
m = makeup water
n = net
o = motor
p = gaseous product
q = supercharger
r = recirculation
s = steam
t = turbine
T = total
v = saturated vapor
w = feed water
1 = inlet
2 = outlet

The chilled water needed for the main cooling coils and chilling coils is provided by a separate absorption chiller system. In charging the steam requirement necessary for its operation, a factor of 1 kg steam for 2.32 MJ was used; this value was obtained from the actual operations of the campus absorption system.

From boiler calculations, the effectiveness of the evaporator was found to be 0.95 based on design operation of the plant [5]. This value was kept constant in the off-design studies. Outlet feedwater temperature from the economizer was set at 5°C below the evaporation temperature to ensure that no boiling occurs in the economizer. The blowdown rate was specified in terms of the ratio $\dot{m}_d/\dot{m}_s$ and was taken to be 0.03 for this study. The calculation of the enthalpy change in the gaseous product was based on a variable specific heat

$$c_p = c_1 T + c_2 \tag{1}$$

where

$$c_1 = (1.622 + 5.444/AF)/1000$$
$$c_2 = 0.2195 + 0.2498/AF$$
$$T = \text{temperature in K}$$

This equation is a fit to values given in [7]. The power drawn by the recirculation pump was fixed at 6.27 kW (5.94 Btu's). The plant and computer program are described in more detail in [8].

Studies

The computer program discussed in the previous section was used to do a parametric study of the off-design operation of this cogeneration plant. Specifically, we studied three aspects: (*i*) reduction of turbine inlet temperature to produce partial loads; (*ii*) use of the main cooling coils; (*iii*) supercharging. To evaluate the effects of each on the plant performance, we established a base or design case for which the inlet conditions are specified in Table 1.

Partial Load. For these runs all inlet conditions conformed to the base case with the exception that the turbine-inlet temperature was varied between 1038°C and 705°C. In practice, this would be accomplished by reducing the fuel flow rate and the generator load for partial load operation.

Main Cooling Coils. For these runs the ambient inlet temperature of the cooling coils was set at 40.5°C, and the outlet temperature was varied from 40.5°C to 18.3°C. All other conditions conformed to the base case. The penalty paid for this cooling is a reduction in net steam output, since steam is required to run the absorption cooler.

Supercharging. For these runs the differential pressure across the supercharger was varied from $P_2 - P_1 = 0$ (i.e., no supercharging) to $P_2 - P_1 = 9.0$ kPa (36 in. water). Otherwise, base case conformance was maintained.

Results and Discussion

Table 1 contains results for the base case, that is, the rated or design capacity of the plant. The plant efficiency calculation contains two terms not included in the steam or electrical efficiencies: the gain in energy from the heat recovery system to the make-up water (positive) and the loss in the blowdown (negative). Since these two terms represent a net gain of energy, the plant efficiency will be greater than the sum of the steam and electrical, η, by 1.4 percent.

Partial Loading Operation. The results of varying the turbine inlet temperature are shown in Fig. 2, with the points at 983°C representing the values for the base case. As turbine inlet temperature is decreased, the steam and electrical outputs decrease almost linearly, because the mass flow rate of gaseous product, the pressure ratio, the isentropic efficiency and the specific heat depend only marginally on the turbine inlet temperature.

Table 1 Design operation

Inlet conditions

Tambient = 18°C—no cooling in the main cooling coils
p_{atm} = 1 atm
Δp in filters—1.74 kPa (7 in. water)
Supercharging—4.23 kPa (17 in. water)
Turbine inlet temperature—983°C
RPM of turbine shaft—14,500
Volumetric airflow rate through generator—0.0787 m^3/s (10,000 CFM)

Output results

m_{ns} = 9408 kg/hr (20,745 lbm/hr)
$P_{elect\,n}$ = 3007 kw
E = 9345 kw
η_s = 53.9
η_{elect} = 26.2
η_{plant} = 81.42

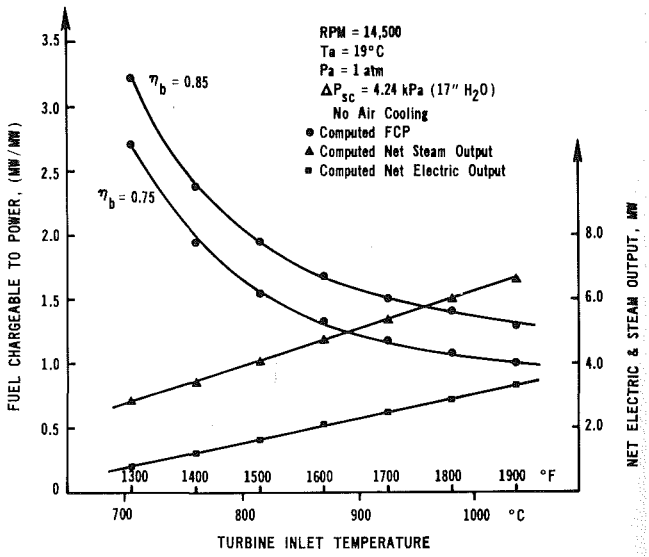

Fig. 2 The effect of reduced turbine inlet temperature on performance

To assess the performance of a cogeneration plant under partial load operation, it is necessary to compare the energy of the fuel consumed per unit of electrical power produced to that for a conventional power plant. Such a figure-of-merit is the fuel chargeable to power, FCP, which is defined as

$$\text{FCP} = \frac{\dot{q}_c - \dot{H}_{sn}/\eta_b}{P_n} \tag{2}$$

The numerator represents the difference between the fuel energy rate for the cogeneration plant and the fuel energy rate for a boiler plant producing the equivalent steam output, where η_b is the thermal efficiency of the conventional boiler plant. As used here, the denominator represents the net electrical output of the cogeneration plant. FCP is similar to the commercially used term heat rate in that it represents the additional fuel energy required per unit of net electrical power output beyond that required for the steam generation (assuming the steam would otherwise be generated by a conventional boiler). The heat rate for a conventional central utility plant would typically be 10,240 Btu/kw-hr, which is equivalent to a thermal efficiency of 33 percent. In this paper, we have made FCP dimensionless (if the conventional heat rate units in BTU/kW-hr are desired, multiply by 3413). FCP as here defined is shown in Fig. 2 as a function of turbine inlet

temperature. Except for $\eta_b = 0.85$ and for the lowest turbine inlet temperature (TIT) of 705°C, the electrical power would be produced more efficiently by the cogeneration unit than it would be by a conventional central utility plant. It is interesting to note that it is possible to have a value of FCP less than 1 without violating the First or Second Law of Thermodynamics since FCP is a function of the efficiency of the hypothetical boiler to which the cogeneration system is being compared.

Cooling Inlet Air. By cooling the inlet air, the density is increased, thereby also increasing the mass flow rate of the air. Since the net electric power produced is proportional to $\dot{m}_a$, it increases linearly with decrease in outlet temperature as shown in Fig. 3. On the other hand, steam must be expended in the absorption chiller system to produce the inlet air cooling effect; hence, a net decrease in steam production occurs under such conditions. The FCP, as shown in Fig. 3, indicates that even though its value increases with cooling, the overall process in still more efficient than that achieved by a conventional central utility plant with an equivalent FCP of 3 (a heat rate of 10,240 Btu/kw-hr).

Another criteria for evaluating the benefit of cooling is the efficiency of the differential increase in the electric power output. A second figure-of-merit is defined to examine the fuel chargeable to the incremental change in net electrical output. It is called fuel chargeable to incremental power.

$$\text{FC}\delta\text{P} = \frac{\Delta\dot{q}_c - \Delta\dot{H}_{n,s}/\eta_b}{\Delta P_n} = \frac{\Delta\dot{q}_c}{\Delta P_n}\left[1 - \frac{\Delta\dot{H}_{ns}}{\Delta\dot{q}_c}/\eta_b\right]$$

If we define the incremental efficiency for the differential electrical power as

$$\epsilon_e = \Delta P_n / \Delta\dot{q}_c \tag{2a}$$

and the incremental efficiency of the differential steam generated as

$$\epsilon_s = \frac{\Delta\dot{H}_{ns}}{\Delta\dot{q}_c} \tag{2b}$$

then

$$\text{FC}\delta\text{P} = \frac{1}{\epsilon_e}(1 - \epsilon_s/\eta_b) \tag{3}$$

While cooling will always produce increased electrical power output, (ΔH_n) may be either positive or negative. FCδP is shown in Fig. 3. These curves show that the incremental power produced by cooling would be thermodynamically more efficient if produced by a commercial central utility plant with an equivalent FCP of 3. Although FCδP is used here for inlet cooling, it is a useful parameter for any design alternative that increases the electric output (whether the steam output increases or decreases).

Supercharging. Since supercharging increases the inlet pressure to the turbine, it also increases the mass flow rate of air, hence net steam and electrical power output of the generator also increases. Countering the power increase will be an increased power consumed in the supercharging process. As shown in Fig. 4, when these factors are considered, the net electrical output decreases slightly. The effect of supercharging is assessed by examining a third figure-of-merit, the differential steam efficiency. It represents the ratio of the incremental heat rate of steam produced to the incremental net fuel heat rate necessary to produce the steam. Thus

$$\eta_{\delta s} = \frac{\Delta\dot{H}_{ns}}{\Delta\dot{q}_c - \dfrac{\Delta P_{ne}}{\eta_e}} = \frac{\Delta\dot{H}_{ns}/\Delta\dot{q}_c}{1 - \dfrac{\Delta P_{ne}}{\Delta\dot{q}_c \eta_e}}$$

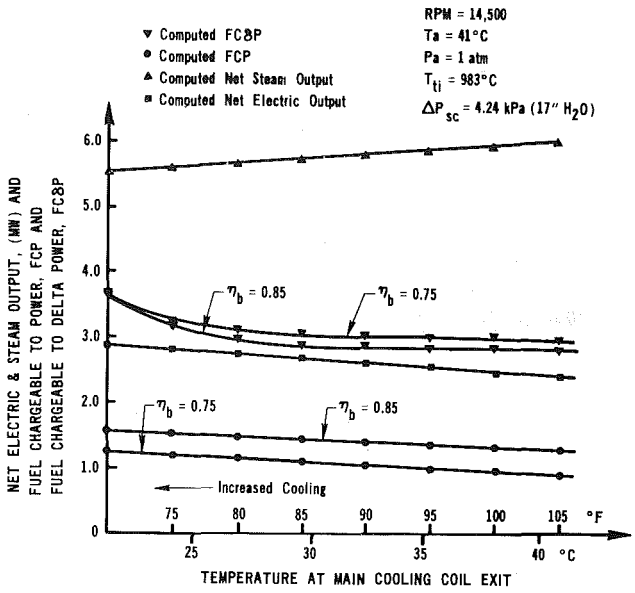

Fig. 3 The effect of inlet air cooling in performance

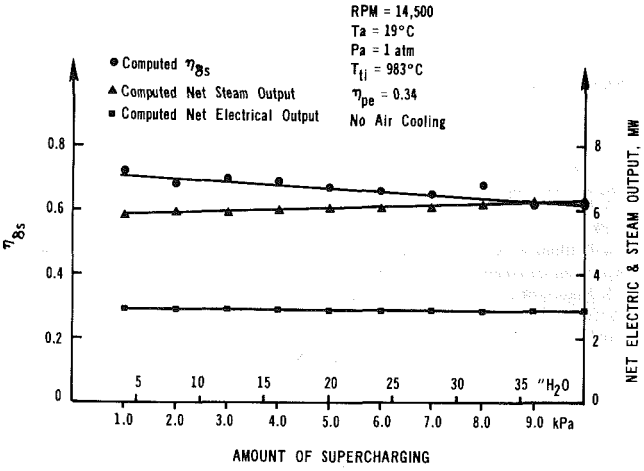

Fig. 4 The effect of supercharging on performance

where η_e is the plant efficiency of a conventional central utility plant. By use of equations 2(*a*) and 2(*b*), the foregoing equation can be written in the form

$$\eta_{\delta s} = \frac{\epsilon_s}{1 - \epsilon_e/\eta_e} \tag{4}$$

This figure-of-merit is shown in Fig. 5. The additional amount of steam produced is accomplished at a thermal efficiency lower than that for a conventional boiler plant.

It has been shown that, thermodynamically, cooling the inlet air or supercharging is not as efficient as obtaining the same incremental increase in electrical power or steam output from conventional plants. However, the total output of the plant is increased in each case. Whether cooling and supercharging are a viable option, then, becomes an economic decision.

Summary

A computer program has been developed to model the thermodynamic performance of a cogeneration plant. This program was used to make a series of parametric studies for (*i*) partial load operation, (*ii*) cooling the inlet air, and (*iii*) supercharging the air prior to entering the turbine. These

results can be useful in analyzing the economics of a cogeneration plant as discussed in [9].

Three figures-of-merit were defined to assess the performance of the plant for the above studies: fuel chargeable to power (FCP), fuel chargeable to incremental power (FCδP), and differential steam efficiency ($\eta_{\delta s}$). FCP has previously been used for studies of cogeneration. FCδP and $\eta_{\delta s}$ are new. By use of these figures-of-merit, it has been shown that, thermodynamically:

(*i*) The electrical power obtained in partial load operation with a reduced turbine inlet temperature is more efficient than that obtained from a conventional central utility plant.

(*ii*) Cooling inlet air temperature is less efficient than obtaining the same incremental power increase from a conventional central utility plant.

(*iii*) Supercharging produces an incremental increase in steam output less efficiently than the same steam obtained from a conventional boiler.

Acknowledgment

The major development of the computer program was done by students as a series of senior design projects under the direction of Professors Baughn and McKillop. The contribution of these students is gratefully acknowledged.

References

1 Wilson, W. B., "Conserving Energy via Cogeneration," *Mechanical Engineering*, Vol. 101, No. 8, Aug. 1979, pp. 21–27.

2 Barnes, R. W., and Wilkinson, B. W., *Cogeneration of Electricity and Useful Heat*, Boca Raton, CRC Press, 1980.

3 Chiogioji, M. H., *Industrial Energy Conservation*, New York, Dekker, 1979.

4 Williams, R. H., "Industrial Cogeneration," PU/CES Report No. 66, Princeton University, May 1978.

5 Martineau, C., Jr., and Boyen, J. L., "Grid-Connected, Electrical-Thermal (Cogeneration) Energy System for University of California, Davis, Calif.," ASME Paper No. 78-GT-134, Dec. 1977.

6 Engine Performance Presentation, Model 501-KB, Allison Gas Turbines, EDR 8064, Dec. 16, 1974.

7 Cohen, H., and Rogers, G. F. C., *Gas Turbine Theory*, 2d ed., Longman, 1972, p. 42.

8 Treleven, K., "Off-Design Operation of a Cogeneration Plant: A Thermodynamic and Economic Analysis," M.S. thesis, University of California, Davis, 1982.

9 Treleven, K., Baughn, J. W., and McKillop, A. A., "A Model for the Economic Analysis of Cogeneration Plants with Fixed and Variable Output," *Energy, the International Journal*, Vol. 8, No. 7, 1983, pp. 547–552.

APPENDIX A

Computation Procedure Used in Computer Program

The equations used in the computational procedure are summarized below. Absolute temperatures were used when appropriate. See the nomenclature for symbols and subscripts.

1 The supercharger outlet temperature is calculated from the pressure ratio using the isentropic efficiency, η_i

$$Tq_2 = T_{l_2}\left[\left(\left(\frac{P_2}{P_1}\right)^{0.286} - 1/\eta_i\right) + 1\right]$$

2 The turbine performance is obtained from a stored data set of $\dot{q}_c$, P_t, $\dot{m}_a$

$$\dot{m}_c = \dot{q}_c / h_c$$

$$\dot{m}_p = \dot{m}_a + \dot{m}_f$$

$$h_p = (\dot{q}_f + \dot{m}_a h_a - P_t)/\dot{m}_p$$

3 The supercharger power is obtained using the isentropic efficiency, η_i

$$P = \dot{m}_a \Delta h_a / \eta_i$$

4 The gearbox energy losses are calculated using

$$P_b = P_t \eta$$

$$\Delta \dot{H}_b = (1-\eta) P_t$$

$$h_{m2} = h_{m1} + \Delta \dot{H}_b / \dot{m}_m$$

5 The generator fan air flow rate and power are given by

$$\dot{m}_g = \dot{V}_g / v_a$$

$$P_f = P_o / \eta$$

6 The total flow rate and steam rate for chilling in the main cooling coils

$$\dot{m}_T = \dot{m}_g + \dot{m}_a$$

$$\dot{m}_s = 0.001 \Delta h_a$$

7 The generator energy losses are

$$P_g = P_b \eta$$

$$h_{w2} = (P_g - P_b)/\dot{m}_g + h_{w1}$$

8 An air heat exchanger energy balance yields

$$h_{a2} = h_{a1} + \epsilon(h_{a2} h(T_{n1}))$$

$$h_{m2} = \dot{m}_g \Delta h_a / \dot{m}_m + h_{m1}$$

9 The steam for the generator air cooling requirement is

$$\dot{m}_s = 0.001 \Delta h_a$$

10 The boiler mass flow rates of steam and feedwater are

$$\Delta h_p = \epsilon(h_p - h_p(t_{w1}))$$

$$\dot{m}_w = \dot{m}_p \Delta h_p / \left(h_{fg} / \left(1 + \frac{\dot{m}_b}{\dot{m}_s}\right) + h_f / \left(\frac{\dot{m}_s}{\dot{m}_b} + 1\right) - (h_f - h_{w1})\right)$$

$$\dot{m}_s = \dot{m}_w / (1 + \dot{m}_b / \dot{m}_s)$$

11 An energy balance for the blowdown heat exchanger gives

$$\dot{m}_d = \frac{\dot{m}_d}{\dot{m}_s} \dot{m}_s$$

$$h_d = h_f - \epsilon(h_f - h_{mb2})$$

$$\Delta H_d = m_b (h_f - h_d)$$

12 The recirculation pump power requirement is

$$P_r = \dot{m}_r P_o \eta_o$$

13 The computer output includes

$\dot{m}_{sn} = \dot{m}_{se} - \dot{m}_s - \dot{m}_{se}$; net steam flow rate

$\Delta H_{sn} = m_s (h_v - h_w)$; net steam energy rate

$P_{jn} = P_f + P_q + P_r$; parasitic electric load

$$\Delta \dot{H}_m = \dot{m}_m (h_d - h_m)$$

$E = P_g + \Delta H_m - P_{jn} - \Delta H_d + \Delta H_{sn}$; useful power

$P_n = P_g - P_{jn}$; net electrical output

$\eta = \Delta \dot{H}_{sn} / \dot{q}_f$ steam

$\eta = P_n / \dot{q}_f$ electrical

$\eta = E / \dot{q}_f$ plant

Development of the Transpiration Air-Cooled Turbine for High-Temperature Dirty Gas Streams

J. Wolf

S. Moskowitz

Curtiss-Wright Corporation,
Wood-Ridge, N.J. 07075

Studies of combined cycle electic power plants have shown that increasing the firing temperature and pressure ratio of the gas turbine can substantially improve the specific power output of the gas turbine as well as the combined cycle plant efficiency. Clearly this is a direction in which we can proceed to conserve the world's dwindling petroleum fuel supplies. Furthermore, tomorrow's gas turbines must do more than operate at higher temperature; they will likely face an aggressive hot gas stream created by the combustion of heavier oils or coal-derived liquid or gaseous fuels. Extensive tests have been performed on two rotating turbine rigs, each with a transpiration air cooled turbine operating in the 2600 to 3000°F (1427 to 1649°C) temperature range at increasing levels of gas stream particulates and alkali metal salts to simulate operation on coal-derived fuel. Transpiration air cooling was shown to be effective in maintaining acceptable metal temperatures, and there was no evidence of corrosion, erosion, or deposition. The rate of transpiration skin cooling flow capacity exhibited a minor loss in the initial exposure to the particulate laden gas stream of less than 100 hours, but the flow reduction was commensurate with that produced by normal oxidation of the skin material at the operating temperatures of 1350°F (732°C). The data on skin permeability loss from both cascade and engine tests compared favorably with laboratory furnace oxidation skin specimens. To date, over 10,000 hr of furnace exposure has been conducted. Extrapolation of the data to 50,000 hr indicates the flow capacity loss would produce an acceptable 50°F (10°C) increase in skin operating temperature.

Introduction

In 1976, the U.S. Department of Energy initiated a multiphase High Temperature Turbine Technology (HTTT) Program with the goal of developing to technology readiness, the turbine component of an industrial gas turbine capable of operation at gas stream temperatures of 2600°F (1427°C) and above. This turbine component, operating on coal-derived liquid or gaseous fuel, will provide electric utilities with an economically and environmentally viable alternative to the use of petroleum fuels or pulverized coal with stack scrubbers.

Analyses of both conventional and advanced combined cycles have shown that increasing the firing temperature and pressure ratio of the gas turbine can substantially improve both the gas turbine specific power output, and the overall power plant efficiency, even though there is a blade aerodynamic performance penalty when using air cooling. The results of one combined cycle study, shown in Fig. 1, clearly show the benefit to the cycle by increasing the gas turbine firing temperature above that of contemporary equipment. In this figure, the range of plant efficiency at a specific firing temperature is a function of the conversion efficiency of the gasifier and the gas cleanup system.

To successfully operate on coal-derived fuel, the high-temperature turbine must withstand, in addition to gas temperatures above the melting point of its constituent materials, entrained gas stream particulates and corrosive compounds which could otherwise severely degrade the

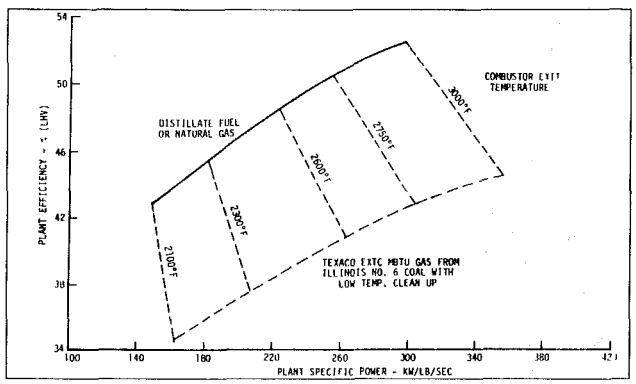

Fig. 1 Combined cycle power plant: 15:1 g.t. compressor pressure ratio optimized reheat steam cycle 2-1/2 in. HG condenser pressure

Contributed by the Gas Turbine Division of THE AMERICAN SOCIETY OF MECHANICAL ENGINEERS for presentation at the 28th International Gas Turbine Conference and Exhibit, Phoenix, Arizona, March 27-31, 1983. Manuscript received at ASME Headquarters December 22, 1982. Paper No. 83-GT-84.
Copies will be available until January 1984.

turbine blading structure and/or performance through erosion, corrosion, and deposition.

Transpiration Air-Cooling Concept

Transpiration air cooling was selected for the critical high-temperature turbine blade and vane airfoils. In this concept, cooling air effuses through a porous wire mesh skin to create an insulating film or boundary layer of cool air on the outer airfoil surfaces. The air for cooling is obtained from the gas turbine compressor component. The turbine blade's porous airfoil skin is attached to an internal structural spar by hub and tip circumferential welds plus spanwise welds which also enclose internal longitudinal cooling air passages between adjacent welds. Figure 2 illustrates the concept. To optimize air usage, each passage is orificed to provide only that quantity of air required to meet design criteria at the local gas stream temperature and pressure conditions. Cooling air is obtained from the lowest compressor stage consistent with each turbine blade row pressure level.

The transpiration air cooling arrangement protects the turbine airfoils from the degrading characteristics of the hot gas stream created by the combustion of coal-derived fuels by providing a continuous protective air blanket surrounding the airfoil so that (*a*) metal temperatures of the skin and spar are maintained at levels commensurate with structural strength requirements, (*b*) solid and liquid particulates in the gas stream are deflected from the airfoil surface, thereby minimizing or eliminating sulfidation, erosion and deposition, and (*c*) skin temperature is cooled below the hot corrosion threshold and skin material oxidation is controlled within predictable and acceptable levels.

While the ability to operate in a dirty gas stream had not previously been evaluated, the transpiration air-cooled blade concept had demonstrated its ability to maintain safe metal temperatures when operating at very high gas stream temperatures. Several thousand transpiration air-cooled blades and vanes have been fabricated in various sizes ranging up to that of the planned commercial power plant gas turbine prior to the current HTTT Program. Stationary turbine cascades and rotating rig engines have been operated for hundreds of hours burning distillate and gaseous fuels at steady-state and cyclic conditions with inlet temperatures up to 3000°F (1649°C) and above.

Recent Turbine Development Test Program

Emphasis in testing under the DOE sponsored HTTT Program has been on evaluation of the erosion, corrosion, and deposition characteristics of the turbine and performance changes resulting from operation in the aggressive atmosphere expected from the combustion of coal-derived fuel. Principal test vehicles were a seven-vane turbine cascade, a low-pressure and a high-pressure rotating rig engine, each incorporating a different single stage turbine. All of the test turbine blades and vanes incorporated porous airfoils made of columbium-stabilized Nichrome V wire and internal structural spars of Stellite 31 material. Airfoil skin construction was predominantly wire wound but woven material was also used.

Because of the difficulty in obtaining coal-derived fuel in the quantities required to operate large scale vane cascades or engines, a simulation was made by seeding distillate jet fuel and natural gas fuel with contaminants. Early cascade tests utilized aluminum oxide particles and fuel-soluble alkali metal compounds. Later cascade and rig engine tests were conducted with ground fly ash obtained from the electrostatic precipitator of a utility boiler burning Illinois No. 6 coal.

The test plan was to operate at levels of particulate size and loading selected on the basis of limited published data and estimates of gasifier output conditions and contemporary gas

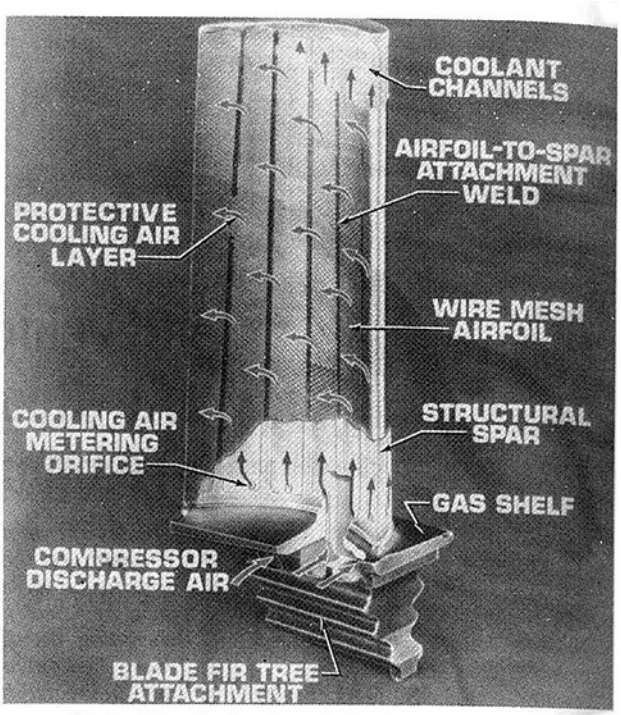

Fig. 2 Transpiration air-cooled turbine blade concept

Table 1 Particulate loading for turbine cascade and rig engine tests

Level	Specification loading in LBG fuel WPPM	Seeding distillate fuel turbine cascade WPPM	Seeding distillate fuel Rig engine WPPM
1	2	42	16
2	11	208	81

Table 2 Particulate size distribution

Level	LBG %	LBG spec. Micron	Aluminum oxide %	Aluminum oxide Micron	Ground fly ash %	Ground fly ash Micron
1	100	<2	100	<1.6	100	<2.5
	80	<1	99.8	<1	88	<1
2	100	<5	100	<6.3	100	<6.3
	80	<2	97	<2	98	<2

cleanup systems. Tables 1 and 2 show, respectively, these particulate loadings and sizes. Later data obtained from a fixed bed gasifier and a "physical" cleanup system consisting of particulate scrubbing and gas cooling elements correlated well with the lowest test specification particle size range and loading. More recent data presented for the Texaco medium Btu coal gasification process with water scrubbing indicate even lower hot gas stream particulate loading and smaller particle sizing than those of the lowest selected values.

Over 900 hr of rotating rig engine testing was accomplished, preceded by almost 400 hrs of stationary turbine vane cascade tests. During the test program, blade and vane airfoil skin examinations were conducted for evidence of corrosion, erosion and deposition of particulates. The following sections describe the test results.

Turbine Vane Cascade Test [1]

Three 100-hr turbine vane cascade tests were conducted at a peak (midspan) gas temperature exceeding 3000°F (1649°C) and with atmospheric exhaust. The first two tests were intended to simulate in 100 hr the equivalent of 300 hr in the

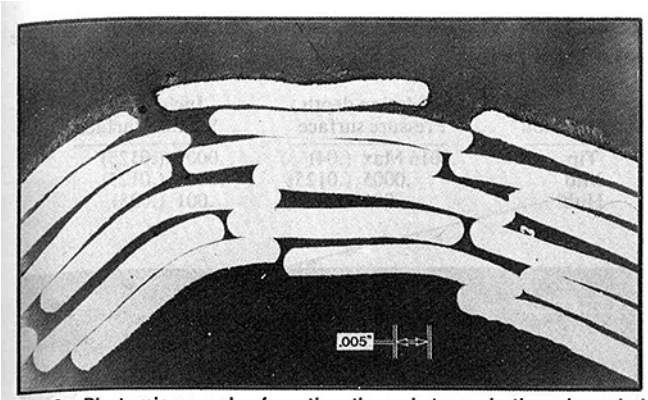

Fig. 3 Photomicrograph of section through transpiration air-cooled turbine rotor blade leading edge

forthcoming low-pressure rig engine. To accomplish this, the specification particulate loadings were trebled, to 120 and 600 wppm, respectively.

Because aluminum oxide particulate was used, appropriate amounts of sodium and potassium compounds were added to the fuel to achieve the level of alkali metal salts expected in a coal-derived gaseous fuel.

Results of the two 100-hr cascade tests with aluminum oxide particulate were quite similar. Visual and microscopic examination of the vane airfoils after test found slight dusting on the convex, or suction sides. The dusting was less than 5 microns thick after the first test at 120 wppm and approximately 15 microns maximum thickness after the second test at 600 wppm particulate loading. After the second test, there was also some particulate on the trailing edge surfaces up to a maximum thickness of 15 microns. The amount of particulate passing through the turbine cascade in these tests exceeded the controlled quantity of aluminum oxide particulate injected into the fuel supply as a result of erosion of the alumina-silica side walls of the combustor sector located upstream of the cascade.

Tests of the vane airfoils to determine cooling air flow characteristics during and after the tests showed flow capacity reductions in the same range as could be expected from oxidation alone at the skin operating temperature of approximately 1300°F (704°C). This indicates that the surface dusting of particulate had no effect on the flow capacity of the porous skin. Results from the first test indicated a maximum of 5 percent reduction in flow. The flow reduction data from the second 100-hr test with 600 wppm particulate loading was similar. Flow characteristics become asymptotic with exposure time in the 50-hr range. The flow reduction rates in both the alumina particulate tests as well as the subsequent test with fly ash particulate, matched the lower bound of the furnace oxidation test data band width for the woven and wound porous materials.

There was no evidence of either erosion or corrosion of the airfoil skin after the two tests with aluminum oxide particulates. The lack of erosion was particularly significant in that the injected sharp-edged aluminum oxide particulate remained hard and abrasive at the rig engine firing temperature, whereas some of the particulates generated from the combustion of coal-derived fuel soften or melt at these temperatures. With regard to the absence of corrosion of the airfoil skin, the 100-hr test time may be considered too short to draw meaningful conclusions.

The third 100-hr tests was conducted with ground fly ash particulate at the Level 1 specified rate of 42 wppm. This level of particulate loading was selected to simulate the conditions to be used in the forthcoming low pressure rig engine test.

Because of a facility malfunction, the vane cooling air temperature for this test was somewhat lower than that of the previous tests. Cooling air flow was increased slightly from the design value to achieve the same velocity exiting the skin into the main air stream as would have been achieved with design flow at the higher temperature. The combination of lower cooling air temperature and slightly higher flow rate produced a lower vane skin temperature of approximately 1050°F (566°C) and thus lower oxidation than was experienced in the two prior tests.

Periodic airfoil permeability flow tests were conducted during this cascade test. After 100 hr of exposure, the flow loss characteristic leveled off at about 2-1/2 percent, at the lower bound of the furnace oxidation test data band width for the airfoil wound mesh at this lower skin temperature.

Low-Pressure Turbine Test [1]

Following a checkout on clean fuel, 650 hr of testing were conducted with fly ash particulate in the 2600°F (1427°C) gas stream entering the complete single-stage turbine at approximately 2.7 atmosphere pressure. All testing was at a particulate loading between 20 to 28 wppm in distillate fuel, or the equivalent of 2 wppm in low Btu gas fuel. Maximum measured particle size for the first 200 hrs of testing was 10 microns, and for the remainder of testing was about 3 microns.

The first 350 hr of testing were with distillate fuel (Jet A) and the final 300 hr were run on natural gas. As noted above, particulate loading was held constant, irrespective of fuel type or particulate size change.

Periodic visual examinations of the outside surfaces of the blades and vanes found varying light amounts of particulate, primarily on the leading edge. Even the lightest deposits created an orange coloration from the iron oxide content of the fly ash. Closer examination of individual airfoils revealed the shallow nature of the deposits in that the individual wire strands remain clearly visible. Generally, it appeared that the airfoil deposits accumulated primarily during the first 50 hr of exposure and then increased only minimally after that.

Microscopic examination of particulate from the surface of the airfoils after early testing revealed a high percentage of discrete particles in the size range of 5 microns and above. A separate test was conducted on an atmospheric discharge combustor rig to determine whether the injected particles undergo size change or agglomeration either when residing in the storage tank and piping system or when passing through the combustion zone. Exhaust samples were collected isokinetically using a modified stack sampling probe behind the combustor exit station and subjected to scanning electron microscope (SEM) analysis for determination of particle size. The particle size distribution in the exhaust samples was found to be in close accord with the measured size distribution of the injected fly ash. Therefore, it was concluded that there is no significant agglomeration of fly ash particles passing through the combustor, and that the major portion of large particles found on the airfoil surface represent the particle size found in the basic fly ash supply. Since only a small percentage of the particles on the airfoil surface was of a small size it was also concluded that the majority of the smaller particles in the hot gas stream were deflected away from the blade and vane airfoil surfaces by the transpiration cooling air or remained entrained in the gas passage flow stream.

Further metallographic analysis revealed that the gas stream particulate which penetrates the airfoil cooling air blanket produces only a surface deposit on the porous mesh airfoil skin. Figure 3 is an enlarged photomicrograph of a section through a vane leading edge after 50 hr of rig engine test with fly ash particulate in the gas stream. Examination of this photomicrograph shows that the particulate has settled only on the outer wires of the first layer of skin material, with

virtually no evidence of bridging over the cooling air pores or particle migration into the subsurface layers.

These deposited particles show little adhesive force and can easily be brushed off. At the vane leading edge only, the outer layers of particulate appear to have remelted or softened from combustor radiant heat to produce a more slaglike appearance on the outer surface.

Periodic flow bench tests were performed on vane and blade airfoils to determine changes in cooling air flow capacity with operating time. The vane test results were quite consistent with those of the earlier cascade test program indicating that the operating flow loss characteristic levels off after the first 100 hr of exposure and is close to that produced by oxidation alone. The results of the rotor blade flow checks show a leveling off of flow loss at under 10 percent, which is well within the requirements for extended operational life and is consistent with the characteristic expected from oxidation alone. The flow bench results corroborated the visual observations of surface deposition discussed above.

A typical rotor blade with an airfoil of 12 × 64 woven mesh was destructively analyzed, using metallographic, SEM, and EDXA examinations, after completing 644 hr of rig engine operation including 500 hr with fly ash particulate in the hot gas stream. The surface degradation results of the analysis are summarized in Table 3. Figure 4 is a photomicrograph of a typical section of the woven airfoil leading edge illustrating the minimal amount of oxidation, and the absence of any evidence of either erosion or hot-corrosion. Fly ash deposits did not penetrate beyond the outer surface wire layer.

High-Pressure Turbine Test [2]

The second turbine test utilized a 7.25:1 pressure ratio rig engine with roughly two times the air and fuel flow of the earlier low pressure rig engine. The 20 wppm level of fuel particulate loading in the low pressure rig engine was maintained, yielding in this later test approximately twice the turbine gas stream particulates of the low pressure rig engine test. Of particular concern, in addition to thermal effects, were the effects of the greater amounts of particulate on performance and turbine section corrosion, erosion, and deposition.

Over 100 hr of testing were completed. Turbine inlet temperature was maintained at 2600°F (1427°C) and above. Transpiration air cooling was again shown to be effective in maintaining satisfactory metal temperatures. Airfoil skin oxidation was minimal, and there was no evidence of sulfidation, corrosion, or erosion. Some light deposition of particulates was encountered but this did not affect porous skin cooling airflow capacity. The rate of airfoil cooling flow capacity loss with operating time was found to be similar to that which occurred during the previous low pressure rig engine test over the same operating time.

The stator vane and rotor blade cooling airflow losses are compared to those of the earlier low pressure rig engine in Fig. 5. This figure shows that, for the test period, the percentage flow loss characteristics of both turbines are similar despite the doubling of turbine section particulate loading in the most recent test. This is additional test demonstration that the primary factor affecting transpiration skin cooling capacity loss is oxidation, and that gas stream particulates in the range expected from the combustion of coal-derived gaseous fuel have a negligible effect.

Metallographic examination of the leading edge of a representative rotor blade found the average depth of oxidation on the surface wires to be 0.0005 inch (0.013 mm); average oxidation on subsurface wires was 0.0001 inch (0.0025 mm). There was no evidence of hot corrosion or erosion. Fly ash deposits were limited to the top layer of wires. Maximum deposit thickness was under 0.002 in. (0.05 mm), with an average thickness of 0.0002 in. (0.005 mm). A magnified photomicrograph of the blade leading edge cross-section is shown in Fig. 6.

Pre-and post-test performance calibrations were run with a jet nozzle area approximating that required to maintain a combustor exit temperature of 2600°F (1427°C) at the design rotor speed of 8600 rpm. Turbine stage efficiencies determined by calculation from measured data indicate about a 1/2

Table 3 Metallurgical examination of low-pressure turbine rotor blade airfoil

Span location	Oxidation depth, Inches (mm) Pressure surface	Suction surface
Tip	.0016 Max (.04)	.0005 (.0125)
Mid	.0005 (.0125)	.0005 (.0125)
Hub	.001 (.025)	.001 (.025)

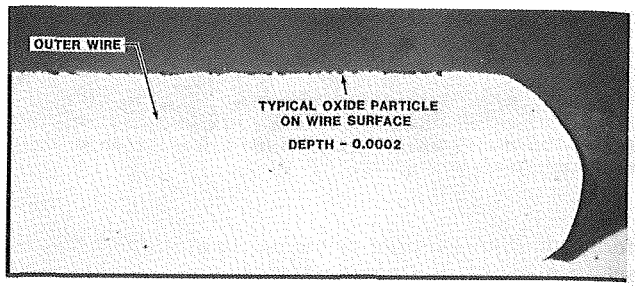

Fig. 4 Photomicrograph of a transpiration air-cooled blade leading edge outer wire after 644 hr of low-pressure rig engine operation

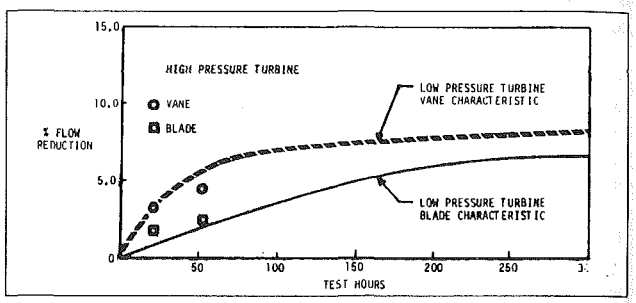

Fig. 5 Transpiration air-cooled turbine cooling flow reduction with hot gas stream particulates

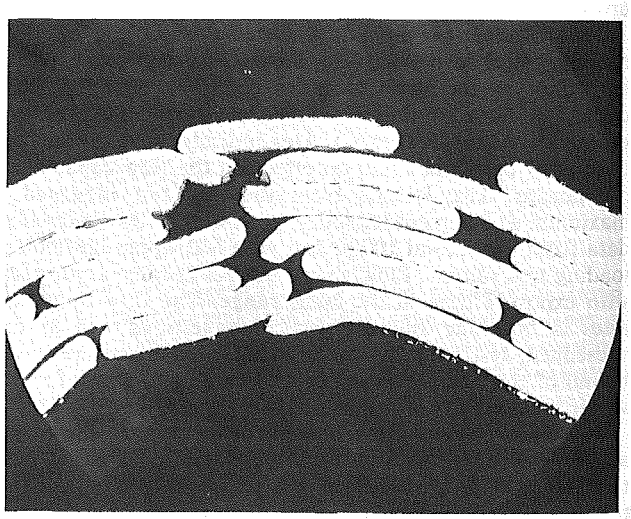

Fig. 6 High-pressure rig engine rotor blade leading edge section at 100X magnification after 53:20 hr of contaminant testing

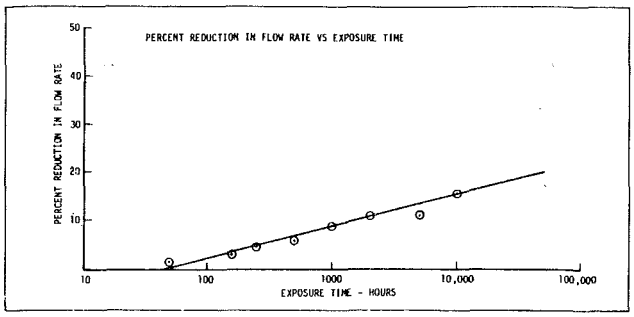

Fig. 7 1350°F furnace oxidation results-nichrome V-Cb wound mesh

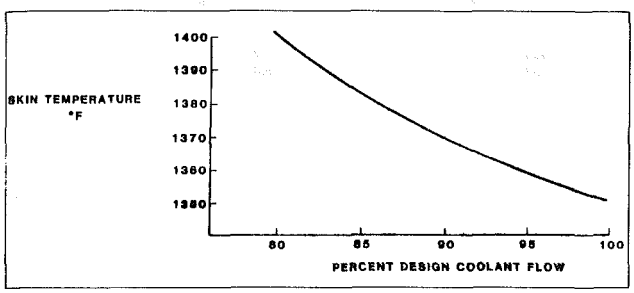

Fig. 8 Effect of reduced coolant flow on transpiration air-cooled blade temperature

percent decrease, which may be within experimental accuracy. These calculations were confirmed by stacking of component sensitivity coefficients to explain differences between pre- and post-test results.

Airfoil Life Prediction

To obtain higher time oxidation characteristics of the porous airfoil skin, a laboratory program was conducted utilizing flat mesh samples exposed to flowing elevated temperature air in a furnace. Comparison of these data with similar permeability loss data taken on instrumented vanes from both cascade and engine tests has shown that laboratory furnace oxidation provides a satisfactory, conservative estimate of the airfoil material oxidation rate in engine operation. Figure 7 is a curve of the permeability reduction experienced by the wound 0.010-in. (0.254-mm)-dia wire Nichrome V-Cb skin sample at 1350°F (732°C). To date, 10,000 hr of exposure have been completed. Extrapolation of these data to 50,000 hr without any intermediate servicing indicates a flow capacity loss of 20 percent. From the curve of Fig. 8, this flow capacity reduction would produce an increase in maximum skin temperature to 1400°F (760°C). Consequently, a 50,000-hr blade life is feasible.

Summary and Conclusions

Over 900 hr of rig engine testing have been accomplished on two different transpiration air-cooled turbines at a turbine inlet temperature primarily between 2600°F (1427°C) and 3000°F (1649°C) and with fly ash particulates in the gas stream. Based on the results of the tests, the following observations and conclusions were made for the blading:

1 There was no mechanical or thermal distress.
2 There was no evidence of erosion or corrosion.
3 Oxidation was minimal.
4 Particle deposition was minimal and limited to the outer strands of the mesh.
5 Deposition did not affect cooling capacity.
6 The airfoil coolant flow loss due to particulate deposit and/or oxidation is within acceptable limits.

Acknowledgment

The authors wish to express their appreciation to Mr. George Manning of the U.S. Department of Energy and Mr. Winfred Crim for their technical guidance during the program conducted under DOE Contract De-AC01-76ET10348 on which this paper is based.

References

1 Curtiss-Wright Topical Report—Low-Pressure Rig Engine Test Program, FE-2291-75A, June 1981.
2 Curtiss-Wright Topical Report—Turbine Spool Technology Rig Fuel Contaminant Tolerance Test, FE-2291-98A, Feb. 1982.

Deposition Results of a Transpiration Air-Cooled Turbine Vane Cascade in a Contaminated Gas Stream

R. Raj
Associate Professor,
Turbomachinery Laboratory,
Department of Mechanical Engineering,
The City College of the City
University of New York,
New York, N.Y. 10031
also, Curtiss-Wright
Corporation Consultant

The experimental data are presented on the deposition of particulate on transpiration air-cooled turbine vanes operating in a cascade for a series of tests using distillate fuel contaminated with alumina or fly ash. The data are discussed in view of the known mechanisms of deposition. Qualitative discussion of the role of electrostatic charge on the deposition in gas turbines is also presented.

Introduction

The electric utility industry is considering the use of coal-derived fuel fired combustion turbines as a means of reducing the dependency on costly imported oil. An integrated gasifier combined-cycle system operating on low or medium Btu gas at moderate turbine inlet temperatures can provide coal pile-to-busbar efficiencies that are in the range of conventional pulverized coal fired plants with flue gas desulfurization. However, operating at turbine inlet temperaures of 2600-3000°F offers an opportunity to achieve plant efficiencies of over 42 percent and at a lower capital cost ($/KW). The effect of increased turbine inlet temperature on plant efficiency and specific power is shown in Fig. 1. These benefits can be achieved by incorporating an advanced cooling concept such as transpiration air cooling to maintain the turbine blade metal temperatures at less than 1350°F, which is below the threshold for hot corrosion attack, an accelerated sulfidation/oxidation phenomena.

In addition to the potential corrosion hazard from gas stream contaminants of molten alkali metal salts, erosion and deposition represent threats to the reliability of turbine blades when operating on coal derived fuels. Erosion does not appear to be a serious problem when the gas stream particulate maximum size is generally below 5 microns since the particles may remain in the streamlines and traverse the aerodynamic gas passage without direct impingement. Where there is particle motion toward the blade surface, the cooling boundary layer can be expected to minimize the impingement effect.

However, deposition can be a problem since the air cooling concept requires that the holes or pores in the surface of the turbine blade must be relatively free from blockage of the path for effusion of the coolant. The phenomena of deposition relies on complex and possibly multiple

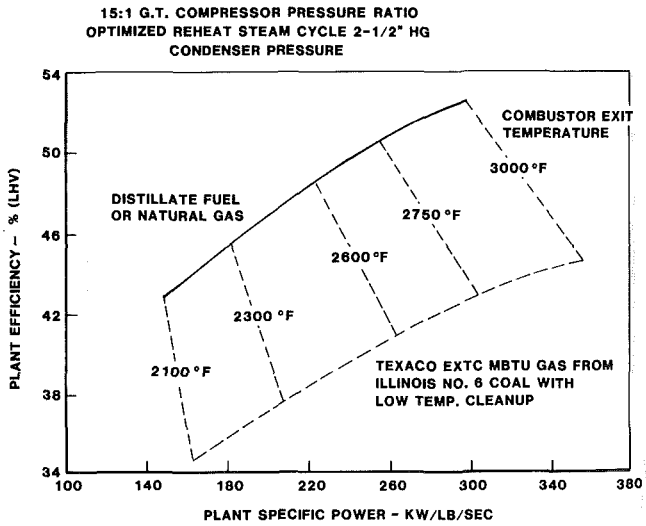

Fig. 1 Combined cycle power plant

mechanisms. The complication to the turbine blade performance due to deposition is twofold. The deposit can reduce the airfoil permeability and result in reduced coolant flow to the surface with an attendant increase in blade metal temperature. This may lead to oxidation, corrosion and strength limitations. Equally important, the deposit may build up to reduce the turbine aerodynamic passage which results in a reduced power output and possibly compressor surge. Gas turbine manufacturers generally stipulate a limit of 5 to 10 percent reduction in power at which point cleaning of the blading is required.

The deposition problem in gas turbines can be considered in two parts. In the first part it is important to know how the particles reach the blade surface and in second part it is im-

Contributed by the Gas Turbine Division of THE AMERICAN SOCIETY OF MECHANICAL ENGINEERS for presentation at the 28th International Gas Turbine Conference and Exhibit, Phoenix, Arizona, March 27-31, 1983. Manuscript received at ASME Headquarters, December 27, 1982. Paper No. 83-GT-130.
Copies will be available until January 1984.

Table 1 Mechanisms for the deposition phenomenon

Bringing particles to blade surface	Retaining particles on blade surface
Direct impingement	
Vapor diffusion	
Turbulent diffusion	Physical
Electrophoresis	Chemical
Thermophoresis	Electrical
Molecular diffusion	Magnetic
Brownian diffusion	
Diffusiophoresis	
Photophoresis	
Magnetophoresis	

Table 2 Particle size range affected by deposition mechanisms

Mechanism	Particle size in microns
Molecular diffusion	0.01 to 0.5
Brownian motion	0.5 to 1
Turbulent diffusion	0.9 to 5
Direct impingement	>5

portant to know how the particles are retained at the blade surface. The mechanisms responsible for bringing the particles to the blade surface and retaining the particles on the blade surface are summarized in Table 1 (reference [1]). The order of effectiveness in which each of the mechanisms come to play may depend upon many factors such as particle size, density, concentration, intensity of static charge, magnetic intensity, temperature of hot gas stream, temperature of blade surface, density of hot gas, pressure of hot gas, blade surface roughness, local turbulence, viscosity of hot gas, velocity of cooling air, and velocity of hot gas stream. Based on particle size alone, preliminary considerations reveal the effectiveness of some of the mechanisms, as shown in Table 2. Extensive theoretical and experimental work is required to establish the order of effectiveness of all the mechanisms relative to each other.

Practically all the available studies refer to part one of the deposition problem. Some of these studies are by Hedley et al. [2, 3], Halstead [4], Vermes [5], Owen [6], Rosner and Chen [7], Menguturk and Sverdrup [8]. These studies have contributed to the understanding of the deposition phenomenon but somehow the experimental results were either not related to a gas turbine environment or were understandably taken for one mechanism while actually other mechanisms acted simultaneously. Several of the available studies, such as by Bowden et al. [9], Mosley and Wisdom [10], reference [11], DeCorso et al. [12], and Wolf et al. [13] present an overall deposition experience obtained on actual gas turbine engines and are useful to evaluate the various analytical efforts.

As part of the U.S. Department of Energy sponsored High-Temperature Turbine Technology (HTTT) program, information on unstudied mechanisms of part one of the deposition problem is being reviewed and the understanding of mechanisms related to retaining the particles on the blade surface in a gas turbine environment is being developed.

This paper examines the experimental data on the deposition of particulate on transpiration air-cooled turbine vanes and discusses the qualitative role of electrostatic charge present on particle deposition.

Transpiration Air Cooled Blade Concept

The essential elements of a transpiration air-cooled blade are shown in Fig. 2. The transpiration cooling of turbine blades involes the effusion of air through the pores of the blade surface. The air is obtained from the discharge of the compressor and is only a fraction of the main stream airflow.

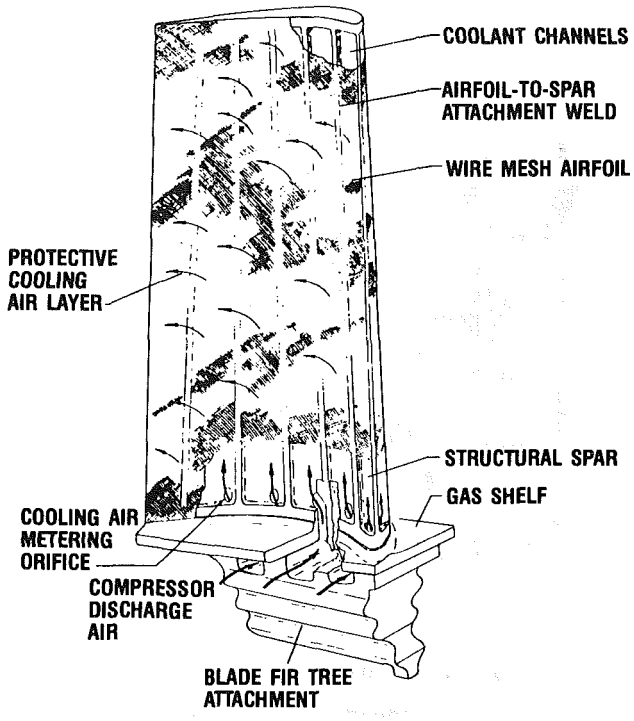

Fig. 2 Transpiration air-cooled turbine blade concept

The effectiveness of transpiration cooling depends upon a number of factors, such as amount of coolant air and the temperature of the inlet hot gas, as well as the type and permeability of the porous material. Air enters the turbine blade through the strut or load-carrying structure which embodies spanwise cooling air passages. Air is fed into the radial channels through metering orifices at the blade base of gas shelf. The air flowing along the channel convectively cools the internal strut. The flow rate through each channel depends upon the external chordwise gas pressure and temperature distribution. The effused air, flowing through the porous blade walls, forms an insulating film separating the blade surface from the main hot gas stream.

The ability to withstand high temperature and protection from erosion of transpiration air cooled blades have been well described in a series of earlier reports [14, 15]. The blade technology and materials used in their manufacture have also been identified in reference [13].

Electrophoresis and Deposition

While many phenomena related to gas turbine deposition have been discussed in the literature, the phenomena of electrophoresis and magnetophoresis apparently have been generally overlooked. These phenomena, however, are widely considered in other engineering applications where their effect is favorable. In the case of gas turbines operating in a contaminated environment both of these phenomen play an adverse role.

An extensive description of the problem of electrophoresis as applied to gas turbines operating on coal or coal-derived fuels is presented in [16]. The particles present in the hot-gas stream in gas turbine are to some extent charged electrically. The charge on particles, in general, appears due to the following phenomena:

(*a*) Injecting a mixture of contaminants and fuel through a burner nozzle and its ignition (as provided in cascade tests operating on fuel "doped" with contaminants).

(*b*) Ionic exchange between solid contaminants and the gas

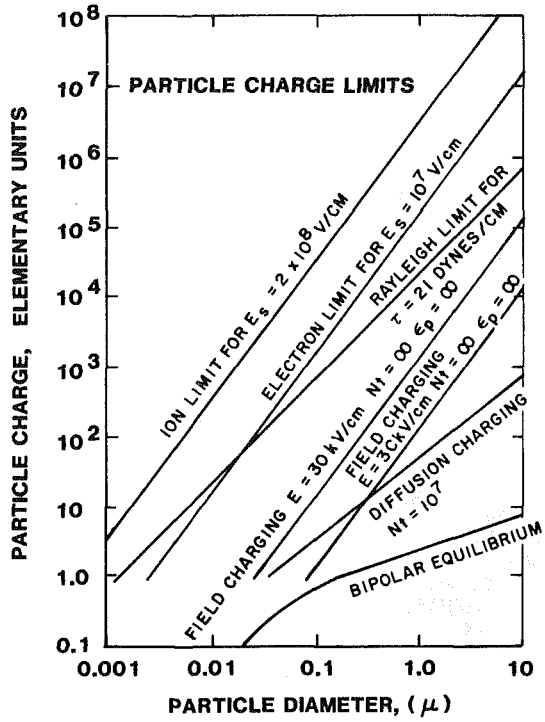

Fig. 3 Particle charge as a function of particle diameter [17]

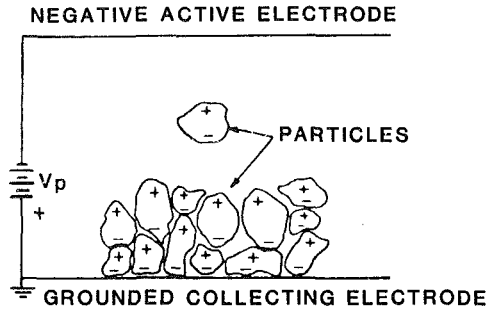

Fig. 4 Dipolar particles in an electric field [18]

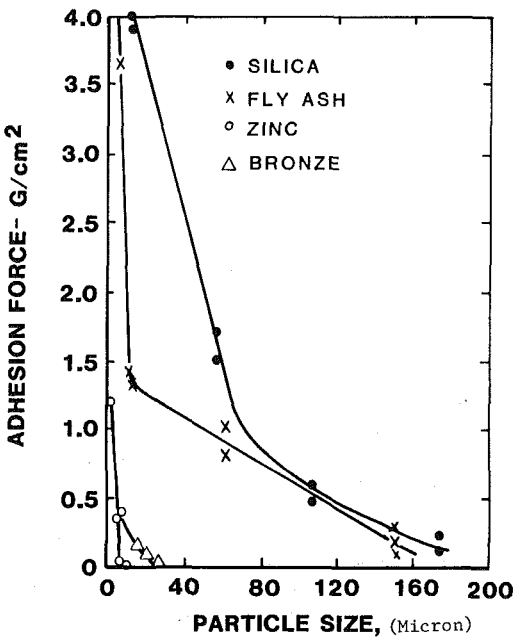

Fig. 5 Measured adhesion force as a function of particle size [18]

presumed to be partially ionized due to high temperature (molecular structural breakdown of coal) and particle agglomeration.

(*c*) Particle friction with solid boundaries such as burner well, cyclones, transmission pipes, turbine casing, etc.

(*d*) Relative motion between dry gas and solid particles.

The first two of the foregoing phenomena are believed to be the dominating factors while the remaining two are also important. It is not certain what contribution the above mentioned phenomena will provide toward establishing the charge type and magnitude. Analysis of this type has not been done before, for either gas turbine or fundamental cases of interest.

In the absence of that detail information, it appears appropriate to measure the total charge on particles in a gas turbine just before the particles enter the turbine blade passage and correlate these results to the individual studies carried out to understand the phenomenon of particle charging. The final result would be verified by measurement of the total deposition on the blade surface. Several experimental tests currently are in progress under the DOE HTTT program to understand the role of electrophoresis on the deposition of gas turbine blades.

Based on available limits of a maximum charge a particular particle can possess, Fig. 3 [17], it is theoretically feasible to evaluate a conservative estimate of the nondimensional nature of this force relative to the other forces. However, it is not certain that the particles in gas turbines indeed will reach a maximum charge limit in actual practice. This is due to the fact that the total charge developed is affected by several parameters surrounding the particle and its physical properties. Further, the charge on particles is based on the assumption that the particle is spherical while in fact the type of coal ash particles in a gas turbine exhaust after the combustion process could be irregular, crystalline, sharp cornered or partially spherical. As a result the contact potential developed between particles or particle to solid surface could be extremely large and would play a decisive role in holding the particles together [Fig. 4], in addition to particle size [Fig. 5], and other parameters [18] discussed earlier.

The fundamental significance of the mechanism of electrophoresis to deposition on gas turbine blades is the fact that this is the only mechanism which is responsible for bringing the particles to the blade surface as well as retaining the particles on the surface.

Experimental Program

Although operation of transpiration air-cooled turbines at very high temperatures has been demonstrated previously on petroleum distillate fuel, the concept had not yet been subjected to the aggressive gas environment from combustion of coal-derived gas. Therefore, a key element of the high-temperature turbine development includes operation initially of a stationary turbine cascade, and subsequently an engine, in order to evaluate the resistance of transpiration air-cooled vanes and blades to an aggressive gas stream environment.

It is well known that there is a shortage of coal-derived low or medium Btu gas facilities, especially for flow quantities to operate large scale cascades or engines. Therefore, testing of turbines in aggressive gas stream conditions had to be simulated initially by "doping" jet fuel with contaminants of either erosive aluminum oxide or fly ash removed from a coal-fired boiler. The alumina was used initially to produce an accelerated evaluation of erosion resistance as well as deposition. The fly ash was used on later tests after establishing a technique for grinding to the required size

Table 3 Particulate size distribution

	LBG spec.		Aluminum oxide		Ground fly ash	
Level	%	Micron	%	Micron	%	Micron
1	100	<2	100	<1.6	100	<2.5
	80	<1	99.8	<1	88	<1
2	100	<5	100	<63	100	<6.3
	80	<2	97	<2	98	<2

Table 4 Chemical analysis of Illinois No. 6 coal fly ash used in test

Constituent	Percent by weight
C	2.37
S	2.20
SiO_2	28.9
Al_2O_3	29.4
Fe_2O_3	25.6
TiO_2	1.67
P_2O_5	0.69
CaO	0.27
MgO	1.10
Na_2O	2.20
K_2O	2.77

Table 5 Cascade operating conditions

Combustor sector airflow	2.1 lb/s (0.95 Kg/s)
Total combustor fuel flow	264 lb/hr (120 Kg/hr)
Peak combustor exit temperature	3400°F (1871°C)
Gas inlet average temperature	2600°F (1427°C)
Vane cooling airflow	0.032 lb/s (0.15 Kg/s)
Vane cooling air supply temperature	325°F (163°C)
Vane skin temperature (average)	1250-1300°F (607-704°C)
Vane spar temperature (average)	600°F (316°C)

distribution and preventing agglomeration during transport and storage of the prepared fly ash.

The initial tests in the HTTT program were directed toward defining the blade areas most susceptible to erosion and deposition, the buildup thickness and the effect on cooling airflow permeability and blade operating temperatures. These tests were conducted in a stationary turbine cascade at 2600-3000°F (1427-1649°C) average inlet temperature with peaks of 3400°F (1871°C) using contaminant added to distillate fuel. The observations from these tests are reported in the following section. Subsequent tests were conducted for about 700 hrs in an engine at similar conditions using fly ash to contaminate the distillate fuel. The engine tests had the same objectives as the cascade but with particular focus on the rotor blades.

Description of the Tests. The data from the cascade were obtained in two sets of tests. The first set ran for a total of 100 hrs each test and comprised of two phases. In the first phase, the fuel was doped with aluminum oxide and amounts of sodium and potassium compounds were added up to an order of magnitude of the alkali contents existing in coal derived gaseous fuel (0.65 wppm). The particulate loading of aluminum oxide was 120 wppm. This loading was about three times the loading specification estblished to simulate engine operation on low Btu gas with a commercial desulfurization system.

In the second phase, which was also executed for 100 hrs, the fuel was again doped with aluminum oxide but the particulate loading was increased to 600 wppm and was about 15 times the loading specification to simulate engine operation with low Btu gas. The particulate size distribution of aluminum oxide is given in Table 3.

The second set of tests also ran for 100 hrs. In this case,

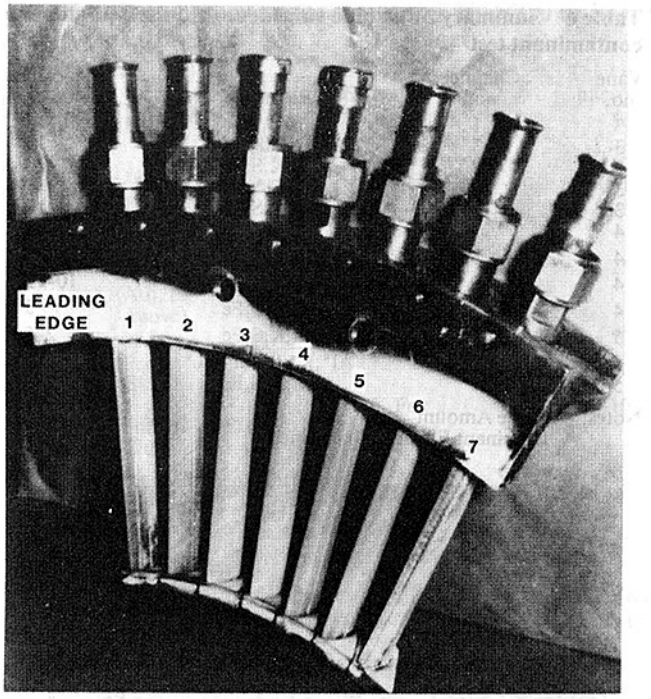

Fig. 6 Turbine cascade after level 2 aluminum oxide contamination test

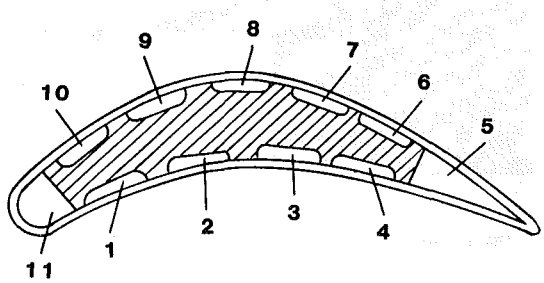

Fig. 7 Turbine vane cooling air channels

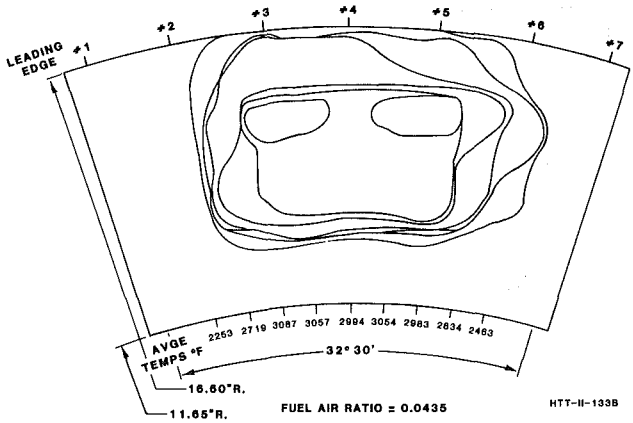

Fig. 8 Cascade combustor isotherm map

the fuel was doped with fly ash. The particle size distribution of fly ash is given in Table 3. The fly ash was obtained from an electrostatic precipitator of an operating utility power plant using Illinois No. 6 coal. The ash was ground to the required level of particulate distribution. The chemical analysis of the Illiois No. 6 coal fly ash is given in Table 4.

The cascade consisted of seven vanes (Fig. 6). The vanes used airfoils that were manufactured by different methods

Table 6 Summary of turbine vane deposition 100 hr alumina contaminant test

Vane no.	Channel no.	Elements	Thickness microns
3	1	Al,S	10–15
3	3	Al	15
3	4	Al,K,S,Ti	5–10
3	8	Al,K,S,Ti*,Na*Si*	5
3	11	Al,K,S,Ti	5–10
4	1	Al,K,S	5–10
4	8	Al,K,S	2–5
4	10	Al,K,S	10–15
4	11	Al,K,S,Fe	5
5	1	Al,K,S,Fe	2–5
5	6	Al*,K*,S*,Si*,Fe*	2
5	11	Al,K,S,Fe	2–5

Notes: *Trace Amount
Dominant Element Underlined

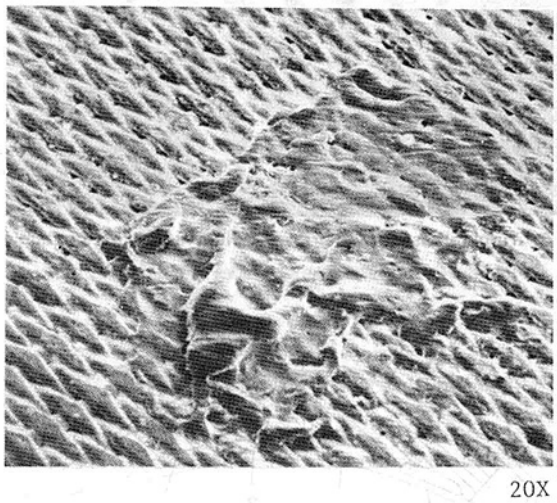

Fig. 9 Alumina agglomeration on vane No. 3—channel 3

and with different wire configurations of columbium stabilized Nichrome V alloy. One method used 0.005 in. (0.13 cm) dia wire which is flattened, wound on a mandrel, and sintered to form a tube. The airfoil is formed from this tube and electron beam welded to narrow ribs on the load carrying internal spar. Another method of airfoil manufacture used 0.005 in. (0.013 cm) dia wire which is woven into flat sheets, layered, and sintered. The internal structural spars were made from Stellite 31 material. Each vane had eleven cooling channels as shown in Fig. 7.

The characteristic parameters selected for the cascade tests are shown in Table 5. The temperature distribution at the inlet to cascade is shown in Fig. 8.

Test Results. The vanes were subjected to three examinations – visual, scanning electron microscopy (SEM), energy dispersive X-ray analysis (EDXA), and cooling air flow checks. The vanes in locations 3, 4, and 5 in the cascade were of special interest since they occupied the central position in the cascade. All of these vanes were of woven mesh type. The diameter of wire used to manufacture the airfoil skin of these vanes was 0.005 in. and the weave was 50 × 250. The vanes 1, 2, 6, and 7 may be affected by endwall effects and were not considered representative.

The vane from position 3 had been degreased in trichlorethylene and the surface brushed with Scotch-Brite before analysis. Vanes from position 4 and 5 were examined in the "as run" condition.

(*a*) *Alumina Contaminant Test.* Elemental analysis indicated aluminum, potassium, sulfur, and iron on all vanes

Fig. 10 Aluminum "map" of particle. Distribution of aluminum is indicated by light areas

Fig. 11 Alumina deposit on vane 3—channel 4

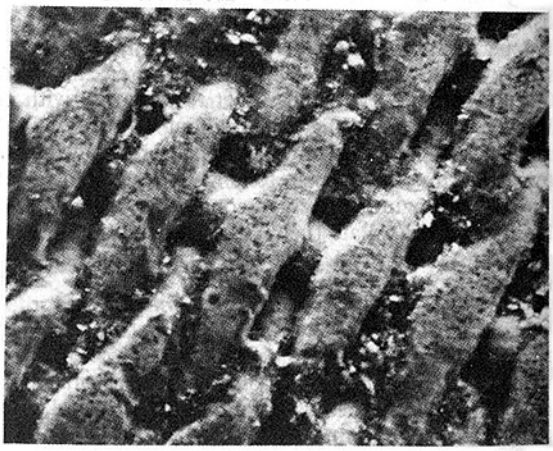

Fig. 12 Alumina particle—vane 4—channel 8

(Table 6). Four of five channels analyzed on vane No. 3 indicated titanium in addition to the above elements. Thickness of the particulate deposition on the porous surface of the airfoil varied from 5 to 15 microns.

Channel 3 had a small agglomerated particle (Fig. 9). This particle was alumina with a thickness of about 15 microns. A map showing the distribution of the aluminum is presented in Fig. 10.

Channel 4 analysis determined aluminum, potassium,

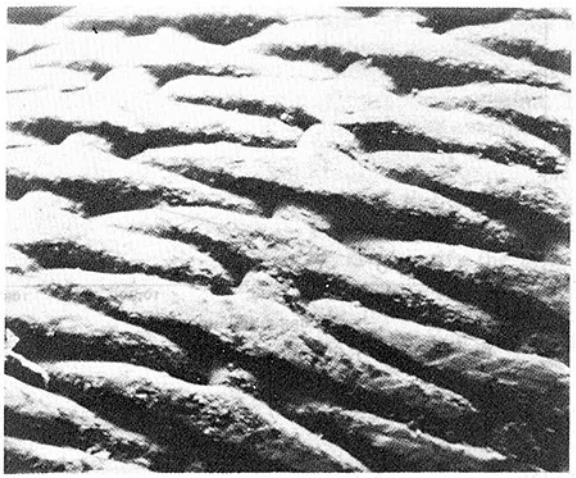

Fig. 13 Alumina particulate—vane 5—channel 11 radius

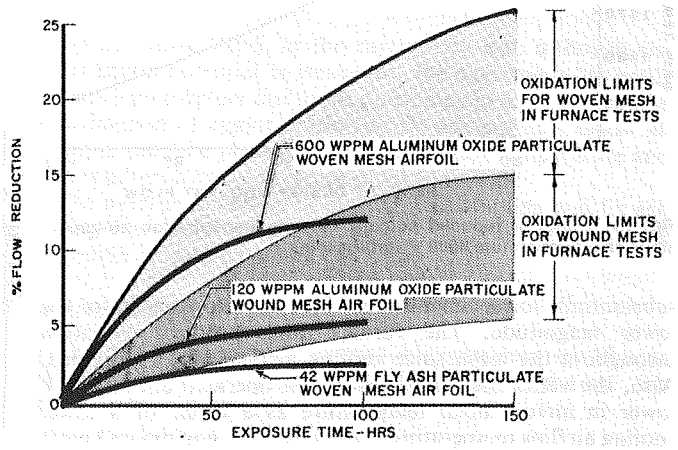

Fig. 14 Vane cooling air flow reduction during turbine cascade contamination test

sulfur and titanium. Particulate thickness on the surface was 5 to 10 microns (Fig. 11)

Channel 8 analysis determined the presence of aluminum, potassium, sulfur, with trace amounts of titanium, sodium, and silicon. Thickness of the particulate layer on the mesh was approximately 5 microns.

EDXA analysis of the Scotch-Brite pad used to brush the vane yielded aluminum and titanium. This may be the source of the titanium found in Channels 4, 8 and 11.

Four channels of the vane No. 4 were analyzed. Aluminum was the primary element with some potassium, sulfur and iron. Particulate deposition thickness varied from 2 microns to 15 microns. The alumina deposit on Channel 8 is shown in Fig. 12.

Three channels were analyzed on vane No. 5. Two channels had particulate consisting primarily of aluminum with some potassium, sulfur and iron. A dark area analyzed on the third channel was primarily nickel. Particulate deposition thickness varied from less than 2 microns to approximately 5 microns. Figure 13 shows the alumina particulate deposit on the leading edge of the vane.

Percentage of air cooling flow reduction for the first level of contamination is shown in Fig. 14. The results of the second level of loading produced essentially similar results; however, a larger flow reduction was observed (Fig. 14), but this was still within the range of flow reduction expected based on the furnace oxidation tests, shown shaded in the figure.

This series of tests also including operating several vanes at

Table 7 Summary of turbine vane deposition 100 hr fly ash contaminant test

Vane no.	Channel no.	Elements	Thickness microns
3	11	Fe,Mn,Si,Ca,Al,K,P,S	~50
3	5	Fe,Si,P,K,Ca,Mn,Al,S	~50
4	11 (1-1/2 above shelf)	Fe,Si,La,Al,K,P,Mg,S	10–15
4	11 (Adj. to above)	Fe,Mn,Si,Ca,K	~250
4	5 (Press. Side)	Fe,Ca,P,Si,K,Al,Mg,Mn	~50
4	5 (Suction Side)	P,K,Fe	5–10

Note: Dominant Element Underlined

higher levels of cooling airflow. The results showed a trend of increased deposition on the suction surface with higher cooling airflow rates. This observation would suggest that thermophoresis is one of the mechanism involved in the deposition.

(*b*) *Fly Ash Contaminant Test.* After 100 hrs of test time, vane No. 3 and 4 were removed and examined. A reddish-brown build-up was noted on the pressure side of the vanes.

In order to identify this particulate, the vanes were analyzed by scanning electron microscope (SEM) and energy dispersive X-ray analysis (EDXA) methods. Areas examined were the leading edges, trailing edges on the pressure side. The results are presented in Table 7.

All of the particulate identified was fly ash. These deposits were thicker on the leading edge and pressure (concave) side of the trailing edge. Particle size diameters ranged from 0.5 microns to 8 microns. Varying amounts of fused fly ash masses were present. Fly ash diameter on the suction (convex) surface ranged from less than 0.5 microns to 2 microns and no fused masses were present.

Diameters of individual fly ash particles on vane No. 3 at the leading edge varied from 0.5 to 8 microns with 2–3 microns being the average diameter. Some agglomeration had occurred. Fusing of particles into amorphous masses was also evident.

Fewer individual fly ash particles were noted on the trailing edge of vane No. 3. There was a greater tendency to agglomeration and the fused masses of particles were more abundant. Fly ash diameters ranged from 0.5 microns to approximately 5 microns.

Examination of an area 1-1/2 in. from the shelf on the leading edge of vane No. 4 revealed the airfoil mesh to be covered with a deposit of fly ash approximately 10–15 microns thick.

Diameters of this fly ash ranged from approximately 0.5 microns to 4 microns with an average of approximately 2 microns. The fly ash, which originally had an irregular shape from grinding, was now spheroidal with some agglomeration but no fused masses. Figures 15(*a*) and (*b*) show the deposit on the leading edge at two magnification levels.

A localized area of heavy fly ash build-up adjacent to the "clean" area was found to have a reddish deposit of about 0.010 in. thick. Particle size of the fly ash ranged from 0.5 microns to 5 microns with an average diameter of 2.5 microns. Agglomeration was evident with areas of fused masses of fly ash.

A fly ash build-up on the pressure side of the trailing edge (Channel 5) of vane No. 4 revealed brown deposit of several

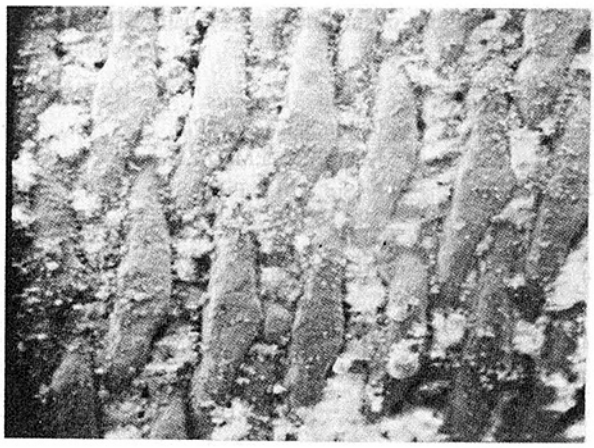

60X

Fig. 15(*a*) Fly ash on mesh

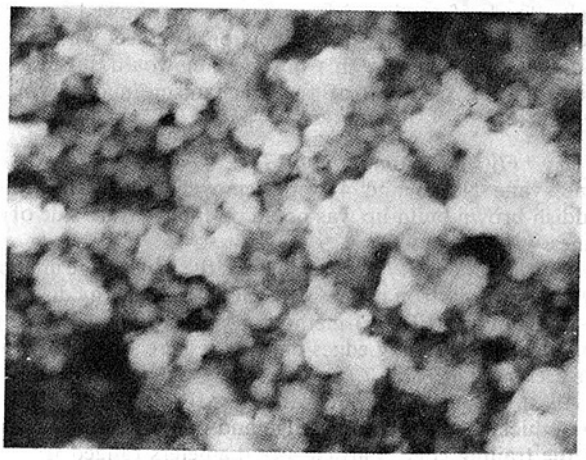

2000X

Fig. 15(*b*) Fly ash on vane 4 leading edge

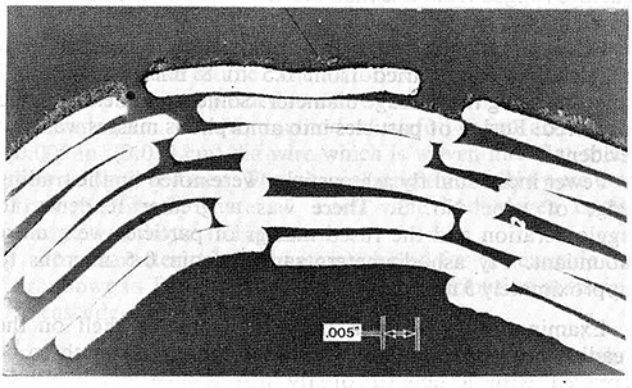

Fig. 16 Micro section through transpiration air-cooled turbine airfoil after test using fly ash in the fuel

thousandths thickness. Particle diameters ranged from 0.5 microns to 5 microns.

Channel 6 of vane No. 4 had a deposit thickness of 5 to 10 microns. Particles were spheroidal and uniform in size; this area had the most uniform size distribution of those examined. The fly ash diameters ranged from less than 0.5 microns to 2 microns with agglomeration but little or no fusing into masses.

Post-test cooling airflow permeability tests were conducted and the results (Fig. 14) again show that the small flow reduction occurs during the initial 50 hours. This is similar in trend to the furnace oxidation tests of the porous mesh but of

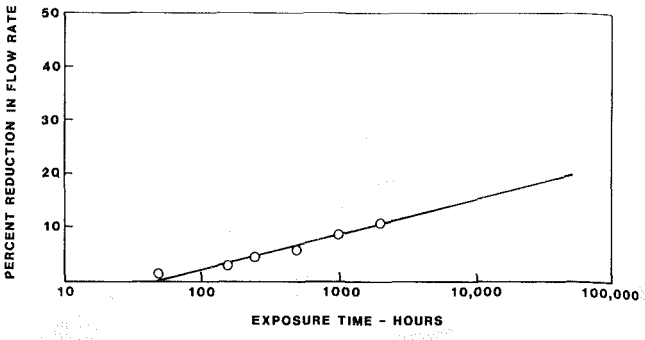

Fig. 17 1350°F furnace oxidation test results

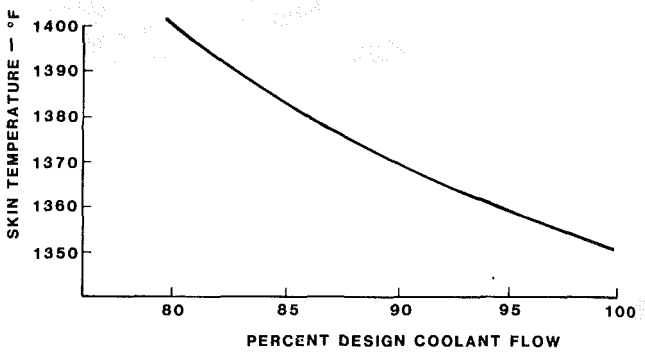

Fig. 18 Effect of reduced coolant flow on transpiration air-cooled blade skin temperature 3000°F turbine inlet

substantially lower magnitude. There are two reasons for the lower magnitude. The furnace tests produce oxidation throughout the mesh since cooling airflow is not provided. Also, the vanes for this series of test operated about 200°F lower in airfoil metal temperature as a result of a lower cooling airflow temperature caused by a test equipment heater malfunction.

Transverse microsections taken through the porous mesh airfoil showed that there was no migration of the particles into the porous mesh structure. The deposition remained on the outer layer of wires forming the airfoil surface (Fig. 16 typical). The air-foil metal temperatures remained cool and within a uniform temperature range throughout the test. This was attributed to (*a*) the airfoil surface pores essentially remaining open, (*b*) the porous nature of the cake deposit, (*c*) the cross-flow within the airfoil wire matrix, and (*d*) the insulating properties of the deposition material on the airfoil surface.

Since the tests suggested that oxidation was a primary mechanism for airflow permeability change, additional furnace oxidation testing of long term duration was initiated. Figure 17 shows the test results through 2000 hrs of a currently on-going 10,000 hr test period. Periodic flow checks have established a straight line characteristic with time on semi-logarithmic plot. Extrapolation of the data to 100,000 hrs indicates a cooling flow reduction of less than 20 percent. The effect of cooling flow reduction on airfoil metal temperature of a transpiration cooled blade at 3000°F gas temperature is shown in Fig. 18. This figure shows that an acceptable 50°F increase in metal temperature can be expected after the 100,000 hrs operating period.

Conclusions

The results of foregoing tests were of significant consequence since practically all the mechanisms such as impingement (controlled by particle size) turbulent diffusion (controlled by boundary layer characteristics), photophoresis (controlled by light), thermophoresis (controlled by tem-

perature gradient) remained the same for both the tests with alumina and fly ash. The phenomenon of diffusiophoresis was weakest in the case of fly ash (lowest loading), yet more deposit was found in the case of fly ash than alumina. This observation indicates that there is more to be examined than just the foregoing mechanisms as is generally mentioned in gas turbine literature.

The properties which are hard to quantify for both the tests with alumina and fly ash are the elctrostatic and the chemical properties, while it is not difficult to quantify the physical properties. The electrostatic and chemical properties are strongly interdependent under the high-temperature conditions existing in gas turbines. One can lead to the consequence of the other. It is these two properties which are believed to have played a major role in the final deposition. This was substantiated by the alumina deposits found on the turbine vanes. It was found that the dust would fly off with a little blowing. This is due to the fact that the electrostatic potential built up between particles which held the particles together during turbine operation had weakened due to change in surrounding conditions and there was no chemcial bonding.

On the other hand, in the case of fly ash, although the electrostatic potential is weakened, the agglomeration holds the particles together due to the phenomenon of sintering. The phenomenon of agglomeration of fly ash particles below 40 microns can take place much below melting temperature and is strengthened by the presence of alkaline salts.

The average thickness of dusting with alumina and fly ash testing was found to vary between 5 to 15 microns with the exception of isolated points.

Acknowledgment

The author wishes to express his gratidute to Mr. S. Moskowitz for various suggestions made during the preparation of this paper.

References

1 Raj, R., and Moskowitz, S., "Some Considerations Concerning Direct Impingement and Deposition on a Transpiration Air-Cooled Blade From a Hot Gas Stream," Presentation at 26th Gas Turbine Conference, Houston, Session 62, Mar. 8-12, 1981.

2 Hedley, A. B., Brown, T. D., and Shuttleworth, A., "Available Mechanisms for Deposition From a Combustion Gas Stream," ASME Paper No. 65-WA/CD-4, 1965.

3 Hedley, A. B., Brown, T. D., and Shuttleworth, A., "Deposition of Oil Ash Constituents From High Temperature Gas Stream," ASME Paper No. 65-WA/CD-3, 1965.

4 Halstead, W. D., "Calculations on the Effects of Pressure and Temperature on Gas Turbine Deposition," Proc. of Conf. organized by Central Electricity Generating Board, Sadbury House, London, 1972, p. 22.

5 Vermes, G., "Thermophoresis-Enhanced Deposition Rates in Combustion Turbine Blade Passages," ASME Paper No. 78-WA/GT-1, 1978.

6 Owen, P. R., "Pneumatic Transport," *J. Fluid Mech.*, Vol. 39, Part 2, 1969, p. 407.

7 Rosner, D. E., and Chen, B. K., "Chemically Frozen Multicomponent Boundary Layer Theory of Salt and/or Ash Deposition Rates From Combustion Gases," *Combustion Science and Technology*, Vol. 20, 1979, p. 87.

8 Menguturk, M., and Sverdrup, E. F., "A Theory or Fine Particle Deposition in 2-D Boundary Layer Flows and Application to Gas Turbines," ASME Paper No. 81-GT-54, 1981.

9 Bowden, A. T., Draper, P., and Rowling, H., "The Problem of Fuel-Oil Ash Deposition in Open-Cycle Gas Turbine," *Proc. of I Mach. E.*, London, No. 167, p. 291.

10 Mosley, W. J., and Wisdom, J. C., "Brown Coal Ash Deposition in the Open-Cycle Gas Turbine," *Journal of Institute of Fuel*, May 1964.

11 "Coal Burning Gas Turbine Project Report on Interdepartmental Gas Turbine Steering Committee," Department of Minerals and Energy Department of Supply, Australian Govt. Pub. Service, Canberrra, 1973.

12 DeCorso, S. M., Vermes, G., Lee, S. Y., Singhal, S. C., and Cohen, A., "Combustion Turbine Design Guidelines Based on Deposition/Corrosion Considerations," ASME Paper No. 80-GT-72, 1980.

13 Wolf, J. C., Moskowitz, S., and Manning, G., "Development of a High Temperature Turbine for Operation on Coal-Derived Fuel," ASME Paper No. 80-GT-168, 1980.

14 Raj, R., "Transpiration Air-Cooled Turbine Blade - A Technology for Future Generation Aircraft and Industrial Gas Turbine Engines Using Coal or Coal-Derived Fuels," 5th ISABE, Paper No. 32, 1981.

15 Raj, R., and Moskowitz, S., "Transpiration Air Protected Turbine Blades - An Effective Concept to Achieve High Temperature and Erosion Resistance for Gas Turbines Operating in an Aggressive Environment," ASME Paper No. 78-GT-100, 1978.

16 Raj, R., "The Role of a Static Charge on the Deposition Rates in Gas Turbines," TR, Curtiss-Wright Corporation, No. CW-WR-81-005, Dec. 1980.

17 Whitby, K. T., and Liu, B. Y. H., *The Electrical Behavior of Aerosols*, Book-Chapter, Aerosol-Science, Edited by C. N. Danies, Academic Press, 1966.

18 Penney, G. W., "Adhesive Behavior of Dust in Electrostatic Precipitation," *J. of Air Pollution Control Association*, Vol. 25, Feb. 1975.

W. Tabakoff
Professor.
Fellow ASME

C. Balan
Graduate Research Assistant.
Student Mem. ASME

Department of Aerospace Engineering
and Applied Mechanics,
University of Cincinnati,
Cincinnati, Ohio 45221

A Study of the Surface Deterioration due to Erosion

Turbomachines are subject to an excessive rate of erosion when operated in dusty environments or exposed to combustion gases of newly developed synthetic fuels or heavy oils. The surface quality of the blades exposed to such particulate flow deteriorates. With time, the surface roughness increases and leads to a decrease in engine performance. This paper presents the results of the experiments carried out in an erosion wind tunnel on 6061T6 aluminum specimens to study the roughness formations. The particles used were silica sand.

Introduction

Materials exposed to particle impacts are eroded and subjected to deterioration of their surfaces quality. This surface deterioration is of considerable interest in turbomachinery subjected to erosion, since it can lead to a significant decrease in engine performance.

The erosion rate is defined as mass or volume of material removed per unit mass of impacting particles. It has been studied by many investigators [1–7]. Most of these works are oriented towards a better understanding of the erosion mechanism. Quantification of the erosion rates and detailed studies of the inelastic collision and rebound of the particles with the target surface are also available [5–7]. These results are of importance in evaluating the life of the equipments subjected to particle erosion. It is well documented that the erosion rate is a strong function of the angle of attack, velocity, particle size, and particle and target materials. The erosion rate for ductile alloys is negligible at 0 deg and it increases rapidly to a maximum around 20 to 25 deg and then decreases slowly to a minimum at 90 deg.

Most of the erosion models stem from the study of single particle impact. The theories range from cutting [1], plowing [2, 3], or local melting [4]. The cutting theory accounts for the material removed as chips equal to the swept volume of the individual particles. The plowing theory explains the plastic deformation and pile-up of material at the exit side of the impact craters to form lips. Material removal is accomplished by brittle fracture of the work hardened lips by subsequent impact of other particles. In reality, the erosion mechanism is a combination of the cutting and plowing actions and possible occasional melting.

Though considerable work has been conducted on the material removal mechanism, a detailed investigation has not been carried out on the surface quality of the impacted material. The material removal by multiparticle impact is associated with an increase in the surface roughness of the eroded part. However, at selective angles of attack the craters join together to form a well defined ripple pattern. Such patterns have been observed by many investigators [8–10]. Finnie and Kabil [8] have presented a theoretical analysis based on the cutting action by single particle impact, which offers a good explanation for the ripple formation. A detailed experimental study of the ripple formation on copper surface was discussed by Carter et al. [10].

Experiments conducted by the present authors on the erosion related performance changes in two-dimensional airfoil cascades [11], revealed that the increase in surface roughness associated with erosion is a major factor in the performance decrease of the cascades. During these experiments, well defined ripples were observed on the airfoil surfaces, as shown in Fig. 1. In order to better understand the increase in surface roughness associated with erosion, experiments were conducted on 6061 T6 flat plate aluminum specimens. A series of experiments were carried out in an erosion wind tunnel using a collimated beam of particles. The particles used were silica sand of 165 and 225 microns mean diameter and particle velocity of 100 m/s.

Experimental Facility and Technique

The experiments were conducted in the erosion tunnel described in great detail in [6]. The erosion tunnel consists of a long acceleration duct into which the particles are fed at a controlled rate. The particles accelerate along with the air to reach steady velocities before impacting on the specimens at the test section. The particles velocities and concentrations in

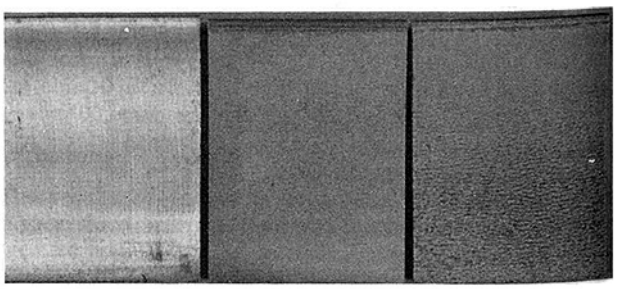

Fig. 1 Eroded blade surfaces

Contributed by the Gas Turbine Division of THE AMERICAN SOCIETY OF MECHANICAL ENGINEERS for presentation at the 28th International Gas Turbine Conference and Exhibit, Phoenix, Arizona, March 27–31, 1983. Manuscript received at ASME Headquarters January 4, 1983. Paper No. 83-GT-213.

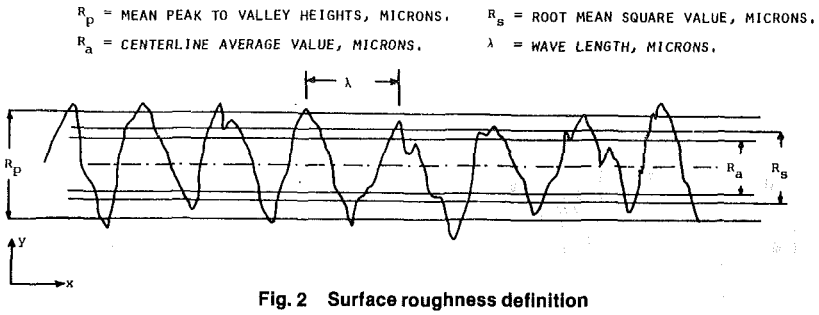

Fig. 2 Surface roughness definition

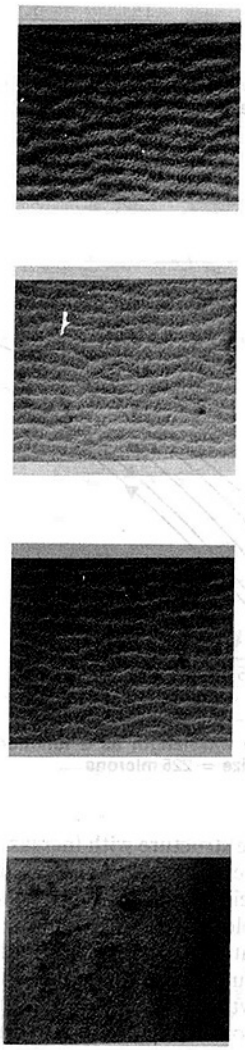

Fig. 3 Micrographs of the eroded specimens at various angles of attack: particle size = 165 microns

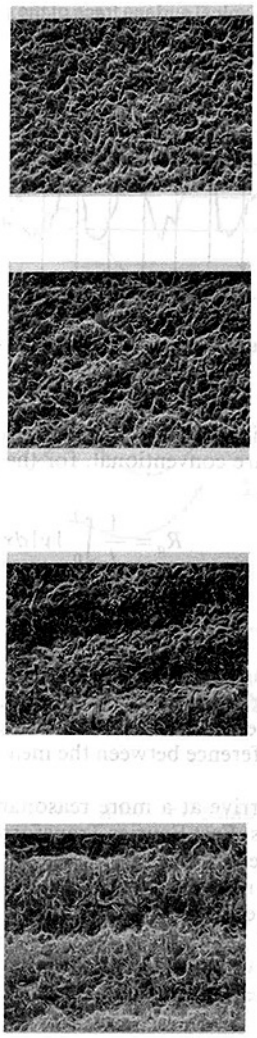

Fig. 4 Development of ripple formation at 30 deg angle of attack: particle size = 165 microns

the tunnel can be controlled exactly. The specimens used were 18 mm × 25 mm in size and 1.8-mm thick.

All experiments were conducted at a fixed concentration equivalent to a particle flux of 12.5 gm/cm^2/min. Before and after each test run, the specimens were weighed accurately using Mettler microbalance. After each test, before weighing, the specimens were washed in acetone, and ultrasonic cleaning was employed. This was followed by Scanning Electron Microscope (SEM) and stereo scan pictures of the eroded specimens. Then the surface trace of the eroded surface was obtained using Sloan Dectak profilometer. The stylus tracking force was 50 mg, the stylus diameter was 25 microns, and the minimum height of the detectable step for this instrument was 25 Angstrom, Å.

These surface traces were then digitized using an electronic digitizing pad. These values were processed to compute the wave length (λ), the centerline average (R_a), the root mean square value (R_s), and the heights of the peak to valley (R_p).

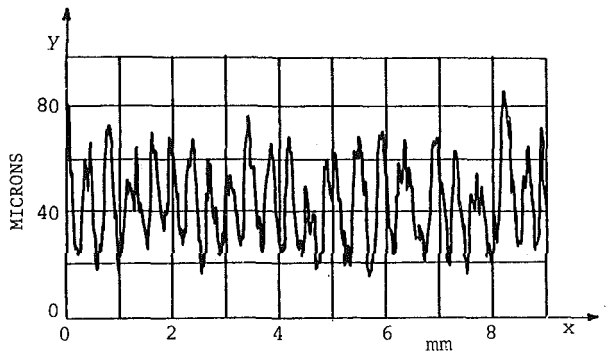

Fig. 5(*a*) Typical surface trace of the eroded surface

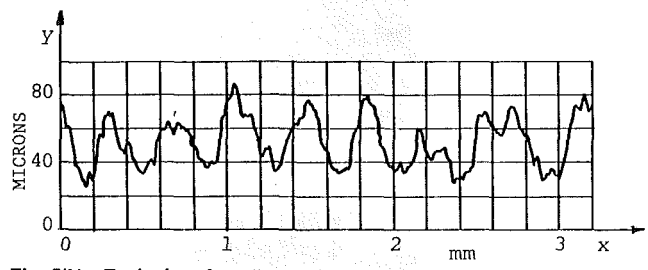

Fig. 5(*b*) Typical surface trace of the eroded surface for expanded *x*-axis

Though the definitions of centerline average and root mean squares values are conventional, for the purpose of clarity in referring to Fig. 2

$$R_a = \frac{1}{l}\int_0^l |y|\,dx \tag{1}$$

$$(R_s)^2 = \frac{1}{l}\int_0^l y^2\,dx \tag{2}$$

where l is the length of the surface trace.

The foregoing equations were used in computing the R_a and R_s values of the eroded surfaces. The R_p values were computed as the difference between the mean heights of the peaks and valleys.

In order to arrive at a more reasonable conclusion on the preceding values, Fast Fourier Transformations of the surface traces were taken, which confirmed the computed λ values. Though there is no definite wave pattern at the 90 deg angle of attack, there are definitely peaks and depressions which are taller or deeper than the R_s values. These values, averaged over the length of the specimen, were used in computing the R_p values for the 90 deg angle of attack.

Results and Discussion

One of the basic parameters that controls the roughness growth on the impacted surface is the total mass or number of particles impacting on unit area of the surface. In the majority of the reported works, attempts are made to correlate the data against the time of exposure to a uniform particle flux. In this paper, an effort is made to present the results as a function of both the time of exposure, t, in min as well as the total mass of particles impacting the surface per unit area, $\dot{m}_{ts}$ in gm/cm^2.

Figures 3(*a–d*) are the micrographs of the eroded specimens at various angles of attack. All these specimens have been impacted by 124 gms of particles per square cm of the sample surface area. It can be observed from these figures that the ripple pattern is present up to about 50 deg angle of attack. Figures 4($a-d$) represent the surface topography at a fixed angle of attack for different amounts of particles impacting the specimen. These figures explain the development of the

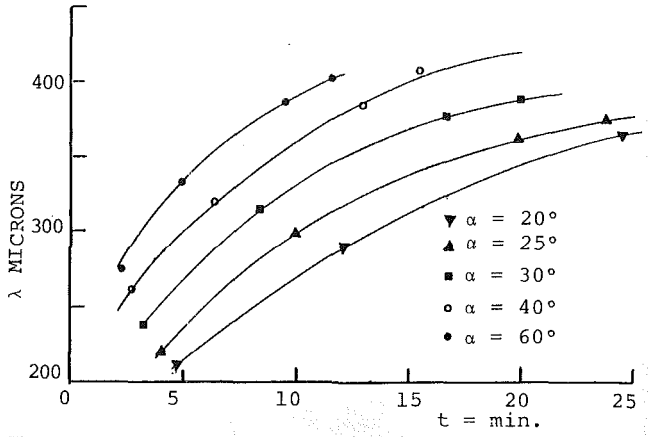

Fig. 6 Mean ripple wavelength variation with time for various angles of attack: particle size = 225 microns

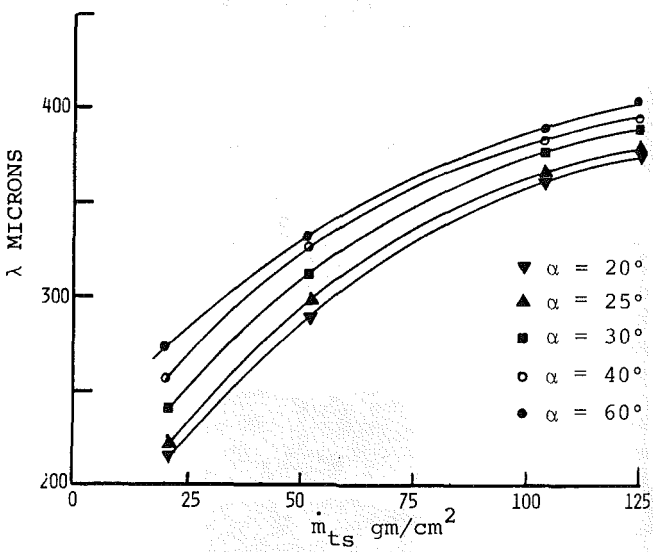

Fig. 7 Mean ripple wavelength as a function of mass of particles impacting: particle size = 225 microns

well-defined ripple structure with increasing an amount of the impacting particles. At very small quantities of particles impacting the specimen, the surface is randomly rough, due to the cutting and plowing tracks. As the amount of particles increases, the craters join together to form a well-defined ripple pattern. Further increasing the amount of particles results in the growth of the ripples amplitude. In addition, the general quality of the surface decreases with icnreased erosion.

The quantification of the parameters associated with the roughness and the ripple structure can be achieved through the centerline average, R_a, the root mean square, R_s, and the peak to valley heights, R_p, as well as the wave length, λ, of the ripple structure. Typical dek tak profilometer surface traces are shown in Figs. 5(*a*) and 5(*b*). From these traces, the R_a, R_s, and R_p values of the roughness elements and the wave length λ of the ripple structure were computed. A plot of the wave length λ as a function of the time of exposure for various angles of attack for 225 microns is given in Fig. 6. It can be seen that the wave length increases with increasing the angle of attack, α, and it reaches a steady-state value with time. When the same results are plotted against the total mass of particles impacting on the unit sample area, there is a considerable difference in the nature of the curves, as shown in Fig. 7. These curves are almost parallel to each other. The

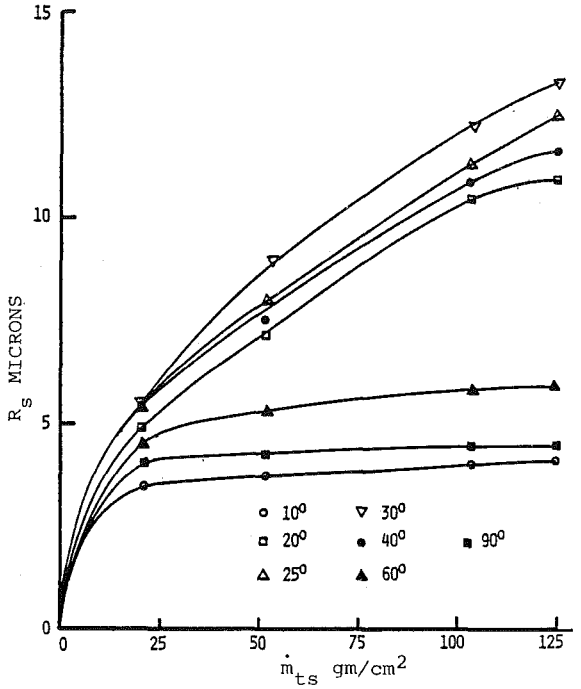

Fig. 8 Root mean square, R_s, values of the roughness heights as a function of mass of particles impacting for various angles of attack

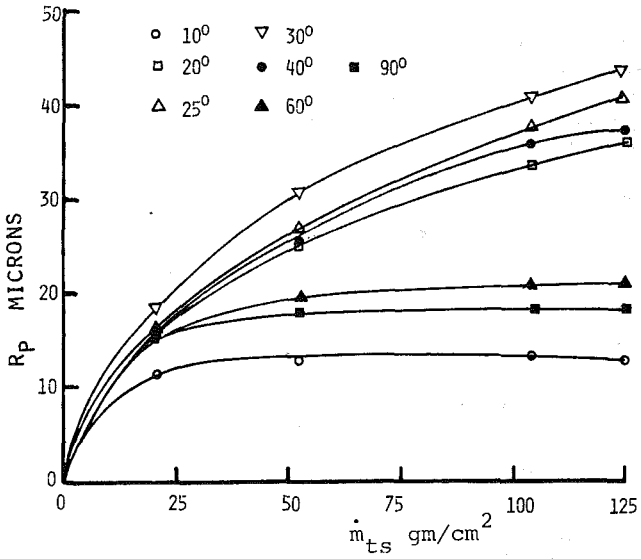

Fig. 9 Peak to valley heights, R_p, of roughness elements as a function of mass of particles impacting for various angles of attack

highest value of λ occurs around 60 deg. The ripple structure is smaller for lower angles. However, the maximum spread in the wavelengths is only about 30 microns, i.e., about 15 percent of the particle size.

The values of the surface roughness, R_s, for various angles of attack as a function of the total mass of particles impacting unit area of the specimen, are shown in Fig. 8. The inspection of this figure shows that the surface roughness rapidly reaches near steady-state values for very low (10 deg) and very high (60 to 90 deg) angles of attack. On the other hand, the roughness values, R_s, are much higher for the angles of attack between 20 to 45 deg. In addition, one can observe that even at these angles, the roughness values show a tendency to stabilize to a steady state. Figure 9 shows a plot of the peak to valley heights as a function of the impacting particle mass.

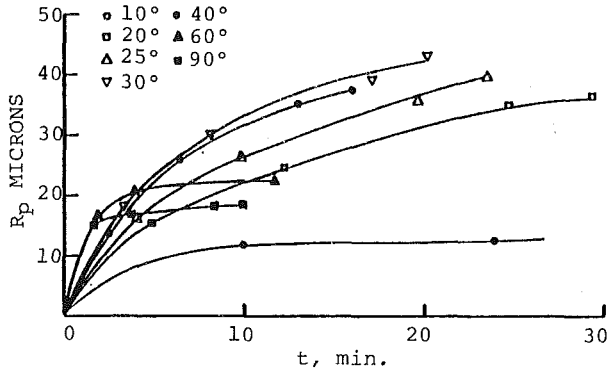

Fig. 10 Peak to valley heights, R_p, of roughness elements as a function of time: particle size = 225 microns

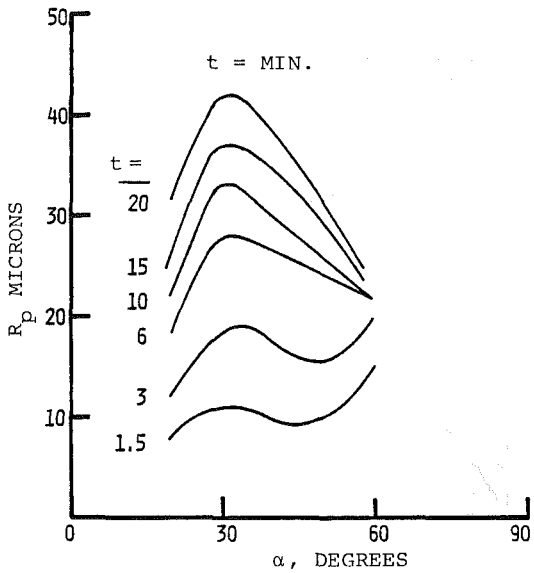

Fig. 11 Variation of roughness heights, R_p, as a function of angle of attack for various times of exposure

The peak to valley heights follow the same trend as the R_s values.

The plot of the R_p as a function of time for various angles of attack is shown in Fig. 10. These curves exhibit different characteristics; for example, at 60 and 90 deg angles of attack, R_p raise very steeply to their steady-state values and then remain constant with time. They intersect the other curves except the curve for 10 deg angle of attack. Figure 11 represents the peak to valley heights that are cross plotted against the angle of attack for various durations of exposure. From this figure, it can be seen that, for very small exposure times, the curves indicate an apparent minimum around 45 to 50 deg angles of attack. For fairly large durations of exposure, the R_p values show an entirely different tendency. All the curves show a maximum R_p around 30 deg. The only comparable experimental results are discussed by Carter et al. [10] for copper surfaces. They observed only a local minimum around 40 deg, but not the change in the nature of these curves as in the present case. It is probable that they have not reached steady-state conditions with the roughness amplitude values in their experiments.

In all the cases tested, it was found that there is a definite relation between the R_s, R_a values and the peak to valley heights, R_p. The relations $R_p = 2.5\ R_s$ and $R_p = 3.1\ R_a$ are valid at all angles of attack and different amounts of erosion within 5 percent accuracy.

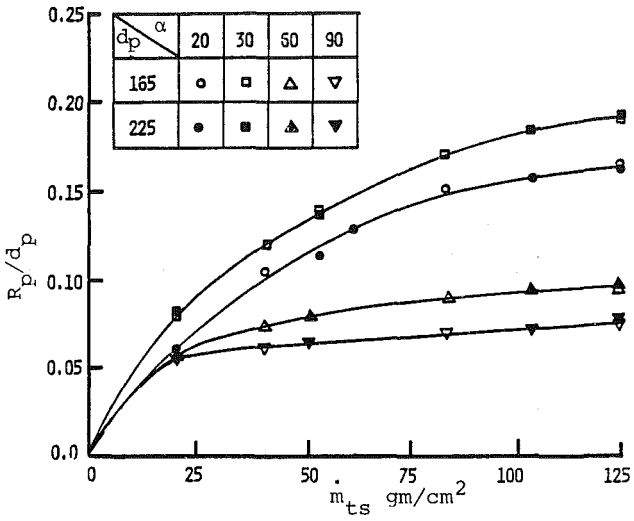

Fig. 12 Nondimensional roughness heights as a function of the mass of particles impacting

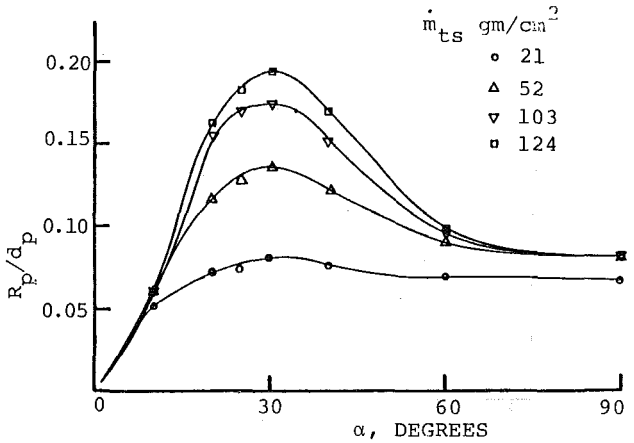

Fig. 13 Variation of the nondimensional roughness heights against angle of attack for different masses of particles impacting: d_p = 225 microns

In order to get a better understanding of the roughness formation, the values of R_p were plotted in nondimensional form versus the total mass of particles impacting per unit area for two particle sizes as shown in Fig. 12. From the inspection of this figure, one can see that the experimental points fall closely on the same curves, for 165 and 225 micron particles. The trend observed indicates that there is a definite asymptotic maximum on the roughness heights with the total mass of particles impacting unit area of the specimen.

Figure 13 shows a plot of the nondimensional roughness heights as a function of the angle for various masses of particles impacting unit area of the specimen. The maximum roughness height occurs around 30 deg angle of attack and the roughness height is approximately slightly less than 0.2 times the particle diameter. The definite relation between the R_a, R_s, and R_p values indicate that there is a good correlation between the various types of surface roughness and some erosion parameters such as angle of attack, the mass of particles impacting the specimen, and particle diameter. However, further investigations are needed on the effect of particle velocities and particle sizes before an empirical corrleation is attempted.

Conclusions

In confirmation with the existing theories and experiments, erosion ripple generation was observed for the angles of attack up to 60 degrees. The wavelength of the ripple structure increases with increasing the angles of attack, and they reach a maximum of about two times the particle diameter.

The surface roughness values increase asymptotically up to a maximum value with increased erosion. The maximum roughness value of about 0.2 times the particle diameter occurs around 30 degree angle of attack. In the absence of any quantitative theoretical models, as in the case of erosion rate prediction, it is necessary to use empirical correlations for the prediction of the surface roughness. The experimental results indicate that the roughness parameters correlate well against the mass of particles impacting unit area of the surface. However, further experiments are needed before any correlation can be attempted. Such a correlation will be very useful in aerodynamics and performance computations of turbomachinery.

Acknowledgments

The authors wish to acknowledge the helpful discourse provided by Dr. John Moetff, Head of Department of Materials Science and Metallurgical Engineering, at University of Cincinnati, Cincinnati, Ohio. This research was sponsored by NASA Lewis Research Center under Grant No. NSG 3218.

References

1 Finnie, I., "Some Observations on the Erosion of Ductile Materials," *Wear*, Vol. 19, 1972, pp. 81–90.

2 Hutchings, I. M., and Winter, R. E., "Particle Erosion of Ductile Metals: A Mechanism of Material Removal," *Wear*, Vol. 27, 1974, pp. 121–128.

3 Tilly, G. P., "Erosion Caused by Airborne Particles," *Wear*, Vol. 14, 1969, pp. 63–79.

4 Smeltzer, G. E., Gulden, M. E., and Compton, W. A., "Mechanisms of Metal Removal by Impacting Dust Particles," *Journal of Basic Engineering*, Sept. 1970, pp. 639–646.

5 Grant, G., and Tabakoff, W., "Erosion Prediction in Turbomachinery Resulting from Environmental Solid Particles," *Journal of Aircraft*, Vol. 12, No. 5, May 1975, pp. 471–478.

6 Tabakoff, W., Kotwak, R., and Hamed, A., "Erosion Study of Different Materials Affected by Coal Ash Particles," *Wear*, Vol. 52, 1979, pp. 161–173.

7 Wakeman, T., and Tabakoff, W., "Measured Particle Rebound Characteristics Useful for Erosion Prediction," ASME Paper No. 82-GT-170.

8 Finnie, I., and Kabil, Y. H., "On the Formation of Surface Ripples During Erosion," *Wear*, Vol. 8, 1965, pp. 60–69.

9 Schallamach, A., "On the Abrasion of Rubber," *Proc. Phys. Soc.*, London, Vol. 67, 1954, pp. 60–69.

10 Carter, G., Nobes, M. J., and Arshak, K. I., "The Mechanism of Ripple Generation on Sand Blasted Ductile Solids," *Wear*, Vol. 65, 1980, pp. 151–174.

11 Tabakoff, W., and Balan, C., "Effects of Solid Particles Suspended in Fluid Flow Through an Axial Flow Compressor Stage," Paper No. 75, Fifth *International Symposium on Air Breathing Engines*, Feb. 16–18, 1981, Bangalore, India.

A. Hamed
Professor.
Mem. ASME

S. Fowler
Student.

Department of Aerospace Engineering
and Applied Mechanics,
University of Cincinnati,
Cincinnati, Ohio 45221

Erosion Pattern of Twisted Blades by Particle Laden Flows

This paper presents the results of a study to predict turbomachine blade erosion by particle laden flows. Using statistical methods, this work combines particle trajectory calculations with experimental erosion data to determine the erosion of blades. The results of the calculations are presented to show the different patterns of blade material removal distribution over the surface of twisted stator blades for different particle sizes.

Introduction

The performance of gas turbine engines is known to deteriorate rapidly when the operating gas is laden with particles. The solid particles can be the product of combustion or can be present in the surrounding atmosphere in the form of dust, salt, or sand. The performance loss can be permanent or temporary, depending on the nature of the particles. The temporary loss of performance was measured experimentally [1] for an axial flow turbine and was shown to be dependent on the rate of the particle to gas mass flow rates. The experimentally measured pressure distribution over compressor and turbine blades [2] showed a reduction in the blade loading when they were tested in a tunnel with gas particle flows. If the particles are erosive they also cause a permanent loss of performance due to the change in the aerodynamic characteristics of the blade, which is caused by erosion.

The erosion of metals by solid particles have been the subject of many experimental investigations. The results of these investigations demonstrate that for a given particle target material combination, the erosion rate is affected by the impacting velocity, impingement angle, and by the metal and gas temperatures [3, 4]. It is very important to correctly simulate these effects in the erosion experiments, in carefully designed erosion tunnels where the gas particle stream conditions can be controlled [5]. Erosion cascade tunnels have also been used to determine experimentally the change in compressor cascade performance due to erosion [6]. The pressure distribution over the blade surface and the inlet and exit total pressure surveys were measured before and after the blades were subjected to erosion by particle laden flows in the tunnel. The change in the airfoil configuration and in its surface-roughness were found to change both blade loading and cascade loss coefficients [6].

The erosion of turbomachine blades can differ significantly from the cascade erosion due to several factors that affect the particle blade impact locations as well as their impacting velocities and impingement angle relative to the blade surfaces. It was shown that the shape of the hub contour and also the radial variation in the blade shape not only affect the particle trajectories but also their radial and circumferential distribution after the blade row [7, 8]. Furthermore, since the velocities of the particles as they leave any blade row are generally different in magnitude and direction than the gas flow field [9], the erosion of the blades in multistage turbomachines is dependent on their stage location.

Particle size has the greatest effect on the particle trajectories, on the frequency of the blade impacts, as well as on the impact conditions. The larger particle trajectories are dominated by their impacts with the blade, and with the hub and tip surfaces, but the smaller particle trajectories are more influenced by the flow field than by their boundary impacts. The rebounding velocities after the surface impacts are different in magnitude and direction from the impacting particle velocities. Rotor impacts in particular can drastically modify the particle trajectories, since circumferential velocities of the rebounding particles can even be higher than the rotor speed itself [9]. All these factors combine to produce different blade erosion patterns for the different particle sizes.

Analysis

The particle dynamics in a gas-solid suspension are determined by the gas-particle interaction and particle-boundary impacts. In turbomachinery applications, the particle concentrations are usually small enough that interparticle interactions are not considered in the trajectory calculations. The particles move in the gas flow under the influence of the drag forces until they impact the blades or annular surfaces. Their velocities after these impacts are dependent upon the magnitude and direction of their impacting velocity, relative to the surface. The accurate representation of the flow field, and of the geometry of the various boundaries, is therefore very important in any method of particle trajectory calculations. Hussein and Tabakoff [9] developed the first method for calculating solid particle trajectories in axial flow compressor and turbine stages [9, 10], that models the particle impacts with the blades and their subsequent rebounds. In this method [9] the representation of the blade airfoil shape and the blade to blade flow field at the mean radius are used in the three-dimensional particle trajectory calculations. A second method was developed by

Contributed by the Gas Turbine Division of THE AMERICAN SOCIETY OF MECHANICAL ENGINEERS for presentation at the 28th International Gas Turbine Conference and Exhibit, Phoenix, Arizona, March 27-31, 1983. Manuscript received at ASME Headquarters January 4, 1983. Paper No. 83-GT-214.

Hamed [11] which is based on the midchannel hub-to-tip solution coupled with a blade-to-blade velocity gradient equation for a three-dimensional flow field representation. The method presented by Beacher, Tabakoff, and Hamed [8] involves a more complex representation of the three-dimensional flow fields.

Particle Dynamics. The equations governing the three-dimensional particle motion in the flow field are written in cylindrical polar coordinates as follows

$$\ddot{r}_p = F(V_r - \dot{r}_p) + r\,\dot{\theta}_p^2 \tag{1}$$

$$r\ddot{\theta}_p = F(V_\theta - r\,\dot{\theta}_p) - 2\dot{r}_p d\dot{\theta}_p \tag{2}$$

$$\ddot{z}_p = F(V_z - \dot{z}_p) \tag{3}$$

where r_p, θ_p, and z_p define the particle location in cylindrical polar coordinates, and V_r, V_θ, V_z represent gas velocities in the radial, circumferential, and axial directions, respectively, and the particle coordinate derivatives are with respect to an inertial frame of reference. The force of interaction between the two phases per unit mass of particles is represented by the first term on the right-hand side of the equations. It is dependent on the relative velocity between the particles and the gas flow, as well as the particle size and shape. The other terms in the equations represent the centrifugal force and Coriolis acceleration.

Particle-Gas Interactions. The interaction force parameter, F, is dependent on the relative velocity between the particles and the gas, on the particle size, and on the gas and particle material densities

$$F = \frac{3}{4}\frac{\rho}{\rho_p}\frac{C_D}{d}[(V_r - \dot{r}_p)^2 + (V_\theta - r\,\dot{\theta}_p)^2 + (V_z - \dot{z}_p)^2]^{1/2} \tag{4}$$

where ρ, ρ_p are the gas and solid particle densities, d the particle diameter, and C_D the drag coefficient. The drag coefficient is a function of the Reynolds number, which is also based on the relative velocity between the particle and the gas. In the trajectory calculations, empirical relations [10] are used for the drag coefficient of spherical particles.

The Flow Field Representation. Traditionally, the complex three-dimensional turbomachinery flow fields are synthesized from two-dimensional flow solutions, on blade-to-blade, and hub-to-tip stream surfaces. The blade-to-blade solutions are used in axial machines with large hub-to-tip ratios, while the meridional solutions are used when the radial variations in the blade shape, or when the axial variation in the inner or outer annulus are significant. The second approach is more appropriate for the case of twisted blades and/or in regions of contoured hub or tip annuli. In this work, the solution of the flow field was obtained using the code of [12], which combines the matrix and the velocity gradient methods in the numerical solution over the midchannel, hub-to-tip stream surface. The velocity gradient equations along the orthogonal grid lines, t, in the hub-tip direction is given by

$$\frac{dV}{dt} = V\left[\frac{\cos^2\beta + \cos(\alpha-\phi)}{r_c} - \frac{\sin^2\beta\cos\phi}{r} + \sin\alpha\sin\beta\cos\beta\frac{d\theta}{dm}\right] + \cos\beta\frac{dV_m}{dm}\sin(\alpha-\phi) + r\cos\beta\frac{dV_\theta}{dm}\frac{d\theta}{dt} \tag{5}$$

where β is the angle between the gas velocity vector and the meridional plane, α is the angle between the meridional streamline and the axial direction, while θ is the angle between the t grid lines and the radial direction, ϕ is the angle between the s-coordinate and the axial direction, r_c is the radius of curvature on the meridional streamlines, V_m and V_θ are the meridional and circumferential gas velocity components, and V is the total gas velocity.

The solution to equation (5) provides the circumferentially averaged flow velocity component and gas density at the midchannel hub-to-tip stream surface. This solution is combined with a blade-to-blade velocty gradient equation to account for the circumferential variation of the flow conditions

$$\frac{\partial V}{\partial\theta} = \cos\beta\frac{d(rV_\theta)}{dm} \tag{6}$$

The flow field computations are performed separately, and the computed flow properties are determined at the grid points of the orthogonal mesh in the midchannel stream surface [13]. The required gas properties at the various locations during particle trajectory calculations are obtained using linear interpolation.

Particle Boundary Interactions. The numerical integration of equations (1-3) from the particle's initial conditions provides the particle trajectories until they impact a solid boundary. After impacting a solid boundary, the magnitude and direction of the particle rebounding velocity is dependent on the particle and target materials, and on the impact conditions. Empirical relations were derived from the results of experimental measurements of the particle rebound characteristics which were obtained using high-speed photography [3] and laser velocimetry [14]. These experimental studies were carried out in special erosion tunnels, which were designed to include the aerodynamic effects in the rebound characteristics. Empirical correlations were derived

Nomenclature

C_D = particle drag coefficient
d = particle diameter (m)
E = blade mass erosion parameter (mgm/m^2/gm)
F = force interaction parameter between the gas and particles (1/s)
m = coordinate along meridional streamline (m)
r = radial distance from the axis (m)
r_c = radius of curvature of meridional streamline (m)
s = distance along orthogonal mesh lines in through flow direction (m)
t = distance along orthogonal mesh lines in direction across flow, (m)
u = normalized stream function
V = flow velocity (m/s)
V_p = particle velocity (m/s)
z = axial coordinate (m)
α = angle between meridional streamline and axial direction (radiance)
β = angle between flow velocity vector and meridional plane (radiance)
θ = angular coordinate (radiance)
ρ = gas density (kg/m^2)
ρ_p = particle density (kg/m^2)
ϕ = angle between s-line and axial direction (radiance)

Subscripts

m = component in direction of meridional streamlines
p = particle
r = component in radial direction
s = component in s-direction
t = component in t-direction
z = component in axial direction
θ = component in tangential direction

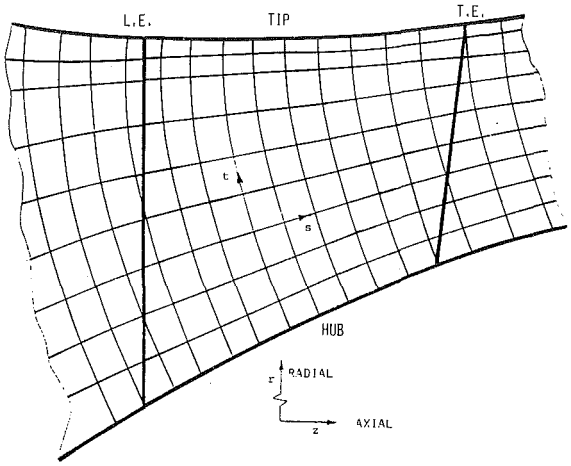

Fig. 1 Meridional projection of the blades and computational grid

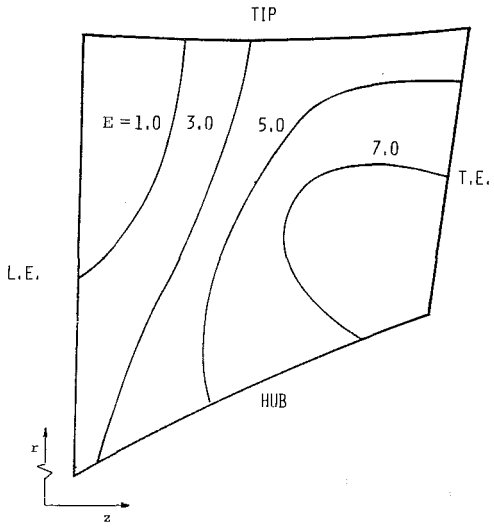

Fig. 2 Blade erosion mass parameter distribution for 100 micron particles

for the statistical distribution parameters of the experimentally measured restitution ratios as functions of the particle impingement angle [3]. These correlations were used in the present study to determine the particle rebounding conditions after blade, hub, or tip impacts.

In the three-dimensional trajectory calculations the impingement angles are determined from the direction of the impinging velocity and the local normal to the impact surface. The same orthogonal grid that is used in the flow computations is also used in the geometric description of the blade surfaces. The vane shapes are described by the θ-coordinates of the midchannel stream surface and by the blade-to-blade passage width, while the hub and tip contours are defined by the (r, z)-coordinates of the grid points at the inner and outer radii.

Blade Mass Erosion Parameter. The experimental measurements in the erosion tunnel provide erosion data in the form of the erosion mass parameter that is equal to the ratio of the eroded mass of target material to the mass of impinging particles [4]. This erosion mass parameter was found to be dependent upon the particle impingement velocity, impingement angle, and on the flow and target temperatures for a given particle target material combination. The computation of blade erosion combines the empirical equation of the mass erosion parameter with the results of the particle trajectory calculations. The distribution of the

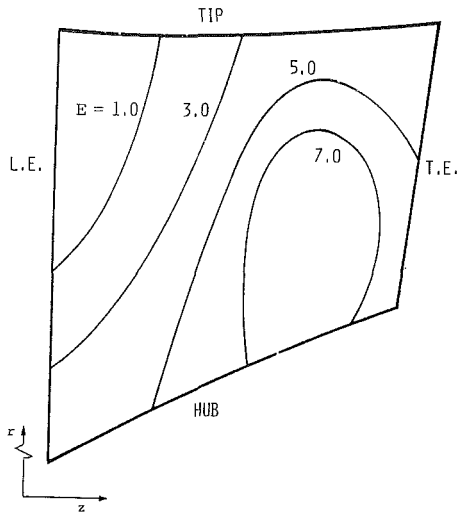

Fig. 3 Blade erosion mass parameter distribution for 50 micron particles

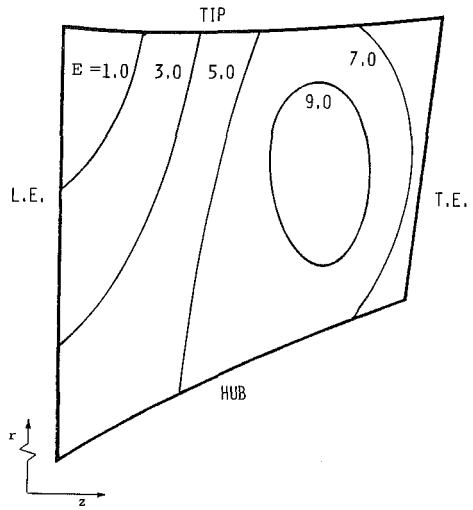

Fig. 4 Blade erosion mass parameter distribution for 20 micron particles

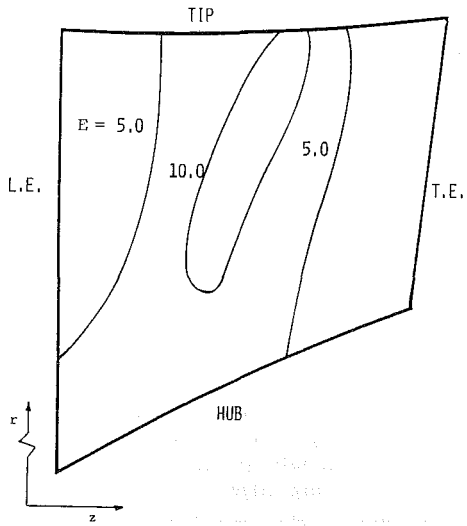

Fig. 5 Blade erosion mass parameter distribution for 10 micron particles

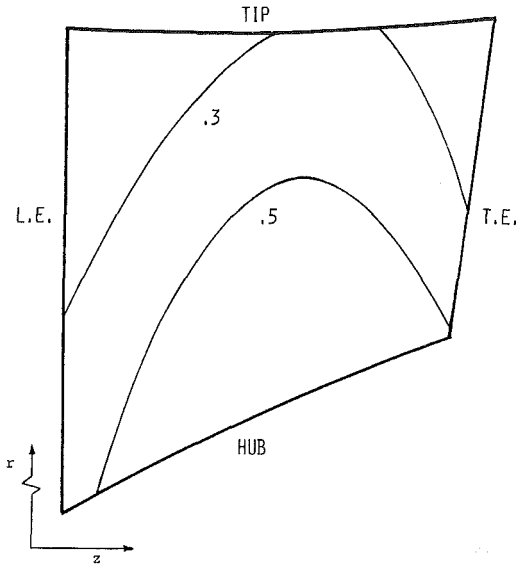

Fig. 6 Frequency of blade surface impact by 100 micron particles

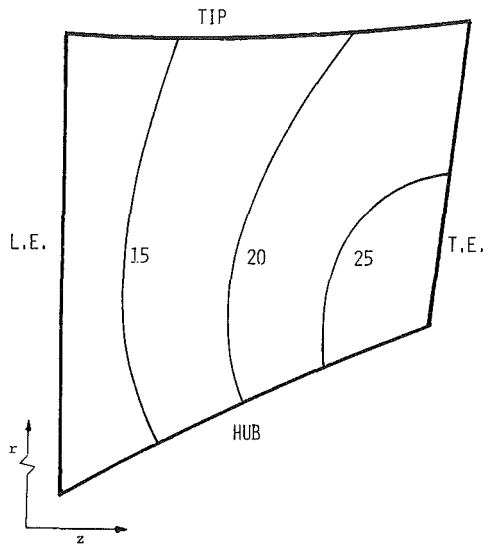

Fig. 8 Local impact angle of 100 micron particles (deg)

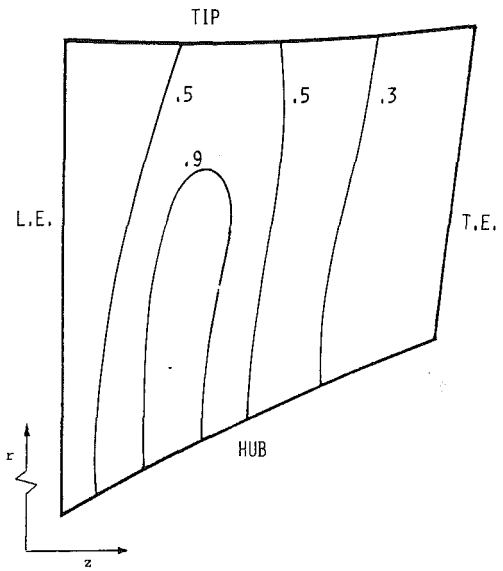

Fig. 7 Frequency of blade surface impact by 10 micron particles

particle impingement velocities and impingement angles and the frequency of particle impacts over the blade surface affect the resulting blade erosion pattern. A different parameter, E, is used to present the computed blade erosion results; it is defined as ratio of the mass of the eroded blade material per unit blade surface area to the total mass of particles ingested by the engine. Using this parameter, E, the computed results representation demonstrates the effects of all parameters influencing the blade erosion pattern, including the number of blades as well as blade, hub, and tip configurations.

Results and Discussions

The erosion pattern in a row of twisted blades were determined by combining the particle trajectory analysis and erosion empirical data using statistical methods. The twisted blades are located in a highly contoured hub region with a tip diameter of 0.335 m and hub-tip ratio of 0.56 and 0.72 at the blade leading and trailing edges, respectively. The radial variation in the blade stagger angle was between 30 deg at the hub to 23 deg at the tip with a constant blade chord of 0.062 m. Because of the hub shape, the flow field calculations were performed in a (40 × 10) grid that extends about one blade chord upstream and downstream of the blade row. The blades themselves were located within a (13 × 10) grid, as shown in Fig. 1. The results of the computations are presented for the erosion of aluminum blades by quartz particle laden flows.

Statistical methods were used in the trajectory calculations with respect to particle distribution at the inlet, where the particle velocities were equal to the local gas velocity. Figures 2–5 show the erosion pattern resulting from particles ranging in size between 10 and 100 microns in diameter. The contours of blade mass erosion parameter, E, over the blade pressure surface show the ratio of the mass of blade material erosion per unit blade surface area per unit mass of ingested particles in (mgm/m^2/gm).

The location of maximum blade erosion is seen to be dependent on the particle size. The maximum erosion for larger particles is seen at the blade hub near the trailing edge. This is the region of both maximum impingement angle (25–30 deg) and maximum number of particle impacts. The impingement angle of 20 deg coincides with the angle of maximum erosion for this particle target material combination. The magnitude of the impact velocity of these large particles was nearly constant along the blade surface, since these large particles continue to move nearly with their initial velocity condition up to the point of impact. On the other hand, the smaller particles rapidly acquire the local flow conditions and have much higher impact velocities but much smaller impact angles than the larger particles. The variation in the erosion pattern with particle size can be seen in Figs. 2–5. As the size of the particle decreases, the blade location of maximum erosion is seen to move both radially and axially away from the hub trailing edge corner. The blade erosion by the small 10 micron particles is shown in Fig. 5, where the maximum blade material removal is found near the blade midchord.

Comparing Figs. 2 and 5, one can see that, not only is the erosion pattern dependent on the particle size, but the amount of material removal changes with particle sizes. The higher values of local blade erosion by the smaller particles is due to multiple particle impacts with the blade surface. Unlike the large particles whose velocities are reduced with each impact, these small particles rapidly acquire the local gas velocity after each impact, with subsequent impacts causing greater erosion damage.

The frequency of particle blade impacts are shown in Figs.

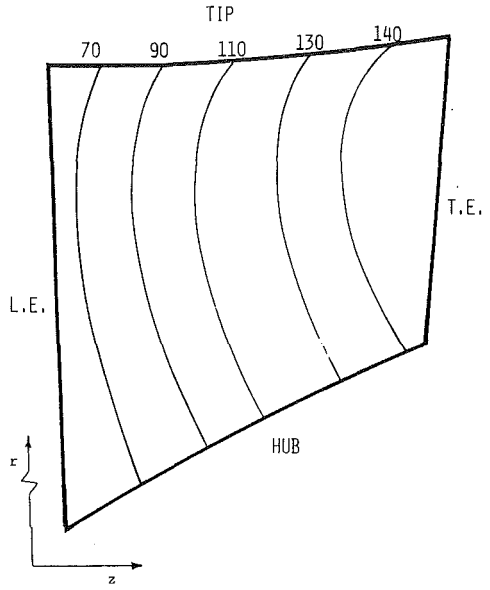

Fig. 9 Local impact velocity of 10 micron particles (m/s)

6 and 7 for 100 micron and 10 micron particles. The labels on the contours in these figures represent the ratio of the mass of particles impacting blade unit surface area to the average mass of particles ingested per unit frontal area at the blade leading edge. One can observe a large difference between the pattern of the impact frequency of smaller and larger particles. In comparing Fig. 6 with Fig. 2, and Fig. 7 with Fig. 5, one must remember that the material removal by erosion is also dependent on the local impact velocity and impingement angles of the particles. The large particle impact angles were dependent on the location of impact (Fig. 8), while the small particles impact velocities varied considerably with the blade impact location (Fig. 9). All these factors combine to produce the erosion patterns of Figs. 2–5.

Conclusion

This work presents the results of a method for calculating turbomachine blade erosion by particle laden flows. Statistical methods are combined with particle trajectory computations and with the experimental data of metal erosion and particle rebound characteristics in the prediction model. The results show that the distribution of material removal by erosion over the blade surface is strongly influenced by the particle size.

Acknowledgment

This research work was sponsored by U.S. Army Research Office under Contract No. DAAG29-82-K-0029.

References

1 Tabakoff, W., Hosny, W., and Hamed, A., "Effect of Solid Particles on Turbine Performance," ASME JOURNAL OF ENGINEERING FOR POWER, Jan. 1976, pp. 47–52.

2 Tabakoff, W., and Hussein, M. F., "Effect of Suspended Solid Particles on the Properties in Cascade Flow," *AIAA Journal*, Vol. 9, No. 8, 1971, pp. 1514–1519.

3 Grant, G., and Tabakoff, W., "Erosion Prediction in Turbomachinery Resulting from Environmental Solid Particles," *Journal of Aircraft*, Vol. 12, No. 5, 1975, pp. 471–478.

4 Tabakoff, W., Hamed, A., and Ramachandran, J., "Study of Metals Erosion in High Temperature Coal Gas Streams," ASME JOURNAL OF ENGINEERING FOR POWER, Vol. 102, Jan. 1980, pp. 148–152.

5 Tabakoff, W., and Hamed, A., "Investigation of Gas Particle Flow in Erosion Wind Tunnel," 7th Annual Conference on Materials for Coal Conversion and Utilization, National Bureau of Standards, Gaithersburg, MD, November 16–18, 1982.

6 Tabakoff, W., Hamed, A., and Balan, C., "Performance Deterioration of an Axial Flow Compressor Stage with Presence of Solid Particles," *Proceedings of the 5th Intern. Symposium on Airbreathing Engines*, 1980.

7 Hamed, A., "Solid Particle Dynamic Behavior Through Twisted Blade Rows," *Proceedings of the Symposium on Particle Laden Flows in Turbomachinery*, 1982, ASME, New York, pp. 33–41.

8 Beacher, B., Tabakoff, W., and Hamed, A., "Improved Particle Trajectory Calculations Through Turbomachinery Affected by Coal Ash Particles," ASME JOURNAL OF ENGINEERING FOR POWER, Vol. 104, Jan. 1982, pp. 64–68.

9 Hussein, M. F., and Tabakoff, W., "Computation and Plotting of Solid Particle Flow in Rotating Cascades," *Computers and Fluids*, Vol. 2, 1974, pp. 1–15.

10 Hussein, M. F., and Tabakoff, W., "Dynamic Behavior of Solid Particles Suspended by Polluted Flow in a Turbine Stage," *Journal of Aircraft*, Vol. 10, No. 7, July 1973, pp. 434–440.

11 Hamed, A., "Particle Dynamics of Inlet Flow Fields with Swirling Vanes," *Journal of Aircraft*, Vol. 19, NO. 9, 1982, pp. 707–712.

12 Katsanis, T., and McNally, W. D., "Revised Fortran Program for Calculating Velocities and Streamlines on the Hub-Shroud Midchannel Stream Surface of an Axial, Radial, or Mixed Flow Turbomachine or Annular Duct: Vol. 1 and 2," NASA TN D8430, and NASA TN D8431, 1977.

13 McNally, W. D., "FORTRAN Program for Generating a Two-Dimensional Orthogonal Mesh Between Two Arbitrary Boudaries," NASA TN D6766, 1972.

14 Tabakoff, W., and Sugiyama, Y., "Experimental Method of Determining Particle Restitution Coefficients," Symposium on Polyphase Flow and Transient Technology Proceedings, 1980.

Steam-Cooled Gas Turbine Casings, Struts, and Disks in a Reheat Gas Turbine Combined Cycle: Part I—Compressor and Combustor

I. G. Rice, P. E.
Consultant,
Spring, Texas 77373
Fellow ASME

High-cycle pressure-ratio (38-42) gas turbines being developed for future aircraft and, in turn, industrial applications impose more critical disk and casing cooling and thermal-expansion problems. Additional attention, therefore, is being focused on cooling and the proper selection of materials. Associated blade-tip clearance control of the high-pressure compressor and high-temperature turbine is critical for high performance. This paper relates to the use of extracted steam from a steam turbine as a coolant in a combined cycle to enhance material selection and to control expansion in such a manner that the cooling process increases combined-cycle efficiency, gas turbine output, and steam turbine output.

Introduction

Aircraft and industrial gas turbines with cycle-pressure ratios of 5 to 7 and with firing temperatures of 1400 to 1500°F[1] have in the past been designed to operate satisfactorily through the proper material selection and known design procedures. Tip clearances of the compressor and turbine rotating blades with respect to the stationary casings were important but not overly critical to the operation of the engines. No special cooling techniques were necessary to control tip clearance for these low-cycle ratios.

Today engines with cycle-pressure ratios of 20 to 30 have been in service for a number of years (aircraft: CF6, JT9, RB-211; and industrial: LM2500, LM5000, and RB-211). Material selection and cooling techniques have been developed to match the expansion of the disks and the rotating blades with the expansion of the stator parts, struts, and casings to retain acceptable blade-tip clearances.

NASA, through a 200,000,000 dollar commercial jet engine program, is currently developing two E^3 technical-readiness engines—one through General Electric and the other through Pratt and Whitney Aircraft—to demonstrate high-performance fan technology with cycle-pressure ratios of 38 to 42 and firing temperatures of 2250°F continuous. Growth versions indicate cycle-pressure ratios up to 44 [1].

These high-ratio, high-temperature engines encounter a far more severe environment which necessitates more careful material selection. Advanced design methods of controlling tip clearance of both the compressor and turbine sections are necessary. Minicomputers and microprocessors are being applied to control the compressor and turbine outer-shell cooling to shrink or expand the casings to maintain close-tip clearance and at the same time prevent tip rubbing. Air is being used to provide the shell cooling either through impingement cooling or convection [2, 3] to accomplish active blade-tip clearance control.

Close-compressor blade-tip clearance is necessary to obtain high-compression efficiency at the elevated pressure and higher compression temperatures where the reduced blading size accentuates the fluid dynamics involved. Tip leakage and recirculation reduces compression efficiency, and if not controlled the higher-cycle-pressure ratios will not provide higher cycle efficiency and a corresponding lower-specific-fuel consumption.

Similarly, turbine-blade-tip clearance is important to prevent gas-blade bypass—particularly in regard to the first-stage blading, where a high-pressure drop of 3 to 4 ratio is being realized through new techniques of blunt-nosed "S"-wall nozzle vanes and a higher degree of reaction in transonic-rotating blades (40 percent reaction and 60 percent impulse).

The prototype E^3 engines are being designed to operate at about 2250°F TIT continuous, using air as the blade, disk, and casing coolant. When considering 2400 to 2700°F TIT continuous for an industrial gas generator, there is a critical ducting area between the high-pressure turbine blading and the low-pressure blading which is subjected to a much higher temperature by about 350°F (2000°F versus 1650°F). The main support struts pass through this ducting to tie the inner barrel, seals, and rear bearing to the outer casing. The higher

[1] See Page 856 for all SI conversion factors.

Contributed by the Gas Turbine Division of THE AMERICAN SOCIETY OF MECHANICAL ENGINEERS for presentation at the 28th International Gas Turbine Conference and Exhibit, Phoenix, Arizona, March 27-31, 1983. Manuscript received at ASME Headquarters December 22, 1982. Paper No. 83-GT-85.
Copies will be available until January 1984.

2000°F environment requires special materials and cooling techniques to cope with the strength of materials and thermal expansion of these parts.

It is not practical to consider using steam as a disk and casing coolant in aircraft engines due to the weight restriction. Industrial gas turbines, on the other hand, do not have these weight restrictions; and steam, a far superior coolant with twice the specific heat and a lower viscosity, can be applied as a coolant—particularly when a combined cycle using a bottoming steam turbine is contemplated.

Steam can be extracted from the steam turbine—optionally desuperheated to saturation temperature, used as the coolant and then readmitted to the steam turbine at a higher temperature to obtain additional steam turbine work before being condensed. A closed system is thus possible whereby no steam is lost to the atmosphere. This prospect is particularly attractive where outer shell, strut, inner barrel, and the exhaust hood and transition duct are concerned. A higher gas turbine reheat temperature can be realized through cooling the power turbine in this manner [4].

Advanced industrial gas turbines are to fire at 2600°F and higher. Considerable research and development money is being spent to accomplish this goal. This research and development, however, is directed toward air cooling (transpiration) and water cooling; steam is not receiving much attention. NASA has made some general studies using steam, but, to this author's knowledge, no specific hardware is being developed. Private American companies, such as GE, have given steam a superficial investigation using the simple-cycle gas turbine, but the reheat gas turbine has not been considered as a contender [5]. Japan is, however, developing a reheat gas turbine for combined cycle operation [6], but air is the coolant.

Previous technical papers [7–13] have dealt with the reheat combined-cycle thermodynamics and steam cooling of the gas turbine rotating blades, stationary vanes, and the power turbine shell. This study focuses on steam cooling the gas generator: the high-pressure-compressor shell, compressor disks, turbine shell, inner barrel, support struts, and diffuser, as well as the turbine disks and internal supporting structure. The subject matter of this study is divided into two parts: Part I deals with the compressor and combustor, whereas Part II covers the gas-generator turbine and power turbine.

Steam cooling, as discussed in Parts I and II ofthis study, makes possible active control of the compressor and turbine blade-tip clearances during start-up, running, and shutdown. Close blade-tip clearance control increases gas-generator efficiency and output and protects against blade-tip rub. Such cooling also increases the allowable stress levels of the various parts because of the resulting appreciable lower metal temperatures; more freedom in material selection is thus made possible. There is an added bonus of reduced disk low-cycle fatigue problems by reducing the temperature differential between hub and rim—particularly during start-up.

Cycle Arrangement

The reheat gas turbine/double-reheat steam turbine (2400 psig 1100/1050/850°F) combined-cycle arrangement being considered is shown in Fig. 1 [4]. The heat transfer surfaces to be discussed in this paper are designated by letters "J" and "K." The cold first-reheate steam at about 600 psia is introduced to the turbine shell for heat exchange J whereas the second cold-reheat steam at about 140 psia is fed to the compressor shell for heat exchange K.

The second steam reheat hot return is mixed with bypass steam in a crossover mixer upstream of the LPT steam turbine. This mixer is lettered "O" in Fig. 1 and a conceptual cross-section is shown in Fig. 2. Reference [4] presents the cycle analysis.

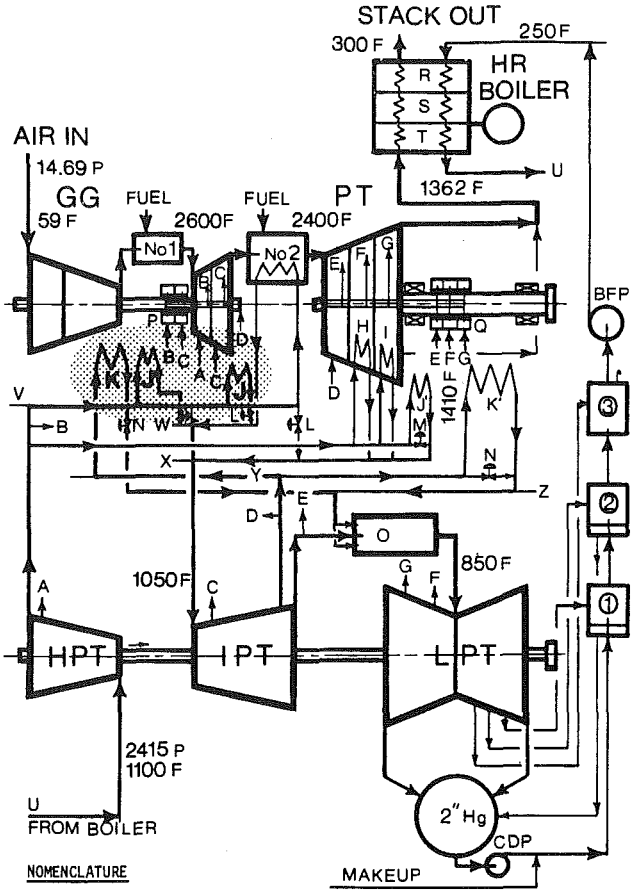

Fig. 1 Schematic diagram of steam-cooled reheat gas turbine for combined-cycle operation

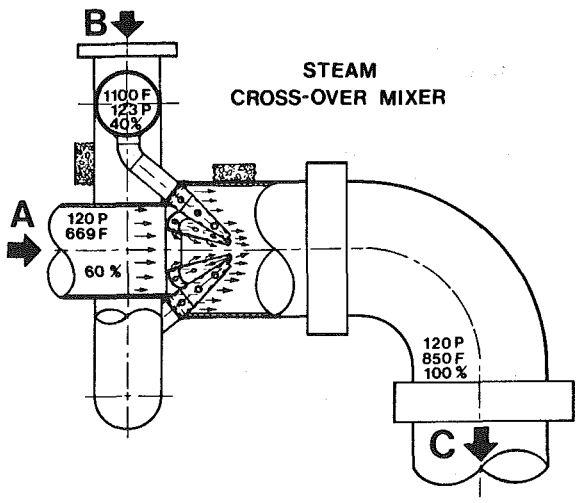

Fig. 2 Low-pressure steam turbine reheat mixer

Alternatives of higher pressure-steam systems can also be considered. Either a supercritical steam pressure of 3500 or 4500 psig can be applied for the double reheat steam cycle for future cycles.

Table 1 Combined-cycle steam turbine data

Steam cycle	2400 PSIG[b] 1100/1050/850°F	3500 PSIG[c] 1000/1050/1050°F	4500 PSIG[c] 1100/1050/1050°F
1st reheat extraction press			
PSIG	589	992	1084
temp. °F	734	705	702
2nd reheat extraction press			
PSIG	125	293	328
temp. °F	701	744	750
Steam turbine cycle efficiency—%[a]	42.0	43.5	46.5
Improvement in combined cycle eff—%	Base	3.6	10.7
Combined cycle efficiency, LHV—%	58.8	59.4	60.7

[a] Based on three stages of feedwater heating to 250°F to heat recovery boiler economizer
[b] Reference [4] data
[c] Reference [14] data

Gas Generator with Steam-Blade Cooling

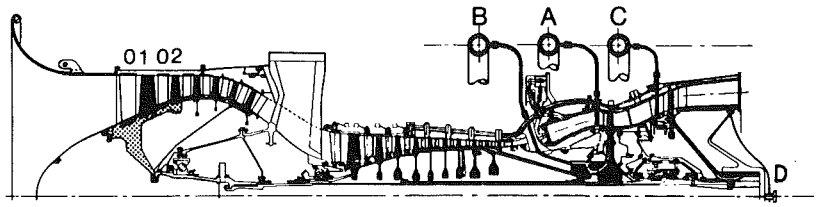

Fig. 3 Conceptual cross section of steam-cooled gas generator based on P & WA 38.6 CPR E[3] development engine

Extraction-steam pressures and temperatures are important when contemplating steam cooling. It is desireable to take advantage of the reheat-steam pressure drops and the available extraction points when considering more advanced cycles presently being proposed by the Electric Power Research Institute (EPRI) [14].

Table 1 presents a tabulation of relative data for the three cycles as applied to the reheat-gas/reheat-steam combined cycle. It can be noted that the full increase in steam-cycle efficiency is not carried over to the overall combined-cycle efficiency. The steam cycle only accounts for about 30 percent of the total power and therefore can only upgrade overall plant efficiency by this ratio of influence. The incentive to go to supercritical steam pressures for the combined cycle is not overly compelling as can be noted on the bottom line when considering the extra initial cost involved and the additional operating and maintenance costs to be expected.

Figure 3 presents the P & WA E[3] engine which has been conceptually modified by the author for steam cooling. Primary-extraction steam passes through steam lines A, B, C, and D to admit cooling steam to the gas generator blading. Line A admits steam to the first-stage nozzle vanes, line B to the first-stage rotating blades, line C to the second-stage nozzle vanes and line D to the second-stage rotating blades. Saturated steam at different pressures (approximately 30 percent above each particular total gas-stream pressure) is applied to cool the vanes and blades. These steam flows steam-blanket the blading in an open cycle whereby the steam is passed through the reheat combustor, power turbine, and heat recovery boiler before being discharged to the atmosphere.

Compressor Shaft, Disk, and Casing Cooling

Reference is made to Fig. 4, which is a plot of cooling-fluid temperature versus compression ratio.

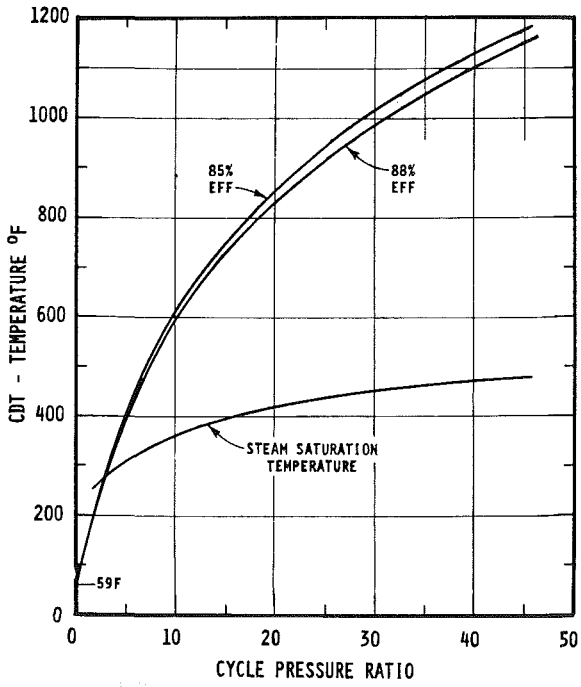

Fig. 4 Contrast in cooling temperatures of CDT air and saturated steam

The very top line in Fig. 4 shows the air temperatures encountered for an 85 percent adiabatic compression efficiency and the next top line for an 88 percent compression efficiency. Note that the temperature level encountered at a 38 cycle-pressure ratio is about 1100°F. The bottom line is a plot of saturated-steam temperature versus pressure. The appreciable difference in cooling temperature between steam and air can be noted; in addition, as shown in Fig. 5, saturated steam at

the high CPR's has elevated specific heat ranging from .8 to .9 BTU/lb°F, providing additional cooling capacity as compared to air with its nearly constant specific heat of only .245.

An enlarged cross section of a portion of the modified E^3 technology gas generator is shown in Fig. 6. The first section of the high-pressure compressor rotor drum to the left side is typically made out of a titanium alloy (Ti 6AL - 4V) which has a coefficient of thermal expansion of 5.0×10^{-6} in/in°F and a low conductivity rate of 50 BTU in/(ft²hr°F). These expansion and conductivity values have to be matched by the outer-casing material characteristics during start-up, running, load changes, stopping, full-load trips and load shedding.

Typically, the high-pressure end of the compressor has disks made out of a nickel-base material such as A-286, Inco 901, or Inco 718 to withstand the high 1000 to 1100°F temperature environment. The thermal expansion of these materials range from 8.0 to 9.8 $\times 10^{-6}$ in/in/°F and the thermal conductivity from 135 to 165 BTU in/(ft²hr°F). These values are considerably higher than those of the titanium-alloy-forward drum and therefore careful matching of the outer-casing material and steam cooling is necessary to control tip clearance.

Extracted steam which has been desuperheated under controlled conditions is used to cool the outer casing and radial compressor struts to the inner casing. The inner casing holds and positions the stator vanes and the shroud strips that encircle the rotating blades. A two-point control sytem is proposed as shown in Fig. 7, where the steam at 140 PSIA and 355°F is admitted at two points, Station 1 and Station 2. The heated steam exits at about 125 PSIA and 600°F and is readmitted to the steam turbine after first being further heated to 1100°F in the PT exhaust area.

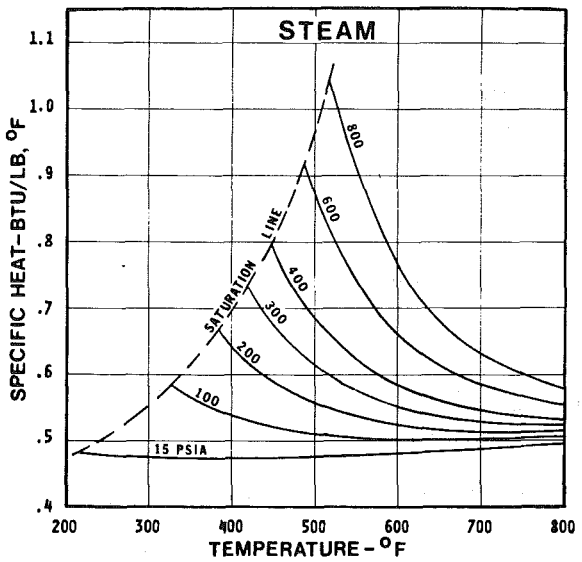

Fig. 5 Specific heats of steam near the saturation line at various pressures

Signals from a minicomputer, microprocessor unit control the two pressure-control valves (PRVs). Inputs to the microprocessor are all the pertinent variables; these are engine speeds (LP compressor, HP compressor, and PT), ambient temperature, gas generator firing temperature, compressor discharge temperature, output, reheat TIT, shell and space temperatures, etc. Variables are fed to the minicomputer as required and programmed.

The amount of steam that is admitted at Stations 1 and 2 control the expansion of the outer casing and compressor-radial support struts (see the enlarged views of Fig. 6 given in Figs. 8(*a*) and 8(*b*)).

The radial support struts each contain extended surface and a flow-control dam (Section $R' - R'$) to create a fast thermal response so that the casing can be cooled or heated rapidly and at a faster rate than the compressor rotor during conditions of load charges, trips, and start-up.

The two inner chambers between Stations 1 and 2 in Fig. 6 are filled with compressor air through bleed hole (orifices). The temperatures corresponding to these two levels of pressure are much lower than the compressor discharge temperature and provide a modest thermal barrier between the inner casing that holds the stator blades and the outer-cylindrical steam chamber.

The two forward inner chambers between Stations 2 and 3 contain bleed steam fed through larger orifices from the outer steam chamber. This steam is at a much lower temperature than the corresponding compressed air (500°F versus 900-1100°F). A thermal barrier is thus established by this low-flow-bleed steam where the steam pressure drop of the radial struts provides the pressure differential for bleed flow. The inner casing that holds the stator blades is subjected to a pressure which is the difference between the air pressure and steam pressure (550 PSIA minus 130 PSIA giving 420 PSIA). Reference is made to Fig. 8(*a*).

When the cooling-steam flow is increased to increase cooling of the radial struts, flow through the two inner chambers increases due to increased pressure drop across the radial struts to provide additional cooling to the inner casing. Thus, the radius of the inner cylinder wall is reduced (see Fig. 8(*b*)).

Cylinder-hoop stress and strain are important. Stress is calculated by the following two formulas for thin-shelled vessels

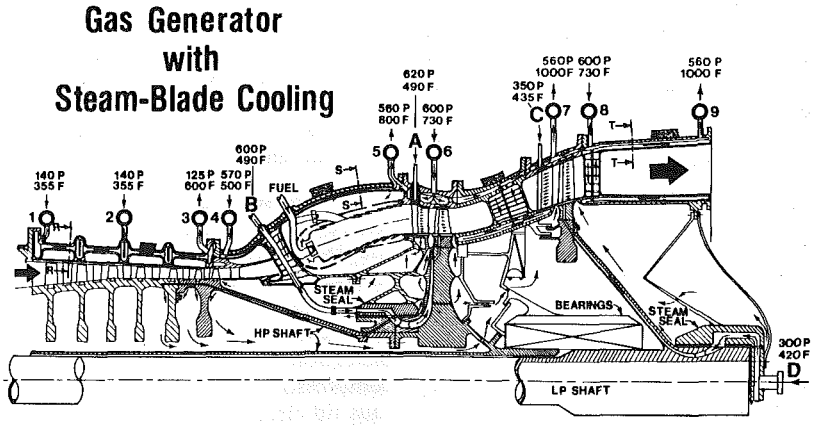

Fig. 6 Cross section of steam-cooled gas generator showing critical area between high-pressure compressor and LPT exit

Fig. 7 Schematic control diagram for blade-tip clearance control using steam as the coolant

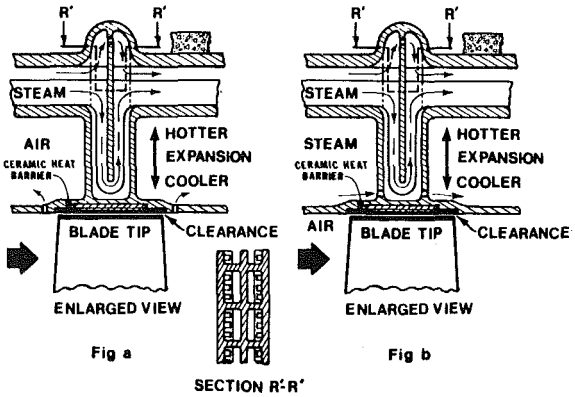

Fig. 8 Cross-sectional views of high-pressure compressor casing showing combination of air and steam isolation for effective blade-tip clearance control using steam as the coolant

$$\sigma_l = \frac{Pr}{2t} \tag{1}$$

$$\sigma_t = \frac{Pr}{t} \tag{2}$$

where σ_l is the longitudinal stress, σ_t is the tangential stress, P is the pressure, r is the radius, and t is the shell thickness. Formula (1) also is used to calculate the stress in a thin-walled sphere [15]. Strain is calculated by applying Hooke's Law where stress is proportional to strain and this ratio is equal to the modulus of elasticity.

The allowable stress for industrial gas turbines at the elevated temperature of 1000 to 1100°F is about 20,000 lbs/in.^{2} for superalloy steels for adequate creep, safety, and stress-rupture protection. The allowable stress increases to about 40,000 lb/in.^{2} when the casing is cooled to 700°F with steam. The pressure-containing cylinder, therefore, can be fabricated out of much thinner material to give a much faster response time. As an example, the casing of a 3-ft-dia shell, when considering hoop stiffeners, can be decreased from .30 in. to .15 in. for a 40 CPR turbine. Also the material can be of a different (lower cost) alloy with thermal expansion and conductivity characteristics to properly match the rotor disks and blades.

The stationary shrouds that surround the rotating blades can be cladded with a ceramic-thermal barrier as shown in the enlarged view of the radial strut. This thermal barrier will reduce the heat transfer to the radial strut and make the strut more responsive to the steam. The barrier coating also provides a good running surface for the blade tips to keep the clearance as small as possible but yet prevent rubbing. This coating also gives a rubbing surface that will prevent galling and severe damage in case of a slight rub.

The steam flow direction is from the low compressor-pressure area to the high-pressure compressor discharge. This procedure matches and balances the temperature rise of both the steam and the compressed air. The approximate temperature rise of the cooling steam is given in Fig. 6.

Insulation covers the compression casing to prevent radiation and convection-heat loss. A low heat loss establishes a stable outer metal environment that is not subject to ambient-air temperature changes.

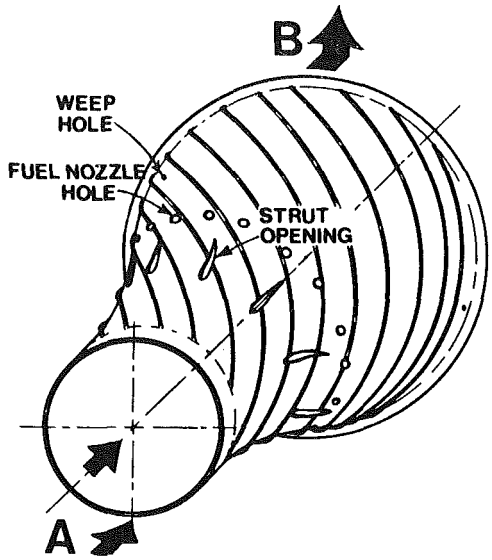

Fig. 9 Compressor-discharge, heat-isolation bladder

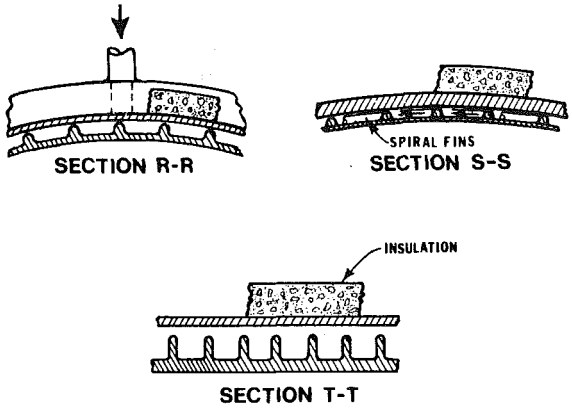

Fig. 10 Cross sections of compressor casing, combustion housing, and turbine casing showing extended surface fins, steam passageway, and outer insulation

Compressor Discharge/Combustor Housing. The spherical compressor discharge/combustor housing which contains the 38–42 atmospheres of pressure at the 1000 to 1100°F temperature can be made up of a thin inner shell and a heavier outer shell as shown in Fig. 6. The shape of this housing is spherical as shown to equalize growth, stresses, and pressure distortion. The same general principles as used for the compressor outer casing are applied to control growth and thus tip clearance of the compressor last stages and the first-stage turbine blades. A thin stainless-steel inner shell, perhaps .030-in. thick is used as a thermal barrier.

Reference is made to Fig. 9 which shows this thin inner stainless-steel bladder. The outer surface is spiral-wound on the outside with approximately .050 in. stainless-steel rectangular-shaped wire of the same material as the bladder. The wire is either continuously pressure-welded to the bladder outer surface or is high-temperature brazed to the outer surface. The bladder assembly is installed prior to the welding of the support struts. The bladder is sealed at all points by welding. A cross section of the installed bladder is shown in Fig. 10, Section S-S.

The spiral windings do the following: (*i*) they add strength to the bladder, (*ii*) they provide a much longer steam-path for heat transfer, (*iii*) they add heat transfer extender surface, (*iv*) they provide backup support against outer shell and (*v*) they provide equal steam-path spacing between bladder and outer shell.

The bladder is equipped with two or three small weep holes about .030 in. in diameter at the exit end to give pressure equalization as a protective device against loss of steam pressure or malfunctioning of the steam control and to protect the bladder during start-up. The small loss in steam will be insignificant.

The proposed steam pressure would be about 570 PSIA (cold steam-reheat line) for the 40 CPR pressure RHGT. The bladder would therefore normally be subjected to about 18 PSI pressure differential.

The 570 PSIA steam enters at Station 4 at 500°F (desuperheated). It heats to about 800°F at the exit Station 5. The outer thick-spherical housing retains the 570 PSIA pressure at a substantially lower temperature than would be experienced with the direct contact of the 1100°F compressor air. The thermal expansion of the outer case is controlled by the steam flow as regulated by the microprocessor. The steam at 560 PSIA is discharged to the steam turbine reheat line.

The steam flow direction is from compressor discharge to turbine nozzle to help balance the temperatures encountered (1100°F CDT and 2600°F TIT).

Stress formula (1) is applicable for a thin-shelled sphere. The allowable spherical-housing stress, S, when considering an industrial gas turbine, can be increased from about 20,000 PSI to 40,000 PSIA when the outer shell is steam cooled and the metal temperature is lowered from 1000°F (average) to 700°F (average). The outer shell thickness can therefore be cut in half. The shell thickness for a 4-ft-dia sphere can be reduced from about .36 in. to about .18 in. There will be far less thermal lag and a faster response to the steam cooling will be accomplished.

The outer shell would be covered with insulation to prevent radiation and convection heat loss, which in the case of an aircraft turbine is not possible because expansion control is accomplished by air sweeping the outer surface.

The same general principle can be applied to an aircraft gas turbine by extracting air at the compressor diffuser exit at impact pressure (about 1 percent higher than compressor discharge). The extraction air is externally cooled and then readmitted at Station 4. The air is then piped directly to the combustor near Station 5 (lower pressure zone by 3–4 percent) through multiple pipes from the bladder. This technique should allow a 50 percent reduction of outer shell material by doubling the allowable stress at the 250°F lower shell temperature and should save 200 to 300 lbs weight per engine of a 50,000 lb thrust size. The fuel could externally cool the air and no heat rate loss would take place. Takeoff pressure and shell temperature are critical items to cope with for an aircraft engine.

Compressor Shaft and Disks. Once the outer compressor casing and discharge housing's thermal expansion are controlled by steam cooling, the inner compressor disks and compressor-conical shaft must be cooled to control the thermal-radial growth of these parts. Steam is used as the coolant. The radial expansion of these rotating parts must match the radial growth of the outer casings.

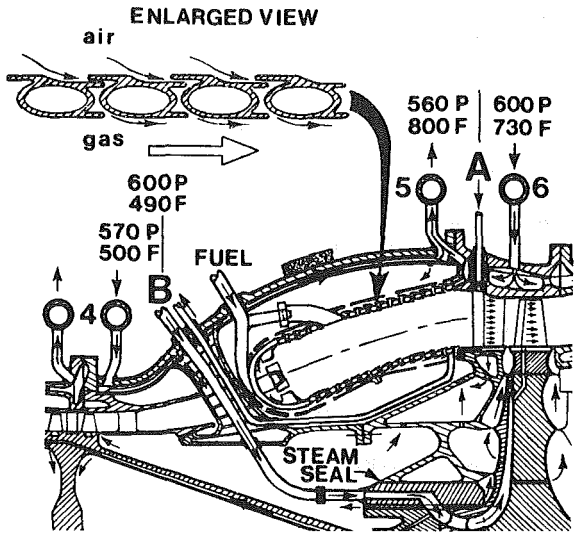

Fig. 11 Steam-cooled combustion liner applying helical coils

A small portion of steam from Point B at 600 PSIA and 490°F (desuperheated) is taken from the small-diameter steam seal and is brought up through the inside of the conical shaft, as shown in Fig. 3. An inner shell provides the passageway. This steam cools the shaft and then flows through passages on the outer periphery of the disks. This steam then impinges on the outer disk surfaces and fills the cavity between the compressor drum and shaft. The steam escapes under the first-stage, turbine-rotor disk as shown by the arrows.

The entire inner cavity is filled with cool steam (550°F versus 1100°F for air). The struts that retain the inner-cavity support members, inner-pressure cylinder, and steam seal are also steam-cooled as shown. The inner-cavity steam is obtained from the spherical-housing steam (see flow arrows in Fig. 6).

Combustion Liner

The compressor discharge temperature of a 40 CPR gas generator reaches 1100°F. Air at this temperature level is rather hot to be used as a combustion-liner coolant—particularly where radiant heat is greater and air is needed for NO_x control. The amount of air available for liner cooling because of the latter is reduced to about 32 percent of the total flow, which in turn necessitates special liner-cooling techniques to limit the liner-peak metal temperature to about 1600°F [18].

Steam cooling in a closed cycle can be used to augment the cooling made available by the 32 percent coolng air. Lower-peak metal temperatures can be achieved and an overall lower combustor pressure drop can be realized. Precious pressure can be saved by using the steam to do a large portion of the critical radiant heat-flux cooling. A 40 psi, steam-pressure drop is available between the steam-turbine, cold-reheat exit, and hot-return steam header to produce the required liner-cooling flow.

Reference is made to Fig. 11 which presents a conceptual cross section of the steam-cooled liner. Steam at 600 psia and 730°F is brought in at Station 6, where a portion is taken to cool the liner. The differential pressure between the compressor discharge (588 psia) and the steam (600 psia) is very low. Tubing blowout strength is not an important factor; small-diameter flattened tubing is proposed.

The annular liner flow is constructed of inner and outer

steam coils similar to what is proposed for the reheat combustor [7, 11] whereby the individual coils are positioned closely together to provide and control the required air-side pressure drop between the compressor discharge and the combustion cavity. Lips can be extended on both sides of the tubes to aid in the pressure/air flow control. The coils can be either helically wound or arranged with flows paths parallel with the direction of combustion flow. Figure 11 shows a helically wound arrangement.

Crossover lines in front of the combustor dome feed the steam from the outer set of cooling coils to the inner coils. These crossover lines are shown in Fig. 11 near the upstream-fuel nozzle.

The heated steam at 1000 to 1100°F flows out of the compressor-discharge housing through pipes which run through the forward structural support struts as shown.

Summary and Conclusion

Steam cooling the compressor and combustor as presented takes advantage of steam's superior cooling properties of high specific heat and allowable pressure drop. A total summary and conclusion is given at the end of Part II of this study.

Acknowledgments

My continuing study of the steam-cooled reheat gas turbine combined cycle has required considerable and ensuing patience, understanding, and time consuming assistance on the part of my wife, Carolyn Keyes Rice. She has, as always, gone above and beyond the call of duty in graciously supporting my efforts and has been most helpful in editing my scripts, lettering my graphs, and preparing the mats, for which I express great appreciation.

References

1 Stewart, W. L., and Weber, R. J., "NASA Research in Aeropropulsion," ASME Paper No. 81-GT-96.

2 Gray, D. E., and Gardner, W. B., "The Energy-Efficient Engine (E^3)—Advancing the State-of-the-Art," ASME Paper No. 80-GT-142.

3 Johnston, R. P., and Ortiz, P., "Future Trends in Sub-sonic Transport Energy-Efficient Turbofan Engines," ASME Paper No. 80-GT-177.

4 Rice, I. G., "The Reheat Power Turbine with Steam Cooling—A Means of Increasing Reheat Temperature, Exhaust Temperature, and Combined-Cycle Efficiency," ASME Paper No. 82-GT-134.

5 Alff, R. K. et al, "The High-Temperature Water-Cooled Gas Turbine in Combined Cycle with Integrated Low BTU Gasification," ASME Paper No. 77-JPGC-GT-7.

6 Hori, A., and Takeya, K., "Outline of Plan for Advanced Research Gas Turbine," ASME Paper No. 81-GT-28.

7 Rice, I. G., "The Combined Reheat-Gas Turbine/Steam Turbine Cycle, Part I—A Critical Analysis of the Combined Reheat Gas Turbine/Steam Turbine Cycle," ASME Paper No. 79-GT-7, ASME JOURNAL OF ENGINEERING FOR POWER, Jan., 1980.

8 Rice, I. G., "The Combined Reheat-Gas Turbine/Steam Turbine Cycle, Part II—The LM 5000 Gas Generator Applied to the Combined Reheat Gas Turbine/Steam Turbine Cycle," ASME Paper No. 79-GT-8, ASME JOURNAL OF ENGINEERING FOR POWER, Jan., 1980.

9 Rice, I. G., "Steam-Cooled Blading in a Combined-Reheat-Gas-Turbine/Reheat-Steam-Turbine Cycle, Part I—Performance Evaluation," ASME Paper No. 79-JPGC-GT-2.

10 Rice, I. G., "Steam-Cooled Blading in a Combined-Reheat-Gas-Turbine/Reheat-Steam-Turbine Cycle, Part II—Design Considerations," ASME Paper No. 79-JPGC-GT-3.

11 Rice, I. G., "The Reheat-Gas Turbine with Steam-Blade Cooling—A Means of Increasing Reheat Pressure, Output and Combined-Cycle Efficiency," ASME Paper No. 81-GT-30, ASME JOURNAL OF ENGINEERING FOR POWER, Jan. 1982.

12 Rice, I. G., and Jenkins, P. E., "Comparison of the HTTT Reheat-Gas-Turbine Combined Cycle with the HTTT Nonreheat-Gas-Turbine Combined Cycle," ASME Paper No. 81-GT-69, ASME JOURNAL OF ENGINEERING FOR POWER, Jan., 1982.

13 Jenkins, P. E., and Rice, I. G., "Blading-Heat Transfer Considerations in a Reheat-Gas-Turbine Combined Cycle," ASME Paper No. 81-GT-155.

14 Bennett, S. B., and Bannister, R. L., "Engineering Assessment of an Advanced Pulverized-Coal Power Plant," EPRI Report CS-2223, Jan. 1982.

15 Bednar, H. H., *Pressure Vessel Design Handbook*, Van Nostrand Reinhold Co., 1981.

16 Nainiger, J. J., "Effect of Thermal-Barrier Coatings on the Performance of Steam and Water-Cooled Gas-Turbine Steam-Turbine Combined-Cycle Systems," NASA Report TM-79057, Dec. 1978.

17 Sawyer, J. W., *Sawyer's Gas-Turbine Engineering Handbook*, 2d ed., Vol. II, Gas Turbine Publications, Stanford, Conn., 1972.

18 Gardner, W. B. et al, "Interim Review of the Energy Efficient Engine (E^3) Program," ASME Paper No. 82-GT-271.

19 Bucy, R. W., "Progress in the Development of Energy Efficient Engine Components," ASME Paper 82-GT-275.

20 Fraize, W. E., and Kinney, C., "Effects of Steam Injection on the Performance of Gas Turbine Power Cycles," ASME Paper No. 78-GT-11.

21 Fraize, W. E., and Kinney, C., "Coal-Fired Gas Turbine Power Cycles Using Steam Injection," CIMAC Paper No. GT-7, 1979.

22 Lewis, J. P., and Kinney, C., "Steam Injection in Medium-BTU Gas-Fueled, High-Temperature Combined Cycle Power Plants," ASME Paper No. 82-GT-274.

23 Rios, J., and Maddagiri, M., "Conditioning Feedwater to Meet Turbine Steam Purity Requirements," American Power Conference, Apr. 1982.

24 Jones, J. L., Flynn, B. R., and Strother, J. R., "Operating Flexibility and Economic Benefits of a Dual-Fluid Cycle 501-KB Gas Turbine Engine in Cogeneration Applications," ASME Paper No. 82-GT-298.

25 Rice, I. G., "The Reheat-Gas-Turbine Combined Cycle," *Mechanical Engineering*, Apr. 1982.

Steam-Cooled Gas Turbine Casings, Struts, and Disks in a Reheat Gas Turbine Combined Cycle: Part II—Gas Generator Turbine and Power Turbine

I. G. Rice
Consultant,
Spring, Texas 77373
Fellow ASME

High-cycle pressure-ratio (38–42) gas turbines being developed for future aircraft and, in turn, industrial applications impose more critical disk and casing cooling and thermal-expansion problems. Additional attention, therefore, is being focused on cooling and the proper selection of materials. Associated blade-tip clearance control of the high-pressure compressor and high-temperature turbine is critical for high performance. This paper relates to the use of extracted steam from a steam turbine as a coolant in a combined cycle to enhance material selection and to control expansion in such a manner that the cooling process increases combined-cycle efficiency, gas turbine output and steam turbine output.

Introduction

Part I of this study covers steam cooling of the compressor and combustor. Part II, which follows, will deal with steam cooling the gas generator and power turbines—their rotors, casings, and struts.[1]

The Introductory Remarks presented in Part I are applicable to Part II and thus are not repeated. It should be pointed out, however, that once steam is considered as the turbine disk and blade coolant, the relative expansion of the disks and blades compared to the casings is disrupted primarily because of the cooler running disks. It follows that proper casing cooling becomes important to maintain blade-tip clearance. Differential expansion between the inner barrel and structures and outer casings must be considered whereby support-strut expansion must be compatible with the casing expansions if cracking between the struts and casings (low-cycle fatigue) is to be avoided.

Fast thermal expansion/contraction response of the casings is necessary. The rotor disks are rather slow to respond; also cooling steam to the blades must be retained, which limits the disk outer radius dimensional control. It is important, therefore, that the casings and struts respond rapidly and evenly under all conditions of start-up, loading, unloading, trips, shutdown, and cool-down. Steam cooling can provide the required flexibility. A miniprocessor/computer can be applied, as outlined in Part I of this study, to control the flow of the cooling steam and thus the thermal expansion of the stationary parts.

It is desirable to start the turbine with ample blade-tip clearances and then reduce the clearances after load has been applied. Likewise, the clearances should be opened up before shutdown. Before start-up, steam can be introduced to both the rotors and casings to provide prerotational warm-up. The relative growth of the disks and blades and of the casings and struts thus can be controlled by modulating the steam flows.

Air has been used for years as the basic gas turbine coolant. It can be pointed out that water was used in the early (1951) General Electric industrial-two-shaft gas turbine to cool the low-pressure turbine shell and second-stage, variable-nozzle stems and bushings. The more recent designs have eliminated the water cooling to simplify the system; however, the water cooling worked quite well but required a separate heat exchanger, another tank, and an extra set of pumps. Water is also a rather harsh coolant and cannot be cut off and started up again without casing-cracking problems.

Steam cooling, in some respects, is simpler than air cooling once thinking is shifted from air to steam. Steam is easy to pipe and has twice the specific heat which reduces the size of the cooling lines. Pressure drop is not as critical as it is for air and greater pressure differentials are available to allow more design freedom for heat exchange surfaces. Steam has been used for years in refineries, chemical plants and indeed steam-power plants to heat both gases and liquids of all kinds. Ample empirical design data are available to ensure accurate heat transfer results. A wide selection of control valves is also available to control steam flow.

Gas turbine engineers tend to think in terms of air cooling primarily because of the aircraft influence in design and

[1] See page 856 for all SI conversion factors

Contributed by the Gas Turbine Division of THE AMERICAN SOCIETY OF MECHANICAL ENGINEERS for presentation at the 28th International Gas Turbine Conference and Exhibit, Phoenix, Arizona, March 27–31, 1983. Manuscript received at ASME Headquarters December 22, 1982. Paper No. 83-GT-86.
Copies will be available until January 1984.

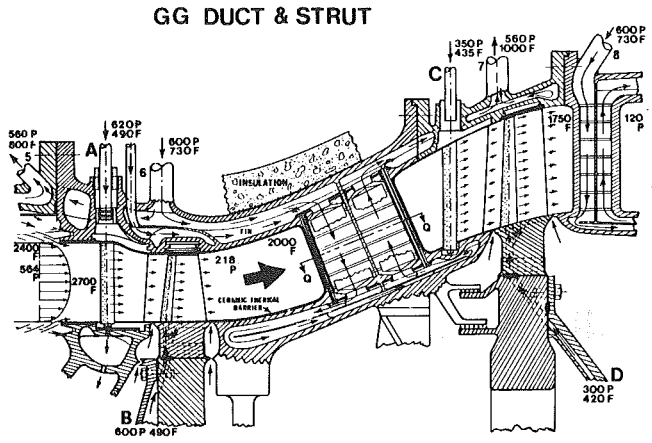

Fig. 1 Enlarged cross section of steam-cooled gas generator casing, strut, and inner barrel showing the hot-gas path

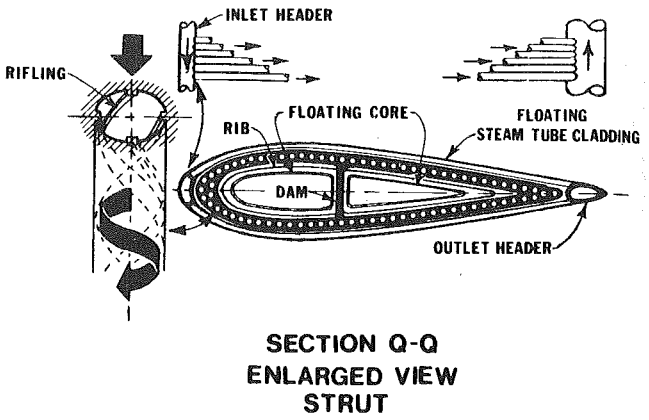

Fig. 2 Cross section of steam-cooled strut showing outer-steam shield and inner-steam riflings

approaches. Research and Development funding is funneled into the aero industry and spinoffs then filter down to the industrial arena. The United States Department of Energy (DOE) has taken a step in recent years to look into different cooling approaches to fit the industrial-gas turbine and combined cycle. Research and development efforts with water cooling are underway, but no meaningful program has been instigated for using steam as the coolant, even though there are valid advantages and a real potential for using steam.

DOE has studied steam injection in a combined cycle [20, 21, 22] as a means of obtaining higher specific power and as a way to offset the loss in power when switching from a medium-Btu gas to high-Btu gas. However, DOE has not presented studies using steam for both cooling and injection.

Steam that is lost out the boiler stack does require high-quality boiler feedwater replacement—the cost of which must be faced and evaluated. Reference [23] gives an overview of high-pressure boiler feedwater makeup requirements. The cooling-tower water evaporation is considerably less due to the reduced steam flow to the condenser. Therefore, the amount of this water treatment is reduced to partially offset the higher-cost boiler feedwater makeup. The total amount of water consumed with steam cooling/injection will be about the same as for the conventional combined cycle [12, 20, 22].

First-Stage Turbine-Disk Expansion

The main flow of steam "B" enters the rotating shaft through openings in a rotating member of the inner shaft. A separate piece that is shrunk-fit on the shaft is used for the transition. The steam then passes up a cavity to the periphery of the first-stage turbine disk. No vanes are present in the cavity to minimize pumping losses. The opening does not act as a compressor. The steam cools the turbine disk and controls expansion thereof. Note that the disk hub is not cut or disturbed as this is the region of highest stress (see Fig. 6, Part I for details).

Turbine Outer Shell, Struts, Inner Barrel, and Diffuser Cooling

The gas generator turbine shell surrounding and downstream of the first-stage nozzle as well as the support struts and inner barrel and diffuser can all be cooled with 600 psia steam turbine cold-reheat steam in a closed-steam system whereby the heated steam is returned to the hot reheat header for readmission to the steam turbine. The cooling/heating serves two functions: one to cool the gas turbine parts and the other to heat the reheat steam.

Reference is again made to Fig. 6 of Part I. Steam enters the turbine shell at Station 6. Part of this steam exits at Point 5 with the majority flowing through the support struts, inner barrel, back out the struts, and then on to Station 7 where the temperature is shown to be 1000°F. This temperature can be as high as 1100°F if necessary where the hot-gas stream between the first and second stages is about 1900°F for a 2600°F TIT 40 CPR gas generator.

Reference is made to Fig. 1 which is an enlarged cross section of Fig. 6 between the combustor outlet and the diffuser (Stations 5 through 8). The stationary shroud that surrounds the first-stage rotating blades is made in segments that fit in grooves in the casing. The surface of the segments that are exposed to the hot gases are coated with a special ceramic-heat barrier which is commonly used in aircraft gas turbines today.

Above the shroud segments there are a series of extended-surface fins about 1/20 in. thick and 3/32 in. apart. These fins greatly increase heat transfer and provide fast thermal response. These fins are enclosed in a special isolation chamber. The chamber is fed with 620 psia saturated steam at 490°F. The flow is controlled and varied by the microprocessor/computer through a PRV. The inner cylindrical wall is thus cooled or allowed to heat to control radial-thermal expansion of the shell. The inner-radial shell expansion must match the overall radial expansion of the disk and blades to maintain tip clearance.

Special attention must be placed on cooling the struts and the internal duct passage between the gas generator first-stage blading and the second-stage nozzle. This passageway carries hot gas at 1900 to 2000°F at a pressure of 200 to 220 psia.

New techniques for bonding ceramic material to metal parts with an underlay of pliable material have been developed the past few years to provide a thermal barrier. These new application techniques are available from various companies. According to NASA Report TM-79057 [16] a .010 in. thickness of plasma sprayed under a bond coat of NiCrALY and an .030 in. overcoat of ythria-stabilized-zirconia ceramic will provide a temperature difference between the gas and metal of 335 to 635°F, depending on the gas temperature level and flow conditions. The zirconia has a low conductivity of 0.75 Btu/hr-ft^2-°F and the NiCrALY conductivity is only 3.9 as reported by NASA. These low figures account for the high-temperature drop.

The inside of the annular ducting is coated with this ceramic thermal barrier to reduce the metal temperature about 400°F. The steam cooling of the casing will reduce the metal surface temperature further to an acceptable level of about 1400°F depending upon the amount of steam cooling.

A further way to isolate or shield the strut from the 2000°F

gas stream is to surround or clad the strut with a series of small-diameter stainless steel (superalloy) tubes about 3/32 in. in diameter with the tubes being arranged parallel with the main-gas flow and touching each other. Steam flows through the tubes (see Fig. 2). The wall thickness of these soda-straw sized tubes is to be very thin for good heat transfer. According to the hoop-stress equation (2) for a thin-shell casing the thickness for an allowable 20,000 psi stress and a 400 psi pressure differential calculates to be .001 in. The tube-wall thickness, for practical considerations, would be .008 to .010 in.—one magnitude greater.

The leading-edge inlet header and trailing-edge outlet headers would be about ¼-in. in diameter with a wall thickness of .015 to .020 in. even though .003 in. would be sufficient to carry the pressure. These tubes are flattened and shaped to match the contour of the strut. Each small tube is welded to the inlet and outlet headers. The ends of the headers are sealed shut. The outer surfaces of the tube or sheet covering are coated with a ceramic-thermal barrier. Sheet superalloy steel could be wrapped around the headers and tubing inside and out and welded to the headers to form a pressure-tight seal.

The tube-shielding sleeve assembly is slipped over each strut, and the open ends of the ¼-in. inlet and outlet headers are welded to the inside outer casing. The cladding assembly is free to float up and down around the strut as the gas stream temperature changes and as the strut is expanded or retracted to control tip clearance.

The thermal-barrier system over the struts and on the outer surface of the steam-cooled tubes insulates the tubes and provides a triple-thermal barrier to the strut: first, a ceramic-thermal barrier on the tubes, second, a steam-tube shielding, and third, another ceramic thermal barrier on the strut itself.

This triple shielding procedure will allow the strut metal temperature to be as low as 800°F. Reduced cooling-steam flow will allow the strut to heat to 1500°F if need be and grow thermally accordingly to match the required blade and disk growth.

The outer casing exposed to the steam is kept at a temperature of 700 to 800°F by the steam entering at 730°F at Station 6.

The radial struts which carry the load of the rear bearing and internal seals and which provide passageways for feed and drain-lube-oil lines must be treated special. These struts not only support the internal parts of the engines but also tie together the inner and outer shells. The overall radial-thermal growth thus controls tip clearance which is particularly important for high-expansion-ratio first-stage rotating blades.

A typically applied method of controlling differential growth between the outer shell, the inner shell, and the inner barrel is to attach the struts tangentially or semitangentially to the inner barrel. The struts, when they expand from temperature increases, rotate the cool inner barrel and thus maintain axial alignment of the inner and outer shells to the barrels. This procedure greatly reduces thermal cracks between the struts and shells.

Reference is again made to Fig. 2, a cross section of one of typically six struts. Cross sections of both the ceramic-coated strut and the steam-tube shield are shown in Fig. 2. The strut, perhaps 6-in. wide, 6-in. high, and 1½-in. thick, has a series of closely spaced holes electro-machined or cast in the shell. These holes are about 1/16 in. to 3/32 in. in diameter. Each hole has riflings broached in it. These riflings provide ridges at a pitch of about 5 rib spirals per inch. Each rib is about .020 in. wide and thick.

These riflings offer three distinct functions: (*i*) they spin the steam to provide a much longer flow path, (*ii*) they provide extended surface area for heat transfer, and (*iii*) they provide a way to create a steam turbulence to increase heat transfer.

Internal cores or sheet-metal inserts are used inside the front and back passages to force the cooling steam to flow next to the strut ribs (cleats, or turbulators as they are sometimes called). Heat transfer is thus improved. Secondly, a pressure drop is created to force some of the steam through the outer rifling holes and the cladding tubes. As the cooling steam is increased, a greater pressure drop occurs, which in turn forces more steam through the rifling holes and cladding tubes.

The cooler steam passes through the front or leading edge of the strut and the hotter steam, heated by the inside barrel, passes through the trailing edge. Therefore, there will be a slight temperature difference causing the leading edge to tilt the outer shell inward to reduce tip clearance of the first-stage rotating blade.

The second-stage rotating blade-tip clearance is controlled by the cooling steam before exiting at Station 7. It is possible to have a separately controlled cooling circuit for the second stage if need be, but tip control here is not as critical as for the first stage.

The diffuser is also cooled with 600 psia steam which flows through the inner and outer shells from Station 8 to Station 9. The aft straightening vanes contain flow dams which separate flow and provide passageways to and from the inner-diffuser cylinder. The temperature of the gas flowing through the diffuser is at a level of 1740°F for the 2600°F TIT-40 CPR gas generator. Cooling either by air or steam is necessary.

The microprocessor minicomputer controls the flow of steam to Stations 6 and 8 through separate pressure-control valves.

Second-Stage Vanes, Disks and Blades

Steam "C" at 350 psia saturated temperature enters the second-stage nozzle vanes as shown in Fig. 6 of Part I. Steam "D" passes through a rear-steam seal to flow up the inside second-stage-shaft cone to the second-stage disk and blades. The steam flowing through the shaft cone and disk cools these parts and thus controls their radial-thermal expansion.

The steam flowing through the outer-turbine shell, struts, inner barrel and diffuser control radial-thermal growth and blade-tip clearance. The temperatures of the outside-stationary parts have to relate to the temperatures of the inside rotating parts to accomplish thermal-expansion control.

First and Second-Stage Shrouds

Thermal-barrier ceramic coatings are used on the stationary-turbine shrouds that surround the rotating blade tips. This insulation restricts the flow of heat to the turbine shell and helps control expansion.

It is important that the outer-turbine shell, inner barrel, and struts have a fast-thermal response. The cooling-steam flow must accommodate a rapid change in firing temperature, particularly during start-up and rapid-load changes. Otherwise, tip rubbing will occur with a possible loss of blades. When very close-tip clearances are considered, this rapid response is necessary. This response is required to match and exceed the radial growth or shrinkage rate of the rotating blades and disks. A fast response is accomplished by incorporating extended finned surface on the hot side of the stationary shell. Reference is made to cross-section T-T, Fig. 10 of Part I, which is typical for the shell, struts, inner barrel, and diffuser. The exact design regarding the number of fins and spacing would require extensive analysis of the disks, blades, shell, struts, and drum; and even rig tests would be required. Fins, however, successfully cool air-cooled aircraft internal-combustion-recip engines, and steam is a far better

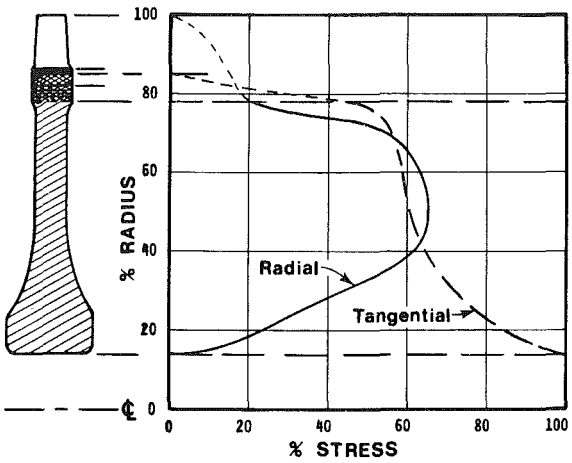

Fig. 3 Radial and tangential stress diagram of a typical gas-turbine disk

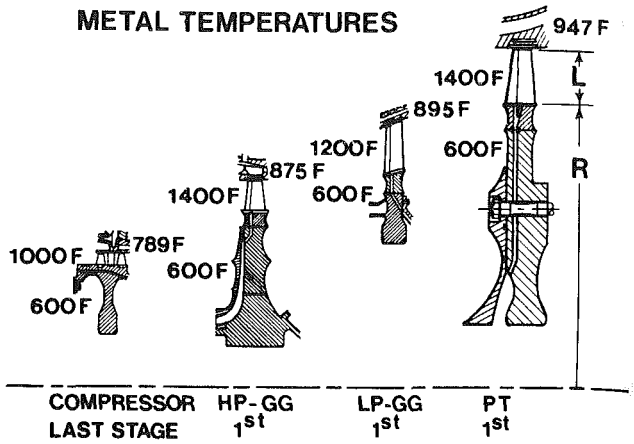

Fig. 4 Typical average metal temperatures of steam-cooled disks and outer casings

coolant than air. The large parts make extended-surface fins possible with a great enough total-surface area required.

Temperatures, Expansion, Materials and Tip Clearances

The disks and casings, where air is the coolant, run hotter in high-pressure-ratio gas turbines than on earlier low CPR units. Extra care must be taken, as a result, in the selection of the materials to make sure they possess the required strength and exhibit compatible thermal expansions for blade-tip control. New air-cooling techniques and more advanced superalloy materials are being developed to cope with the new temperature-pressure conditions.

Steam, a superior coolant to air, offers a way to cool the disks and casings to a lower temperature. The last-stage compressor disk, for instance, can be cooled to an average hub to rim temperature of 600°F whereas the air-cooled disk will operate at a comparable temperature level of 800 to 900°F. Similarly, steam-cooled turbine disks will operate at a 600°F level versus 900 to 1000°F for air. Also a much greater temperature differential for air cooling will take place between hub to rim.

Cooling the disks greatly increases allowable stress levels but, on the other hand, it upsets the balance between casing-thermal growth and disk-thermal growth. Steam cooling of the outer casing and stationary parts then, as previously discussed, becomes necessary so that blade-tip clearance can be controlled and maintained.

Steam is made available from a small boiler before the gas turbine is started. Steam is introduced to the gas turbine rotors, blading, and casings in a controlled manner to warm up these parts to about 300°F before the gas turbine is fired. This warm-up reduces thermal shock considerably and allows positive blade-tip clearance control during start-up. Clearances can be opened up for light-off by steam-heating and thus expanding the outer casings.

After the gas turbine is running and up to speed, steam flow to the disks, blading, and casings is regulated to control tip clearance. The minicomputer/microprocessor provides the proper signal to control cooling steam to the various parts.

Steam cooling also is automatically adjusted in case the gas turbine experiences a sudden load change requiring either an increase or decrease in firing temperature. Likewise, in case of a full-load trip, the amount of cooling steam to the shell and disks can be adjusted to insure proper casing and disk thermal expansion and thus tip clearance.

The disks have a greater thermal capacity and a slower response time than the casings—particularly in regard to the compressor. It is a distinct advantage, therefore, to use steam as a coolant to control both disk and casing expansion during coast-down and static cool-down. Steam from an accumulator or extracted steam from the steam turbine is used. The outer compressor casing in an air-cooled turbine tends to cool off faster than the disks and tip rubbing can occur. "Squealer" tips on the turbine-blade tips have a very thin extension that can rub away and prevent seizure. Rubbed tips, however, give greater running clearances and performance is lost. Steam cooling will prevent this loss and minimize the need for "squealer" tips.

Tip-clearance control must be accurate, precise, and reliable where close running clearances of ten to twenty-thousandths of an inch are contemplated. These clearances, under precise control, can be opened up to sixty or seventy thousandths of an inch during start-up and coast-down to prevent any possible rub or seizure.

Without blade-tip control an ample clearance of sixty-thousandths of an inch has to be present all the time to protect against sudden temperature changes. This excessive clearance reduces both compressor and turbine efficiency during operation. Fuel consumption is increased and power output is reduced.

Disk and Casing Growth. Growth of the rotating disks is brought about by two factors. First, the rotational or centrifugal forces cause the disk to elastically distort or expand. Second, the disks thermally grow as the temperature is increased. Outer casings experience elastic-hoop growth due to the pressure. The thermal growth can be readily varied and controlled. It is about six times greater than the elastic strain and dominates, as will be shown. Conversely, the elastic growth tends to remain constant over the operating range of the gas turbine. Inner casings can experience elastic contraction due to compression forces.

The two-fold displacements (thermal expansion and elastic strain) are represented by the following two formulas

$$\text{Radial strain,}\quad \epsilon_r = \frac{\sigma_r - u\sigma_t}{E} + \alpha(T_2 - T_1) \tag{3}$$

$$\text{Hoop strain,}\quad \epsilon_t = \frac{\sigma_t - u\sigma_r}{E} + \alpha(T_2 - T_1) \tag{4}$$

where σ_r = radial stress—lb/in.^{2}
σ_t = tangential stress—lb/in.^{2}
u = Poisson's ratio (considered .3 for steel)
E = modulus of elasticity
α = coefficient of thermal exp—in./in.°F

Table 1 Steam-cooled-reheat gas turbine material selection and temperatures for tip clearance control 40 CPR – 2600/2400°F

Rotor	HP-Comp last stage	HP-GG Turbine, first stage	LP-GG Turbine, first stage	PT Turbine, first stage
1 Material				
disk	INCO 718	INCO 718	INCO 718	INCO 718
blade	INCO 718	U-700	U-500	U-500
2 E – tensile modulus psi × 10^{-6}				
disk	29.0	29.0	29.0	29.0
blade	29.0	32.4	29.4	29.4
3 α – Mean coef. of therm exp. in./in.°F × 10^6				
disk	8.0	8.0	8.0	8.0
blade	8.0	7.74	7.80	7.80
4 Thermal conductivity Btu-in./(ft^{2}hr°F)				
disk	135	135	135	135
blade	135	143	127	127
5 Stress (average)-lb/in.^{2}				
disk	40,000	40,000	40,000	40,000
blade	5,000	10,000	10,000	10,000
6 R_D-radius of disk-in.	16	19	23	28
7 L-length of blade-in.	2	3.5	4.5	5.0
8 T_D-temp. of disk (Avg)-°F	600	600	600	600
9 T_B-temp. of blade (Avg)-°F	1000	1400	1200	1400
10 ΔR_D-growth of disk-in.				
elastic	.015448	.018345	.0222069	.027035
thermal	.067840	.080560	.0975200	.118720
subtotal	.083248	.098905	.1197269	.145755
11 ΔL-growth of blade-in.				
elastic	.0003448	.0010802	.0015306	.0017007
thermal	.0148800	.0360300	.0396630	.0518700
subtotal	.0152248	.0371102	.0411936	.0535707
12 Total growth-in.	.098515	.136015	.160920	.199325
13 Distribution				
% elastic	16.0	14.3	14.8	14.4
% thermal	84.0	85.7	85.2	85.6
Casing				
14 Material	12-CR-ST Type 422	12-CR-ST Type 422	12-CD-ST Type 422	12-CR-ST Type 422
15 E – tensile modulus psi × 10^{-6}	30.6	30.6	30.6	30.6
16 α – Mean coef. of therm exp. in./in.°F × 10^6	6.7	6.7	6.7	6.7
17 Thermal conductivity Btu-in./(ft^{2}hr°F)	196	196	196	196
18 Pressure – psia	565	500	250	100
19 Stress (avg w/Stiffeners) lb/in.^{2}	20,000	20,000	10,000	5,000
20 R_c–radius of casing–in.	18.0	22.5	27.5	33.0
21 $\Delta R_c = \Delta R_D + \Delta L$ – in.	.098515	.136015	.16092	.199325
22 % of radius	.547	.605	.585	.604
23 T_c–casing temp.–°F	789	875	895	947

T_1 = ambient temperature—°F
T_2 = metal temperature—°F

A typical disk stress versus radius plot for both tangential and radial stress is presented in Fig. 3 [17]. Formulas (3) and (4) can be applied to a hypothetical and simplified example of a steam-cooled gas turbine to illustrate the selection of materials, thermal growth, centrifugal-force growth, and pressure-force growth of the various parts. A typical gas generator of 300 lbs/s air flow will be used.

Known allowable and measured stress levels can be used for the disks and casings. Also, it can be assumed that the disks are shaped to give constant or near constant stress levels from the hub to the rim. A stress value of 40,000 lb/in.^{2} can be assumed for the disks, 20,000 lb/in.^{2} for the forward casing and 10,000 and 5,000 lb/in.^{2} for the rear casings. An average temperature of 600°F can be assumed for the steam-cooled turbine compressor and turbine disks. Also, the metal temperatures of the compressor blades (1000°F), the HP GG turbine blades (1400°F), the LP GG turbine blades (1200°F), and the first-stage PT blades (1400°F) can be assumed as typical values. Radial blade stresses are assumed to be 5,000 lbs/in.^{2} for the compressor and 10,000 lbs/in.^{2} for the turbine. Exact strain values of a particular turbine design can be calculated by a computer program using a finite-element approach. The actual values can be verified by x-rays through component rig testing and final unit testing.

The outer-casing metal temperatures can be calculated by applying formulas (3) and (4). Table 1 presents a tabulation of the material selection, material physical properties, growth values, and finally outer-casing temperatures required to maintain constant-tip clearance for the gas turbine.

It can be noted that approximately 15 percent of the growth

is attributed to the elastic growth and that 85 percent comes from the thermal growth; therefore, the thermal growth is dominant and tip-clearance control must be accomplished through temperature control of the disks and casing. Also, it can be observed that the total growth is appreciable and amounts to about .5 percent of the radius as given in line 22.

The casing calculated temperatures, line 23, indicate that the steam temperatures available are some 200°F below the casing temperatures which provides a reasonable delta temperature between the cooling steam and the various casings. The cooling system is entirely practical and lends itself to temperature control of the different casing segments.

The relative sizes of the various disks and blades are given in Fig. 4. This diagram also presents the various metal temperatures assumed for the disks and blades and the calculated casing temperatures.

The casing temperatures, line 23, clearly show that the compressor discharge casing will operate at a lower temperature than the HP-GG first stage casing by some 87°F. These figures show the need for the internal stainless-steel combustion casing bladder to isolate the CD temperature and the required direction of flow of the cooling steam from compressor discharge to the turbine.

The casing metal temperatures of an air-cooled, high-cycle, pressure-ratio gas turbine by necessity will be considerably higher than the casing temperatures of a similar steam-cooled gas turbine. Reference is made to Fig. 5 which shows typical temperatures for an air-cooled unit on top and calculated temperatures for a steam-cooled unit on the bottom. The difference in temperatures can be noted to be about 400°F.

The air-cooled casings must operate at the elevated temperatures because the disks operate at much higher temperatures due to the elevated temperature of the compressed air used as the coolant. The cooling air temperature to the first stage disk would be about 1000°F inlet compared to about 500°F saturated steam. Also the specific heat of steam is twice that of air—thus offering a greater heat sink.

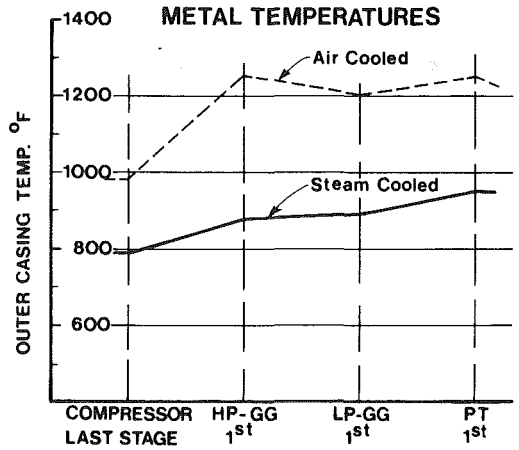

Fig. 5 Typical average steam-cooled casing temperatures compared with air-cooled values

The air-cooled outer casing must operate without any insulation; whereas the steam-cooled casing has a heat-retention insulation covering to prevent heat leakage and a loss to the cycle. The insulation also affords a way to control outer metal skin temperature under varying ambient temperature conditions.

Sensitivity. The sensitivity of the outer casing can be calculated and then evaluated to ascertain if the rate of change in tip clearances is acceptable with all parameters using steam as a coolant.

Formula (4) can be applied again for increases and decreases in case temperature above and below the neutral temperatures shown in line 23 of Table 1. The results of these calculations are given in Fig. 6. This last figure shows that a 100°F increase or decrease in case temperature will increase or decrease tip clearance respectively as follows: (*i*) compressor last stage, .0121 in.; (*ii*) GG-HP first stage, .0158 in.; (*iii*) GG-LP first stage, .0184 in.; and (*iv*) PT-first stage, .0221 in. Figure 16 also shows the relationship between casing thermal growth and disk and blade thermal growth as can be noted by the dashed lines.

The magnitude of these values are quite practical for an engine of the size contemplated (air flow of 300 lbs/s) and indicate that an initial blade-tip clearance at ambient temperature of the engine could be in the order of .020 in. and that this magnitude of clearance could be maintained under all running conditions.

This graph also shows that it is important to insulate the outside of the casings so that the casing temperatures can be maintained by the cooling steam. Aircraft gas generators using ambient-air cooling do not have the outside of the casings insulated. Air is forced over the outer surface in an unregulated manner by fans to cool the casing as required. The heat is rejected with the atmospheric-pressure cooling air and the rejected heat is lost from the cycle. This heat is retained in the steam in the steam-cooled arrangement and is not lost from the cycle.

Material Selection. The materials selected for the disks, blades, and outer casings are typical for today's modern gas turbine. Future gas turbines using advanced powdered superalloy metallurgy for disks and single-grain crystals for turbine blades will become available for industrial gas turbines in a few years. The casings are generally fabricated out of a high-alloy steel as shown in line 14. It can be noted that this type of material has a much lower coefficient of thermal expansion than the disk (6.7×10^{-6} versus 8.0×10^{-6}). Therefore, the casing can operate at a higher temperature than the disk (800 versus 600°F) to be compatible with the cooling steam.

Another factor can be observed from Table 2 and that factor relates to conductivity and the response rate of the

Correction factors for Standard International (SI) Units

	Multiply	By	To Obtain	
(in.)	inch	2.54×10^{-6}	meter	(m)
(ft)	feet	.3048	meter	(m)
(lbs)	pounds (mass)	.4535924	kilograms	(Kg)
(psi)	pounds per square inch	6894.757	Newtons per square meter	(N•m/m)
(psia)	pounds per square inch absolute	6894.757	Pascal	(Pa)
(fps)	feet per second	.3048	meters per second	(m/s)
(Btu)	British thermal units	1055.056	Joules	(J)
(Btu/lb)	British thermal unit per pound	2326.000	Joules per kilogram	J/Kg
(°F)	degrees Fahrenheit	$\frac{°F + 459.67}{1.8}$	Kelvin	(K)
(°F)	degrees Fahrenheit	$\frac{°F - 32}{1.8}$	Celsius	(°C)

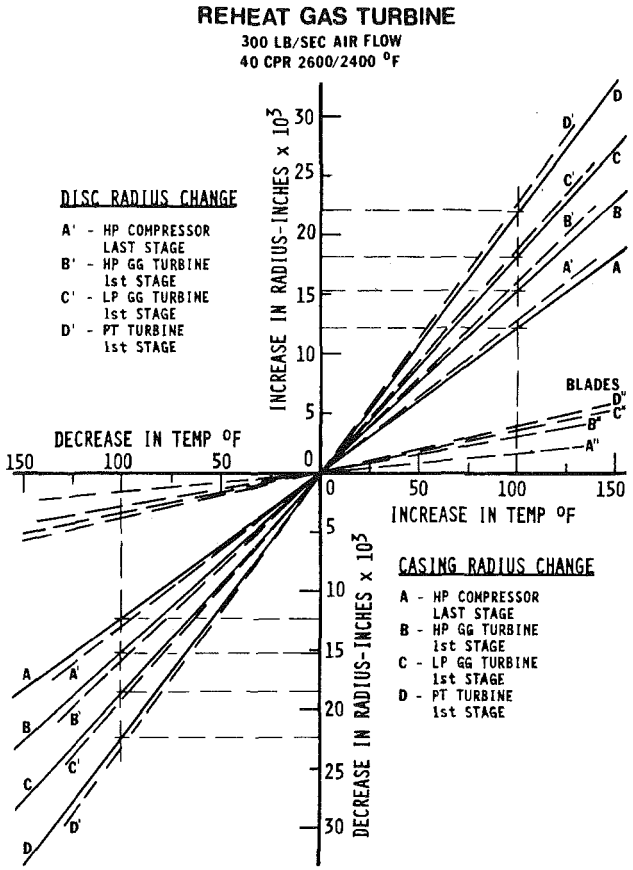

Fig. 6 Sensitivity chart for steam-cooled gas turbine blade-tip control

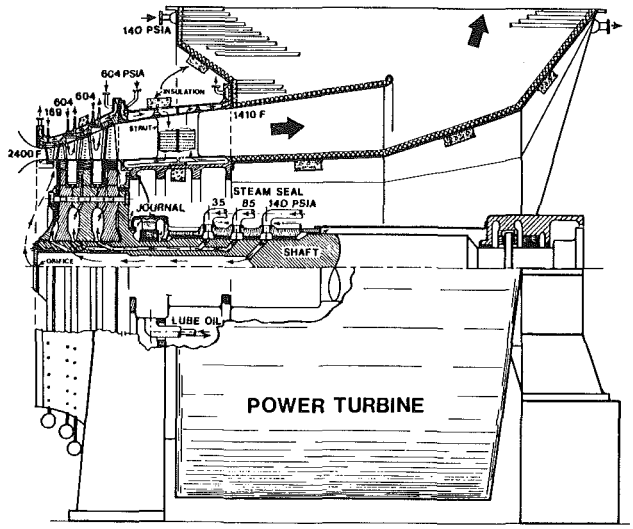

Fig. 7 Steam-cooled power turbine

casing relative to the disks. It can be seen that the thermal conductivity of the casing material is notably greater than for the disks (196 versus 135). Therefore, the casing should respond faster to the steam cooling than the disks, assuming equal specific heats of the different alloys. The casings, being thin and less massive than the disks, can be expanded or contracted as necessary at a faster rate than the disks and independent of the disks to control tip clearances at all times—prestart, warm-up, and start-up, running, load changing, trip-outs, coast-downs and static cool-down.

Steam-Cooled Power Turbine

The same general steam-cooling approach can be applied to the power turbine as is outlined for the gas generator. Reference is made to Fig. 7, which shows a conceptual cross section of a steam-cooled power turbine. The details of this three-stage-overhung power turbine with an 8 expansion ratio were previously presented as referenced in Part I of this study [4]. Figure 1 of Part I presents the cycle diagram and shows the various power-turbine heat-exchanger areas. Heat balance data on the cycle were presented in [4].

Steam is used at different pressure levels as shown in Fig. 7. The casings, struts, and inner barrel as well as the second and third nozzle vanes are cooled with a closed cycle whereby no steam is lost to the atmosphere. The heated steam is readmitted to the steam turbine, expanded and then condensed.

An open-cycle, steam-cooling system is employed for the first-stage nozzle vanes and for the three stages of rotating blades. The blade steam is introduced through a steam seal at the required three different steam extraction pressures. The steam seal is shown in Fig. 7 located between the two journal bearings. The spent cooling steam mixed with the gas passes through the heat-recovery boiler where a considerable amount of its heat is transferred back to the cycle before being exhausted to the atmosphere.

Aircraft Versus Industrial CPRs

It appears at the present time that 38 CPR is about as high as economically feasible for aircraft engines. When the CPR is increased above this value, any gain in cycle efficiency is offset by the added weight of the compressor casing, combustor housing and turbine shells. Also, the higher compressor-discharge temperature necessitates heavier last-stage compressor disks.

When considering a modified steam-cooled gas generator as previously discussed, there is no reason why an industrial-gas generator could not be built for a 40 to 44 CPR to optimize the reheat-gas-turbine reheat-steam turbine combined cycle for the higher 2600°F TIT projected.

Cooling-Steam Flow Rates

The cooling-steam flow rates for the GG shell, struts, barrels, etc. are very small compared to the total air flow of the gas generator. These flow rates are also small compared to the primary coolants for the nozzle vanes and rotating blades (A, B, C, and D) and are perhaps only 15 percent of these primary values. The PT cooling-flow rates will be somewhat higher due to the larger areas involved.

The core flow rate of a 50,000 lb thrust fan-jet gas generator is about 275 lb/s. The total steam cooling rate for primary cooling open system (points A, B, C, and D) is calculated to be about 6 percent of the air flow or 16.5 lbs/s (59,400 lbs/hr) which is considerable steam. It is estimated that the compressor casing, tubing, shell, strut, barrel, and diffuser total-steam flow would be about 9,000 lbs/hr in a closed system where no steam is lost.

This steam flow is available from the 604 psia first-steam-reheat header and the 140 psia second-steam-reheat header for the 2400 psig steam-turbine arrrangement. Ample pressure is available to force the steam through the various passages and extended-surface fins. There is some 50 psi total pressure present from the steam turbine reheat-pressure drop. In the case of the 604 psi steam, the flow will be part of the reheat-combustor-cooling steam where there is an ample supply present. In the case of the 140 psia extraction steam flow is available with an adequate pressure drop of 20 psi to provide the working force for cooling.

The 140 psia steam at 701°F is extracted from the IPT steam turbine one stage before the crossover line to the LPT. This extracted steam, after being desuperheated, is then heated through the process of cooling the gas generator casings and stationary parts, the power turbine casings and stationary parts and the transition duct to the boiler.

The 123 psia heated steam at 1100°F flows back to the crossover line to the steam turbine where it is mixed with the IPT steam in a crossover mixer. A conceptual cross-sectional drawing of the mixer is shown in Fig. 2 of Part I. Steam at 123 psia and 1100°F is fed into a donut header to which is connected a number of mixing nozzles—perhaps six in number. These nozzles are shown at an angle. Each contains a number of properly spaced holes to allow the hot steam to disperse and mix with the cooler steam. In this way, the hot 1100°F steam at 123 psia mixes with the cooler 669°F 120 psia steam.

The 3 psia pressure differential (about 2½ percent pressure drop) should be ample to obtain good mixing. The right-angle turn to the LPT turbine will greatly aid in the mixing process and stabilize temperatures. The homogeneous mixture of steam at 850°F then enters the center-inlet scroll to the double-flow LPT steam turbine.

Summary and Conclusion

It has been shown in Parts I and II of this paper that steam is a practical way to cool the stationary and internal rotating parts of a high-cycle pressure-ratio gas generator and reheat gas turbine when firing at high inlet temperatures of 2600/2400°F rotor inlet temperatures. Steam also makes possible disk cooling of the compressor and turbine rotors to greatly reduce the temperature differential between hub and rim; and disk low-cycle fatigue problems are reduced.

Steam, due to its appreciable better physical characteristics over air offers a way to control blade-tip clearances of the last stages of the high-pressure compressor, the gas-generator turbine and the power turbine which is vital to high performance and low-specific fuel consumption. A microprocessor minicomputer can be applied to accomplish cooling-steam flow control. Steam extracted from the steam turbine in a combined-cycle mode of operation can be taken from the cold reheat lines to take advantage of the existing and inherent steam-pressure losses. This steam can be desuperheated to the saturation temperature as needed to obtain maximum heat-carrying capacity before being used as the coolant. The hot steam is returned to the steam turbine to develop incremental steam turbine power.

Although supercritical pressure steam cycles are being proposed by EPRI there does not appear to be a compelling advantage in terms of combined-cycle heat rate to go beyond the present-day industry-accepted 2400 psig level. Growth exists in the second reheat of a 2400 psig system whereby the second reheat can extend from the proposed 850°F level to perhaps 1000°F.

Response time and sensitivity to metal temperatures of the gas turbine casings and support struts are important considerations. The lighter parts of an aero-derivative gas generator of the type being developed through the NASA-sponsored program appear to be more suitable to steam cooling than the heavier industrial-type turbines.

Steam cooling can maintain cooler stationary and rotating parts than air cooling and thus allows more freedom in material selection due to higher allowable stresses being possible at the lower temperatures. Thermal expansion varies appreciably with different metals. High-nickel superalloys exhibit some 20 percent higher coefficients of expansion than high-strength steels. The steam-cooled casings can be made out of high-strength steels with lower thermal-expansion rates to better match the high-nickel disk expansion rates. The casings would operate at higher temperatures than the disks to provide better casing to steam temperature differentials.

Considerable research and development work is needed before the steam-cooled reheat gas turbine can become a reality, but this paper shows that steam-cooling a high-cycle pressure-ratio gas turbine in a combined-cycle mode of operation is a practical and realistic method of cooling the parts and controlling blade-tip clearances.

Acknowledgments

Appreciation is expressed for the devoted assistance of my wife, Carolyn Keyes Rice, on page 7 of Part I.

References

All references for this two-part paper are included at the end of Part I.

Gas Turbine Compressor Interstage Cooling Using Methanol

J. A. C. Fortin

M. F. Bardon

Department of Mechanical Engineering,
Royal Military College of Canada,
Kingston, Ontario, Canada K7L 2W3

An earlier study demonstrated the theoretical potential of the concept of injecting methanol into a gas turbine compressor inlet as a means of increasing cycle thermal efficiency. To attain the full potential of such a system, continuous shifting vapour/liquid equilibrium is required which would pose formidable difficulties in practice due to the presence of liquid in the compressor blading. This study evaluates a more practicable configuration in which the alcohol is injected between stages of a multistage machine so that, due to the higher air temperatures, evaporation is complete before the mixture enters subsequent stages. Through a computer analysis, it is shown that this arrangement would retain most of the potential of the concept while greatly reducing the design and operating problems.

Introduction

It is well known that methanol can be successfully used as a fuel in conventional gas turbine combustion chambers [1, 2]. As a simple replacement for kerosene in a conventional cycle, it in fact gives comparable or slightly improved performance. However, some recent analytical studies [3, 4] have demonstrated that a considerable increase in thermal efficiency is theoretically possible if the unique properties of methanol are used to advantage. The proposed technique makes use of alcohol injection into the compressor.

Injection of alcohol or water/alcohol mixtures has been used in the past to increase the power output of aircraft gas turbines during takeoff. The work previously reported in [3] demonstrated that the technique could also be used to increase cycle thermal efficiency by as much as 15 percent. It is noteworthy that this technique is not applicable when using an ordinary hydrocarbon fuel because efficiency would instead decrease. This difference between alcohol and hydrocarbons results from the different fuel properties, mainly, latent heat and stoichiometric fuel-air ratio. The combination of these two characteristics results in a large charge cooling effect referred to as evaporative intercooling when used deliberately in a Brayton cycle engine. Now ordinary compressor intercooling via heat exchangers reduces compressor work and so increases net work; however, unless an exhaust gas energy recuperator is used, the cycle efficiency drops because the heat removed must later be replaced by additional fuel. Hence, alcohol injection in aircraft tacitly accepts reduced efficiency for increased power. However, alcohol evaporation does not actually represent an energy loss from the working fluid since the cooling effect is counterbalanced by an equivalent increase in the fuel's heating value when it changes from liquid to vapour. Consequently, an engine designed to accommodate this effect could in principle achieve worthwhile efficiency improvements, as well as increased work per unit mass of air flow.

In the calculations used to determine the benefit theoretically possible using this technique [3], the best case was assumed, namely: that the alcohol was injected upstream of the compressor, achieved vapor/liquid equilibrium before compression began, and thereafter, maintained equilibrium during the remainder of the evaporation within the compressor. From a practical viewpoint, it is readily apparent that achieving this maximum theoretical benefit would be difficult because it requires (*i*) that droplet sizes be very small so that evaporation will be sufficiently fast to maintain equilibrium; (*ii*) that the increased mass flow of gas due to the steadily increasing quality of methanol vapor be accounted for in the compressor design; and (*iii*) that the liquid droplets not cause serious erosion of the compressor blades. Although all three of these areas of potential difficulty may ultimately be manageable, they present a rather formidable obstacle to a manufacturer considering implementation of such a system. One possible interim measure which might eliminate all three factors at the cost of a reduced efficiency gain would be the injection between stages so that (*i*) alcohol would be injected only after sufficient compression had occurred to raise the air temperature to a level allowing rapid and complete evaporation before the remainder of the compression took place; (*ii*) although different stages of the compression would have different mass flow, each would be constant rather than variable as in the case of continuous evaporation, permitting standard design procedures; and (*iii*) there would be no erosion of blading.

Figures 1 and 2 show schematically the two versions of an unregenerated gas turbine using continuous shifting equilibrium and interstage cooling. The purpose of this paper is to examine the interstage evaporative cooling concept using a realistic cycle analysis so as to determine whether the potential benefits are still sufficiently large to justify the development effort required to put the system into practice.

Contributed by the Gas Turbine Division of THE AMERICAN SOCIETY OF MECHANICAL ENGINEERS for presentation at the 28th International Gas Turbine Conference and Exhibit, Phoenix, Arizona, March 27-31, 1983. Manuscript received at ASME Headquarters January 11, 1983. Paper No. 83-GT-230.

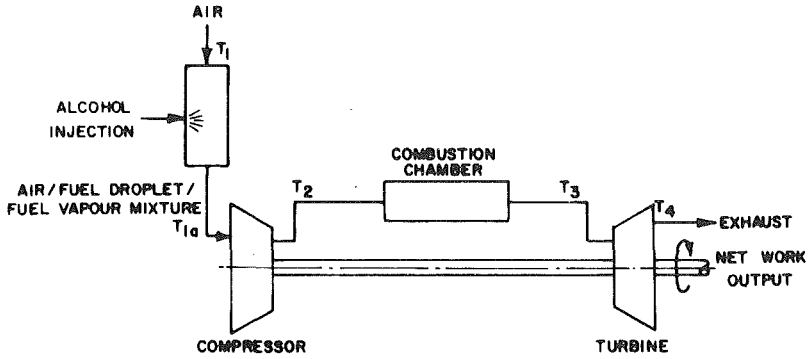

Fig. 1 Gas turbine with methanol injection upstream of the compressor

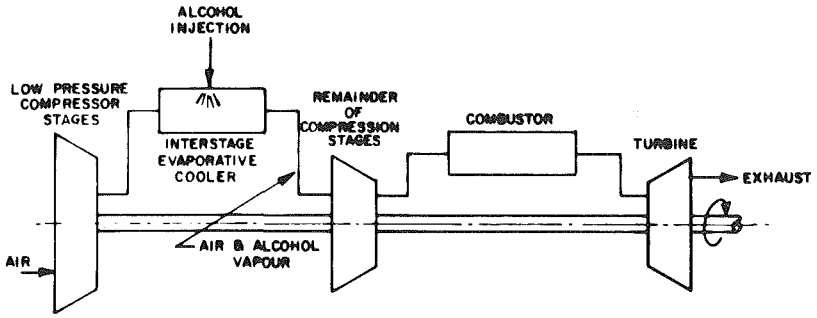

Fig. 2 Methanol injection between compressor stages

Cycle Model

The computer calculation details for the continuous shifting equilibrium case have been given elsewhere [3]. As a brief summary, (*i*) gas properties were determined using temperature dependent specific heats and the ideal gas law, (*ii*) the Antoine equation was used to determine methanol vapour pressure when required, (*iii*) component efficiencies were defined in the customary ways and representative peak values were used in all calculations, (*iv*) pressure losses were neglected, (*v*) in the evaporator, liquid fuel at ambient

Nomenclature

A,B,C = constants used in Antoine equation (A8)
a = coefficient used in equation (A1)
b = coefficient used in equation (A1)
c = coefficient used in equation (A1)
C_p = constant pressure molar specific heat J/mol K
d = coefficient used in equation (A1)
e = coefficient used in equation (A1)
H = total enthalpy, J
$\bar{h}$ = molar specific enthalpy, J/mol
k = ratio of specific heats
n = number of moles
P = pressure (total mixture pressure if unsubscripted)
P_r = single stage pressure ratio
R = universal gas constant = 8.314 J/mol K
S = total entropy, J/K
$\bar{s}$ = molar specific entropy J/mol K
T = absolute temperature, K
η = efficiency

Subscripts and Superscripts

a = value for air
b = reference to the combustion chamber
c = reference to the compressor
f = value for fuel if no superscript is used
^0f = used for enthalpy of formation, i.e., h_f^0
fg = change in property during evaporation
$^0_{fg}$ = change in property during evaporation at reference temperature, 25°C
g = reference to fuel vapour
i = reference to ith component of a mixture
l = reference to liquid fuel
s = reference to state after an isentropic process
st = reference to value for a single compressor stage
t = reference to turbine
1,2 = general sequential values
1,1a,2,x,3,4 = points during cycle as defined in Fig. 1
0 = value at reference temperature, 25°C

Table 1 Comparison of cycle performance at T_{max} = 1055 K

	Cycle thermal efficiency	% efficiency gain	Specific work (kJ/kg of air flow)
Conventional cycle	0.315	-	181
Evaporative intercooling (continuous shifting equilibrium)	0.349	11	212
Interstage evaporative intercooling between			
Stages 1 and 2	0.346	9.8	209
2 and 3	0.342	8.5	205
3 and 4	0.338	7.3	200
4 and 5	0.334	6.1	197
5 and 6	0.330	4.9	193
6 and 7	0.327	3.8	191
7 and 8	0.324	2.8	188
8 and 9	0.321	1.8	186
9 and 10	0.318	0.9	184

Table 2 Comparison of cycle conditions at constant cycle thermal efficiency

	Cycle thermal efficiency	Turbine inlet temperature (K)	Temperature reduction (K)
Conventional cycle	0.315	1055	-
Evaporative intercooling (continuous shifting equilibrium)	0.315	924	131
Interstage evaporative intercooling between			
Stages 1 and 2		934	121
2 and 3		947	108
3 and 4	↑	960	95
4 and 5	0.315	973	82
5 and 6	↓	986	69
6 and 7		999	56
7 and 8		1013	42
8 and 9		1027	28
9 and 10		1041	14

temperature was mixed with the incoming air and assumed to evaporate adiabatically and irreversibly such that vapor/liquid equilibrium was attained at the outlet. The Appendix gives further details along with some data used in the calculations.

Basis of Comparison. There are endless combinations of multistage compressors with evaporation between stages at various points. The particular case used here to compare interstage evaporative cooling with the case of continuous shifting equilibrium was that of an unregenerated engine having a 10-stage compressor with an overall pressure ratio of 10 and a peak turbine inlet temperature of 1055 K. As indicated in the appendix, the overall adiabatic compressor efficiency was taken to be 0.85.

Assuming negligible change in the value of specific heat for air over the operating temperature of a multistage compressor, then the relationship between individual stage efficiency, η_{st}, and overall compressor efficiency, η_c, may be shown to be given by

$$\eta_{st} = \left(P_r^{\frac{k-1}{k}} - 1\right) \Big/ \left[\left[1 + \frac{1}{\eta_c}\left(P_r^{\frac{n(k-1)}{k}} - 1\right)\right]^{\frac{1}{n}} - 1\right] \quad (1)$$

where k = ratio of specific heats
n = number of stages
P_r = single stage pressure ratio

Using this relationship, the assumed overall compressor efficiency of 0.85 implies a stage efficiency of approximately 0.886, because the individual stage pressure ratio must be about 1.26 to give an overall ratio of 10 after 10 stages.

Results and Discussion

Table 1 shows the overall cycle efficiency and specific work possible when alcohol injection occurs between various stages of the 10-stage compressor assumed as the basis of comparison. Each case shown has the same maximum turbine inlet temperature of 1055 K, which means that the fuel-air ratios are slightly different. This is because earlier evaporation induces cooler temperatures at all downstream points in the machine unless fuel flow is increased. This effect is considered in further detail later.

As expected, injection between stages results in values of efficiency and work output lying between the two extremes of continuous shifting equilibrium and conventional combustor injection. Taking the case of injection between stages 2 and 3, for example, it is seen that the cycle efficiency is still increased by 8.5 percent compared to the theoretical maximum improvement of about 11 percent for this pressure ratio and peak cycle temperature. Some study is required to determine whether, for example, methanol evaporation in the 62°C air leaving the second stage would be sufficiently fast to avoid the presence of liquid at the third stage inlet without an excessively long connnecting passage between the stages.

In addition to being a method for increasing overall cycle thermal efficiency, methanol injection offers a means of reducing peak turbine inlet temperature, without suffering a resultant efficiency reduction. Table 2 shows the results of

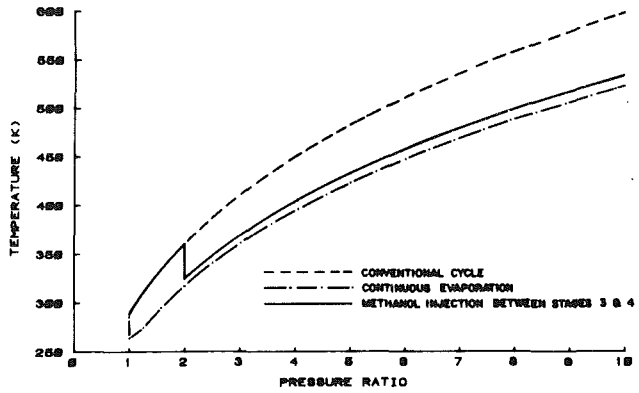

Fig. 3 Effect of methanol evaporation on gas temperature within the compressor

cycle calculations in which the fuel injection rate was selected so that the overall cycle efficiency with evaporative intercooling would be the same as that of a conventional cycle.

Figure 3 shows the temperature distribution within the compressor to illustrate the effects of the methanol evaporation. As in Table 1, the calculations were performed such that the turbine inlet temperature was 1055 K for all configurations.

Conclusions

From the results of this study, it is concluded that the significant improvement in cycle thermal efficiency theoretically possible using methanol injection in the compressor would be only slightly reduced by using injection between stages of a multistage machine rather than upstream of the compressor. This would have the advantage of avoiding liquid within the blading by allowing rapid and complete evaporation of the methanol in the higher temperatuare air resulting from one or more stages of compression. Furthermore, although the gas flow rates and properties for compressor stages upstream and downstream of the point of injection would be different, they would be constant and precisely known for each part of the machine, thus eliminating the formidable design difficulties associated with the theoretical case of continuous evaporation within the compressor blading.

The only remaining serious obstacle to implementation of such a system is the combustion chamber design to burn the lean homogeneous mixture delivered by the compressor. A catalytic combustor would be ideal. Pilot injection of a small fraction of the fuel in a conventional combustor might also be feasible, although it would result in a smaller efficiency gain.

References

1 Klapatch, R. D., "Gas Turbine Emissions and Performance on Methanol Fuel," ASME-IEE Joint Power Generation Conference, Portland, Sept. 28-Oct. 1975.

2 Weir, A. Jr., von Kleinsmid, W. H., and Danko, E. A., "Test and Evaluation of Methanol in a Gas Turbine System," Electric Power Research Institute, Palo Alto, Calif., report AP-1712, Feb. 1981.

3 Bardon, M. F., "Modified Brayton Cycles Utilizing Alcohol Fuels," ASME JOURNAL OF ENGINEERING FOR POWER, Vol. 104, No. 2, Apr. 1982.

4 Bardon, M. F., and Fortin, J. A. C., "Methanol Dissociative Intercooling in Gas Turbine Compressors," ASME Paper No. 82-GT-176, presented at the 27th International Gas Turbine Conference, London, Apr. 19-23, 1982.

5 Wark, R., *Thermodynamics*, McGraw-Hill, New York, 1977.

6 *Standard Handbook for Mechanical Engineers*, 8th ed., edited by T. Baumeister, McGraw-Hill, 1978.

7 *Lange's Handbook of Chemistry*, 11th ed., edited by J. A. Dean, McGraw-Hill, N.Y. 1973.

8 Wilhoit, R. C., and Zwolinski, B. J., "Physical and Thermodynamic Properties of Aliphatic Alcohols," *J. Phys. Chem. Ref. Data*, Vol. 2, Supp. 1, 1973, pp. 1.40-1.54.

9 Hagen, D. L., "Methanol as a Fuel: A Review with Bibliography," SAE Paper 770792, Detroit, Sept. 26-30, 1977.

APPENDIX

Cycle Calculation Methods

Gas Properties. In order to determine the properties of the gases at various points during the cycle, the components were assumed to behave both individually and collectively as ideal gases with temperature-dependent specific heats of the following form

$$C_p = a + bT + cT^{-1} + dT^{-1/2} + eT^{-2} \tag{A1}$$

where

C_p = constant pressure molar specific heat, J/mol K
a,b,c,d,e = coefficients characteristic of the gas concerned
T = absolute temperature, K

Table 3 shows the values of the coefficients used in the foregoing equation for the gases considered in this study. Air was taken to be composed of 21 mole percent oxygen and the remainder nitrogen. Combustion was assumed to be essentially complete as far as gas composition was concerned; therefore, only CO_2 and H_2O were produced during the burning of the fuel, which was considered to be completely consumed in the combustor. Consequently, the gas entering the turbine consisted only of the original nitrogen, excess oxygen, and the two products of combustion.

With the assumptions stated above, the sensible enthalpy of a gas at temperature T above the reference temperature T_0 is

$$\bar{h} - \bar{h}_f^o = \int_{T_o}^{T} C_p dT$$

$$= a(T - T_o) + \frac{b}{2}\left[T^2 - T_o^2\right] + c\ ln\left\{\frac{T}{T_o}\right\}$$

$$+ 2d\left[T^{1/2} - T_o^{1/2}\right] - e\left[T^{-1} - T_o^{-1}\right] \tag{A2}$$

where

$\bar{h}$ = molar specific enthalpy, J/mol; and $\bar{h}_f$ = specific enthalpy of formation at $T° = 25°C$.

Likewise, the entropy may be expressed as

$$\bar{s} - \bar{s}_f^o = \int_{T_o}^{T} \frac{C_p}{T} dT - \bar{R} ln(P/P_o)$$

$$= a\, ln(T/T_o) + b(T - T_o) - c\left[T^{-1} - T_o^{-1}\right]$$

$$- 2d\left[T^{-1/2} - T_o^{-1/2}\right] - \frac{e}{2}\left[T^{-2} - T_o^{-2}\right]$$

$$- \bar{R} ln(P/P_o) \tag{A3}$$

where $\bar{s}$ = molar specific entropy, J/mol K; $\bar{s}_f^o$ = absolute entropy at the reference state, J/mol K; $\bar{R}$ = universal gas constant, 8.314 J/mol K; P = partial pressure of the gas; P_o = reference state pressure = 1 atm.

For a mixture of N gases, equation (A2) becomes

Table 3 Coefficients for specific heat equation (A1) (adapted from [5, 6]; temperature in K, C_p in J/mol K)

O_2	48.178	0	3 556	− 536	0
N_2	39.6	0	− 8 066	0	1 498 000
CO_2	67.8	0	− 15 200	0	1 821 000
H_2O	83.09	0	17 400	− 1 860	0
CH_3OH	8.37	0.125 5	0	0	0

Table 4 Component efficiencies

Compressor	0.85
Combustor	0.98
Turbine	0.90

Table 5 Other data used in the cycle calculations

Property	Units	Substance	Source	Value
$\bar{s}_f^0$	J/mol K	O_2	5	205.03
		N_2	5	191.50
		CO_2	5	213.64
		H_2O(g)	5	188.72
		$CH_3OH(l)$	5	126.80
		CH_3OH(g)	5	239.70
$\bar{h}_f^0$	J/mol	O_2	5	0
		N_2	5	0
		CO_2	5	− 393 520.
		H_2O	5	− 241 820.
		$CH_3OH(l)$	5	− 238 660.
		CH_3OH(g)	5	− 200 670.
C_p	J/mol K	$CH_3OH(l)$	-	82.1
Air intake temperature	K	-	-	289

$$H=\sum_{i=1}^{N} n_i\bar{h}_{fi}^{o}+\sum_{i=1}^{N} n_i a_i(T-T_o)+\sum_{i=1}^{N}\frac{n_i b_i}{2}\left[T^2-T_o^2\right]+\sum_{i=1}^{N} n_i c_i ln(T/T_o)+\sum_{i=1}^{N} n_i d_i\left[T^{1/2}-T_o^{1/2}\right]-\sum_{i=1}^{N} n_i e_i\left[T^{-1}-T_o^{-1}\right] \quad \text{(A4)}$$

where H = total mixture enthalpy, J; n_i = number of moles of component i in the mixture.

Similarly, equation (A3) becomes

$$S=\sum_{i=1}^{N} n_i\bar{s}_{fi}^{o}+\sum_{i=1}^{N} n_i a_i ln(T/T_o)+\sum_{i=1}^{N} n_i b_i(T-T_o)-\sum_{i=1}^{N} n_i c_i\left[T^{-1}-T_o^{-1}\right]-2\sum_{i=1}^{N} n_i d_i\left[T^{-1/2}-T_o^{-1/2}\right]-\frac{1}{2}\sum_{i=1}^{N} n_i e_i\left[T^{-2}-T_o^{-2}\right]-\sum_{i=1}^{N} n_i\bar{R}ln(P_i/P_o) \quad \text{(A5)}$$

Liquid Properties. The specific heat for methanol was taken to be constant so its enthalpy and entropy were determined as follows

$$\bar{h}=\bar{h}_f^0+C_p(T-T_0) \quad \text{(A6)}$$

and

$$\bar{s}=\bar{s}_f^0+C_p ln(T/T_0) \quad \text{(A7)}$$

Component Efficiencies.

Compressor Efficiency. Adiabatic compressor efficiency was defined as

$$n_c=\frac{\bar{h}_{2s}-\bar{h}_1}{\bar{h}_2-\bar{h}_1} \quad \text{(A8)}$$

where

$\bar{h}_1$ = specific enthalpy of the air at the compressor inlet
$\bar{h}_2$ = specific enthalpy of the air at the compressor outlet
$\bar{h}_{2s}$ = enthalpy which would exist after an isentropic compression from state 1 to the same compressor exit pressure, P_2

In the case of the continuous shifting equilibrium cycle, the working fluid's composition is not the same at the compressor inlet and outlet. Therefore, the following more general but equivalent form was used

$$n_c=\frac{H_{2s}-H_{1a}}{H_2-H_{1a}} \quad \text{(A9)}$$

where

H_{1a} = total mixture enthalpy at the compressor inlet
H_2 = total mixture enthalpy at the actual compressor outlet
H_{2s} = total mixture enthalpy which would exist after an isentropic compression from the same initial state to the same outlet pressure, P_2

Both equations (A8) and (A9) define the adiabatic compressor efficiency as the ratio of ideal work to actual work required.

Combustion Chamber Efficiency. Combustion chamber efficiency was defined as the ratio of actual sensible enthalpy rise during combustion to the ideal sensible enthalpy rise for complete adiabatic combustion. Hence

$$\eta_b = \frac{\sum_{i=1}^{N} n_{i3}(\bar{h}_i - \bar{h}^0_{fi})_3 - \sum_{i=1}^{N} n_{i2}(\bar{h}_i - \bar{h}_{fi})_2}{\sum_{i=1}^{N} n_{i3}\bar{h}^0_{fi3} - \sum_{i=1}^{N} n_{i2}\bar{h}^0_{fi2}} \tag{A10}$$

where states 2 and 3 are at combustor inlet and outlet, respectively.

Turbine Efficiency. Turbine adiabatic efficiency was defined as

$$\eta_1 = \frac{\bar{h}_3 - \bar{h}_4}{\bar{h}_3 - \bar{h}_{4s}} \tag{A11}$$

where

$\bar{h}_3$ = enthalpy at turbine inlet
$\bar{h}_4$ = enthalpy at turbine exhaust
$\bar{h}_{4s}$ = enthalpy after an isentropic expansion from state 3 to the same turbine exit pressure

When the fuel saturation pressure was required, it was determined using the Antoine equation [7] with coefficients taken from the data of Wilhoit and Zwolinski [8]. Converted to SI units, the relationship is

$$\log_{10} P_f = 7.022\,40 - 1\,474.08/(T - 44.02) \tag{A12}$$

where

P_f = methanol saturation pressure, kPa
T = temperature, K

Simplified Mathematical Representations of Heavy-Duty Gas Turbines

W. I. Rowen
Manager-Control Systems,
Gas Turbine Division,
General Electric Company,
Schenectady, N. Y. 12345
Mem. ASME

This paper provides simplified mathematical representations of heavy-duty gas turbines that are suitable for use in dynamic power system studies and in dynamic analyses of connected equipment. The full range of heavy-duty, single-shaft gas turbines, from 18 MW (24,000 HP) and 106 MW (142,000 HP), is covered, as well as both liquid and gas fuel systems, parallel and isolated operation, droop and isochronous governors, and the impact of both air- and hydrogen-cooled generators on the characteristics of the model. Alterations to the models, for the purpose of further simplification, are also discussed.

Introduction

During the past several years, requests have been received for simplified mathematical models of General Electric gas turbine generators to be used as input for comprehensive studies of gas turbine users' power systems. The intent of these studies has been the investigation of power system stability, the development of dispatching strategy, and contingency planning for system upsets. Invariably, each request has placed the emphasis on keeping the model "simplified" yet flexible enough to represent different units with different characteristics. This paper is intended to answer these requests with a unified approach that offers the broadest possible base of applicability.

Terminology used throughout the block diagrams and supplementary tables is shown in the nomenclature section. In general, this terminology is kept in the per unit system with the exception of temperatures. (Per unit values are the decimal equivalents of percent values. In the percent system, 100 equals the design value, while in the per unit system 1.00 equals the design value.) Real equivalents of per unit values for the values for the various machines sizes are presented in both English and metric units, as are equations associated with the temperature control system. Notes to the figures are kept sequentially, and a specific note such as No. 1, for Fig. 1, will also apply to Figs. 4, 5, and 6 as called out in the specific figure. The system gains, coefficients, and time constants included in this paper represent design and calculated values. They have been verified by test and actual field experience accumulated from numerous installations in many different applications.

The subject of this paper has been limited to simple cycle, single-shaft, generator drive gas turbines only, because inclusion of combined cycle installations or two-shaft gas turbines would tend to make the paper inordinately long and complex. Specific limits of applicability of the information contained are shown in Table 1. Item 2, limitation of the allowable speed range to 95—107 percent of rated speed, is intended to cover the expected operating speed range in its extremes, while still preventing excursions into the regions where the gas turbine no longer responds linearly or where discontinuities due to control actions are encountered. It should also be noted that this paper concentrates on the functional representation of the gas turbine and its control, and is therefore independent of whether the control is Speedtronic[2] Mark I, or Mark II or Mark IV.

Table 1 Limits of applicability

1	For simple cycle, single-shaft, generator drive only	
2	Allowable speed range = 95 to 107 percent of rated speed	
3	Open inlet guide vanes only, i.e. no heat recovery	
4	ISO conditions apply, i.e.,	
	Ta = 59°F	Pa = 14.696 psia.
	= 15°C	= 101.325 kpa.

Simplified Single-Shaft Gas Turbine Simulation

Figure 1 represents a simplified block diagram for a single-shaft gas turbine, together with its control and fuel systems, as it would be represented for isolated generator drive service. Notes 1 through 8 specify details applicable to this model, and Table 2 specifies unit ratings and per unit values, by turbine Model Series and generator type, in both English and metric units.

The control system includes speed control, temperature control, acceleration control, and upper and lower fuel limits. The representation of the speed governor is suitable for either droop or isochronous control and operates on the speed error formed between a reference made up of one per unit speed plus the digital setpoint, compared with actual system or rotor speed. A droop governor is a straight proportional speed

Contributed by the Gas Turbine Division of THE AMERICAN SOCIETY OF MECHANICAL ENGINEERS for presentation at the 28th International Gas Turbine Conference and Exhibit, Phoenix, Airzona, March 27-31, 1983. Manuscript received at ASME Headquarters December 21, 1982. Paper No. 83-GT-63.
Copies will be available until January 1984.

[2] Registered trademark of the General Electric Company

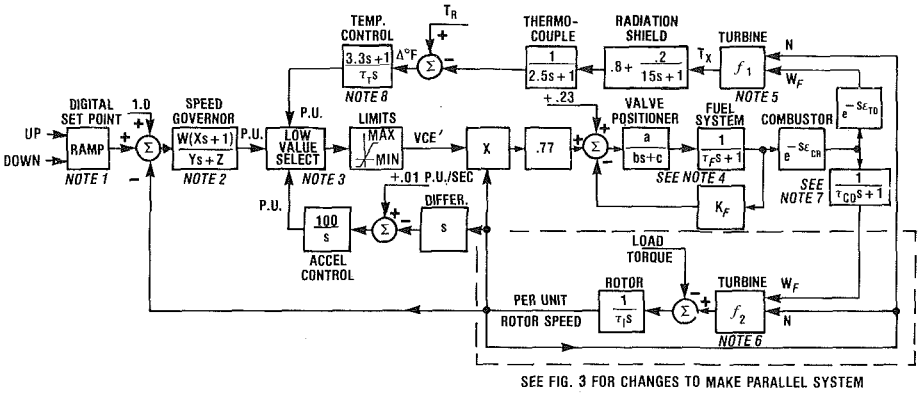

Fig. 1 Simplified single-shaft gas turbine simulation block diagram for isolated operation[3]

[3] Notes for Fig. 1:

1 Digital setpoint time for −5 percent to +7 percent speed change

Model	Synchronizing	Time for 12% Change* Manual	Normal	Fast load
5001M,P	6 Min.	1.5 Min.	12 Min.	1.5 Min.
6001B	GES	1.5 Min.	12 Min.	~
7001B,E		18 Min.	36 Min.	4.5 Min.
9001B	4.5 Min.	12 Min.	48 Min.	~
9001E	μ-Sync	18 Min.	36 Min.	~

*No-load to ISO-rated load is 1/3 of time shown if droop setting is 4%.

2 Speed governor transfer function coefficients

Type	w	x	y	z
Droop	K_D	0	.05	1
Isoc.	30	2.5	.10	0

K_D = 1/Droop; K = 25 typically for 4 percent droop setting.
Droop setting is adjustable from 2 to 10 percent.

3 VCE′ limits are typical by Max = +1.5 PU; Min = −0.1 PU (no load = 0.0 PU; rated load = +1.0 PU)

4 Fuel system characteristics

Type	Model	a	b	c	τ_F	K_F
Gas	All	1	0.05	1	0.40	0
Liquid	5&6	10	1	0	0.10	1
Liquid	7&9	1	0.20	1	0.10	0

5
$f_1 = T_X = T_R - 700(1 - W_F) + 550(1 - N)$ in English units
$= T_X = T_R - 390(1 - W_F) + 306(1 - N)$ in metric units

6 f_2 = turb. torque = $1.3(W_F - .23) + .5(1 - N)$

7 Gas turbine dynamic characteristics

Model Series	ϵ_{CR}	τ_{CD}	ϵ_{TD}
5 & 6	.01	.10	.02
7 & 9	.01	.20	.04

8 τ_T = 450 in °F or 250 in °C

controller in which the output is proportional to the speed error. An isochronous governor is a proportional-plus-reset speed controller in which the *rate of change* of the output is proportional to the speed error. Therefore, the output of an isochronous governor will integrate in a corrective direction until the speed error is zero. For isochronous control, the digital setpoint remains at zero deviation from the frequency reference, and the gas turbine matches the system load up to its rated capability. The speed governor is the primary means of gas turbine control under part-load conditons.

The digital setpoint is the normal means for controlling gas turbine output when operating in parallel and using a droop governor. The digital setpoint is equivalent to a logic-controlled counter and digital-to-analog converter that generates a ramp function at a selectable, predetermined rate. Several different rates are available depending on Model Series and mode of operation. There are two modes of synchronizing, one which uses a conventional synchronizing relay, operating on the setpoint using a 6-min. time period, and the other a microprocessor-based synchronizer, using a 4.5-min time period. Setpoint time periods subsequent to synchronizing can be either manual, which is under the control of the operator using the raise/lower switch, or automatic/remote, which is at the normal rate. The MS5001 Series and 7001 Series also have available, as an option, a fast load rate which is eight times the normal. It should also be noted that the digital setpoint is reset to 100.3 percent in the event that the generator breaker is opened. This is intended to minimize speed overshoot on load rejection as well as reduce the time required for resynchronizing.

Temperature control is the normal means of limiting gas turbine output at a predetermined firing temperture, independent of variation in ambient temperature or fuel characteristics. Since exhaust temperature is measured using a series of thermocouples incorporating radiation shields, there is a small transient error due to the time constants associated

Nomenclature[1]

a, b, c = fuel system transfer function coefficients
w, x, y, z = governor transfer function coefficients
K_D = governor gain
K_F = fuel system feedback
N = per unit turbine rotor speed
s = Laplace operator
T_R = turbine rated exhaust temperature, °F or °C
T_X = turbine exhaust temperature, °F or °C
VCE' = per unit fuel command/per unit speed
W_F = per unit fuel flow
ϵ_{CR} = combution reaction time delay
ϵ_{TD} = turbine and exhaust system transport delay
τ_{CD} = compressor discharge volume time constant
τ_F = fuel system time constant
τ_I = turbine rotor time constant
τ_T = temperature controller integration rate

[1] Units for all time functions are in seconds except for digital set point times, which are in minutes.

Table 2 Turbine-generator characteristics and constants[4]

English units

Model	Turbine rpm	Rating MW	Rated T_R °F	Torque Ft-Lb	Inertia Lb-Ft^2	τ_I s
5001M	5100	18.2	955	25,200	24,600	16.2
5001P	5100	24.8	919	34,200	36,100	17.5
6001B	5100	35.9	1020	49,500	44,900	15.1
7001B	3600	60.0	950	117,400	185,900	18.5
7001E	3600	75.0	1004	146,700	176,400	14.1
7001E[a]	3600	75.0	1004	146,700	153,000	12.2
9001B	3000	82.6	950	193,800	500,300	25.2
9001E	3000	106.7	972	250,400	474,700	18.5
9001E[a]	3000	106.7	972	250,400	439,500	17.1

Metric units

Model	Turbine rpm	Rating MW	Rated T_R °C	Torque Kg-M	Inertia Kg-M^2	τ_I s
5001M	5100	18.2	513	3,484	1,037	16.2
5001P	5100	24.8	493	4,728	1,521	17.5
6001B	5100	35.9	549	6,844	1,892	15.1
7001B	3600	60.0	510	16,231	7,834	18.5
7001E	3600	75.0	540	20,282	7,434	14.1
7001E[a]	3600	75.0	540	20,282	6,447	12.2
9001B	3000	82.6	510	26,793	21,083	25.2
9001E	3000	106.7	522	34,619	20,004	18.5
9001E[a]	3000	106.7	522	34,619	18,521	17.1

ISO package ratings are shown for base load and distillate Gas ratings are normally 2 percent higher.
[a]Hydrogen-cooled generator; all others are air-cooled

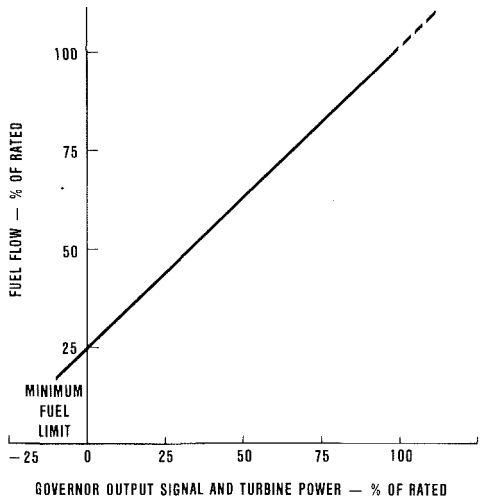

Fig. 2 Relationship between governor output signal and turbine fuel flow

with the measuring system. Under normal system conditions, where gas turbine output is determined by the slow rate of digital setpoint, these time constants are of no significance to the load limiting function. However, where increasing gas turbine output is the result of a reduction of system frequency and therefore may occur quite rapidly, exhaust temperature measurement system time constants will result in some transient overshoot in load pickup. The design of the temperature controller is intended to compensate for this transient characteristic.

Acceleration control is used primarily during gas turbine startup to limit the rate of rotor acceleration prior to reaching governor speed, thus ameliorating the thermal stresses encountered during startup. This control serves a secondary function during normal operation, in that it acts to reduce fuel flow and limit the tendency to overspeed in the event that the turbine generator separates from the system. This action is most beneficial where separation is the result of a breaker other than the generator breaker, in which case the digital setpoint is *not* reset to 100.3 percent as previously described.

These three control functions—speed governing under part-load conditions, temperature control acting as an upper limit, and acceleration control to prevent overspeeding—are all inputs to a low value selector. The output of the low value selector, which is called *VCE'*, is the lowest of the three inputs, whichever requires the least fuel. Transfer from one control to another is bumpless and without any time lags. The output of the low value selector is compared with maximum and mininum limits. Of the two, the maximum limit acts as a backup to temperature control and is not encountered in normal operation; the minimum limit is the more important dynamically. This is because the minimum limit is chosen to maintain adequate fuel flow to insure that flame is maintained within the gas turbine combustion system. This is typically set at a torque deficiency of approximately 10 percent, is a "hard" limit, and represents a maximum rate of deceleration or torque absorption from the system.

This capability of transiently absorbing power from the connected system is unique to the gas turbine and sets it apart from other large prime movers such as steam and hydro turbines. It is normally limited to a maximum steady-state deficiency of 5 percent by the reverse power relay, which will open the generator breaker on an inverse time-current characteristic. The reverse power relay setting is adjustable and in special circumstances can be set to take full advantage of the negative power capability of the gas turbine. It should be noted that the reverse power relay is not a protective device, but is used primarily as part of the normal shutdown sequencing.

Gas turbine fuel systems are designed to provide energy input to the gas turbine in proportion to the product of the command signal (*VCE'*) times the unit speed. This is analogous to the actual mode of operation of the fuel system, since liquid fuel pumps are driven at a speed proportional to turbine rotor speed and since gas fuel control is accomplished in two stages, with the output pressure of the first stage being

[4]Turbine constants are subject to change without notice

proportional to rotor speed. The net effects is to reduce the turndown ratio of the primary fuel control from approximately 50:1 to 6:1.

From a dynamic standpoint, gas turbines have many differences from steam turbines. One of the more obvious differences is the need for a significant fraction of rated fuel to support self-sustaining, no-load conditions. This amounts to approximately 23 percent and is one of the economic driving forces to minimize operating time at full-speed, no-load conditions. As a result, the active fuel control range of the governor is from 16–100 percent, thus providing for a negative torque contribution of approximately 10 percent, as previously mentioned. To allow the use of governor parameters comparable to steam and hydro turbines, the governor operates from 0–100 percent of active load range. This range must then be corrected to 23–100 percent fuel flow range to be compatible with the thermodynamics of the turbine. This relationship between governor output signal and fuel flow is shown in Fig. 2.

As mentioned previously, the fuel gas control system consists of two valves in series, the first of which controls the pressure between the two valves as a function of speed. The second valve has a linear area versus lift characteristics and is aerodynamically designed so that sonic velocities are attained at the controlling area with flange-to-flange valve pressure ratios as low as 1.25. If valve position is maintained proportional to the *VCE′* signal, the net result is a flow rate of fuel gas which is proportional to the produce of *VCE′* and turbine speed. The response of the pressure control portion of the system may be neglected for this type of simplified study

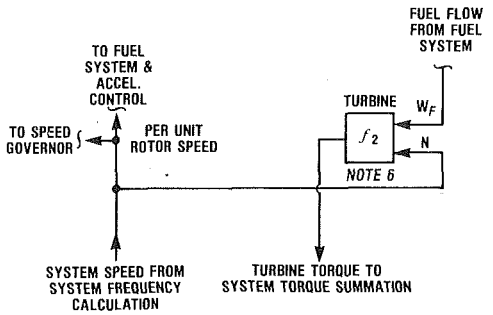

Fig. 3 Modification to Fig. 1 for parallel operation (Note 9: add turbine-generator rotor inertia to overall system inertia; Note 10: system calculations are by user)

because of the small volume between the two valves and the higher gain of the first or pressure controlling valve. Therefore, there are only two time constants of importance in the gas system. The first is that associated with the gas control valve positioning system, and the second is the volumetric time constant associated with the downstream piping and fuel gas distribution manifold.

There are two types of liquid fuel control systems that are used on single-shaft gas turbines. Both of these are bypass systems in which part of the output of a constant volume fuel pump is returned to the pump suction. The amount of fuel bypassed is determined by measuring fuel flow going to the turbine and making that number agree with the total fuel command, which is the product of *VCE′* and turbine speed. The larger gas turbines utilize a closed position loop on the bypass valve, which is an inner loop within the flow feedback signal. The smaller gas turbines, the MS5001 and 6001 series, do not utilize an inner position feedback signal, and therefore close the loop around a pure integrating positioner on the bypass valve by means of only the flow feedback signal. Fuel compressibility and inertia in the system between the bypass valve and the flow measurement are represented by a relatively small time constant.

The gas turbine proper is essentially a linear, nondynamic device with the exception of the rotor time constant. There is a small transport delay associated with the combustion reaction time, a time lag associated with the compressor discharge volume, and a transport delay to transport the gas from the combustion system through the turbine. Representative values are shown in Note 7 of Fig. 1. In the context of the rotor and connected system time constants and the relatively slow setpoint ramp rates, these short-term dynamic characteristics can be ignored.

Both the torque and exhaust temperature characteristics of the single-shaft gas turbine are essentially linear with respect to fuel flow and turbine speed over the 95–107 percent speed range to which these models are limited. The torque equation is accurate to within 5 percent at part load, and is significantly more accurate at the 100 percent design rating. The exhaust temperature equations are somewhat less accurate at part load; however, since temperature control is only active at the design point, the impact of the part load inaccuracy is negligible to the overall simulation. Table 2 provides basic turbine characteristics in both English and metric units as a function of Model Series. Some of the larger gas turbines are

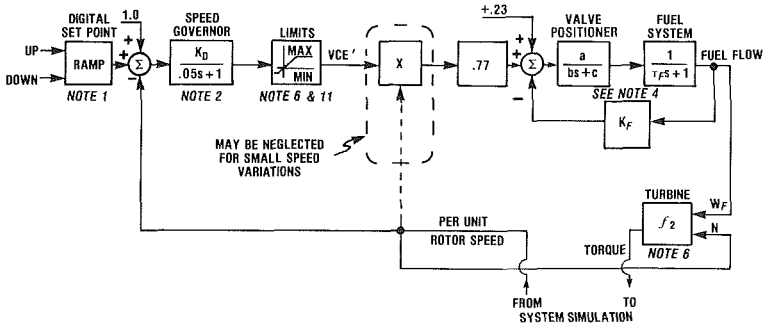

Fig. 4 Additional simplifications to block diagram of Fig. 1 (Note 11: Set Max VCE′ limit = rated load = + 1.0 PU)

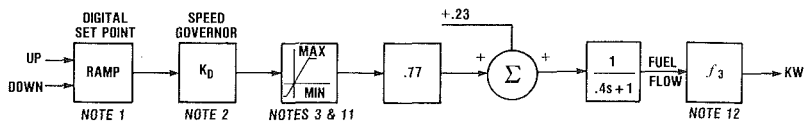

Fig. 5 Simplified block diagram for very "stiff" systems (Note 12: f_3 = KW = 1.3(W_F − .23))

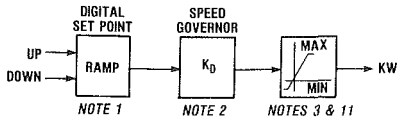

Fig. 6 Simplified block diagram for very large "stiff" systems

available with either air- or hydrogen-cooled generators. This only affects the inertia, and therefore the rotor time constant, as shown in Table 2. By way of definition, the turbine rotor time constant is defined as the time necessary for the rotor to double its speed if the initial rate of speed change is maintained after removal of rated load torque.

Simulation of Parallel Operation

The configuration shown in the lower right-hand corner of Fig. 1 is indicative of the system configuration for simulating an isolated generator drive gas turbine. Most system studies involve the simulation of numerous units all operating in parallel. With the exception of system torque balances and frequency calculations, all previous discussions apply to the models regardless of whether the gas turbine is operating as an isolated unit or in a parallel configuration. The changes necessary to merge the gas turbine model with a system model are shown in Fig. 3. In this case, the turbine generator rotor inertia should be added to the overall system inertia.

Simplifications to the Models

Most simplifications to the model presented in Fig. 1 are associated with parallel operation in a relatively "stiff" system, in which speed variation is significantly less than the 95–107 percent limitation of the model of Fig. 1. Under these conditions of limited frequency variation, several simplifications can be made to reduce the complexity of Fig. 1. First of all, since parallel operation is the only type envisioned, the speed governor can be changed to a droop-only configuration. Secondly, if the frequency variations are not greater than ± 1 percent, acceleration control will not become active except under load-loss situations, and acceleration control can be eliminated. Lastly, since gas turbine output is predominantly controlled by the digital setpoint, the need for the interactive limit imposed by temperature control is significantly diminished, thereby allowing elimination of temperature control, as well as the need for the low value selector. Where temperature control has been eliminated, the upper load limit can be satisfactorily approximated by reducing the maximum fuel limit to level corresponding to rated load. These changes are shown in Fig. 4. Previous notes from prior figures still apply as noted. As mentioned previously, the minor dynamic characteristics of the gas turbine can also be eliminated.

Further simplification of Fig. 4 is possible in the case of parallel operation where the system inertia relative to the gas turbine is very large and system time constants are very long. For this situation many of the shorter time constants associated with the speed governor and fuel control systems can be ignored. Again, if frequency variations are small enough so as to be negligible, then fuel flow and therefore turbine output, will be a direct function of the speed governor command. These additional changes are shown in Fig. 5.

In the final analysis, where system time constants are very long relative to those associated with the gas turbine, gas turbine output will be essentially proportional to the position of the digital setpoint times the governor gain. This is shown in Fig. 6. Although this last simplification may appear to make the model trivial, it is nevertheless an adequate representation of a relatively small gas turbine in a very large system. There are no guidelines that can be put down with regard to how far model simplification should be carried since it is very much a function of the size and characteristics of the connected system. Considerable engineering judgment and detailed knowledge of equipment characteristics are required to insure against oversimplification.

Summary

This paper has attempted to present mathematical representations of General Electric heavy-duty gas turbines that would be suitable for use as input to power system stability studies. The models have been tailored to cover the full spectrum of generator drive gas turbines and appropriate turbine-generator characteristics; constants have been included in both English and metric units. All conventional fuel systems, for both liquid and gas, have been discussed, and special operating conditions such as isolated operation and use of isochronous governors have also been touched upon. Simplifications to the models, and the appropriate rationale have also been discussed. Engineering judgment must be used in conjunction with careful evaluation of the intended purpose prior to use of the simplified models.

D. W. Leffler
Manager of Projects,
Power Systems Engineering, Inc.,
Houston, Texas
Assoc. Mem. ASME

B. S. Roberts
Chief Generation Engineer,
Bahamas Electricity Corporation,
Nassau, Bahamas

Conversion of a Heavy-Duty Industrial Gas Turbine to Combined Cycle

This paper discusses the evaluation, design, and operation of a combined-cycle plant for Bahamas Electricity Corporation in Nassau, Bahamas. The plant was designed to provide maximum fuel efficiency, satisfactorily operate to 40 percent load, and includes provisions for heavy oil firing in the gas turbine. The system was started up July, 1982 and has been in successful operation since then.

Introduction

In the 1970s, the Bahamas Electricity Corporation's (BEC) power generation system on New Providence Island, Bahamas, consisted of simple-cycle gas turbines, a conventional oil-fired steam plant and three diesels. When fuel costs began to rise rapidly, BEC decided that improvements were necessary to increase the fuel efficiency of the system. In 1979, BEC contracted with Power Systems Engineering, Inc. to evaluate the installation of a combined-cycle system on their most efficient gas turbine. The results of this evaluation were presented to the BEC Board and approved. Power Systems was awarded the contract for Project Management, Engineering Design, Procurement, and Construction Management. The plant was subsequently designed and constructed, with initial operation beginning in July, 1982.

This paper describes the BEC system evaluation, the combined-cycle system design, and initial operation of the combined-cycle plant.

Background

Bahamas Electricity Corporation (BEC) initiated studies in 1976 with a view of determining future generating plant requirements for New Providence Island, Bahamas, for the following ten years. The study considered the forecast of demand during that period, the capacity and life of existing equipment, additional capacity as required by the demand forecast and factors determining the type of plant to be installed.

Spiralling oil prices of the mid 1970s resulted in correspondingly high and continuous increases in operating costs for BEC. Continuous monitoring of the various cost components of producing a unit of electricity made it clear that the predominant factor was fuel cost. Further, as significant cost increases were projected to continue in the 1980s, it was necessary for particular emphasis to be placed on minimizing the overall cost of fuel and thereby significantly reducing the cost of electricity production. Therefore, decisions concerning selection and commissioning of a new plant were heavily influenced by fuel cost considerations.

The installed generation equipment which was under consideration totaled 101,000 kW and was made up as follows:

	Design rating kW	Fuel	Average heat rate Btu/kWh (HHV)
Blue Hills station			
Gas turbine no. 1	14,000	no. 2	18,750
Gas turbine no. 2	14,000	no. 2	18,750
Gas turbine no. 3	13,000	no. 2	18,750
Gas turbine no. 4	14,000	no. 2	18,750
Gas turbine no. 5	20,000	no. 2	15,500
	75,000		
Clifton Pier			
Steam turbine no. 1 and 4	8000	no. 6	19,000
Steam turbine no. 2	6000	no. 6	19,000
Diesel alternator no. 2	6000	no. 6	10,500
	20,000		
Soldier Road			
Diesel alternator no. 1	3000	no. 2	10,500
Diesel alternator no. 2	3000	no. 2	10,500
	6000		

The maximum daytime load in 1978 was 60.0 MW reducing to a load of 26 MW at night.

Contributed by the Gas Turbine Division of THE AMERICAN SOCIETY OF MECHANICAL ENGINEERS for presentation at the 28th International Gas Turbine Conference and Exhibit, Phoenix, Arizona, March 27–31, 1983. Manuscript received at ASME Headquarters, December 23, 1982. Paper No. 83-GT-88.
Copies will be available until January 1984.

System Evaluation

A cost comparison was made of installed generation equipment and existing operating patterns with various combinations of additional generation equipment and projected revised operating patterns. All known generation equipment options were considered including steam turbines, diesels, gas turbines, combined cycle, solar, nuclear, and wind. Certain options were eliminated in the preliminary stages as they were obviously impractical when factors such as required unit output(s), present state of technology, delivery, availability of relevant local skilled labor and capital cost were considered.

Options selected for detailed consideration were as follows:

- Gas Turbines
- Diesels
- Steam Turbines
- Combined Cycle (Gas Turbine/Steam Turbine)

Projected costs over the life of the plant for each option were evaluated taking into consideration the impact of capital cost, repair and maintenance, fuel, and operation costs. Consideration was also given to fuel oils presently used by BEC as well as possible alternatives.

In June of 1978, a report was presented to the BEC board of Directors which contained the following statement: "The present average cost of generating one unit of electricity is 6.06 cents/kWh. The total cost of new diesels, at current prices is 4.78 cents per unit generated and of GT-5 combined cycle, 4.49 cents per unit generated. Therefore, the effect of installing new diesel plant converting GT-5 to combined cycle will be to reduce generation costs."

The report further stated that total projected generation costs (cents/kWh) in 1981-1982 for the various options compared with present costs would be as follows at 1978 prices:

	Present	1 × 7000 kW diesel	2 × 7000 kW diesel	2×7000 kW diesel plus combined cycle
Fuel	4.26	3.99	3.69	3.23
Operations	0.40	0.33	0.33	0.33
Maintenance	0.71	0.71	0.71	0.71
	5.37	5.03	4.73	4.27
Depreciation	0.44	0.44	0.51	0.66
Interest	0.25	0.21	0.28	0.37
Total Cost	6.06	5.68	5.52	5.30

As a result of the above, the Board approved the recommendation to proceed with the installation of 2 × 7000 kW diesel engines and the conversion of the most efficient gas turbine (GT-5) to a combined cycle unit. This decision subsequently led to selection of Power Systems Engineering, Inc. to carry out project management, engineering services, construction management, and start-up associated with the combined cycle project.

System Design

Heat Recovery Boiler and Steam Turbine System. The existing gas turbine (GT-5) selected for the combined cycle previously exhausted to a heat recovery boiler which supplied steam to a desalination plant. This plant has operational problems and had been idle for approximately six years. Design steam conditions on the existing boiler were 250 psig, 425°F, with a 370°F stack temperature. Reuse of this boiler for the new combined cycle system was evaluated. It was

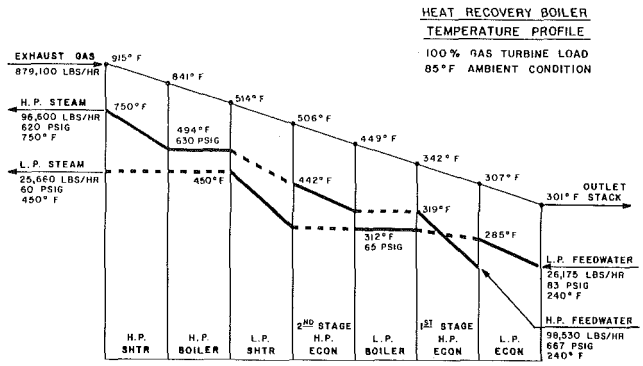

Fig. 1

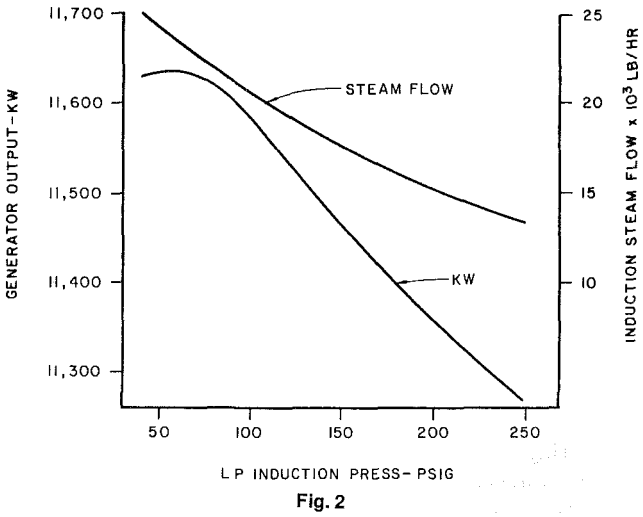

Fig. 2

determined that the cost to refurbish this boiler plus the additional operating cost due to decreased cycle efficiency, as determined by the steam pressure and temperature, would make the installation of a new boiler more cost effective.

Several boiler configurations were evaluated. To obtain the maximum utilization of the exhaust heat from the gas turbine, it was determined that the boiler stack temperature would be designed for 300°F at base load conditions. This temperature would provide the optimum system efficiency while allowing for the use of fuels containing higher sulphur which BEC may use in the future. To obtain the design stack temperature of 300°F, it was necessary to specify a two pressure level boiler. The high-pressure steam pressure and temperature were evaluated relative to the increased cycle efficiency and the additional capital cost of the equipment. The most cost effective design for the high pressure boiler was determined to be 600 psig, 750°F, producing 96,600 lb/hr of steam. This was based on a boiler design pinch point of 20°F. The boiler design temperature profile for the exhaust gas and water/steam side is shown in Fig. 1.

An evaluation was made between the low pressure boiler directly supplying the deaerator and low pressure steam being inducted into the steam turbine with deaerator steam extracted from the steam turbine at a lower pressure. To determine the low-pressure steam pressure for induction into the steam turbine, an evaluation at various pressures with constant high-pressure steam flow, pressure, temperature, and boiler pinch point was conducted. Low-pressure steam pressures over the range of 50 psi to 250 psi were evaluated to determine the most efficient level. This evaluation is shown in Fig. 2, and is based on lowering the stack temperature as low

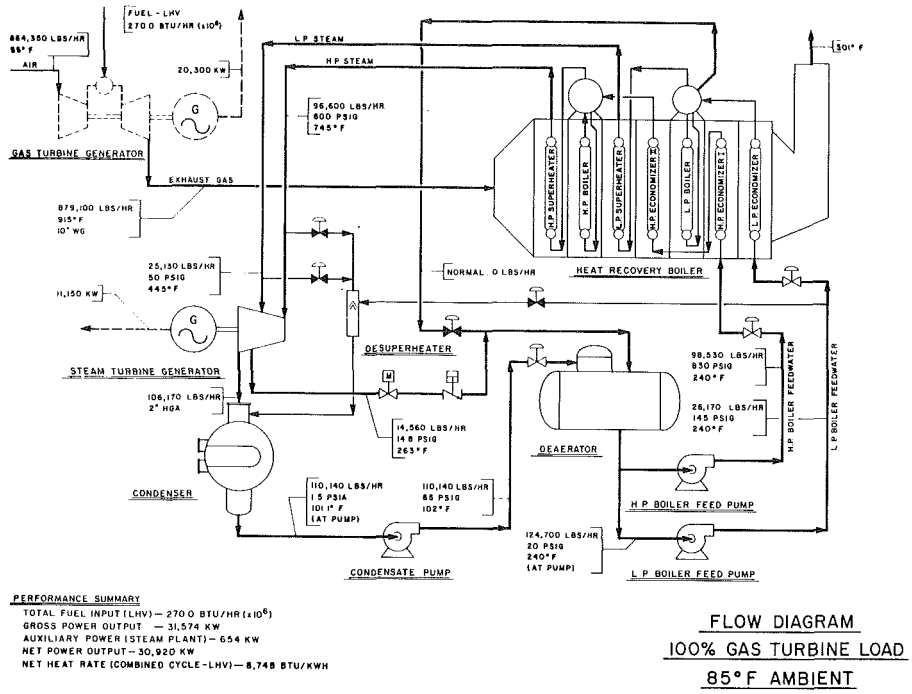

Fig. 3

as possible at any given steam pressure and calculating the corresponding kW output of the turbine at constant turbine efficiency. This curve is very flat over the range of steam pressures from approximately 60 to 80 psi. At a steam pressure of 75 psi the stack temperature is 300°F. When delivering the low-pressure steam directly to the deaerator, the stack temperature was calculated to be 325°F, with a corresponding reduction in power output of 500 kW when compared to inducting 75 psi steam. Therefore, the design with 75 psi steam inducted into the turbine was selected for the final design.

The main criteria in designing the combined cycle system was to obtain high efficiency and have a system that was capable of being base loaded during the day and operate down to 40 percent load at night. The two major restrictions on part load operation are excessive moisture in the final turbine stages and a steaming economizer. By introducing superheated low-pressure steam into the turbine, the turbine exhaust moisture content at 40 percent load was decreased. The temperature for the low-pressure steam was set at 450°F, based on obtaining as low a part load operation as possible while still utilizing the maximum available exhaust heat. The economizer tubes were vertical and connected to headers at the top which were connected to the steam drum. This allowed steam generated in the economizers at part load to be vented to the steam drum.

The boilers were designed for future firing of heavy oil in the gas turbine. The boiler tubes were specified to have four (4) fins per in. with 3/4 in. height. In addition, the boiler design incorporated sootblower lanes, and the exterior boiler piping and platforms were designed for the future addition of sootblowers and soothblower piping.

The condenser cooling water was supplied from an underground sea water system with a design temperature of 85°F. This water was reinjected into the ground as described in another section of this paper. The design turbine exhaust pressure was set at 2″ HgA. This was based on an economic analysis which considered the cost of water supply wells and the cost of wells for reinjection of the water, as well as the condenser.

The turbine was designed with a controlled induction point to admit steam from the low-pressure boiler and an uncontrolled extraction point which maintained the deaerator pressure at 15 psig at full load down to 5 psig at 40 percent load. At low loads the turbine extraction pressure will drop below 5 psi. At this point, steam will be admitted directly from the low-pressure boiler header to the deaerator for steam supply. Heaters were provided in the deaerator to allow rapid startup.

The existing gas turbine exhaust bypass stack was left in place to provide a means to conduct the initial start-up and checkout. After the initial start-up, a blank-off plate was to be inserted under this stack to eliminate any heat loss through the damper.

BEC also wanted to be able to operate the gas turbine with the steam turbine out of service. Since the exhaust bypass stack would not be used in normal operation, a steam bypass system and desuperheater were installed on both low-pressure and high-pressure steam. This system bypassed steam around the steam turbine to the condenser when the steam pressure increased to a specified pressure. This allows operation of the gas turbine with the steam turbine out of service.

Makeup water for the system was to be provided from existing municipal water supply. Since the water supply in Nassau is not suitable as boiler feedwater, a water treatment unit consisting of a single train, strong acid/strong base demineralizer was installed to provide condensate quality makeup of approximately 10 gpm with a 30 gpm maximum.

The flow diagram defining the selected system is shown in Fig. 3. The design steam turbine output is 11,150 kW with a combined cycle heat rate of 8748 Btu/kWh (LHV). Figure 4 shows this system when operating at 40 percent load with a steam turbine output of 3580 kW and a heat rate of 12,804 Btu/kWh (LHV). This system meets the design criteria of high efficiency at base load while permitting maximum turndown with a heat rate lower than all other turbines on the system. The comparison of the combined cycle heat rate to the simple cycle gas turbine heat rate is shown in Fig. 5.

Cooling Water System. An investigation wass conducted to determine whether it would pay to utilize groundwater for once-through condensing cooling as opposed to a cooling tower. Since the groundwater could be supplied to the con-

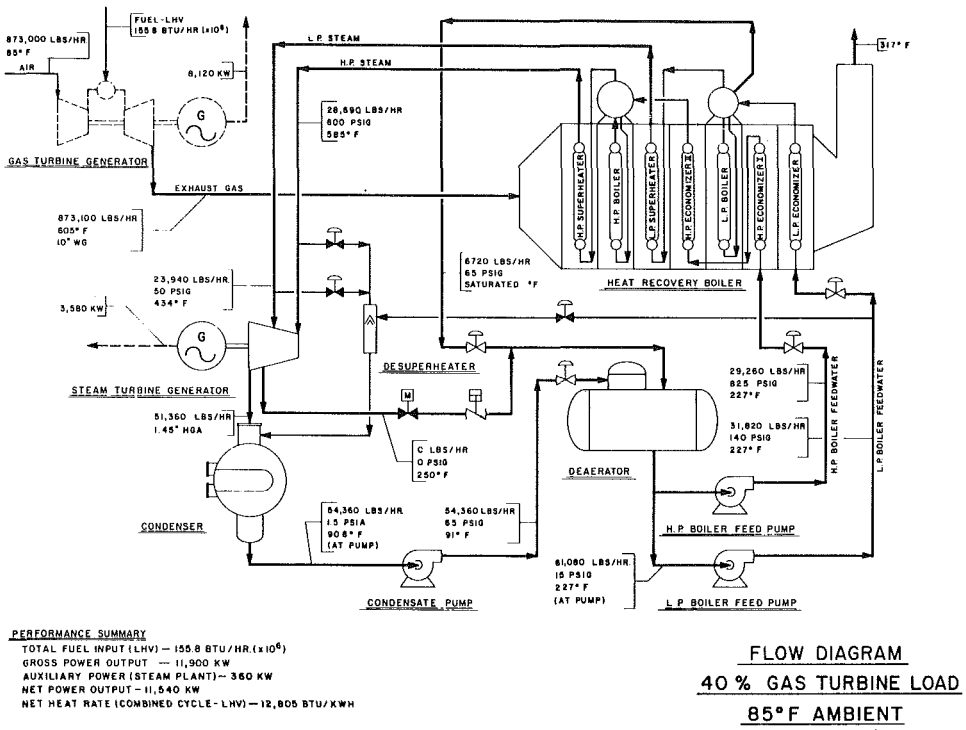

Fig. 4

denser at 85°F, it was determined that the reduction in condenser pressure would pay for the additional cost of the water well systems. Four existing water supply wells (200 ft depth), which had been used for supply of water for the old desalination plant, were available for this project. In addition, there were four existing reinjection wells available from this old system. It was determined that the existing well design criteria could not be used for design of the system and that a pumping test should be conducted on these wells. However, to conduct a full-scale test would have been too expensive. Therefore a pumping test was conducted on the wells at a low capacity and data extrapolated to determine the capability for supply of this project. One area of concern for this test was the extrapolation of the data from a test flow of 2000 gpm to a total required design flow of 13,000 gpm from all four wells, including the effect on the groundwater level drawndown. Since the original wells had been specified for a total supply of 9600 gpm, the existing data showed that the wells would be marginal for supply of this water. The pumping test data also showed that the wells may be marginal; however, this could not be determined conclusively. Due to the substantial cost for installing an additional well, it was decided that the existing wells would be utilized and if these wells could not meet the new pumping requirements, additional wells would be drilled after start-up. During operation of the old desalination plant, water was recirculating from the reinjection wells back to the supply wells. Therefore, reuse of the reinjection wells was not considered. It was decided that the new reinjection wells would be drilled as far from the supply wells as practical within the property limits of BEC. The two new reinjection wells were also specified to be double cased wells drilled to a depth of 600 ft to prevent any problems with recirculation water and also provide a method to determine if the outer casing had failed.

Since the supply wells were already in place and the casing sizes fixed, it was determined that submersible pumps could not be used in this application. Therefore, it was decided to purchase horizontal, centrifugal pumps with the best available NPSH and largest suction lift to try to eliminate any problems

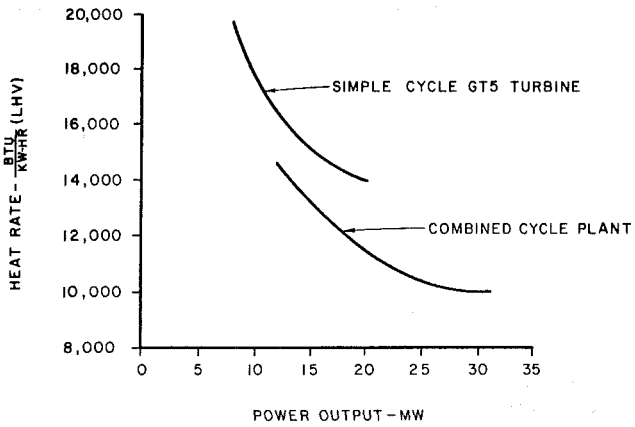

Fig. 5

from cavitation. The design NPSH of these pumps was 3.5 ft with a design suction lift of 25 ft.

Plant Layout

The plant layout is shown in Fig. 6. This layout provides access for maintenance to all critical areas. Maintenance of the turbine generator can be performed from one side by using mobile cranes. The turbine auxiliary equipment is located at the end of the turbine area and is also accessible from the side and the end. The high-pressure and low-pressure boiler feed pumps are located under the deaerator and are accessible from the turbine maintenance area or the area between the boiler and turbine. The area between the boiler and turbine are sized to allow truck or small mobile crane access. Walkways were provided for access to all critical areas on the boiler with interconnecting walkways between the boiler, deaerator, and both turbine maintenance areas. The water treatment area is located at the back of the control building with all equipment readily accessible. The condensate storage tanks and transfer pumps are accessible to tank

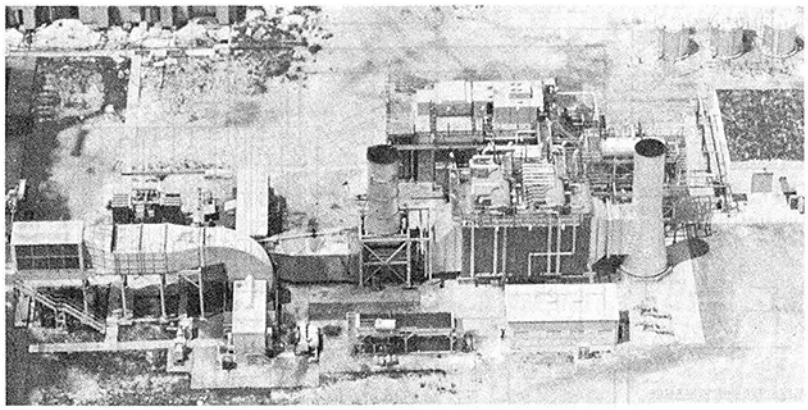

Fig. 6 Plant layout

trucks. If the water supply is interrupted at this plant, condensate can be trucked in from another location.

The control building was located to allow the operator to view the main equipment area. The control building contains a battery room, water analysis lab, storage room, and control room which contains the motor control center and main control panel. The control panel is located adjacent to the windows so that the operator can view the main equipment areas while operating the equipment.

System Reliability

A critical design requirement for this system was reliability. The boiler feed pumps, condensate pumps, and makeup water pumps all have 100 percent standby capacity. The standby pumps automatically start upon loss of the normal operating pump. The main cooling water pumps do not have spare capacity because of the excessive cost of an additional well. However, the plant can operate at reduced load with one of these pumps out of service. A complete spare cooling water pump was purchased to allow fast replacement of these pumps. Spare pump rotors and other critical spare parts for other pumps and equipment were purchased to allow quick repair of all components.

The auxiliary power supply for this plant is a dual feed from the existing 11 kV auxiliary system and the gas turbine bus. The motor control centers incorporate the buses with the normal operating pump motors connected to one bus and the alternate pump motors connected to the other. Both of these buses can be fed from either auxiliary power supply and will be automatically transferred on loss of power.

System Operation

The plant was designed to be operated with one operator in the control room and one roving operator. The controls are located on a central control board located in the control room. Water quality is continuously monitored in a room adjacent to the control room. The control system is an electronic analog system designed to provide ease of operation. The control systems are automatic and can be controlled and monitored from the control room. The generator can be synchronized from this control room or from the main control room which is central to the plant. Critical parameters are also monitored and annunciated in the main control room. Synchronization will normally take place in the main control room.

Results and Operating Experience

The plant began producing power in July 1982, and has operated satisfactorily since this time. It was commissioned on September 17, 1982, with the stack temperature measured at 291°F at design ambient temperature. Based on an annual availability of 90 percent, the payout period for this project is approximately 24 months.

The water wells have operated satisfactorily and no pump cavitation has been noted. The bypass stack was used for initial start-up of the system and has since been blanked off to eliminate leakage. The system has been operated at part load down to 16 MW without difficulty. All control systems are operating as designed including continuous operation of the gas turbine when the steam turbine is tripped. The combined cycle steam system design described in this paper has demonstrated high efficiency and the capability of operating satisfactorily over a wide range of conditions.

Power Systems Engineering operated the plant for two months until BEC operators were trained. A preventive maintenance training program and operator training for this system continued for the first six months of operation.

H. I. H. Saravanamuttoo
Chairman,
Department of Mechanical and
Aeronautical Engineering,
Carleton University,
Ottawa, Canada
Director,
GasTOPS Ltd.,
Ottawa, Canada
Mem. ASME

B. D. MacIsaac
President,
GasTOPS Ltd.,
Ottawa, Canada
Assoc. Mem. ASME

Thermodynamic Models for Pipeline Gas Turbine Diagnostics

Thermodynamic models suitable for use as diagnostic tools for pipeline gas turbines have been developed. A basic requirement was the prediction of the performance of gas turbines subject to in-service deterioration, including effects such as compressor fouling, foreign object damage, and turbine damage. This was met by creating thermodynamic models capable of operation over the complete running range expected, with a provision for introducing arbitrarily controlled degradations. Models for a variety of types of gas turbines currently in pipeline use have been tested, demonstrating good agreement with user experience. The models are extremely flexible in use and may be used either for investigation of specific problems or to increase user understanding of operating problems.

Introduction

The American Gas Association contracted with GasTOPS Ltd., Ottawa, Canada, to develop thermodynamic models of gas turbines for application to gas pipeline operations. The incentive of the program was to develop a better understanding of gas turbine behavior by pipeline users, a prime requirement being the ability to predict engine health from field measurements. A knowledge of engine condition is important both for assessment of operating *efficiency* and diagnosis of engine *deterioration*, and early prediction of in-service deterioration can result in significant savings in both fuel and overhaul costs. In the event of deterioration taking place, it is important to be able to diagnose the cause, permitting appropriate maintenance action to be taken; this could range from routine servicing to complete removal and overhaul. Thermodynamic models were perceived as a method of permitting in-depth study of the behavior of gas turbines, both in good condition and as a result of specified defects.

Literature Survey

Engine manufacturers normally provide users with performance specifications for a nominal engine; information provided would usually include the variation of power output and thermal efficiency (or heat rate) with ambient conditions, along with suitable limiting values for safe operation or long life. This information is essential to the user, to ensure that the gas turbine is capable of meeting the anticipated power requirements. In the event of engine deterioration, however, the information provided is of minimal help and the operator has no capability of identifying the cause of the problem; the severity of the problem could range from atmospheric fouling of the compressor, which can be corrected by compressor cleaning, to severe mechanical damage requiring complete overhaul of the unit. Before the user can make informed decisions, it is necessary that he be able to predict the performance of the gas turbine over its expected running range. Performance prediction methods are described in [1] and will be discussed later.

Once the operator understands the methods required to predict the performance of *healthy* engines, thought must be given to the changes in performance resulting from engine deterioration. Engine Health Monitoring (EHM) is a term applied to the many methods used for surveillance of a power plant; methods include vibration monitoring, oil analysis (e.g., SOAP or ferrography), visual inspection, and performance monitoring. The very nature of pipeline operations, with engines running for extremely long hours at fairly high power settings, offers more scope for performance analysis than almost any other application. With the massive increase in value of gas being pumped around North America and the large quantities of power consumed, it is clear that a small percentage saving in fuel used is a very large sum of money.

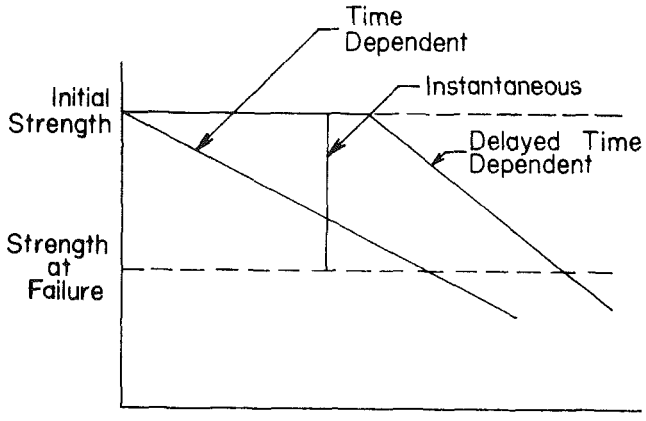

Fig. 1 Types of failure

Contributed by the Gas Turbine Division of THE AMERICAN SOCIETY OF MECHANICAL ENGINEERS for presentation at the 28th International Gas Turbine Conference and Exhibit, Phoenix, Arizona, March 27-31, 1983. Manuscript received at ASME Headquarters January 12, 1983. Paper No. 83-GT-235.

Reid [2] showed that for a typical 9000-kw gas turbine fuel costs averaged about 160 dollars per hour and maintenance costs 7–10 dollars per hour (1977 data, Canadian dollars).

An excellent treatise on the principles involved in machinery monitoring has been published by Davies [3], who notes that there are essentially *three* types of failures common to all machines: time-dependent, delayed time-dependent and instantaneous (these are shown in Fig. 1).

The *instantaneous* failures, typical of fatigue failure of compressor blades, give no warning. No amount of monitoring, at any expense, will detect the onset of these types of failures. This is a fact that is often lost on the designers of EHM systems.

The *delayed time-dependent* failures are those for which there is no detectable change until some point in the life of the machine after which a deterioration is observable. This kind of failure allows some time for corrective action but depends very much on the ability to observe the point at which degradation first begins. It is clearly a candidate for EHM but, because nothing is observable for a long (and undetermined) time, it will require a very sophisticated system to identify it as real.

The pure *time-dependent* type of failure is also a candidate for EHM. For known components with a well defined rate of degradation, a very simple EHM system is sufficient. For gas turbines, the rates of degradation are seldom known and are not likely to be linear. Examples are known where, in pipeline operation, deterioration has been very slight; Avon engines have shown an increase in heat rate of 1 percent per 10,000 hrs, which is clearly not detectable with normal field instrumentation.

Performance Monitoring defines the subset of EHM procedures which is concerned with the thermodynamic behavior of the engine and its ability to produde a specified power for a given fuel input. There is clearly a strong coupling between the thermodynamic behavior of the engine and its mechanical health, and if accurate estimates of its thermodynamic state can be made on a continuous basis, it can be used to anticipate and prevent further and more costly mechanical damage. Three possible methods of using performance analysis are:

(*i*) Trend analysis
(*ii*) Trend analysis with baselines
(*iii*) Gas path analysis

At its simplest level, trend monitoring merely allows the operator to keep track of the directly observed readings, whereas *Gas Path Analysis* uses the instrument readings to deduce other more critical cycle parameters that cannot normally be measured in the field (e.g., turbine inlet temperature and air flow). One of the basic problems with simple trend monitoring is that if different power settings are used from day to day there can be considerable scatter in the data even for a perfectly healthy engine. The majority of trend monitoring performed today uses baseline data in order to more easily determine when engine performance is deviating from the norm; it is usually convenient to plot the differences between the *measurements* and the baseline data as a function time. Data produced by this method tends to be "jagged," and it is *not* easy to pick up trends automatically without a considerable amount of data "smoothing," although manually plotted trends may be identifiable. An example of the use of this method is given in [4], where data obtained from a hovercraft using manual data gathering and existing instrumentation was successfully analyzed making use of a programmable calculator. The application of programmable calculators for Gas Path Analysis was discussed in [5], where an extremely simple system for deducing airflow and turbine inlet temperature was presented.

It is often felt that manual data recording is not adequate for performance monitoring, but this is frequently because of lack of planning of log sheets, poor instrumentation readouts, and perhaps most important of all, lack of motivation by the operator. It is disheartening for an operator to take a large number of readings with great diligence, only to find them ignored at head office. The final result is often that when results are eventually looked at much later, many errors and omissions are encountered. This problem was addressed by the present authors [6] with the development of an analysis package for in-field verification of engine data. The basic method was to use a mathematical model to check readings for consistency with known baseline data; both engine and instrumentation problems could be detected. The computational requirements were met using a computer already available for station control purposes.

Some notable work in the area of performance monitoring and EHM has been carried out by TransCanada PipeLines. The work of Reid [2] was referenced earlier, and he suggested that a 3 percent drop in efficiency was enough to justify an engine overhaul regardless of its mechanical health. This figure was arrived at by noting that fuel costs were of the order of 20 times maintenance costs per fired hour. Regular use of performance testing and analysis has become an integral part of TCPL operations and Scott [7] published a review of accomplishments in applying these techniques, including resizing of power turbine nozzles, calibration of exhaust gas temperature, and attending to regenerator leakage problems. Another useful technique, also described by Scott [8], was the use of the *change* in compressor airflows, giving an extremely simple but effective means of indicating compressor fouling. In a recent paper, Williams [9] has described the use of simple mathematical models used to test for consistency with engine measurements, where individual defects can be entered into simple cycle calculations until agreement with engine results is achieved. TransCanada PipeLines is one of the few major users who have openly published their work in performance monitoring. It should be noted that all of these successful programs were based on manual data gathering, an extremely significant factor in keeping the system cost and risk low, representing a very necessary first step in gaining acceptance of the system.

The recent decline in the cost of computing suggests that it would be technically feasible to *collect* the data automatically, the next logical step being to *interpret* it automatically. Probably the earliest published work in this area came from the US Army AIDAPS (Automatic Inspection Diagnostic and Prognostic System) program, conceived for use with military helicopters [10]. Hamilton Standard developed techniques for this program which were eventually marketed for industrial gas turbines. This system, called TRENDS, is essentially a computerized process which accepts readings from as many sensors as possible, which are automatically and continuously recorded and compared with baselines and limits [11]. If a limit is exceeded, a diagnostic message is printed, possibly with a prognosis and suggested maintenance action. This system has had only limited market penetration, but has been installed on a large oil pipeline in the Middle East where it is intended to gather data from a large number of gas turbines [12].

It is noteworthy that large amounts of money and engineering effort have been expended by some very large aircraft and military users, but industry acceptance is still not widespread and many users remain sceptical regarding the claims made for very sophisticated systems. Morever, the requirements for pipeline usage are totally different to those of airlines, air forces or navies: differences arise because of different usage of engines, operational requirements, and perhaps most important of all, the skills and training levels of

available manpower. The success of TransCanada PipeLines is very impressive and appears to have resulted from a clear understanding of the *engineering* requirements followed by careful experimentation, including the use of calibrated instrumentation when required; clearly demonstrated economic gains were obtained without large scale expenditure on hardware or automated systems.

Development of Thermodynamic Models

Successful applications of EHM in pipeline operations are dependent on a clear understanding of the *engineering* problems involved, and these are centered on the machinery installation; thus, a prerequisite for an effective system is a detailed understanding of gas turbine behavior. Once the primary base of knowledge has been established the next requirement is to predict the effects of engine deterioration; this is important both from the viewpoint of operating efficiency and also continued safe operation of the engine. Experienced operators will know the most common problems occurring in the field, but may not know the effects of less frequent mechanical problems. Williams [9] listed the most common problems encountered, in order of frequency, as follows:

(*i*) Compressor efficiency
(*ii*) Compressor mass flow
(*iii*) Leakage (overboard)
(*iv*) Leakage (internal)
(*v*) HP turbine efficiency
(*vi*) LP turbine efficiency
(*vii*) HP turbine flow function
(*viii*) LP turbine flow function

It would appear, then, that the most common problems are related to compressor fouling, seal problems, and turbine damage.

In the past, attempts have been made to implant mechanically damaged components in gas turbines to measure the resulting deterioration without notable success. This is clearly an extremely expensive method, and it is not possible to implant severely damaged components because of the likelihood of causing further more serious damage; in any case, changes in performance may result merely from stripping and rebuilding an engine with the same parts. The only feasible method of systematically investigating engine deterioration is by the use of *mathematical models*, based on established thermodynamic techniques. The models, of course, must be validated against available field data to be credible to the users.

While Trend Analysis is a useful and essential technique, it is somewhat limited in its capability; while engine deterioration may be detected, the cause of the problem is probably not identifiable. The judicious use of Gas Path Analysis, however, can help in focussing attention of the likely causes of the problem. Thus, Trend Analysis and Gas Path Analysis should be regarded as complementary rather than competing systems; one possible pipeline approach is for Trend Analysis to be used in the field by operators and Gas Path Analysis to be used by engineering staff based in a central location.

The success of any EHM system will be strongly dependent on the level of acceptance of users at all levels, and operators must be clearly aware of both the advantages and limitations of any system. It will take some time for operators to become confident of the system, and it is especially important that false warnings of trouble be kept to an absolute minimum. Use of an overly complex system may result in a series of both hardware and software problems with the maintenance system itself, which may obscure problems occurring in the machinery system. It is also important that instrumentation

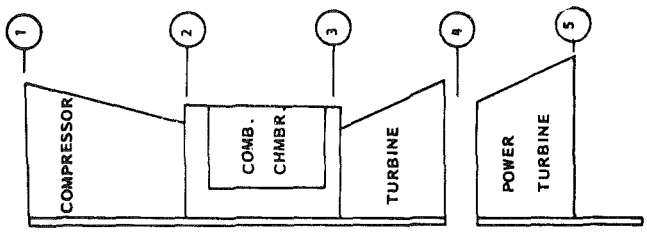

Fig. 2 Free turbine engine

problems should not be interpreted as engine problems, and instrumentation failure or deterioration should be detectable by the EHM system.

Development of a system suitable for pipeline operations is clearly not a "black box" type of problem and should be firmly based on an understanding of the *machinery system* to be monitored and an appreciation of the operating problems at compressor stations.

Instrumentation Considerations. The level of instrumentation required is dependent on the type of performance analysis to be carried out, and the EHM system should be regarded as a tool which improves the operator's ability to interpret the information obtained from the instruments. The primary purpose of monitoring the equipment is to maintain surveillance over its condition; the motivation is a mixture of safety, availability, and performance, with increases in fuel cost making performance monitoring more important than it has been in the past.

In accordance with the need for user acceptance, it is clear that, as far as possible, *existing* instrumentation should continue to be used; any system that purposes major additions to the sensor complement is extremely unlikely to receive serious consideration. Any suggestions for extra instrumentation must be fully justified to the user and may only be considered for new applications without being retrofitted to existing installations. Thermodynamic models of differing levels of complexity may be considered, depending on the anticipated use (e.g., by the user in the field or by engineering staff at a central base). Three possibilities should be considered.

(*i*) Simple models for early warning of engine degradation. This would require the minimum in sensor control.

(*ii*) Detailed models used in conjunction with an engine performance test; it is anticipated that additional sensors would be fitted for such a test.

(*iii*) Automatic or semiautomatic systems using telemetered data, online analysis, and trending of data. This could only be justified in unmanned stations or more complex stations where computer control is already in use.

Gas path analysis may be effective with a very small increase in sensor requirements, but an automated system would require a substantial increase. Until the simpler systems have won user acceptance, there is little point in considering complex systems.

While these thermodynamic models may be used in conjunction with field data to *identify* engine health, they cannot be used to *predict* the effect of component models; while models of this complexity may not be directly used by pipeline operators, they can play a useful and cost effective role in the development of data driven models intended to analyze field measurements.

Detailed Component Models

Rationale. The use of detailed mathematical models is the only feasible method of systematically investigating the effects of various levels of degradation of individual com-

ponents, e.g., compressor fouling, foreign object damage, or turbine mechanical damage. Models of this type offer the advantage of great flexibility, being able to cover the entire operating range of the engine, and they can be used to investigate problems which had not been considered at the start of the investigation. They can also predict the values which should be seen by the instrumentation and can be used to check the validity of the instrumentation on particular installations. Perhaps the most important feature is the capability of *controlled* fault implementation, where component flow and efficiency characteristics may be modified to represent differing levels of degradation. This in turn, can lead to the development of *fault matrices* which show the expected changes in measured parameters for a specified fault. Some engine manufacturers provide the user with "small change" data, showing such effects as a 1 percent drop in turbine efficiency; data of this sort is produced from detailed component models which will now be discussed.

Structure. Any gas turbine is a collection of discrete components, each of which may be fully described in thermodynamic terms. The single-spool, free-turbine engine (Fig. 2) is the most useful to consider when explaining the methods required for prediction of engine performance. Typical requirements might be the prediction of performance between low power and maximum power ratings for standard inlet conditions, or the variation of maximum power with ambient temperature. The eventual goal is to predict the effects of mechanical degradation on output, efficiency, and limiting temperatures.

Performance prediction methods depend on the application of physical laws to relate the flow rates and pressure ratios in each component; to achieve steady-state operation of the gas turbine, it is necessary to maintain a balance of *flow* between each of the major components and a balance of *power* between the compressor and its driving turbine, and also between the power turbine and the load.

Since the flow through each of the major components is generally described by a set of empirically derived maps which, in turn, are expressed in nondimensional form, it has been found convenient to define the equations describing the steady-state behavior of the gas turbine in nondimensional form. For example, if bleed and fuel flows are neglected, a balance of *flow* between the compressor and the gas generator turbine would require that

$$W_3 = W_1$$

where W_1 = compressor flow

W_3 = turbine flow

In nondimensional form, this equation becomes

$$\frac{W_3\sqrt{T_3}}{P_3} = \frac{W_1\sqrt{T_1}}{P_1} \cdot \frac{P_1}{P_2} \cdot \frac{P_2}{P_3} \cdot \sqrt{\frac{T_3}{T_1}} \tag{1}$$

where

$\frac{W_3\sqrt{T_3}}{P_3}$ = turbine nondimensional flow

$\frac{W_1\sqrt{T_1}}{P_1}$ = compressor nondimensional flow

P_2/P_1 = compressor pressure ratio

P_3/P_2 = combustor pressure ratio

T_3/T_1 = nondimensional turbine temperature ratio

For compatibility of *work* between the compressor and its driving turbine

$$W_1 C_{pc} \Delta T_{12} = W_3 C_{pt} \Delta T_{34} \eta_m$$

Hence

$$\Delta T_{12} = \Delta T_{34} \frac{W_3}{W_1} \frac{C_{pt}\eta_m}{C_{pc}}$$

In nondimensional form, since $W_3 = W_1$

$$\frac{\Delta T_{12}}{T_1} = \frac{\Delta T_{34}}{T_3} \cdot \frac{T_3}{T_1} \cdot \frac{C_{pt}\eta_m}{C_{pc}} \tag{2}$$

Thus, two equations, (1) and (2), for T_3/T_1 are obtained and the engine operating point which satisfies both must be found by trial and error, using data obtained from the highly nonlinear component characteristics. The procedure by which this is done is often referred to as *component matching*.

For the free power turbine example of Fig. 2, flow compatibility with the power turbine and the gas generator must also be established. By writing the governing equations in a form similar to equation (1) and (2) above, it is possible to set up relatively simple procedures for solving them, and the calculations can readily be carried out on a digital computer of relatively modest capacity.

Estimation of Component Characteristics. The major problem facing the user intent on the development of component-based models is the lack of availability of component data. This is primarily due to the fact that data, such as compressor and turbine characteristics are highly proprietary to each individual manufacturer. This sort of data would only be obtained at the early stages of an engine development program, and for some engines currently in service the compressor development work may go back to the early 1950s; thus even if the data were no longer considered particularly sensitive, it may be difficult to locate. From time to time, however, component characteristics may be published in the open literature.

It has been found possible to obtain quite adequate estimates of both compressor and turbine characteristics by relative scaling of component maps, and methods developed by the authors have been validated for several specific engines.

Every major component of a gas turbine is designed to meet a performance specification at the nominal design point of the engine. All other data for that component can be presented relative to the design condition as follows:

(suffices D and R refer to "design" and "relative" values)

$$Q_R = \frac{W\sqrt{T}}{P} \Big/ \left(\frac{W\sqrt{T}}{P}\right)_D$$

$$N_R = \frac{N}{\sqrt{T}} \Big/ \left(\frac{N}{\sqrt{T}}\right)_D$$

$$PR_R = (PR - 1)/(PR_D - 1)$$

$$TR_R = (TR^{\epsilon} - 1)/(TR_D^{\epsilon} - 1)$$

$$\epsilon = \gamma/\gamma - 1$$

Where PR is the pressure ratio and TR is the temperature ratio, related to the pressure ratio by the isentropic efficiency of the component. The four parameters are sufficient for complete definition of the component performance.

If the data describing components of a given class of design are plotted in the relative form described below, there is very considerable similarity between different units. In the case of turbines, these data collapse quite well, with the major variable being the value of the choking pressure ratio, which is a function of the number of stages; indeed, in the absence of *any* turbine data, reasonable results could be obtained by using the theoretical flow relationships for a convergent nozzle. The compressor data are somewhat more complicated in that the shape of the speed lines change as the flow through

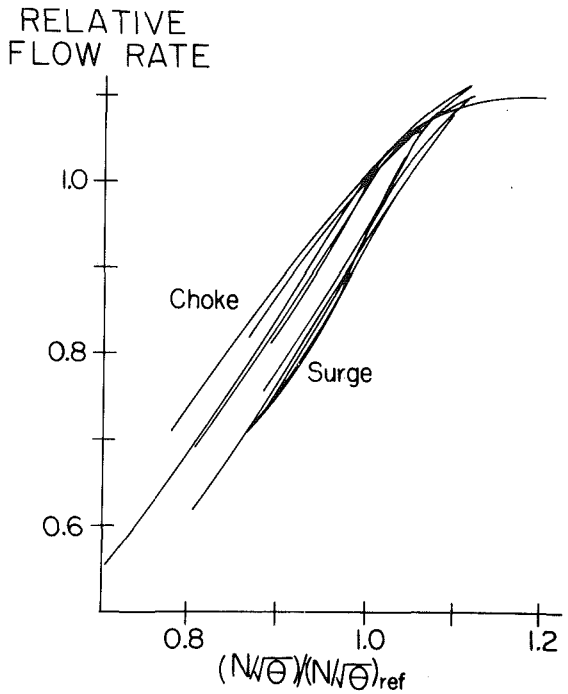

Fig. 3 Variation in relative flow range

the unit increases. It has been found that if the change of relative flow and pressure ratio from surge to choke is plotted as a function of relative speed, these data collapse well enough to use an average curve for each. An example of the variation in relative flow range for five axial compressors is shown in Fig. 3.

These compressors covered a significant range of engine sizes and pressure ratios, and it is particularly notable how the surge values of flow rate collapse when presented in this form. A similar plot can be formed for relative pressure ratio and relative temperature ratio (i.e., efficiency) thus giving two points on each speed line. These points, together with typical average shapes, are sufficient to build up a generalized compressor map for each class of compressor considered. A generalized map for multistage axial compressors is shown in Fig. 4.

For purposes of the current work, the reader is reminded that the absolute accuracy of the engine model is of no great consequence; as long as the major performance effects are represented accurately, the model can be used as a useful validation tool over the entire running range. It must, therefore, be a *believable* representation of an engine of its class but it need not model any specific engine. If a user had a particular interest in a specific engine, however, he could quite readily carry out modifications to the estimated component data until a good match with known engine operating parameters was obtained. Models were developed for the following classes of engine:

(*i*) Single-shaft, simple cycle
(*ii*) Two-shaft, simple cycle
(*iii*) Two-shaft, regenerative cycle
(*iv*) Three-shaft, simple cycle

The models showed good agreement at the approximate engine design points, and based on a more detailed comparison of off-design performance of other shaft power engines previously modeled, it is confidently expected that the prediction of off-design performance will be quite good. They will certainly be adequate for the purpose of validating EHM models.

Typical Results. Having estimated compressor and turbine

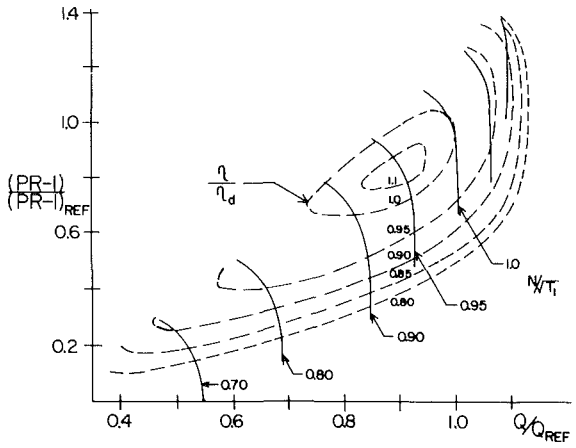

Fig. 4 Generalized compressor characteristic

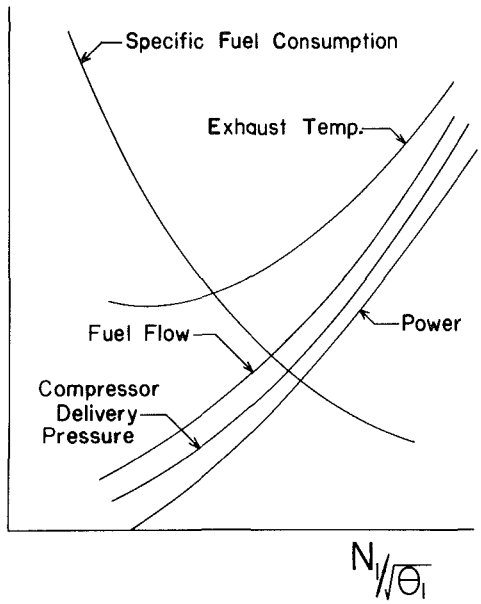

Fig. 5 Performance variation

characteristics for the appropriate engine design point, the computer model can be used to generate the baseline performance for a "nominal" or healthy engine. Results are most usefully plotted as functions of compressor nondimensional speed as shown in Fig. 5. The rapid variation of both power and turbine inlet temperature with rotational speed should be noted, remembering that the combination of centrifugal stress and blade temperature will determine the creep life of the turbine.

To generate data for an engine subject to in-service deterioration, it is necessary to modify the component data, changing flow rates and efficiency, or modify the internal bleed flows to simulate problems such as excessive seal leakage or regenerator leakage. From very limited data available from one major pipeline operator, compressor fouling effects were simulated by a simultaneous reduction of 7 percent in flow and 2 percent in compressor efficiency; this was implemented on the compressor characteristic by multiplying all flow rates by 0.93 and all efficiencies by 0.98. In the case of the turbine, the flow rate is primarily determined by the nozzle areas and the effect of mechanical damage to the rotor was simulated by a reduction in turbine efficiency with no change in nondimensional flow. Turbine flow areas, and hence, the flow function $M\sqrt{T}/P$, may be affected by erosion, corrosion, or bowing due to excessive

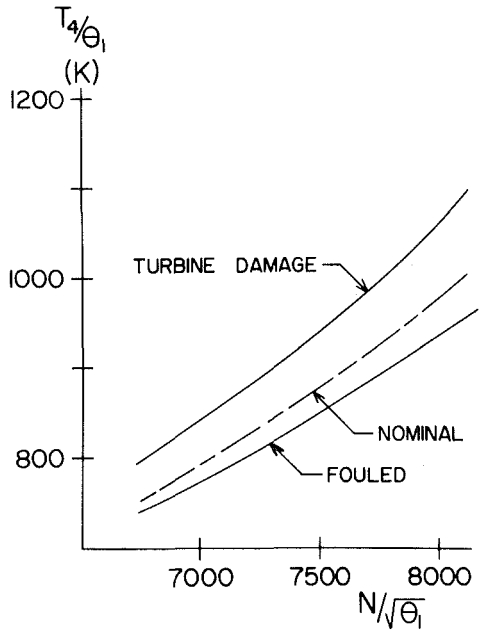

Fig. 6 Effect of deterioration on T_4

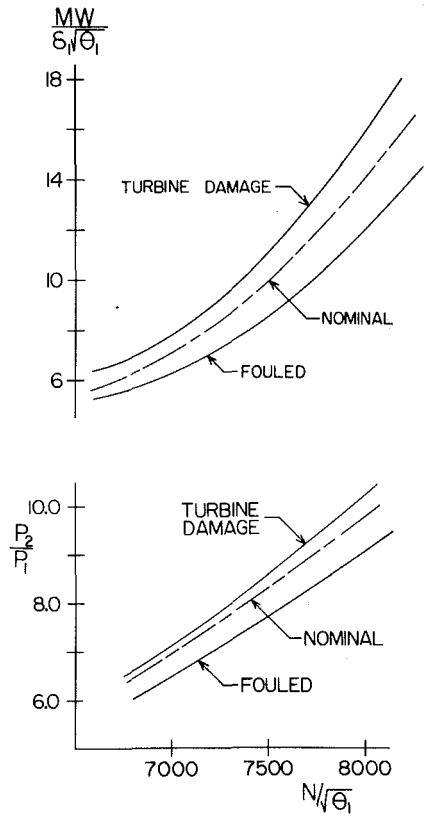

Fig. 7 Effect of deterioration on CPR and power

temperatures. Each of these faults could be introduced in a controlled manner to permit in-depth study of the expected behavior of a deteriorated engine. In addition to engine faults, sensor faults could also be introduced, with both bias and random measurement errors included; this permitted the study of a healthy engine subjected to erroneous instrumentation.

Two-Shaft, Simple Cycle. The basic performance of this engine type, one of the most widely used configurations in pipeline operation, can readily be understood by considering the behavior of a simple jet engine; the aero-derivative gas

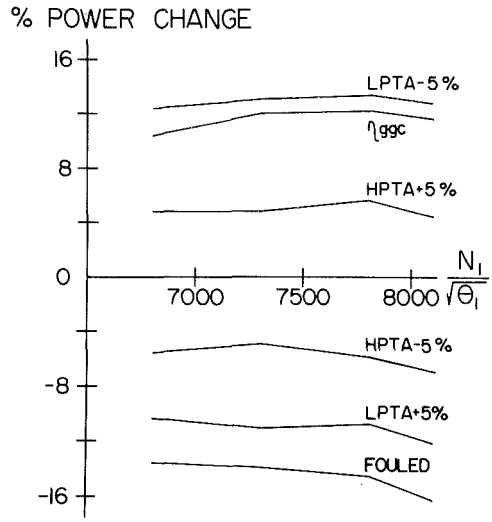

Fig. 8 Effect of different faults

turbine owes its existence to the fact that the flow characteristics of a propelling nozzle and power turbine are almost identical. Setting the fuel flow determines the speed of the gas generator rotor, which in turn fixes the flow, pressure, and temperature at entry to the power turbine; these then determine all other parameters, such as power, turbine temperatures, and fuel flow as shown in Fig. 5.

A hypothetical engine with performance similar to the widely used Rolls Royce Avon was modelled. The nominal value of compressor speed was taken to be 7500 rpm at standard conditions (1.013 bar and 288K) and performance calculations were carried out over a range of $N/\sqrt{\theta_1}$, from 6800–8100 rpm.

Figures 6–7 show the variation of power turbine inlet temperature (T_4), compressor pressure ratio (P_2/P_1), and power (MW) as functions of gas generator speed ($N/\sqrt{\theta_1}$). Turbine mechanical damage was simulated by scaling isentropic efficiency by 0.98. At first glance, it appears contradictory that turbine damage causes power to *increase* at a specified value of speed; this, however, is entirely due to the fact that the damaged turbine has to operate at a higher temperature to maintain the specified speed. In practice control limits would result in a decrease in T_4, P_2/P_1, and power, this being primarily due to the reduction in compressor flow allowing the compressor to operate at a lower pressure ratio while operating against a fixed turbine resistance. It should be noted, however, that if the decrease in compressor efficiency were substantially larger than specified, T_4 could increase.

It is instructive to consider the effects of various faults on power output over a reasonable range of speeds. Figure 8 shows six different simulated faults, and it can be seen that the percentage changes are fairly constant with speed; the three effects showing increases in power are due to operation at excessive turbine temperatures, and could occur provided the temperature remained within allowable limits. It can be seen that the largest nozzle area changes on the power turbine are much more significant than changes in the gas generator turbine.

Little field data were available for checking the model, but an interesting comparison of predicted effects of compressor fouling was made against data provided by a pipeline operating Avon engines. The difference between compressor delivery pressure and decrease in flow for a number of engines is shown in Fig. 9, which shows a considerable amount of scatter but a definitely observable trend. Two levels of compressor fouling, 7 percent on flow, 2 percent on efficiency and 3 percent on flow, 1 percent on efficiency, were modeled

as shown in Fig. 10; the estimated loss in compressor delivery pressure from field tests for 3 percent decrease in flow shows excellent agreement with the model results for mild fouling.

It is known that excessive seal leakage can lead to a major loss in power. If seal leakage from compressor delivery is returned before the power turbine nozzles, the effect of an increase in leakage is twofold; first, the turbine must operate at a higher temperature to maintain compressor speed, and second, the injection of a considerable flow into the turbine nozzles causes an increased blockage effect (similar to reducing throat area), pushing the turbine to a still higher temperature. This effect was modeled, as shown in Fig. 11. For the nominal engine, the seal leakage was assumed to be 2 percent, giving 9.25 MW at a power turbine inlet temperature of 820K at the design speed of 7500 rpm. The power curve for 8 percent seal leakage appears to be markedly higher. The effect of maintaining a limit on T_4, however, must be considered. If the value of T_4 is maintained at 820 K, it can be seen that the speed must be reduced to 7050 rpm, with a resulting loss of power of about 20 percent. These results were found to be in good agreement with the experience of operators.

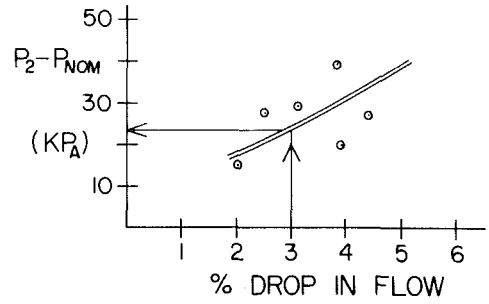

Fig. 9 Effect of fouling (experimental)

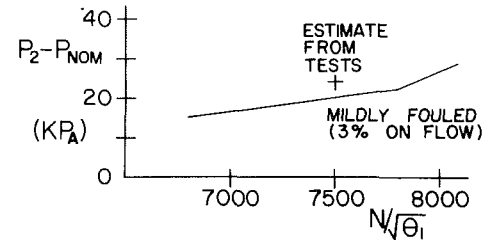

Fig. 10 Effect of fouling (simulation)

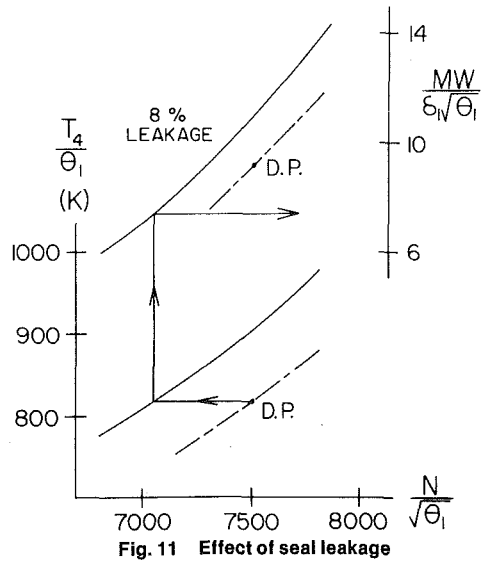

Fig. 11 Effect of seal leakage

The modeling technique was used to evaluate fault matrices, concentrating on the more probable faults. Turbine distress, for example, is much more likely in the higher temperature environment of the gas generator turbine than in the power turbine; in any case, a reduction in power turbine efficiency would simply result in a loss of power with no other parameters changed.

Fault matrices require that one parameter be considered as the independent variable; possible choices include $N/\sqrt{\theta_1}$, EPR, $MW/\delta_1\sqrt{\theta_1}$, and fuel flow. As a result of the performance investigations, speed, and power looked the most promising. The fault matrix based on *constant speed* is considered first.

	T_4	P_2/P_1	SHP	W_f	EPR
Fouled compressor	↓	↓	↓	↓	↓
Excess leakage	↑	≐	↑	↑	↑
$\eta_{\text{gas gen turbine}}$	↑	↑	↑	↑	↑
A_{LPT} (increase)	↓	↓	↓	↓	↓

It can be seen that based purely on *qualitative* considerations the effects of a fouled compressor appear the same as an increase in power turbine area; the *quantitative* variations will not be the same, but it is difficult to give general guidelines on this to an operator. The most useful primary parameters to observe are T_4 and P_2/P_1 (or P_2).

The fault matrix using *power* as the independent variable, however, permits further deductions to be made.

	T_4	P_2/P_1	$N/\sqrt{\theta_1}$	W_f	EPR
Fouled compressor	≐	≐	↑	≐	≐
Excess leakage	↑	↓	↓	≐	≐
$\eta_{\text{gas gen turbine}}$	↑	↓	↓	↑	≐
A_{LPT} (increase)	↓	↑	↑	≐	≐

The differing effects of compressor fouling and turbine throat area changes are clearly seen. Fuel flow only varies significantly for a damaged gas generator turbine.

Thus, the use of *two* fault matrices greatly enhances the diagnostic capability. For the operator in the field, speed is the more useful independent variable, being readily displayed and measured. Power, which is probably not directly available without calculations on the gas compressor, is more likely to be useful to engineering staff as an additional source of information.

Two-Shaft, Regenerative Cycle. The foregoing methods could be applied to a *fixed geometry* regenerative cycle, but many of the regenerative engines in pipeline operation make use of a variable geometry power turbine, with the throat area and swallowing capacity varied by rotating the power turbine nozzles. Analysis of GE Frame 3 units in U.S. pipeline service showed that approximately 80 percent were of the variable geometry regenerative type. With this type of application, the power turbine inlet temperature is held approximately constant as load is decreased, to improve heat rate. This mode of operation means that T_4 is no longer a useful measure for investigating engine faults.

Regenerator faults may appear as leakage, increased pressure loss or decreased effectiveness; leakage is by far the most important effect. For a hypothetical engine similar to a GE Frame 3, for example, it was found that doubling the regenerator pressure losses caused a drop of only 5 percent in power at design speed, whereas 10 percent regenerator leakage

caused 27 percent reduction in power; changes in heat transfer effectiveness only appear as small changes in fuel flow and heat rate.

As for the simple cycle gas turbine, it appears that two fault matrices should be used, as shown below:

Constant speed

	SHP	W_f	P_2/P_1	Heat rate	
Fouling	↓	↓	↓	≙	Healthy
η_{ggt}	↓	↓	≙	↑	regenerator
Leakage	↓	↓	↓	↑	Regenerator
ΔP doubled	↓	≙	≙	↑	faults
ϵ down	≙	↑	≙	↑	

Constant power

	$N/\sqrt{\theta_1}$	W_f	P_2/P_1	Heat rate	
Fouling	↑	≙	≙	≙	Healthy
η_{ggt}	↑	↑	↑	↑	regenerator
Leakage	↑	↑	↑	↑	Regenerator
ΔP doubled	↑	≙	≙	↑	faults
ϵ down	≙	↑	≙	↑	

Three-Shaft, Simple Cycle. Although three shaft engines (i.e., twin spool gas generators with a free power turbine) are not as widespread in pipeline uses as two shaft engines, performance analysis is somewhat more demanding and thermodynamic modelling was found to give a considerable insight into engine behavior.

The effects of mechanical damage can be detected by a shift in the rotor speed relationship; although the spools are *mechanically* independent, there is a strong aerodynamic coupling caused by the need for flow compatibility between the two compressors. Damage on the LP rotor, either to the turbine or compressor, causes an increase in HP speed for a given LP speed, with the opposite effect for HP rotor damage as shown in Fig. 12 [13].

Compressor fouling is rather harder to model for a twin-spool compressor, and two possibilities were investigated,

(*i*) LP Compressor fouled, HP compressor unaffected
(*ii*) Both LP and HP compressor fouled.

Intuitively, the effects of fouling are more likely to influence the early stages of the compressor; by the time the LP compressor is severely fouled, however, it is unlikely that the HP will be unaffected, and deposits may bake on the higher temperature blading at the rear. It is not unreasonable to assume that the final result may be midway between the two cases. The rotor speed relationship is shown in Fig. 13, and it is seen that the mean value of the two cases gives a reasonable agreement; it is, however, difficult to see what use can be made of the speed relationship to detect fouling.

Examining the variations of power turbine inlet temperature (T_7), overall compressor pressure ratio (P_3/P_1), and power, however, show that fouling may be detected by a drop in pressure ratio and power with little change in T_7 (Figs. 14, 15, and 16). It is particularly noteworthy that the two models for fouling show relatively little difference, but are quite different from the effects caused by mechanical damage.

It can be seen that the use of detailed component models can provide an in-depth understanding of engine problems not previously available to an operator. These models, although they have demonstrated the types of fault matrix to be expected, are not proposed for field use. The requirements for the operator in the field must be satisfied using *data-driven* models.

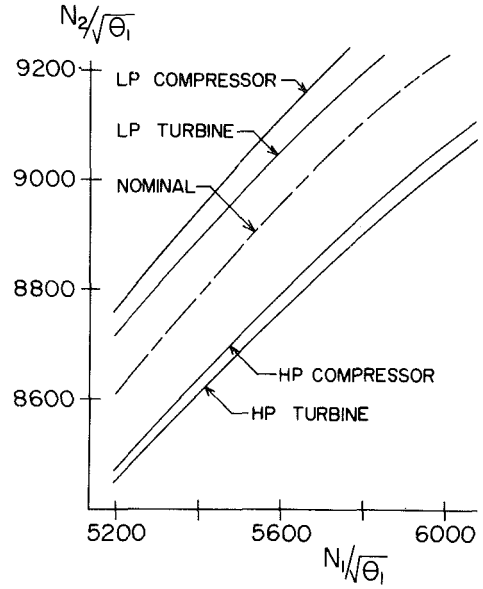

Fig. 12 Rotor speeds for twin spool engine

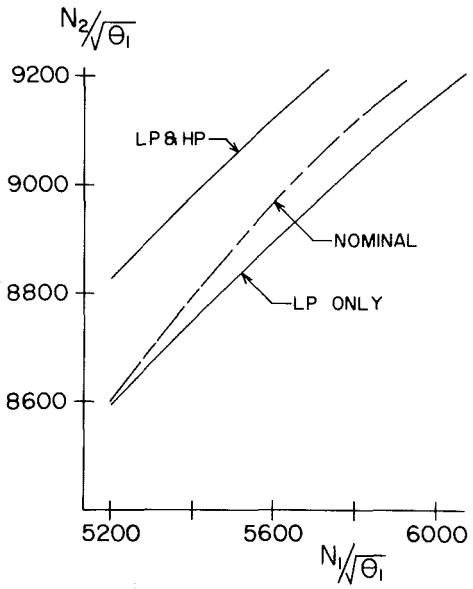

Fig. 13 Effect of fouling on rotor speeds

Thermodynamic Models for EHM Systems

Basic Philosophy. The determination of engine performance levels and their deviation from normal condition is the legitimate domain of thermodynamic or gas path analysis (GPA). The major functional aspects are presented in Fig. 17. Following conversion of the data to engineering units, they must be corrected to standard atmospheric conditions. These corrected data are then to be processed through a thermodynamic analysis which makes use of physical laws governing the behavior of the engine to deduce other cycle parameters which were not measured. Clearly these thermodynamic analyses must be tailored to the particular engine being monitored. The results of the thermodynamic analysis define the complete array of cycle performance parameters. To be of any value to the performance engineers, they must be compared to standard baselines and deviations from these baselines computed, time tagged and added to a data base containing historical trends.

The final functional block in the GPA section of the EHM

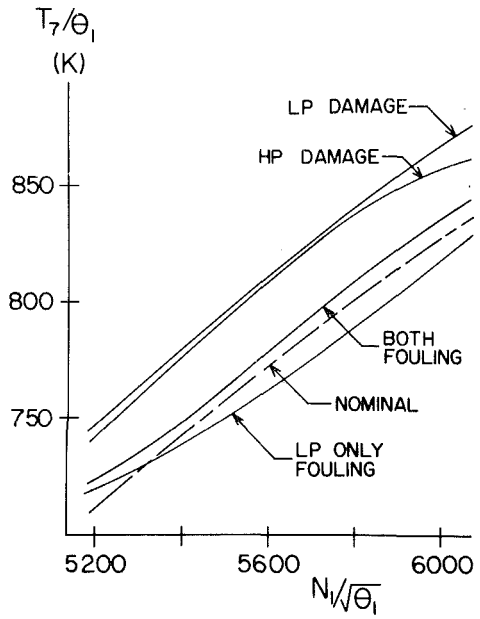

Fig. 14 Effect of fouling on T_7

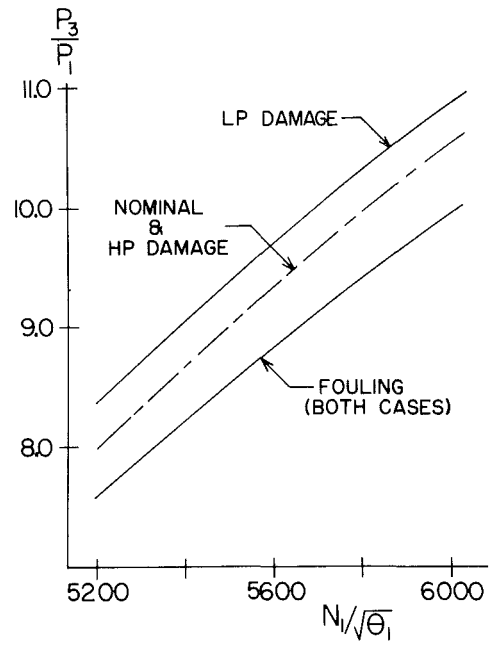

Fig. 15 Effect of fouling on CPR

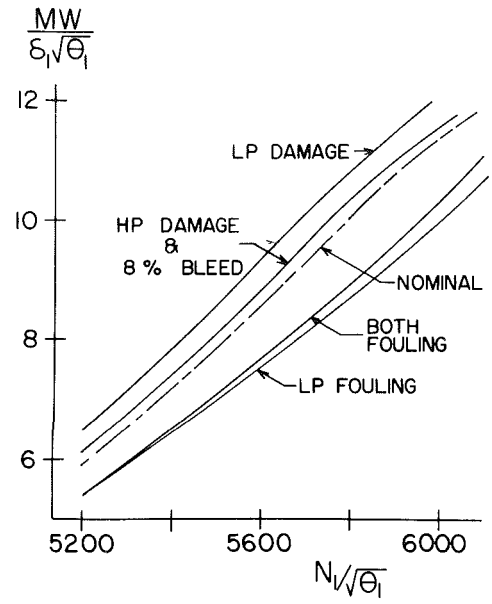

Fig. 16 Effect of fouling on power

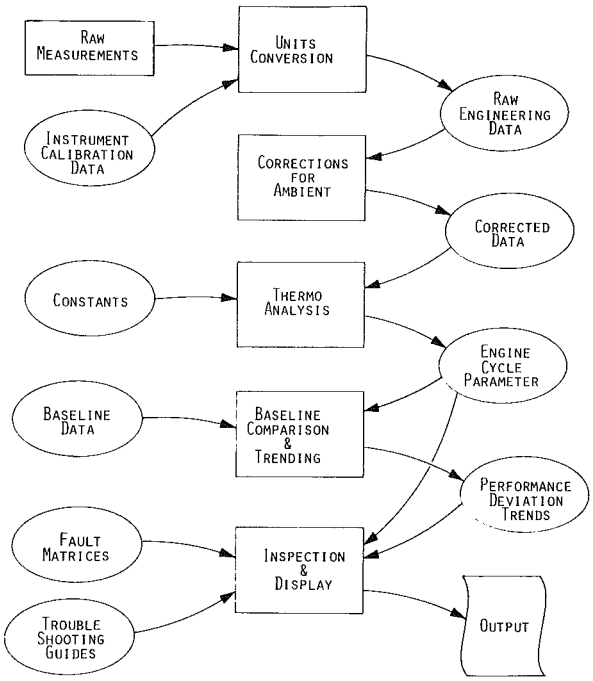

Fig. 17 Functional aspects of EHM system

package is that of inspection and display. It is emphasized that automation has been considered only insofar as manipulation of the data is concerned. The system described allows visual display of the trends, comparison of the data at any point in time with a fault matrix and a means of displaying this comparison. Judgement of the results together with recommended action has been left entirely in the hands of the engineering staff. The philosophy of the design, therefore, places the computer in a subservient role to the operations engineers on the argument that they are the only means by which the system can be adapted to new engines or new problems.

Data Collection Considerations. Application of such a system to a pipeline presents a number of unique problems that need to be drawn to the attention of the reader. The pipeline is geographically spread out, making data collection more of a problem than might be the case with a centralized facility. The basic requirements for data collection to support a pipeline EHM system are completeness and reliability of information. Since most of the current pipelines will likely operate their EHM system with manually gathered data, all possible precautions should be taken to ensure that the data is a reasonably reliable set of information. To achieve this, there is a requirement for simplifying the collection process together with a rough determination of data validity. Two levels of inspection are suggested, as follows:

Level 1 Inspection. At this level, the station personnel have little or no time and/or training and the simplest possible check of the engine is suggested. Under these circumstances, a book of tabular data should be provided which contains the following information.

	Parameters to be inspected	Functional dependence
Single-shaft	Exhaust temp	T_{amb}, N, P_c
Two-shaft, simple cycle	Power turbine inlet temp	T_{amb}, N_1
Two-shaft, regenerative cycle	Compressor delivery pressure	T_{amb}, N_1
Three-shaft	Power turbine inlet temp	T_{amb}, N_1

Level 2 Inspection. General baselines for each engine type can readily be made available either in chart form or in functional form. Collected data is then inspected as follows:

(*i*) Corrected to ambient pressure and temperature
(*ii*) All baselines for which there are measurements are accessed using the functional dependence indicated in level 1 to obtain baseline data for the current operating point
(*iii*) Measurement deviation computed

Conclusions

The use of thermodynamic models shows considerable promise for EHM in pipeline application of gas turbines. The ability to study the effects of degradation in a systematic manner is especially valuable. Thermodynamic models are best used as an engineering tool to provide information to engineering personnel, rather than in a completely automated system.

Acknowledgment

The research for this paper was conducted under the sponsorship of the Pipeline Research Committee of the American Gas Association incident to PRC project number PR-154-128, "Development of Thermodynamic Models of Gas Turbines and Centrifugal Compressors." The authors gratefully acknowledge both the financial support and the advice of individual members of the committee.

References

1 Cohen, H., Rogers, G. F. C., and Saravanamuttoo, H. I. H., "Gas Turbine Theory," 2nd ed., Longman, 1972.

2 Reid, D. E., "Impact of Increased Fuel Prices on Gas Turbine Operations and Maintenance," Second Symposium on Gas Turbine Operations and Maintenance, National Research Council of Canada, 1977.

3 Davies, A. E., "Principles and Practice of Aircraft Powerplant Maintenance," Institute of Marine Engineers, 1977.

4 Karanjia, D. J., and Saravanamuttoo, H. I. H., "A Cost Effective Engine Health Monitoring System for On-Board Use on Hovercraft," ASME Paper No. 80-GT-185, 1980.

5 Saravanamuttoo, H. I. H., "A Low Cost, On-Site Performance Monitoring System," ASME Paper No. 79-GT-24, 1979.

6 Agrawal, R. K., MacIsaac, B. D., and Saravanamuttoo, H. I. H., "An Analysis Procedure for Validation of On-Site Performance Measurements for Gas Turbines," ASME JOURNAL OF ENGINEERING FOR POWER, Vol. 101, No. 3, 1979, pp. 405-414.

7 Scott, J. N., "Improving Turbo Compressor Efficiency Via Performance Analysis Techniques," ASME Paper 77-GT-53, 1977.

8 Scott, J. N., "Axial Compressor Monitoring by Measuring for Intake Depression," Third Symposium on Gas Turbine Operation and Maintenance, National Research Council of Canada, 1979.

9 Williams, L. J., "The Use of Mathematical Modelling in the Analysis of Gas Turbine Compressor Unit Test Data," ASME Paper No. 81-GT-217, 1981.

10 Belrose, T. D., "Automatic Inspection, Diagnostic and Prognostic System," AGARD-CP-165, 1974.

11 Urban, L. A., "Condition Monitoring of Turbine Engines and Gas Compressors for Gas Line Pumping," First Symposium on Gas Turbine Operation and Maintenance, National Research Council of Canada, 1974.

12 Temple, T. W., Foltz, F. L., and Jamallail, H. R., "A Gas Turbine Maintenance Information System for the Saudi-Arabian East-West Crude Oil Pipeline," ASME Paper 80-GT-107, 1980.

13 Matthee, F. A. H., and Saravanamuttoo, H. I. H., "Development of a Low Cost Performance Monitoring System for Use On-Board Naval Vessels," ASME Paper No. 82-GT-297, 1982.

I. Macdougall[1]
Research Officer.

R. L. Elder
Senior Research Fellow.

School of Mechanical Engineering,
Cranfield Institute of Technology,
Cranfield, England

Simulation of Centrifugal Compressor Transient Performance for Process Plant Applications

The development of a theoretical model capable of simulating centrifugal compressor transient performance (including compressor surge) is detailed. Simulation results from a Fortran computer program are compared with measured compressor transient data. Good simulation of compressor transients between stable operating points, and compressor presurge flow oscillations has been obtained. General application criteria are presented for the geometric distribution of model elements within a compressor system. Model applications and future work are outlined.

Introduction

Within industry, the use of large centrifugal compressors is widespread in applications such as compression of process gases and pipeline pumping. The transient operation of these compressors is, as yet, little understood. Still less well understood is the compressor interaction with plant controls during rapid transients, such as compressor surge, start-up, sudden changes in gas composition, and the like. Thus the design of control systems to regulate the behavior of the plant during transient operation is difficult and, in many cases, results in inefficient design due to, on the one hand, overspecification, and on the other, underestimation of the problems which can lead to catastrophic failure of critical plant components.

To improve this situation, a much better understanding of installed dynamic compressor performance is required. To gain this understanding, a research program has been carried out which developed a mathematical model capable of simulating compressor transient performance, including compressor surge, within a process environment. The model was originally developed for aerospace applications, and has been extensively modified for industrial uses where the working fluid need not necessarily be air. The model has been implemented in a Fortran computer program. In addition to this, transient test data have been acquired using a large, single-stage centrifugal compressor.

This paper describes the mathematical model and compares simulated with measured compressor performance during transient operation. Both surge transients and transients between stable operating points are considered.

2 Basic Theory

There are two basic requirements of the model if it is to successfully simulate process plant compressor transients:

(*i*) the model should be sufficiently representative of the dynamic fluid flows involved to be capable of simulating compressor surge

(*ii*) there should be sufficient thermodynamic flexibility within the model to deal with both the nonideal gases typically found in this application and changes in gas composition

Numerous compressor models have been published. The simpler models [1–6] are not capable of simulating compressor surge, although the work of Fasol [5, 6] has produced good results when simulating transfers between stable compressor operating points.

To satisfy the first requirement (above) the proposed model is based upon dynamic forms of the conservation relations. To achieve a concise model the flow is assumed to be one dimensional. Models of this type are not new; for instance the work of Kuhlberg [7] and Willoh [8] suggest models which are capable of simulating compressor surge. Greitzer [9] also uses a similar model to that proposed here to simulate post-stall compressor behavior. It is from this work that Elder [11–13] derived the basic model used in this study.

Although thermodynamic flexibility has been built into some models (Davis [1]) the combination of thermodynamic flexibility and adequate dynamics has not been pursued. In the method proposed here, the model incorporates the polytropic analysis due to Schultz [13] with the dynamic equations previously described. The reason for choosing the Schultz analysis is its flexibility and its general acceptability.

A detailed derivation of the proposed model is given in Appendix A. In addition a brief outline of the major factors are presented here. During the analysis the integral forms of the momentum and continuity equations are applied to a generalized element (Fig. 1).

Momentum:

$$-\int_v \frac{\partial \rho \bullet \bar{v}}{\partial t}\, dv = \int_s P_s d\bar{s} + \int_s \rho \bar{v} \bullet \bar{v}\, d\bar{s} + \int_v \bar{F}\, dV$$

[1] Currently with General Electric, Cincinnati, Ohio

Contributed by the Gas Turbine Division of THE AMERICAN SOCIETY OF MECHANICAL ENGINEERS for presentation at the 28th International Gas Turbine *Conference and Exhibit, Phoenix, Arizona, March 27–31, 1983. Manuscript* received at ASME Headquarters December 7, 1982. Paper No. 83-GT-25.
Copies will be available until January 1984.

Continuity:

$$-\int_v \frac{\partial \rho}{\partial t}\, dv = \int_s \rho \bar{v} \cdot d\bar{s}$$

Energy:

$$-\int_v \left(\frac{\partial Ui}{\partial t} + \frac{\partial \mathrm{KE}}{\partial t}\right) dV = \int_s \rho(h+\mathrm{KE})\bar{v} \cdot d\bar{s} + \int_v E dv$$

The flow is assumed to be one dimensional in the axial direction, with a mean flow area, and that Mach numbers are relatively low (<0.3) at the element boundaries. The so-called "lumped" parameter distribution is then assumed. This involves assuming the terms under the integrals on the L.H.S. of the above equations are constant across the element.

The equations then become:

Momentum:

$$\frac{dw_1}{dt} = \frac{Am}{\Delta x}\,(P_{t1} - P_{t2} + F_{\mathrm{NET}}) \tag{1}$$

Continuity:

$$\frac{d\rho_2}{dt} = \frac{1}{Am\Delta x}\,(w_1 - w_2) \tag{2}$$

Energy:

$$Am\Delta x \frac{d}{dt}\left(C_v T_s + \frac{1}{2}\rho v_x^2\right)_2 = (\rho A v_x H)_1 - (\rho A v_x H)_2 + E_{\mathrm{NET}} \tag{3}$$

where F_{NET} represents the force exerted by the element on the flow and E_{NET} represents the element work input.

For this model, previous work (Elder [11]) has shown that the dynamics of the energy equation add little to the accuracy of the model; therefore, for simplicity, they are neglected. Hence

$$H_2 = H_1 + \frac{E_{\mathrm{NET}}}{w_1} \tag{4}$$

The resulting model relationships consist of a set of nonlinear ordinary differential equations. In order to numerically solve the equations, they are simulated using, in this case, digital techniques. In its application, this method implies similar assumptions to those used in the method of characteristics (see for example Benson [14]), and no fundamental advantage is claimed for the lumped parameter model used here. Kuhlberg [7], however, has noted that the method of characteristics becomes cumbersome when applied to a compressor and the current authors would support this suggestion. The details of the model derivation, above, differ from those of Kuhlberg [7], Willoh [8], and Greitzer [9], who used an actuator disk and associated volume. This is largely a superficial difference, however, as the resulting equations are very similar. The different approach has been taken here because the authors feel development of the models can more readily be made from this approach, Elder [10].

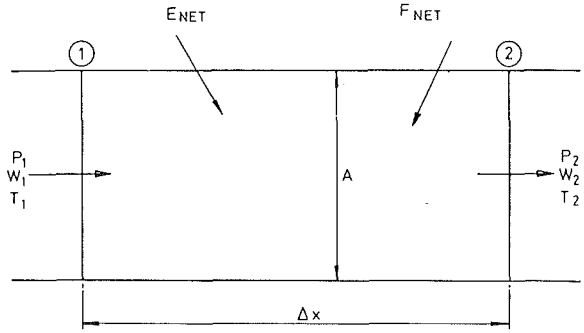

Fig. 1 Generalized one-dimensional flow element

The thermodynamic model uses a simple equation of state, namely

$$\frac{P_T}{\rho} = ZRT \tag{5}$$

together with the Schultz relationships to define the polytropic compression paths where

$$Wp = \frac{Cp\ T_1}{\left(\frac{1}{e} + x\right)}\left[\left(\frac{P_{t_2}}{P_{t_1}}\right)^m - 1\right] \tag{6}$$

$$m = \frac{ZR}{Cp}\left(\frac{1}{e} + x\right) \tag{7}$$

$$Ws = \frac{Wp}{e} + \Delta \mathrm{KE} \tag{8}$$

and

$$T_2 = T_1\left(\frac{P_{t_2}}{P_{t_1}}\right)^m \tag{9}$$

Equation (2) is modified (see Appendix A) to produce

$$\frac{dP_2}{dt} = \frac{ZRT_1}{(1-m)V}\,(w_1 - w_2) \tag{10}$$

The dynamic equations thus derived may be applied to any type of system element (duct, compressor, valve, etc.) by suitable calculation of the F_{NET} and E_{NET} factors. To calculate F_{NET} and E_{NET} a quasi-steady assumption is made such that the instantaneous element inlet conditions may be used to calculate the value of F_{NET} and E_{NET} from steady-

Nomenclature

A = cross-sectional area, m^2
C_p = specific heat at constant pressure, J/kg K
C_v = specific heat at constant volume, J/kg K
e = polytropic efficiency
E = energy, J
F = body force, Pa
h = enthalpy, J/kg
H = stagnation enthalpy, J/kg
KE = kinetic energy, J
m = polytropic index
M = Mach number
P = pressure, Pa
R = gas constant, J/kg K
s = surface area, m^2
t = time, s
T = temperature, K
U_i = internal energy, J/kg
v = velocity, m/s
V = volume, m^3
W = mass flow rate, kg/s
W_p = polytropic head, J/kg
W_s = shaftwork, J/kg
x = axial length, m
X = compressibility function
Z = compressibility factor
ΔKE = change in kinetic energy, J
Δx = element length, m
γ = ratio of specific heats
ρ = density, kg/m
τ = time constant, s

Subscripts

m = mean value
NET = net value
s = static value
t = stagnation value
0 = initial steady-state value
1 = element inlet
2 = element outlet
∞ = final steady-state value

state information, the values of E_{NET} and F_{NET} being continually updated as the inlet flow variables change.

Characteristics are generally available for the compressor element which allow the values of polytropic head and efficiency to be determined from the instantaneous volume flow rate (see Fig. 2). Thus, using the Schultz relationships

F_{NET} = Steady-state pressure rise =

$$P_{t_1}\left(\left[\frac{Wp}{C_p T_1}\left(\frac{1}{e}+x\right)1\right]^{\frac{1}{m}}-1\right)$$

and

$$E_{NET} = W_s \bullet W_1$$

or

$$T_2 = T_1 + \frac{W_s}{C_p}$$

Note that during a compressor transient the compressor operating point is not necessarily limited to be on the compressor steady-state characteristics.

To model the test compressor systems (described later in this paper) further types of elements were developed to represent upstream and downstream ductwork. For simple pipe elements, F_{NET} is equated to the pressure loss in the pipe (either using measured data or using simple pipe friction), and E_{NET} is zero. Throttle valve elements were also developed, using isentropic nozzle flow relationships, which included opening and closing area versus time schedules to permit fast transients to be introduced into the system.

Thus a simple model has been developed which is relatively easy to apply to different types of compressor system elements. To solve the equations, a system geometry distribution is necessary, together with element characteristics and inlet conditions, and working fluid data. In this case, the downstream boundary condition is set by a nozzle venting to ambient.

3 Compressor Test

The compressor tested was a single-stage centrifugal machine with impeller tip dia of 600 mm, and it used air as the working fluid. Compressor performance ranges up to a pressure ratio of 1.8 with a maximum of approximately 30,000 c.f.m. ($\simeq$10 kg/s). The driver unit was an electric motor, the compressor speed remaining constant at about 10,000 rpm. A set of variable inlet guide vanes was fitted.

A schematic test layout is shown by Fig. 3. Fast transients were introduced into the system by a pneumatically operated butterfly valve (stroking time: 1.05 s closing; 0.66 s opening). High-performance pressure transducers were mounted on the test compressor to provide transient measurement of compressor inlet mass flow, and compressor inlet and outlet pressure.

Steady-state compressor characteristics were measured (Fig. 2). Of the compressor transient data taken, two transients are considered here. At a fixed inlet guide-vane setting, the blow-off valve was opened and closed such that the compressor operating point moved from one stable point to another, and back again. Secondly, the blow-off valve was closed from a fixed, stable operating point such that the compressor entered full surge cycles.

4 Simulation of Measured Compressor Transients

To simulate the compressor system, a geometric distribution of elements is required. To establish this, two criteria are used. Firstly a frequency parameter is used which relates the ability of the model to simulate perturbations within a certain bandwidth. Secondly, a criterion of approximately equal element volumes is used to avoid the

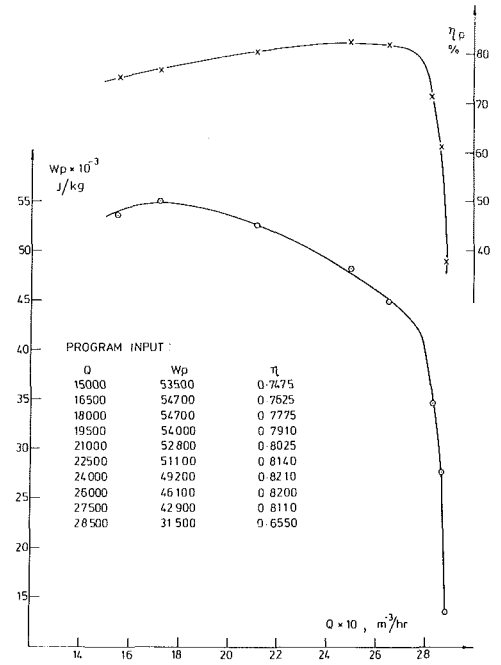

Fig. 2 Compressor characteristic from steady-state testing

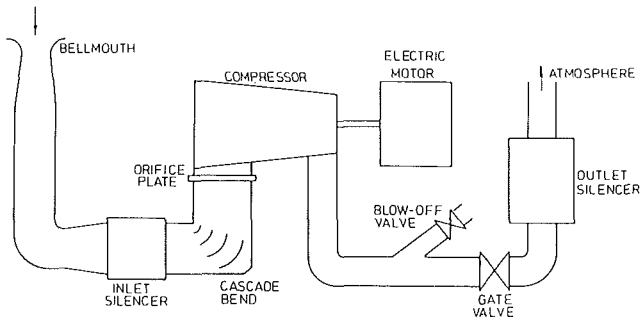

Fig. 3 Compressor test rig schematic

problem becoming numerically "stiff." (In practice if large and small elements are adjacent, it is noted that they do not appear to "communicate" in a realistic manner.) The final geometric distribution is a compromise between the two criteria.

Simulation results are compared with measured compressor transients in Figs. 4, 5, and 6. In all cases, the blow-off valve initiates the transient at $t = 0.2$ s. Point-to-point transient simulation with the blow-off valve closing (Fig. 4) produces slight mass flow and pressure discrepancies, with decaying flow oscillations at the end point. Simulation of the blow-off valve opening (Fig. 5) between stable operating points produced a slightly high pressure-time history. This may be due to inaccuracy in the blow-off valve opening characteristic. It is worth noting the simulation of the "kinks" in the pressure and mass flow curves (Fig. 5) which are similar to those measured. Simulation of presurge oscillations (Fig. 6) occurs at about the correct point in time, and at the correct point on the compressor characteristic. Further, the frequency response is of the correct order of magnitude.

Post-transient oscillations are to be noted particularly in (Fig. 4). These are readily observed in the theoretical predictions and can also be seen in the experimental data although the scatter in these results makes this less clear. Frequencies of the experimental and theoretical results are closely equal but the phases differ by a small amount probably due to the misalignment of the transient start. As closely as could be defined the frequency shown was that of a

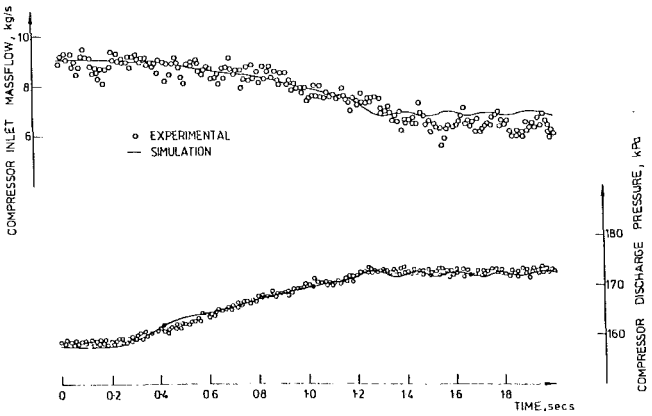

Fig. 4 Point-to-point compressor transient, blow-off valve closing

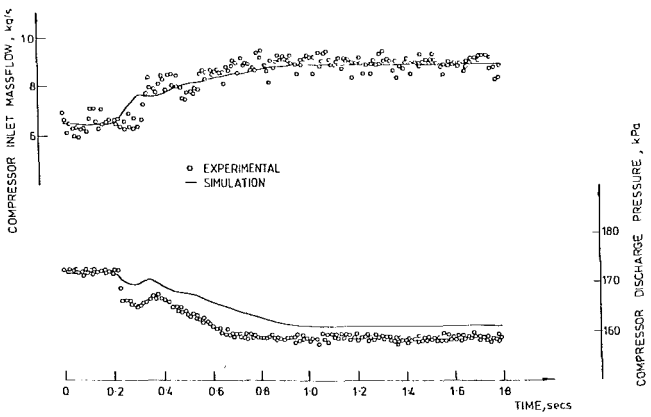

Fig. 5 Point-to-point compressor transient, blow-off valve opening

sound wave travelling through the system. The ability of the system to simulate wave structures is a feature of the method and has been noted in work carried out since. It is also interesting to note that the post-transient oscillations are much more persistent when the final operating point on the compressor characteristics is nearer surge, i.e., in Fig. 4, than in Fig. 5. This can be attributed to the system being more stable where the compressor characteristic has a larger negative gradient.

5 Discussion

The derivation of the mathematical model has involved several assumptions; their effects are discussed here. First, a one-dimensional flow is assumed. Although this appears to be a drastic simplification of the complex flow structures known to exist the assumption has often [1–15] been made and in so far as the objectives of this project have been concerned, does not appear to be a limiting factor. Second, the assumption of relatively low Mach numbers implies that the element boundaries should be chosen to comply with this requirement. Third, the justification for neglecting the dynamics of the energy equation is simply that results are little affected and computational complexity is much reduced [10]. Finally, both the lumped parameter and quasi-steady assumptions impose frequency limitations on the model. These limitations are not serious so long as the following conditions are fulfilled.

(Element length) $<<$ (Wavelength of the flow perturbation)

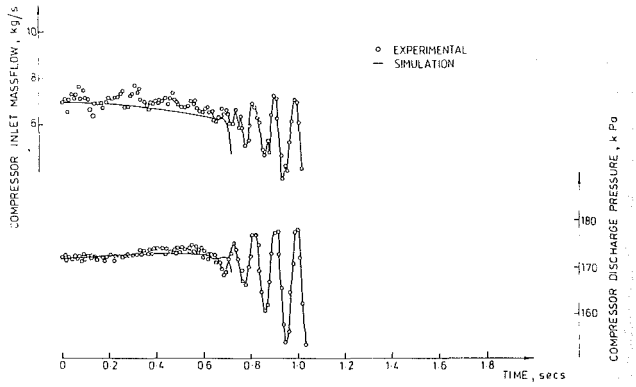

Fig. 6 Compressor transient into surge

In practice for the cases studied, this limits element lengths to about 2 or 3 m.

General application rules for the geometric distribution of elements have been formulated. The first, relating element length with a frequency parameter, is based upon the work of Elder [10] and is derived from a comparison of the lumped parameter model and the true partial differential solution. The critical frequency parameter obtained from this study is set such that the error between the two solutions is small (less than 5 percent). The second criterion, namely approximately equal element volumes, is necessary to ensure that elements will interact with each other in the correct time scale (i.e., avoid a numerically "stiff" system).

The above discussion, in part, relates to the stability of the model solution. The Cranfield computer model uses, in its solution of the differential equations a fourth-order Runge-Kutta technique which produces an error estimate at each time step. This is used to alter the time-step during the integration. It is interesting to note that the element lengths and time-steps produced by the model are comparable to those produced by the conditionally stable method of characteristics (see, for instance [15]), where the Courant-Freidrichs-Lewy stability criterion is used. Both in this area, and in the assumptions made, there are certain similarities between the method of characteristics and the method used here, although the derivations follow totally different paths. It is thought that the method used here is slightly easier to apply in the case of a compressor.

The simulation results presented here represent a considerable amount of model validation work. During this work it was found that the geometry distribution, through the effects of element interactions, have a considerable effect on the oscillatory behavior of the simulation. Further, the shape of the compressor characteristic, and its absolute level, had a large effect upon the accuracy of the simulation in terms of absolute pressures and mass flows and in the time taken for oscillatory behavior to be exhibited. Thus, when comparing simulated with experimental results, the accuracy of the geometry and compressor characteristic inputs is of major importance. A further possible source of error was the system inlet mass flow which is used to determine, via a stage stacking routine, the element inlet conditions. The experimental values were, unfortunately, rather scattered (Figs. 4, 5, and 6) and thus the simulation input was a mean value only. As previously noted, a further source of inaccuracy may be the experimental blow-off valve characteristics.

Given the possible sources of inaccuracy, the simulation results presented (Figs. 4, 5, and 6), are considered to be in good agreement with the experimental data and compare favorably with other published results. Simulation of compressor transients between stable operating points has been

carried out with only minor, explicable errors. Note the duration of the transient closely follows the blow-off valve stroking time.

Simulation of compressor presurge flow oscillations has also been performed with good results. The ability to simulate this type of compressor transient is a feature of this model which is not available in many other compressor models. It is not reasonable to expect a model of this type to simulate full compressor surge cycles without an accurate knowledge of the negative mass flow compressor characteristics. If such a characteristic were available, it is thought that the model would be capable of simulating full surge cycles; the work of Greitzer [7] is perhaps indicative of this.

6 Model Development

Development of the model described here is continuing. This will include further comparisons between simulated and experimental transient results using a turbocharger type compressor. It is considered that the model is only limited in its applications by the input data available. The modeling of any type of process system element together with its control system is possible. This simulation of multistage compressors, parallel interconnected process paths, steam turbine driver units, and the use of nonideal gases are all under consideration.

7 Conclusions

A mathematical model capable of simulating centrifugal compressor transient performance within a process system has been developed and implemented in a Fortran computer program. The model is applicable to any type of process system component, and can deal with nonideal gases. A comparison with measured compressor transient performance has shown that:

1 Simulation of transients between stable operating points has been performed with reasonable accuracy.

2 Simulation of compressor presurge flow oscillations has been performed with good accuracy in terms of both the variable time history and the oscillatory behavior of the flow.

3 The simulation results presented compare favorably with those published elsewhere, especially those relating to presurge flow oscillations.

4 The accurate simulation of transient performance is contingent upon accurate model input data, especially system geometry and compressor characteristics.

5 The computer code has been prepared in a modular fashion to permit different studies to be easily made. In addition to the project described here, multistage axial and centrifugal machines and steam turbine drivers have been simulated.

In addition to this, general criteria have been formulated for the distribution of compressor system geometry.

8 Acknowledgments

The authors wish to thank the Science Research Council for supporting this work. Thanks are also due to Mr. J. S. Anderson of I.C.I. Limited for his, and I.C.I.'s continuing interest and support.

References

1 Davis, F. T., and Corripio, A. B., "Dynamic Simulation of Centrifugal Compressors using a Real Gas Equation of State," *Proc. Fifth Annual University of Pittsburgh Conf. on Modeling and Simulation*, Pittsburgh, Pa., Apr. 1974.

2 Dean, R. C., Jr., and Young, L. R., "The Time Domain of Centrifugal Compressor and Pump Stability and Surge," ASME *Symposium on Centrifugal Compressor and Pump Stability, Stall and Surge*, Mar. 1976.

3 Rothe, P. H., and Runstadler, P. W., Jr., "First-Order Pump Surge Behaviour," *Journal of Fluids Engineering*, Dec. 1978, pp. 459-466.

4 Fasol, K. H., and Tuis, L., "Identification of Blast Furnace Air Supply System," Paper No. 8.6, 4th IFAC Symposium on Identification and System Parameter Estimation, Tbilisi, Sept. 1976.

5 Fasol, K. H., Gronau, M., and Tuis, L., "Possibilities of Theoretical and Experimental Identification of Blast Furnace Air Supply System," (In German), VDI Berichte, Vol. 276, 1977, pp. 81-85.

6 Fasol, K. H., and Gronau, M., "Modeling and Simulation of a Chemical Process Plant Blast Supply System," IMACS Symposium on Simulation of Control Systems, Vienna, Sept. 1978.

7 Kuhlberg, J. F., Sheppard, D. E., King, E. O., and Baker, J. R., "The Dynamic Simulation of Turbine Engine Compressors," AIAA Paper No. 69-486, AIAA 5th Propulsion Conference.

8 Willoh, R. G., and Seldner, K., "Multistage Compressor Simulation Applied to the Prediction of Axial Flow Instabilities," NASA TM X - 1880, Sept. 1969.

9 Greitzer, E. M., "Surge and Rotating Stall in Axial Flow Compressor: Part II—Experimental Results and Comparisons with Theory," ASME JOURNAL OF ENGINEERING FOR POWER, Apr. 1978, p. 199.

10 Elder, R. L., "Mathematical Modeling of Axial Flow Compressors," Ph.D. thesis, Leicester University, 1972.

11 Corbett, A. G., and Elder, R. L., "Stability of an Axial Flow Compressor With Steady Inlet Conditions," *Journal of Mechanical Engineering Science*, Vol. 16, No. 6, 1975.

12 Corbett, A. G., and Elder, R. L., "Mathematical Modeling of Compressor Stability in Steady and Unsteady Flow Conditions," *Unsteady Phenomena in Turbomachinery*, AGARD CP - 177, 1976.

13 Schultz, J. M., "The Polytropic Analysis of Centrifugal Compressors," JOURNAL OF ENGINEERING FOR POWER, Jan. 1962, pp. 62-82.

14 Benson, R. S., and Whitfield, A., "Application of Nonsteady Flow in a Rotating Duct to Pulsating Flow in a Centrifugal Compressor," Paper No. 20, Proc. I. Mech. E., 1967-68, Vol. 182, pt. 3H, pp. 184-196.

15 Benson, R. S., Garg, R. D., and Woollatt, D., "A Numerical Solution of Unsteady Flow Problems," *International Journal of Mechanical Science*, 1964, Vol. 6, pp. 177-244.

APPENDIX

Derivation of the Mathematical Model

The derivation below considers the integral form of the continuity, linear momentum, and energy equations applied to the generalized flow element (Fig. 1). Therefore

Continuity:

$$\int_v \frac{\partial \rho}{\partial t}\, dV = \int_s \bar{v} \cdot ds \tag{11}$$

Linear momentum:

$$\int_v \frac{\partial \rho \cdot \bar{v}}{\partial t}\, dv = \int_s P_s \cdot d\bar{s} + \int_s \bar{v} \cdot \bar{v} \cdot ds + \int_v \bar{F}\, dV \tag{12}$$

Energy:

$$\int_v \left(\frac{\partial Ui}{\partial t} + \frac{\partial \mathrm{KE}}{\partial t} \right) dV = \int_s \rho (h + \mathrm{KE}) v \cdot ds + \int_v E\, dV$$

Since $Ui = C_v \cdot Ts$, and $h + \mathrm{KE} = h + \frac{1}{2}\rho v^2 = H$, and assuming that $\int E\, dV = E_{\mathrm{NET}}$, then the energy equation is simplified to

$$-\int_v \frac{\partial}{\partial t} \left(C_v \cdot Ts + \frac{1}{2} \rho \bar{v} \cdot \bar{v} \right) dV = \int_s H \bar{v} d\bar{s} + E_{\mathrm{NET}} \tag{13}$$

Now, assuming axial flow

Continuity:

$$-\int A \frac{\partial \rho}{\partial t}\, dx = (\rho u\, A)_1 - (\rho u\, A)_2 = w_1 - w_2 \tag{14}$$

Momentum:

$$-\int A \frac{\partial \rho u}{\partial t}\, dx = -(\rho v_x{}^2 A + P_s A)_1 - (\rho u_x{}^2 A + P_s A)_2 + \int P_s \cdot ds_x + F_x$$

where

$$F_x = \int_v F_x dV$$

It is now assumed that the final two terms of this equation

may be combined to provide a simple pressure force × mean flow area term, i.e.,

$$-\int A\frac{\partial \rho v}{\partial t} = -(\rho v_x{}^2 A + P_s A)_1 - (\rho v_x{}^2 A + P_s A)_2 + F_{\text{NET}} Am \tag{15}$$

Energy:

$$\int A\frac{\partial}{\partial t}\left(C_v \cdot t_s + \frac{1}{2}\rho v_x{}^2\right)dx = (\rho A v_x H)_1 - (\rho A v_x H)_2 + E_{\text{NET}} \tag{16}$$

Further simplification of (15) is possible by utilizing perfect gas relationships:

$$\rho v_x{}^2 A + P_s A = A(P_s + \rho v_x{}^2) = AP_s\left(1 + \frac{v_x{}^2}{RT_s}\right) = AP_s(1+\gamma \mathrm{M}_x{}^2) = AP_T\left[\frac{(1+\gamma \mathrm{M}_x{}^2)}{1+\frac{(\gamma-1)}{2}\mathrm{M}^2}\right]^{\gamma/(\gamma-1)}$$

since in practice it is found that the axial Mach number is similar to the actual Mach number. Expanding this expression binomially and neglecting Mach number terms of order four and higher.

$$\rho v_x{}^2 A + P_s A = AP_T\left(1 - \frac{\gamma}{2}\mathrm{M}^2\right)$$

For the intended application, the flow Mach number is likely to be small, i.e., $\mathrm{M}^2 << 1$, thus

$$\rho v_x{}^2 A + P_s A = AP_T$$

Using this relationship, and assuming a mean flow area for the element, equations (14) and (15) became

Momentum:

$$\int \frac{\partial w}{\partial t}dx = Am(P_{t_1} - P_{t_2} + F_{\text{NET}}) \tag{17}$$

Continuity:

$$-\int A\frac{\partial \rho}{\partial t}dx = w_1 - w_2 \tag{18}$$

and omitting the dynamics of the energy equation reduces (16) to

Energy:

$$H_2 = H_1 + \frac{E_{\text{NET}}}{w_1} \tag{19}$$

Finally, a lumped parameter distribution is assumed such that

$$\frac{d\rho_2}{dt} = \frac{1}{Am\Delta x}(w_1 - w_2) \tag{20}$$

$$\frac{dw_1}{dt} = \frac{Am}{\Delta x}(P_{t_1} - P_{t_2} + F_{\text{NET}}) \tag{21}$$

The last three equations are the basis of the dynamic model.

One further transformation is required. From the polytropic analysis [13] it is seen that

$$P_t \cdot \rho^{\frac{1}{1-m}} = \text{constant}$$

thus

$$\frac{d\rho}{dt} = \frac{(1-m)}{ZRT}\frac{dP_t}{dt}$$

and hence equation (20) may be written

$$\frac{dP_2}{dt} = \frac{ZRT}{(1-m)V}(w_1 - w_2) \tag{22}$$

Equations (19), (20), and (21) are used directly by the computer program, and are applied to any type of element by suitable definition of F_{NET} and E_{NET}.

On the Transient Interaction of Centrifugal Compressors and Their Piping Systems

C. R. Sparks
Director of Engineering Physics,
Applied Physics Division,
Southwest Research Institute,
San Antonio, Texas 78284

The problems of surge and other low-frequency pulsation phenomena in centrifugal compressors are described in terms of both machine (head curve) characteristics and the flow impedance characteristics of its attached piping. Flow stability criteria are presented in terms of net modal damping, as the combination of piping acoustic damping and equivalent negative damping of the compressor in the surge region of its performance curve. Surge and instability frequencies are related to acoustic reactance of the piping system. Finally, theoretical concepts are verified both by electrical analog models and by field and laboratory data on real compressors. This paper provides some new and significant findings on the dynamic interaction of centrifugal compressors with piping systems and describes the basic phenomena underlying these interactions. Good agreement is shown between predicted and measured surge frequencies, and for those termed "piping resonance surge" produced by high flow offsets or flat spots in the head curve.

Introduction

This paper deals with low frequency pulsation phenomena in centrifugal compressors and will describe an analysis approach that has proven useful in describing and controlling these transient effects. By defining the compressor piping in terms of both its steady-state and transient (pulsation) impedances, some new insight is provided into: (*i*) the mechanisms of surge, (*ii*) the ability of a compressor to amplify external low frequency pulsations, and (*iii*) the self-generation of low frequency pulsations at flows substantially above normal surge conditions. The higher frequency components of compressor pulsations, i.e., those pulsations associated with blade passing frequency and its harmonics, are not treated.

Emphasis for this work has come from a number of field experiences with large industrial machines where low-frequency pulsations caused problems ranging from fatigue of internal components to flow measurement errors caused by pulsations in the piping. While many such problems could be solved from a basic understanding of piping acoustics, the field tests seemed to raise more questions than they answered. Salient observations from field test work and from early experimental work in the laboratory dealing with compressor-piping transient interaction are summarized below.

(*i*) It has been shown that a compressor can either amplify or attenuate external pulsations (as from a reciprocating compressor or from vortex flow) if these are introduced into either the suction or discharge piping.

(*ii*) Even when no external source of pulsations exists in the piping system, low frequency pulsations can be experienced at levels sufficiently high to fatigue compressor internals or severely shake the piping. Such effects have been observed at flows substantially above the normal machine surge point.

(*iii*) Resultant pulsation problems can often be mitigated by changing the pulsation response of the compressor piping (lengths, diameters, etc.). High level pulsations have been observed at frequencies ranging from less than 1 Hz to several hundred Hertz. Frequencies are not harmonically related to—and do not vary with—compressor speed.

(*iv*) The severe pulsation frequencies normally correspond to one of the major system acoustic resonances of the piping systems, and measurements along the piping show a strong standing wave pattern, often existing across or through the compressor.

(*v*) Pulsation levels are most severe when the compressor is situated at or near a velocity maximum (pressure minimum) in the pulsation standing wave field.

(*vi*) The onset, frequency, and severity of machine surge can also vary as the piping system is changed. Surge point (and frequency) as measured in a test stand often bears little relationship to those characteristics observed with field piping.

(*vii*) External pulsations can induce premature surge in a centrifugal (e.g., paralleling a centrifugal with a reciprocating compressor).

(*viii*) Some machines exhibit little if any evidence of surge. This tendency is especially noticed when compressor piping is small and little discharge volume is available.

(*ix*) Surge frequency can often be predicted by analyzing the pulsation response of the compressor piping.

The Compressor Dynamic Response (CDR) theory

Contributed by the Gas Turbine Division of THE AMERICAN SOCIETY OF MECHANICAL ENGINEERS for presentation at the 28th International Gas Turbine Conference and Exhibit, Phoenix, Arizona, March 27-31, 1983. Manuscript received at ASME Headquarters January 12, 1983. Paper No. 83-GT-236.

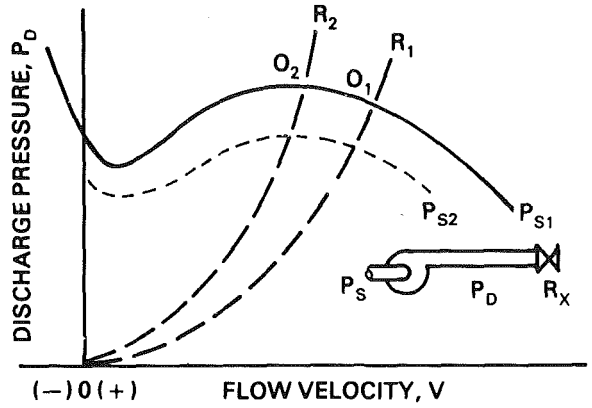

Fig. 1 Effects of pipe flow resistance on compressor operating point

developed below helps explain many of these phenomena in at least qualitative terms. From these basic concepts, quantitative simulation techniques have been developed and proven for many of the phenomena described. Work on the CDR theory is still in progress in areas such as predicting surge amplitude and in the effects of rotating stall and other flow separations on surge and low flow performance.

Approach

The field experience just described suggests a strong influence exerted by the piping on observed transient response and flow stability within centrifugal compressors. Even the so-called deep surge or machine surge is profoundly affected by the flow dynamics of the attached piping. The approach presented below is intended to help correlate field observations with machine characteristics and piping flow impedance. The analysis process involves superimposing pipe impedance curves on the compressor head curve in a manner similar to that used for designing an electronic amplifier stage. Circuit analysis techniques can then be used to explain many of the pulsation and surge phenomena observed in real machines.

Two important simplifying assumptions are made. First, that linear acoustic theory describes the pulsation response in a piping system with large pulsation amplitudes and net convective flow. The adequacy of this assumption for simulating industrial compressor systems has been verified by some 30 years of operation of the Southern Gas Association (SGA) Analog at Southwest Research Institute (SwRI) and will not be detailed in this paper. The second assumption is that the steady-state head curve also defines compressor response under transient conditions. This is undoubtedly an oversimplification after surge is well established, but appears adequate for predicting surge threshold and frequency. It also appears adequate for predicting compressor response to external pulsations; slight changes in average head or flow do not significantly affect pulsations.

The discussions that follow draw from at least three disciplines: fluid dynamics, acoustics, and electronics. An attempt has been made to keep the contribution from each area in the simplest possible terms, to facilitate explanation of basic concepts. The approach taken, therefore, will be to start with oversimplified concepts and add complexities from the real world as needed to give correlation between theory and experiment.

Compressor Dynamic Response (CDR) Theory

Figure 1 illustrates a typical head curve[1] for a centrifugal compressor, and a sketch of a simplified compressor piping which will be used as the initial physical example. In the system shown, the compressor suction is at atmospheric pressure, while discharge pressure is controlled by flow through a constrictive orifice or valve labeled R_X. As long as the pressure ratio is low and flow is subsonic through the constriction, supply pressure to the valve is related to approximately the square of flow velocity:

$P = P_D = R_X V^2$
P = pressure across the valve
P_D = pressure supplied by compressor
V = flow velocity
R_X = a constant (approximately) for a given valve setting, analogous to flow resistance.

This square law dependence is also depicted in Fig. 1, where the valve resistance lines are labeled R_1 and R_2 for two valve settings. The operating point (0_1) is defined as the intersection of the compressor curve and the load curve (R_1). If we reduce the orifice size or valve opening, the load curve changes as illustrated by curve (R_2) and a new operating point (0_2) results.

If, instead of a valve for flow resistance, the discharge line is a long pipeline, the operating point would be defined by a similar square law equation

$$P_D = \frac{f}{2D}\rho V^2 \cdot L \tag{1}$$

or

$$P_D = R_X V^2 \tag{2}$$

where:

f = pipe friction factor
ρ = fluid density
R_X = the d-c (steady flow) resistance of the pipe.

$$R_X = \frac{f}{2D}\rho L$$

As long as changes in flow or valve setting are slow, the load line and head curve define system discharge pressure. For example, if suction pressure is modulated slowly, the operating point will track up and down the R_X line. If R_X is varied, the operating point will move up and down the compressor curve.

[1] Note that the compressor performance curve is shown in terms of discharge pressure and flow velocity. This coordinate system allows us to superimpose pipe flow impedance and compressor characteristics on the same plot. Each performance curve, therefore, assumes a known suction pressure and compressor speed.

Nomenclature

c = acoustic velocity
D = pipe diameter
f = friction factor
F = frequency
L = pipe length
N_s = Strouhal number
n = an integer
P = static pressure
p = acoustic pressure amplitude
Q = volume flow rate
R = pipe flow resistance (P/V^2)
r = acoustic resistance, Re (p/v)
V = flow velocity
v = acoustic particle velocity
Z = complex acoustic impedance (p/v)
ρ = gas density
Δ = differential

When suction pressure is modulated rapidly however, the operating point will no longer track the steady-state R_X line or the compressor curve. Instead of R_X, the acoustic impedance of the discharge piping will control the transient relation between pressure modulation and flow modulation about the operating point. Acoustic theory shows that the acoustic impedance looking into a long (semi-infinite) pipe is purely resistive and is numerically equal to the characteristic impedance of the fluid in the line. If we use lower case letters to denote pulsation amplitudes, the acoustic pressure amplitude (p) is related to the velocity modulation amplitude (v) in a semi-infinite (long) line as follows

$$p = \rho c v \tag{3}$$

where

ρc = the specific acoustic impedance of the fluid; i.e., the product of density and acoustic velocity

Instantaneous total static pressure, $P(t)$, then is $(P_D + p)$, or

$$P(t) = (P_D + p) = \frac{f}{2D}\rho V^2 L + \rho c v \tag{4}$$

$$= R_X V^2 + r v$$

where:

r = acoustic resistance (characteristic impedance)
$v = v_o \sin \omega t$

The value of R_X therefore sets the operating point 0 (assuming a given compressor speed and suction pressure), while the value of r defines the slope of the impedance (load) line passing through the operating point (Fig. 2). The value of r thereafter defines the relationship between pressure p and particle velocity v. For typical gas pipeline operating conditions (ρ, c, etc.), acoustic resistance is a small fraction of the steady-state flow resistance, i.e., $p/v << P/V$, as illustrated in Fig. 2.

It should be emphasized that whenever suction pressure modulation frequencies are in the acoustic range, the load line, r, (passing through the static operating point 0) totally defines the relation between (p) and (v) in the piping, and acoustic modulations of the operating point must follow this line. If operating point slowly shifts, then the line, r, will shift with it, but without a change in slope. The effect of convective flow velocity on acoustic pipe impedance is very second-order in most industrial plant applications.

Figure 3 illustrates a typical compressor/piping interaction map, assuming interaction of piping and the compressor pipe impedance is strictly resistive. The effects of reactive impedances in producing reflections, standing waves, and phase shift between p and v will be discussed shortly.

Pulsation Amplification by a Compressor. In Fig. 3, if suction pressure (P_{s0}) is modulated from P_{s2} to P_{s1}, then flow (V) varies from V_2 to V_1 and discharge pressure varies from P_2 to P_1. The ratio of $(P_2 - P_1)$ to $(P_{s2} - P_{s1})$ defines the amplification or attenuation of pressure pulsations as they pass through the compressor, at least for the simplified case of a traveling wave and a long discharge line. If the piping impedance is very low (the dynamic load line is nearly horizontal), then $P_1 - P_2$ can approach zero and the compressor will effectively attenuate suction pressure pulsations. In that case, flow variations $(V_1 - V_2)$ can be substantial. Under the foregoing conditions and for all pulsation frequencies of practical concern, both the compressor curve and the pulsation impedance of the discharge line will influence flow and discharge pressure modulations for a given modulation of suction pressure. The magnitude of the piping's pulsation impedance (i.e., its slope) can be any positive value from near zero (shown as a horizontal slope) to very high (a vertical slope). The phenomena of pulsation

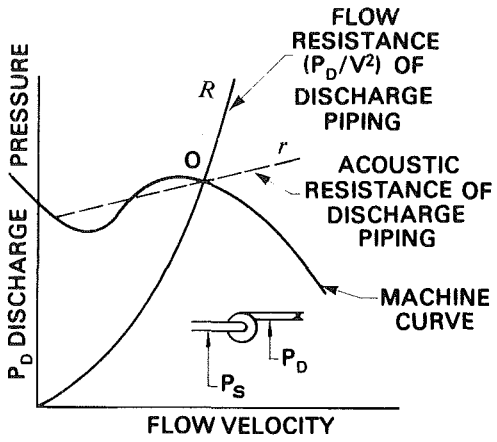

Fig. 2 Performance curve of an idealized centrifugal machine showing steady-state and acoustic load lines

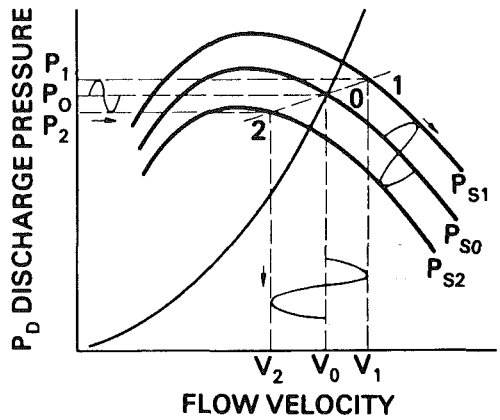

Fig. 3 Effect of modulating compressor suction prssure on discharge pressure and discharge flow velocity

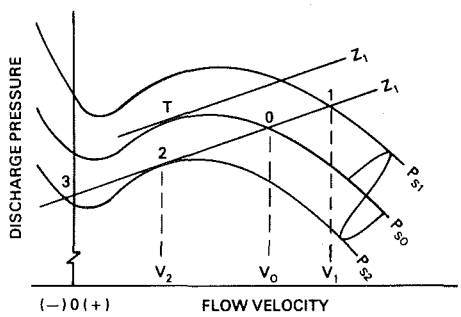

Fig. 4 Bistable nature of system surge when suction pressure falls to P_{s2}

amplification and attenuation have been observed in the laboratory using a test compressor and varying the pipe lengths and pulsation frequencies.

For purely resistive piping systems (traveling rather than standing waves), amplification of suction pulsations are most severe when high impedance (small diameter) discharge piping is used. For real piping systems, this condition is seldom realized, and the presence of reflected (back traveling) waves changes the design rule, as discussed later.

Stability Limits (Nonreactive Piping). Before proceeding with the inclusion of reactive impedance components into the CDR concepts (area discontinuities, etc.), the use of acoustic load lines helps shed some interesting light on compressor surge or stability limits.

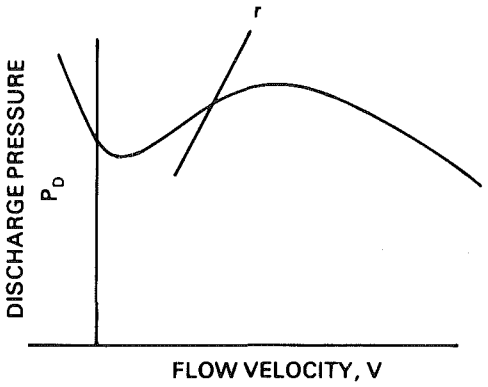

Fig. 5 Acoustic resistance line which will prevent surge

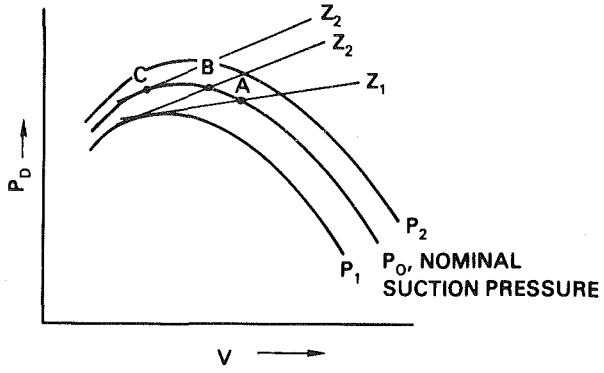

Fig. 6 Compressor stability (surge) limits for various line impedances and external pulsation levels

To illustrate the conditions required for surge, consider a set of compressor curves as in Fig. 4, with operating point 0 and load line Z_1. If suction pressure is modulated between P_{s1} and P_{s2}, the system is stable. As flow drops from point 0 to 2, the compressor is able to supply the pressure required by the piping. If suction pressure falls below P_{s2}, the compressor is unable to make discharge pressure in the positive flow region, and flow collapses to point 3. The pipe begins to backflow, as required by its load line Z_1. Subsequent increases in suction pressure or decreases in discharge pressure (as from decreased withdrawal from the suction piping, from backflow, or from acoustic reflections) can drive the operating point back up the load line with resulting large fluctuations in flow, particularly if the load line is very flat. The cycle then repeats.

The limit of stability is affected not only by the head curve but also the load line slope and any coexisting pulsations. If suction pulsations are from P_{s1} to P_{s2}, the surge limit is defined by point 0, where Z_1 is tangent to the P_{s2} line. If no pulsations are present, the surge limit is T, where the Z_1 line is tangent to the steady-state operating curve (P_{s0}). Thus, pulsations move the surge point from point T to point 0.

To illustrate a condition where surge cannot occur, consider Fig. 5. In this case, the piping impedance line is assumed very steep, and in fact is steeper than the back portion of the compressor head curve. When flow is reduced, pipe pressure requirements always fall faster than the compressor curve (i.e., slope of the pipe impedance line > slope of head curve), and the compressor is always able to supply adequate pressure. While flow separations, rotating stall and other vortex generation phenomena can occur in such a situation, the bistable condition described in the preceding paragraph cannot occur because the overall flow regime is quite stable.

Points A and B in Fig. 6 are the surge limits for the nominal head curve shown, assuming two different piping impedances Z_1 and Z_2 and a modulating suction pressure between P_1 and P_2. If no pulsations are present, the surge point is C, assuming pipe impedance Z_1.

A more generalized form of the graphical representation of compressor and piping curves is shown in Fig. 7. In this curve, suction pressure is not atmospheric, and discharge is assumed to be a constant pressure vessel or pipeline P_L. The steady flow resistance curve (depicting pressure drop in the discharge lateral) is the dotted square law curve labeled R_X. Once the static and dynamic load lines are properly located, the analysis process is identical to that previously described.

In subsequent paragraphs it will be shown that the acoustic impedance of a real piping system is a function of frequency. Thus, Z_1 and Z_2 may exist simultaneously for a given piping system, but represent different frequencies. It follows that a compressor will surge at that frequency which represents the lowest impedance of its attached piping. Since the lowest

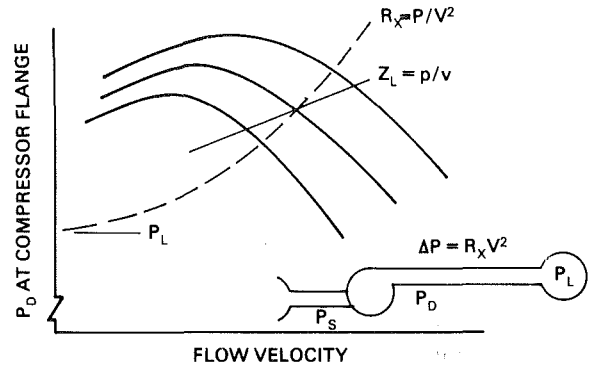

Fig. 7 Graphical application of pipe impedance concepts to high-pressure systems

impedance always appears in the standing wave field at a velocity maximum (pressure minimum), the compressor should surge in a mode which finds the compressor situated nearest a velocity maximum. As noted earlier this is exactly what has been observed both in the laboratory and in the field.

System Acoustic Damping. It is interesting to note that many of the characteristics of surge can be explained using relatively simple network theory, especially those involving flow stabilty limits. If, for example, we consider the compressor as a pressure source and a restricting (controllable) orifice, then we can define the orifice resistance necessary to simulate a compressor P_D curve. In Fig. 8(a), P_L is supply pressure minus the orifice drop; i.e., $P_L = P_0 - \Delta P$. Note that between points A and B, the required orifice resistance is negative, i.e., as flow increases orifice pressure drop decreases. If we attach piping with a damping line r_1 as shown in Fig. 8(b), the system is stable because the positive damping afforded by piping is greater than the negative damping of the compressor. For load line r_2, however, the system is unstable at the operating point 0 because negative damping R_{02} is greater than load damping r_2.

This approach was confirmed using electronic simulation, and the electronic system did indeed become unstable. In addition, the simulation frequencies were very close to observed surge frequencies of the laboratory compressor for a broad range of piping dimensions. Surge frequencies could be accurately predicted using the electronic model. The implication is, of course, that surge is a system instability, dependent only upon head curve and piping configuration. In either the electronic or fluid systems, conditions are not stable in the negative damping region, unless external damping is sufficient to make total damping positive. The system may be made up of a centrifugal compressor, electrical generator, or

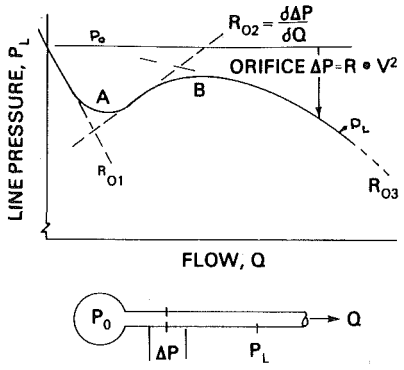

A. SIMULATED COMPRESSOR SOURCE, SHOWING NEGATIVE DAMPING FROM A TO B

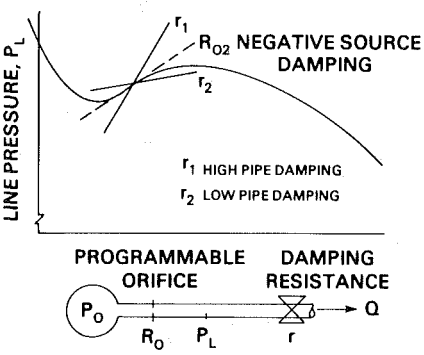

B. PIPE ACOUSTIC DAMPING IN COMPARISON TO SOURCE NEGATIVE DAMPING

Fig. 8 Flow stability criteria for a passive piping system using a hypothetical flow controlling orifice to simulate a compressor head curve

even a reciprocating compressor. The instability or surge does not occur because external driving forces (vortex formation, flow separations, etc.) are greater than damping forces; it is simply a result of inherent instability (actually, bistability), and it will be unstable even when no external (or internal) exciting forces are present. While stall, flow separation, or any of various possible vortex generators may play an important part in shaping the head curve in the region of surge, the simulation tests show that surge itself is a rather different mechanism whose onset is determined by system acoustic damping and whose frequency is determined largely by attached piping.

Reactive Piping Systems

The piping impedances provided by real piping systems are substantially more complex than those of the semi-infinite, constant diameter pipe described earlier. Any change in flow diameter affords reflection points for pulsations, and pipe lengths strongly influence piping resonant frequencies. The net effect is an extreme variation in pipe impedance as a function of frequency, and preferred frequencies or resonances are quite pronounced.

Complex piping system made up of various discrete lengths, diameters, branches, volumes, and constrictions will exhibit dynamic transfer characteristics which will amplify pulsations at some frequencies and attenuate them at others. In this action, the piping characteristics are almost directly analogous to electrical circuitry or delay lines, wherein the inertial (inductance) and stiffness (capacitance) characteristics

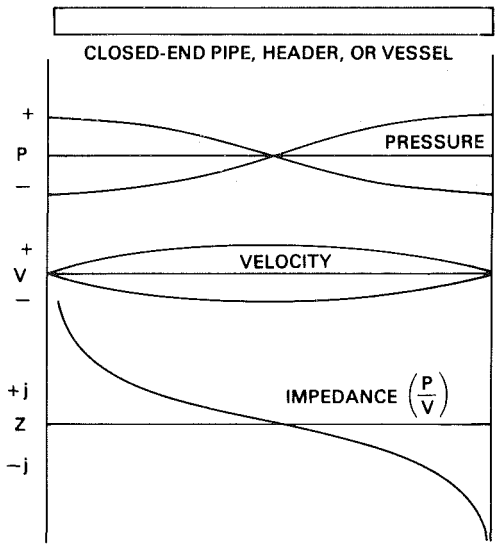

Fig. 9 Standing wave plots of a closed-end pipe resonance showing variations in pressure, flow and impedance as a function of distance along the pipe

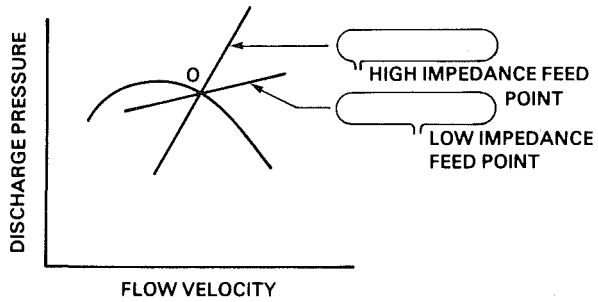

Fig. 10 Simple configurational effects on pipe acoustic impedance

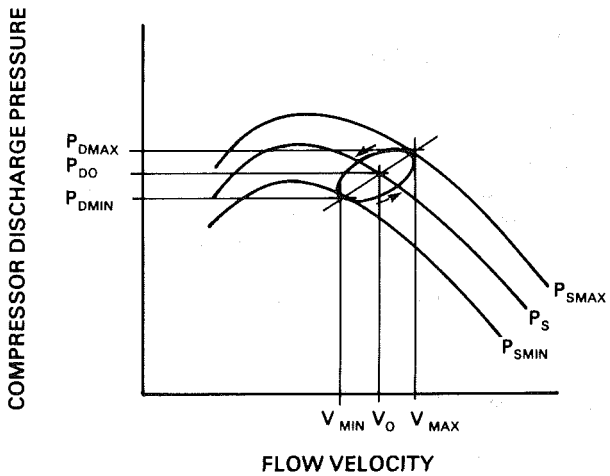

Fig. 11 Orbit of flow versus pressure into a reactive piping system, demonstrating phase shift between *p* and *v*

are quite linear, but the resistance is nonlinear with flow. In flowing piping systems, the acoustic resistance is a direct function of the ρV^2 pipe frictional losses. These far overshadow conventional acoustic dissipation effects such as molecular relaxations for the range of flows normally encountered in industrial piping systems. This distributed impedance network can amplify low-level pulsation up to as much as a factor of 100 (i.e., acoustic Q's up to 100 or so), depending on frequency, pipe size, flow, termination impedance, and fluid properties.

Since the reactive flow impedances (distributed acoustic inertia and stiffness) of a piping system are quite linear, conventional acoustic theory can be used to define resonant frequencies, mode shapes, and filtering characteristics even for rather high flow velocities. The nonlinear damping only affects the amplitude or sharpness of the resonance peaks. Using elementary physics, resonances of individual piping segments can be very simply described from "organ pipe" resonance theory.

In order to illustrate the influence of finite length piping, consider the standing wave modes of a simple closed-closed pipe section (i.e., capped at each end). Figure 9 shows both the pressure and velocity standing wave patterns at resonance. By dividing pressure (p) by velocity (v), the impedance (z) along the pipe is plotted for its lowest (half-wave) resonance.

From this impedance plot, it may be seen that reactive impedance is zero at the point of pressure minimum (velocity maximum). If a centrifugal compressor feeds into the center of such a pipe or vessel, a very low resistive impedance (or slope) is seen. Alternatively, if the feed-in point is near a capped end, a very high reactive impedance is seen by the compressor.

From earlier discussions, one might expect to illustrate the effects of reactive impedances simply by changing slope of the load line. This would imply a situation as shown in Fig. 10, where two loaded lines pass through the operating point 0.

Unfortunately, the process is more complex because of phase shift between pressure and flow near resonance. At resonance, this shift is 90 deg (in time) for single degree of freedom systems and tends to produce an elliptically shaped orbit rather than a single straight line. If pressure and flow were measured at a pressure maximum point in the piping, the load line would indeed be nearly a straight vertical line (large p, zero v). At a velocity maximum, it would be nearly horizontal (large v, zero p). At all intermediate measurement points, at all frequencies off-resonance, or in systems with substantial damping, the load lines are actually orbits, as illustrated in Fig. 11, at least for sinusoidal pulsations and flows well above surge.

If now the operating point is moved up the compressor head curve (e.g., by throttling flow), surge once again results when the compressor head curve cannot supply the instantaneous pressure required by the piping. Now, however, pipe flow pulsations are defined by an orbit instead of a straight line. A graphical illlustration of the orbital conditions which will produce surge is much more complex than for a nonreactive piping system, but the effects are the same. When surge occurs, the orbit can become quite distorted because of the compressor's participation in the generation process. A hypothetical and relatively simple orbit shape is illustrated in Fig. 12. Figure 13 shows a similar orbit as measured in the laboratory using a small test compressor. Other orbits (i.e., taken with other piping configurations) are shown in Fig. 14.

The acoustic reflections and standing waves which occur in real piping systems add complexity to the analysis process and modify some of the piping design rules suggested earlier. For example:

(i) Pulsation amplification by the compressor can best be defined by comparing pulsation amplitudes with the compressor off and on. Because of standing wave patterns through the compressor, simple measurements of pulsation levels in suction and discharge are highly dependent upon measurement point location.

(ii) Pulsation amplification of a standing wave is most pronounced when the compressor is located near a velocity maximum in the standing wave field. For wide band pulsations, maximum amplification will be experienced by those frequency components which have a velocity maximum at the compressor. As a rather low impedance device, the compressor couples most effectively at these low impedance points in the piping.

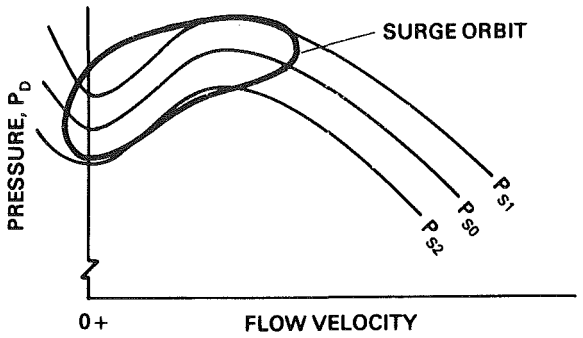

Fig. 12 Surge orbit for a simple piping system as suggested by compressor dynamic response theory

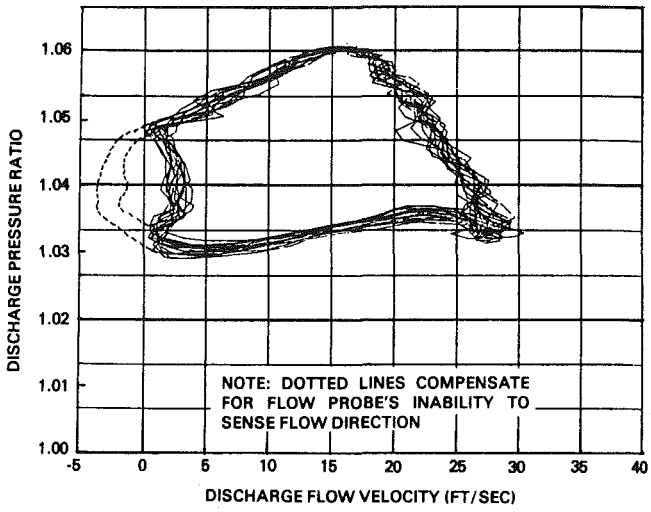

Fig. 13 Surge orbit from single stage compressor at 18,000 rpm

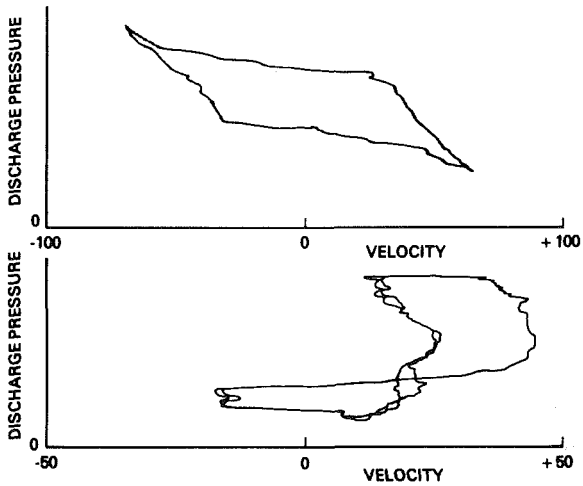

Fig. 14 Surge orbits for other piping systems of increased complexity

(iii) Surge will also occur at the frequency for which the compressor location is most nearly a velocity maximum. The onset of surge is controlled by the net modal system damping, but once it occurs its amplitude is influenced both by the proximity of the compressor to a pure velocity maximum and by the depth of the low flow valley in the head curve.

In summary, the acoustics of a compressor piping system can play a significant, if not controlling, part in the pulsation

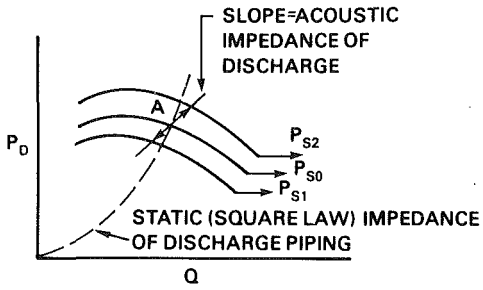

A. RESISTIVE PIPING SYSTEM

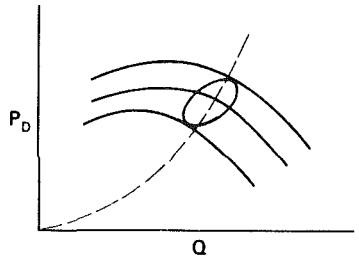

B. REACTIVE PIPING SYSTEM

Fig. 15 Typical response map of a centrifugal compressor for low frequency modulations of suction pressure

and surge response of a centrifugal. It is not surprising, for example, that test stand data on compressor surge often bears little relation to surge after the machine is installed. However, the analysis process for both pulsations and surge in reactive piping systems is sufficiently complex that the hand or graphical analysis techniques described earlier must give way to more sophisticated simulation models. One such model is the SGA Centrifugal Analog described and illustrated in a later section.

Suction Piping

Note that all discussions to this point have ignored the suction piping, chiefly to keep complexity of the discussion within manageable limits. It is obvious that suction piping is of equal importance to the discharge piping, and test results show that standing wave acoustic patterns are usually established including both suction and discharge piping. To fully define system response, it is of course necessary to include suction piping characteristics in the system analysis. Discussions at this level of complexity do not add a great deal to the understanding of basic system interaction; again, a more comprehensive simulation model is required, as described in a later section. By extending the approach taken in the foregoing discussions, however, some of the more obvious effects of suction piping on pulsation orbits can be anticipated.

Effects of Other Perturbation Sources on Orbit Shape

Previous discussions and illustrations of the dynamic response of centrifugal compressors have assumed the source of transient perturbation to be suction pressure. When suction pressure is modulated, the resultant orbit on the P_D versus Q map is defined by the discharge piping acoustic impedance. Figure 15 illustrates these orbits for the simplified case of resistive piping and for the more general case of reactive piping systems. In the general case, phase shift between flow and discharge pressure causes the orbit to become an elliptical, and the axis of the ellipse is dependent upon the phase angle between P_D and Q at the points of measurement. The shape of the orbit is strongly dependent upon the location of

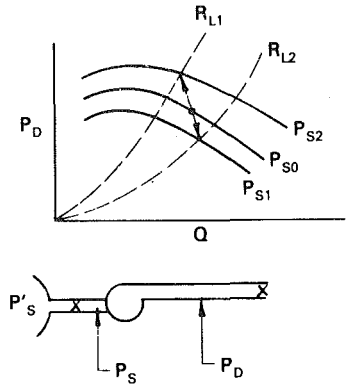

A. VARYING P_D, BUT WITH FLOW RESISTANCE IN SUCTION LINE

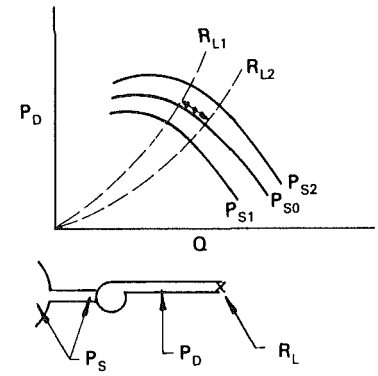

B. VARYING FLOW RESISTANCE R_L, CONSTANT P_S

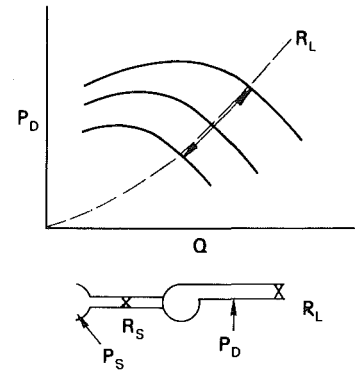

C. VARYING SUCTION VALVE OPENING (R_S), CONSTANT P_S AND R_L

Fig. 16 Typical pulsation orbit orientations for several pulsation sources

P_D and V measurement points. If both P_D and V are measured at a pressure maximum (velocity minimum) in a strongly resonant system, the orbit will be almost vertical, while at a velocity maximum (pressure minimum), the orbit would be horizontal. The orbit can be of almost any orientation off resonance. If P_D and V are not measured at the same point, 180 deg phase shifts are noted whenever the sensing point is moved past a zero crossing of either the p or v standing wave.

Thus orbit shapes are strongly dependent upon the location

of measurement points, as well as upon the piping impedance. They are also dependent upon the source of pulsations. Modulations of discharge pressure, for example, produce different orbits than modulations of suction pressure. Pulsations introduced by pressure variations (e.g., a reciprocating compressor) produce different orbit orientations than those produced by variable flow constrictions (e.g., a "hunting" regulator valve). Figure 16 illustrates some of the basic concepts, but assumes nonreactive piping systems and very slow transients for clarity.

Piping Resonance Surge

Flow separations can occur at any of several points in a compressor, e.g., in the impeller, diffuser, or in virtually any flow section if it is improperly designed or if it is operating at some condition substantially apart from its original design conditions (perhaps from a change in service). A single-stage compressor used in some of the supporting research for this paper has a vaned diffuser which functions poorly at intermediate to low flow rates. Such a condition is illustrated in Fig. 17.

The effect of the offset shown in Fig. 17 is to produce a flat spot or reverse slope portion of the head curve at flows well above the surge point. This has the effect of greatly reducing modal damping by increasing apparent negative resistance of the head curve in that flow region. It has long been recognized that such flat spots in the head curve can cause pulsation and vibration problems in centrifugal compressors and pumps. No technology has been available, however, to define when these problems will occur, how severe they might be, what causes them, or how they can be controlled.

The self-generated pulsation problems caused by flat spots or offsets in compressor head curves have been coined "piping resonance surge." The mechanism is identically the same as machine surge, but the dynamic amplitude is usually not as severe. If piping reactance and amplification is neglected, an orbit, such as that shown in Fig. 18, will result. As the operating point is moved from very high flow up the head curve, a bistable condition occurs at point A in Fig. 18, and conditions jump to B. Point B is unstable, however, for steady-state operation, since it does not fall on the R_X line, and continued oscillations are likely. Piping reactance is likely to cause a rebound of the operating point, and an instability similar to surge will occur. The bifurcated orbit shown in Fig. 18 is therefore an oversimplification. Passive pipe reactance will tend to reestablish an ellipse while the compressor tends to drive the operating point back to the head curve. Coupling between the very nonlinear compressor and the linear pipe impedance finally determine orbit shape.

Note that the compressor curve shown in Fig. 17 is for one rpm and one suction pressure only. Changing either parameter can move the point of offset relative to the peak of the curve. Thus, a compressor which was well designed for one application might be subject to anomalous flat spots at another condition. An example of a less idealized performance curve is given in Fig. 19 and illustrates the change in curve shape and potential instability region as rpm changes.

Sources of External Pulsations

Reciprocating compressors are an obvious source of external pulsations, especially at many gas pipeline compressor stations. Experience both in the field and with the SGA Analog have shown that pulsations from reciprocating compressors can in fact be amplified by centrifugal compressors, while in other cases pulsations from the piston compressor can throw the centrifugal unit into surge.

A less obvious but important source of piping pulsations are those caused by flow past a branch line. While such pulsations are normally of rather low amplitude at velocities

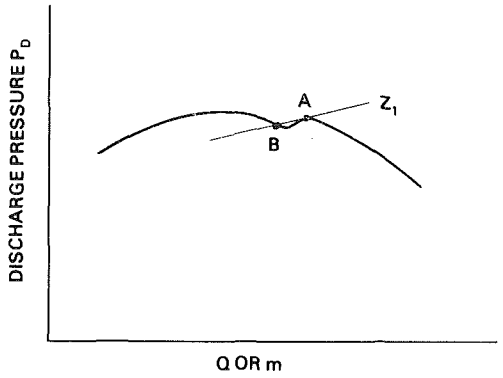

Fig. 17 Compressor head curve showing the effect of an offset relative to a piping load line

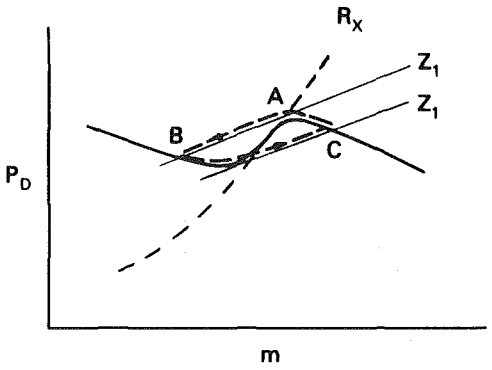

Fig. 18 Simplified orbit of operating points caused by head curve offset

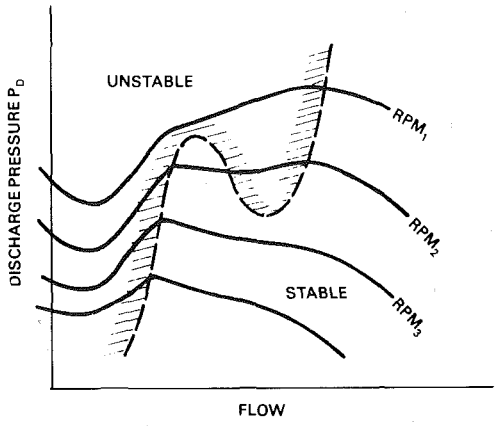

Fig. 19 Effect of changing operating conditions on compressor head curve

below 100 fps, the amplification afforded by centrifugal compressors can sometimes amplify these to severe and sometimes injurious levels. Field measurements at pipeline compressor installations have shown amplified levels up to several hundred psi.

In all cases, the frequency of flow induced pulsations is controlled by the acoustics of the branch pipe, often a closed bypass or recycle line. At certain flow velocities in the main piping, vortex generation at the mouth of the stub will produce pulsations both in the stub and the main piping. Testing with various diameter ratios shows that such shedding usually occurs between a Strouhal number (N_s) between 0.25 and 0.55, where

$$N_s = \frac{FD}{V} \tag{5}$$

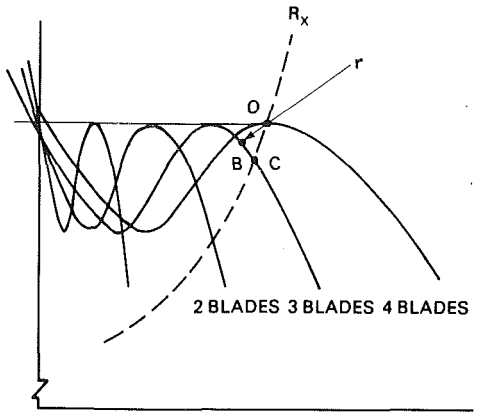

Fig. 20 When one blade stalls, the operating point shifts from 0 to B, along the dynamic load line *r*. Continued operation with a blocked passage would see migration to point C, to satisfy flow requirements.

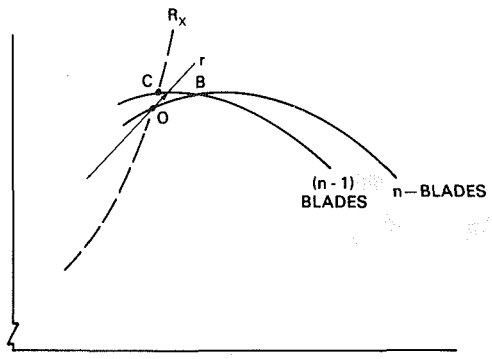

Fig. 21 Stall at point 0 would cause head to jump to point B, and an increase in instantaneous flow. Continued blockage would cause a shift to point C to satisfy steady flow requirements.

and F is an acoustic resonant frequency of the branch pipe, D is its diameter, and V is the average pipe flow velocity. Although length of the branch stub defines the pulsation frequency, flow velocity and the acoustics of the main piping system determine whether the vortex shedding will occur. Again, a rather detailed simulation technique is required to appropriately simulate the acoustic interaction of the branch and main piping, but once this is accomplished, rather good predictions can be made of the conditions under which vortex generation will result and of pulsation frequency. Research is now underway to verify amplitude prediction techniques.

Stall Effects on Surge

The effect of stall or other flow separations within the compressor is usually expected to result in a local drop in compressor head. Consider the hypothetical performance curve for a four-vane compressor shown in Fig. 20. The total flow results from the four blades operating in parallel, and the curves for one, two, three, and four blades are shown. The compressor operating point is at 0 and a dynamic load line (r) characterizes pipe impedance. If one blade stalls, pipe flow must follow the load line (r) to point B for three blades. Both flow and head drop suddenly, as defined by the pipe impedance (time constant). If blade 4 were to continue in a blocked or choked mode, the operating point would migrate to point C to satisfy stabilized flow requirements of the piping and compressor. As the stall cell rotates relative to the blades, stall choking can come and go, producing a jump in head curve as defined by the piping. The resulting pulsation wave form can be extremely complex, since dwell time at 0 and B depend on stall rotation, while transit time between 0 and B is a strong function of pipe impedance. By providing a local drop of the head curve in its low flow portion, the stall effect increases the likelihood of surge.

It seems likely that the opposite effect might be possible as well. In Fig. 21, if stall occurs at point 0, then head can jump from the normal curve (for n blades) to that for $(n - 1)$ blades. In this case, head is increased. Flow may increase or decrease depending upon the stall point and the orientation of the load line; for the load line shown, it would increase.

While these are simplified representations of complex phenomena, they appear to help explain why stall often produces surge, and why step function changes are sometimes observed at low flow when field measurements are made of compressor performance.

It follows that any phenomenon which causes a local drop in head curve can have serious implications with regard to stability of compressor and piping systems. Preswirl into a compressor, for example, can cause head curve variations by either improving or degrading the angles of attack (for example, the effects of variable inlet guide vanes). It follows that split flow inlets might have similar problems because of unequal angles of attack around the compressor eye.

Normally, stall frequencies are somewhat higher than surge frequencies simply because of the geometries involved. Since stall patterns are established circumferentially, their frequency is strongly influenced by machine geometry and operating conditions. Their onset can be affected by attached piping, preswirl, split flow inlets, etc., but their frequency should be only slightly affected by piping. As such, it should be possible to define a great deal about stall from shop tests. This is in contrast to surge, because surge onset, frequency, and amplitude are all strongly controlled by the attached piping configuration.

Implementing CDR Concepts in Compressor System Analyses

The process of graphically superimposing pipe impedance on the compressor head curve is useful for explaining CDR concepts in simple piping systems. However, it has obvious limitations in deriving quantitative results for complex piping systems. Branched piping systems with changes in pipe diameter normally have many resonance modes, and defining real and imaginary acoustic impedance components at an arbitrary point in the piping throughout the range of possible surge frequencies defies hand calculation. It is clear that graphical techniques must give way to more powerful simulation techniques, but they do serve to guide the simulation process.

The approach taken by SwRI in performing both pulsation and surge studies has involved development of a centrifugal compressor analog simulator. This method of simulation was chosen by SwRI largely because of its compatibility with existing analog simulation equipment used for reciprocating compressor analysis over the past 30 years, under sponsorship of the SGA's Pipeline and Compressor Research Council. As a result of some 30 years operation of the SGA Analog for reciprocating compressor problems, a good deal of background experience with both piping pulsations and analog simulation was available. The only development required was that of the centrifugal compressor analog itself. The requirements were simply to develop an electrical charge transfer pump, capable of simulating a compressor head curve of almost arbitrary shape, while providing appropriate input, output, and transfer impedances at all frequencies. Such an analog was developed and several are now in use in a design and problem-solving capacity.

The original versions were linear devices, in the sense that they simulated only a limited (straight-line) portion of the

head curve at the proposed operating point. This analog (Fig. 22) is particularly useful for pipeline installations involving both reciprocating and centrifugal compressors, as it served chiefly to simulate the centrifugal's ability to amplify externally generated pulsations. In essence it provides a description of the pulsation response of the entire piping system to external pulsations, but does not simulate surge or piping resonance surge.

A later version, shown in Fig. 23, is the Nonlinear Centrifugal Analog (NLCA). The entire head curve (excluding backflow) can be digitally programmed into this device, although its simulation is totally analog. Most of its use to date has been in research activities to further investigate surge phenomena (especially surge amplitude) and piping effects. Use of these analogs in research and design studies has provided considerable additional insight into the mechanisms and control of low-frequency pulsation and surge in centrifugal compressors. Table 1 shows a comparison of surge frequencies measured in the laboratory versus those predicted by the NLCA. These data show that predictions of surge frequency are quite accurate for a wide range of piping dimensions on both suction and discharge.

Fig. 22 SGA linear centrifugal analog

Fig. 23 SGA nonlinear centrifugal analog

Field Correlation

Subsequent to completion of the manuscript, a surge test was conducted on a 10,000 horsepower pipeline compressor as a basis for evaluating the surge simulation capability of the centrifugal analog. A comparative summary of field and analog results is given in Table 2.

Conclusions

Given below are a series of conclusions from the compressor dynamic response theory presented in the preceding sections. Note the similarity of these conclusions to the list of observations from laboratory and field data as presented in the Introduction.

(*i*) The theory demonstrates the action of a compressor in amplifying or attenuating externally generated pulsations and shows these actions to be dependent upon:

Table 1 Observed surge frequencies as a function discharge piping variations for both the centrifugal analog and a laboratory compressor[a]

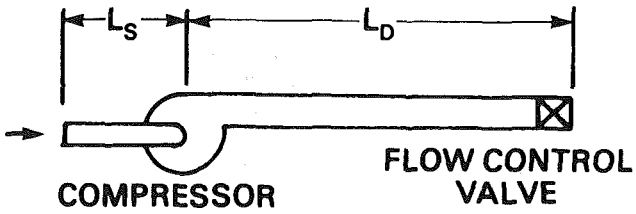

L_s, in.	L_d, in.	Surge Frequency
3	89.0	32.0
3	142.0	21.25
3	177.0	17.25
3	198.0	15.4
3	229.0	13.5
3	250.0	12.45
3	270.0	11.45
3	300.0	10.40
3	349.0	9.05
3	400.0	7.95
3	510.0	6.3
3	750.0	4.3
3	900.0	3.25

[a] Similar results were obtained for more complex piping systems involving branches and volumes.

Table 2 Comparison of centrifugal compressor analog surge predictions with measured values for a large pipeline compressor

	Analog	Field	% Diff.
Surge period, s	1.10	1.12	8.9
Minimum surge flow, lb/s	110	100	10.0
Peak surge flow, lb/s	287	305	5.9
Minimum surge pressure, psi	916	931	1.6
Peak surge pressure, psi	960	960	0

(*a*) Compressor head curve
(*b*) Piping impedance (including phase characteristics)
(*c*) The (quiescent) operating point
(*d*) Pulsation frequency content

These characteristics can be quantitatively simulated using electronic simulation techniques.

(*ii*) External pulsations can cause the onset of compressor surge at flows substantially above normal surge point, and the mechanism of surge inducement is relatively well understood.

(*iii*) Surge frequency is a function of piping acoustic response and is largely unrelated to compressor internals once the compressor head curve is established.

(*iv*) By using electronic analog simulation techniques, rather effective estimates can be made of the actual machine surge point and surge frequency if a reliable head curve is available.

(*v*) Surge characteristics of a machine (amplitude, onset and frequency) as measured on the test stand will bear little resemblance to that observed in the field, unless flow conditions, piping configuration, and external pulsations (if any) are the same.

(*vi*) Use of a piping system with a high acoustic impedance at the compressor location can virtually eliminate any noticeable surge effects and can permit operation well behind the normal peak point on the head curve.

(*vii*) High impedance piping, however, can increase the tendency of the compressor to amplify suction pulsation levels and may result in high amplitude (nonsurge) pulsations throughout the compressor piping.

(*viii*) Severe length resonances in the suction and discharge piping should be avoided in design, as these can amplify the natural perturbations (flow-induced vortex formations, etc.) to the point that physical damage can result, or the machine is thrown into premature surge.

(*ix*) Complex system resonances (involving both suction and discharge piping) should be analyzed at the piping design stage and detuned where possible. Compressors should be located in the piping so as to avoid the velocity maxima points of strong acoustic resonances.

Acknowledgment

This paper is based upon research conducted at Southwest Research Institute for the Southern Gas Association's Pipeline and Compressor Research Council.

Aerodynamic Tests on Centrifugal Process Compressors—the Influence of the Vaneless Diffusor Shape

K. Ludtke
Manager, Aerodynamics
Tubocompressors,
Borsig GmbH,
Berlin, West-Germany

Shop performance tests were conducted on a four-stage industrial centrifugal compressor. The first stage consisted of a radial plenum inlet, an open inducer type impeller with high hub/tip ratio and radial exit blades, a short vaneless diffuser, and a scroll including a conical diffuser. These stages with high flow coefficients and high tip speed Mach numbers are sometimes used as a first stage with multistage process compressors to increase the volumetric capacity of the given casing and reduce the number of stages. We have four versions of the vaneless diffuser with a radius ratio of 1.46: wide parallel walled, narrow parallel walled, constant area tapered, and reduced area tapered. The influence of these modifications was tested within a tip speed Mach number range of 0.94 to 1.07. Improvement of turn-down was obtained by narrowing and tapering. But the two extremely narrow diffusers reduced the rated point efficiencies beyond acceptable limits. The wide parallel walled diffuser has the highest efficiency and the most unfavorable surge, whereas the constant area diffuser achieved 10 percent better surge without practically any detrimental effects on efficiency.

The Use of Open or Closed Impellers in Multistage Process Compressors

Multistage centrifugal compressors for the chemical industry are normally equipped with shrouded impellers with backward curved blades.

Open inducer type impellers with radial exit blades are sometimes used as a first stage for the purpose of increasing the volumetric capacity of a given casing and also to reduce the number of stages.

Due to a higher tip speed and a higher head coefficient this type of stage in conjunction with closed backward curved impellers increases the casing volume flow potential by 20 percent and generates a 100 percent greater polytropic head than a conventional backward curved shrouded wheel. Thus for multistage compressors it leads to a smaller frame size and one stage less, which represents a considerable amount of capital cost. Figure 1 shows an example of a ten-stage, two-casing steam turbine driven air compressor with a first stage open radial impeller.

Open radial impellers however have lower efficiencies, smaller turndowns, and flatter characteristic curves than conventional designs.

The lower efficiency and the flat curve of an individual stage do not have a significant impact on the overall performance of multistage compressors.

The small turndown, however, can spoil the compressor surge limit especially in the case of variable-speed turbine driven units, where constant discharge pressure part-load operation is achieved by speed reduction, which in turn means that the first stage surges first. Thus the compressor turndown is determined by the surge limit of the first stage.

A number of shop tests were conducted on the first stage of a four-stage air compressor to improve the surge limit.

The Test Compressor

The test compressor shown on Fig. 2 during the shop performance test is a four-stage steam turbine driven centrifugal air compressor with three intercoolers. The impellers are arranged back-to-back to reduce recirculation losses and are located separately between a radial inlet and a scroll. They are stepped down in diameter toward the discharge end for better efficiency (see the cross-sectional drawing on Fig. 3). The first stage is an open impeller with axial inducer and radial exit blades (blade exit angle 90 deg). The second and third stage are backward-curved impellers with twisted blades (so-called three-dimensional blades), fourth impeller has nontwisted two-dimensional blades.

The actual suction volume flow of 100 000 m^3/h is compressed from 1 to 7.5 bar at a speed of 7300 1/min. The turbine has a maximum power of 11 000 kW.

The first stage has an outer diameter of 920 mm and runs at the rated point with a tip speed Mach number of 1.00 (tip speed over inlet sonic velocity).

Contributed by the Gas Turbine Division of THE AMERICAN SOCIETY OF MECHANICAL ENGINEERS for presentation at the 28th International Gas Turbine Conference and Exhibit, Phoenix, Arizona, March 27-31, 1983. Manuscript received at ASME Headquarters, December 23, 1982. Paper No. 83-GT-87.
Copies will be available until January 1984.

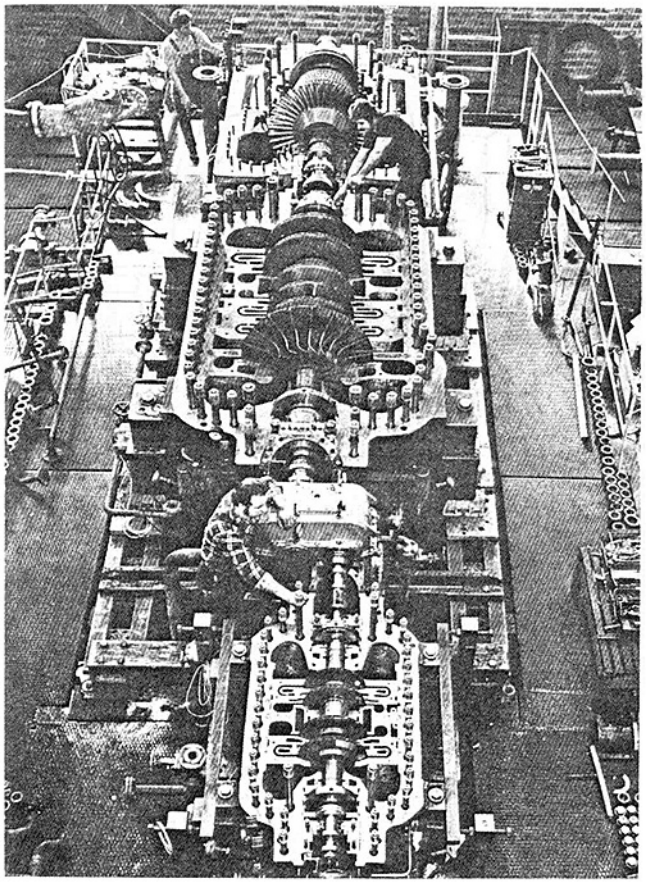

Fig. 1 Example of a steam turbine driven two-casing air compressor with first stage open impeller (not tested)

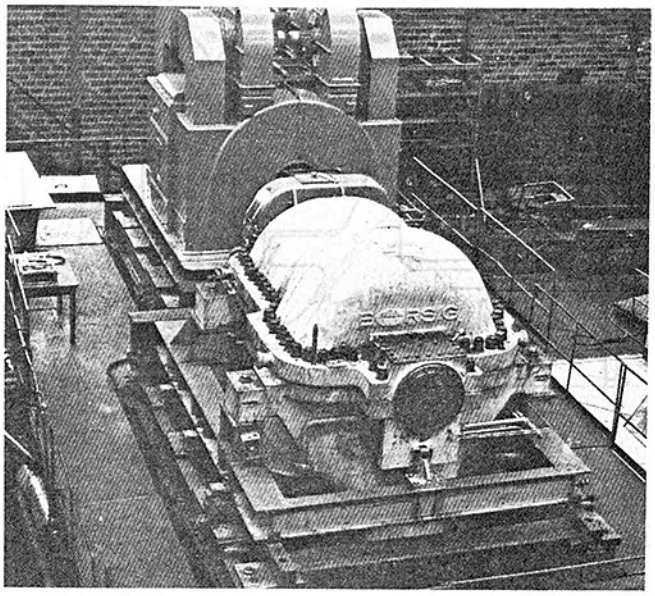

Fig. 2 The four-stage test compressor in the shop test facility

To cope with the requirements of rotordynamics, the hub-tip ratio of 0.293 is relatively high. Typical also for multistage process compressors is the relatively short vaneless diffuser ratio of 1.46 from wheel outlet to scroll inlet. The scroll, developing partly outside the casing body, is of the one-sided off-set type, whose cross section changes from circular to oval to save on axial length. The scroll is followed by a conical diffuser with an area ratio of 2:1. The inducer camberline is parabolic. The conical blades were cut from the solid hub material by means of a five-axis, NC-milling machine. To avoid blade vibrations, the inducer carries a narrow welded-on shroud band (for other dimensions see Fig. 4). The plenum inlet duct directs the flow from radial to axial direction. The inlet flange is 1000 mm in diameter. The discharge flange is 600 mm in diameter.

Objective of Tests

The tests concentrated on the crucial item of the compressor: the first stage. This specially designed high flow, high head stage, which is uncommon with industrial compressors, determines the feasibility of the concept outlined above. Stages 2, 3, and 4 are conventional standard components with well-known characteristics and favorable turndowns.

Two questions were to be answered by the test:

(*a*) Can the surge limit of the open impeller be improved without altering the impeller?

(*b*) Can the complete characteristic curve of a stage like that be shifted to smaller volume flows without changing the impeller?

Question (*a*) refers to the extension of the operational range

Nomenclature

d_2 = impeller tip diameter, m

h_p = pol. head at test condition,

$$\mathrm{RT}_s \frac{k\eta_p}{k-1}\left[\left(\frac{p_d}{p_s}\right)^{\frac{k-1}{k\eta_p}} - 1\right] \mathrm{kJ/kg}$$

h_{pred} = reduced polytropic head, $h_p\,(R_0 T_{os}/RT_s)$ kJ/kg

k = ratio of heat capacities, 1.4

M_{u_2} = tip speed Mach number at test condition, $u_2/\sqrt{\mathrm{k}RT_s \cdot 10^3}$

$\dot{m}$ = mass flow at test condition kg/s

p_d = discharge pressure (total) at test condition, bar

p_s = suction pressure (total) at test condition, bar

R = gas constant at test conditions, kJ/kg K

R_0 = 0.28705, reference gas constant (dry air), kJ/kg K

T_d = discharge temperature at test condition, K

T_{os} = 288.15, reference suction temperature, K

T_s = suction temperature (total) at test condition, K

u_2 = tip speed at test condition, m/s

$\dot{V}$ = $\dot{m}RT_s/(10^2 \cdot p_s)$ suction volume flow at test condition, m^3/s

$\dot{V}_{red}$ = $\dot{V}\sqrt{R_0 T_{os}/RT_s}$ reduced suction volume flow, m^3/s

φ = flow coefficient, $\dfrac{\dot{V}}{(\pi/4)d_2{}^2 u_2}$

ψ_p = pol. head coefficient, $h_p.2000/u_2{}^2$

η_p = polytropic efficiency (total to total),

$$\frac{k-1}{k}\,\frac{\ln(p_d/p_s)}{\ln(T_d/T_s)}$$

Subscripts

max = maximum

opt = optimum (η_p = max)

RP = rated point

SL = surge limit

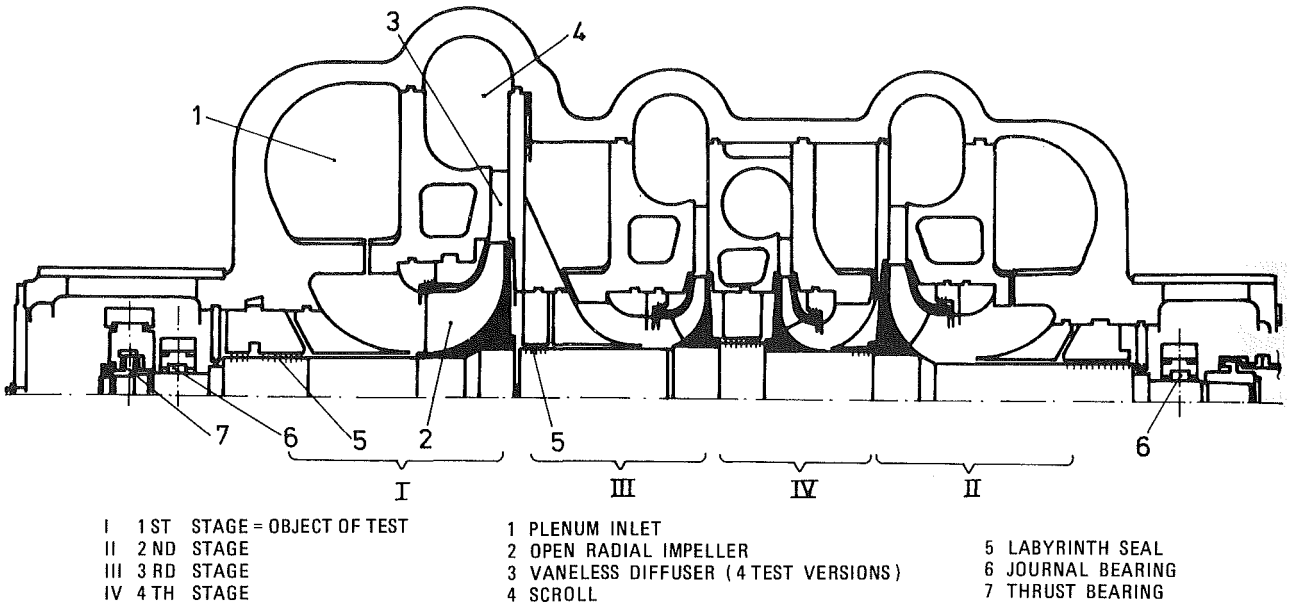

Fig. 3 Cross-sectional drawing of test compressor

of a multistage variable-speed compressor having a first stage open radial exit impeller. What are the consequences with regard to head, efficiency and other parameters?

The background of question (*b*) is more general: can a stage with a fixed-geometry open impeller be used for a range of rated volume flows rather than for one rate point only? This is relevant when planning on standardization by means of a finite number of fixed geometry components.

Test Variables and Test Program

It was decided to measure the performance curve of the first stage with four different versions of the vaneless diffuser (see Fig. 5).

	Axial width			
Version	impeller exit b_2 (at dia) mm	diffuser inlet b_3 (at dia) mm	diffuser exit b_4 (at dia) mm	diffuser shape
0	55(920)	55(940)	55(1340)	parallel walled, base geometry
2	55(920)	55(940)	29(1340)	highly tapered
2a	55(920)	55(940)	38(1340)	constant area
3	55(920)	29(1050)	29(1340)	parallel walled, width reduced

Version 0 is the most common diffuser design used with industrial centrifugal compressors; the diffuser width is the same as the impeller exit width.

Version 2 represents a diffuser that starts with the impeller exit blade contour angle and then gradually reduces its meridional area by 33 percent from inlet to outlet. Static pressure recovery takes place by reduction of the tangential velocity component only.

Version 2a is a diffuser with an approximately constant meridional area from inlet to outlet.

Version 3 is parallel walled from $d/d_2 = 1.14$ to 1.46 with a transition zone from 1.0 to 1.14 formed by a radius. The axial width of the parallel part is only 53 percent of the impeller exit width and there is the same area reduction of 33 percent from diffuser inlet to outlet as for Version 2.

The following test program was conducted in the shop test facility:

Version	suction p_s bar	conditions t_s °C	tip speed Mach number Mu2		
0	0.9-0.95	5-8	0.94	1.01	
2	0.88-0.97	8-10	0.94	1.01	1.07
2a	0.89-0.96	8-24	0.95	0.98	1.07
3	0.9-0.97	7-9	0.94	1.01	1.07

Test Arrangement and Instrumentation

The downward-oriented suction nozzle was directly connected by a straight pipe of 2.3 m length and 1000 mm dia to the large suction tunnel in the basement of the test facility. Three hundred and fifty mm upstream of the suction flange, four combined Kiel probes were located for total pressure and total temperature measurement spaced 90 deg.

Discharge total pressure and temperature were measured with two combined Kiel probes spaced 90 deg and located 400 mm downstream of the discharge nozzle with a 600-mm dia. As shown on Fig. 6, the mass flow was measured by a DIN 1952-orifice in the 800-mm dia discharge pipe with $10 \times D$ and $5 \times D$ of straight pipe before and after the orifice, respectively. Flow equalizers and straighteners were located in the suction pipe and before and after the orifice. Flow measurement was checked by Prandtl-tube measurement in the suction and discharge pipe in two planes in each case. Curve points were set by actuation of a butterfly valve of DN 800 on the discharge side. A second valve of DN 400 served for approaching the surge limit, being detected by piezzo quartzes located in the suction pipe in conjunction with an oscillograph. During the measurement of the first stage the other stages were suction throttled and operated near their own surge points to reduce compressor power inlet.

The test driver used was a 6500 kW variable-speed electric motor of 1500 1/min with a gear increaser. Motor and gearbox are test facility equipment (see Fig. 2).

Test Performance Curves

Figures 7.1 to 7.4 present the measured performance curves

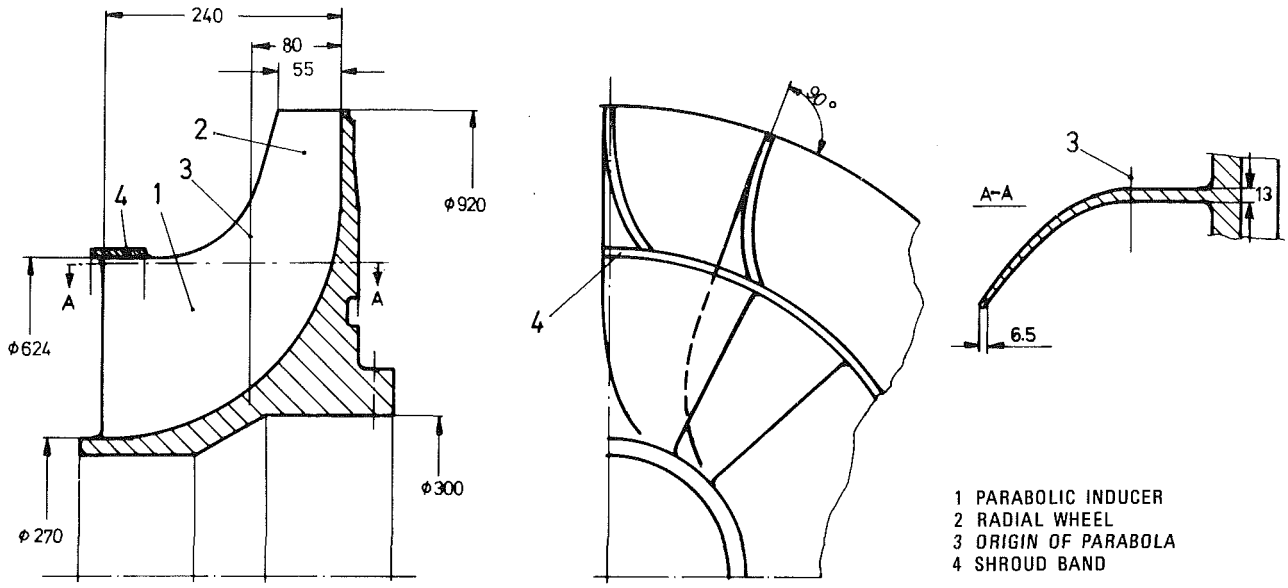

Fig. 4 The test impeller

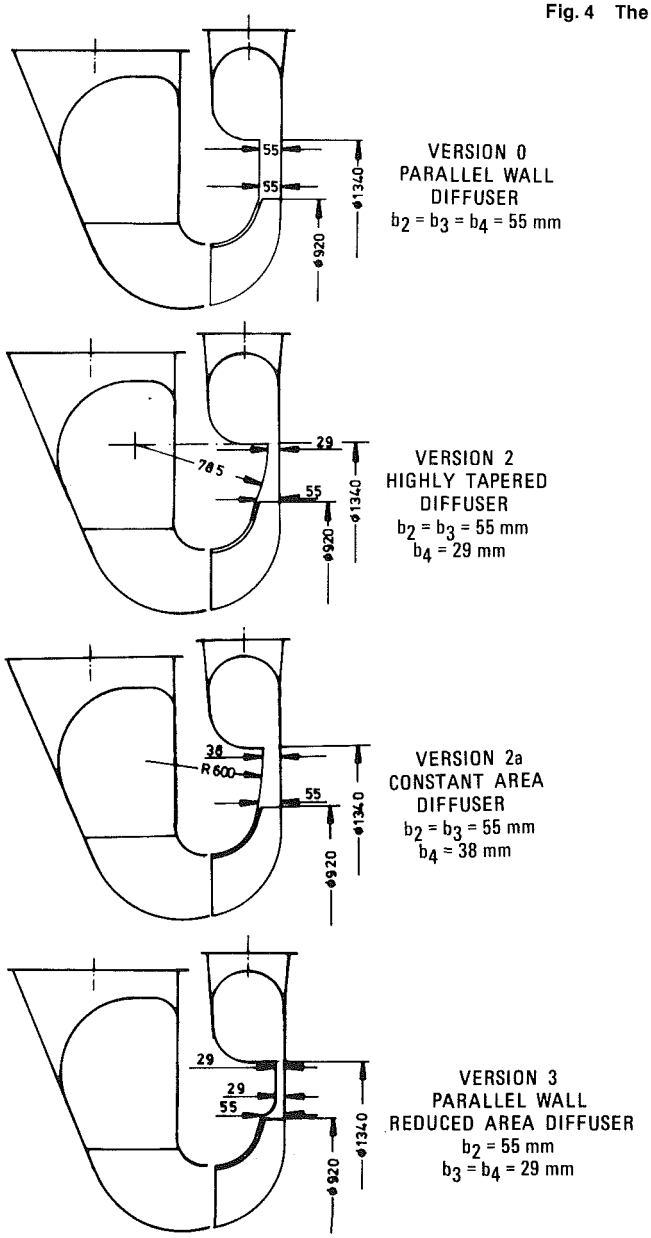

Fig. 5 Test diffuser modifications

in the form of reduced polytropic head and polytropic efficiency versus reduced suction volume flow with the tip speed Mach number as a parameter. The solid lines are measured, the dashed lines are interpolated or extrapolated curves and the dash-dotted lines are measured surge limits.

The reduced values are those that would have been achieved if the compressor had run under the reference conditions of $R_0 = 0.28706$ kJ/kg K (dry air gas constant) and $T_{so} = 288.15$ K (suction temperature) at the same tip speed Mach number as actually tested. Therefore all these performance curves can be compared directly with each other.

Comparative Test Evaluation

For the purpose of comparison the volume flow was converted into the flow coefficient φ, the polytropic head into the head coefficient ψ_p. Both are dimensionless.

Choke Point. Figure 8.1 shows the "choke flow coefficient" versus Mach number. The terms "choke" in this context is referred to as the "maximum measurable volume flow" under the described test conditions. It is only a few percentage points off the real choke, where the head is zero. The graph shows (besides the well-known fact that the maximum flow coefficient reduces with increasing Mach number) that the choke point of the base configuration (Version 0) is virtually not affected by diffuser tapering, neither by moderate (Version 2a) nor by radical tapering (Version 2). However a considerable reduction of parallel walled diffuser width of 47 percent (Version 3) leads to a choke point decrease of only 4 percent.

Surge Limit. Surge limit is defined at constant Mach number (or speed) as it can be detected by intensive pressure fluctuations on the oscillograph and by the characteristic noise. The surge-choke ratio is considerably improved by all of the diffuser modifications (see Fig. 8.2): At 0.95 Mach the surge-choke ratio of Version 0 is improved by 10 percent (Version 2a), 20 percent (Version 3) and 24 percent (Version 2); at 1.01 Mach the numbers are 12, 24, and 26 percent, respectively. If only surge is considered, Version 2 is the most favorable. Another conclusion can be drawn from these surge measurements: the surge-choke ratio of Version 0 deteriorates faster with increasing Mach number than all other versions because the diffuser exit area is too large for the higher compression and therefore more prone to flow instability.

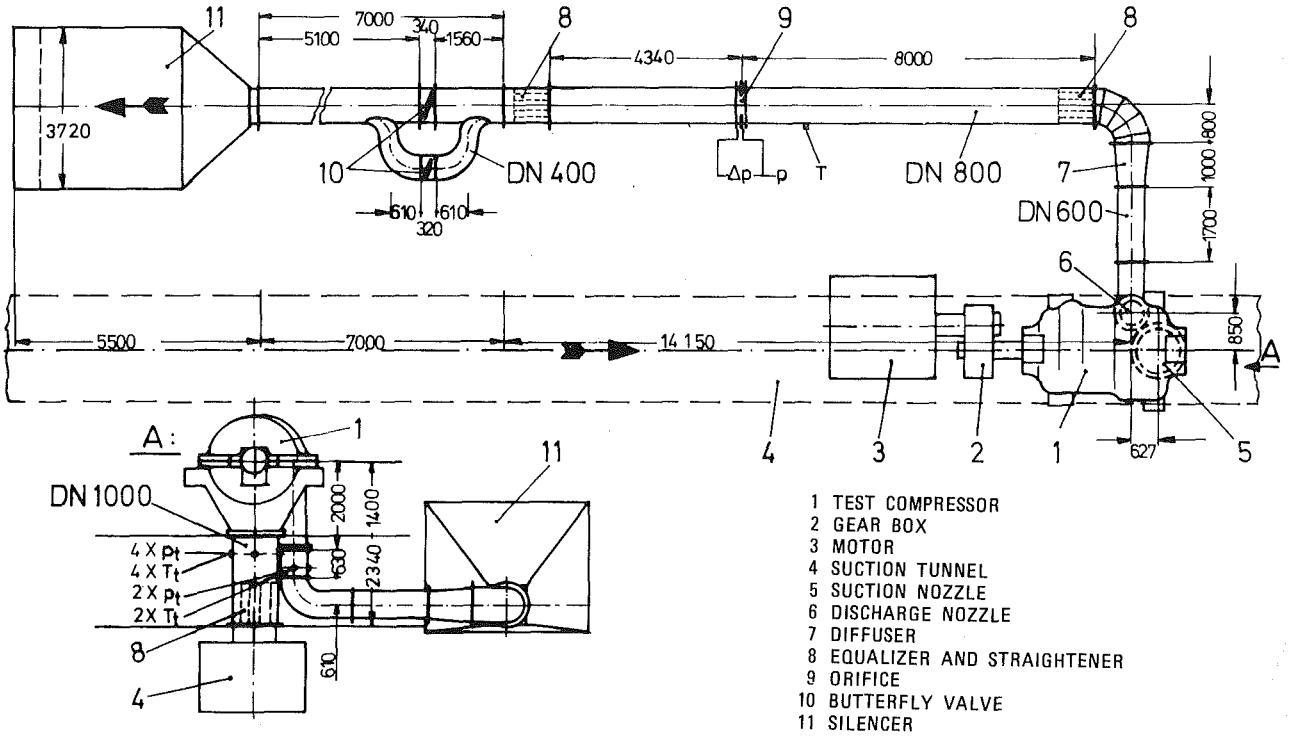

Fig. 6 Test arrangement

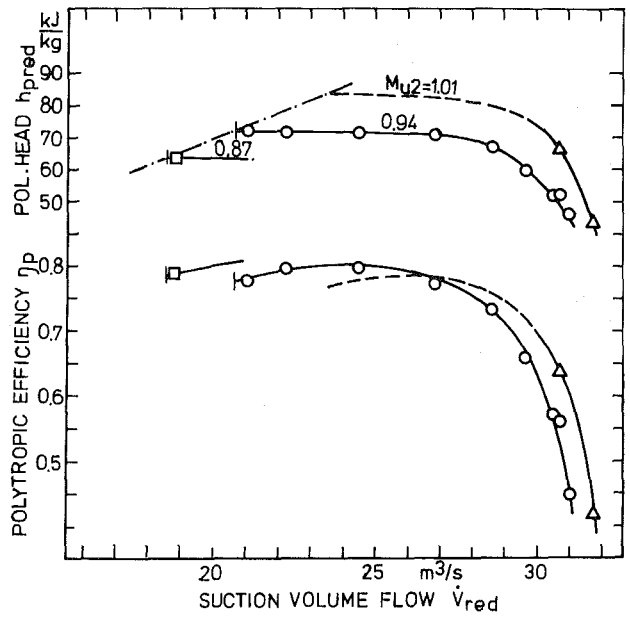

Fig. 7.1 Perfomance curves, version 0

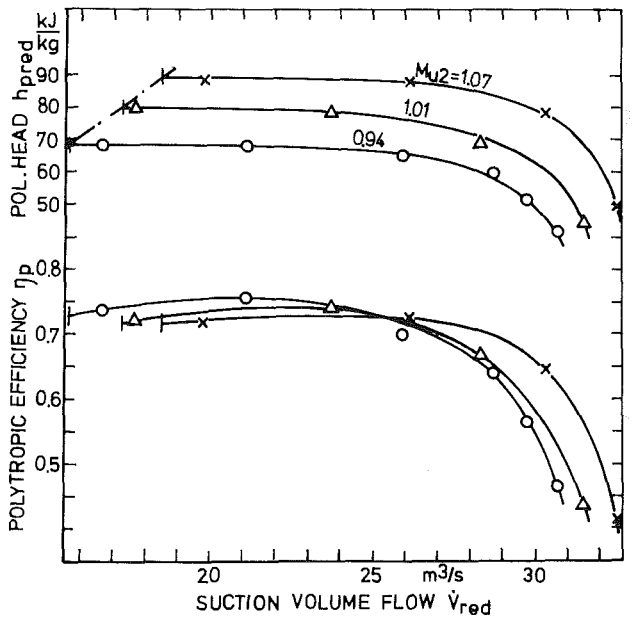

Fig. 7.2 Performance curves, version 2

Best Efficiency Point. Besides improvement of surge, one has to consider other criteria to fully assess the modifications. One of course is the efficiency maximum with the pertaining "optimum" flow and head coefficient. Efficiency in these tests is defined as flange-to-flange total polytropic stage efficiency including the losses of the radial inlet duct, impeller, diffuser, scroll, and conical diffuser. Version 0 has the highest efficiency of all modifications: 80 percent at Mach 0.94 and 78 percent at Mach 1.01. Version 2a is 1 point less, Version 2 is 5 points less at Mach 0.94 and 4 points at Mach 1.01. Version 3 drops even further to 6.5 (Mach 0.94) and 5.5 points less (Mach 1.01)!

Figure 8.4 and 8.5 show that the narrower the diffuser, the more the optimum flow coefficient approaches the surge point. Version 2a sees an average shift of the optimum flow coefficient of minus 9 percent compared to the base version 0, version 2 shifts an average of minus 13 percent and version 3 even 34 percent, which in this case means: the surge is the best efficiency point (see Fig. 8.5).

What these results boil down to is the following: diffuser narrowing not only reduces the maximum efficiency but also shifts the maximum efficiency closer to the respective surge points, which yields another reduction for the possible rated point! The rated point must be reasonably located between the

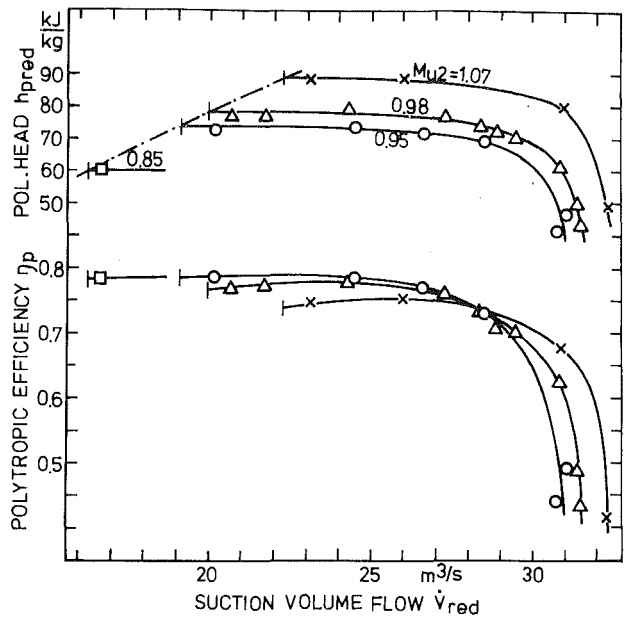

Fig. 7.3 Performance curves, version 2a

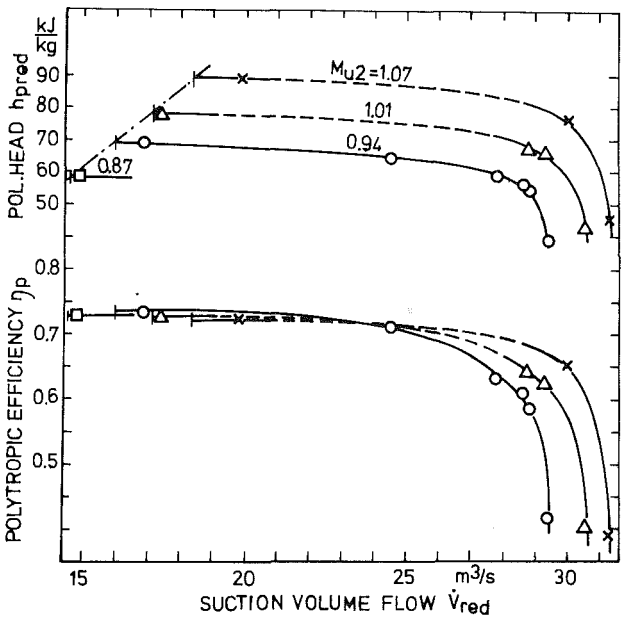

Fig. 7.4 Performance curves, version 3

choke and the surge and should preferably, but not necessarily, coincide with the optimum if the optimum in turn comes too close to the surge. In these cases the rated point must be an off-optimum point!

Diffuser width reduction not only means efficiency and optimum flow decrease. It also results in decreasing polytropic head coefficients, as can be seen from Fig. 8.6. At Mach 1.01, the head coefficient drops from 1.37 (version 0) to 1.35 (2a), to 1.34 (2), and to 1.305 (3). This means that for narrowed diffusers the polytropic head will be lower for a constant tip speed Mach number. To generate the same polytropic head, the Mach number is to be progressively increased because head coefficients tend to become smaller for higher Mach numbers (see Fig. 8.6).

Rated Point. Since for this type of impeller the best efficiency point cannot always be identical with the rated point, as has been shown, we must differentiate between optimum

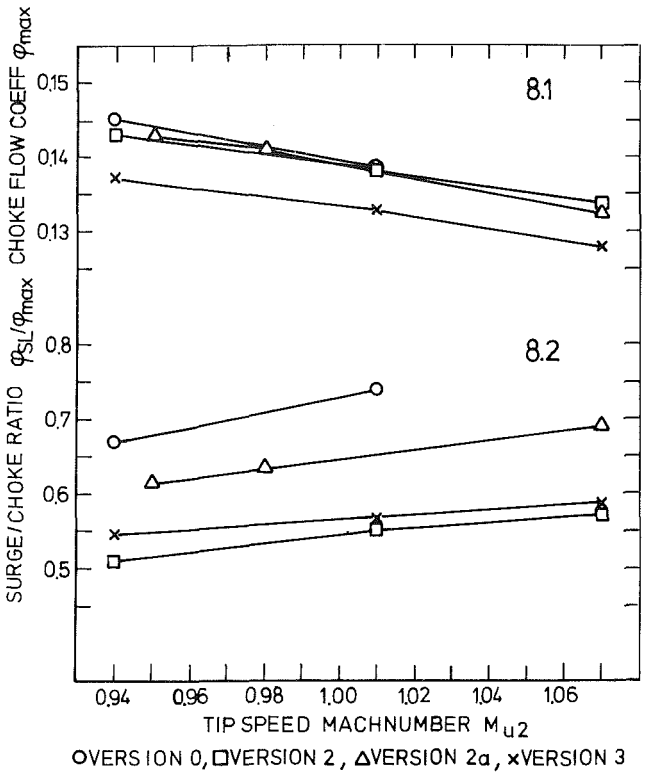

Fig. 8.1–8.2 Comparative test evaluation, choke and surge

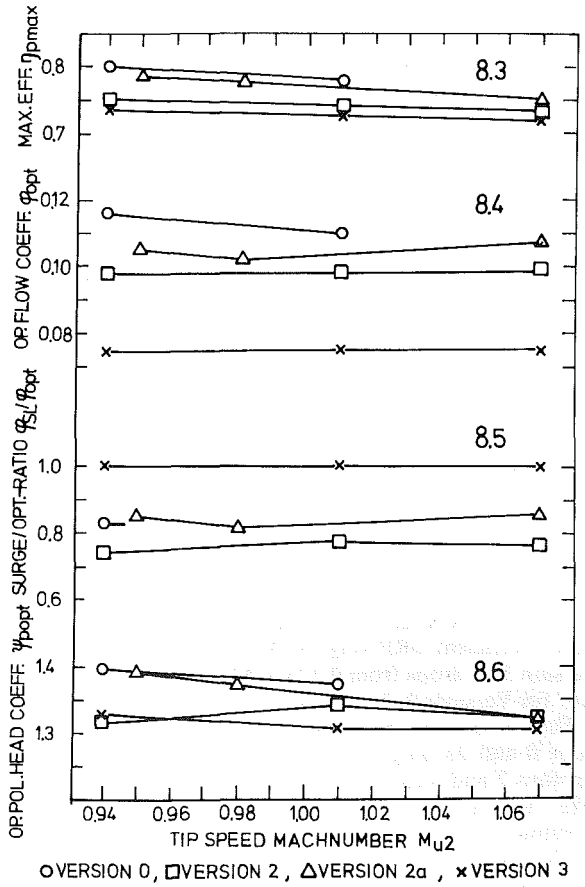

Fig. 8.3–8.6 Comparative test evaluation, best efficiency point

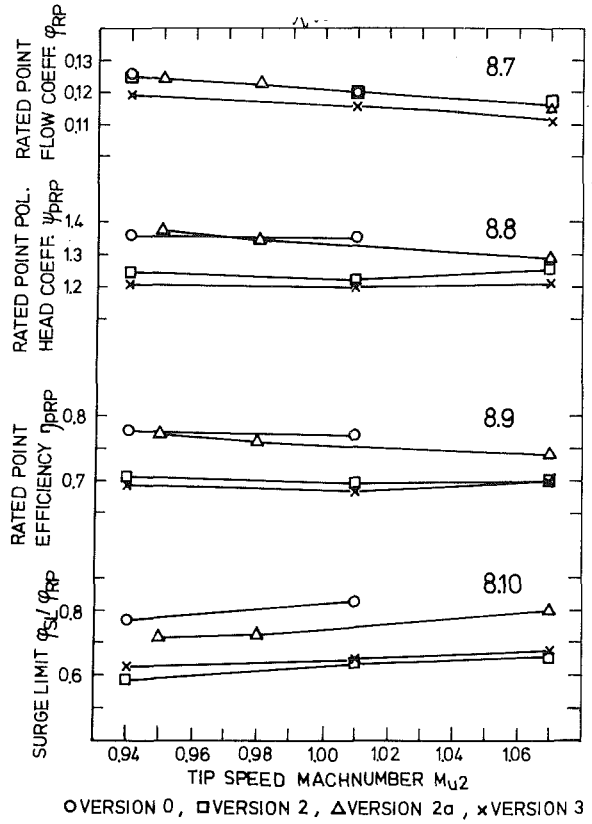

Fig. 8.7-8.10 Comparative test evaluation, rated point

and rated point. The latter, sometimes referred to as "design point" normally represents, in conjunction with the individual rated points of the other stages, the guarantee point of the compressor. How can a reasonable rated point of the test stage be defined? There is no generally valid answer. If the specification calls for a turbine driven compressor with favorable turndown and the open radial impeller is only one stage among others, the rated point should be placed as far away from surge as possible, which reduces rated point efficiency, polytropic head coefficient, and overload range. If a constant speed multistage compressor is specified where the compressor surge is normally determined by the individual surge limit of the last stage, the rated point of the open radial stage should be placed closer to the optimum, resulting in a higher efficiency and overload range, but in a less favorable surge of this stage, which in this case does not affect so much the overall compressor performance.

So the location of the rated point depends to a large degree on the specific application. To have a basis for further discussion the rated point was placed such, that for all of the measured curves the choke point was assumed to be 115 percent of rated. The charts on Figs. 8.7 to 8.10 are basis on this assumption:

Since φ max is one single line (Fig. 8.1) so is the rated point flow coefficient φRP (Fig. 8.7), again with the exception of Version 3. It drops from 0.125 at Mach 0.94 to 0.116 at Mach 1.07 for Versions 0, 2, and 2a.

The rated point head coefficients and efficiencies of versions 0 and 2a only differ by 3 percent maximum, whereas versions 2 and 3 cause a significant drop of both parameters (Fig. 8.8 and 8.9): 9 percent (version 2) and 11 percent (version 3) less than version 0.

The surge-rated point ratio (Fig. 8.10) is similar to the surge-choke ratio (Fig. 8.2): it deteriorates with rising Mach number and improves with diffuser narrowing. At Mach 1.01 the surge limits are: 83 percent (version 0), 75 percent (2a), 65 percent (3), and 63 percent (2).

So diffuser tapering and narrowing improve surge considerably and leave the rated volume flow virtually unchanged, but lead to severe sacrifices in polytropic head and efficiency.

Conclusions

The Optimum Test Diffuser. An overall relative assessment of choke, surge, optimum, and rated point criteria for the diffuser versions results in the following table:

		Diffuser versions			
		0	2	2a	3
Choke	φ_{max}	+	+	+	−
Surge	φ_{SL}	−	+	+	+
Optimum	$\eta_{p\,max}$	+	−	+	−
Location of optimum	φ_{op}	+	+	+	−
Rated point	φ_{RP}	+	+	+	−
	$(\psi_P,\eta_P)_{RP}$	+	−	+	−

+ . . . .positive assessment
− . . . .negative assessment

Version 3. For the tested Mach number range of 0.94 to 1.07, the radical parallel width reduction of the diffuser (version 3) achieves favorable surge limits of between 63 and 69 percent relative to the rated point (Fig. 8.10). All other criteria have to be rated negative: the choke and rated volume flow reduce by 4 percent average; the maximum efficiency is the lowest of all versions: 72 to 73 percent (Fig. 8.3); the optimum volume flow coincides with the surge, so that the rated point sees another efficiency decrease down to values of 69 and 70 percent (Fig. 8.9). This drop of 8 efficiency points from version 0 is excessive even in case of process compressors with 10 stages and more. Version 3 therefore is not acceptable.

Version 2. The radical diffuser tapering leads to the most favorable surge limit of all versions: 59 to 65 percent relative to the rated point (Fig. 8.10). The choke volume flow is identical with version 0. The optimum is reasonably located away from surge (Fig. 8.4 and 8.5). Rated point polytropic head coefficient and efficiency however are below normally acceptable limits (7 points efficiency drop from version 0). Therefore, version 2 can only be applied in the rare cases where a multistage process compressor has to operate at low part-loads most of the time at the cost of the rated point efficiency; that may lose 2 to 4 points depending on the number of compressor stages.

Version 0. For the Mach numbers tested, the wide parallel walled diffuser yields the most unfavorable surge limits of 77 to 83 percent (Fig. 8.10). At Mach 1.07, which was not tested on this version, surge may extrapolate to 90 percent. All other criteria are rated positive: the highest maximum efficiencies (Fig. 8.3), highest optimum flow and head coefficients (Figs. 8.4 and 8.6), and the highest rated point head coefficients and efficiencies (Figs. 8.8 and 8.9) of all versions. Version 0 should not be applied in cases where a large turndown is essential and a variable-speed prime mover is used. In case of constant-speed prime movers with compressor suction throttling, the first stage surge may be less relevant, since the compressor surge is normally determined by the last stage.

Version 2a. The constant area tapered diffuser gets an overall positive rating: the choke flow is identical with version 0 (Fig. 8.1); the surge limit is 72 to 80 percent relative to the rated point, an average 10 percent better than version 0 (Fig. 8.10); the maximum efficiency is only 1 point lower than version 0 (Fig. 8.3); the rated point flow and head coefficients are identical with version 0 and the rated point efficiency is zero to 2 points lower than version 0.

So a substantial surge improvement of 10 percent, which actually saves 10 percent energy at low partloads, is achieved at practically no sacrifices on the rated point efficiency of the multistage compressor.

Version 2a can be recommended in all cases where a favorable surge limit is required and the first-stage open impeller determines the compressor surge.

Surge Improvement And Shift of Characteristic Curves. Two questions were to be answered by the tests:

(*a*) Can the surge limit be improved?

(*b*) Can the performance curve be shifted?

Question (*a*) has a positive answer: Yes, the surge limit of a centrifugal compressor stage with the described geometry and aerodynamic parameters can definitely be improved by modifications of the vaneless diffuser without changing the impeller.

Question (*b*) has to be answered with "no." At the test Mach number range of around 1.0, overload and partload ranges of open impellers are relatively small compared to closed impellers with backswept blades. So the concept of a geometrically fixed standard impeller line with defined rating ranges rather than rating points, as they are used for closed impellers, has to be abandoned for high Mach number open impellers with radial exit blades. An individually designed stage with a thoroughly defined rating point should preferably be applied for this type of stage configuration.

Aerodynamic Tests on Centrifugal Process Compressors—Influence of Diffusor Diameter Ratio, Axial Stage Pitch, and Impeller Cutback

P. Lindner
Supervisor,
Research Department,
Borsig Gmbh, Berlin, West Germany

Almost all process compressors manufactured today are built in accordance with the fixed geometry modular system. It is not always possible to accurately predict the operational behavior of a compressor, particularly in such cases where a deviation from the standard solution is advisable or even necessary. This paper describes and analyses by means of experimental measurements the influence of three different stage modifications (axial stage pitch, shortening of the vaneless annular diffusor, blading cut-back). The results given here are directly related to engineering practice as they enable the design engineer to apply realistic efficiences even for modified stages in the early planning stage.

Introduction

In 1971, the author's company commenced the construction of turbocompressors in accordance with the modular design system, by which all flow components such as impellers with their relevant diaphragms (annular diffusor, return vane stage, exit scroll, etc.) are fixed in their geometry. A considerably large number of modular elements can be obtained by adopting a system of sufficiently close gradiation in geometric dimensions. This system thus allows coverage of all possible cases of application.

The basic idea behind the modular design system is this: we assign to each stage an adequately limited "rating range" rather than a "rating point."

The family of impellers, theoretically developed based on the aerodynamic laws of similarity, have backward curved blades and cover a φ-range of 0.01 to 0.1. Narrow impellers (small φ-value, small eye diameter) have nontwisted blades; wide impellers (large φ-value, large eye diameter) by contrast have twisted blades for better adaption to local flow conditions. The impeller outlet width is graduated in 2 steps in order to cope with the greater reduction in volume involved with the compression of heavier gases in the impeller such as higher hydrocarbons, chloride, freon, etc.

The annular diffusors that follow the impeller are vaneless and have parallel walls. The diffusor-diameter ratio is the same for all types of impellers and is $DF = 1.65$ (except in the case where the impeller is functioning as a final stage).

The inwardly directed return vane blading serves to reduce the vortex in the medium flow. Depending on the compressor size, 18 to a maximum of 24 nontwisted profile blades are arranged in the return vane passage. The described standard, impellers which were developed on a theoretical basis, were experimentally tested during a comprehensive test program in the shop test facility.

During these tests the impellers are either tested individually or in pairs, with or without a scroll in a compressor frame of the normal series. Measurements carried out were not just limited to the suction and discharge nozzles. In fact, measurements were carried out in the flow passages of the diaphragms. By means of this method we obtain detailed information on loss distribution in the various flow components in addition to measured characteristic curves for the individual impeller types.

Objectives

Based on this knowledge we then proceeded to systematically extend the test program. Measurements were carried out on stage modifications for the purpose of finding out what influence

(*a*) a shortened annular diffusor, or
(*b*) a change in the axial stage pitch, or
(*c*) blading cut-back

has on the operational behavior of a compressor stage.

The tests are directly related to engineering practice. Case dimensions are essentially determined by means of the diffusor-diameter ratio and axial stage length in multistage process compressors with vaneless annular diffusors. If a compressor stage with given impeller geometry is to achieve a good stage efficiency, then the vaneless annular diffusor must not be selected too small. On the other hand, a diffusor which is too long must be avoided for cost reasons. By reducing the axial stage pitch, either the shaft can be shortened (this can be significant from the aspect of rotor-dynamic properties) or the number of stages per shaft can be increased.

Contributed by the Gas Turbine Division of THE AMERICAN SOCIETY OF MECHANICAL ENGINEERS for presentation at the 28th International Gas Turbine Conference and Exhibit, Phoenix, Arizona, March 27-31, 1983. Manuscript received at ASME Headquartes December 28, 1982. Paper No. 83-GT-172.

Blade cutbacks are always necessary in such cases where the user specifices adherence to certain interim pressures or requires limitation of the rotational speed, and/or when maximum stage discharge temperatures are not to be exceeded during compression of certain gases such as chlorine. Test results are dealt with and discussed in this paper.

Influence of the Axial Stage Pitch

Test Objectives. For economical reasons, we are endeavored to fulfill the customer specifications (e.g., discharge pressure or polytropic head) with the minimum possible number of casings, meaning, we try to accommodate as many impellers as possible on one shaft.

When impellers with a particularly high maximum intake capacity are used, the number of stages per shaft upwards is limited. A long and thin shaft (which is then considered soft and tends to bend easily) results from the use of small hub diameters and the large axial widths of such high capacity impellers.

If back-to-back impellers are required for balancing axial thrust, the bearing span must be increased because of the balance piston located in the shaft center. The shaft as a whole must be increased in length. Long and thin shafts have considerable static deflection and this has its disadvantages from the aspects of rotor dynamics.

Assuming rigidly supported bearings, the ratio of the first critical speed to the operating speed is about or below 40 percent. If we also consider that the damping properties of the oil film in the bearings produce a further reduction of the first critical speed (as opposed to the value calculated with rigidly support bearings), then resonances with higher natural frequencies are unavoidable (particularly with high-speed compressors).

Safe and reliable operation is possible in this particular case due to the oil film damping and the associated limitation of the vibration path amplitudes in the bearings. However, the API 617 (Nov. 1979) states that no critical speed (such speeds where the vibration path amplitudes indicate maximum peaks) are allowable in a range of 15 percent below the lowest operating speed and 20 percent above the highest operating speed. Remedies can only be provided in such cases when the stiffness of the shaft is improved as a whole for design engineering aspects. With impellers having a given geometry there is only then the possibility of shortening the bearing span by reducing the axial stage pitch.

The axial stage pitch referred to here is understood as the span between the return blading and the impeller hub disk, Fig. 1. A small axial stage pitch now implies that the flow, after leaving the return vanes, must be guided in a very short distance from the radial into the axis parallel direction.

Compared to the configuration of a large axial stage pitch, it is no longer possible to smooth out any irregularities in the exit velocity profile of the return vanes. The follow-up impeller is thus negatively influenced.

However, it can be expected that major gradients occur in the velocity distribution as a result of a sudden and sharp change of flow direction. The flow to the follow-up impeller is thus affected with a resulting deterioration of efficiency.

In order to examine the influence of the axial stage pitch we

Nomenclature

a = axial stage length, mm
a_{0t} = sonic velocity at compressor inlet, m/s
b_2 = exit blade width (identical with diffusor width), mm
c = absolute velocity, m/s
d = diameter, mm
DES = blade cutback ratio, $DES = d_2^*/d_2$
DF = diffusor diameter ratio, $DF = d_4/d_2$
h_p = polytropic head, kJ/kg
l = axial impeller length, mm
LS = axial stage pitch, $LS = a/d_2$
M_{u2} = tip speed Mach number
N = rotational speed, rpm
p = pressure, bar
R = gas constant (R = 0.288 kJ/kg K for air), kJ/kg K
s = slip factor
t = temperature, K
u_2 = tip speed, m/s)
$\dot{V}$ = volume flow, m^3/s
w = relative velocity, m/s
z = compressibility factor (z = 1.0 for air)
k = isentropic exponent (k = 1.4 for air)
φ = inlet flow coefficient
φ_3 = exit flow coefficient
Ψ_p = polytropic head coefficient
η_p = polytropic efficiency

Subscripts

0 = compressor inlet (suction nozzle, measuring plane "S")
1 = impeller inlet
2 = impeller exit
3 = behind impeller exit, diffusor inlet
4 = diffusor exit
D = discharge diffusor (measuring plane "D")
opt = optimum
p = polytropic
t = related to total conditions
* = blading cutback

Formulas

polytropic head

$$h_p = z_{0t} \cdot R \cdot t_{0t} \frac{k}{k-1} \cdot \eta_p \cdot \left[\left(\frac{p_{Dt}}{p_{0t}} \right)^{\frac{k-1}{k \cdot \eta_p}} - 1 \right]$$

polytropic head coefficient

$$\psi_p = 2 \cdot s \cdot \eta_p = \frac{2000 \cdot h_p}{u_2^2}$$

polytropic efficiency

$$\eta_p = \frac{k-1}{k} \cdot \frac{ln[p_{Dt}/p_{0t}]}{ln[t_{Dt}/t_{0t}]}$$

inlet flow coefficient

$$\varphi = \frac{4 \cdot 10^6 \cdot \dot{V}_{0t}}{\pi \cdot u_2 \cdot d_2^2}$$

exit flow coefficient

$$\varphi_3 = \frac{c_{m3}}{u_2}$$

sonic velocity at compressor inlet

$$a_{0t} = \sqrt{z_{0t} \cdot k \cdot R \cdot t_{0t} \cdot 10^3}$$

tip speed Mach number

$$M_{u_2} = \frac{u_2}{a_{0t}}$$

rotational speed

$$N = \frac{6 \cdot 10^4 \cdot u_2}{\pi \cdot d_2}$$

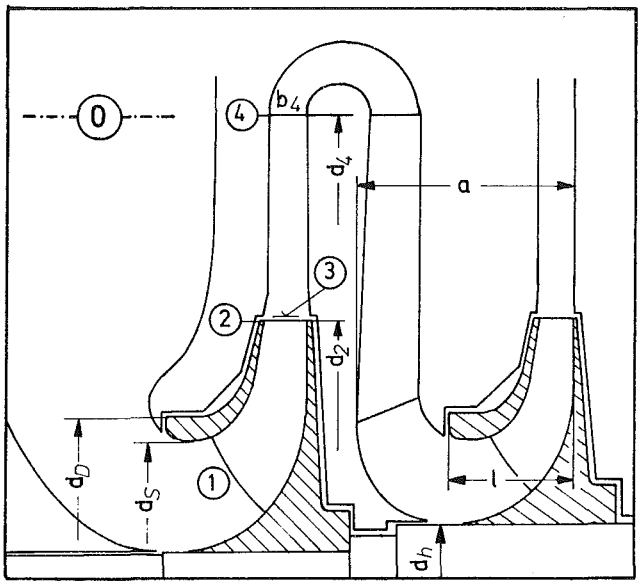

Fig. 1 Compressor stage geometry

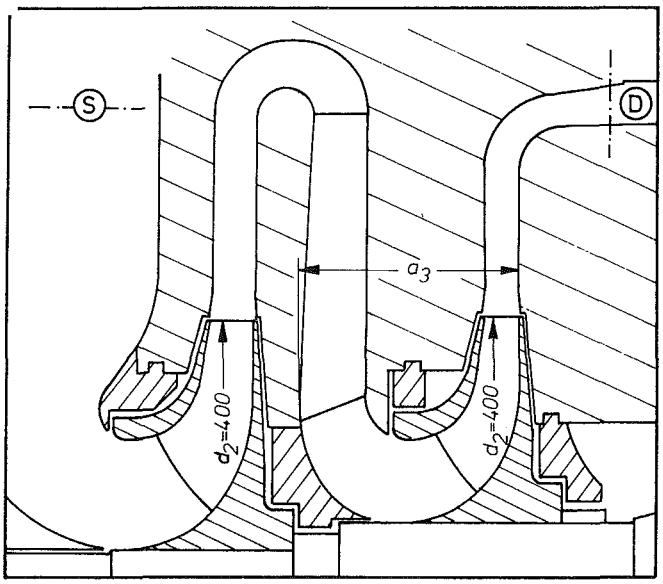

Fig. 2 Arrangement of impellers to investigate the axial stage pitch, test series A (high flow coefficient impellers), normal stage pitch (LS = 0.347)

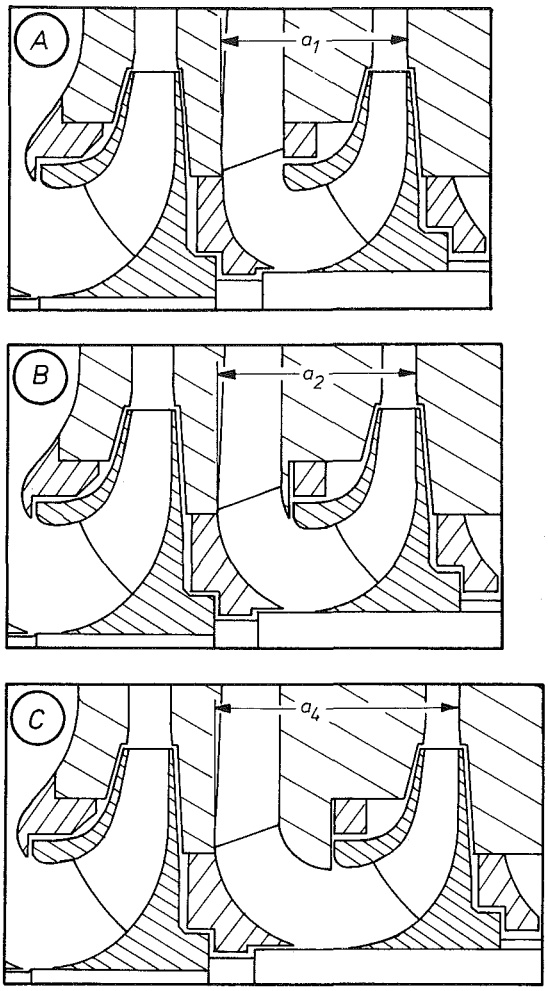

Fig. 3 Modification of the axial stage pitch, test series A (high flow coefficient impellers): A, extreme minimum stage pitch (LS = 0.297); B, minimum stage pitch (LS = 0.321); C, maximum stage pitch (LS = 0.390)

have carried out tests with two different impeller combinations in the shop test facility.

Test Procedure. In the test series A, two impellers with high level intake capacities were examined. These impellers were in a compressor casing of the conventional series, Fig. 2. As already stated earlier on in this paper, the standard impellers with high level intake capacity have twisted blades. Both impellers have an outside diameter of d_2 = 400 mm. A vaneless annular diffusor with parallel side walls ($b_2 = b_4$; DF = 1.65), a 180 deg crossover bend with subsequent return vanes were arranged between the impellers. The axial stage pitch related to the impeller outside diameter was varied from LS = 0.297 to 0.390, Fig. 3.

The flow medium (in this case air) was admitted to the inlet impeller via a plenum inlet and leaves via a discharge diffusor arranged after a 90 deg bend after the vaneless annular diffusor of the second impeller.

The compressor was driven by a 600 kW-steam turbine (speeds: max. 9600 rpm) with a 1:1.7 transmission gear system. The test arangement can be seen in Fig. 4. The most important geometric data of the stage group is compiled in the Tables 1 and 2.

In the test series B two impellers with average intake capacity were examined in the same compressor casing, Fig. 5. The test arrangement is similar to that of the test series A. The impeller blades in this case are also backward-curved but are not twisted because of the narrow inlet ducts. The outside impeller diameter, as also in the case of test series A, was d_2 = 400 mm for both impellers.

Two different axial stage pitches, LS = 0.195 and 0.244, were examined. Tables 1 and 2 show the corresponding geometry data of the stage group for the test series B.

Combined Kiel-probes were used for data acquistion of total pressure and total temperature due to insensitivity to changes in the directions of flow. Measuring points selected were the suction nozzles (in Figs. 2 and 5 indicated by the measuring plane "S") and the discharge diffusor (indicated by the measuring plane "D" Figs. 2 and 5). The arrangement of the measuring points can be seen in Fig. 6.

Test Results. The results of the tests on the influence of the axial stage pitch are shown in Figs. 7–10 for the series A (impellers with high level intake capacity) and for the series B (impellers with average intake capacity) in Fig. 11.

The polytropic efficiency, η_p, and the polytropic head, h_p, versus the suction volume $\dot{V}_{ot}$ are entered. Thus, the

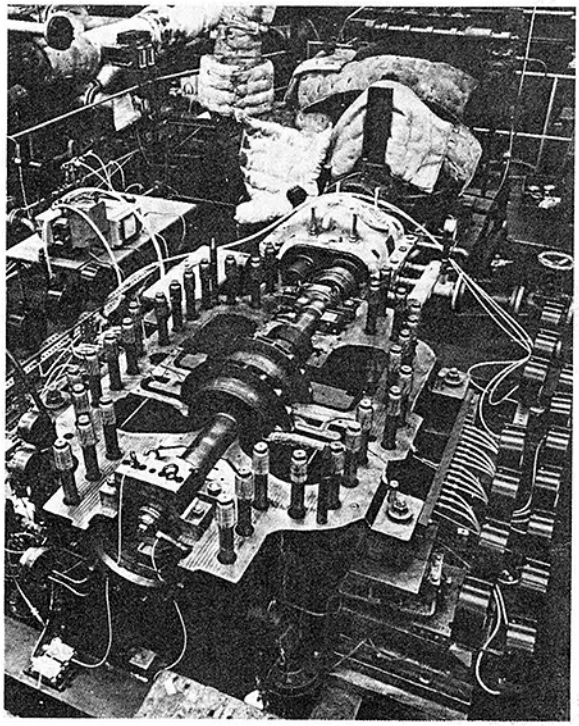

Fig. 4 Test compressor with removed upper casing half; picture shows high flow coefficient impellers, test series A

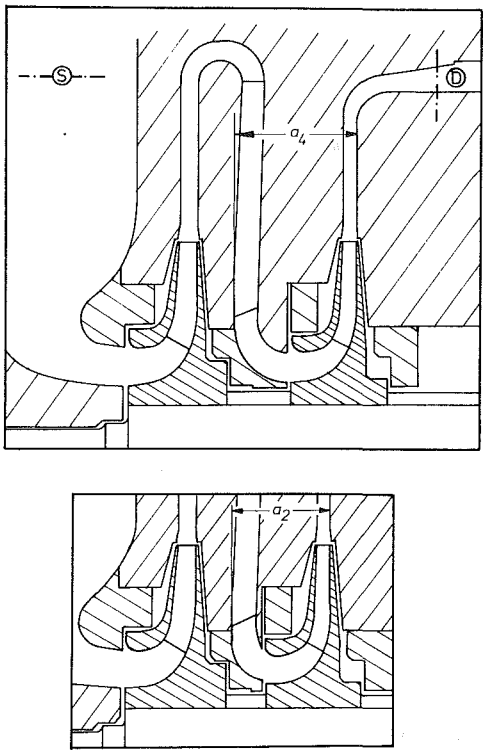

Fig. 5 Arrangement of impellers to investigate the axial stage pitch, test series B (medium flow coefficient impellers): Top, maximum stage pitch (LS = 0.244) Bottom, minimum stage pitch (LS = 0.195)

assumption that sharp changes in flow direction after leaving the return blading must be avoided is only partically confirmed.

With regard to series A, it is interesting to note that,

Table 1

Symbol	Dim.	Test Series A		Test Series B	
$b_2 = b_4$	mm	26.6	21.3	12.9	10
d_2	mm	400	400	400	400
d_4	mm	660	660	660	660
		Impeller 1	Impeller 2	Impeller 1	Impeller 2

Table 2

No.	Designation	LS = a/d_2	LS = a/d_2
1	extreme minimum	0.297	-----
2	minimum	0.321	0.195
3	normal	0.347	-----
4	maximum	0.390	0.244
		Test Series A	Test Series B

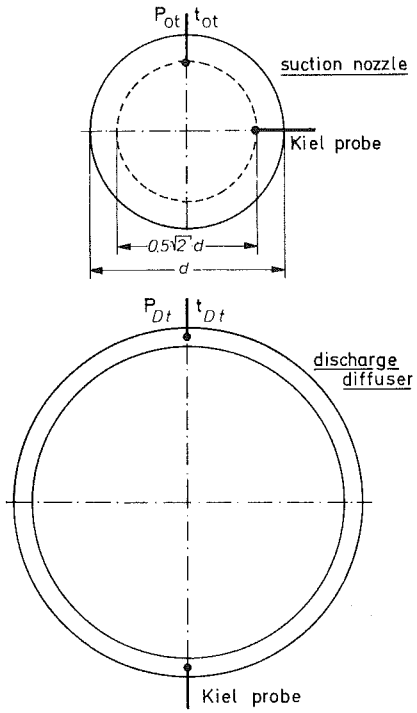

Fig. 6 Test instrumentation

disregarding the isolated scattered points due to measurement faults (LS = 0.321 in Fig. 7 and in part also LS = 0.390 in Fig. 10), the location and the level of the efficiency optimum are not influenced by a change in the axial stage pitch, Figs. 7–10.

Only a distinct deviation from optimum point indicates a growing deterioration of efficiency with decreasing axial stage pitch. The influence of the stage pitch is best seen near surge and choke range. In this case, a mild change in the direction of flow (large axial stage pitch) produces the best efficiency, whereas an abrupt change in the direction of flow (small axial stage pitch) produces the lowest efficiency, with an upward tendency as the tip speed increases.

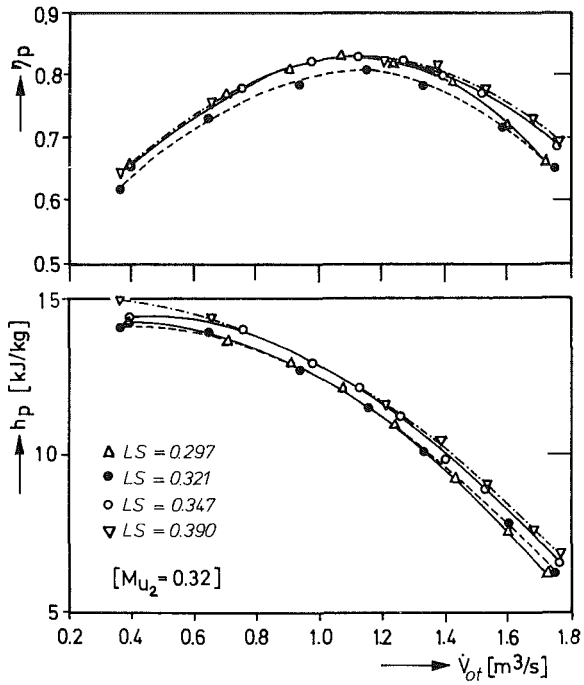

Fig. 7 Influence of the axial stage pitch, measured performance curves, test series A

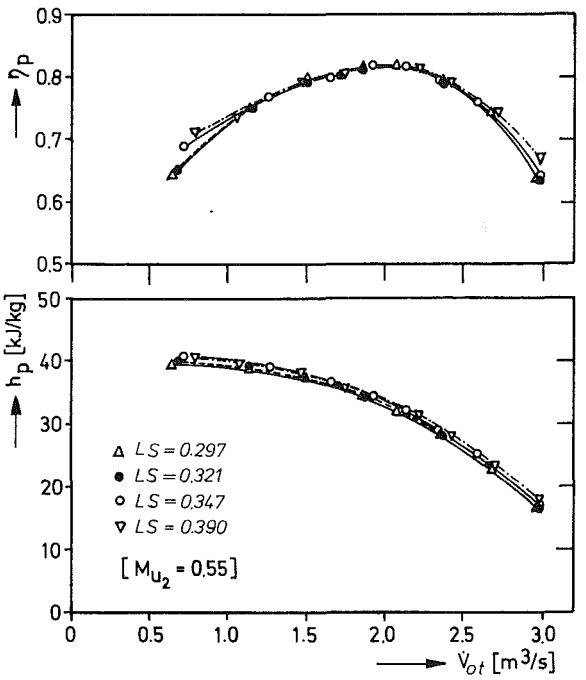

Fig. 8 Influence of the axial stage pitch, measured performance curves, test series A

With regard to the polytropic head, h_p, it is also interesting to note in the series A that there are no appreciable differences between maximum and normal stage pitch (LS = 0.390 and 0.347) on one hand and between minimum and extreme minimum stage pitch (LS = 0.321 and 0.297) on the other, up to average tip speed Mach numbers (Figs. 7–9).

The group with the smaller axial stage pitches over the entire range of the curve produces a 3 to 4 percent less polytropic head than the group with the larger axial stage pitches. If, however, the tip speed continues to increase ($M_{u2} \geq 0.75$), an increased spreading of the measuring values

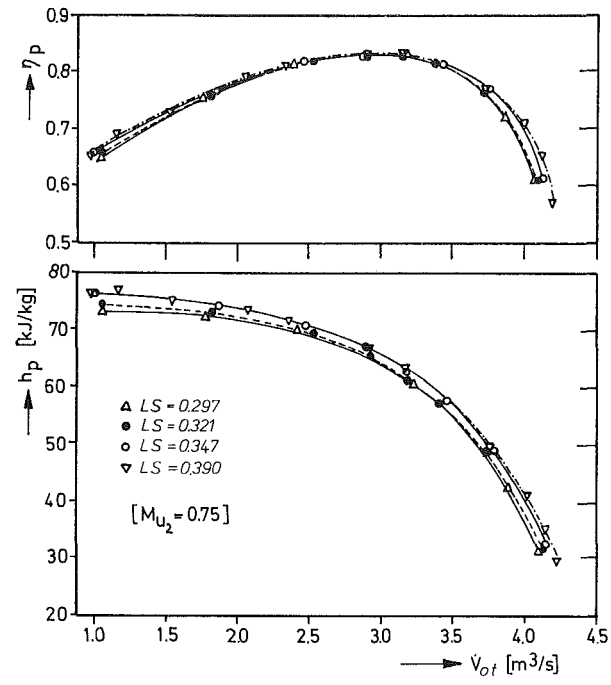

Fig. 9 Influence of the axial stage pitch, measured performance curves, test series A

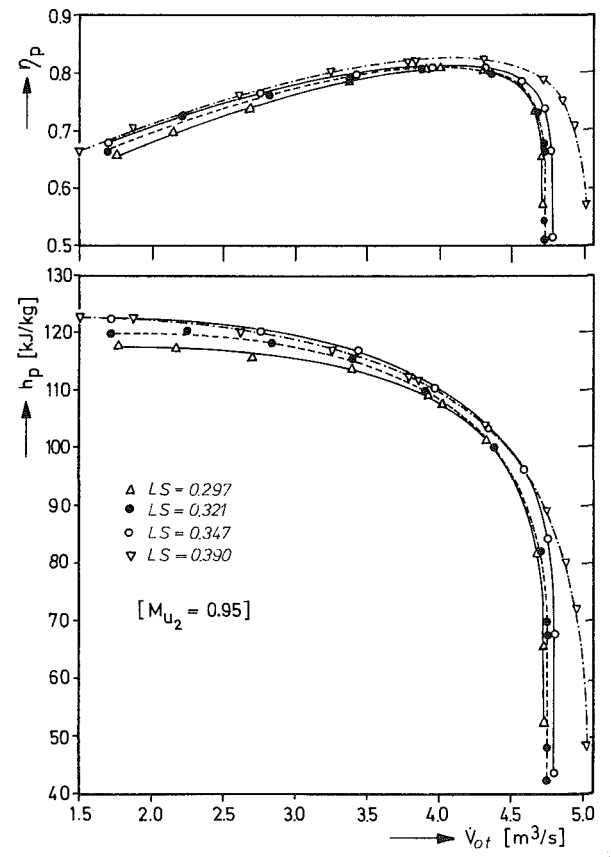

Fig. 10 Influence of the axial stage pitch, measured performance curves, test series A

between the minimum and extreme minimum stage pitch, particularly in the part-load range of the curve, can be found. On the other hand, this Mach number effect is not to be found at normal and maximum stage pitch, Figs. 9 and 10.

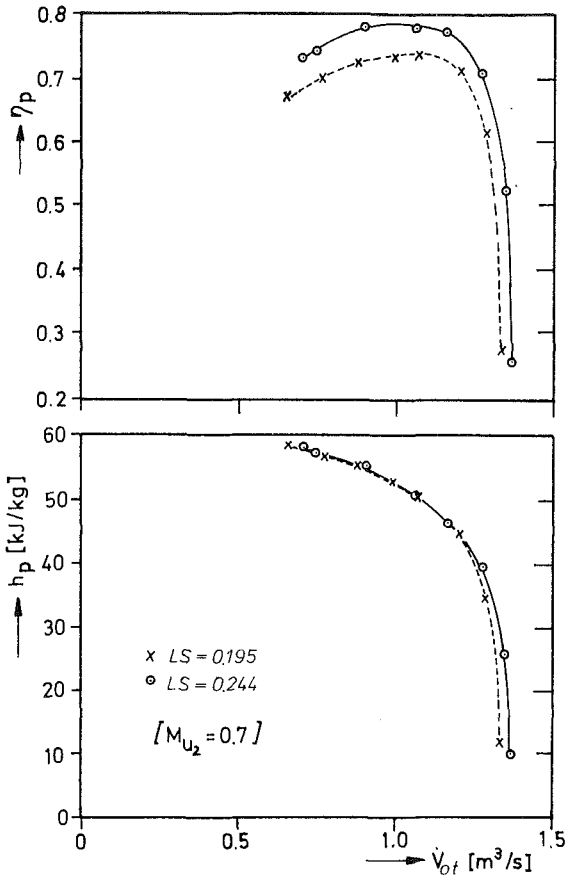

Fig. 11 Influence of the axial stage pitch, measured performance curves, test series B

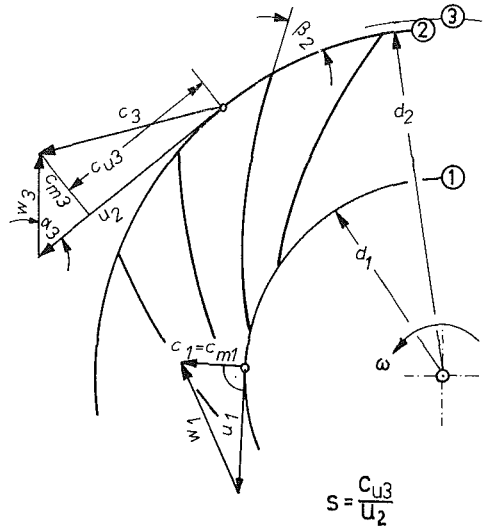

Fig. 12 Velocity triangles for impellers with backward curved blades

It is evident from Fig. 11 that the results of test series A simply cannot be transferred on impellers with various intake capacities.

In the test series B (impellers with medium intake capacity), the axial stage pitch has a considerable influence on the stage group efficiency behavior. Over the entire curve range the shorter axial stage pitch produces clearly inferior efficiency, Fig. 11.

The reason for this is that, where narrow impellers are concerned (small φ-value), the ratio of the labyrinth flow through the impeller seal to the main flow is greater than in the case of wide impellers. The labyrinth flow is fed transversely into the main flow within the inlet bend. With decreasing axial stage pitch the labyrinth flow now enters the main flow in an area with higher gradients in the velocity profile. The additional transverse component of the labyrinth flow increases the tendency to separation of the low energy flow particles in the main flow, so that there is the danger that a vortex can occur. If the vorteces separate they must be carried on by the main flow, thus constituting a loss of energy.

In summing up, the influence of the axial stage pitch can be interpreted as follows:

Subject to the smaller labyrinth flow (related to the main flow) and positively influenced by the otherwise smooth guidance of flow in the inlet bend, the influence of the axial stage pitch in wide impellers is only of subordinate importance. A reduction of the axial stage pitch of 18 percent (from $LS = 0.390$ to 0.321) does not produce any appreciable efficiency loss (in fact, the optimum point remains unchanged), while the polytropic head, h_p, drops on average by about 3 to 4 percent. However, where narrow impellers are concerned, the axial stage pitch has an appreciable influence. This is explainable by the effect of the transverse componente of the relatively large labyrinth flow when it enters the main flow. A reduction of the axial stage pitch of 20 percent (from $LS = 0.244$ to 0.195) causes a deterioration of the efficiency of approx. 7 to 10 percent.

Generally speaking, meaning, independent of the φ-value of the impellers, it can be said that by increasing the axial stage length, the curve range—except for high tip Mach numbers— is hardly influenced at all.

Influence of the Diffusor-Diameter-Ratio

Objectives. The annular diffusor downstream of the impeller serves the purpose of converting the relatively high kinetic energy in the gas into compression energy with a minimum loss.

Vaneless diffusors are presently applied in most cases in industrial compressors in order to achieve a wide operation range. Pressure conversion in vaned annular diffusors is in principle more efficient than in vaneless annular diffusors. However, the stator vanes have a certain influence on the impeller flow and this expresses itself—in addition to other effects—in a limitation of the stable operation range also.

Where stator vanes are concerned, the leading edges are no longer incident-free for off-design operation. Wake regions are formed which have a great influence on the diffusor exist velocity profile.

There are two significant disadvantages involved with the vaneless diffusor as opposed to the advantages (wide operation range, insensitivity to changed operating conditions, simple design):

(*i*) The vaneless diffusor is inferior to the vaned diffusor with regard to efficiency.

(*ii*) From the outlet velocity triangle (Fig. 12), it can be derived that an adequate pressure conversion can only be achieved by means of a significant reduction of the peripheral component of the velocity, c_u. According to the law of angular momentum for a nonviscous flow

$$r \cdot c_u = r_3 \cdot c_{u3} = \text{constant}$$

from which we can derive that the effectiveness of the vaneless annular diffusor almost exclusively depends on its diameter ratio, $DF = d_4/d_2$.

If good stage efficiencies are to be achieved, the radial extent of the diffusor must be selected large enough.

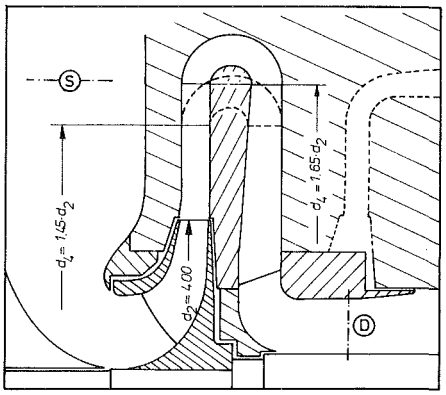

Fig. 13 Arrangement of impellers to investigate the diffusor diameter ratio

The following values for industrial compressors have been proven during the course of experience:

(*a*) Impellers with radial exit blades: $DF = 1.8$ to 2.0
(*b*) Impellers with backward curved blades: $DF = 1.6$ to 1.7

An increase of these values does not make sense. Due to a longer flow path, the dissipation losses increase and the static pressure recovery rises insignificantly in relation to the hardware cost.

However, if the diameter ratio falls short of the aforementioned values, the static pressure rise is imperfect and the stage efficiency decreases. Since the diffusor length determines the casing frame size (and therefore the hardware costs to a great extent), it is most important to find out about the optimum diffusor diameter ratio. In other words: How far can the diffusor length be reduced for a given efficiency reduction?

Since up to now the understanding of the complex flow mechanism is still fragmentary, theoretical models which describe diffusor losses do not supply generally accepted rules. Even the boundary layer theory cannot explain the influence of the opposite diffusor wall. Of course, from a physical point of view, it makes sense to break down the diffusor losses into friction and dissipation, but for numerical calculations one has to apply empirical assumptions.

Altogether, the calculation of optimum diffusor configurations on a theoretically basis can only be approximate. On the other hand the process compressor manufacturer must achieve a high prediction accuracy for the efficiency in order to fulfill contract guarantees. This also applies in cases where the design deviates from standard solutions. Therefore, the influence of diffusor diameter ratio was experimentally tested in the shop test facility in two test series.

Test Performance. In the first test series, the diffusor diameter ratio was $DF = d_4/d_2 = 1.65$. As described earlier in this paper, this is the normal diffusor for standard impellers not operating as a final stage with discharge scroll. The selection of the diffusor diameter ratio for the second test series was based on following facts:

The casing and the impeller diameter steps of the standard line are matched so that such a wide wheel, one step larger in diameter, can be put in the same casing if the diffusor ratio is reduced to $DF = 1.45$.

To conduct the tests, the same compressor was used that was described in the "Test Procedure" section (test series A); the second impeller, however, was removed and replaced by a suitable diaphragm part, Fig. 13. The stage geometry is given in Table 1, left column, the diffusor outer diameter is reduced, according to the selected diffusor ratio of $DF = 1.46$, to $d_4 = 580$ mm. For the shorter diffuser, the return vanes were completely redesigned.

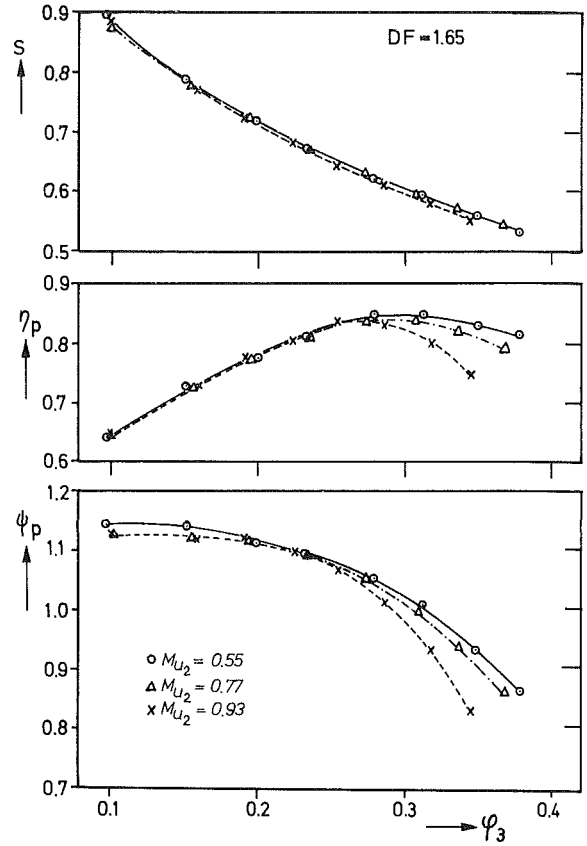

Fig. 14 Influence of the diffusor length, measured performance curves, long diffusor ($DF = 1.65$)

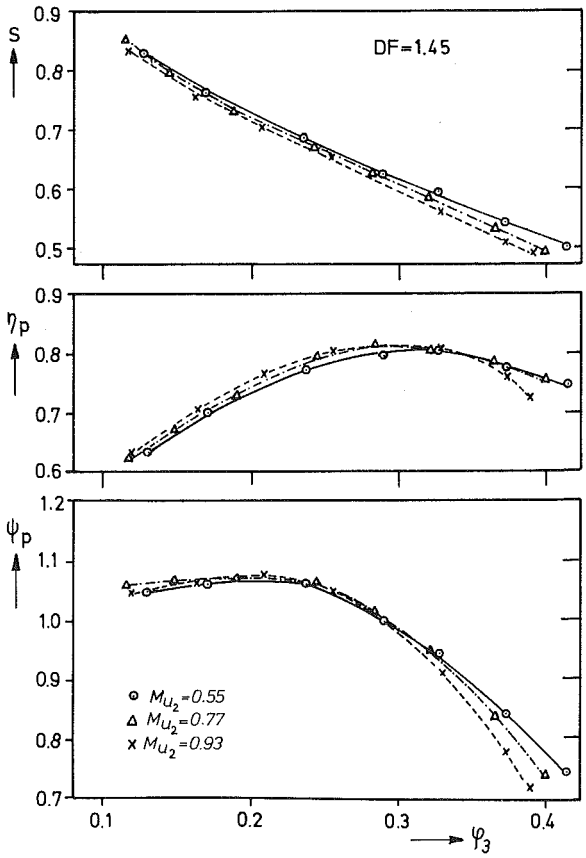

Fig. 15 Influence of the diffusor length, measured performance curves, short diffusor ($DF = 1.45$)

The measurement of total pressure and total temperature in the suction nozzle (measuring plane "S") and in the discharge diffusor (measuring plane "D") was carried out again with combined Kiel-probes. Test instrumentation was similar to that shown in Fig. 6.

Test Results. The test results on the influence of diffusor diameter ratio are given in Fig. 14 (long diffusor, $DF = 1.65$) and in Fig. 15 (short diffusor, $DF = 1.45$), respectively.

The chart shows the slip factor, s, the polytropic efficiency, η_p and the polytropic head coefficient, ψ_p, versus the exit volume coefficient φ_3. A comparison of both diffusors are shown on Fig. 16.

As expected, the pressure rise is imperfect by shortening the diffusor length, so that polytropic efficiency will decrease. A 12 percent diffusor ratio reduction causes an efficiency decrease of approximately 3 percent at optimum point. In the part-load range the efficiency decrease is as high as 5 percent.

Since the slip factor, s, is a characteristic impeller parameter, it remains constant in case of diffusor changes. Therefore, the polytropic head coefficient, ψ_p, behaves similarly like the polytropic efficiency, η_p.

The performance curve offset (Fig. 16) is remarkable. Compared to the long diffusor, the short diffusor causes an approximate 10 percent shift of the performance curve with regard to higher exit flow coefficients, φ_3. This can be explained by a lesser reduction of the meridional velocity component in the short diffusor.

As can be seen from the stage geometry the diffusor width/length ratio in 0.0403 (long diffusor) and 0.0458 (short diffusor). This parameter which is characteristic for a comparative assessment of the diffusor is also of great practical significance.

At a given diffusor length, d_4, a multistage compressor frame size with constant diameter impellers is determined by the widest wheel. This has the following consequenecs for the other narrower impellers on the same shaft:

(*i*) At the same diffusor length the width/length ratio becomes smaller with narrower impellers. At the same time the casing is no longer fully utilized.

(*ii*) At full utilization of the casing, however, the diffusor length can be increased, thus producing a positive impact on the static pressure recovery. On the other hand, the width/length-ratio of the diffusor is further reduced.

Further tests must prove the general validity of the described tests. In particular, it must be shown whether these results can be transferred to diffusor configurations of constant diffusor ratio and varying width/length-ratio.

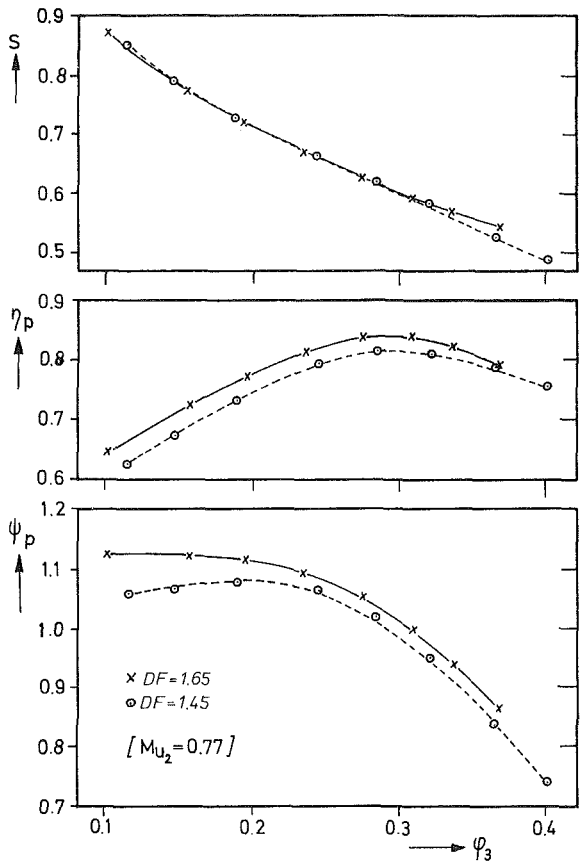

Fig. 16 Influence of the diffusor length, comparison: long versus short diffusor

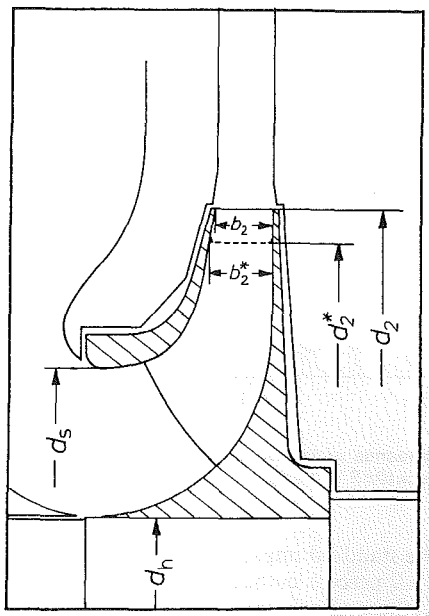

Fig. 17 Impeller geometry with extended shrouds

Influence of Blade Cutback

Test Objective. Blade cutback, which involves blade trimming but leaving shroud and hub disk as is, is an appropriate means of reducing the polytropic head of an impeller. This becomes necessary if performance curves of individual stages are to be shifted to avoid mismatching. As described before, a fixed geometry modular system requires certain rating ranges. Therefore, there may be cases with multistage process compressor where, at the compressor rated point, some of the stages operate at far off-design points inspite of narrow diameter stepping.

Without changing the basic concept, impellers can thus be forced to operate close to their best-efficiency-points. On the other hand blade trimming is required if the specification calls for limitations of sidestream pressures, speeds, or maximum discharge temperatures.

The extending impeller disks form a rotating annular diffusor. Since the relative velocity, w, is smaller and more radially directed than the absolute velocity, c (see Fig. 12), the friction losses in a rotating diffusor become smaller than in a comparable stationary diffusor.

This is the reason why the rotating diffusor was given great attention [1].

The efficiency however can only be increased up to a certain maximum amount of blade cutback. For higher cutbacks, the radial flow path length near the shroud is no longer sufficient to achieve an acceptable velocity distribution at the impeller exit.

Table 3

Symbol	Dim.			
$b_2 = b_4$	mm	26.6		
d_2	mm	400 (= $d_{2\ disc}$)		
d_4	mm	580		
b_2^*	mm	26.6	27.2	28.7
d_2^*	mm	400	382	365
DES	--	1.0	0.955	0.9125
		No. 1	No. 2	No. 3

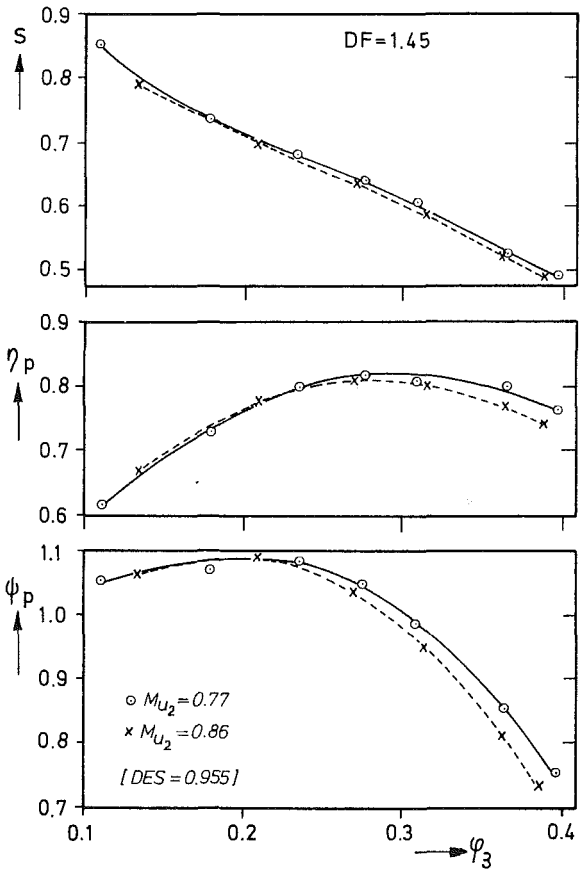

Fig. 18 Influence of blade cutback, measured performance curves small cutback (*DES* = 0.955)

Since the standard impeller diameters are stepped in such a way that a 9 percent cutback reaches the next small impeller diameter, the cutback tests were not intended to find out about the maximum permissible blade trimming but to generate experimentally based design criteria.

Test Performance. To conduct the blade trimming tests, the single-stage compressor, described in "Test Performance" section, with the short diffusor (DF = 1.45) was used, see Fig. 13.

The impeller blades were cut in two steps, with the disks remaining unchanged. The first step was a blade diameter cut from d_2 = 400 mm to d_2^* = 382 mm, which is a 4.5 percent decrease. The second cut was d_2^* = 365 mm (8.75 percent increase.

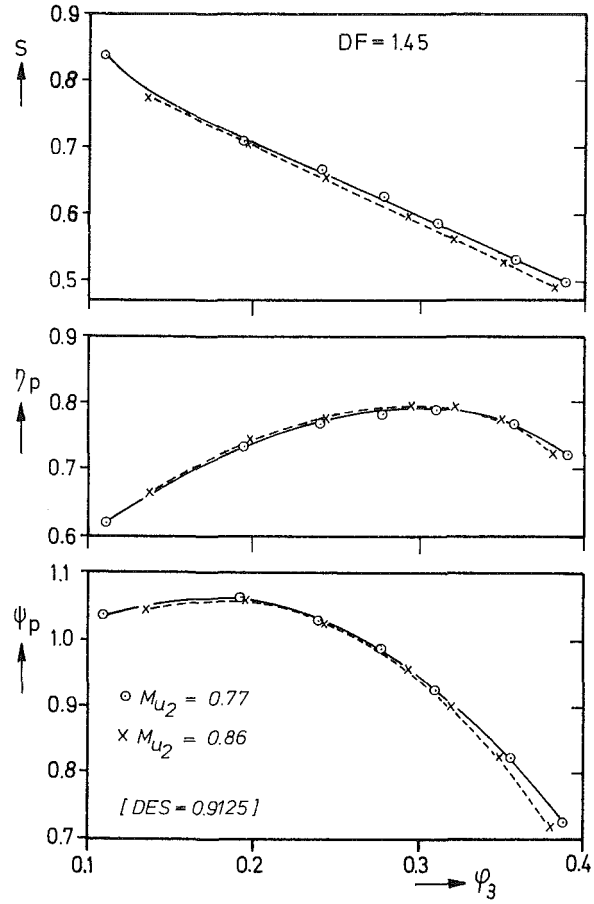

Fig. 19 Influence of blade cutback, measured performance curves large cutback (*DES* = 0.9125)

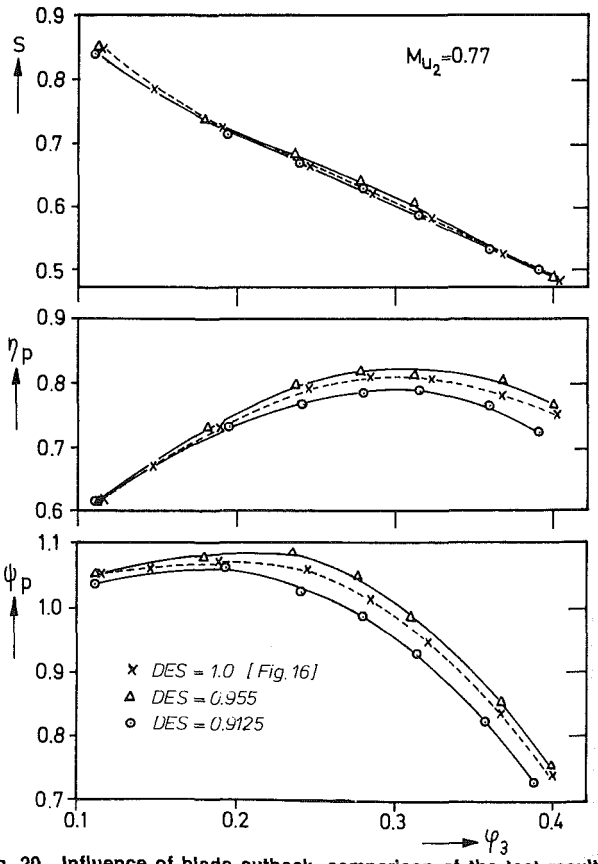

Fig. 20 Influence of blade cutback, comparison of the test results, M_{u2} = 0.77

Table 3 shows the stage geometry. Measuring stations and data acquisition of total pressure and total temperature were identical to the diffusor tests.

Test Results. The test results on the influence of blade cutback are exhibited on Fig. 18 (small cutback ratio, $DES = 0.955$) and on Fig. 19 (large cutback ratio, $DES = 0.9125$).

The charts show slip factor, s, polytropic efficiency, η_p, and polytropic head coefficient, ψ_p, versus exit flow coefficient, φ_3.

Figure 20 compares the non-cutback wheel (see Fig. 15) with the two cutback wheels. The small cut-back increases the maximum polytropic stage efficiency by 1.3 percent (from 0.815 to 0.826). The large cutback sees an efficiency reduction of 2.8 percent (from 0.815 to 0.792) with regard to the non cut-back impeller. The volumetric location of the efficiency maximum, $\varphi_{3\,\mathrm{opt}}$, remains unchanged.

In spite of an unchanged volumetric range, the part-load efficiency curves approach each other, whereas the overload efficiency curves diverge. Since the blade cutback has only a minor influence on the slipfactor (Fig. 20, top), the impeller exit flow conditions must have stayed approximately the same. This assumption makes sense because the selected cut-back ratios are relatively small. On the other hand the rotating diffusor must then be the cause for the described efficiency change.

So the advantages of the rotating diffusor prevail with the small cutback rate, achieving an additional static pressure recovery. The large cutback rate, however, causes additional friction losses in the gaps between the diaphragm walls and the extending impeller disks.

Compared with the non-cutback wheel a small cutback achieves a higher polytropic head coefficient, ψ_p, of 1 to 2 percent. The large cutback however reduces the polytropic head coefficient by 3 to 5 percent.

Summary

To improve rotordynamics the shaft of a multi-stage process compressor with wide impellers can be shortened. The pertaining reduction of the axial stage pitch does not influence the polytropic efficiency significantly.

Shafts with medium and narrow impellers are not jeopardized rotordynamically. By shortening the axial stage pitch the number of stages per casing can be increased at an efficiency sacrifice of 7 to 10 percent.

The frame size is determined by the length of the vaneless annular diffusor. If, for cost reduction purposes, the diffusor ratio is reduced, the efficiency decreases. Tests have revealed efficiency detriments of 3 to 5 percent for a diffusor ratio reduction of 18 percent.

The polytropic head can be reduced by blade trimming. The extending impeller disks form a rotating diffusor, which at small cutback rates of 4.5 percent yields an increase of the polytropic efficiency and polytropic head of approximately 1 percent. At large cutback rates of 8.75 percent, however, polytropic efficiency and head drop by 3 to 5 percent.

References

1 Sapiro, L., "Effect of Impeller Extended Shrouds on Centrifugal Compressor Performance as a Function of Specific Speed," ASME paper 82-GT-228, 1982.

A New Look at Performance Analysis of Centrifugal Compressors Operating With Mixed Hydrocarbon Gases

N. S. Nathoo
Mem. ASME

W. G. Gottenberg
Fellow ASME

Shell Development Company
Houston, Texas 77001

A program was undertaken to examine the thermodynamic performance of multistage centrifugal compressors operating with hydrocarbon gas mixtures. Experimental aspects included methods for accurate measurement of such variables as the pressure and temperature of the process gas stream before and after each compressor stage and the acquisition of gas samples and their analysis. Emphasis was placed on development of an analytical technique using an equation-of-state representation for the gas mixture to evaulate its thermodynamic properties. This permitted integration of the exact thermodynamic equations developed by Schultz in 1962 for describing the compression path of the gas stream. The effect of the variation of the so called polytropic volume exponent, n, on the performance parameters was examined. The special case of the polytropic path, i.e., n considered a constant, was shown to be acceptable in most practical applications. The technique was validated by examples of field tests and by comparison with test cases reported in the literature.

Introduction

The thermodynamic performance analysis of centrifugal compressors has been dealt with quite extensively in the literature. References [1–3], among others, provide an insight into the methods used for performance evaluation. The commonly used "*n*" methods usually employed perfect gas relations and, in some cases, did not properly characterize the compression path followed by the gas medium. The real gas integral equations for representing the compression path of a gas stream were derived first by Schultz [4]. However, the equations could not be solved exactly because of difficulty in predicting the detailed thermodynamic properties of hydrocarbon gas mixtures (see [5]). An alternate approach to Schultz's method was described in [6]. This method was postulated to be more accurate for compression processes where the discharge pressure exceeded 10 MPa (1450 psia). This approach, however, was also approximate to some extent. In addition to the analytical approximations, the procedures to acquire experimental data, especially gas samples, from field installations have not been generally well defined.

In order to obtain a more accurate prediction of the performance of such compressors, an effort was undertaken to develop:

(*a*) Experimental techniques for the acquisition of such variables as pressure, temperature, flow rate, and gas samples at the suction and discharge sides of each stage[1] of compression

(*b*) An equation-of-state approach to predict the thermodynamic properties of gas mixtures and couple them with the equations developed by Schultz to permit their exact integration.

A brief description of the experimental technqiues is contained herein; complete details appear in a related paper [7]. The analytical techniques extending the work of [4] are supported by examples of field tests and by comparison with test cases reported previously. In addition, the effect of the variation of the so-called polytropic volume exponent, *n*, on the performance parameters is examined. The special case of the polytropic path, i.e., *n* considered a constant, is shown to be acceptable in most practical applications.

Experimental Techniques

A preliminary evaluation of the effect of measurement error of the basic quantities, such as temperature, pressure, and flow rate of the gas stream, had raised some doubt about the suitability of the usual process control plant instrumentation for evaluating compressor performance. For example, is the temperature indicated by a thermocouple in a thermowell near the wall of a large duct truly representative of

Contributed by the Power Division and for publication in the Journal of Engineering for Power. Manuscript received at ASME Headquarters June 9, 1983.

[1] In this paper, except where otherwise noted, a "stage" of compression may include multiple impellers between the suction and discharge ends with intercooling being present between stages.

the average temperature of the gas stream at that axial location? To answer such questions it was deemed necessary to employ special instrumented probes that could permit radial traverses of suction and discharge ducts for acquiring measured variables such as stagnation pressures and temperatures and gas stream axial velocity pressure. The same probe was also used to acquire gas stream samples. Therefore, the probe would: (*a*) provide a laboratory calibrated means of acquiring accurate data, and (*b*) serve to determine the accuracy of existing plant instrumentation.

A detailed description of the probe, its insertion device, the data acquisition procedure and its discussion appears in [7]. In summary, the sensor end of the probe is wedge-shaped and has ports which are connected through internal passages, to a static and differential pressure transducer at the end that remains outside the duct. The probe tip also has an imbedded thermocouple for temperature measurement. Access for the probes is gained through gate valves at existing process instrumentation taps and an insertion device is used to position the probe in the duct while it is under pressure. Gas samples can be obtained through the static pressure ports of the probe. The use of the probe has indicated that the static pressure and temperature of the gas stream are fairly constant across the radius of the compressor ducts. This is a result of the well-stirred nature of the gas stream. The latter condition was verified by the velocity profile as obtained with the probe and the estimation of the Reynold's number for the flow condition. It was also shown that if plant instruments are properly calibrated, good agreement can be obtained between their output and those from the probe. However, there were some exceptions and for that reason, it is suggested that the probe may be used initially to establish the accuracy of the plant instrumentation. Needless to say, accurate pressure, temperature and flow measurements are essential for a proper evaluation of performance.

As has been mentioned, the probe was also used to acquire gas samples. For this purpose, the probe tip was inserted at several radial positions in the duct and gas samples acquired. An extensive series of tests was performed to determine whether radial sampling location in the duct influenced measured composition. It was concluded from the analysis of these gas samples that no systematic variation was found with radial location. However, it was determined that gas samples acquired directly from a wall tap (i.e., without a probe) were leaner in higher molecular weight constituents than samples taken with the probe. From this observation, it was concluded that a gas sample should be acquired with a probe that projects at least 1 in. into the gas stream.

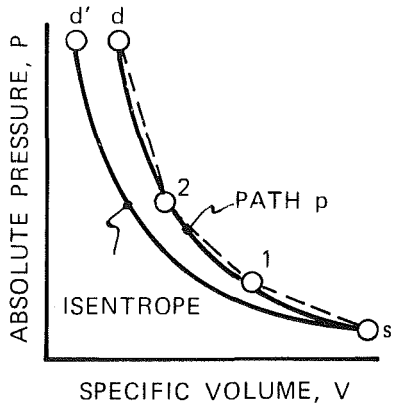

Fig. 1 Pressure volume diagram for gas compression in a centrifugal compressor [4]

It was also determined that the gas sample flask should be heated to the same temperature as the gas stream prior to the acquisition of the sample. This heating is required in order to prevent any of the initial hot gas stream (during purging) condensing and adhering to the "cold" wall of the flask. In addition, the gas sample flask should be reheated to the same temperature prior to and during discharge of the gas sample into the gas analysis instrument. Incidentally, the composition of the gas samples was determined using a mass spectrometer.

Analytical Development

Equations for the Compression Path. For the sake of convenience, the method described by Schultz [4] is summarized below. Consider a multi-impeller, adiabatic stage of compression of a real homogeneous gas. If the state of the gas is known at the suction (inlet) and discharge (outlet) ends, it can be represented on a P-V plane as shown in Fig. 1.

Let path p be a continuous curve connecting points s and d and let curve sd′ represent an isentropic path to the same discharge pressure. For a steady flow, adiabatic process the net shaft work, W, is given by

$$W = H_d - H_s + \frac{v_d^2 - v_s^2}{2g} \tag{1}$$
$$= \Delta H + \Delta KE$$

where H is gas enthalpy and v is gas velocity. Along path p, let W_p equal net reversible mechanical work input

Nomenclature

a,b = parameters of phase composition, temperature, and critical properties
f = polytropic head factor, see equation (11)
g = acceleration of gravity, $m \cdot s^{-1}$ ($ft \cdot s^{-1}$)
k = ratio of specific heat capacities (C_p/C_v)
m = defining equation (7*a*)
n = polytropic exponent (see also defining equation (7*b*))
p = path followed by gas in compression process
v = gas velocity, $m \cdot s^{-1}$ ($ft \cdot s^{-1}$)
C_p = specific heat capacity at constant pressure, $kJ \cdot kg^{-1} \cdot °K^{-1}$ ($Btu \cdot lbm^{-1} \cdot °R^{-1}$)
C_v = specific heat capacity at constant volume, $kJ \cdot kg^{-1} \cdot °K^{-1}$ ($Btu \cdot lbm^{-1} \cdot °R^{-1}$)
H = gas enthalpy $kJ \cdot kg^{-1}$ ($Btu \cdot lbm^{-1}$)
N = number of moles
P = absolute pressure, Pa ($lbf \cdot in^{-2}$)
Q_p = net reversible heat input, $kJ \cdot kg^{-1}$ ($Btu \cdot lbm^{-1}$)
R = gas constant, $kJ \cdot kg^{-1} \cdot °K^{-1}$ ($ft^2 \cdot s^{-2} \cdot °R^{-1}$)
S = gas entropy, $kJ \cdot kg^{-1} \cdot K^{-1}$ ($Btu \cdot lbm^{-1} \cdot °R^{-1}$)
T = absolute temperature, K (°R)
V = specific volume, $m^3 \cdot kg^{-1}$ ($ft^3 \cdot lbm^{-1}$)
W = net shaft work in steady flow adiabatic process, $kJ \cdot kg^{-1}$ ($Btu \cdot lbm^{-1}$)
W_p = net reversible mechanical work input, $kJ \cdot kg^{-1}$ ($Btu \cdot lbm^{-1}$)
Z = compressibility factor
η_p = efficiency along path p
ρ = gas density, $kg \cdot m^{-3}$ ($lbm \cdot ft^{-3}$)

Subscripts

s = suction
d = discharge
is = isentropic
P = along path p (see Fig. 1)

$$= \int_{P_s}^{P_d} V dP$$

Q_p = net reversible heat input

so that

$$\Delta H = Q_p + W_p \tag{2}$$

One measure of the compressor efficiency can be defined by

$$\eta_p = \frac{W_p}{W_p + Q_p} = \frac{W_p}{H_d - H_s} = \frac{\int_{P_s}^{P_d} V dP}{H_d - H_s}$$

$$= \frac{\text{Reversible Work Input}}{\text{Enthalpy Rise}} \tag{3}$$

If η_p is assumed to be a constant along p, then p is defined to be a path with a governing equation

$$\eta_p = V \frac{dP}{dH} \tag{4}$$

where η_p is that constant for which p passes through points s and d. It may be noted that along the isentropic path, $dS = 0$. Because

$$dH = VdP + TdS \tag{5}$$

it follows that $\eta_p = 1$ along the isentrope which is an expected conclusion.

The only assumption inherent in the preceding analysis has been that of a constant efficiency along the compression path; this appears to be a valid and logical assumption. However, if the state of the gas at intermediate points 1, 2 (i.e., between adjacent impellers) is not known, then it is further assumed that all impellers between points s and d have the same constant efficiency η_p. In order to determine the constant efficiency path, it can be shown that any one of the following equations must be integrated.

$$\frac{P}{T}\frac{dT}{dP} = m \tag{6a}$$

$$\frac{P}{V}\frac{dV}{dP} = -\frac{1}{n} \tag{6b}$$

$$\frac{P}{Z}\frac{dZ}{dP} = \frac{n-1}{n} - m \tag{6c}$$

where Z is the usual compressibility factor and

$$m = \frac{ZR}{C_P}\left(\frac{1}{\eta_p} + X\right) \tag{7a}$$

$$n = \frac{1}{Y - m(1+X)} \tag{7b}$$

and

$$X = \frac{T}{Z}\left(\frac{\partial Z}{\partial T}\right)_P = \frac{T}{V}\left(\frac{\partial V}{\partial T}\right)_P - 1 \tag{7c}$$

$$Y = 1 - \frac{P}{Z}\left(\frac{\partial Z}{\partial P}\right)_T = -\frac{P}{V}\left(\frac{\partial V}{\partial P}\right)_T \tag{7d}$$

$$L = 1 + \frac{T}{Z}\left(\frac{\partial Z}{\partial T}\right)_V = \frac{T}{P}\left(\frac{\partial P}{\partial T}\right)_V \tag{7e}$$

Equations (6*a*) and (6*b*) can be rewritten as a pair in expanded form as

$$\frac{dT}{dP} = \frac{V}{C_P}\left[\frac{1}{\eta_P} + \frac{T}{V}\left(\frac{\partial V}{\partial T}\right)_P - 1\right] \tag{8a}$$

$$\frac{dV}{dP} = \left(\frac{\partial V}{\partial P}\right)_T + \frac{V}{C_P}\left(\frac{\partial V}{\partial T}\right)_P \left[\frac{1}{\eta_P} + \frac{T}{V}\left(\frac{\partial V}{\partial T}\right)_P - 1\right] \tag{8b}$$

It can be seen that the right-hand sides of these two differential equations are a function of both the efficiency of compression and the thermodynamic properties of the gas medium at each point along the compression path. Therefore, it is obvious that they cannot be integrated without the knowledge of both of these entities. However, η_p is itself an unknown at this time and is one of the variables to be determined.

Given these difficulties, Schultz postulated that both m and n were relatively constant compared to P, V, and T. In that case, equation (6*b*) results in the familiar form

$$PV^n = \text{constant} \tag{9}$$

where n is now referred to as the polytropic volume exponent, and the path p is called the polytropic path. Now equation (9) can be used as the path equations, and n and W_p (numerator in equation (3)) can be determined as

$$n = \frac{\log(P_d/P_s)}{\log(V_s/V_d)} \tag{10a}$$

$$W_p = \int_{P_s}^{P_d} V dP \simeq \frac{n}{n-1}(P_d V_d - P_s V_s) \tag{10b}$$

Schultz had recognized that n would vary along the compression path. To compensate for the effect of this variation on the calculation of W_p, he postulated that a correction factor, f, could be developed as

$$f = \frac{H_{d_{is}} - H_s}{\frac{n_{is}}{n_{is}-1}(P_d V_{d_{is}} - P_s V_s)} \tag{11}$$

where

$H_{d_{is}}$ = enthalpy of gas at discharge assuming an isentropic compression, and $V_{d_{is}}$ = volume of gas at discharge assuming an isentropic compression, and

$$n_{is} = \frac{\log(P_d/P_s)}{\log(V_s/V_{d_{is}})}$$

This correction factor, termed the polytropic head factor, would be applied to the calculation of the head, W_p, so that now

$$W_p = f\frac{n}{n-1}(P_d V_d - P_s V_s) \tag{12}$$

Equation (12) would then be used in lieu of equation (10*b*) to calculate W_p. However, it may be noted that Schultz could not ascertain the validity of the application of the correction factor.

In reference [6], Mallen et al. proposed the use of

$$T\frac{dS}{dT} = C \text{ (a constant)} \tag{13}$$

as the equation to be used for describing the compression path. They concluded that this equation provided a more accurate representation for cases where the discharge pressure exceeded 10 MPa (1450 psia). Equation (13) results in

$$W = (H_d - H_s) - Q \tag{14}$$

where

$$Q = \frac{(S_d - S_s)(T_d - T_s)}{\ln(T_d/T_s)}$$

as the relation for computing the work done in the compression process. It was further concluded that without ex-

perimental evidence, it could not be proven that equation (14) would result in a better estimate than equation (12).

In order to calculate the efficiency of the compression process for the case of n = constant or for the path represented by equation (13), it is necessary to calculate the enthalpy change $(H_d - H_s)$ and the entropy change $(S_d - S_s)$ incurred by the gas (see equations (3) and (14)). If the gas being compressed is a pure (single) entity, then it is a relatively straightforward procedure to determine ΔH from the Mollier diagram of the gas. However, this presents a difficulty for the case of hydrocarbon gas mixtures. A method outlined in [8] utilizes a tabular procedure to obtain entropy, enthalpy, and specific heat of gas mixtures based on ideal gas properties of the constituents. Sources of concern are the need to interpolate from tables of ideal gas properties and the accuracy of the pseudocritical pressure and temperature corrections applied to the results. Moreover, automation of the procedure via a computer is complicated by the need to store a vast amount of data. The overall results, therefore, cannot be expected to be very accurate.

Calculation of Thermodynamic Properties. In the present work, an equation-of-state representation of the gas mixture was developed to calculate the detailed thermodynamic properties required for the performance computation. The Redlich-Kwong-Soave (RKS) equation-of-state [8, 9] has been modified for use within Shell and was further adapted for use in the performance calculations. The modified RKS equation may be written as

$$P = \frac{RT}{V-b} - \frac{a(T)}{V(V+b)} \tag{15}$$

where a and b are parameters which, in general, are explicit functions of the phase composition, temperature, and pure component critical properties and characterization parameters. Whenever needed, the determination of various parameters is supported by experimental data. In general, the equation has been proven to be successful in predicting the phase behavior over a temperature range of 114–846 K (−200–1000°F) and a pressure range of 0–10MPa (0–1450 psia).

The first step in any property calculation procedure is to perform a material (flash) calculation in order to determine the phase compositions. A by-product of this calculation is the compressibility factor(s) of the phase(s). Given the pressure and temperature, these provide the mixture volumes which can be used in the following exact thermodynamic relationships.

$$H - H^\circ = \int_V^\infty \left[P - T\left(\frac{\partial P}{\partial T}\right)_{V,N} \right] dV + PV \tag{16a}$$

$$S - S^\circ = \int_V^\infty \left[\frac{NR}{V} - \left(\frac{\partial P}{\partial T}\right)_{V,N} \right] dV + R\Sigma n_i \ln\left(\frac{V}{N_i RT}\right) \tag{16b}$$

$$C_p - C_p^\circ = \frac{\partial}{\partial T}(H - H^\circ)_P \tag{16c}$$

$$C_V = C_P - T\left(\frac{\partial V}{\partial T}\right)_P \left(\frac{\partial P}{\partial T}\right)_V \tag{16d}$$

In the above equations N is the number of moles of each constituent. H, S, C_P and C_V are the enthalpy, entropy, heat capacity at constant pressure, and heat capacity at constant volume, respectively. The superscript "0" indicates the corresponding ideal gas value of that property. It may be noted that a data base consisting of pure component properties forms part of the overall computation scheme.

In order to evaluate the performance of a compression stage, the following information would be required:

(*a*) Suction and discharge pressures
(*b*) Suction and discharge temperatures
(*c*) Composition of the gas stream
(*d*) Volumetric flow rate on either suction or discharge side.

With the knowledge of the gas mixture composition, the equation-of-state (equation (15)) is used on the right-hand sides of equations (16*a–d*) to calculate the thermodynamic properties. These in turn can be used, along with equation (10), to determine the efficiency of the compression stage along a polytropic path (n considered a constant).

Alternatively, n need not be considered a constant. Using the aforementioned information, equations (8*a*) and (8*b*) can also be integrated numerically starting with the suction conditions, and with some assumed value of η_p, the two equations can be integrated simultaneously until the independent variable, P, equals the measured discharge pressure. The calculated value of the variable T at that point is compared with the actual (measured) value of the discharge temperature. The entire integration procedure is iterated with various values of η_p until the calculated and measured value of the temperature, T, agree with each other. This determines the efficiency, η_p, of the compression path and, therefore, the compression path itself. Knowing the latter, i.e., V is now known as a function of P along the compression path, the work

$$W_p = \int_{P_s}^{P_d} V dP$$

can be evaluated. The enthalpy change can be calculated either using equation (3) or internally by the property evaluation procedure described earlier.

The technique developed here can be used to obtain results either via the exact integration of equations (8*a*) and (8*b*) or the approximate approach—either equations (10*a*) and (12) or equation (14). Its use can be best exemplified by test cases reported in [4] and [6] and an example from an operating Shell plant. These examples along with one from [3] are presented below.

Effect of Variation of n. Consider the example from [4] of the compression of Freon-12 from P_s = 69 kPa (10 psia), T_s = 250 K (−10°F) to P_d = 896 kPa (130 psia), T_d = 372 K (210°F). This is a typical example of determining the performance characteristics of a compressor from operating data. Table 1 shows the results of [4] as compared with those from the present work—both with n assumed to be a constant. As may be seen, there is good agreement between the two sets of results. Figure 2 shows the variation of m and n along the compression path as obtained from the numerical integration of equations (8*a*) and (8*b*) for this case. A change of −9.8 and −7.5 percent occurs, respectively, in m and n from suction to discharge conditions. Although, this variation is significant by itself, there is very little difference between the efficiency and work done along the compression path calculation via the "exact" versus the "approximate" (n-constant) methods. This can also be seen in Table 1.

A similar situation occurs for the compression of a hydrocarbon gas mixture. The case in point is a four-stage process gas compressor in one of the Shell ethylene plants. The gas mixture for the first stage of this compressor consists of 21 different constituents ranging in molecular weight from 2 to 95 as shown in Table 2. In addition to hydrocarbons from C_2's to C_7's, the mixture contains gases such as hydrogen, nitrogen, and carbon dioxide. This composition is typical for the remaining stages as well. The suction and discharge

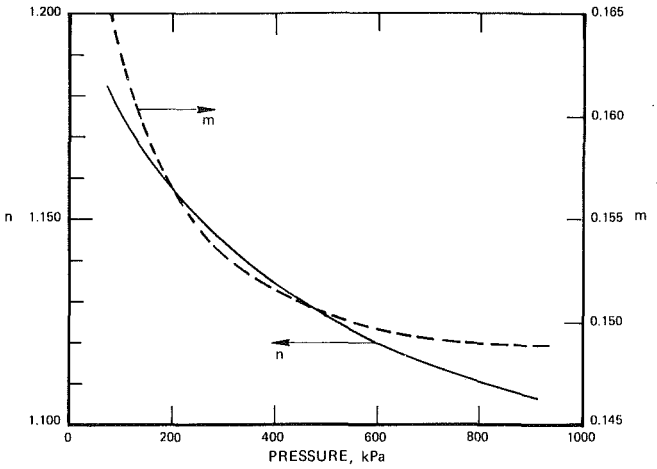

Fig. 2 Variation of *n* and *m* over compression path for Freon-12

Table 1 Comparison of results from [4] and present work for compression of Freon-12

		Reference [4] n = Constant	Present Work n = Constant	Present Work "Exact" n ≠ Constant
Pressure, kPa / psia	Suction	68.9 / 10.0		
	Discharge	896.3 / 130.0		
Temperature, °K / °F	Suction	249.8 / −10.0		
	Discharge	372.0 / 210.0		
Enthalpy Change, kJ·kg⁻¹ / Btu · lbm⁻¹		68.94/29.64	68.64 / 29.51	
Entropy Change, kJ·kg⁻¹ · °K⁻¹ / Btu · lbm⁻¹ °R⁻¹		0.0564 / 0.01347	0.0561 / 0.01340	
n	Suction	1.1488	1.1488	1.181
	Discharge			1.106
Work Input, kJ·kg⁻¹ / ft-lbf · lbm⁻¹		51.664 / 17285	51.772 / 17321	51.698 / 17297
Efficiency		0.749	0.754	0.753

conditions for the first stage are shown in Table 3 along with the performance parameters calculated via the "exact" and "approximate" methods. In this case, as well as for the three other stages, a difference of approximately 1/2 of 1 percent exists between the efficiency (and the work done) calculated by the two methods. Similar differences have also been observed for the compression of gas mixtures ranging in molecular weight from 6 to 42.

The final example to be considered is from [6]. This concerns the compression of ethylene from $P_s = 2.5\text{MP}_a$ (363 psia), $T_s = 310\text{K}(98.3°\text{F})$ to $P_d = 50\ \text{MP}_a$ (7252 psia), $T_d = 570$ K (566°F). This is the extreme case where a difference of 3 percent exists in the calculated work of compression between the approach of [6] (equation (14)) and Schultz (equation (12)). This is shown in Table 4. To be compatible, the work input was calculated using the present analysis; these recomputed values appear in column 1 and 2 of Table 5. They differ from those of Table 4 by about 2 percent. The likely cause of the discrepancy is the difference in the pure component property data base that underlies the calculation of enthalpy and entropy. Also shown in this table are the corresponding efficiencies of compression (work done divided by change in enthalpy). Column 3 of Table 5 shows the results obtained by integrating equations (8*a*) and (8*b*) numerically for this case. As may be seen, the efficiency and, therefore, the work input, falls in between those calculated by the two

Table 2 Typical gas composition for the first stage of a four-stage centrifugal compressor

Component Number	Component Molecular Weight	Component Mole Percent (Mean of 3 Tests)
1	2.01	11.62
2	16.04	24.30
3	26.03	0.32
4	28.05	26.77
5	30.07	6.97
6	40.06	0.17
7	42.08	12.17
8	44.09	0.58
9	54.09	3.10
10	54.10	4.39
11	58.12	0.43
12	66.12	0.80
13	68.12	2.07
14	70.13	1.27
15	72.15	0.24
16	80.14	0.47
17	84.16	0.26
18	86.17	0.29
19	88.12	0.17
20	78.18	1.90
21	92.14	0.70

Table 3 Comparison of "approximate" and "exact" analysis for the compression of a mixed hydrocarbon gas

		"Approximate" n = Constant	"Exact" n ≠ Constant
Pressure, kPa / psia	Suction	180.98 / 26.25	
	Discharge	409.88 / 59.45	
Temperature, °K / °F	Suction	307.87 / 94.50	
	Discharge	363.55 / 194.72	
Enthalpy Change, kJ·kg⁻¹ / Btu · lbm⁻¹		99.32 / 42.70	
Entropy Change, kJ·kg⁻¹ · °K⁻¹ / Btu · lbm⁻¹ °R⁻¹		0.0795/0.0190	
n	Suction	1.249	1.266
	Discharge		1.231
Work Input, kJ·kg⁻¹ / ft-lbf · lbm⁻¹		72.99 / 24423	73.49 / 24589
Efficiency		0.735	0.740

aforementioned methods. Furthermore, the difference between the "exact" and "approximate" cases is no more than 1-1/2 percent.

In summary, it can be said that in most practical cases, the assumption of *n*-constant leads to fairly accurate results. The added computation time required for integrating equations (8*a*) and (8*b*) may not be justified unless very accurate results are desired. In the opinion of the present authors and within the context of the present work, it does not appear that the formulation of [6] offers any significant advantage over the now generally accepted method of Schultz.

Application to Compressor Design. In the selection of a centrifugal compressor, the following design parameters are usually known:

(*a*) Suction side:
- Gas pressure
- Gas temperature
- Volumetric flow rate

(*b*) Discharge side
- Gas pressure
- Gas temperature range

(*c*) Gas composition

(*d*) Nominal compressor efficiency (supplied by the manufacturer)

The selection process requires the calculation of the discharge temperature after the choice of a compressor section has been made to ensure that it falls within the specified range. The present analysis can be used in one of two ways to calculate the discharge temperature. For the case of *n*-constant, the computer program (based on this analysis) is run interatively with different values of discharge temperature until the calculated efficiency corresponds to the desired chosen nominal efficiency. Alternatively, the chosen efficiency is used directly in the integration of equations (8*a*) and (8*b*), and the discharge temperature is obtained as a result. This entire process becomes quite straightforward as shown in the example below.

Reference [3] considered the compression of benzene vapor from 101 kPa (14.7 psia) and 383 K (230°F) to 2.07 MPa (300 psia) using a polytropic efficiency of 70 percent. An iterative procedure was used in [5] to determine the discharge temperature for each of the five stages chosen for this application. The results of [5] are shown in Table 6 alongside those obtained from the application of equations (8*a*) and (8*b*). The discharge temperature for each stage is used as the suction temperature for the following stage. Although only minor differences may be noted between the two methods, the present approach can considerably reduce the selection effort because of its noniterative character.

Table 4 Comparison of results for the compression of ethylene via analysis of [4] and [6] (taken from [6])

		Reference [4]	Reference [6]
Pressure, mPa / psia	Suction	2.5 / 362.6	
	Discharge	50.0 / 7252.0	
Temperature, °K / °F	Suction	310.0 / 98.3	
	Discharge	570.0 / 566.3	
Work Input, kJ · kg^{-1} / ft-lbf · lbm^{-1}		350.30 / 117204.7	361.00 / 120784.4

Summary

Performance calculations for multistage centrifugal compressors are of importance not only in process design and equipment selection, but also in assessing performance of machinery in actual plant conditions. Field testing requires consistently obtained data for performance calculation and that has been carefully discussed. Another practical difficulty associated with compressors in chemical plant service is that they frequently operate on gas mixtures whose composition is not certain and therefore must be determined. Knowing the gas stream composition, it was shown that computer-based equations-of-state could be used to provide accurate thermodynamic properties of typical gas mixtures as well as pure components.

Having the ability to calculate the thermodynamic properties of gas mixtures, it was next possible to reexamine the assumptions made in the polytropic path analysis which has proven to be so useful for compressor analysis. By means of specific examples, it was shown that the usual assumption of *n*, the polytropic volume exponent, being constant along the compression path, is valid in a practical sense. For instance, equivalent values for work and efficiency were obtained when compared with the more exact method of numerically evaluating the path integrals. Also, it was shown that a previous criterion of the polytropic process calculation

Table 5 Comparison of results for the compression of ethylene via analysis of [4], [6], and present work

		Reference [4] *(Recalculated)*	Reference [6] *(Recalculated)*	Present Analysis "Exact"
Pressure, kPa / psia	Suction	2.5 / 362.6		
	Discharge	50.0 / 7352.0		
Temperature, °K / °F	Suction	310.0 / 98.3		
	Discharge	570.0 / 566.3		
Enthalpy Change, kJ·kg^{-1} / Btu · lbm^{-1}		450.04/193.50		
Entropy Change, kJ·kg^{-1} · °K^{-1} / Btu · lbm^{-1} °R^{-1}		0.1926 / 0.046		
n	Suction	1.1450	–	1.294
	Discharge			1.738
Work Input, kJ·kg^{-1} / ft-lbf · lbm^{-1}		359.47 / 120276	367.84 / 123077	365.44 / 122274
Efficiency *		0.799	0.817	0.812

* $\frac{\text{Work Input}}{\text{Enthalpy Change}}$

Table 6 Comparison of results of [3] and present work for compression of benzene

		Stage 1		Stage 2		Stage 3		Stage 4		Stage 5	
		Reference [3]	Present Work	Reference [3]	Present Work	Reference [3]	Present Work	Reference [3]	Present Work	Reference [3]	Present Work
Pressure, kPa (psia)	Suction	101.35 (14.7)		213.73 (31.0)		434.36 (63.0)		858.38 (124.5)		1682.3 (244.0)	
	Discharge	213.73 (31.0)		464.36 (363.0)		858.38 (124.5)		1682.3 (244.0)		2068.4 (300.0)	
Temperature, °K (°F)	Suction	383.1 (230.0)	383.1 (230.0)	414.3 (286.0)	415.4 (288.0)	444.9 (341.0)	446.8 (344.5)	475.4 (396.0)	478.1 (400.9)	508.2 (455.0)	510.4 (461.0)
	Discharge	413.3 (286.0)*	415.4 (288.0)*	444.9 (341.0)*	446.8 (344.5)*	475.4 (396.0)*	478.1 (400.9)*	508.2 (455.0)*	510.4 (461.0)*	519.3 (475.0)	522.9 (481.4)
Work Input, kJ · kg^{-1} / ft-lbf · lbm^{-1}		29.89 (10000.0)	30.76 (10291.0)	29.89 (10000.0)	30.88 (10333.0)	29.89 (10000.0)	30.67 (10263.0)	29.89 (10000.0)	30.30 (10139.0)	11.81 (2950.0)	9.08 (3038.0)

* *Discharge temperatures for each stage are calculated quantities and are used as suction temperatures for the next stage.*

method for extreme discharge pressures is not warranted if accurate thermodynamic properties are used.

To summarize, performance calculations using the polytropic process with n-constant for mixed hydrocarbon gases give satisfactory results. In performing such calculations, it has been found necessary and convenient to use computer-based equations-of-state to obtain accurate thermodynamic properties of gas mixtures.

References

1 Edmister, W. C., *Applied Hydrocarbon Thermodynamics*, Gulf Publishing Company, Houston, Texas, 1961.

2 Hall, J. W., "Thermodynamics of Compression—A Review of Fundamentals," ISA Paper 76-582, 1976.

3 Church, D. M., "Centrifugal Gas Compressor—Parts 1-3," *Chemical Engineering*, Mar. 5, 19, and Apr. 2, 1962.

4 Schultz, J. M., "The Polytropic Analysis of Centrifugal Compressors," ASME JOURNAL OF ENGINEERING FOR POWER, Jan. 1962.

5 ASME Power Test Codes, "Compressors and Exhausters," PTC 10—1965, pp. 3.

6 Mallen, M., and Saville, G., "Polytropic Processes in the Performance Prediction of Centrifugal Compressors," I. Mech E. Conference Publications, 1977.

7 Nathoo, N. S., and Gottenberg, W. G., "Measuring the Thermodynamic Performance of Multistage Compressors Operating on Mixed Hydrocarbon Gases," Proceedings of the Tenth Turbomachinery Symposium, Texas A&M University, 1981.

8 Technical Data Book, *Petroleum Refining*, American Petroleum Institute.

9 Chao, K. C., and Robinson, R. L., ed. *Equation of State in Engineering and Research*, Advances in Chemistry, Series #182, American Chemical Society, 1979.

Effects of Anomalous Rotor Joints on Turbomachine Dynamics

N. Klompas
Gas Turbine Division,
General Electric Company,
Schenectady, N.Y. 12345
Mem. ASME

Mechanisms simulating rotor joint restoring moments different from the common axisymmetric elastic hinge are derived and their effects on the dynamics of a complete turbomachine are calculated by impressing equivalent perturbing moments. A mechanism for locking subsynchronous whirl to a fractional frequency is described and supporting experimental observations are discussed. Sample analysis shows the possibility of self-sustained synchronous whirl due to preload asymmetry.

Introduction

The technical literature does not treat the effects on turbomachine vibration of rotor joints that do not comply with the common axisymmetric elastic model and, hence, are called anomalous. The theoretical work on transverse rotor cracks does cover a mechanism which may be encountered in a mechanical joint; however, other mechanisms may also be encountered. Grabowski [1] treats the vibrational effect of a transverse crack interacting with stationary rotor deflection. His analysis accounts for only the rotor and involves complicated mathematical processes which do not provide physical interpretation and may be difficult for the engineer to implement. Another area of associated work is that covering asymmetric shafts in generators. Again, the model covers neither the range of possible mechanisms nor the complete turbomachine application; the paper by Inagaki, Kanki, and Shiraki [2] represents this work. Nevertheless, these theoretical presentations and associated experimental observations provide insight into and correlation with the present theory.

Reference [3] derives a method of analyzing the response of a complete turbomachine to unbalance. The present paper develops various mechanisms that may simulate the effects of an anomalous rotor joint. These mechanisms may be applied to the basic linear model of [3] or of any other method. Although they may involve nonlinear phenomena, the mechanisms and their effects can be visualized and verified.

Theory

The present theory is an extension of that developed in [3] to calculate response of a complete turbomachine to forces and moments due to unbalance. Perturbing moments are now impressed into rotor joints to simulate specific characteristics which do not conform to the axisymmetric elastic assumption of the model. In this extended analysis, it is necessary first to postulate a mechanism to represent the behavior of an anomalous joint and then iteratively to obtain a solution where the perturbing moment and the resulting motion satisfy the conditions imposed by the mechanism. The result is the steady response of the complete turbomachine. If the solution contains no stimulus due to unbalance and if stability with respect to the impressed whirl speed can be shown, the result is self-sustained whirl or, technically, a limit cycle.

The original method of linear analysis may be used to account for the restoring moment of a rotor joint which is not purely elastic and/or axisymmetric. Derivation of the conditions which the solution must satisfy to simulate different characteristics of the joint is presented in Appendix A.

The elliptical coordinates introduced in [3] will be used to define some conditions in analysis of the complete system. Appendix B defines those coordinates. The only difference from the definition of [3] is that the positive phase angle is now in the direction of lead rather than lag. This direction is now consistent with that of other angles. Definition of the different mechanisms derived in Appendix A follows.

Synchronous. In a synchronous solution where the slope increment across the joint is $\Delta y'_{r1}{}^{+}$, $\Delta y'_{r1}{}^{+*}$, $\Delta y'_{r1}{}^{-}$, $\Delta y'_{r1}{}^{-*}$ and correction is being made for higher, by ΔK, joint stiffness in the principal plane of $\Delta y'_{r1}{}^{+*}$, the correcting moment must be, in the order corresponding to the components of the slope increment, 0, $\Delta y'_{r1}{}^{+*}\ \Delta K$, $\Delta y'_{r1}{}^{-}\ \Delta K/2$, $\Delta y'_{r1}{}^{-*}\ \Delta K/2$. A third harmonic is also generated and is calculated by impressing the perturbing moment $\Delta y'_{r1}{}^{-}\ \Delta K/2$, $\Delta y'_{r1}{}^{-*}\ \Delta K/2$, 0, 0 in conjunction with $\Omega = 3\omega$.

A correcting moment may be derived to account for initial joint preload where, as shown in Fig. 1, the joint remains rigid until the restoring moment reaches the breaking moment, M_o. This representation of joint preload is an idealization of contacting flat surfaces clamped axially by either distributed tie rods or a central tie rod. The representation of a joint where the assumption of negative breaking moment may be justified is shown in Fig. 2. This representation may apply to a flanged joint distorted thermally so as to develop a gap over the portion of the face which transmits compressive stress. The stiffness of the joint then is reduced until this contact and, hence the original stiffness, are reestablished. If the joint is fully loose, the lower stiffness would be zero.

If the restoring moment of the joint is represented in the

Contributed by the Gas Turbine Division of THE AMERICAN SOCIETY OF MECHANICAL ENGINEERS for presentation at the 28th International Gas Turbine Conference and Exhibit, Phoenix, Arizona, March 27-31, 1983. Manuscript received at ASME Headquarters December 29, 1982. Paper No. 83-GT-175.

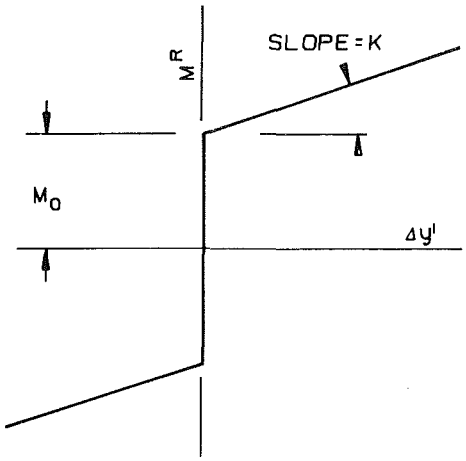

Fig. 1 Restoring moment of joint with inadequate preload

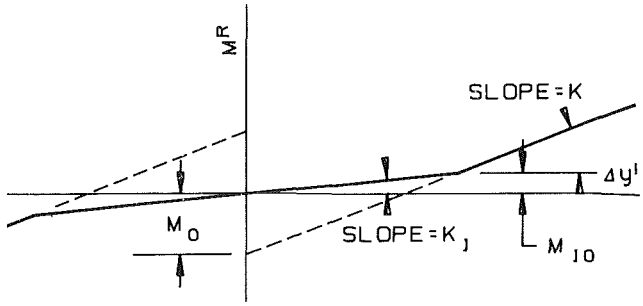

Fig. 2 Restoring moment of joint with initial looseness

elliptical coordinates as $M^R_{a1}, M^R_{b1}, \alpha^R_1, \phi^R_1$, the perturbing moment must be $M^P_{a1}, M^P_{b1}, \alpha^R_1, \phi^R_1$, where

$$M^P_{a1} = M_o M^R_{a1} / |M^R_{a1}|$$
$$M^P_{b1} = M_o M^R_{b1} / |M^R_{b1}| \quad (1)$$
$$\text{if } M_o > |M^R_{a1}|, M^P_{a1} = 0$$
$$\text{if } M_o > |M^R_{b1}|, M^P_{b1} = 0$$

and if $|M^R_{a1}|$ or $|M^R_{b1}| < M_{Io}$, the correction for asymmetric stiffness should be added to the perturbing moment.

A moment correcting for asymmetric preload may also be added to the perturbing moment. To simplify its illustration, the slope increment is assumed 90 deg ahead of the primary reference plane as shown in Fig. 3. The moment ΔM_o in the plane at angle θ, in direction of spin from the primary reference plane, is produced by nonuniform preload which may contain either or both deviations: concentration of lower than average preload in the vicinity of angle θ and of higher than average preload in the vicinity of angle $\theta + \pi$. If the slope increment in elliptical coordinates is $\Delta y'_a, \Delta y'_b, \alpha', \pi/2$ where $\Delta y'_a$ and $\Delta y'_b$ are both positive, the corresponding addition to the perturbing moment may be calculated. However, it is necessary first to determine that θ is not close to $\pi/2$ or $-\pi/2$. Otherwise, the contribution to ΔM_o due to the lower or the higher preload deviation, respectively, would vanish because it would coincide with the compressive region of the joint, which is assumed small. The effect of preload asymmetry is then accounted for by adding to the perturbing moment the two components

$$\Delta M_o \cos\theta, \Delta M_o \cos\theta, \alpha', 0 \quad (2)$$

Nomenclature

A = aspect ratio of ellipse defining $\Delta y'$, dimensionless
C = amplitude coefficient of limit cycle $M^P_l / \Delta M_o$, dimensionless
D = major deflection at joint/M^P_l, /lb(/N)
$\bar{i}, \bar{j}$ = orthogonal pair of unit vectors defining whirl frame of reference, dimensionless
K = axisymmetric stiffness coefficient representing joint in linear model, lb in/rad (Nm/rad)
K_I = initial axisymmetric stiffness coefficient of nonelastic joint, lb in/rad (Nm/rad)
ΔK = difference between principal stiffness coefficients of joint, lb in/rad (Nm/rad)
M^R = restoring moment of rotor joint, lb in (Nm)
M^P = perturbing moment impressed in rotor joint, lb in (Nm)
M^P_l = constant forward perturbing moment of limit cycle analysis, lb in (Nm)
M_{Io} = moment in rotor joint corresponding to limit of K_I, lb in (Nm)
M_o = moment in rotor joint corresponding to limit of preload, lb in (Nm)
ΔM_o = moment in rotor joint due to asymmetry of preload, lb in (Nm)
m = preload asymmetry parameter $M_o/\Delta M_o$, dimensionless
ΔM_f = moment in rotor joint due to friction, lb in (Nm)
S = major value of $\Delta y'/M^P_l$, /lb in (/Nm)
t = time, s
$\Delta y'$ = increment of slope due to rotor joint flexing, dimensionless
α = orientation angle of ellipse axes, rad
α^R = orientation angle of ellipse axes defining M^R, rad
α' = orientation angle of ellipse axes defining $\Delta y'$, rad
ϕ = phase angle of lead relative to primary plane, rad
ϕ^P = phase angle defined in sample analysis, rad
ϕ^R = phase angle defining M^R, rad
ϕ' = phase angle defining $\Delta y'$, rad
Ω = angular speed of whirl, rad/s
ω = angular speed of spin, rad/s
θ = angle relative to reference plane, rad

Subscripts

a = along ellipse axis rotated through α from x-axis
b = along ellipse axis rotated through α from y-axis
r = whirl
1,2,3,. . .n = Ω/ω, order of harmonic relative to spin speed
n = dummy variable indicating order of harmonic

Superscripts

* = in coordinates 90 deg ahead of primary reference
\+ = forward whirl
− = backward whirl

which lags the slope increment by 90 deg and $\Delta M_o \sin\theta$, $\Delta M_o \sin\theta$, α', $\pi/2$, which is in phase with the slope increment.

Stationary Deflection. Stationary deflection due to gravity should assume the average joint stiffness of $K + \Delta K/2$, or $K + \Delta K/4$ in the event of one-directional asymmetry as due to a breathing crack, in the static calculation. The static value of joint flexing may then be used in calculation of the perturbing moment at whirl speed of 2ω necessary to account for the vibratory effect of spin.

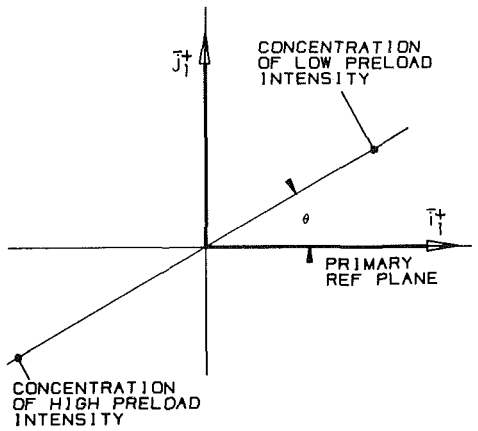

Fig. 3 Reference coordinates of asymmetric preload

Half-Frequency. To obtain the response to a known stimulus at whirl speed of one-half spin speed, elastic asymmetry of the joint is accounted for by using the average stiffness $K + \Delta K/2$ in the linear analysis. Stimulus may be generated by friction within the flexing joint. If the slope increment in elliptical coordinates is $\Delta y_a'$, $\Delta y_b'$, α', ϕ' where $\Delta y_a'$ and $\Delta y_b'$ are positive values, and a constant moment on ΔM_f is produced by friction, the necessary perturbing moment is ΔM_f, ΔM_f, α', $\phi' - \pi/2$.

It would be possible to include at least one harmonic of the half-frequency whirl. Accounting for elastic asymmetry of the joint would require the corresponding correcting moments to be included in the perturbing moments at whirl speeds of $3\omega/2$ and $5\omega/2$. The lower harmonic is due to forward joint flexing, which is assumed to dominate because the frictional moment is forward. It should be possible to derive the component of the frictional moment due to the total joint flexing that should be included in the perturbing moment at whirl speed of $3\omega/2$.

Other Subsynchronous. Periodic whirl at a nonfractional frequency is not possible if elastic asymmetry is present in the rotor joint. If the rotor is axisymmetric, friction induced whirl would occur at the whirl speed of a resonance which is sensitive to that particular stimulus. However, the exact conditions of asymmetry, etc., that would cause the motion to lock into a fractional whirl speed which is near a resonant speed have not yet been determined; the subject of nonperiodic self-sustained whirl has not yet been deeply explored.

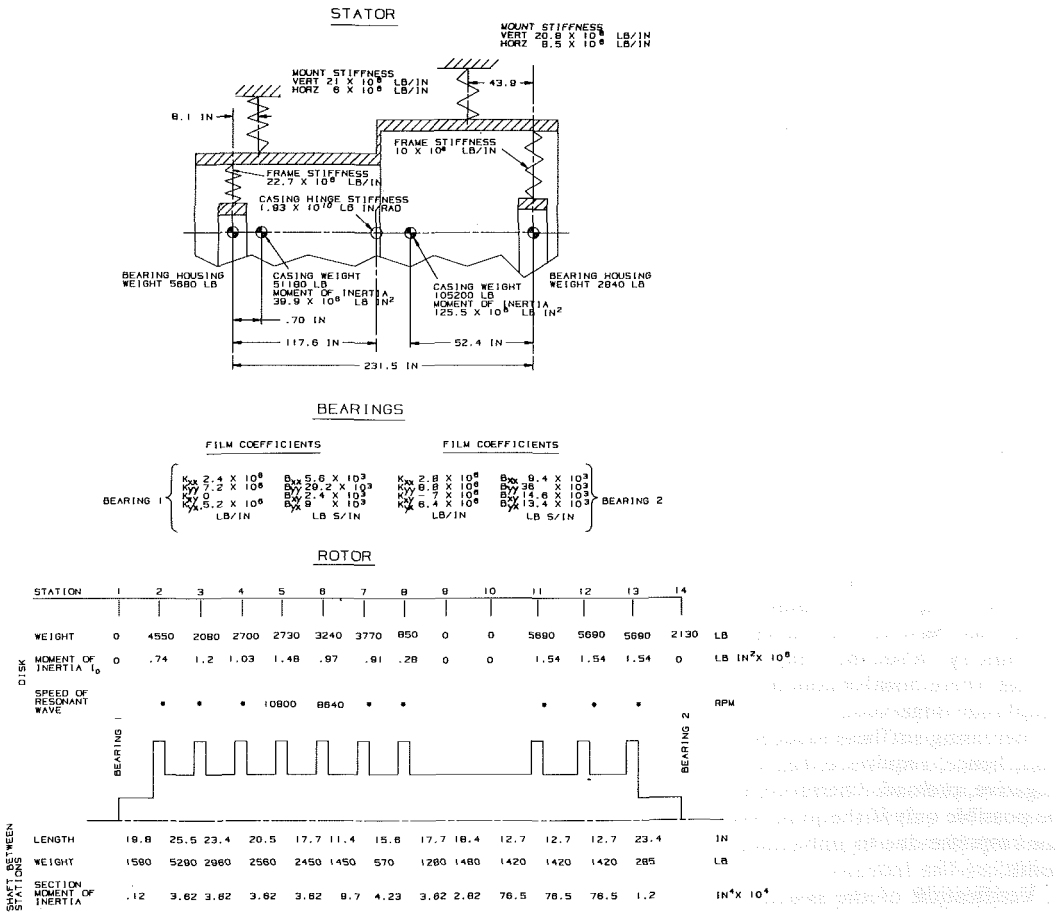

Fig. 4 Model of sample analysis. Conversion Factors: (m) = (in.) × 2.54 × 10^{-2}, (m^4) = ($in.^4$) × 4.162 × 10^{-7}, N = (lb) × 4.448, (N/m) = (lb/in.) × 1.751 × 10^2, (N/m^2) = ($lb/in.^2$) × 6.895 × 10^3, (Nm^2) = (lb $in.^2$) × 2.870 × 10^{-3}, (Ns/m) = (lb s/in.) × 1.751 × 10^2, (Nm/rad) = (lb in./rad) × .1130

Sample Analysis

The model of a hypothetical large gas turbine analyzed previously [3]—the original definition of the model is repeated in Fig. 4—for unbalance response is now used to illustrate the effect of exceeding the breaking moment in an asymmetrically preloaded joint on synchronous whirl. Sensitivity to this effect at design speed of 3600 rpm is highest if the casing hinge stiffness is increased to 2.05×10^{10} lb in/rad from 1.93×10^{10} shown in the figure. Therefore, this higher stiffness is used in the analysis to follow. An elastic hinge is added to the model at station 8.

An arbitrary constant forward perturbing moment defined in elliptical coordinates as $M^P{}_1$, $M^P{}_1$, 0, ϕ^P was impressed into the joint in a series of analyses with only the stiffness of the joint being varied. The phase angle, ϕ^P, of the perturbing moment was corrected for each solution to attain $\phi' = \pi/2$. The results of these analyses are summarized in Fig. 5. The parameters shown are:

ϕ^P, the phase angle of the perturbing moment corresponding to $\phi' = \pi/2$

A, the aspect ratio, major axis/minor axis, of ellipse defining $\Delta y'$

D, major deflection of the joint/$M^P{}_1$

S, major increment of slope across the joint/$M^P{}_1$

A single solution is interpreted, by similarity, to represent limit cycles associated with a range of asymmetric preload conditions defined by a combination of the ratio $m = M_o / \Delta M_o$ and the angle θ. From equations (1) and (2) the following equations are obtained.

$$M^P{}_1 \cos\phi^P = M_o(\cos\theta)/m$$

$$M^P{}_1 \sin\phi^P = M_o[1 + (\sin\theta)/m] \tag{3}$$

Dividing the first equation by the second yields

$$m = \cos\theta \tan\phi^P - \sin\theta \tag{4}$$

The first of equations (3) yields

$$C = \cos\theta / \cos\phi^P \tag{5}$$

where $C = M^P{}_1 / \Delta M_o$ is the coefficient which represents the amplitude of the limit cycle.

The two parameters pertaining to amplitude shown in Fig. 5 may be transformed into the corresponding displacements of the limit cycle by the equations:

$$\text{major deflection of joint} = CD\Delta M_o$$

$$\text{major increment of slope across joint} = CS\Delta M_o \tag{6}$$

All other resultants of the original solution may be transformed by the multiplier $C\Delta M_o / M^P{}_1$.

The combinations of preload conditions that would translate to a limit cycle are shown in Fig. 6 as a plot of θ versus m for a range of joint stiffnesses. Also, the coefficient, C, is shown. The range of θ is limited essentially from -75 deg to 75 deg to illustrate the necessity for avoiding interference between the planes of joint flexing and of preload asymmetry. Also, this range is limited further for low stiffnesses where bistable conditions are calculated and the lower amplitude is ignored.

Increasing stiffness reduces the highest possible value of m and, hence, requires either very high asymmetry or low, or negative, preload. Therefore, the limit cycle eventually would be possible only if the joint were loose. It would converge to the response due to unbalance associated with a kink at the joint.

Verification of the system analysis as described in [3] is retained. The work absorbed by the joint is now calculated and compared to that dissipated by the bearings. Compatibility and equilibrium across the joint, including the effect of this perturbing moment, are verified.

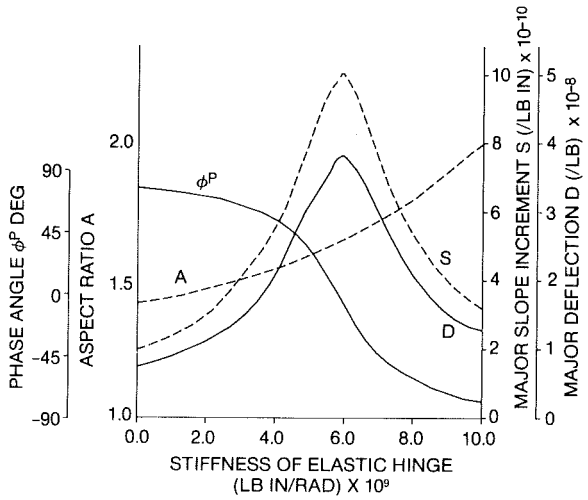

Fig. 5 Summary of linear analyses leading to interpretation of limit cycles. Conversion Factors:
(/N) = (/lb) × .2248
(Nm/rad) = (lb in./rad) × .1130
(/Nm) = (/lb in.) × 8.851

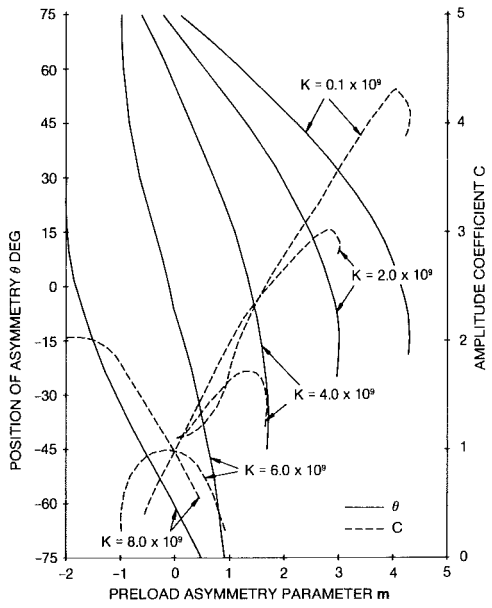

Fig. 6 Parametric plot of limit cycles

Experimental Observations

The experiment of Kottke and Menning [4] where transverse cracks in a steam turbine rotor were thermally opened and closed by variation of steam temperature provides good evidence that an asymmetric joint may cause absorption of energy into synchronous whirl. Their first harmonic amplitude increased by approximately 80 percent when the crack opened and returned to its original value with the crack closed. They also show evidence of the second harmonic produced by stationary deflection. This harmonic arises in significant amplitude only when the crack is opened.

A clear transition from synchronous whirl to half-frequency whirl was recorded in operation of the test rig

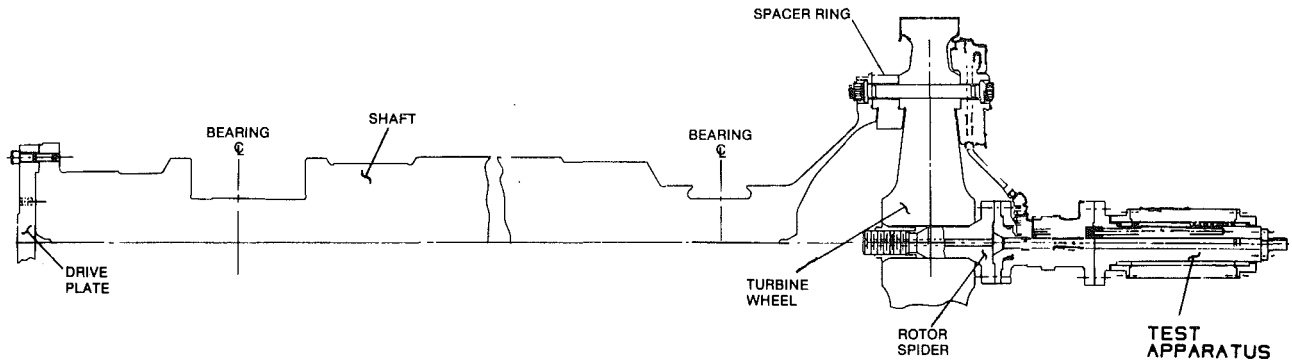

Fig. 7 Rotor of test rig

illustration in Fig. 7. The basic rotor is supported in two journal bearings with its large disk overhung. This rotor-bearing system was known to be stable. However, in support of the particular test, an additional apparatus was attached outboard of the disk. This apparatus contained a rotating element, designated rotor spider, which was joined by shrinking its end into the cylindrical bore of the disk.

Although the necessary tests were successfully completed, considerable difficulty arose because of vibration. Several trials resulted in high synchronous vibration degenerating into high half-frequency vibration. After each such incident, a kink at the joint to the apparatus was found. Increasing the interference at this joint only raised the speed at which the transition in frequency occurred.

Sensitivity of the system to frictional excitation in the joint at half-frequency was confirmed analytically using the present method. It is theorized that an asymmetric preload in the cylindrical joint is produced by manufacturing variations of the mating cylindrical surfaces. Also elliptical synchronous precession produces the highest loads in one direction. Therefore, the joint breaks loose in one plane and provides the conditions necessary for self-sustained whirl at half-frequency. When the whirl is fully developed, the synchronous dynamic forces due to initial kinking of the joint disappear. Instead the kinking converts into cyclic flexing of the joint and the resulting forces are satisfied by the half-frequency whirl. On the other hand, the synchronous whirl reduces to low amplitude.

Although the recorded data of these rig tests are not now accessible for presentation, almost identical behavior of a similar rotor has been presented by Botman and Samaha [5]. They show a large component of half-frequency response at spin speed approximately 70 percent above the critical speed. An explanation for this whirl being of substantially lower speed than that of the synchronous resonance is evident. Since the half-frequency orbit at the disk is backward, it is likely that disk precession is also backward. Therefore, the resonant whirl speed at half-frequency is lower than the critical speed observed synchronously.

Botman and Samaha attribute, without evidence, the half-frequency whirl to nonlinear properties of the oil-film dampers. Their results show evidence of structural asymmetry in the rotor support. However, their vertical inclination of the rotor and the inherent axisymmetry of oil-film dampers and frictionless bearings reduce the probability of significant forced eccentricity which might be suspected of producing the timing mechanism. Moreover, Pan and Tonnesen [6] and the author [7] have shown that asymmetric effects associated with squeeze-film dampers produce harmonics rather than subharmonics.

The data presented by Botman and Samaha provide further evidence of the present theory. There exists a second resonance which would contribute to the amplitude of this periodic sybsynchronous whirl. Frictional moment is generated in the forward direction, and probably the harmonic moment due to asymmetry is largely due to forward joint flexing. A harmonic of the half-frequency whirl would, therefore, be expected at whirl speed of $3 \times 27/2 = 40.5$ krpm. Also, according to [7], elliptical orbits across the oil films would produce forces at this speed. This harmonic indeed is in the influence of the second critical speed. Moreover, gyroscopic stiffening would be lower because of lower spin speed and the effective critical speed may be closer to 40.5 krpm than is indicated by the synchronous response. Therefore, the half-frequency whirl at 27 krpm is probably the result of interaction between two resonant modes, one of whirl speed below and the other above the spin speed.

Discussion

The characteristics of the joint assumed in the sample analysis derive from the idealization which comprises preload through elastic tie rods clamping between two flat surfaces which, when loaded beyond the breaking moment, pivot about a point at the radius of the tie rods. Also the deviations of low and high preload are equal. Although this ideal model is compromised in practice, it should be useful in investigation of system sensitivity to possible joint behavior. An exact solution to a particular vibration of a system is usually not possible because all conditions are not known.

The results of the sample analysis are not intended to indicate likelihood of the synchronous limit cycle in practice; the limit cycle shown appears confined to a very narrow range of conditions. Rather, they are intended to illustrate that joint asymmetry may cause absorption of energy into synchronous whirl. The more likely effect would be transient augmentation of normal steady synchronous whirl.

The constant frictional moment assumed in sub-synchronous whirl would be expected in joints where the sliding occurs only in the axial direction. Joints comprising shrink fits, usually referred to in connection with friction induced whirl, would probably comply with this assumption. However, joints which do not comply may be common. Marmal, Smalley, and Tecza [8] treat a spline joint with frictional forces proportional to the amplitude of motion across the joint. A face spline may behave similarly if sliding on the contact surfaces should occur. Such joints would be more destabilizing because the frictional moment would increase with amplitude. Therefore, limitation of amplitude might require some other nonlinear mechanism in the system.

The lack of precise theory on the stability of a sub-synchronous fractional-frequency limit cycle should not be a detriment; the exact frequency of a potential self-sustained whirl is not of great concern to the engineer. However, it is important to recognize that rotor asymmetry may provide a timing mechanism to lock subsynchronous whirl into an exact frequency. A theory that such a timing mechanism may be produced externally to the rotor is represented by Childs [9].

However, such an external mechanism does not appear to be dominant in the present experimental observations.

Friction effects are usually simulated in linear analysis by equivalent viscous damping. Marmal, Smalley, and Tecza [8] so simulate a spline coupling in calculating onset of friction induced rotor instability. However, their equivalent viscous damping coefficient is based on the total energy dissipated by friction rather than the energy transmitted into subsynchronous motion of particular joint flexing amplitude and whirl speed. They do not show that application of their damping coefficient produces the equivalent transmitted energy. In contrast, the present theory impresses the appropriate component of the frictional moment to motion at the whirl speed of interest. Also, it suggests a derivation of the component applicable to its lowest existing harmonic, or other harmonics.

The present method of analysis may be applied to account for discrete nonlinear effects other than those illustrated. For example, a perturbing force may be impressed in the fluid film of a bearing to determine sensitivity of the system to possible nonlinear characteristics. The effects of rub or aerodynamic interaction between the rotor and the stator may be investigated. The perturbing moment or force may be applied in any linear analytical method which produces precise response to discrete variations in model and stimulus. The verification analyses derived in [3] should confirm the suitability of the analytical method selected.

Summary and Conclusions

Mechanisms have been derived to simulate the restoring moments of possible anomalous—not axisymmetric and elastic as commonly assumed in linear analysis—rotor joints. The difference between the restoring moment of the postulated mechanisms and of an assumed linear model is impressed as a perturbing moment in linear analysis of a complete turbomachine. A solution is attained if the perturbing moment and the resulting flexing of the joint correspond to the conditions of the postulated mechanism.

Sample analysis has been performed to illustrate possible self-sustained synchronous whirl due to inadequate and asymmetric preload in a joint. The correspondence between the perturbing moment and the joint flexing was attained by defining a range of conditions that may be satisfied by a single linear solution. A continuum of possible limit cycles representing variations in a joint of a hypothetical gas turbine was thus calculated.

Simulation of frictional moment sustaining subsynchronous whirl and, possibly, a harmonic was discussed. A mechanism where stiffness asymmetry locks subsynchronous whirl into circular frequency, which is an exact fraction of spin speed, was derived. Experimental observations of half-frequency whirl were cited as evidence of this mechanism.

Acknowledgment

The author is indebted to E. L. Teaney for assistance in preparation of figures for this and previous papers.

References

1 Grabowski, B., "The Vibrational Behavior of a Turbine Rotor Containing a Transverse Crack," ASME *Journal of Mechanical Design*, Jan. 1980, pp. 140–146.

2 Inagaki, T., Kanki, H., and Shiraki, K., "Response Analysis of a General Asymmetric Rotor-Bearing System," ASME *Journal of Mechanical Design*, Jan. 1980, pp. 147–157.

3 Klompas, N., "Unbalance Response Analysis of a Complete Turbomachine," ASME JOURNAL OF ENGINEERING FOR POWER, Jan. 1983, pp. 184–191.

4 Kottke, J. J., and Menning, R. H., "Detection of a Transverse Crack in a Turbine Shaft—The Oak Creek Experience," *ASME Paper No. 81-JPGC-Pwr-19*.

5 Botman, M., and Samaha, M. A., "Experiments on the Dynamic Behavior of a Supercritical Rotor," ASME *Journal of Mechanical Design*, Apr. 1982, pp. 364–369.

6 Pan, Coda H. T., and Tonnesen, J., "Eccentric Operation of the Squeeze-Film Damper," ASME *Journal of Lubrication Technology*, July 1978, pp. 369–378.

7 Klompas, N., "Blade Excitation by Elliptical Whirling in Viscous-Damped Jet Engines," JOURNAL OF ENGINEERING FOR POWER, Apr. 1981, pp. 326–330.

8 Marmal, R. A., Smalley, A. J., and Tecza, J. A., "Spline Coupling Induced Nonsynchronous Rotor Vibrations," ASME *Journal of Mechanical Design*, Jan. 1980, pp. 168–176.

9 Childs, D. N., "Fractional-Frequency Rotor Motion Due to Nonsymmetric Clearance Effects," ASME JOURNAL OF ENGINEERING FOR POWER, July 1982, pp. 533–542.

APPENDIX A

Simulation of a Nonelastic and/or Nonsymmetric Rotor Joint

The rotor joint is simulated by an axisymmetric, elastic hinge in the linear model. Variations in its restoring moment due to its differences from the assumed elastic hinge must be accommodated by appropriate mechanisms. Derivation of mechanisms representing some possible characteristics of a joint follow.

Elastic and Asymmetric. The restoring moment and the flexing motion across a joint are called M^R and $\Delta y'$, respectively, and their directions in a plane of reference are defined in Fig. 8. Their representation as vector components is shown in Fig. 9 for synchronous motion where $\Omega = \omega$. The pair of reference unit vectors, $\bar{i}_1^+$, $\bar{j}_1^+$, which travel forward are stationary with respect to the rotor and coincide with the principal axes of the hinge. The axisymmetric hinge stiffness, K, in the basic model is that which applies in the plane of vector $\bar{i}_1^+$. The difference between this assumed stiffness and that in the plane of vector $\bar{j}_1^+$, ΔK, will be accounted for by impressing the equivalent perturbing moment in the joint. This moment is applied internally in direction of the elastic restoring moment as shown in Fig. 8. It accounts for error in the linear model associated with each component of joint flexing as follows:

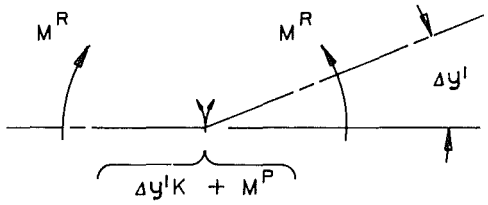

Fig. 8 Restoring moment and flexing in plane of reference

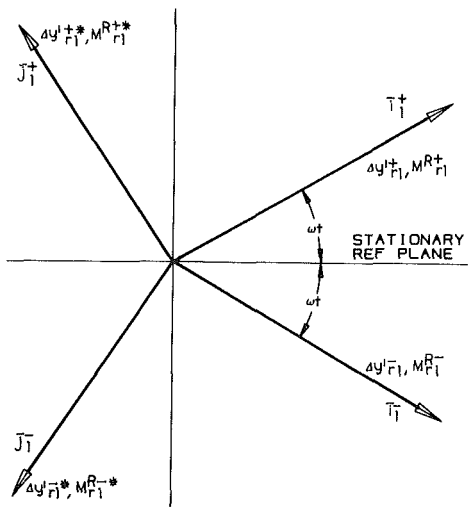

Fig. 9 Restoring moment and flexing as vector components

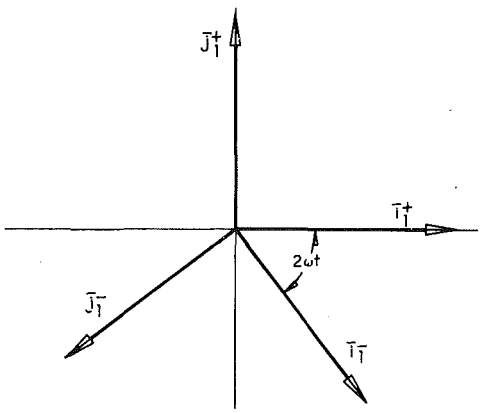

Fig. 10 Reference vectors with respect to spinning frame

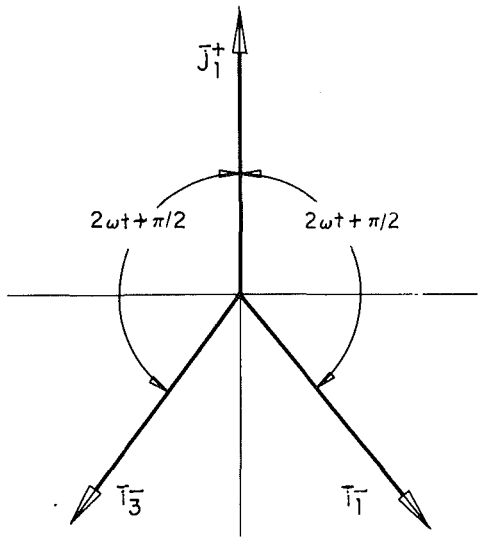

Fig. 11 Reference vectors to define oscillating moment in spinning rotor

$\Delta y'^{+}_{r1}$: The response of the hinge is correctly represented by the linear model.

$\Delta y'^{+*}_{r1}$. The model attributes the wrong stiffness to the plane of this component. The moment $\Delta y'^{+*}_{r1}\ \Delta K\ \bar{j}_1^+$ corrects this error.

$\Delta y'^{-}_{r1}$. This component travels backward at an angular speed of 2ω relative to rotor. The constant moment accounted for by the linear model must be corrected to represent the effect of traveling over the asymmetric stiffness. This effect is best visualized by coordinate transformation to the frame of reference defined by the pair of reference vectors $\bar{i}_1^+$, $\bar{j}_1^+$. Accordingly, Fig. 10 shows the reference vectors $\bar{i}_1^-$, $\bar{j}_1^-$ as they rotate with respect to the elastic asymmetry. The moment due to $\Delta y'^{-}_{r1}$ is seen as $\Delta y'^{-}_{r1}\ (K\bar{i}_1^- - \Delta K \sin 2\omega t\, \bar{j}_1^+)$.

The model accounts for the component associated with the vector $\bar{i}_1^-$ and the perturbing moment must contain the oscillating component in the direction of $\bar{j}_1^+$. This oscillating component is transformed into the sum of two constant components associated with reference unit vectors traveling forward and backward at speed 2ω symmetrically about $\bar{j}_1^+$. Figure 11 shows that the backward component is associated with the reference unit vector $\bar{i}_1^-$. A new pair of reference vectors, $\bar{i}_3^+$, $\bar{j}_3^+$ are defined to accommodate the forward component which is then associated with $\bar{i}_3^+$. The two equivalent components then are

$$(\Delta y'^{-}_{r1}\ \Delta K/2)(\bar{i}_1^- + \ + \bar{i}_3^+)$$

The component associated with the reference vector $\bar{i}_1$ can be accounted for by a perturbing moment in the synchronous analysis. However, the other component cannot be so satisfied; it is orthogonal to synchronous motion and produces the third harmonic at whirl speed of 3ω.

$\Delta y'^{-*}_{r1}$. Similar derivation to that for $\Delta \hat{y}_{r1}^-$ leads to the necessary correcting moment of

$$(\Delta y'^{-*}_{r1}\ \Delta K/2)(\bar{j}^-{}_1 + \bar{j}^+{}_3)$$

It would be possible to use the linear model to analyze the response of the third harmonic. This harmonic would in turn require a correcting moment with orthogonal components of third order which would produce a further harmonic at whirl speed of 5ω and would interact with the synchronous solution.

A similar derivation may be obtained for subsynchronous whirl where all four components of joint flexing travel with respect to the rotor. The linear model need only assume an effective stiffness of $K+\Delta K/2$ for the hinge to avoid the necessity of a correcting moment. However, moments at higher whirl speeds of $2\omega-\Omega$ and $2\omega+\Omega$ are produced by the forward and backward components, respectively. Therefore, a periodic solution is possible only if the whirl speed is an exact fraction of the spin speed. For example, if $\Omega=\omega/2$, harmonics at whirl speeds of 3Ω and 5Ω are produced.

Another condition where the equivalent joint stiffness of an asymmetric joint is the average of the principal stiffnesses arises in stationary deflection. There remains a component of moment which must be satisfied by the second harmonic.

The asymmetry of the stiffness may contain a further complication; the variation in stiffness, ΔK, may apply only in one direction of the associated principal axis. This condition can be accommodated in synchronous motion by assuming an asymmetric preload, to be defined below. For half-frequency whirl, for stationary deflection and for higher harmonics a good approximation would be to continue using the average stiffness with the correction now at $\Delta K/4$. This approximation would be correct for the particular whirl speed of the analysis, but would not satisfy orthogonal components of moment at other speeds.

Nonelastic. Two nonelastic effects that may be significant are those associated with preload and friction. Figure 1 shows the relationship of the restoring moment to the flexing of a preloaded joint; elastic behavior is assumed after the breaking moment, M_o, is exceeded. It is conceivable that insufficient preload and/or thermal deformation may reduce the breaking moment to zero. Thermal deformation causing joint separation may produce the conditions shown in Fig. 2. The joint responds elastically until the gap on the compression side of the joint is closed, and the original stiffness is recovered. If flexing exceeds closing of the gap, the joint may be represented by the stiffness and an initial breaking moment which is negative.

A further influence may be due to asymmetric preload. Assume that the slope increment of joint flexing is associated with the reference vector j_1^+. Also assume that the nonuniformity of the preload is such that concentrations of lower than average and higher than average preload lie in the plane of angle θ as shown in Fig. 3. If neither concentration of preload is in the region of compression centered on the vector j_1^+, the moment ΔM_o in direction of angle θ is produced. Hence, the restoring moment of the joint must be corrected by the term

$$\Delta M_o(\cos\theta\, \bar{i}_1^+ + \sin\theta\, \bar{j}_1^+)$$

Perturbing moments derived above to account for asymmetric preload satisfy equilibrium only at the instances when the slope increment vector passes its ellipse axis. If this vector is defined by a circle, equilibrium is maintained throughout the cycle. However, if it is defined as an ellipse, the necessary

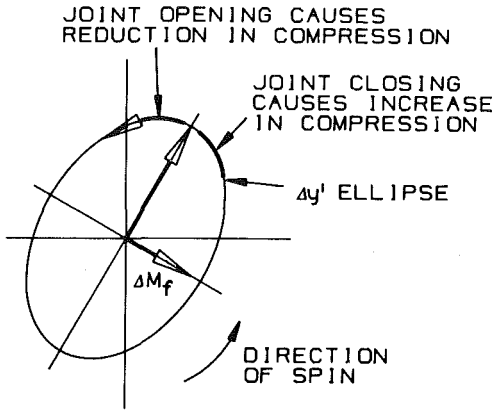

Fig. 12 Cause of frictional moment

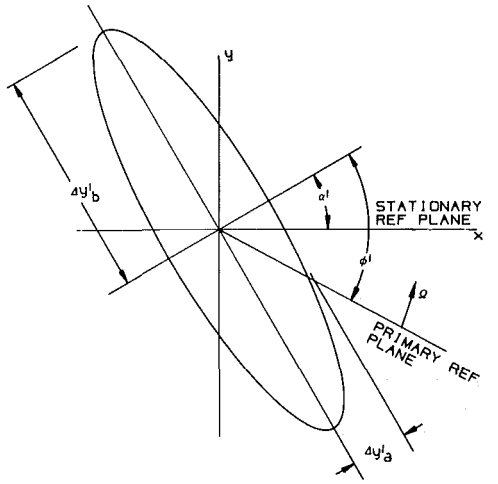

Fig. 13 Joint flexing definition in elliptical coordinates

constant angle between the slope increment vector and the correcting component of moment varies in the region between the axes. However, the effect of this variation in one quadrant is cancelled in the next. Therefore, the results obtained at the whirl speed of the analysis remain correct; only possible higher harmonics are ignored.

Subsynchronous whirl may be affected by friction in a flexing joint. Figure 12 illustrates the slope increment across the joint as a vector at the instant it passes its major ellipse axis. The forward rotation of the joint relative to the vector produces frictional forces which are compressive in the quadrant lagging and tensile in the quadrant leading the vector. The result is a moment which lags by 90 deg. If friction exists also at the tensile side of the joint, an additional moment of the same phase angle is produced. The net frictional moment is shown as ΔM_f.

The assumption of constant frictional moment and phase angle is satisfied only at the principal axes of a slope increment vector. The angular velocity of this vector is at its peak at the minor axis; the direction of the frictional moment would reverse if this velocity should exceed the spin speed. Also, because the magnitude of the slope increment varies between its principal axes, the phase angle of lag would be greater than 90 deg in the quadrants where the magnitude is increasing and less than 90 deg in the quadrants where the magnitude is decreasing. This error due to ellipticity is similar to that of a squeeze-film damper [7]. The third harmonic of whirl circular frequency is excited.

If the slope increment across the joint at the whirl speed of interest and that at its lowest existing harmonic, with whirl speed of 3Ω, are added, a nonelliptical slope increment vector is obtained. The frictional moment due to this combined joint flexing should contain orthogonal components which are applied as perturbing moments in independent linear analyses at the two whirl speeds. Solution of a limit cycle would be attained when the joint flexing obtained from each of these analyses and the perturbing moments applied to them match. A residue of the moment would remain unsatisfied and would excite yet higher harmonics.

It is clear that the frictional moment applicable to the subsynchronous whirl speed of interest is the constant value of ΔM_f at lag angle of 90 deg as initially postulated. That applicable to the harmonic would require a four-dimensional Fourier analysis which will not now be derived. However, some of its implications will be discussed.

If the circular frequency of the harmonic is greater than the spin speed, increasing amplitude might produce reversals in the direction of the frictional moment and, hence, a limiting value of the amplitude. However, if the subsynchronous whirl speed is substantially lower than the spin speed, and the slope increment of the harmonic is small, the harmonic may be excited directly by the frictional moment despite its circular frequency.

APPENDIX B

Definition of Elliptical Coordinates

Figure 13 illustrates a vector quantity with direction and amplitude varying as in the solution of the linear analysis at one whirl speed. For convenience, the slope increment across a joint is represented. The magnitude associated with any direction is represented by the corresponding radial distance from the origin to the ellipse. The orientation angle of the ellipse axes is designated α'. The component $\Delta y'_a$ is on the axis displaced by α' from the stationary reference plane. The phase angle ϕ' represents the location of the whirl primary reference plane, which rotates at whirl speed Ω, at the instant of the slope increment defined by the dimension $\Delta y'_a$. Therefore, the phase angle is the lead angle in relation to the primary reference plane of the slope increment on an axis of the ellipse and on the side designated by the sign of the appropriate component $\Delta y'_a$ or $\Delta y'_b$. If the signs of the two components are the same, the motion of the vector is forward; if the signs are opposite, the motion is backward.

The periodicity of the coordinates permits different combination of components to represent the same vector. If 180 deg are added or subtracted from the phase angle the signs of $\Delta y'_a$ and $\Delta y'_b$ are reversed. Also, if 90 deg are added or subtracted from the orientation angle, the values of $\Delta y'_a$ and $\Delta y'_b$ are interchanged.

An Investigation Into the Effect of Side-Plate Clearance in an Uncentralized Squeeze Film Damper

R. A. Cookson

L. J. Dainton

Applied Mechanics Group,
School of Mechanical Engineering,
Cranfield Institute of Technology,
Cranfield, Bedford MK43 OAL, England

An experimental investigation has been carried out into the influence of side-plate flow restrictors on the performance of a squeeze film damper bearing. The experimental rig used was a flexible rotor with a disk positioned midway between two squeeze film damper bearings. One of the squeeze film dampers was fitted with side plates that could be adjusted and accurately located with respect to the squeeze film damper journal. It has been found that the influence of the side-plate clearance on the ability of the squeeze film damper to reduce the amplitude of the central disk can be considerable if the side-plate clearance is less than the radial clearance. As the side-plate clearance reduces towards zero, the effectiveness of the squeeze film damper diminishes until the amplitudes obtained are the same as those measured when the rolling-contact bearing is rigidly supported. An interesting type of precessing elliptical orbit was discovered for conditions where the "jump" phenomenon was operating.

Introduction

One of the many design criteria to which the gas turbine manufacturer must work, is the limitation of vibration, either within the gas turbine or transmitted to the surrounding structure. The most common causes of vibration are engine order excitation of disks and blades and synchronous excitation due to unbalance. In service, the level of vibration, set to very fine limits by the manufacturer, may increase due to material loss from the blades or be caused by the bowing of shafts and uneven distortion of blades produced by thermal gradients. In the final analysis, the level of vibration may become unacceptable to the customer and require some costly exercise for its alleviation.

The minimization of rotor vibration within gas turbines has been achieved over the last 10 to 15 years by the use of squeeze film damper bearings. In its simplest form the squeeze film damper consists of a fluid-filled annular cavity surrounding the outer race of a rolling contact bearing. This annular cavity is usually filled with engine oil, and the clearance between the bearing housing and the outer race of the bearing (journal) is generally in the order of 0.1 mm to 0.2 mm.

A major variation in the design of squeeze film dampers exists. One type allows the bearing to settle freely to the bottom of the clearance circle until unbalance causes it to lift off. The other type has the bearing outer race supported by a set of cantilever springs (known collectively as a squirrel cage), so that the bearing is held centrally within the clearance circle. The first of these two types is that usually used by engine manufacturers in the United Kingdom, and is often referred to as an uncentralized squeeze film damper, while the second is that most often adopted by manufacturers in the United States. These two design variants are shown in Fig. 1.

From Fig. 1 it can be seen that side (or end) plates can be employed with either uncentralized or squirrel-caged squeeze film dampers. However, in the former case they have the dual role of restricting flow and also restraining the movement of the outer race, whereas in the latter case their flow restricting capabilities could be provided by, say, an "O"ring.

Although it may be desirable, even necessary, to limit the

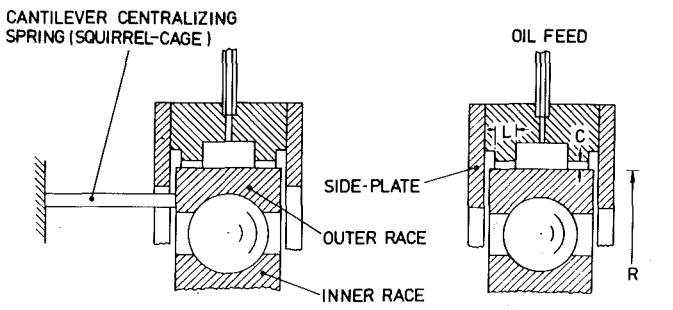

(a) CENTRALIZED VERSION (b) UNCENTRALIZED VERSION

Fig. 1 Centralized and uncentralized squeeze-film dampers

Contributed by the Gas Turbine Division of THE AMERICAN SOCIETY OF MECHANICAL ENGINEERS for presentation at the 28th International Gas Turbine Conference and Exhibit, Phoenix, Arizona, March 27-31, 1983. Manuscript received at ASME Headquarters December 29, 1982. Paper No. 83-GT-176.

flow of oil through the squeeze film damper, and hence to the rolling-contact bearing, there must be a strong possibility that the restriction of flow will influence the vibration inhibiting performance of the device. For example, from very simple considerations it can be seen that the restriction of flow will raise the pressure at outlet from the damper land, and that this in turn will increase the average load-carrying capacity of the squeeze film. However, since it is known that the level of cavitation within the fluid-film also influences the performance of a squeeze film damper [1], and that there is a tendency for cavitation bubbles to persist after the low-pressure condition has passed [2], it can be seen that the vibration inhibiting properties of the damper could vary with the fluid flow rate. By the same token, this influence is probably at its greatest in a squeeze film damper fitted with "O" rings, since in that case the axial flow of the fluid would be zero.

There have been a number of theoretical studies in which an attempt was made to assess the influence of the end seal on the performance of a squeeze film damper, for example, [3] and [4]. In [3], a number of end seal conditions, including side plates, were studied, while for [4] a conclusion was reached that side plates fitted to squirrel caged, squeeze film dampers could increase the damping coefficient if the side-plate clearance was reduced.

It was, therefore, the main aim of this experimental investigation to study the influence of side-plate clearance on the effectiveness of uncentralized squeeze film dampers. A subsidiary aim was to investigate the result of positioning the damper journal on one side of the axial clearance, a condition which could occur with an uncentralized squeeze film damper which was subjected to an axial load. At a much simpler level it was also decided to attempt to discover the position taken up by the journal within the axial clearance when it was allowed to move freely.

Since it is possible that the influence of the side-plate clearance could vary with the effectiveness in vibration inhibiting terms, of the squeeze film damper, and with the operating unbalance levels, these characteristics of the system have been taken as variables in this experimental investigation. Previous studies [5] have allowed us to correlate the effectiveness of an uncentralized squeeze film damper in terms of certain dimensionless parameters, in particular the bearing parameter, B. Therefore, it was decided to study the effect of side-plate clearance on a squeeze film damper configuration that was known to have good vibration inhibiting properties ($B = 0.146$), and another which was known to have relatively poor vibration inhibiting properties ($B = 0.694$). Three unbalance levels were used, defined by $U = 0.1, 0.2$, and 0.3.

Experiment

The experimental investigation reported in this paper utilizes an existing rig which was used by Kossa [6] in his work on determining the effectiveness of squeeze film dampers. In this rig, a centrally located disk is mounted on a shaft which is supported by two squeeze film damped rolling contact bearings. However, for the present investigation one of the bearing pedestals has been modified in such a way as to allow the side-plate clearance to be accurately adjusted and measured over a relatively large range (see Fig. 2).

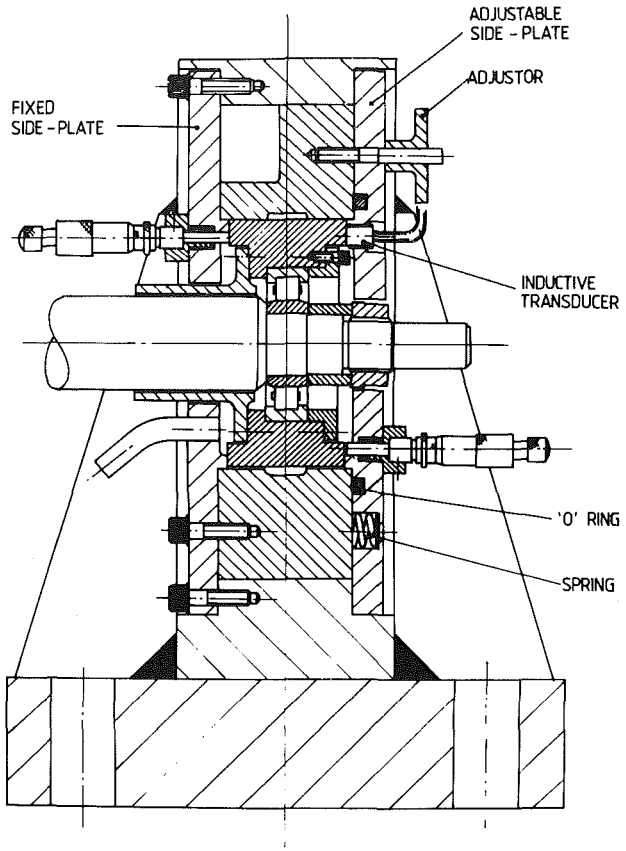

Fig. 2 Bearing pedestal with adjustable side-plate

It is a feature of this rig, which is described more fully in [6], that the squeeze film clearance and the operating land widths can be changed so as to give different damper characteristics, these characteristics being defined in non-dimensional form in the manner described in [5]. However, in the earlier experiments the side-plate clearances were maintained at a constant value which was greater than the radial clearance.

For the present investigation, one of the side plates was kept fixed, while the other was fully adjustable, being located by six studs and adjusting nuts (although definition of the plane of the side plate could obviously be achieved with three adjusters, it was felt that better control could be maintained over the small clearances being used, if six adjusters were incorporated in the design). Unwanted movement or vibration, of this side plate was prevented by the presence of

Nomenclature

B = bearing parameter ($\mu RL^3/m\omega_c c^3$), nondimensional
c = radial clearance, m
e_u = unbalance eccentricity, nondimensional
F_u = unbalance force ($me_u\omega^2$), N
G = rotor peak-to-peak amplitude, m
g = gravitational acceleration, m/s^2
L = squeeze film bearing land length, m
m = mass, kg
R = journal radius, m
U = unbalance parameter ($F_u/mc\omega^2$), nondimensional
$\bar{W}$ = gravity parameter ($mg/mc\omega_c^2$), nondimensional
ω = rotor angular speed, (rad/s)
μ = fluid viscosity, Ns/m^2
ω_c = first pin-pin critical speed, rad/s
Ω = speed ratio (ω/ω_c), nondimensional

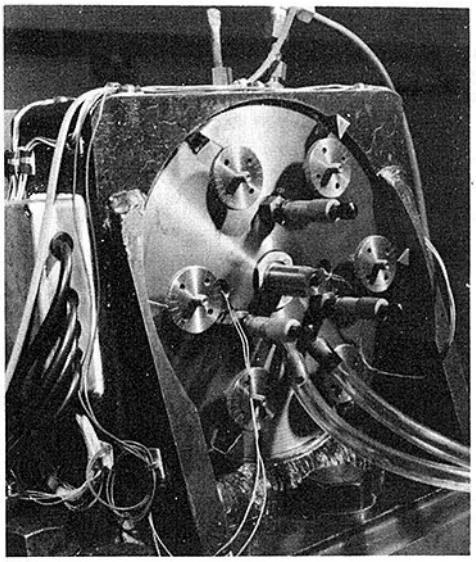

Fig. 3 Adjustable side-plate

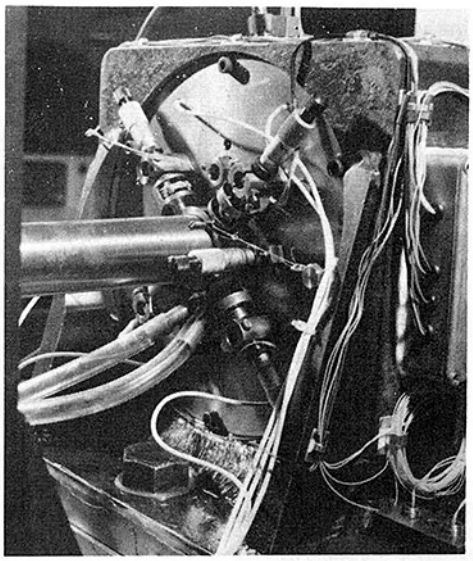

Fig. 4 Fixed side-plate and journal amplitude measurement

Table 1

	Radial clearance c(mm)	Land length L(mm)	Average viscosity μ(Ns/m^2)	Unbalance (gm.cm)	Unbalance parameter U	Gravity parameter $\bar{W}$	Bearing parameter B
First configuration	0.191	15.24	1.70×10^2	17.00	0.1	0.089	0.146
	0.191	15.24	1.70×10^2	34.00	0.2	0.089	0.146
	0.191	15.24	1.70×10^2	51.00	0.3	0.089	0.146
Second configuration	0.127	15.24	2.39×10^2	11.33	0.1	0.134	0.694
	0.127	15.24	2.39×10^2	22.66	0.2	0.134	0.694
	0.127	15.24	2.39×10^2	33.99	0.3	0.134	0.694

six coiled springs located on the adjuster screws. Similarly, leakage of damper oil, other than through the side-plate clearance, was prevented by the inclusion of a sealing "O" ring. During these tests the side-plate clearances for the other bearing pedestal were kept equal to the radial clearance.

Micrometer barrels were positioned on either side of the bearing housing, primarily to allow the side-plate clearance to be measured, but also so that the damper journal could be positioned within the side-plate clearance for some tests.

The orbits of the squeeze film damper journal, and of the central disk, were monitored by means of two pairs of linked inductive transducers in each case. Unfortunately, because of the limitations on available space, the journal transducers are mounted on 45 deg axes, whereas the disk transducers are mounted vertically. Hence, in linking together appropriate disk and journal orbits, one orbit must be rotated through 45 deg relative to the other.

The radial depth of the side plate was kept at about 5 mm since this is approximately the dimension employed in modern gas turbines. Earlier tests have shown that a greater depth of narrow clearance will affect the performance of the squeeze film damper.

Oil was supplied to the squeeze film and to the rolling contact bearings from a gear pump which provided a maximum pressure of about 200 kN/m^2 (30 psi). However, most of the tests reported here were carried out with an oil supply pressure of about 35 kN/m^2 (5 psi). The oil temperature was monitored at the entrance to the damper in order that the viscosity could be determined accurately. The oil used throughout this investigation was Turbine Oil 3.

A sectional view of the bearing pedestal with adjustable side plate is given in Fig. 2, and Figs. 3 and 4 are photographs of the pedestal from the adjustable side plate and fixed side-plate sides, respectively.

Results

In this investigation, two configurations of the uncentralized squeeze film dampers were employed. These configurations are defined by bearing parameter B values of 0.146 and 0.694, respectively. The first of these configurations is known to have good vibration inhibiting properties [6], whilst from the same source the vibration inhibiting properties of the second version are known to be relatively poor. The basic data for the two series of tests are contained in Table 1.

The measured first (pin-pin) critical speed for the rotor operating on active squeeze film dampers was 7230 rpm (ω_c = 757.1 rad/s).

For the experiments aimed at investigating the effect of side-plate clearance on the rotor response, a range of side-plate clearances from much greater than the radial clearance down to zero, were used. Similarly, a speed range from Ω = 0.4 to 1.4 was used. While these variations of the properties of the variable side-plate pedestal were being tested, the side-plate clearances of the other pedestal were maintained at the same value as the radial clearance.

A typical set of oscilloscope traces of the orbits of both the disk (midspan) and the journal when B = 0.146 and U = 0.1 are contained in Fig. 5. It should be noted that the ellipse major axis should be vertical since these readings were taken near the critical speed (Ω = 0.997). The apparent 45 deg orientation is produced by the positioning of the transducers.

From the maximum amplitudes obtained from the

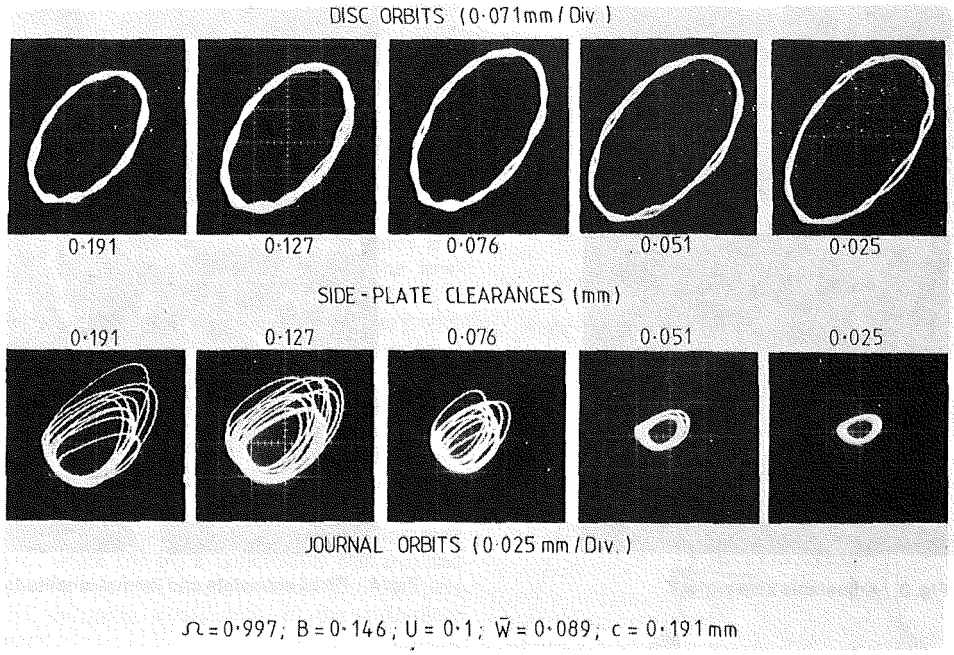

Fig. 5 Journal and disk orbits for various side-plate clearances

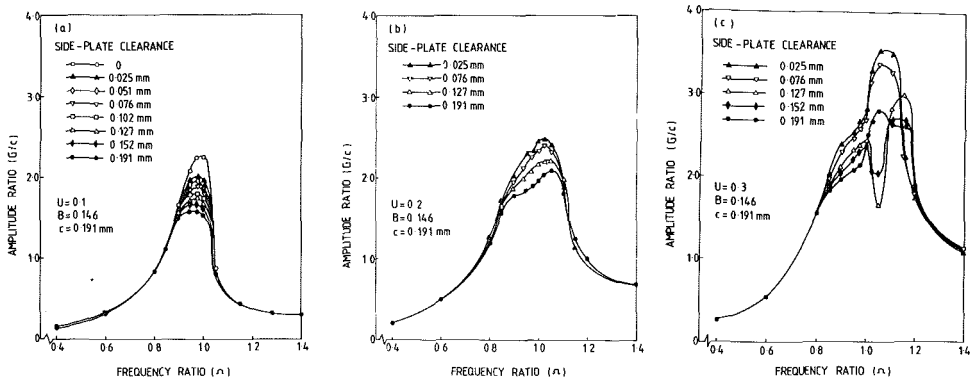

Fig. 6 The variation of response of an effective squeeze film damper (B = 0.146) with side-plate clearance for three levels of unbalance

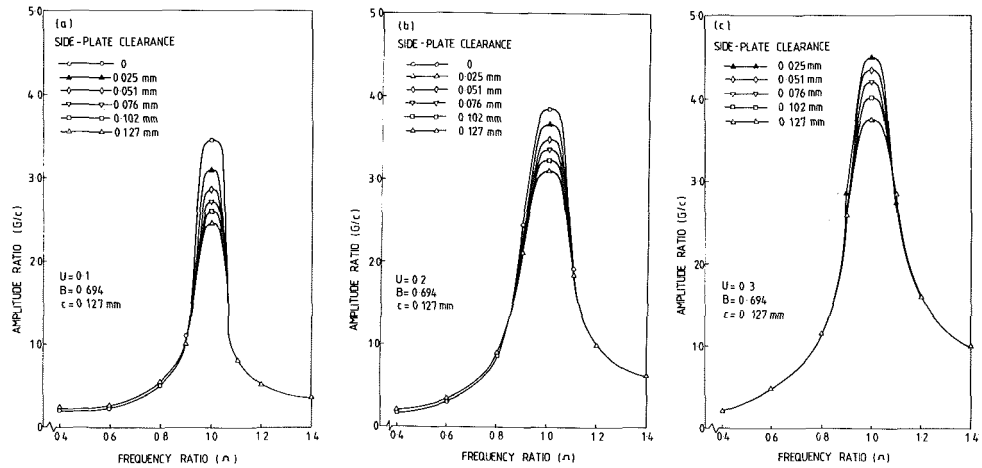

Fig. 7 The variation of response of a relatively ineffective squeeze film damper (B = 0.694) with side-plate clearance for three levels of unbalance

oscilloscope traces (for example Fig. 5) response curves, such as those shown in Figs. 6 and 7, can be produced. Figure 6 is a plot of the amplitude ratio (nondimensionalized to the radial clearance) against the speed ratio, for the more effective of the two squeeze film damper configurations B = 0.146. The response for three levels of unbalance are shown. Figure 7 is a similar trio of plots for the less effective of the squeeze film dampers where B = 0.694.

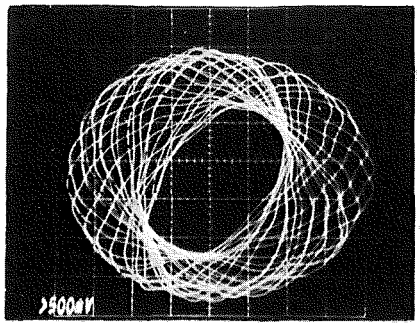

U = 0·3 ; B = 0·146 ; Ω = 0·985 ; c = 0·191 mm

PHOTOGRAPH EXPOSURE 0·2 Sec.

Fig. 8 Precessing jump orbit

The trace obtained for the apparently unstable region on Fig. 6(*c*), that is, where $U = 0.3$ and the side-plate clearance is 0.152 mm, is given in Fig. 8.

During this investigation other results were obtained, for example, the response curves produced when the squeeze film damper journal was translated axially until one of the clearances closed up. Also, a study was made of the interaction between oil supply pressure and side-plate clearance. Unfortunately, there is not enough room in this report to include these results, but they can be found in [7]. However, the normal positioning of the journal within the total axial clearance was observed at every stage and will be commented upon later.

Discussion

The results from the foregoing experiments clearly showed, as would probably be expected, that side-plate clearance did not affect the squeeze film damper performance until it became less than the radial clearance. However, once the side-plate clearance is less than the radial clearance, it clearly begins to affect the rotor response as can be seen from Figs. 6 and 7. As the side-plate clearance is reduced below 0.191 mm (which is the radial clearance), it can be seen that the disk amplitude grows larger until the side-plates pinch the journal and a condition, equivalent to that encountered when the rolling-contact bearing is rigidly fixed, is reached. The amplitudes shown on Figs. 6 and 7 would almost certainly have been greater if side-plate clearances had been reduced on both bearing pedestals. As it is, the squeeze film damper effect of the unadjustable pedestal helps to reduce the maximum amplitude experienced.

From Figs. 6 and 7, it can be seen that the increase in amplitude at the critical speed as the side-plate clearance reduces from a value equal to that of the radial clearance down to 0.025 mm is greater for the less effective squeeze film damper ($B = 0.694$) than for the more effective device. Of course, the absolute value of the amplitude is also greater, by definition, and the percentage increase is approximately the same (12.5 percent) for both configurations. Similarly, the percentage amplitude increase from the condition where the side-plate clearance equals the radial clearance to the condition where it is equal to 0.025 mm remains fairly constant at all levels of unbalance.

The results shown by Fig. 6(*c*) are particularly interesting since they appear to indicate the onset of the "jump phenomenon" as previously reported by [8], [2], and [9]. Figure 6(*c*) shows the disk amplitudes for large unbalance $U = 0.3$ and for side-plate clearances from 0.025 mm to 0.191 mm. The response curves for side-plate clearances of 0.025 mm, 0.076 mm, and 0.191 mm (that is, the two smallest and the largest) behave very much as expected, but the response curves for intermediate side-plate clearances, 0.127 mm and 0.152 mm, show a large drop in the peak amplitude in the region of the critical speed. The points within the troughs on the 0.127 and 0.152 mm curves of Fig. 6(*c*) indicated stable orbits of the small amplitude shown. Whereas in transit from point to point, the amplitude was seen to "jump" from the small orbit to a large orbit in a random manner. The process of jumping from a small to a large orbit, and vice-versa, has been well documented, for example, in [8], [2], and [9], but in the tests reported here a third mode of orbiting appears to exist. In this mode, an elliptical orbit is taken up with a minor axis equal to that of the small circular orbit and a major axis equal to that of the large orbit. The axis of this ellipse then precesses at some unpredictable rate. Figure 8 shows this precession lasting for 0.2 s and hence producing a composite photograph of several superimposed ellipses. This orbit mode was always observed when a jump occurred from a small orbit to a large orbit, or from a large orbit to a small orbit. However, the rate of precession would vary from occasion to occasion. This would appear to suggest that some part of the unbalance force causes the change in attitude of the elliptical orbit, with the rate of precession depending upon the forces present.

In general, the application of an axial load to offset the squeeze film journal within the axial clearance gave a reduced effectiveness when the side-plate clearance approached the radial clearance and a slightly increased effectiveness for small side-plate clearances. For intermediate clearances the effectiveness was almost unchanged. For a fuller description, see [7].

Whenever the squeeze film damper journal was forced to one extreme or other of the axial clearance, it always returned to a position roughly in the center of the clearance and tended to hunt slightly about that position. Consideration of equilibrium would perhaps suggest that this should be so.

Conclusions

The effect of side-plate clearances that are smaller than the radial clearance could be considerable. As the side-plate clearance was reduced, the effectiveness of the squeeze film damper in reducing the amplitude of whirl of the midspan disk was severely reduced. The rotor response tended towards the rigid support response when the squeeze film operated with small side-plate clearances.

Side-plate clearances larger than the radial clearances were found not to reduce the performance of the squeeze film damper.

The reduction in effectiveness of the squeeze film damper was approximately the same in percentage terms for a device which was known to be a good inhibitor of vibration, as for one which was known to be poor in those terms. Similarly, the percentage loss in effectiveness was approximately the same whether the unbalance parameter U was 0.1, 0.2, or 0.3. Obviously, the reduction in absolute terms (amplitude) could be quite different.

If the squeeze film damper journal was forced to one side or the other of the axial clearance, the effectiveness of the squeeze film damper was found to decrease if the side-plate clearance was approximately the same as the radial clearance, while it could increase if the side-plate clearance was small. When released, the journal always took up a position approximately in the middle of the axial clearance.

An interesting orbit mode was observed under conditions

when the "jump" phenomenon could take place. An elliptical orbit or small orbit minor axis and large orbit major axis was found to precess at a constant rate.

References

1 Humes, B., and Holmes, R., "The Role of Subatmospheric Film Pressures in the Vibration Performance of Squeeze-Film Bearings," *J. Mech. Eng. Sci.*, Vol. 20, No. 5, 1978, pp. 289–293.

2 White, D. C., "The Dynamics of a Rigid Rotor Supported on Squeeze Film Bearings," *Proceedings of the I. Mech. E., Conf.*, "Vibrations of Rotating Systems," 1972, pp. 213–229.

3 Marmol, R. A., and Vance, J. M., "Squeeze Film Damper Characteristics for Gas Turbine Engines," ASME *J. Mech. Des.*, Vol. 100, No. 1, 1978, pp. 139–146.

4 Toshio, M., Hoshiya, S., Sofue, Y., Matsuki, M., and Torisaki, T., "Oil Squeeze-Film Dampers for Reducing Vibration of Aircraft Gas-Turbine Engines," ASME Paper No. 79-GT-133, 1979.

5 Cookson, R. A., and Kossa, S. S., "The Vibration Inhibiting Properties of Uncentralized Squeeze Film Dampers Supporting a Flexible Rotor," JOURNAL OF ENGINEERING FOR POWER, Oct. 1981, pp. 781–787.

6 Kossa, S. S., "Theoretical and Experimental Investigation of Uncentralized Squeeze-Film Damper Bearings," Ph.D. thesis, Cranfield Institute of Technology, 1980.

7 Dainton, L. J., "An Investigation into the Effect of Side-Plate Clearance on Squeeze-Film Damper Bearings," M.Sc. thesis, Cranfield Institute of Technology, 1982.

8 Cooper, S., "Preliminary Investigations of Oil Films for the Control of Vibration," *Proc. Lub. and Wear Conf.*, I. Mech. E., 1963, London, pp. 305–315.

9 Mohan, S., and Hahn, E. J., "Design of Squeeze Film Damper Supports for Rigid Rotors," ASME *J. Eng. for Ind.*, 1974, pp. 976–982.

A. B. Palazzolo
Senior Research Engineer,
Southwest Research Institute,
San Antonio, Texas 78284

Bo Ping Wang
Associate Research Professor.

W. D. Pilkey
Professor.
Department of Mechanical
and Aerospace Engineering,
University of Virginia,
Charlottesville, Va.

Component Synthesis of Multicase, Rotating Machinery Trains by the Generalized Receptance Approach

A method is presented for computing the eigenvalues of multicase, coupled, rotating machinery trains. The method is based on a synthesis technique which utilizes generalized receptance formulas, previously derived by the authors. These formulas improve the accuracy of the computed receptance when only an incomplete set of modes is available. A nonsynchronous, gyroscopic, two-rotor example is examined to illustrate the synthesis procedure.

Introduction

Various approaches have been proposed for computing the eigensolutions of a large structure by utilizing data from its isolated components. The ultimate goals of these schemes are to produce accurate eigensolutions of the assembled structure, to minimize computer time, and to minimize computer storage requirements.

A popular synthesis technique is component mode synthesis, which was first derived by Hurtz [1]. Here the eigenvectors of the total system are restricted to a vector subspace, W, similar to a Rayleigh-Ritz-type analysis [2]. This reduces the dimensions of the resulting matrix eigenvalue problem.

For accurate results the subsapce (W) must be spanned by a "physically sensible" set of basis vectors. The basis vectors include modes from the isolated components, modeled with artificial boundary conditions, and so-called "constraint" modes. Constraint modes are derived by applying the Guyan reduction technique to degrees of freedom which lie on an interface shared by neighboring components. This is discussed further in Imbert's [3] excellent review of modal synthesis methods.

The main body of the synthesis literature has been devoted primarily to undamped or proportionately damped structures, described by symmetric property matrices (**M**, **K**, **C**). The eigensolution synthesis algorithm presented in this paper is applicable to the general case when **M**, **K**, and **C** are unsymmetric. It is particularly useful in solving rotating structure problems, or in cases where isolated dampers are present. An example of the former case is examined in detail in this paper.

Critical rotating machinery trains used in petrochemical or power utility industries are usually modeled, at some design stage, for rotor bearing stability. A simple diagram of a mutlicase train is shown in Fig. 1. The entire train, its supporting structure, and its piping network form an assemblage of rotating and stationary structure components. The

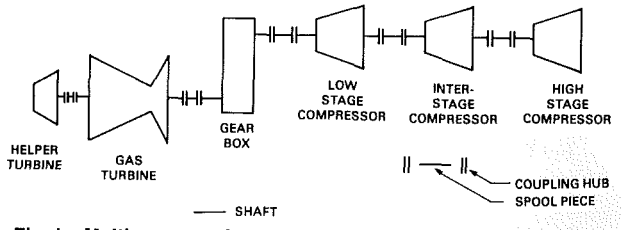

Fig. 1 Multicase, rotating machinery train for syngas compression

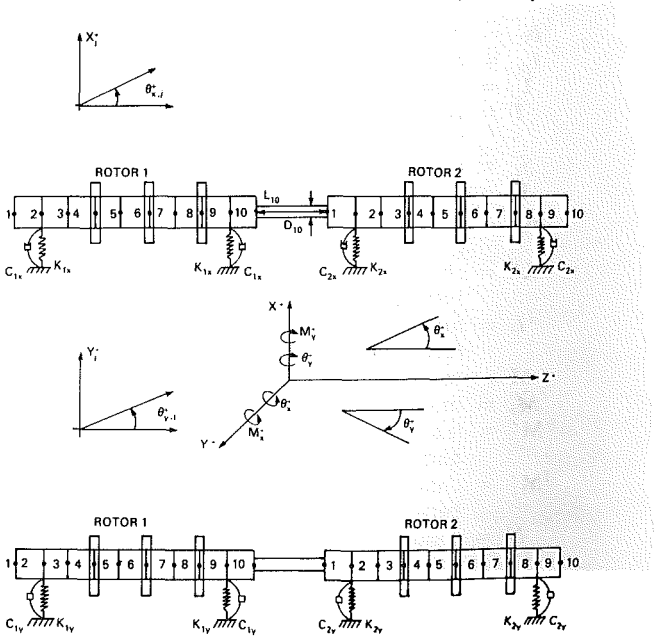

Fig. 2 Two rotor machinery train for illustrating the synthesis procedure

Contributed by the Gas Turbine Division of THE AMERICAN SOCIETY OF MECHANICAL ENGINEERS for presentation at the 28th International Gas Turbine Conference and Exhibit, Phoenix, Arizona, March 27-31, 1983. Manuscript recieved at ASME Headquarters December 29. 1982. Paper No. 83-GT-229.

eigensolutions of each individual rotor are usually obtained by assuming approximate boundary conditions at the ends, isolating the rotor from the remainder of the train. These assumptions may not be valid, especially when two rotors are joined by solid couplings.

This paper presents a mathematical algorithm for computing the eigenvalue of coupled, multicase, rotating machinery trains via a synthesis technique. The components are considered here to be the uncoupled rotors. The proposed solution procedure utilizes generalized receptance matrix formulas previously derived by the authors [4]. The approximate assumption of proportional damping is not imposed, permitting the rotor model to include disk gyroscopics, bearing and seal stiffness and damping, and centrifugal impeller aerodynamic stiffness. The accuracy and efficiency of the algorithm are tested by analyzing the idealized two rotor system showing in Fig. 2.

Theory—Component Synthesis Formulations

The governing equations of motion for rotor-bearing stability analysis state that the column vectors of the second-degree square lambda matrix

$$\alpha^2\mathbf{M}+\alpha\,\mathbf{C}+\mathbf{K}$$

are linearly dependent. For a system of N *uncoupled* rotors, this conditions may be expressed, using the direct stiffness assembly method [5], as

$$\{\alpha_i^2 \begin{bmatrix} {}^1\mathbf{M} & \mathbf{0} & \dots & \mathbf{0} \\ \mathbf{0} & {}^2\mathbf{M} & \dots & \mathbf{0} \\ \cdot & \cdot & \cdot & \cdot \\ \cdot & \cdot & \cdot & \cdot \\ \cdot & \cdot & \cdot & \cdot \\ \mathbf{0} & \mathbf{0} & \dots & {}^n\mathbf{M} \end{bmatrix} + \alpha_i \begin{bmatrix} {}^1\mathbf{C} & \mathbf{0} & \dots & \mathbf{0} \\ \mathbf{0} & {}^2\mathbf{C} & \dots & \mathbf{0} \\ \cdot & \cdot & \cdot & \cdot \\ \cdot & \cdot & \cdot & \cdot \\ \cdot & \cdot & \cdot & \cdot \\ \mathbf{0} & \mathbf{0} & \dots & {}^n\mathbf{C} \end{bmatrix}$$

$$+ \begin{bmatrix} {}^1\mathbf{K} & \mathbf{0} & \dots & \mathbf{0} \\ \mathbf{0} & {}^2\mathbf{K} & \dots & \mathbf{0} \\ \cdot & \cdot & \cdot & \cdot \\ \cdot & \cdot & \cdot & \cdot \\ \cdot & \cdot & \cdot & \cdot \\ 0 & 0 & \dots & {}^n\mathbf{K} \end{bmatrix} \begin{bmatrix} {}^1\mathbf{\Lambda}_i \\ {}^2\mathbf{\Lambda}_i \\ \cdot \\ \cdot \\ \cdot \\ {}^n\mathbf{\Lambda}_i \end{bmatrix} = \mathbf{0}, \quad N\times 1$$

or

$$\{\alpha_i^2\ \mathbf{M}+\alpha_i\ \mathbf{C}+\mathbf{K}\}\ \mathbf{\Lambda}_i=\mathbf{0} \tag{1}$$

The ${}^j\mathbf{M}$, ${}^j\mathbf{C}$, and ${}^j\mathbf{K}$ are the property matrices for the jth uncoupled rotor, and have dimensions ${}^j\mathbf{N}\times{}^j\mathbf{N}$, i.e.,

$$\mathbf{N}=\sum_{j=1}^{n}{}^j\mathbf{N} \tag{2}$$

Nomenclature

$\mathbf{C}$ = damping matrix
${}^{ij}\mathbf{C}'$ = damping "coupling" matric between components i and j
${}^i\mathbf{C}'$ = change in the damping matrix of component i, between the uncoupled and coupled states
$\mathbf{F}(\lambda)$ = receptance matrix defined by equation (8)
${}^iF_{kj}(\mu)$ = kj element of the receptance matrix for uncoupled rotor i
$g(\lambda)$ = a form of a characteristic equation for the coupled system
I_{Ti} = transverse moment of inertia of station i
I_{pi} = polar moment of inertia of station i
$\mathbf{I}_j$ = $j\times j$ unit matrix
$\mathbf{J}$ = vector containing the non-null row (or column) numbers of $\mathbf{S}(\lambda)$
j_i = ith member of $\mathbf{J}$
$\mathbf{K}$ = stiffness matrix
${}^{ij}\mathbf{K}'$ = stiffness "coupling" matrix between components i and j
${}^i\mathbf{K}'$ = change in the stiffness matrix of component i between the uncoupled and coupled states
${}^iL$ = number of eigenvectors used in computing the receptances for uncoupled rotor i
$\mathbf{M}$ = mass matrix
$\bar{M}_i$ = lumped mass at station i
${}^{ij}\mathbf{M}'$ = mass "coupling" matrix between components i and j
${}^i\mathbf{M}'$ = change in the mass matrix of component i, between the uncoupled and coupled stated
N = total number of independent degrees of freedom in the entire system
n = total number of uncoupled rotors
p = total number of non-null rows (or columns) in matrix $\mathbf{S}(\lambda)$
$\mathbf{S}(\lambda)$ = matrix which defines the difference between the coupled and uncoupled states
α_i = ith eigenvalue of the uncoupled system
${}^j\alpha_i$ = ith eigenvalues of the uncoupled rotor i
$\mathbf{\Lambda}_i$ = ith eigenvector of the uncoupled system
${}^j\mathbf{\Lambda}_i$ = ith eigenvector of the jth uncoupled rotor
ω = rotor pin rate in rad/s
λ = eigenvalue of he coupled system
ψ = eigenvector of the coupled system
${}^j\psi$ = portion of the coupled system eigenvector corresponding to rotor j
ξ = vector of generalized coordinates
δ_m = mth left eigenvector

Symbols

$-$ = matrix, vector designator
T = right superscript implies matrix or vector transpose
Δ = change in a quantity

$$(\mathbf{A})\ \begin{matrix} l_1 & l_1 & \dots & l_s \\ m_1 & m_2 & \dots & m_r \end{matrix} = \begin{bmatrix} A_{l_1M_1} & A_{l_1M_2} & \dots & A_{l_1M_r} \\ A_{l_2M_1} & A_{l_2M_2} & \dots & A_{l_2M_r} \\ \cdot & \cdot & \cdot & \cdot \\ \cdot & \cdot & \cdot & \cdot \\ \cdot & \cdot & \cdot & \cdot \\ A_{l_sM_1} & A_{l_sM_2} & \dots & A_{l_wM_r} \end{bmatrix}$$

$= s\times r$ submatric of $\mathbf{A}$

where A_{ij} is the ij element of matrix $\mathbf{A}$

$$(\mathbf{X})\ (l_1\ l_2\ \dots\ l_s)=(X_{l_1}\ X_{l_2}\ \dots\ X_{l_s})^T$$

where X_i is the ith element of vector X

$\hat{-}$ = condensed matrix-vector quantity
i = imaginary unit, $\sqrt{1}$
${}^i(\ )$ = left superscript i designates structural component i
$(\mathbf{A})_k$ = kth column of $\mathbf{A}$
$(\mathbf{A})_k$ = kth jrow of $\mathbf{A}$
${}^jX_k$ = X translatory displacement at station K of rotor j

The mass matrix ${}^{j}\mathbf{M}$ is block diagonal with a typical block for the local ith station

$$\begin{bmatrix} {}^{1}\bar{M}_i & 0 & 0 & 0 \\ 0 & {}^{j}\bar{I}_{Ti} & 0 & 0 \\ 0 & 0 & {}^{j}\bar{M}_i & 0 \\ 0 & 0 & 0 & {}^{j}\bar{I}_{Ti} \end{bmatrix} \tag{3}$$

The variation rate matrix ${}^{j}\mathbf{C}$ is composed of viscous damping terms from bearing and seal force linearization and gyroscopic (Coriolis) contributions from disk spinnutation coupling [6]. The gyroscopic contribution is block diagonal with a typical block for the local ith station given by

$$\begin{bmatrix} 0 & 0 & 0 & 0 \\ 0 & 0 & 0 & \omega({}^{j}I_{pi}) \\ 0 & 0 & 0 & 0 \\ 0 & -\omega({}^{j}I_{pi}) & 0 & 0 \end{bmatrix} \tag{4}$$

The ${}^{j}\mathbf{K}$ matrix contain stiffness terms for linearization of the hydrodyamic and aerodynamic forces at the bearings, seals, and impellers, plus beam element structural stiffness for the shaft. The displacements of the jth rotor are arranged in the ${}^{j}N+1$ vector

$${}^{j}\psi^{T}=[{}^{j}X_1\ {}^{j}\theta_{x,1}\ {}^{j}Y_1\ {}^{j}\theta_{y,1}\vdots{}^{j}X_2\ {}^{j}\theta_{x,2}\ {}^{j}Y_2\ {}^{j}\theta_{y,2}\vdots\ldots] \tag{5}$$

Equations of motion for the uncoupled rotor systems are given by

$$\{\lambda^2(\mathbf{M}+\Delta\mathbf{M})+\lambda(\mathbf{C}+\Delta\mathbf{C})+(\mathbf{K}+\Delta\mathbf{K})\}\psi=\mathbf{0},\quad (n\times 1)(6a)$$

where $\Delta\mathbf{M}$, $\Delta\mathbf{C}$, $\Delta\mathbf{K}$, and ψ are partitioned matrices defined by

$$\Delta\mathbf{M}=\left[\begin{array}{c|c|c|c} {}^{1}\mathbf{M}' & {}^{12}\mathbf{M}' & \ldots & {}^{1n}\mathbf{M}' \\ \hline {}^{21}\mathbf{M}' & {}^{2}\mathbf{M}' & \ldots & {}^{2n}\mathbf{M}' \\ \hline \cdot & \cdot & \cdot & \cdot \\ \cdot & \cdot & \cdot & \cdot \\ \cdot & \cdot & \cdot & \cdot \\ \hline {}^{n1}\mathbf{M}' & {}^{n2}\mathbf{M}' & \ldots & {}^{n}\mathbf{M}' \end{array}\right]$$

$$\Delta\mathbf{C}=\left[\begin{array}{c|c|c|c} {}^{1}\mathbf{C}' & {}^{12}\mathbf{C}' & \ldots & {}^{1n}\mathbf{C}' \\ \hline {}^{21}\mathbf{C}' & {}^{2}\mathbf{C}' & \ldots & {}^{2n}\mathbf{C}' \\ \hline \cdot & \cdot & \cdot & \cdot \\ \cdot & \cdot & \cdot & \cdot \\ \cdot & \cdot & \cdot & \cdot \\ \hline {}^{n1}\mathbf{C}' & {}^{n2}\mathbf{C}' & \ldots & {}^{n}\mathbf{C}' \end{array}\right]$$

$$\Delta\mathbf{K}=\left[\begin{array}{c|c|c|c} {}^{1}\mathbf{K}' & {}^{12}\mathbf{K}' & \ldots & {}^{1n}\mathbf{K}' \\ \hline {}^{21}\mathbf{K}' & {}^{2}\mathbf{K}' & \ldots & {}^{2n}\mathbf{K}' \\ \hline \cdot & \cdot & \cdot & \cdot \\ \cdot & \cdot & \cdot & \cdot \\ \cdot & \cdot & \cdot & \cdot \\ \hline {}^{n1}\mathbf{K}' & {}^{n2}\mathbf{K}' & \ldots & {}^{n}\mathbf{K}' \end{array}\right]$$

$$\psi^{T}=[{}^{1}\psi^{T}\vdots{}^{2}\psi^{T}\vdots\ldots\vdots{}^{n}\psi^{T}] \tag{6b}$$

The matrices ${}^{ij}\mathbf{M}'$, ${}^{ij}\mathbf{K}'$, and ${}^{ij}\mathbf{C}'$ contain terms which represent the physical connection between rotors i and j. The matrices ${}^{i}\mathbf{M}'$, ${}^{i}\mathbf{C}'$, and ${}^{i}\mathbf{K}'$, contain terms for connecting rotor i to the remaining $(n-1)$ rotors, and terms which represent the internal changes experienced by the ith rotor due to the coupling.

Define the following $N\times N$ matrix corresponding to the uncoupled system

$$\mathbf{F}(\lambda)=\begin{bmatrix} {}^{1}\mathbf{F}(\lambda) & \mathbf{0} & \ldots & \mathbf{0} \\ \mathbf{0} & {}^{2}\mathbf{F}(\lambda) & \ldots & \mathbf{0} \\ \cdot & \cdot & \cdot & \cdot \\ \cdot & \cdot & \cdot & \cdot \\ \cdot & \cdot & \cdot & \cdot \\ \mathbf{0} & \mathbf{0} & \ldots & {}^{n}\mathbf{F}(\lambda) \end{bmatrix} \tag{7}$$

where

$${}^{i}\mathbf{F}(\lambda)=(\lambda^{2i}\mathbf{M}+\lambda^{i}\mathbf{C}+{}^{i}\mathbf{K})^{-1} \tag{8}$$

The matrix ${}^{i}\mathbf{F}(\lambda)$ is referred to as a generalized receptance matrix since

$${}^{i}\mathbf{F}(i\omega)=(-\omega^{2\,i}\mathbf{M}+i\omega^{i}\mathbf{C}+{}^{i}\mathbf{K}^{-1}) \tag{9}$$

is the familiar expression for a receptance matrix [7]. Substitute the change of basis

$$\psi=\mathbf{F}\,\xi \qquad (N\times 1) \tag{10}$$

into equation (6a)

$$\{\mathbf{I}_N+\mathbf{S}(\lambda)\mathbf{F}(\lambda)\}\xi=\mathbf{0}\quad (N\times 1) \tag{11}$$

where

$$\mathbf{S}(\lambda)=\lambda^2\Delta\mathbf{M}+\lambda\,\Delta\mathbf{C}+\Delta\mathbf{K} \qquad (N\times N) \tag{12}$$

is referred to as an effective coupling-modification matrix.

Each rotor model often contains a large number of "lumped mass' stations, yet only two stations are typically involved when two rotors are coupled. These stations usually represent the two coupling hubs which are bolted to the spool piece shaft. For this reason, the coupling matrix $\mathbf{S}(\lambda)$ is highly sparse. This sparsity is quantified by entering the numbers of non-null rows (or columns) of $\mathbf{S}(\lambda)$ into the integer set $\mathbf{J}$, i.e.,

$$J=(j_1 j_2\ldots j_p) \tag{13}$$

By equation (11) it can be shown easily that

$$\xi_k\equiv 0,\quad k\in\mathbf{J} \tag{14}$$

Substitute (14) into (11)

$${}^{\xi}j_r+\tilde{\mathbf{S}}_r(\lambda)\bar{\mathbf{F}}(\lambda)\tilde{\xi} \tag{15}$$

$r=1,2,\ldots p$ where

$$\bar{\mathbf{F}}(\lambda)=(\mathbf{F})\begin{pmatrix} 1 & 2 & \ldots & N \\ j_1 & j_2 & \ldots & j_p \end{pmatrix},N\times p \tag{16}$$

$$\xi=(\xi)(j_1 j_2\ldots j_p),\quad p\times 1 \tag{17}$$

$$\tilde{\mathbf{S}}_r(\lambda)=(\mathbf{S})_{1\ 2\ \ldots\ j_r\ \ldots\ N},\ 1\times N \tag{18}$$

Only elements $j_1, j_2\ldots j_p$ of $\mathbf{S}_r(\lambda)$ can be nonzero. Utilizing this information in equation (15) yields

$$(\mathbf{I}_p+\hat{\mathbf{S}}(\lambda)\hat{\mathbf{F}}(\lambda))\hat{\xi}=\mathbf{0},p\times 1 \tag{19}$$

where

$$\hat{\mathbf{S}}(\lambda)=(\mathbf{S})\begin{pmatrix} j_1 & j_2\ldots j_p \\ j_1 & j_2\ldots j_p \end{pmatrix},p\times p \tag{20}$$

$$\hat{\mathbf{F}}(\lambda)=(\mathbf{F})\begin{pmatrix} j_1 & j_2\ldots j_p \\ j_1 & j_2\ldots j_p \end{pmatrix},p\times p \tag{21}$$

Table 1 Geometric properties of the uncoupled rotors

Shafts

$^1\omega = {}^2\omega = 1200.0$ rad/sec $= 11,459.0$ rpm
$^1D = {}^2D = 5.0$ inches $= 12.7$ centimeters
$^1L = {}^2L = 108.0$ inches $= 2.743$ meters
$^1E = {}^2E = 30.0 \times 10^6$ lb/in^2 $= 2.068 \times 10^{11}$ N/m^2
$\rho = 0.000732$ 1 bm/in^3 $= 20.273$ kg/m^3

Discs

$^1L_D = {}^2L_D = 0.5$ in $= 1.27$ centimeters
$^1D_D = {}^2D_D = 22.0$ in $= 55.9$ centimeters

Bearings

$K_{1x} = 50,000.0$ lb/in $= 8.757 \times 10^6$ N/m
$K_{1y} = 75,000.0$ lb/in $= 13.135 \times 10^6$ N/m
$C_{1x} = 50.0$ lb sec/in $= 8757.0$ N.sec./m
$C_{1y} = 100.0$ lb sec/in $= 17513.0$ N.sec./m
$K_{2x} = 1.15 \times 10^6$ lb/in $= 201.4 \times 10^6$ N/m
$K_{2y} = 0.65 \times 10^6$ lb/in $= 113.8 \times 10^6$ N/m
$C_{2x} = 1000.0$ lb sec/in $= 0.175 \times 10^6$ N.sec/m
$C_{2y} = 500.0$ lb sec/in $= 0.0876 \times 10^6$ N.sec/m

Combining equations (10) and (14) gives

$$\psi = \bar{\mathbf{F}}(\lambda)\hat{\xi}, \quad N \times 1 \tag{22}$$

The necessary condition for the existence of coupled system modes is seen from equations (19) and (22) to be

$$g(\lambda) = \text{determinant}\,(\mathbf{I}_p + \hat{\mathbf{S}}(\lambda)\hat{\mathbf{F}}(\lambda)) = 0 \tag{23}$$

The zeroes of equation (23) are the eigenvalues

$$\lambda_q = S_q + i\,\omega_q \tag{24}$$

of the coupled system of rotors. The decay rate of oscillation in the qth mode is determined from S_q and the frequency of this mode is ω_q.

Theory—Receptance Computation

The zeroes of equation (23) are obtained by utilizing an iterative approach such as the Muller or Newton-Raphson Methods [8]. The $p \times p$ matrix $\mathbf{S}(\lambda)$ is easily evaluated for each guess of λ, by employing equations (12) and (20). The evaluation of $\mathbf{F}(\lambda)$ for each guess of λ is much more difficult, as can be seen by inspection of equations (7), (8), and (21). Each term in $\mathbf{F}(\lambda)$ is an element of a matrix which is the inverse of a second-degree, square lambda matrix, whose dimensions are normally very large. Inverting each matrix in equation (8) to obtain $\mathbf{F}(\lambda)$ for each guess of λ would be computationally inefficient. A better approach is to evalute each element of $\mathbf{F}(\lambda)$ without inverting the entire matrix which represents its corresponding rotor. This goal can be achieved by utilizing the spectral representation [9]

$$^iF_{kj}(\lambda) = \sum_{m=1}^{2(^iL)} \frac{^i\Lambda_{km}\,{}^i\delta_{jm}}{^ia_{2m}(\lambda - {}^i\alpha_m)} \tag{25}$$

where

$$(^i\alpha_m^2\,{}^i\mathbf{M} + {}^i\alpha_m\,{}^i\mathbf{C} + {}^i\mathbf{K})\,{}^i\Lambda_m = \mathbf{0} \tag{26}$$

$$(^i\alpha_m^2\,{}^i\mathbf{M}^T + {}^i\alpha_m\,{}^i\mathbf{C}^T + {}^i\mathbf{K}^T)\,{}^i\delta_m = \mathbf{0} \tag{27}$$

$$^ia_{2m} = {}^i\delta_m{}^T(2\,{}^i\alpha_m\,{}^i\mathbf{M} + {}^i\mathbf{C})\,{}^i\Lambda_m = \mathbf{0} \tag{28}$$

The expression in equation (25) becomes exact when the number of modes (^iL) calculated for the ith uncoupled rotor is equal to the total number of degrees of freedom (^iN), including all masters and slaves, contained in the ith rotor model. The ratio of the calculated to total number of modes for any uncoupled rotor will typically lie in the range

$$0.05 < {}^iL/{}^iN < 0.3 \tag{29}$$

The question naturally arises, if there is a way to improve the accuracy of equation (25) when the number of available modes (^iL) for each uncoupled rotor is fixed. The derivation of a series of formulas to accomplish that goal is included in [4]. These formulas are utilized for eigensolution reanalysis in [10]. The accuracy of each generalized receptance matrix element is shown to be dependent on the number of property matrix terms included in its expansion. This is quantified by introducing a "higher mode factor," given the variable identifier R, where R is some nonnegative integer. The $R = 0$ formula is equation (25), and the $R = 1$, 2, and 3 expressions are listed below

$R = 1$

$$^iF_{kj}(\lambda) = (^iK^{-1})_{kj} + \lambda \sum_{m=1}^{2(^iL)} \frac{^i\Lambda_{km}\,{}^i\delta_{jm}}{^ia_{2m}\,{}^i\alpha_m(\lambda - {}^i\alpha_m)}$$

$R = 2$

$$^iF_{kj}(\lambda) = (^i\mathbf{K}^{-1})_{kj} - \lambda(^i\mathbf{K}^{-1})_{\bar{k}}\,{}^i\mathbf{C}(\{i\tilde{\mathbf{K}}^{-1})_j + \lambda^2 \sum_{m=1}^{2(^iL)} \frac{^i\Lambda_{km}\,{}^i\delta_{jm}}{^ia_{2m}\,{}^i\alpha_m(\lambda - {}^i\alpha_m)} \tag{31}$$

$R = 3$

$$^iF_{kj}(\lambda) = (^i\mathbf{K}^{-1})_{kj} - \lambda(^i\mathbf{K}^{-1})_{\bar{k}}\,{}^i\mathbf{C}(\{i\tilde{\mathbf{K}}^{-1})_j - \lambda^2\{(^i\mathbf{K}^{-1})_{\bar{k}}\,{}^i\mathbf{M}(^i\mathbf{K}^{-1})_j - (^i\mathbf{K}^{-1})_{\bar{k}}\,{}^i\mathbf{C}\,{}^i\mathbf{K}^{-1}\,{}^i\mathbf{C}(^i\mathbf{K}^{-1})_j\} + \lambda^3 \sum_{m=1}^{2(^iL)} \frac{^i\Lambda_{km}\,{}^i\delta_{jm}}{^ia_{2m}\,{}^i\alpha_m{}^3(\lambda - {}^i\alpha_m)} \tag{32}$$

These formulas may at first appear to involve excessive numerical operations. This is misleading, though, since:

(*i*) Only a small submatrix ($\mathbf{F}(\lambda)$, equation (21) of the system's generalized receptance matrix ($\mathbf{F}(\lambda)$, equation (7) is computed at each iteration in solving equation (23).

(*ii*) Evaluation of equation (32) does not require calculating $^iN \times {}^iN$ matrix products, since only a scalar results.

(*iii*) Expressions such as $(^i\mathbf{K}^{-1})_{\bar{k}}\,{}^i\mathbf{C}\,{}^i\mathbf{K}^{-1}\,{}^i\mathbf{C}\quad(^i\mathbf{K}^{-1})_j$ are calculated and stored only once, and then used for all subsequent iterations.

A Numerical Example

The purpose of this example is to illustrate the algorithm outlined in the preceeding sections. Figure 2 shows a simplified drawing which represents a solidly coupled, two-case machinery train. The various properties of both rotors are contained in Table 1. The coupling spool piece, which connects the two rotors, has the following length and diameter

$$L_{10} = 24.0 \text{ in.} = 50.96 \text{ cm}$$
$$D_{10} = 3.0 \text{ in.} = 7.62 \text{ cm}$$

Computations were performed on a CDC CYBER 172 digital computer. To establish an accuracy and efficiency comparison benchmark, the coupled system's eigenvalues were determined with the eigenvalue solver EISPACK [11].

For this example,

$$n = 2, {}^1N_1 = {}^2N_2 = 40, N = 80$$

The equations of motion for the coupled rotor system are derived from equations (6) as

Table 2 Accuracy comparison of the coupled rotor's 14 lowest eigenvalues (error realpart, error imaginary part)

i	EISPACK λ_i	R = 0 % Error
1	(-18.03, 217.55)	(.22173, .03066)
2	(-11.59, 191.38)	(.00312, .03637)
3	(-6.734, 292.09)	(2.75945, .23745)
4	(-8.982, 314.63)	(1.97105, .21967)
5	(-43.11, 362.03)	(-.16263, .34179)
6	(-94.298, 412.30)	(.08395, .21921)
7	(-49.53, 614.02)	(1.20658, 1.09287)
8	(-70.82, 635.08)	(.04760, .80694)
9	(-10.00, 1001.2)	(.41424, .07366)
10	(-10.00, 1071.0)	(.-1598, .06661)
11	(-191.5, 1088.5)	(.41844, -1.0373)
12	(-84.83, 1196.9)	(6.99039, .80504)
13	(-442.43, 1100.1)	(.03118, -.03559)
14	(-240.95, 1388.9)	(1.5584, 3.17748)

i	R = 1 % Error	R = 3 % Error
1	(.00079, .00002)	(.00004, .00001)
2	(.00154, -.00000)	(-.00012, -.00002)
3	(.04835, .00052)	(-.00127, -.00040)
4	(.01236, -.00041)	(.00156, .00037)
5	(.00530, .00120)	(.00019, -.00007)
6	(.00189, .00033)	(-.00016, .00007)
7	(-.04442, .01352)	(.00257, -.00016)
8	(.04036, -.00129)	(-.00230, .00028)
9	(.10547, .00091)	(.0020-7, -.00034)
10	(.12377, .00093)	(.00328, .00033)
11	(-.04345, -0.02547)	(-.00259, -.00081)
12	(.11005, .02925)	(.00351, .00166)
13	(-.00101, -.00080)	(-.00005, -.00004)
14	(.30162, .07716)	(.01200, .00301)

$$\{\lambda^2\left(\begin{bmatrix}{}^1\mathbf{M} & \mathbf{0}\\ \mathbf{0} & {}^2\mathbf{M}\end{bmatrix}+\begin{bmatrix}{}^1\mathbf{M}' & {}^{12}\mathbf{M}'\\ {}^{21}\mathbf{M}' & {}^2\mathbf{M}'\end{bmatrix}\right)+\lambda\left(\begin{bmatrix}{}^1\mathbf{C} & \mathbf{0}\\ \mathbf{0} & {}^2\mathbf{C}\end{bmatrix}+\begin{bmatrix}{}^1\mathbf{C}' & {}^{12}\mathbf{C}'\\ {}^{21}\mathbf{C}' & {}^2\mathbf{C}'\end{bmatrix}\right)+\left(\begin{bmatrix}{}^1\mathbf{K}' & \mathbf{0}\\ \mathbf{0} & {}^2K\end{bmatrix}+\begin{bmatrix}{}^1\mathbf{K}' & {}^{12}\mathbf{K}'\\ {}^{21}\mathbf{K}' & {}^2\mathbf{K}'\end{bmatrix}\right)\}\begin{bmatrix}{}^1\psi\\ {}^2\psi\end{bmatrix}=\mathbf{0} \tag{33}$$

The generalized receptance matrix is obtained from equations (7) and (8)

$$\mathbf{F}(\lambda)=\begin{bmatrix}{}^1\mathbf{F}(\lambda) & \mathbf{0}\\ \mathbf{0} & {}^2\mathbf{F}(\lambda)\end{bmatrix} \tag{34}$$

where

$$\begin{aligned}{}^1\mathbf{F}(\lambda)&=(\lambda^2\,{}^1\mathbf{M}+\lambda\,{}^1\mathbf{C}+{}^1\mathbf{K})^{-1}\\ {}^2\mathbf{F}(\lambda)&=(\lambda^2\,{}^2\mathbf{M}+\lambda\,{}^2\mathbf{C}+{}^2\mathbf{K})^{-1}\end{aligned} \tag{35}$$

The primed matrices in equation (33) contain only terms which result from the connection between the two rotors in Fig. 2. These matrices are highly sparse, as indicated below where *only* the non-null partitions are listed

	37	38	39	40	41	42	43	44	
37	$\bar{m}_{10}/2$								${}^1X_{10}$
38		$\bar{I}_{T,10}/2$							${}^1\theta_{x,10}$
39			$\bar{m}_{10}/2$						${}^1Y_{10}$
40				$\bar{I}_{T,10}/2$					${}^1\theta_{y,10}$
41					$\bar{m}_{10}/2$				${}^2X_1$
42						$\bar{I}_{T,10}/2$			${}^2\theta_{x,1}$
43							$\bar{m}_{10}/2$		${}^2Y_1$
44								$\bar{I}_{T,10}/2$	${}^2\theta_{y,1}$

$\Delta\underline{C}$

	37	38	39	40	41	42	43	44	
37	0	0	0	0					${}^1X_{10}$
38	0	0	0	□					${}^1\theta_{x,10}$
39	0	0	0	0					${}^1Y_{10}$
40	0	-□	0	0					${}^1\theta_{y,10}$
41					0	0	0	0	${}^2X_1$
42					0	0	0	□	${}^2\theta_{x,1}$
43					0	0	0	0	${}^2Y_1$
44					0	-□	0	0	${}^2\theta_{y,1}$

$$\square=\omega\frac{\bar{I}_{p,10}}{2} \tag{36}$$

$\frac{E_{10}I_{10}}{L_{10}^3}$

	37	38	39	40	41	42	43	44	
37	12	$6L_{10}$	0	0	-12	$6L_{10}$	0	0	${}^1X_{10}$
38	$6L_{10}$	$4L_{10}^2$	0	0	$-6L_{10}$	$2L_{10}^2$	0	0	${}^1\theta_{x,10}$
39	0	0	12	$6L_{10}$	0	0	-12	$6L_{10}$	${}^1Y_{10}$
40	0	0	$6L_{10}$	$4L_{10}^2$	0	0	$-6L_{10}$	$2L_{10}^2$	${}^1\theta_{y,10}$
41	-12	$-6L_{10}$	0	0	12	$-6L_{10}$	0	0	${}^2X_1$
42	$6L_{10}$	$2L_{10}^2$	0	0	$-6L_{10}$	$4L_{10}^2$	0	0	${}^2\theta_{x,1}$
43	0	0	-12	$-6L_{10}$	0	0	12	$-6L_{10}$	${}^2Y_1$
44	0	0	$6L_{10}$	$2L_{10}^2$	0	0	$-6L_{10}$	$4L_{10}^2$	${}^2\theta_{y,1}$

where

$$\bar{I}_{T,10}=\bar{M}_{10}(D_{10}^2/16+L_{10}^2/12)$$

$$\bar{M}_{10}=\pi D_{10}^2L_{10}\rho/(4g)\quad \bar{I}_{p,10}=\bar{M}_{10}D_{10}^2/8 \tag{37}$$

Since the only non-null partitions of $\Delta\mathbf{M}$, $\Delta\mathbf{C}$, and $\Delta\mathbf{K}$ are shown in equations (36), the sparsity integer set of equation (13) becomes

$$\begin{aligned}\mathbf{J}&=(j_1\ j_2\ j_3\ j_4\ j_5\ j_6\ j_7\ j_8)^T\\ &=(3738\ 39\ 40\ 41\ 42\ 43\ 44)^T\end{aligned} \tag{38}$$

with p equal to eight. The condensed effective coupling matrix, $\mathbf{S}(\lambda)$, as defined by equations (12) and (20), becomes

$$\hat{\mathbf{S}}(\lambda)=\lambda^2(\Delta\mathbf{M})\begin{pmatrix}37 & 38 & 39 & 40 & 41 & 42 & 43 & 44\\ 37 & 38 & 39 & 40 & 41 & 42 & 43 & 44\end{pmatrix} \tag{39}$$

$$+\lambda(\Delta\mathbf{C})\begin{pmatrix}37 & 38 & 39 & 40 & 41 & 42 & 43 & 44\\ 37 & 38 & 39 & 40 & 41 & 42 & 43 & 44\end{pmatrix}$$

Table 3 Efficiency comparison between the EISPACK and generalized receptance approach

	EISPACK (all eigenvalues) computed)	Generalized receptance approach (lowest 14 eigenvalues computed)		
		$R-0$	$R=1$	$R=3$
	cp s	cp s	cp s	cp s
Disjoint substructures 1 and 2[a]		67.90	69.59	68.40
Coupled system	152.4	26.40	27.30	31.45
Total central processor time	152.4	94.30	96.89	99.85

[a] Includes computation time for obtaining the eigensolution and property matrix terms in equations 26–30

$$+(\Delta\mathbf{K}) \quad \begin{pmatrix} 37 & 38 & 39 & 40 & 41 & 42 & 43 & 44 \\ 37 & 38 & 39 & 40 & 41 & 42 & 43 & 44 \end{pmatrix}$$

The condensed generalized receptance matrix as defined by equations (21) and (39) is given by

$$\hat{F}(\lambda) = (\mathbf{F}) \quad \begin{pmatrix} 37 & 38 & 39 & 40 & 41 & 42 & 43 & 44 \\ 37 & 38 & 39 & 40 & 41 & 42 & 43 & 44 \end{pmatrix} \tag{40}$$

Combine equations (34) and (40)

$$\hat{\mathbf{F}} = \left[\begin{array}{cccc|cccc} {}'F_{37,37} & {}'F_{37,38} & {}'F_{37,39} & {}'F_{37,40} & & & & \\ {}'F_{38,37} & {}'F_{38,38} & {}'F_{38,39} & {}'F_{38,40} & & & & \\ {}'F_{39,37} & {}'F_{39,38} & {}'F_{39,39} & {}'F_{39,40} & & & \mathbf{0} & \\ {}'F_{40,37} & {}'F_{40,38} & {}'F_{40,39} & {}'F_{40,40} & & & & \\ \hline & & & & {}^2F_{11} & {}^2F_{12} & {}^2F_{13} & {}^2F_{14} \\ & & \mathbf{0} & & {}^2F_{21} & {}^2F_{22} & {}^2F_{23} & {}^2F_{24} \\ & & & & {}^2F_{31} & {}^2F_{32} & {}^2F_{33} & {}^2F_{34} \\ & & & & {}^2F_{41} & {}^2F_{42} & {}^2F_{43} & {}^2F_{44} \end{array}\right] \tag{41}$$

The elements of this matrix are evaluated, for each value of λ, in the iterative solution of equation (23) by Muller's method [8]. These elements are computed from the $R = 0$, 1, and 3 generalized receptance matrix formulas, given by equations (25), (30), and (32), respectively. Fourteen complex conjugate eigensolution pairs ($^iL = 14$) were utilized. The uncoupled rotor-model solutions were calculated with the generic eigenvalue solver EISPACK.

EISPACK [11] was also utilized in producing "exact" coupled system eigenvalues to provide a benchmark, for efficiency and accuracy comparisons with the receptance algorithm.

Table 2 lists the fourteen [14] lowest *coupled* system eigenvalues arranged according to the magnitude of their impaginary parts. The table compares the accuracy between the receptance based algorithm and the EISPACK results. The maximum error decreases from 7.0 percent, with the $R = 0$ receptance formula (equation (25), to 0.012 percent with the $R = 3$ receptance formula (equation (32)).

These results show that the accuracy of the coupled system's eigenvalues, that are obtained from the iterative solution of equation (23), is substantially increased when the hybrid receptance formulas (equation (30–32)) are employed.

Table 3 compares the computation time for calculating the eigenvalues. The receptance algorithm requires approximately only one-fifth of the computer time for the EISPACK solution. This assumes that the uncoupled rotor eigensolutions are available from prior computation. The additional cost for utilizing the hybrid receptance formulas (equations 30 and 32), instead of the pure spectral representation (equation 25) is seen to be relatively insignificant.

Discussion and Conclusions

A systematic procedure has been presented for computing the eigenvalues of a coupled, rotating machinery train. The eigenvalues are zeroes of a nonlinear algebraic equations, containing elements of the receptance matrices for the uncoupled rotors. The elements are computed from spectral-property matrix receptance formulas, previously derived by the authors [4]. A numerical example was presented which demonstrates the efficiency and accuracy of the procedure.

It is tacitly assumed that no uncoupled rotor has repeated eigenvalues and that no uncoupled system eigenvalue remains invariant during the synthesis. Due to the lack of ideal symmetry characteristics both of these conditions are usually satisfied in actual rotating machinery trains.

References

1 Hurty, H. C., "Dynamic Analysis of Structural Systems Using Component Modes," *AIAA Journal*, Vol. 3, No. 4, Apr. 1965, pp. 678–685.

2 Bathe, K. J., and Wilson, E. L., *Numerical Methods in Finite Element Analysis*, 1st ed., Prentice-Hall, New Jersey, 1976.

3 Imbert, J. F., "A Survey of Current Capability for Dynamic Analysis of Complex Structures," *Finite Element Methods in the Commercial Environment*, ch. 20, edited by J. Robinson, Robinson and Associates, 1978.

4 Palazzolo, A. B., Wang, B. P., and Pilkey, W. D., "A Receptance Formula for General Second-Degree Square Lamba Matrices," *Inter. Jour. for Numerical Methods in Engineering*, Vol. 18, 1982, pp. 829–843.

5 Martin, H. C., *Introduction to Matrix Methods of Structural Analysis*, 1st ed., McGraw Hill, New York, 1966.

6 Frazer, R. A., Duncan, W. J., and Collar, A. R., *Elementary Matrices*, 1st ed., MacMillan, New York, 1947, pp. 277–279.

7 Bishop, R. E. D., *The Mechanics of Vibration*, 1st ed., Cambridge at the University Press., 1960.

8 Hamming, R. W., *Introduction to Applied Numerical Analysis*, 1st ed., McGraw Hill, New York, 1971.

9 Lancaster, P., *Lamdba Matrices and Vibrating Systems*, 1st ed., Pergamon Press, Toronto, 1966.

10 Palazzolo, A. B., Wang, B. P., and Pilkey, W. D., "Eigensolution Reanalysis of Rotor Dynamnic Systems by the Generalized Receptance Method," ASME 82-GT-262, presented at 1982 ASME Gas Turbine Conference, London, England.

11 Forsythe, G. E., Malcolm, M. A., and Moler, C. B., *Computer Methods for Mathematical Computations*, 1st ed., Prentice Hall, 1977.

J. Mowill
Corporate Vice President,
Technology.

S. Strom
Manager,
Flowpath Development.

Kongsberg Våpenfabrikk, Norway

An Advanced Radial-Component Industrial Turbine Engine

The first engine of a new family of high performance, industrial radial turbines is presented. The new single-shaft, 1500-kW site rated KG3 is built upon extensive experience from the field proven KG2 of the same nominal power. The KG3 is being developed both as a simple cycle and recuperated engine providing specific fuel consumptions in the range of 0.29–0.19 kg/kW-hr (0.47–0.32 lbs/hp-hr). This engine makes use of a high specific speed, high pressure ratio centrifugal compressor combined with a very high tip speed uncooled radial turbine to obtain optimized aerodynamic matching. Several novel design features are described.

Background

The design philosophy of the first engine in a new series of radial gas turbines engines, the KG3, is similar in design concept to the first Kongsberg engine, the KG2 (Fig. 1). The KG2 uses a single stage centrifugal compressor and a radial inflow turbine in a single shaft rotor assembly.

The emphasis at Kongsberg has always been on simplicity and ruggedness. After more than 5 million operating hrs in marine and industrial applications, the radial inflow turbine has left no doubt as to its merits in demanding operating conditions.

Applications for the current Kongsberg engines, the 1600-kW KG2 and the 3000-kW KG5, include electrical power packages for merchant ships, fire control water pumps, cogeneration, stand-by, and mobile power plants. More than seven hundred units have been delivered over a 10-year period.

Kongsberg's gas turbine components and new engine technologies are being developed by their new corporate organization designated Radial Turbomachinery Research (RTR). The Corporation's Gas Turbine Division, as well as external organizations and firms, constitute RTR's customers and co-developers.

In 1978, Kongsberg was confronted with the problem how to achieve a post-1990 energy competitive engine design without compromising the basic design that had made the KG2 successful.

Furthermore, it was required that not only should the new engine be fuel efficient, it should also be low enough in first cost in order to replace the current KG2 in its existing market areas where efficiency is not of primary importance. Like the KG2 and KG5, the new engine would be designed for a major overhaul period of a minimum of 25,000 hrs.

Based on the new centrifugal compressor technology developed from the 6.5:1 pressure ratio KG5 compressor and on improved structural and aerodynamic properties of an advanced radial inflow turbine, several new engine designs were initiated by RTR during 1980.

The development of a high peripheral speed radial inflow turbine was pursued as a priority effort to achieve good thermal efficiency without the use of cooling. A 780 m/s (2550 ft/s) test model is shown in Fig. 2. One of the key elements in this new design is the use of the GATORIZING[R] process to forge the KG3 turbine rotor. Pratt & Whitney's Government Products Division, under contract from Kongsberg has demonstrated the forging of a subscale KG3

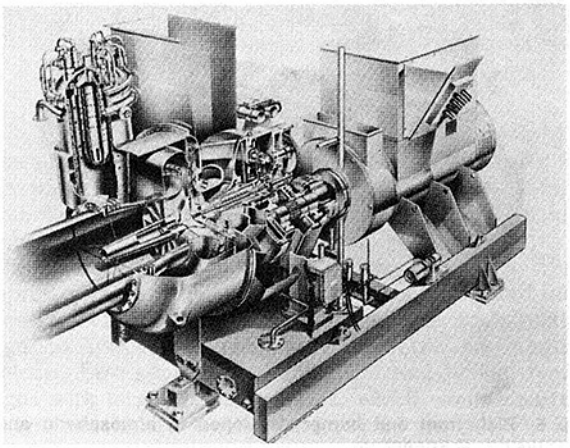

Fig. 1 Kongsberg KG2 1500-KW generator set

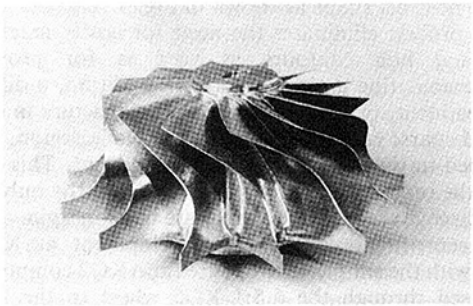

Fig. 2 Radial turbine test wheel showing Kongsberg's deeply scalloped configuration

Contributed by the Gas Turbine Division of THE AMERICAN SOCIETY OF MECHANICAL ENGINEERS for presentation at the 28th International Gas Turbine Conference and Exhibit, Phoenix, Arizona, March 27–31, 1983. Manuscript received at ASME Headquarters January 6, 1983. Paper No. 83-GT-221.

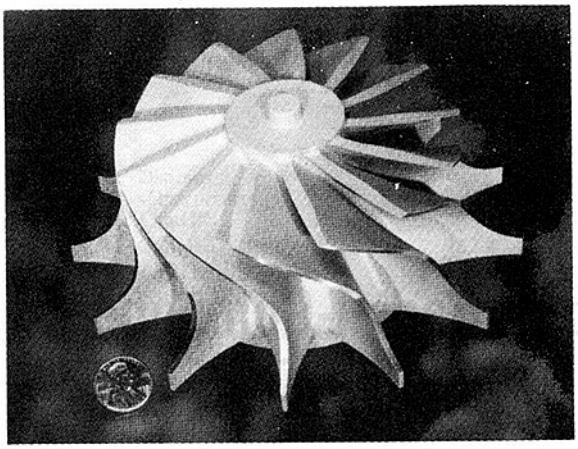

Fig. 3 One-third scale turbine rotor isothermally forged (Gatorized^{R}) to near net shape (KFAC 78935)

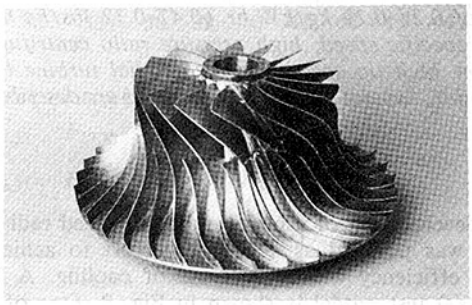

Fig. 4 Advanced 9:1 Pressure ratio centrifugal compressor for the KG3 engine

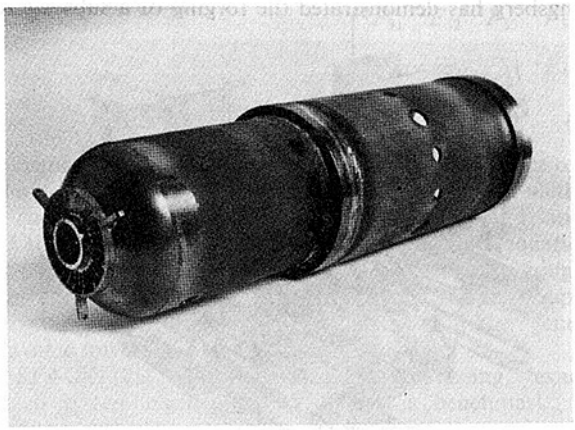

Fig. 5 Rich front end burner developed in atmospheric and full pressure rigs at Kongsberg

rotor to near net shape as shown in Fig. 3. The rear net shape forging process eliminates the need for costly machining of blade and hub contours as well as for providing a homogeneous fine grain material. In addition, a differential heat treatment, producing a fine grain structure in the rotor hub and coarse equiaxed grains in the blade region, has been developed in the subscale turbine component. This gives the blades the required high creep strength and the hub the high tensile strength required for adequate burst margin.

The centrifugal compressor development at Kongsberg started with the simple 4:1 pressure ratio KG2 compressor and progressed through the 6.5:1 KG5 wheel to the latest 9:1 design for the KB3 shown in Fig. 4. This wheel was designed for a total to static adiabatic efficiency of 82 percent, with an

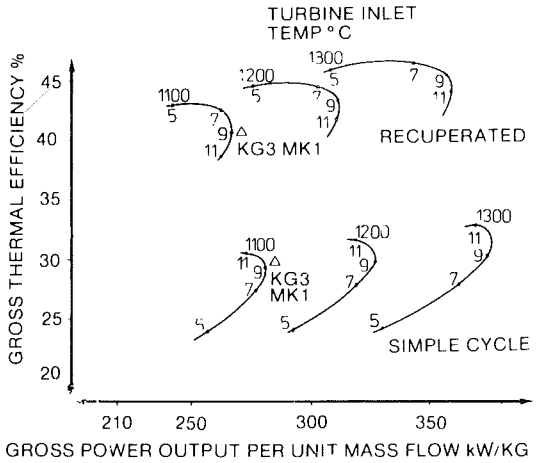

Fig. 6 Design point selection chart for the KG3 engine

exit Mach number of 0.1. This performance is 1-2 percent above the current state-of-the-art.

A new series of low wall-temperature, low pattern factor combustors have been in development since 1980. Figure 5 shows a "Rich Front End" development can. The combustors are being developed both in atmospheric and full pressure rigs.

KG3 Design and Development

The KG3 is developed with two main market considerations in mind:

1 To gradually replace the KG2 in the 1500-kW market range. Here, a simple rugged design combined with low initial cost are essential features.

2 To enter the continuous on site power generation market both with and without recuperator by means of a much improved fuel consumption.

Studies of several engine concepts revealed that with Kongsberg's field experience, design capabilities, and aerothermo know-how the design criteria could be best met with an engine based on a single stage centrifugal compressor and single stage radial turbine. Figure 6 shows the cycle performance of this type of gas turbine.

The optimum pressure ratio/temperature match is different for a single stage radial gas turbine than for an all axial or axicentrifugal combination, due to a different efficiency variation with pressure ratio. The turbine inlet temperature is mainly limited by creep considerations in the uncooled radial turbine rotor. The choice of pressure ratio is limited by the maximum work that can be efficiency extracted over a single stage radial turbine and by the obtainable pressure ratio over a single stage centrifugal compressor. Figure 6 shows that for the simple cycle, a pressure ratio above 11:1 would be desired for maximum efficiency, while the maximum specific power is obtained at about 9:1. The recuperated cycle requires a pressure ratio of about 6:1 for maximum thermal efficiency at the design point; however, when part load efficiency and recuperator size are considered, a higher pressure ratio is preferred. This also benefits the simple cycle version. The selected design point with major engine data is given in Table 1, showing the span between the first production version KG3 - 11 and anticipated growth version KG3 - 13. Part load fuel consumption curves are shown in Fig. 7 (a og b).

To achieve this performance level of the components, careful matching of the specific speed of the centrifugal compressor and the radial turbine is required. Optimum specific speed for centrifugal compressors is about 100 and for radial turbines 80, as shown [6] and [11]. For a single shaft engine, the ratio of specific speeds between the turbine and the

Table 1 KG3 performance data

	KG3-11	KG3-13
Simple cycle		
Power output, gross KW	1654	2310
Thermal efficiency, gross % (lb/hphr)	29.0 (.470)	30.6 (.447)
Recuperated cycle		
Power output, gross KW	1580	2200
Thermal efficiency, gross % lb	37.1 (0.369)	43.2 (0.317)
Recuperator effectiveness	0.88	0.88
General data		
Compressor pressure ratio	9.0	9.0
Combustor system pressure loss %	0.05	0.05
Compressor mass flow, kg/s (lbs/s)	6.44 (14.2)	6.44 (14.2)
Rotor speed (rpm)	35,115	35,115
Compressor efficiency (adiabatic)	0.82	0.83
Turbine tip speed, m/s (ft/s)	779 (2550)	779 (2550)
Turbine efficiency (total diffuser exit static)	0.88	0.88
Combustor exit temperature, °C	1108	1315
Average rotor tip metal temperature, °C	835	972
Turbine exhaust temperature, °C	581	718

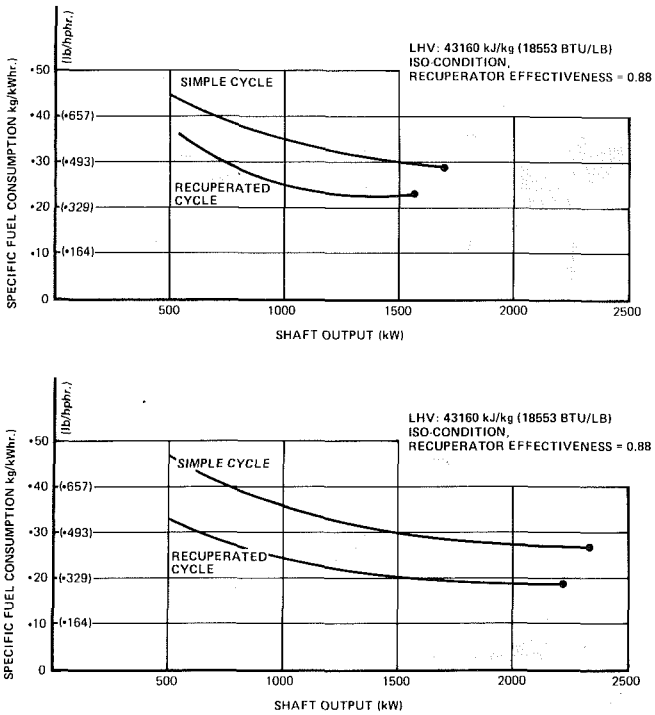

Fig. 7 Predicted part-load performance: (*a*) KG3-11; (*b*) KG3-13

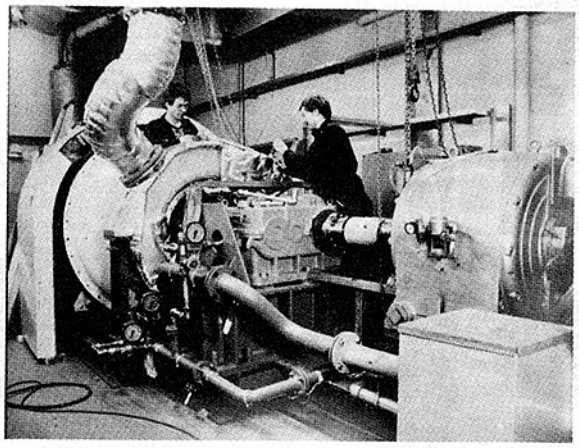

Fig. 8 Compressor component development rig

compressor is dependent on firing temperature, burner pressure loss and cycle pressure ratio.

The selected pressure ratio for the obtainable firing temperature allows both compressor and the turbine to operate near optimum specific speed.

Compressor Design. The KG3 centrifugal compressor with its high pressure ratio and optimum specific speed leads to relative inlet Mach numbers above 1.4. Great care was required in designing the transonic inducer portion. The compressor has 15 full blades and 15 splitter blades with a large sweepback designed to maintain low aerodynamic loading throughout the blade channel both in the hub-shroud plane and in the blade-to-blade plane. The 4:1 area ratio Composite Channel Diffuser with a cylindrical tailpipe and a radial plate diffuser will bring the flow down to 0.1 Mach number at the diffuser exit (see Fig. 13).

The design has been confirmed in the compressor rig shown in Fig. 8. The rig accommodates a full engine size compressor run at subatmospheric inlet conditions to reduce the rig power requirements. The KG3 compressor map is shown in Fig. 9 (these data have been adjusted to atmospheric Reynolds number conditions).

The stress analysis of such high tip-speed centrifugal compressors and turbines require the use of advanced three-dimensional finite element analysis methods for structural design to minimize stress nonuniformity and vibration problems. Less sophisticated analytical tools would require designs with larger safety margins, which would constrain aerodynamic shake and cause reduced performance. The KG3 will be operating at constant speed, thus avoiding the cyclic loading experienced in variable speed multishaft engines.

Radial Turbine Design. Radial turbines have been used extensively for small engine applications and turbochargers, rather for its low cost than for good performance. In these applications no serious attempts have been made to either optimize the radial turbine aerodynamically or to understand the complex flow field. The radial turbine is most advantageously used in high work situations, where high tip-speed results in a large temperature difference between the gas total temperature and the blade relative stagnation temperature (i.e., metal temperature). This difference will constitute a delta of 250°C for the KG3. Additionally, the maximum blade metal temperature appears when the blade stresses are zero, such that the critical life blade-section will be at even lower metal temperatures due to the rapid fall in total

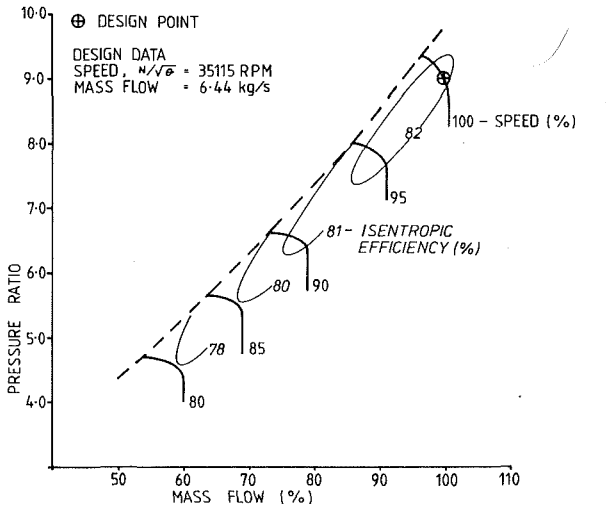

Fig. 9 KG3 compressor map

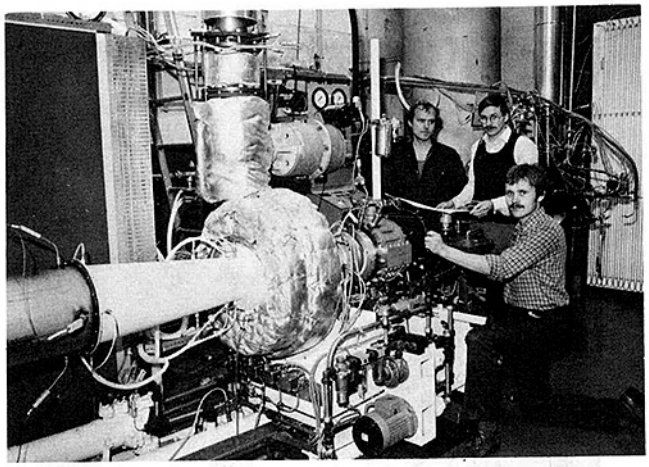

Fig. 10 Turbine component development rig currently in operation at Kongsberg

temperature with decreasing radius. This allows a much higher cycle temperature for an uncooled radial rotor than would be possible with an uncooled axial turbine or more conventional radial turbines with moderate tip speeds [2]. Figure 17 shows diagrammatically temperature and stress distribution.

The resulting temperature capability of an uncooled radial turbine has therefore become as high as that of moderately cooled axial turbines or similar to cooled radial turbines being proposed. The advantage of the cooled stages, however, is more than lost due to performance penalties both in aerodynamic efficiency and overall cycle losses.

The radial turbines in the Kongsberg KG2 and KG5 operate with total-total isentropic efficiencies above 90 percent with minimal aerodynamic development. Based on this experience and on extensive rig development the KG3 efficiency level was established as shown in Table 1. The turbine development rig is shown in Fig. 10. Figure 11 gives a comparison of radial turbine efficiency of Kongsberg's design and other state-of-the-art turbine designs versus pressure ratio.

Engine Description. All the engine components have been demonstrated prior to the first KG3 light up, either by using established technology from KG2 or KG5, such as was the case with the well proven Kongsberg "slow-melt" tilting pad bearings, or by component development, such as was done for the centrifugal compressor and the radial turbine. Figure 12 shows the KG3 engine, the Simple Cycle version, Fig. 12(*a*), and the Recuperated Version, Fig. 12(*b*).

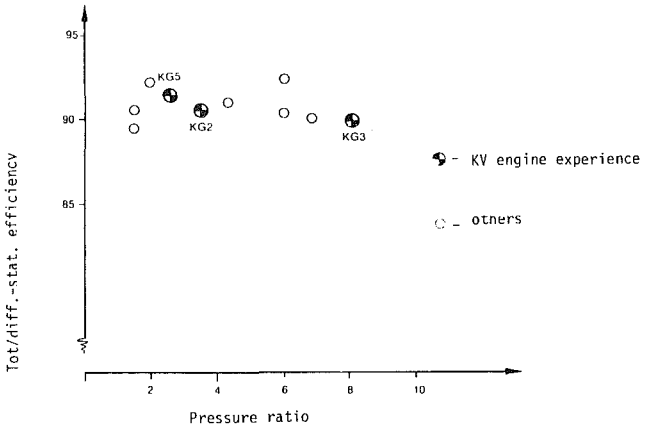

Fig. 11 Kongsberg engine turbine efficiencies compared to other state-of-the-art turbine component efficiencies

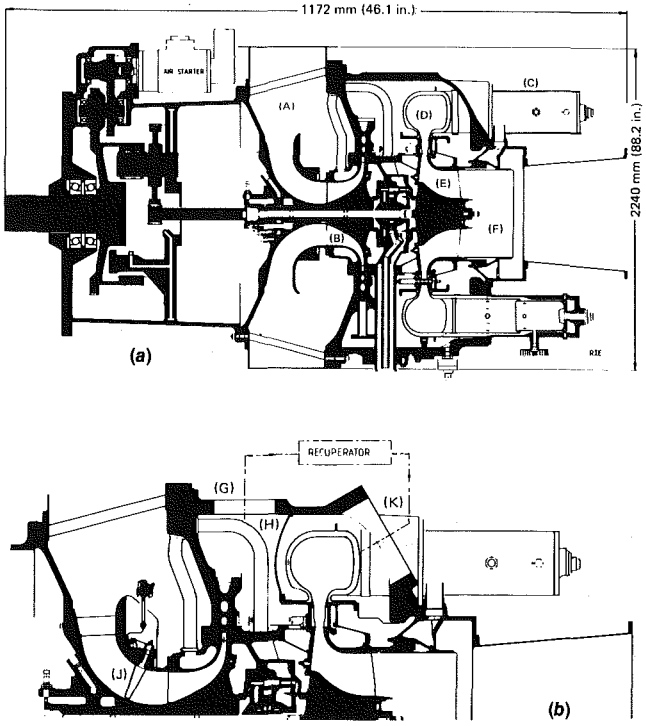

Fig. 12 KG3 engine cross sections: (*a*) simple cycle version; (*b*) recuperated version

Air enters the structural inlet (A) and into the 9:1 pressure ratio single stage centrifugal compressor (B). Seal air for the midrotor bearing is bled from the compressor at an intermediate station. The compressed air leaves the Composite Channel Diffuser, shown in Fig. 12, and passes to six reverse flow axially mounted combustors (C) via a double wall "doughnut" manifold (D) designed to give sufficient cooling to maintain life with a minimum of pressure loss. The combustion gases pass through air cooled nozzles and into the radial inflow turbine (E).

The KG3 design has a number of patented features, among which is the vortex controlled short diffuser (F), which uses compressor backside leakage air as the driving medium for an exhaust diffuser ejector. A star-compound type reduction gear takes the 35,000 rpm of the rotor down to standard 50/60 cycle generator speeds.

The mechanical differences between the simple cycle and the recuperative versions of the KG3 area are shown in Fig. 12(B).

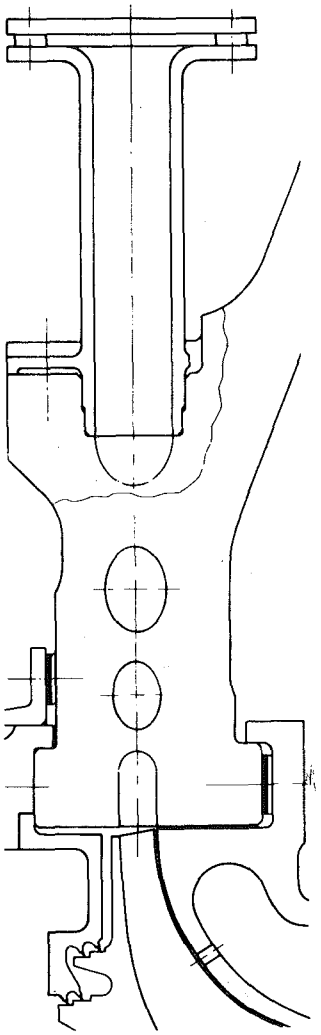

Fig. 13 Composite channel diffuser for the KG3 compressor consisting of a channel diffuser followed by a circular pipe and a radial plate diffuser with a total area ratio of 10:1

- Port for pressure vessel discharge (G)
- Flow barrier (H)
- Variable inlet guide vanes (J) Fig. (14)
- Recuperator return ports (K)

The recuperated pressure vessel with the discharge/return ports is made from a heat resistant cast alloy compared to nodular cast iron in the simple cycle version. Figure 15 shows a considerable size reduction of the KG3 pressure vessel compared to the KG2.

The KG3 engine design incorporates passive clearance control to help ensure best efficiencies under normal operating conditions. This is achieved through mechanical design and the selection of materials with matched thermal expansion coefficients. Whereas the KG3 constitutes a complete industrial design optimized for land and sea applications, the design incorporates certain technologies which have been proven in aircraft design. The cooled turbine nozzle is an example of this (Fig. 16). The radial nozzle design is different from their axial aircraft counterparts but the cooling technology is very similar.

Program Status

At the time of submitting this paper, the following had been accomplished in the KG3 program:

- Design

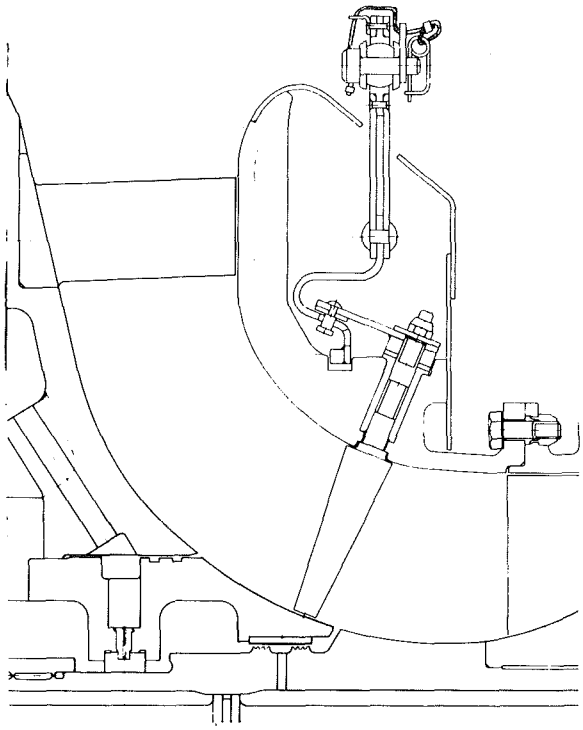

Fig. 14 Variable inlet guide vane system consisting of a fixed and a variable set of vanes. The system imparts up to 30 deg preswirl to the compressor inlet air with low pressure loss, and thus improves part load performance for the recuperated version.

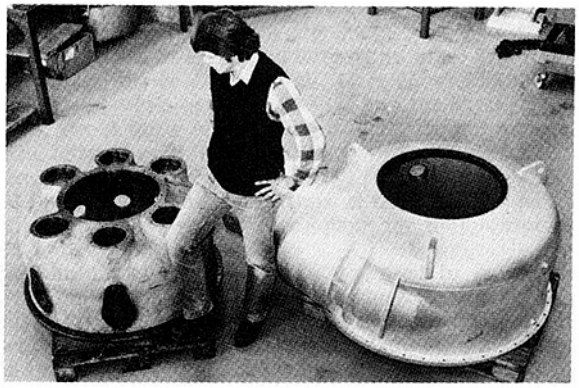

Fig. 15 Comparison of KG3 (left) and KG2 pressure vessels

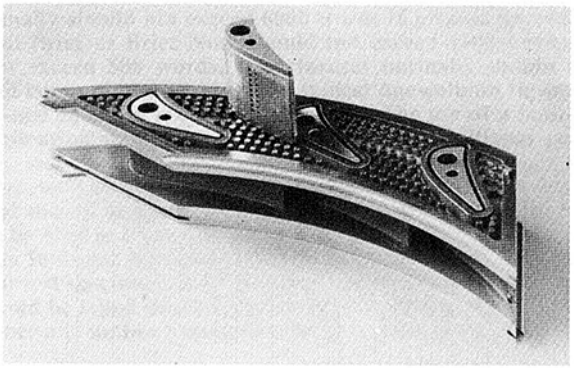

Fig. 16 Cooled radial turbine nozzle segment for the KG3

- Component testing for the KG3-11 version
- All materials and components on order
- Prototype assembly well under way
- Preproduction series partially initiated by the Gas Turbine Division
- Engine development testing underway

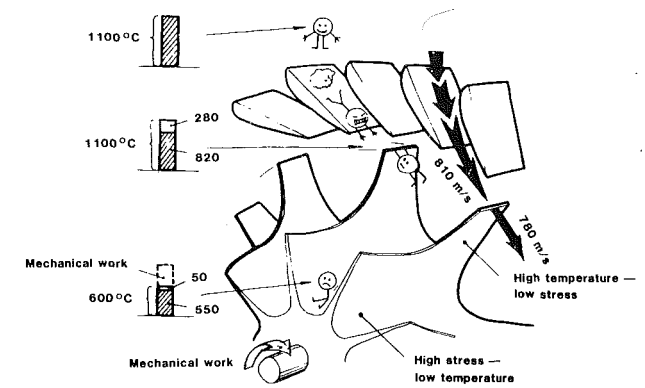

Fig. 17 Symbolic description of temperature/stress distribution in radial turbines

The first production series of the KG3-11 will have a single alloy rotor, modified AF2-IDA. Later engine models are planned with dual alloy turbine rotors.

The first production engines will be available within 1984. Field qualification arrangements are currently being made with major potential users of the engine.

Following the start of the KG3 program, additional engine designs have been initiated, both as single shaft or two shaft designs. Recuperated, as well as Simple Cycle engines, are contemplated which will utilize the radial technology under development at Kongsberg.

Conclusions

It has been possible to combine the simple rugged design of the current KG2 with new aerodynamic and materials technology to develop the KG3 with a significant improvement in performance compared with the best current turbines. It is expected that the KG3 will see numerous applications in the on-site electric power generation field, with or without exhaust heat recovery.

Generic designs utilizing the basic KG3 technology can be expected to result in a family of radial engines in the years to come.

References

1 Wood, H. J., "Current Technology of Radial Inflow Turbines for Compressible Fluids," ASME JOURNAL OF ENGINEERING FOR POWER, Vol. 85, Jan. 1963, pp. 72–83.

2 Mowill, R. J., "Justification for an All-Radial 1600 HP Gas Turbine Engine," ASME Paper No. 70-GT-33.

3 Arnold, D. G., and Balje, O. E., "High Temperature Potential of Uncooled Radial Turbines," ASME JOURNAL OF ENGINEERING FOR POWER, Vol. 100, Apr. 1978, pp. 294–302.

4 Wood, H. J., "Performance Potential of Single Stage Gas Turbine Engines," *Proceedings of 8th Intersociety Energy Conversion Engineering Conference*, Philadelphia, Aug. 1973, pp. 286–297.

5 Billman, L. S., and Walker, B. H., "Status of Forged Turbine Rotor Technology," ASME Paper No. 80-GT-100.

6 Rodgers, C., "Specific Speed and Efficiency of Centrifugal Impellers," Performance Prediction of Centrifugal Pumps and Compressors, *25th Annual International Gas Turbine Conference*, New Orleans, La., Mar. 1980, pp. 191–200.